Cosmic-ray Hydrodynamics: Theory, Numerics, Applications

Timon Thomas

Kumulative Dissertation
zur Erlangung des akademischen Grades
”doctor rerum naturalium”
(Dr. rer. nat.)
in der Wissenschaftsdisziplin Theoretische Astrophysik

eingereicht an der
Mathematisch-Naturwissenschaftlichen Fakultät
Institut für Physik und Astronomie
der Universität Potsdam
und
Leibniz-Institut für Astrophysik Potsdam (AIP)

Ort und Tag der Disputation:
Potsdam am 21.09.2022

Betreuer: Prof. Dr. Christoph Pfrommer
Mentor: Dr. Udo Ziegler
Gutachter: Prof. Dr. Christoph Pfrommer
Prof. Dr. James Stone
Prof. Dr. Greg Bryan

Published online on the
Publication Server of the University of Potsdam:
https://doi.org/10.25932/publishup-56384
https://nbn-resolving.org/urn:nbn:de:kobv:517-opus4-563843

Abstract

Cosmic rays (CRs) are a ubiquitous and an important component of astrophysical environments such as the interstellar medium (ISM) and intracluster medium (ICM). Their plasma physical interactions with electromagnetic fields strongly influence their transport properties. Effective models which incorporate the microphysics of CR transport are needed to study the effects of CRs on their surrounding macrophysical media. Developing such models is challenging because of the conceptional, length-scale, and time-scale separation between the microscales of plasma physics and the macroscales of the environment. Hydrodynamical theories of CR transport achieve this by capturing the evolution of CR population in terms of statistical moments. In the well-established one-moment hydrodynamical model for CR transport, the dynamics of the entire CR population are described by a single statistical quantity such as the commonly used CR energy density.

In this work, I develop a new hydrodynamical two-moment theory for CR transport that expands the well-established hydrodynamical model by including the CR energy flux as a second independent hydrodynamical quantity. I detail how this model accounts for the interaction between CRs and gyroresonant Alfvén waves. The small-scale magnetic fields associated with these Alfvén waves scatter CRs which fundamentally alters CR transport along large-scale magnetic field lines. This leads to the effects of CR streaming and diffusion which are both captured within the presented hydrodynamical theory. I use an Eddington-like approximation to close the hydrodynamical equations and investigate the accuracy of this closure-relation by comparing it to high-order approximations of CR transport.

In addition, I develop a finite-volume scheme for the new hydrodynamical model and adapt it to the moving-mesh code Arepo. This scheme is applied using a simulation of a CR-driven galactic wind. I investigate how CRs launch the wind and perform a statistical analysis of CR transport properties inside the simulated circumgalactic medium (CGM).

I show that the new hydrodynamical model can be used to explain the morphological appearance of a particular type of radio filamentary structures found inside the central molecular zone (CMZ). I argue that these harp-like features are synchrotron-radiating CRs which are injected into braided magnetic field lines by a point-like source such as a stellar wind of a massive star or a pulsar.

Lastly, I present the finite-volume code Blinc that uses adaptive mesh refinement (AMR) techniques to perform simulations of radiation and magnetohydrodynamics (MHD). The mesh of Blinc is block-structured and represented in computer memory using a graph-based approach. I describe the implementation of the mesh graph and how a diffusion process is employed to achieve load balancing in parallel computing environments. Various test problems are used to verify the accuracy and robustness of the employed numerical algorithms.

Zusammenfassung

Kosmische Strahlung (CR) ist ein allgegenwärtiger und wichtiger Bestandteil astrophysikalischer Umgebungen wie des interstellaren Mediums (ISM) und des Intracluster-Mediums (ICM). Ihre plasmaphysikalischen Wechselwirkungen mit elektromagnetischen Feldern beeinflussen ihre Transporteigenschaften weitgehend. Effektive Modelle, die die Mikrophysik des CR-Transports einbeziehen, sind erforderlich, um die Auswirkungen von CRs auf die sie umgebenden makrophysikalischen Medien zu untersuchen. Die Entwicklung solcher Modelle ist eine Herausforderung, aufgrund der konzeptionellen, Längenskalen-, und Zeitskalen- Unterschiede zwischen den Mikroskalen der Plasmaphysik und den Makroskalen der Umgebung. Hydrodynamische Theorien des CR-Transports erreichen dies, indem sie die Entwicklung der CR-Population in Form von statistischen Momenten erfassen. Im etablierten hydrodynamischen Ein-Moment Modell für den CR-Transport wird die Dynamik der gesamten CR-Population durch eine einzige statistische Größe wie der häufig verwendeten CR-Energiedichte beschrieben.

In dieser Arbeit entwickle ich eine neue hydrodynamische Zwei-Momenten Theorie für den CR-Transport, die das etablierte hydrodynamische Modell um den CR-Energiefluss als zweite unabhängige hydrodynamische Größe erweitert. Ich erläutere, wie dieses Modell die Wechselwirkung zwischen CRs und gyroresonanten Alfvén-Wellen berücksichtigt. Die mit diesen Alfvén-Wellen verbundenen kleinskaligen Magnetfelder streuen die CRs, was den CR-Transport entlang großskaligen Magnetfeldlinien grundlegend verändert. Dies führt zu den CR-Strömungs- und Diffusioneffekten, welche beide in der neu vorgestellten hydrodynamischen Theorie erfasst werden. Ich verwende eine adaptierte Eddington Näherung, um die hydrodynamischen Gleichungen zu schließen und untersuche die Genauigkeit dieser Näherung, indem ich sie mit Näherungen höherer Ordnung für den CR-Transport vergleiche.

Darüber hinaus entwickle ich ein Finite-Volumen-Schema für das neue hydrodynamische Modell und passe es an den mitbewegten Gitter Code Arepo an. Dieses Schema wird mittels einer Simulation eines CR-getriebenen galaktischen Windes angewendet. Ich untersuche, wie CRs den Wind beschleunigen und führe eine statistische Analyse der CR-Transporteigenschaften innerhalb des simulierten zirkumgalaktischen Mediums (CGM) durch.

Ich zeige, dass das neue hydrodynamische Modell das morphologische Erscheinungsbild eines neu-entdeckten bestimmten Typs von filamentartigen Radiostrukturen, welcher in der zentralen molekularen Zone (CMZ) auffindbar ist, erklären kann. Ich schlage vor, dass es sich bei diesen harfenartigen Strukturen um synchrotronstrahlende CRs handelt, die zuvor von einer punktförmigen Quelle wie dem stellaren Wind eines massereichen Sterns oder eines Pulsars in geflochtene Magnetfeldlinien injiziert wurden.

Schließlich stelle ich den Finite-Volumen-Code Blinc vor, der adaptive Gitterverfeinerungstechniken (AMR) verwendet, um Simulationen von Strahlungs- und Magnetohydrodynamik

(MHD) durchzuführen. Das Gitter von BLINC ist blockstrukturiert und wird im Computerspeicher mittels eines graphbasierten Ansatzes dargestellt. Ich beschreibe die Implementierung des Gittergraphen und wie ein Diffusionsprozess eingesetzt wird, um einen Lastausgleich in parallelen Rechenumgebungen zu erreichen. Verschiedene Testprobleme werden verwendet, um die Genauigkeit und Robustheit der verwendeten numerischen Algorithmen zu überprüfen.

Contents

1 Motivation and Structure of this Thesis

Cosmic rays (CRs) are charged particles with trans- to fully relativistic energies. They predominantly interact with their surroundings through electromagnetic fields because their number densities are low which renders collisional interactions subdominant. The Lorentz force is also the driving process that accelerates galactic CRs at supernovae (SNe) shocks through the diffusive shock acceleration mechanism (Axford et al., 1977; Bell, 1978; Blandford and Eichler, 1987). Once they left their acceleration side, CRs travel along magnetic field lines into the ISM where they provide an additional and important pressure component (Boulares and Cox, 1990; Everett et al., 2008; Naab and Ostriker, 2017). CRs with MeV energies influence the ionization balance and, consequently, the chemistry of molecular clouds (Padovani et al., 2009). The GeV-CR subpopulation provides most of the bulk CR energy density. The forces exerted by these CRs are able to expel gas from star-forming galaxies by driving galactic winds (Ipavich, 1975; Breitschwerdt et al., 1991; Zweibel, 2017). Inside the IGM, CRs redistribute energy released by active galactic nuclei (Loewenstein et al., 1991; Guo and Oh, 2008; Ehlert et al., 2018).

To investigate CR dynamics inside these astrophysical media, understanding the transport of CRs along magnetic field lines is crucial. This transport has different characters depending on the typical scales on which the magnetic field lines fluctuate.

CRs are tied to magnetic field lines if their gyroradii are small compared to the scales of the magnetic field. This relates the trajectories of CRs to the large-scale magnetic field topology. Turbulent structures inside these magnetic fields can effectively scatter the CR population and cause CRs to participate in a super-diffusion process as nearby magnetic fields diverge through turbulent motions (Lazarian and Yan, 2014; Sampson et al., 2022).

On smaller scales, CRs are directly scattered by magnetic fluctuations. There are two competing scenarios for the origin of these fluctuations. First, in the external-confinement picture, large-scale interacting magnetic fields propagate to smaller scales inside the turbulent magnetohydrodynamic (MHD) cascade until CRs can resonantly interact with them (Yan and Lazarian, 2002, 2004). Second, CR can self-confine through the gyroresonant streaming instability (Kulsrud and Pearce, 1969) where CRs excite gyroresonant Alfvén waves in a collective effort through a plasma-physical process and are scattered by these waves later (Zweibel, 2013). Recent studies investigating the consequences of both pictures conclude that neither a single picture in isolation nor a combination of both is sufficiently general to explain all observational

traces of CR propagation (Hopkins et al., 2021d; Kempski and Quataert, 2021).

Without this scattering, CRs travel on purely ballistic trajectories through their surrounding medium. In the presence of scattering, CRs participate in a statistical diffusion process (Shalchi, 2009a; Schlickeiser, 1989). If the scattering has a preferred direction, then the bulk of CRs can start to stream in this direction. This is the case if scattering is provided by either externally- or self-generated gyroresonant Alfvén waves. The motional electric field of these Alfvén waves exerts an additional force on the CRs along the direction of the mean magnetic field. This results in the CR streaming effect where bulk statistical quantities such as CR number or energy density are transported with the local Alfvén speed (Skilling, 1975; Ko, 1992).

Hydrodynamical models can be used to describe these microphysical transport effects. They describe the dynamics of the CR population in terms of a few statistical moments. This captures the essence of small-scale processes and allows for effective CR transport models that can be used to investigate the impact of CRs on large-scale astrophysical environments. First instances of such hydrodynamical models use a single statistical quantity and describe the CR dynamics in a one-moment approximation. The possibility of CR-driven galactic winds and CR-modified shocks can be investigated in this setting using one-dimensional flux-tube approaches (Ipavich, 1975; Drury and Völk, 1981; Breitschwerdt et al., 1991). With the advent of high-performance computers and advanced numerical techniques, the impact of CRs can be analysed in three dimensions and in arbitrary magnetic field topologies (Hanasz et al., 2013; Salem and Bryan, 2014; Pfrommer et al., 2017a; Ruszkowski et al., 2017). In the last few years, the implications of CR-driven galactic winds on the evolution of galaxies experienced a surge of interest. This is accompanied by the development of more sophisticated hydrodynamical CR transport models (Jiang and Oh, 2018; Girichidis et al., 2020; Ogrodnik et al., 2021; Hopkins et al., 2021a).

Numerically integrating the CR diffusion process while adhering to the second law of thermodynamics is possible using special numerical limiter techniques (Sharma and Hammett, 2007). Designing numerical schemes for the CR streaming process is challenging because standard numerical discretizations are subject to numerical instabilities. These instabilities can be averted using effective but unphysical regularization techniques (Sharma et al., 2009). Jiang and Oh (2018) propose to include a second moment in the hydrodynamical theory to describe the evolution of bulk velocity of the CR population. They show that this approach is not plagued a numerical instability.

In this work, we derive a new two-moment approximation for CR transport following the idea of Jiang and Oh (2018), develop numerical schemes to integrate the resulting equations of CR hydrodynamics, analyse the transport and wind-launching processes of CRs inside a galactic wind, and investigate radio filaments inside the CMZ.

We use Heaviside Lorentz units throughout this work, denote $\boldsymbol{ab}$ as the dyadic product of vectors $\boldsymbol{a}$ and $\boldsymbol{b}$, and define $:$ as the double-dot product of two rank-2 tensors.

Thesis outline

In Chapter 2, we provide an introduction to theoretical aspects of CR self-confinement. We review the theory of quasilinear diffusion and rederive the growth rate of the gyroresonant streaming instability. The derivations are conducted with first-principle calculations and start with the interaction between a charged particle and electromagnetic fields as described by Newton-Maxwell's equations.

In Chapter 3, we derive a new hydrodynamical theory for CR transport. This theory is based on a two-moment approximation for CR transport and uses an Eddington-like approximation for the closure of the hydrodynamical equations. We account for the scattering of CRs and gyroresonant Alfvén waves in the self-confinement picture. Special care is taken to derive the scattering terms for this process. The derivation is based on the quasilinear theory and approximations are made to ensure that the resulting scattering terms are covariant. The energy contained in Alfvén waves is described as an additional fluid. The system of CR, Alfvén waves, and thermal particles is coupled through forces exerted by magnetic fields. Energy exchange between the three fluids is mediated by plasma-physical processes.

In Chapter 4, we investigate the closure problem of hydrodynamical theories in the context of our newly developed theory for CRs. We revisit this problem for radiation hydrodynamics and demonstrate the failure of this model for optically-thin media. By comparing the closure for our CR-focused hydrodynamical theory to more sophisticated closures and higher-order approximations, we find that the closure problem for CR hydrodynamics is less severe and even absent in the case of strong scattering.

In Chapter 5, we develop a finite-volume scheme for the new equations of CR hydrodynamics. This scheme is adapted to the moving-mesh code Arepo and uses a path-conservative finite-volume discretization for non-conservative transport terms. A semi-implicit second-order Runge-Kutta scheme with adaptive timestepping is derived to enable an accurate integration of the scattering terms. These schemes are thoroughly tested using a variety of test problems to assess their accuracy and robustness.

In Chapter 6, we use this new numerical scheme to investigate a simulated CR-driven wind launched from disk galaxy that is situated inside a $10^{11}\,M_{\odot}$ halo. We identify the force exerted by the CR-Alfvén wave interaction as the underlying reason for the wind-launching because it dominates over other forces that act on the gas at the wind-launching site inside the disk-halo interface. Furthermore, we perform a statistical analysis of the CR diffusion coefficient and the effective CR transport speeds inside the CGM of the galaxy. This reveals that CR transport inside the CGM cannot be described by steady-state assumptions concerning the effective transport speed of CRs.

In Chapter 7, we introduce a possible formation scenario for a particular type of non-thermal filaments (NTFs) inside the CMZ which were observed in great detail by the MeerKAT radio telescope. They appear as triangular-shaped systems, are composed of parallel strings, and resemble harps. We propose that a point-like source injects CRs into (spatially and/or temporally) intermittent magnetic flux tubes. By comparing the morphology of CR populations in idealized simulations with the observed NTFs, we find that the general structure of the radio harps can be matched by a CR population that is streaming and diffusing inside the magnetic flux tubes.

In Chapter 8, we present Blinc – a new finite volume code for the equations of MHD and radiation hydrodynamics with AMR capabilities based on a block-structured representation of the computational mesh. Mesh connectivity is realised using a graph-based approach. A diffusive load balancer is developed to distribute work on parallel computers. The divergence constrained of the MHD equations is accounted for using constrained transport (CT) or the Powell scheme. We validate the implemented numerical schemes through various test problems. We show that results computed with the Powell scheme are qualitatively comparable to results computed with the CT scheme although divergence errors introduce quantitative differences.

2 Theoretical Background

We use this chapter to discuss some basic aspects of the CR transport theory. Because most CR transport phenomena are collective processes that occur in magnetized media, the analytical tools that we are using are known from plasma and statistical physics. To keep these matters tractable, we will focus on those topics that will be used in the following chapters of this work and abandon the idea to present a general introduction to this subject. In particular, we will review two topics of quasilinear theory: 1) we will derive the Fokker-Planck equation for CR transport and the associated momentum-space diffusion coefficients for the interaction with Alfvén waves that are propagating along the mean magnetic field and 2) we will derive the growth rate of the gyroresonant streaming instability of Alfvén waves, which is triggered by the CRs. The discussion here and in later chapters will show that both phenomena are tightly connected.

The equations of motion of a non-relativistic particle with mass m, charge q, momentum $\boldsymbol{p}$, and velocity $\boldsymbol{v}$ in an electromagnetic field is given by:

$$\frac{\mathrm{d}\boldsymbol{p}}{\mathrm{d}t} = \frac{\mathrm{d}m\boldsymbol{v}}{\mathrm{d}t} = q\left[\boldsymbol{E} + \frac{\boldsymbol{v}\times\boldsymbol{B}}{c}\right], \tag{2.1}$$

where $\boldsymbol{E}$ is the electric field and $\boldsymbol{B}$ is the magnetic field.

It is instructive to solve this equation for a vanishing electric and uniform magnetic field. Written out in Cartesian components, the equations of motion read as:

$$\frac{\mathrm{d}}{\mathrm{d}t}\begin{bmatrix} v_x(t) \\ v_y(t) \\ v_z(t) \end{bmatrix} = \frac{qB}{mc}\begin{bmatrix} +v_y \\ -v_x \\ 0 \end{bmatrix}, \tag{2.2}$$

if we orientate the direction of the magnetic field along the z-axis. This system of differential equations can be readily solved to give:

$$\boldsymbol{v}(t) = \begin{bmatrix} v_x(t) \\ v_y(t) \\ v_z(t) \end{bmatrix} = \begin{bmatrix} v\sqrt{1-\mu^2}\sin(\Omega t+\varphi) \\ v\sqrt{1-\mu^2}\cos(\Omega t+\varphi) \\ v\mu \end{bmatrix}, \tag{2.3}$$

where v is the particle speed, μ is the cosine of the particle's pitch angle, φ its initial phase and, $\Omega = qB/mc$ is the gyrofrequency. The four quantities v, μ, φ, and Ω are constants of motion. The two transverse velocity components are rotating. The particle position can be calculated to:

$$\boldsymbol{x}(t) = \begin{bmatrix} x(t) \\ y(t) \\ z(t) \end{bmatrix} = \begin{bmatrix} -v\sqrt{1-\mu^2}\cos(\Omega t+\varphi) + x_0 \\ +v\sqrt{1-\mu^2}\sin(\Omega t+\varphi) + y_0 \\ v\mu t + z_0 \end{bmatrix}, \tag{2.4}$$

where (x_0, y_0, z_0) is the initial particle position. The particle performs a gryomotion in the plane that is perpendicular to the magnetic field. Along the direction of the magnetic field, the particle performs a uniform motion.

It may seem counterintuitive to start our discussion with non-relativistic particles but it turns out that the important aspects of the quasilinear theory are present in this regime. To obtain the expressions that are valid for relativistic particles, it is sufficient to replace the (non-relativistic) gyrofrequency with its relativistic counterpart $\Omega \leftarrow qB/\gamma mc$, where γ is the Lorentz factor of the particle. A textbook derivation valid for relativistic particles can be found in Schlickeiser (2002).

2.1 Polarization and Helicity

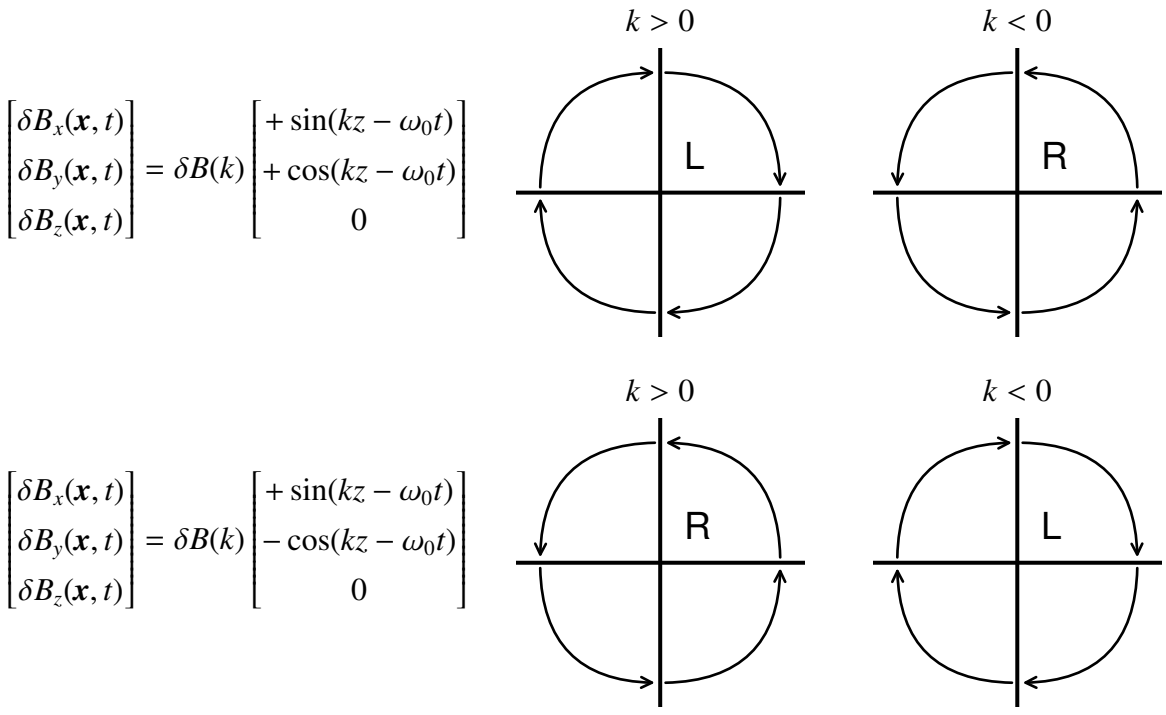

Figure 2.5: On the definition of helicity of transverse waves for the two basis vectors. x- and y-axes are in the plane of the paper and the z-axis is pointing out of the paper. Left- and right-handedness are abbreviated by L and R, respectively.

We shortly discuss different ways of how to define the sense of rotation of a given vector field. A common approach is to define helicity and polarization for vector fields using the rotation properties of the argument of the $\exp(\mathrm{i}x)$ function in the complex plane. Using Fourier-

decomposition methods, a real vector field can be written in terms of a vector consisting of complex valued functions. To avoid confusion between the rotation of the vector components in the complex plane and the actual rotation of the real vector, we will continue to describe vectors as real valued functions and in terms of the $\sin(x)$ and $\cos(x)$ functions. In this approach, a transverse wave in the magnetic field can be decomposed into the following two basis vectors (which differ by the sign of the y component):

$$\delta\boldsymbol{B}(\boldsymbol{x},t) = \begin{bmatrix} \delta B_x(\boldsymbol{x},t) \\ \delta B_y(\boldsymbol{x},t) \\ \delta B_z(\boldsymbol{x},t) \end{bmatrix} = \delta B(k) \begin{bmatrix} +\sin(kz-\omega_0 t) \\ \pm\cos(kz-\omega_0 t) \\ 0 \end{bmatrix} \tag{2.5}$$

upto an unimportant phase, where k is the wave number and ω_0 is the wave frequency. Both basis vectors rotate in the plane that is perpendicular to the direction of the mean magnetic field. The sense of rotation of this vector field depends on k, ω_0 and whether t or z varies. We define that:

Polarization is the sense of rotation for fixed z but varying t,

Helicity is the sense of rotation for fixed t but varying z.

We illustrate the definition for helicity in Fig. 2.5 where we provide a finding chart to identify left- and right-handed helicity. Note that both definitions are dependent on the observer and are not proper. We, as an observer, can take the point of view of a particle and also define for this particle that the

Polarization of the probed magnetic field $\delta\boldsymbol{B}(\boldsymbol{x}(t),t)$ is its sense of rotation for varying t.

This definition depends on the actual motion of the particle and on possible differences in particle and wave phase velocities. We consider a particle in a medium with a strong, uniform, and constant magnetic field and an additional perturbing magnetic field that originates from a transverse wave. Assume that the magnetic field strength of the transverse wave is so weak that the resulting motion is still well described by the free gyration around the constant magnetic field. In this case, the probed magnetic field is given by

$$\begin{bmatrix} \delta B_x(\boldsymbol{x}(t),t) \\ \delta B_y(\boldsymbol{x}(t),t) \\ \delta B_z(\boldsymbol{x}(t),t) \end{bmatrix} = \delta B(k) \begin{bmatrix} +\sin\left(k\left(\mu v - \frac{\omega_0}{k}\right)t\right) \\ \pm\cos\left(k\left(\mu v - \frac{\omega_0}{k}\right)t\right) \\ 0 \end{bmatrix}. \tag{2.6}$$

We see that the polarization of the field depends on two parameters: the wave number k and the Doppler shifted velocity $(\mu v - \omega_0/k)$ where ω_0/k is the phase speed of wave.

2.2 Quasilinear Theory

We are now moving our attention away from a single particle and describe a population of particles in a statistical framework. The evolution of a distribution function f which contains all the statistical phase-space information about the particle population is given Boltzmann-Vlasov equation:

$$\frac{\partial f}{\partial t} + \boldsymbol{v} \cdot \frac{\partial f}{\partial \boldsymbol{x}} + \boldsymbol{F} \cdot \frac{\partial f}{\partial \boldsymbol{p}} = 0, \tag{2.7}$$

$$\text{or} \quad \frac{\partial f}{\partial t} + \boldsymbol{v} \cdot \frac{\partial f}{\partial \boldsymbol{x}} + \frac{\partial}{\partial \boldsymbol{p}} \cdot (\boldsymbol{F} f) = 0. \tag{2.8}$$

Both forms are equivalent if and only if $\boldsymbol{\nabla}_p \cdot \boldsymbol{F} = 0$ which holds true for the electromagnetic force:

$$\boldsymbol{F} = q\left[\boldsymbol{E} + \frac{\boldsymbol{v} \times \boldsymbol{B}}{c}\right]. \tag{2.9}$$

We analyse this equation in the following setting: assume that particles primarily follow trajectories that are defined by a strong force $\boldsymbol{F}$ but experience additional perturbing forces $\delta\boldsymbol{F}$ that slightly change their original trajectories. These perturbing forces are assumed to fluctuate on time scales comparable or shorter than other characteristic time scales of the particles. We strive for an effective generalization of the Boltzmann-Vlasov equation that allows us to study the motion through phase space in a statistical approach.

The perturbing or fluctuating forces will also introduce perturbations of the particle distribution so that we need to perturb the Boltzmann-Vlasov equation with:

$$f \longrightarrow f + \delta f, \tag{2.10}$$

$$\boldsymbol{F} \longrightarrow \boldsymbol{F} + \delta\boldsymbol{F}, \tag{2.11}$$

where we assume that both perturbations are stochastic and their ensemble averages vanish:

$$\langle \delta A \rangle = 0 \quad \text{with} \quad \delta A \in \{\delta f, \delta \boldsymbol{F}\}. \tag{2.12}$$

Because the small fluctuation forces seed the perturbations in the particle distribution in the first place, we can also assume that the fluctuations in the particle distribution are small as well. To separate the dynamics of the mean and fluctuating particle distributions, we perturb

the Boltzmann-Vlasov equation and take the ensemble average of the result. We get for the non-fluctuating particle distribution that

$$\frac{\partial f}{\partial t} + \boldsymbol{v} \cdot \frac{\partial f}{\partial \boldsymbol{x}} + \boldsymbol{F} \cdot \frac{\partial f}{\partial \boldsymbol{p}} + \frac{\partial}{\partial \boldsymbol{p}} \cdot \langle \delta \boldsymbol{F} \delta f \rangle = 0. \tag{2.13}$$

By subtracting this result from perturbed Boltzmann-Vlasov equation, we calculate the corresponding evolution equation for the fluctuations in the particle distribution to be:

$$\frac{\partial \delta f}{\partial t} + \boldsymbol{v} \cdot \frac{\partial \delta f}{\partial \boldsymbol{x}} + \boldsymbol{F} \cdot \frac{\partial \delta f}{\partial \boldsymbol{p}} + \delta \boldsymbol{F} \cdot \frac{\partial f}{\partial \boldsymbol{p}} + \frac{\partial}{\partial \boldsymbol{p}} \left(\delta \boldsymbol{F} \delta f - \langle \delta \boldsymbol{F} \delta f \rangle \right) = 0. \tag{2.14}$$

The last term in this equation is negligible because it is 2nd-order in fluctuations and thus small compared to all other terms. We continue with:

$$\frac{\partial \delta f}{\partial t} + \boldsymbol{v} \cdot \frac{\partial \delta f}{\partial \boldsymbol{x}} + \boldsymbol{F} \cdot \frac{\partial \delta f}{\partial \boldsymbol{p}} + \delta \boldsymbol{F} \cdot \frac{\partial f}{\partial \boldsymbol{p}} = 0. \tag{2.15}$$

We find a solution to this partial differential equation by converting it into an ordinary differential equation: instead of solving this equation for arbitrary $\boldsymbol{x}$ and $\boldsymbol{p}$, we solve it along a trajectory of a particle, which has the following equations of motions:

$$\frac{\mathrm{d}\boldsymbol{x}}{\mathrm{d}t} = \boldsymbol{v}, \tag{2.16}$$

$$\frac{\mathrm{d}\boldsymbol{p}}{\mathrm{d}t} = \boldsymbol{F}, \tag{2.17}$$

which defines a new coordinate system and Eq. (2.15) reduces to:

$$\frac{\mathrm{d}\delta f}{\mathrm{d}t} = - \delta \boldsymbol{F} \cdot \left. \frac{\partial f}{\partial \boldsymbol{p}} \right|_{\boldsymbol{x}(t), \boldsymbol{p}(t), t}. \tag{2.18}$$

This equation has the simple solution:

$$\delta f(t) = - \int_{-\infty}^{t} \mathrm{d}t' \, \delta \boldsymbol{F}(\boldsymbol{x}(t'), t') \cdot \frac{\partial f}{\partial \boldsymbol{p}}(\boldsymbol{x}(t'), p(t'), t'). \tag{2.19}$$

Inserting Eq. (2.19) back into Eq. (2.13) results in:

$$\frac{\partial f}{\partial t} + \boldsymbol{v} \cdot \frac{\partial f}{\partial \boldsymbol{x}} + \boldsymbol{F} \cdot \frac{\partial f}{\partial \boldsymbol{p}} = \frac{\partial}{\partial \boldsymbol{p}} \cdot \left\langle \int_{-\infty}^{t} \mathrm{d}t' \, \delta \boldsymbol{F}(\boldsymbol{x}, t) \delta \boldsymbol{F}(\boldsymbol{x}(t'), t') \cdot \frac{\partial f}{\partial \boldsymbol{p}}(\boldsymbol{x}(t'), p(t'), t') \right\rangle. \tag{2.20}$$

Note that this equation is independent of δf. This is a strong statement because the fluctuating forces might seed arbitrary perturbations in the particle distribution. But, we do not need to know the actual realization of these fluctuating components to investigate the evolution of the mean particle distribution. The evolution of f is entirely determined by the forces and their fluctuations.

Once we assume that the momentum derivative of f does not vary faster in time than the force fluctuations, it can be approximated by a constant value in the temporal integral and we arrive at the Fokker-Planck equation:

$$\frac{\partial f}{\partial t} + \boldsymbol{v} \cdot \frac{\partial f}{\partial \boldsymbol{x}} + \boldsymbol{F} \cdot \frac{\partial f}{\partial \boldsymbol{p}} = \frac{\partial}{\partial \boldsymbol{p}} \cdot \int_{-\infty}^{t} \mathrm{d}t' \, \langle \delta \boldsymbol{F}(t) \delta \boldsymbol{F}(\boldsymbol{x}(t'), t') \rangle \cdot \frac{\partial f}{\partial \boldsymbol{p}} \tag{2.21}$$

This equation states that the fluctuating forces induce a phase-space diffusion of the particle population. We introduce the matrix-valued momentum diffusion coefficient:

$$\mathbf{D} = \int_{-\infty}^{0} \mathrm{d}s \, \langle \delta \boldsymbol{F}(\boldsymbol{x}, t) \delta \boldsymbol{F}(\boldsymbol{x}(t+s), t+s) \rangle \tag{2.22}$$

$$= \int_{-\infty}^{0} \mathrm{d}t \, \langle \delta \boldsymbol{F}(\boldsymbol{x}, 0) \delta \boldsymbol{F}(\boldsymbol{x}(t), t) \rangle \,, \tag{2.23}$$

where we arrived at the second line after using the homogeneity of time to shift the time integration. Consequently, the momentum diffusion coefficient is the autocorrelation of the perturbation forces. To get a physical understanding of this equation, we need to recall that the fluctuating forces induce small perturbations into a particle's momentum. Particles continuously experience these stochastic forces. This leads to a random motion through phase space. The effective speed of this motion depends on the strength of the effective fluctuating forces. Hence, the diffusion coefficient must depend on the fluctuating forces in some way. The diffusion coefficient is given in the specific form of an autocorrelation because fluctuating forces at two different points in time can constructively or destructively interfere which can be measured using this quantity.

2.2.1 Pitch Angle Scattering by an Alfvén Wave

The Fokker-Planck equation (2.21) is general in the sense that we only needed a few restrictive assumptions about the nature of the fluctuating forces to derive it. In this work, we are interested in the propagation properties of CRs. These charged particles interact with electromagnetic fields. Alfvén waves are an important type of electromagnetic (to be precise magnetohydrodynamical) waves and are thought to have a strong influence on the transport of GeV CRs (Zweibel, 2013). We will focus on the interactions between CRs and Alfvén waves and restrict ourselves to Alfvén waves propagating along the direction of the mean magnetic field. This type of Alfvén waves can be characterized as incompressible, transverse perturbations of an ideal MHD fluid where the perturbation of the transverse mean-velocity and magnetic field are given by

$$\frac{\delta \boldsymbol{u}}{v_\mathrm{a}} = -\frac{\delta \boldsymbol{B}}{B} \quad \text{and} \quad \omega_0 = \omega_0(k) = v_\mathrm{a} k, \tag{2.24}$$

where v_a is the Alfvén velocity. In the MHD approximation, the electric field vanishes in a frame that is comoving with the mean-flow at velocity $\boldsymbol{u}$:

$$\boldsymbol{E} = -\frac{\boldsymbol{u} \times \boldsymbol{B}}{c}. \tag{2.25}$$

We perturb this equation in the presence of an Alfvén wave, which yields in the comoving frame:

$$\delta\boldsymbol{E} = -\frac{\delta\boldsymbol{u} \times (\boldsymbol{B} + \delta\boldsymbol{B})}{c} = -\frac{\delta\boldsymbol{u} \times \boldsymbol{B}}{c} = -\frac{\boldsymbol{v}_\mathrm{a} \times \delta\boldsymbol{B}}{c}. \tag{2.26}$$

The perturbing force exerted by an Alfvén wave is given by

$$\delta\boldsymbol{F}(x,t) = q\left(\delta\boldsymbol{E} + \frac{\boldsymbol{v} \times \delta\boldsymbol{B}}{c}\right) = q\frac{(\boldsymbol{v} - \boldsymbol{v}_\mathrm{a}) \times \delta\boldsymbol{B}}{c}, \tag{2.27}$$

where the magnetic field is given by

$$\delta\boldsymbol{B}(\boldsymbol{x}(t),t) = \begin{bmatrix} \delta B_x(\boldsymbol{x}(t),t) \\ \delta B_y(\boldsymbol{x}(t),t) \\ \delta B_z(\boldsymbol{x}(t),t) \end{bmatrix} = \delta B(k) \begin{bmatrix} +\sin(k(\mu v - v_\mathrm{a})t) \\ \pm\cos(k(\mu v - v_\mathrm{a})t) \\ 0 \end{bmatrix}, \tag{2.28}$$

Expanding the force in Cartesian coordinates gives:

$$\delta\boldsymbol{F} = \begin{bmatrix} \delta F_x \\ \delta F_y \\ \delta F_z \end{bmatrix} = \frac{q}{c} \begin{bmatrix} -(v\mu - v_a)\delta B_y, \\ +(v\mu - v_a)\delta B_x, \\ +v_x\delta B_y - v_y\delta B_x \end{bmatrix}. \tag{2.29}$$

We do not continue our calculation of the pitch-angle diffusion coefficient in these coordinates but in spherical momentum coordinates given by p, μ, φ where the Cartesian momentum coordinates are given by:

$$\boldsymbol{p} = \begin{bmatrix} p_x \\ p_y \\ p_z \end{bmatrix} = \begin{bmatrix} p\sqrt{1-\mu^2}\sin(\varphi) \\ p\sqrt{1-\mu^2}\cos(\varphi) \\ p\mu \end{bmatrix}. \tag{2.30}$$

We use this coordinate system because it will simplify the following calculations. This is because one of the fluctuating forces in the diffusion coefficient of Eq. (2.23) is evaluated along the trajectory of an unperturbed particle. In our case, this trajectory is given by the gyration of a particle along the mean magnetic field. The corresponding phase-space trajectory is stated in Eq. (2.3) and resembles our definition for the phase-space coordinates in spherical coordinates.

The force exerted along the direction of the pitch-angle coordinate is:

$$\delta F_\mu = \frac{\mathrm{d}\mu}{\mathrm{d}t} = \frac{\mathrm{d}}{\mathrm{d}t}\frac{p_z}{p} \tag{2.31}$$

$$= \frac{1}{p}\frac{\mathrm{d}p_z}{\mathrm{d}t} - \frac{p_z}{p^2}\frac{\mathrm{d}p}{\mathrm{d}t} \tag{2.32}$$

$$= \frac{1}{p}\frac{\mathrm{d}p_z}{\mathrm{d}t} - \frac{\mu}{p}\frac{\mathrm{d}p}{\mathrm{d}t} \tag{2.33}$$

$$= \frac{q}{pc}(v_x\delta B_y - v_y\delta B_x) - \frac{q\mu}{p}\frac{\boldsymbol{v}}{v}\cdot\delta\boldsymbol{E} \tag{2.34}$$

$$= \frac{q}{pc}(v_x\delta B_y - v_y\delta B_x) - \frac{q\mu}{vpc}(v_x v_\mathrm{a}\delta B_y - v_y v_\mathrm{a}\delta B_x) \tag{2.35}$$

$$= \frac{q}{pc}\left(1 - \frac{\mu v_\mathrm{a}}{v}\right)(v_x\delta B_y - v_y\delta B_x). \tag{2.36}$$

Inserting the magnetic fields from Eq. (2.28) and the velocities from Eq. (2.3) results in:

$$\delta F_\mu(t) = \frac{vq\delta B(k)}{pc}\sqrt{1-\mu^2}\left(1 - \frac{\mu v_\mathrm{a}}{v}\right)\ [\pm\sin(\Omega t + \varphi)\cos(k(\mu v - v_\mathrm{a})t) - \cos(\Omega t + \varphi)\sin(k(\mu v - v_\mathrm{a})t)] \tag{2.37}$$

$$= \pm\frac{vq\delta B(k)}{pc}\sqrt{1-\mu^2}\left(1 - \frac{\mu v_\mathrm{a}}{v}\right)\sin(\Omega t + \varphi \mp k(\mu v - v_\mathrm{a})t) \tag{2.38}$$

We are now in the position to calculate the pitch-angle diffusion coefficient. If we insert the μ-force from Eq. (2.38) into the Eq. (2.23) then we get:

$$D_{\mu\mu} = \int_{-\infty}^{0}\mathrm{d}t\,\left\langle\delta F_\mu(0)\delta F_\mu(t)\right\rangle \tag{2.39}$$

$$= \frac{v^2q^2\delta B^2(k)}{p^2c^2}\left(1-\mu^2\right)\left(1 - \frac{\mu v_\mathrm{a}}{v}\right)^2\int_{-\infty}^{0}\mathrm{d}t\,\langle\sin(\varphi)\sin(\Omega t + \varphi \mp k(\mu v - v_\mathrm{a})t)\rangle \tag{2.40}$$

$$= \frac{v^2q^2\delta B^2(k)}{p^2c^2}\left(1-\mu^2\right)\left(1 - \frac{\mu v_\mathrm{a}}{v}\right)^2\int_{-\infty}^{0}\mathrm{d}t\,\Big\langle\cos(\Omega t \mp k(\mu v - v_\mathrm{a})t)\sin^2(\varphi) + \sin(\Omega t \mp k(\mu v - v_\mathrm{a})t)\sin(\varphi)\cos(\varphi)\Big\rangle. \tag{2.41}$$

So far, we did not restrict our discussion to any specific particle distribution. In the following, we will do so and only consider gyrotropic particle distributions defined by $\partial_\varphi f = 0$. This will simplify our calculations. Using the uniform distribution is also appropriate because this choice minimises our prior information about f and, consequently, this distribution maximises the entropy. Evaluating the ensemble averages for a uniform distribution in φ results in:

$$\frac{1}{2\pi}\int_0^{2\pi}\mathrm{d}\varphi\ \sin^2(\varphi) = \frac{1}{2} \quad \text{and} \quad \frac{1}{2\pi}\int_0^{2\pi}\mathrm{d}\varphi\ \sin(\varphi)\cos(\varphi) = 0 \tag{2.42}$$

and we arrive at:

$$D_{\mu\mu} = \frac{v^2 q^2 \delta B^2(k)}{2p^2c^2}\left(1-\mu^2\right)\left(1-\frac{\mu v_\mathrm{a}}{v}\right)^2 \int_{-\infty}^{0} \mathrm{d}t\, \cos(\Omega t \mp k(\mu v - v_\mathrm{a})t). \tag{2.43}$$

This integral frequently appears in our calculations and we carefully evaluate it to:

$$\int_{-\infty}^{0} \mathrm{d}t\, \cos(\Omega t \mp k(\mu v - v_\mathrm{a})t) = \frac{1}{2}\int_{-\infty}^{\infty} \mathrm{d}t\, \cos(\Omega t \mp k(\mu v - v_\mathrm{a})t) \tag{2.44}$$

$$= \frac{1}{4}\int_{-\infty}^{\infty} \mathrm{d}t\, e^{\mathrm{i}t(\Omega \mp k(\mu v - v_\mathrm{a}))} + e^{-\mathrm{i}t(\Omega \mp k(\mu v - v_\mathrm{a}))} \tag{2.45}$$

$$= \pi\delta(k(\mu v - v_\mathrm{a}) \mp \Omega) \tag{2.46}$$

Substituting this expression into Eq. (2.43) yields our final expression for the pitch-angle diffusion coefficient:

$$D_{\mu\mu} = \frac{\pi}{2}\frac{v^2 q^2 \delta B^2(k)}{p^2c^2}\left(1-\mu^2\right)\left(1-\frac{\mu v_\mathrm{a}}{v}\right)^2 \delta(k(\mu v - v_\mathrm{a}) \mp \Omega) \tag{2.47}$$

$$= \pi\Omega^2 \frac{\delta B^2(k)}{B^2}\frac{1-\mu^2}{2}\left(1-\frac{\mu v_\mathrm{a}}{v}\right)^2 \delta(k(\mu v - v_\mathrm{a}) \mp \Omega) \tag{2.48}$$

The δ-function defines a resonance condition for the interaction with parallel-propagating Alfvén waves:

$$0 = k_\mathrm{res}(\mu v - v_\mathrm{a}) \mp \Omega. \tag{2.49}$$

Only Alfvén waves that fulfill this resonance condition can influence particles with velocity v, pitch-angle μ, and gyrofrequency Ω. To discuss this interaction, let us focus on particles with

$$\mu > \frac{v_\mathrm{a}}{v} \quad \text{or} \quad \mu v - v_\mathrm{a} > 0 \quad \text{and} \quad \Omega > 0. \tag{2.50}$$

We solve Eq. (2.49) for the resonant wave number k_res and insert the result into the first basis vector of the Alfvén wave magnetic field in Eq. (2.28). This yields:

$$k_\mathrm{res} = +\frac{\Omega}{\mu v - v_\mathrm{a}} \quad \text{and} \quad \begin{bmatrix}\delta B_x(\boldsymbol{x}(t),t)\\ \delta B_y(\boldsymbol{x}(t),t)\\ \delta B_z(\boldsymbol{x}(t),t)\end{bmatrix} = \delta B(k)\begin{bmatrix}\sin(\Omega t)\\ \cos(\Omega t)\\ 0\end{bmatrix}. \tag{2.51}$$

The magnetic field has the same rotation direction and frequency as the particle. We see that $k_\mathrm{res} > 0$ which states that this wave has left-handed helicity. The magnetic field as probed by the particle has left-handed polarization. We get for the second basis vector and sign in the resonance condition that:

$$k_\mathrm{res} = -\frac{\Omega}{\mu v - v_\mathrm{a}} \quad \text{and} \quad \begin{bmatrix}\delta B_x(\boldsymbol{x}(t),t)\\ \delta B_y(\boldsymbol{x}(t),t)\\ \delta B_z(\boldsymbol{x}(t),t)\end{bmatrix} = \delta B(k)\begin{bmatrix}-\sin(\Omega t)\\ -\cos(\Omega t)\\ 0\end{bmatrix}, \tag{2.52}$$

which, again, can be identified as an Alfvén wave with left-handed helicity and polarization. Note that helicity and polarization have the same sense of rotation here because of our particular parameter choices. For $\mu v - v_\mathrm{a} < 0$, both waves have right-handed helicity and left-handed polarization as seen by the particle.

2.2.2 Quasilinear Diffusion

We expand our analysis from an individual Alfvén wave to a spectrum of Alfvén waves by integrating Eq. (2.48) over the wave number k. The resulting integral can be readily integrated to give:

$$D_{\mu\mu} = \frac{1-\mu^2}{2}\left(1 - \frac{\mu v_\mathrm{a}}{v}\right)^2 \nu(k_\mathrm{res}), \tag{2.53}$$

where we defined the Alfvén wave scattering frequency to be:

$$\nu(k) = \pi\Omega\frac{|k|\delta B^2(k)}{B^2}. \tag{2.54}$$

Furthermore, we can calculate remaining non-vanishing components of the diffusion coefficient matrix once we evaluate the component of the fluctuating force along the p-direction to

$$\begin{aligned}
\delta F_p &= \frac{\mathrm{d}p}{\mathrm{d}t}, && (2.55)\\
&= q\frac{\boldsymbol{v}}{v}\cdot\delta\boldsymbol{E}, && (2.56)\\
&= \frac{q}{vc}(v_x v_\mathrm{a}\delta B_y - v_y v_\mathrm{a}\delta B_x), && (2.57)\\
&= \frac{q v_\mathrm{a}}{vc}(v_x\delta B_y - v_y\delta B_x). && (2.58)
\end{aligned}$$

Expressing this result in terms of the δF_μ force component will tremendously simplify our calculations:

$$\delta F_p = \left(1 - \frac{\mu v_\mathrm{a}}{v}\right)^{-1} p\frac{v_\mathrm{a}}{v}\delta F_\mu. \tag{2.59}$$

The μ-p and p-μ components of the diffusion coefficient matrix are:

$$\begin{aligned}
D_{\mu p} = D_{p\mu} &= \int_0^\infty \mathrm{d}t\left\langle\delta F_\mu(0)\delta F_p(t)\right\rangle && (2.60)\\
&= \left(1 - \frac{\mu v_\mathrm{a}}{v}\right)^{-1} p\frac{v_\mathrm{a}}{c}\int_0^\infty \mathrm{d}t\left\langle\delta F_\mu(0)\delta F_\mu(t)\right\rangle && (2.61)\\
&= \left(1 - \frac{\mu v_\mathrm{a}}{v}\right)^{-1} p\frac{v_\mathrm{a}}{c}D_{\mu\mu} && (2.62)\\
&= p\frac{v_\mathrm{a}}{c}\frac{1-\mu^2}{2}\left(1 - \frac{\mu v_\mathrm{a}}{v}\right)\nu(k_\mathrm{res}). && (2.63)
\end{aligned}$$

The last non-vanishing entry in the diffusion coefficient tensor is the p-p component:

$$D_{pp} = \int_0^\infty \mathrm{d}t \left\langle \delta F_p(0) \delta F_p(t) \right\rangle \tag{2.64}$$

$$= \left(1 - \frac{\mu v_\mathrm{a}}{v}\right)^{-2} p^2 \frac{v_\mathrm{a}^2}{c^2} \int_0^\infty \mathrm{d}t \left\langle \delta F_\mu(0) \delta F_\mu(t) \right\rangle \tag{2.65}$$

$$= \left(1 - \frac{\mu v_\mathrm{a}}{v}\right)^{-2} p^2 \frac{v_\mathrm{a}^2}{c^2} D_{\mu\mu} \tag{2.66}$$

$$= p^2 \frac{v_\mathrm{a}^2}{c^2} \frac{1-\mu^2}{2} \nu(k_\mathrm{res}). \tag{2.67}$$

Collecting all three components in a single expression gives:

$$\begin{bmatrix} D_{\mu\mu} \\ D_{\mu p} \\ D_{pp} \end{bmatrix} = \nu(k_\mathrm{res}) \frac{1-\mu^2}{2} \begin{bmatrix} \left(1 - \frac{\mu v_\mathrm{a}}{v}\right)^2 \\ p \frac{v_\mathrm{a}}{c} \left(1 - \frac{\mu v_\mathrm{a}}{v}\right) \\ p^2 \frac{v_\mathrm{a}^2}{c^2} \end{bmatrix}, \tag{2.68}$$

which completes our calculation of the diffusion coefficients for the interaction between CRs and Alfvén waves propagating along the direction of the magnetic field. A trivial extension to Alfvén waves propagating in the opposite direction is achieved by replacing $v_\mathrm{a} \to -v_\mathrm{a}$. This concludes our derivation of the diffusion coefficients of CRs in the quasilinear theory.

The theory can be generalized to contain the effects of arbitrary perturbations in the electromagnetic fields (Kulsrud and Pearce, 1969; Schlickeiser, 2002), to include 2nd-order effects (Shalchi and Schlickeiser, 2005), to be valid in non-linear regime (Shalchi, 2009b), or to account for magnetohydrodynamical turbulence (Yan and Lazarian, 2004).

2.2.3 Gyroresonant Streaming Instability

In the previous discussion, we focused on the effects that Alfvén waves have on CR propagation through phase space. We implicitly assumed that these Alfvén waves were generated through some external source and interacted with the CRs but did not consider a possible backreaction of the CRs on the Alfvén waves. This backreaction is given in the form of the gyroresonant streaming instability where CRs are able to excite Alfvén waves (Kulsrud and Pearce, 1969). We are now calculating the growth rate of this instability.

Particles influence electromagnetic fields through their currents. The current driven by the perturbation in the particle distribution is:

$$\delta \boldsymbol{j} = \int \mathrm{d}^3 p \, q \boldsymbol{v} \, \delta f = \int \mathrm{d}^3 p \, q \boldsymbol{v} \int_{-\infty}^{t} \mathrm{d}t' \, \delta \boldsymbol{F} \cdot \left. \frac{\partial f}{\partial \boldsymbol{p}} \right|_{\boldsymbol{x}(t'), \boldsymbol{p}(t'), t'}, \tag{2.69}$$

where we used Eq. (2.19) to remove the fluctuating component of the particle distribution. To proceed, we evaluate the momentum space gradient in spherical momentum coordinates to:

$$\frac{\partial f}{\partial \boldsymbol{p}} = \left(\frac{\partial f}{\partial p} \boldsymbol{e}_p + \frac{\sqrt{1-\mu^2}}{p} \frac{\partial f}{\partial \mu} \boldsymbol{e}_\theta \right), \tag{2.70}$$

where $\boldsymbol{e}_p$ is the unit vector in p-direction and $\boldsymbol{e}_\theta$ is the unit vector in $\theta = \cos^{-1}(\mu)$ direction. Note that a derivative of f with respect to φ does not appear because we are still assuming that f is gyrotropic. The projections of this gradient onto the fluctuating forces includes two terms:

$$\boldsymbol{e}_p \cdot \delta \boldsymbol{F} = \delta F_p \quad \text{and} \quad \sqrt{1-\mu^2} \boldsymbol{e}_\theta \cdot \delta \boldsymbol{F} = \delta F_\mu \tag{2.71}$$

which can be evaluated using Eqs. (2.36) and (2.58) and can be combined to give:

$$\begin{aligned} \delta \boldsymbol{F} \cdot \frac{\partial f}{\partial \boldsymbol{p}} = \frac{\sqrt{1-\mu^2}}{p} \frac{q v_\mathrm{a}}{c} \left[p \frac{\partial f}{\partial p} + \left(\frac{v}{v_\mathrm{a}} - \mu \right) \frac{\partial f}{\partial \mu} \right] \times \\ \left[\sin(\Omega t + \varphi) \delta B_y - \cos(\Omega t + \varphi) \delta B_x \right]. \end{aligned} \tag{2.72}$$

We insert this expression into Eq. (2.69). Furthermore, we assume that the momentum space derivatives do not vary as much as the fluctuating forces and approximate these derivatives as a constant in the resulting temporal integral. This yields:

$$\begin{aligned} \delta \boldsymbol{j} = \int \mathrm{d}^3 p \, \frac{\sqrt{1-\mu^2}}{p} \frac{q^2 v_\mathrm{a}}{c} \left[p \frac{\partial f}{\partial p} + \left(\frac{v}{v_\mathrm{a}} - \mu \right) \frac{\partial f}{\partial \mu} \right] \times \\ \boldsymbol{v} \int_{-\infty}^{0} \mathrm{d}s \left[\sin(\Omega s + \varphi) \delta B_y - \cos(\Omega s + \varphi) \delta B_x \right] \Big|_{\boldsymbol{x}(t+s), t+s}, \end{aligned} \tag{2.73}$$

where we also shifted the time integration range. We perform the φ-integration of the momentum integral over the velocity components. Once the intergration is performed, we reintroduce the φ integral to absorb a 2π factor and to keep our notation compact. We get for the transverse components of the perturbation current:

$$\begin{aligned} \begin{bmatrix} \delta j_x \\ \delta j_y \end{bmatrix} = \int \mathrm{d}^3 p \, v \frac{1-\mu^2}{p} \frac{q^2 v_\mathrm{a}}{c} \left[p \frac{\partial f}{\partial p} + \left(\frac{v}{v_\mathrm{a}} - \mu \right) \frac{\partial f}{\partial \mu} \right] \times \\ \int_{-\infty}^{0} \mathrm{d}s \begin{bmatrix} \cos(\Omega s) \delta B_y + \sin(\Omega s) \delta B_x \\ \sin(\Omega s) \delta B_y - \cos(\Omega s) \delta B_x \end{bmatrix} \Bigg|_{\boldsymbol{x}(t+s), t+s}. \end{aligned} \tag{2.74}$$

The transverse components of the magnetic fields evaluated at $\boldsymbol{x}(t+s)$ and time $t+s$ can deduced from Eq. (2.28):

$$\begin{bmatrix} \delta B_x \\ \delta B_y \end{bmatrix} \Bigg|_{\boldsymbol{x}(t+s), t+s} = \delta B \begin{bmatrix} +\sin\left(k(z + s\mu v) - \omega_0 (t+s)\right) \\ \pm \cos\left(k(z + s\mu v) - \omega_0 (t+s)\right) \end{bmatrix} = \delta B \begin{bmatrix} +\sin\left(kz - \omega_0 t + sk(\mu v - v_\mathrm{a})\right) \\ \pm \cos\left(kz - \omega_0 t + sk(\mu v - v_\mathrm{a})\right) \end{bmatrix} \tag{2.75}$$

To proceed, some manipulations of the trigonometric functions appearing in the temporal integral are necessary. We get for the functions in the δj_x entry after inserting these magnetic fields:

$$\pm \cos(\Omega s)\cos\left(kz - \omega_0 t + sk(\mu v - v_\mathrm{a})\right) + \sin(\Omega s)\sin\left(kz - \omega_0 t + sk(\mu v - v_\mathrm{a})\right) \tag{2.76}$$

$$= \pm \cos\left(kz - \omega_0 t + sk(\mu v - v_\mathrm{a}) \mp \Omega s\right) \tag{2.77}$$

$$= \pm \cos(kz - \omega_0 t)\cos\left(sk(\mu v - v_\mathrm{a}) \mp \Omega s\right) \mp \sin(kz - \omega_0 t)\sin\left(sk(\mu v - v_\mathrm{a}) \mp \Omega s\right), \tag{2.78}$$

while a similar expression holds for the δj_y component. We can use Eq. (2.46) to perform the s-integration and have:

$$\begin{bmatrix}\delta j_x \\ \delta j_y\end{bmatrix} = \pi \int \mathrm{d}^3 p\, v \frac{1-\mu^2}{p}\frac{q^2 v_\mathrm{a}}{c}\left[p\frac{\partial f}{\partial p} + \left(\frac{v}{v_\mathrm{a}} - \mu\right)\frac{\partial f}{\partial \mu}\right]\begin{bmatrix}\delta B_y \\ -\delta B_x\end{bmatrix}\delta(k(\mu v - v_\mathrm{a}) \mp \Omega), \tag{2.79}$$

which is our final expression for the perturbation current.

We are now in the position to discuss the influence of this current on the electromagnetic fields. Their evolution is dictated by Maxwell's equations:

$$c\boldsymbol{\nabla} \times \boldsymbol{E} = -\frac{\partial \boldsymbol{B}}{\partial t}, \tag{2.80}$$

$$c\boldsymbol{\nabla} \times \boldsymbol{B} = \frac{\partial \boldsymbol{E}}{\partial t} + \boldsymbol{j}_\mathrm{tot}, \tag{2.81}$$

where the total current $\boldsymbol{j}_\mathrm{tot} = \boldsymbol{j}_\mathrm{th} + \boldsymbol{j}$ is partly provided by thermal particles ($\boldsymbol{j}_\mathrm{th}$) and the CRs ($\boldsymbol{j}$). We perturb these equations by introducing a single wave-mode perturbation in the electromagnetic fields via

$$\begin{bmatrix}\delta\boldsymbol{E}(\boldsymbol{x}, t) \\ \delta\boldsymbol{B}(\boldsymbol{x}, t)\end{bmatrix} = \begin{bmatrix}\delta\boldsymbol{E}(\boldsymbol{k}, \omega) \\ \delta\boldsymbol{B}(\boldsymbol{k}, \omega)\end{bmatrix}\exp\left(\mathrm{i}\boldsymbol{k}\cdot\boldsymbol{x} - \mathrm{i}\omega(\boldsymbol{k})t\right), \tag{2.82}$$

which represents an Alfvén wave with wavenumber $\boldsymbol{k}$, wave frequency $\omega = \omega_0 + \mathrm{i}\Gamma$, and wave growth rate Γ. The evolution equations for this perturbation can be readily found and read as:

$$c\boldsymbol{k} \times \delta\boldsymbol{E} = \omega\delta\boldsymbol{B}, \tag{2.83}$$

$$\mathrm{i}c\boldsymbol{k} \times \delta\boldsymbol{B} = -\mathrm{i}\omega\delta\boldsymbol{E} + \delta\boldsymbol{j}_\mathrm{tot}, \tag{2.84}$$

where we dropped the $\boldsymbol{k}$ and ω dependencies for readability. These equations can be combined into a single expression:

$$\mathrm{i}c^2\boldsymbol{k} \times (\boldsymbol{k} \times \delta\boldsymbol{B}) = -\mathrm{i}\omega^2\delta\boldsymbol{B} + c\boldsymbol{k} \times \delta\boldsymbol{j}_\mathrm{tot}. \tag{2.85}$$

We assume that the perturbations caused by the CRs are small. The growth rate Γ will also be small because this growth is directly caused by the presence of the CRs perturbation. We can thus expand the ω^2-term to give:

$$\mathrm{i}c^2\boldsymbol{k}\times(\boldsymbol{k}\times\delta\boldsymbol{B}) = -\mathrm{i}\left(\omega_0^2 + 2\mathrm{i}\omega_0\Gamma\right)\delta\boldsymbol{B} + c\boldsymbol{k}\times(\delta\boldsymbol{j}_{\mathrm{th}} + \delta\boldsymbol{j})\,. \tag{2.86}$$

Either of following two arguments can be used to derive:

$$2\omega_0\Gamma\delta\boldsymbol{B} = c\boldsymbol{k}\times\delta\boldsymbol{j} \tag{2.87}$$

First, we can sort all terms in Eq. (2.86) by their relative size. The two terms in Eq. (2.87) are the only ones that are connected to the perturbations induced by the CRs. They belong to the same order in a hypothetical expansion of Eq. (2.86), are small, and must balance one another. Second, let us assume that there are no perturbing currents from the CRs, which implies neither growing nor damping of Alfvén waves. In this situation, Alfvén waves are still solutions of the MHD equations and, consequently, of Maxwell's equations. Thus, all other terms in Eq. (2.86) balance each other. This expression holds because we can remove all terms associated with unperturbed Alfvén waves. This leaves us with the two terms in Eq. (2.86) which have to balance one another.

Writing this equation in Cartesian coordinates yields:

$$2\omega_0\Gamma\begin{bmatrix}\delta B_x\\ \delta B_y\end{bmatrix} = kc\begin{bmatrix}-\delta j_y\\ \delta j_x\end{bmatrix}. \tag{2.88}$$

By inserting the perturbation current from Eq. (2.79), we get our final expression for the wave growth rate:

$$\Gamma = \pi\int \mathrm{d}^3p\,\frac{1-\mu^2}{2}\frac{q^2v}{p}\left[p\frac{\partial f}{\partial p} + \left(\frac{v}{v_{\mathrm{a}}} - \mu\right)\frac{\partial f}{\partial\mu}\right]\delta(k(\mu v - v_{\mathrm{a}}) \mp \Omega). \tag{2.89}$$

As for the quasilinear diffusion process, the δ-function defines a resonance condition. Here, we interpret it slightly differently and from the viewpoint of the Alfvén waves: only CRs propagating such that

$$k(\mu v - v_{\mathrm{a}}) \mp \Omega = 0 \tag{2.90}$$

can interact with the Alfvén waves of wave number k to damp or excite them. The resonance condition is fulfilled when the gyromotion of the CRs is in resonance with the Doppler-shifted wave oscillation. This justifies the name *gyroresonant streaming instability*. Whether the Alfvén waves will be damped or grow depends on the sign of the velocity-derivatives terms in the brackets.

This process belongs to the class of instabilities driven by a velocity space anisotropy of f. The growth rate might also be analysed further for a particle distribution with anisotropic temperatures to calculate the growth rate of the firehose-instability (Ichimaru, 1973).

In the next chapter, we will show that both the gyroresonant streaming instability and quasilinear diffusion need to be simultaneously taken into account in order to derive self-consistent hydrodynamical models for CR transport. In particular, we will show that Alfvén waves gain energy through the gyroresonant streaming instability at the exact same rate as CRs are losing energy by the quasilinear diffusion process. This result is expected because both processes are based on the same mutual and energy-conserving electromagnetic interaction. Yet, it is a non-trial result because the derivations for the quasilinear diffusion and the gyroresonant instability are different. They diverge after the fluctuations have been introduced in the Boltzmann-Vlasov equation in Eq. (2.15) and significant approximations have been made afterwards to derive the final expressions in Eqs. (2.68) and (2.89).

3 Cosmic-ray hydrodynamics: Alfvén-wave regulated Transport of Cosmic Rays

This chapter is based on the published paper by Thomas, T. ; Pfrommer, C.:
Monthly Notices of the Royal Astronomical Society, Volume 485, Issue 3, p.2977-3008
I presented parts of this work in my master thesis. I list the differences between the contents of my master thesis and the presented manuscript in the commented publication list.

Star formation in galaxies appears to be self-regulated by energetic feedback processes. Among the most promising agents of feedback are cosmic rays (CRs), the relativistic ion population of interstellar and intergalactic plasmas. In these environments, energetic CRs are virtually collisionless and interact via collective phenomena mediated by kinetic-scale plasma waves and large-scale magnetic fields. The enormous separation of kinetic and global astrophysical scales requires a hydrodynamic description. Here, we develop a new macroscopic theory for CR transport in the self-confinement picture, which includes CR diffusion and streaming. The interaction between CRs and electromagnetic fields of Alfvénic turbulence provides the main source of CR scattering, and causes CRs to stream along the magnetic field with the Alfvén velocity if resonant waves are sufficiently energetic. However, numerical simulations struggle to capture this effect with current transport formalisms and adopt regularization schemes to ensure numerical stability. We extend the theory by deriving an equation for the CR momentum density along the mean magnetic field and include a transport equation for the Alfvén-wave energy. We account for energy exchange of CRs and Alfvén waves via the gyroresonant instability and include other wave damping mechanisms. Using numerical simulations we demonstrate that our new theory enables stable, self-regulated CR transport. The theory is coupled to magneto-hydrodynamics, conserves the total energy and momentum, and correctly recovers previous macroscopic CR transport formalisms in the steady-state flux limit. Because it is free of tunable parameters, it holds the promise to provide predictable simulations of CR feedback in galaxy formation.

3.1 Introduction

CRs are pervasive in galaxies and galaxy clusters and likely play an active role during the formation and evolution of these systems. CRs, magnetic fields, and turbulence are observed to be in pressure equilibrium in the midplane of the Milky Way (Boulares and Cox, 1990), suggesting that CRs have an important dynamical role in maintaining the energy balance of the interstellar medium (ISM).

This equipartition could be the result of a self-regulated feedback process: provided that CR and magnetic midplane pressures are supercritical, their buoyancy force overcomes the magnetic tension of the dominant toroidal magnetic field, causing it to bend and open up (Parker, 1966; Rodrigues et al., 2016). CRs stream and diffuse ahead of the gas into the halo along these open field lines and build up a pressure gradient. Once this gradient overcomes the gravitational attraction of the disc, it accelerates the gas, thereby driving a strong galactic outflow as shown in one-dimensional magnetic flux-tube models (Breitschwerdt et al., 1991; Zirakashvili et al., 1996; Ptuskin et al., 1997; Everett et al., 2008; Samui et al., 2018) and three-dimensional simulations (Uhlig et al., 2012; Booth et al., 2013; Salem and Bryan, 2014; Pakmor et al., 2016a; Simpson et al., 2016a; Girichidis et al., 2016; Pfrommer et al., 2017b; Ruszkowski et al., 2017; Jacob et al., 2018). If the CR pressure is subcritical, the thermal gas can quickly radiate away the excess energy, thus approaching equipartition as a dynamical attractor solution.

Seemingly unrelated, at the centres of dense galaxy clusters the observed gas cooling and star formation rates are reduced to levels substantially below those expected from unimpeded cooling flows (Peterson and Fabian, 2006). Most likely, a heating process associated with radio lobes that are inflated by jets from active galactic nuclei offsets radiative cooling. Apparently, the cooling gas and nuclear activity are tightly coupled to a self-regulated feedback loop (McNamara and Nulsen, 2007). A promising heating mechanism can be provided by fast-streaming CRs, which resonantly excite Alfvén waves through the "streaming instability" (Kulsrud and Pearce, 1969). Scattering off of this wave field (partially) isotropizes these CRs in the reference frame of Alfvén waves, which causes CRs to stream down their gradient (Zweibel, 2013). Damping of these waves transfers CR energy and momentum to the thermal gas at a rate that scales with the CR pressure gradient and provides an efficient means of suppressing the cooling catastrophe in cooling core clusters (Loewenstein et al., 1991; Guo and Oh, 2008; Enßlin et al., 2011; Fujita and Ohira, 2012; Pfrommer, 2013; Jacob and Pfrommer, 2017a,c; Ehlert et al., 2018). Hence, in sharing energy and momentum with the thermal gas, CRs may play a critical role in galaxy formation and the evolution of galaxy clusters.

CRs interact with the thermal gas through particle collisions as well as through collisionless

processes. Low-energy (MeV to GeV) CRs are important for collisional ionization and heating of the interstellar medium. In particular the ability of CRs to deeply penetrate into molecular clouds (where ultra-violet and X-ray photons are absorbed) makes them prime drivers of cloud chemistry (Dalgarno, 2006; Ivlev et al., 2018; Phan et al., 2018) and responsible for the evolution of these star-forming regions. Hadronic particle interactions generate secondary decay products that emit characteristic signatures from radio to gamma-ray energies, thereby enabling studies of the spatial and spectral CR distribution.

Energetic protons with energies of a few GeV, which dominate the total CR energy density, are mostly collisionless and interact via collective phenomena mediated by the ambient magnetic field. Being charged particles, CRs are bound to follow individual magnetic fields lines, which become modified as a result of the dynamical evolution of the CR distribution. Hence, in combination with the toroidal stretching of magnetic fields due to differential rotation of galactic discs, CR-induced gas motions can twist and fold magnetic structures, thereby amplifying and shaping galactic magnetic fields via a CR-driven dynamo (Hanasz et al., 2004).

Generally, these collective, collisionless interactions can be subdivided into CR transport processes at the microscale, the mesoscale and the macroscale. While CR interactions at the microscale are modelled with kinetic theory, CR transport at the macroscale is treated in the hydrodynamic picture in which the full phase space information of CRs is condensed to a few variables that describe the system such as energy density, pressure, and number density. Interactions at the mesoscale combines elements of both descriptions and enables studies of, e.g., the structure of collisionless shocks (Caprioli and Spitkovsky, 2013). Different scientific questions select the approach that is best suited for a problem at hand. While we always seek for clarity and apply Occam's razor as a basic principle of model building, the richness of physics may force us to move elements from kinetic theory into the hydrodynamic picture to more faithfully capture the physics of CR transport on larger scales.

The kinetic picture of the underlying plasma assumes a sufficiently dense plasma that is well described by a distribution function. This is equivalent to requiring that many particles within a characteristic energy range be present on the plasma scale. Typically, problems such as the growth of kinetic instabilities and damping processes are addressed within kinetic theory. In particular, the non-resonant hybrid instability that excites right-handed circularly polarized Alfvén waves by the current of energetic protons, can potentially explain magnetic amplification and CR acceleration to (almost) PeV energies at supernova remnants (Bell, 2004). Kinetic instabilities at shocks are important for energy exchange between electrons and protons and in building up the momentum spectrum of energetic particles (Spitkovsky, 2008; Caprioli and

Spitkovsky, 2014). Thus, this approach provides a crucial input to modelling multi-frequency observations across the entire electromagnetic spectrum of supernova remnants (e.g., Morlino and Caprioli, 2012; Blasi and Amato, 2012), galaxies (Breitschwerdt et al., 2002; Recchia et al., 2016), and galaxy clusters (Brunetti and Lazarian, 2011; Pinzke et al., 2017). However, to obtain a complete (non-linear) picture of a system, the dynamics on the CR gyroscale or at least the growth time-scale of a particular instability needs to be resolved. This requirement prohibits us from directly treating kinetic effects in global simulations of astrophysical objects such as galaxies or jets of active galactic nuclei.

Hence, to model CR transport in the ISM, the circumgalactic medium (CGM) or the intracluster medium (ICM), we have to resort to a hydrodynamic prescription. Traditionally, this was done by taking the energy-weighted moment of the Fokker-Planck equation for CR transport, yielding the CR energy equation (Drury and Völk, 1981; McKenzie and Völk, 1982; Völk et al., 1984). This equation shows that CRs are transported through a combination of advection with the thermal gas as well as streaming and diffusion. In the ideal magneto-hydrodynamic (MHD) approximation, magnetic fields are flux-frozen into the thermal gas and thus advected with the flow. The collisionless CRs are bound to gyrate along magnetic field lines and are also advected alongside the moving gas. As CRs propagate along the mean field, they scatter at self-generated Alfvén waves, which causes them to stream down their gradient with a macroscopic velocity that is substantially reduced from their intrinsic relativistic speed. MHD turbulence that was driven at larger scales by energetic events and successively cascaded down in scale can also scatter CRs, redistributing their pitch angles, but conserving their energy (Zweibel, 2017). This can be described as anisotropic diffusion where the main transport is along the local direction of the magnetic field (Shalchi, 2009b).

As a closure of these approaches, CR diffusion is modelled with a prescribed coefficient that is usually taken to be constant and not coupled to the physics of turbulence, and CR streaming is always assumed to be in steady state. However, neither of these two approaches is providing the correct prescription of CR transport (Wiener et al., 2017b). Moreover, due to the non-linear property of the streaming equation, an ad-hoc regularization is applied that adds numerical diffusion to the solution (Sharma et al., 2010), questioning the results in regime of shallow gradients. Hence, these considerations reinforce the need for a novel description of CR transport that cures these weaknesses.

Recently, Jiang and Oh (2018) used an ansatz to reinterpret CR transport as a modification of radiation hydrodynamics. They showed numerically, that their resulting set of equations captures the streaming limit of CR transport while conserving the total energy and momentum.

However, in their picture, the conversion between mechanical and thermal energy mediated by CRs is in general not fully accounted for and, as we will show here, they adopt an incomplete treatment of CR scattering. In this work, we provide a first-principle derivation of such an improved CR transport scheme while emphasizing the deep connection between radiation and CR hydrodynamics throughout this work.

This paper is organized as follows. In Section 3.2, we show the complete set of MHD and CR transport equations as a reference and derive those in the remainder of this work. In Section 3.3, we use the Eddington approximation for the two-moment approximation of CR transport. In Section 3.4, we derive equations accounting for the energy and pitch-angle scattering of CRs by Alfvénic turbulence. In Section 3.5, we derive transport equations for Alfvén waves, which are coupled (i) to the gas via damping mechanisms and (ii) to the CR population by the streaming instability. In Section 3.6, we couple the forces and work done by the CR-Alfvénic subsystem to the MHD equations and address energy and momentum conservation in the Newtonian limit. In Section 3.7 we show that the presented theory contains the classical streaming-diffusion equation of CR transport in the steady-state flux limit and discuss spectral extensions of the new theory. We show a numerical demonstration of our coupled transport equations for the energy densities contained in CRs and Alfvén waves in Section 3.8 and compare our theory to other approaches in the literature. We conclude in Section 3.9. In Appendix 3.10, we show how pure CR diffusion emerges mathematically by neglecting the electric fields of Alfvén waves, thereby emphasizing the need of CR streaming for a full description of CR transport. We present an alternative derivation of the scattering terms in Appendix 3.11 that clarifies the approximation used to derive our CR transport equations. In Appendices 3.12 and 3.13, we present semi-relativistic derivations of the Vlasov and CR hydrodynamical equations using a covariant formalism. In Appendix 3.14, we derive the lab-frame equations for CR hydrodynamics expressed in comoving quantities and discuss energy and momentum conservation. We denote the frame that is comoving with the gas as the comoving frame and use the Heaviside system of units throughout this paper.

3.2 Equations of CR Hydrodynamics

The equations for ideal MHD coupled to non-thermal CR and Alfvén wave populations are given by:

$$\frac{\partial \rho}{\partial t} + \boldsymbol{\nabla} \cdot (\rho \boldsymbol{u}) = 0, \tag{3.1}$$

$$\frac{\partial \rho \boldsymbol{u}}{\partial t} + \boldsymbol{\nabla} \cdot (\rho \boldsymbol{u}\boldsymbol{u} + P\mathbf{1} - \boldsymbol{B}\boldsymbol{B}) = \boldsymbol{g}, \tag{3.2}$$

$$\frac{\partial \boldsymbol{B}}{\partial t} + \boldsymbol{\nabla} \cdot (\boldsymbol{B}\boldsymbol{u} - \boldsymbol{u}\boldsymbol{B}) = 0, \tag{3.3}$$

$$\frac{\partial \varepsilon}{\partial t} + \boldsymbol{\nabla} \cdot [\boldsymbol{u}(\varepsilon + P) - (\boldsymbol{u} \cdot \boldsymbol{B})\boldsymbol{B}] = \boldsymbol{u} \cdot \boldsymbol{g} + Q_+ + Q_-, \tag{3.4}$$

where $\mathbf{1}$ is the unit matrix and $\boldsymbol{a}\boldsymbol{b}$ is the dyadic product of vectors $\boldsymbol{a}$ and $\boldsymbol{b}$. Gas density, mean velocity, and the local mean magnetic field are denoted by ρ, $\boldsymbol{u}$ and $\boldsymbol{B}$. The total force exerted by CRs, Alfvén waves and the thermal gas is denoted by $\boldsymbol{g}$ and will be defined below. The MHD pressure and energy density are given by

$$P = P_{\rm th} + \frac{\boldsymbol{B}^2}{2}, \tag{3.5}$$

$$\varepsilon = \frac{\rho \boldsymbol{u}^2}{2} + \varepsilon_{\rm th} + \varepsilon_B, \tag{3.6}$$

where $P_{\rm th}$ is the thermal pressure, $\varepsilon_{\rm th}$ and $\varepsilon_B = \boldsymbol{B}^2/2$ are the thermal and magnetic energy densities, respectively. $Q_\pm$ are the source terms of thermal energy due to Alfvén wave energy losses as detailed in Section 3.5. All pressures and the respective energy densities are related by equations of states:

$$P_{\rm th} = (\gamma_{\rm th} - 1)\varepsilon_{\rm th}, \qquad \gamma_{\rm th} = \frac{5}{3}, \tag{3.7}$$

$$P_{\rm cr} = (\gamma_{\rm cr} - 1)\varepsilon_{\rm cr}, \qquad \gamma_{\rm cr} = \frac{4}{3}, \tag{3.8}$$

$$P_{\rm a,\pm} = (\gamma_{\rm a} - 1)\varepsilon_{\rm a,\pm}, \qquad \gamma_{\rm a} = \frac{3}{2}, \tag{3.9}$$

where $P_{\rm cr}$ is the CR pressure and $P_{\rm a,\pm}$ are the ponderomotive pressures due to presence of Alfvén waves on scales that are resonant with the gyroradii of (pressure-carrying GeV to TeV) CRs. This enables a well-defined separation of scales in comparison to the large-scale magnetic field.

We augment these evolution equations of MHD quantities by a CR-Alfvénic subsystem, which encompasses the hydrodynamics of CR transport that is mediated by Alfvén waves.

As we will show in this work, this subsystem describes the transport of CR energy density ($\varepsilon_{\rm cr}$), CR momentum density along the mean magnetic field ($f_{\rm cr}/c^2$), where $f_{\rm cr}$ denotes the CR energy flux density, and Alfvén-wave energy density ($\varepsilon_{\rm a,\pm}$), where the $\pm$ signs denote co- and counter-propagating waves with respect to the large-scale magnetic field. Note that $\varepsilon_{\rm cr}$ and $f_{\rm cr}$ are measured with respect to the comoving frame while $\varepsilon_{\rm a,\pm}$ is measured in the lab frame:

$$\frac{\partial \varepsilon_{\rm cr}}{\partial t} + \boldsymbol{\nabla}\cdot[\boldsymbol{u}(\varepsilon_{\rm cr}+P_{\rm cr}) + \boldsymbol{b} f_{\rm cr}] = \boldsymbol{u}\cdot\boldsymbol{\nabla}P_{\rm cr} - \boldsymbol{v}_{\rm a}\cdot\boldsymbol{g}_{\rm gri,+} + \boldsymbol{v}_{\rm a}\cdot\boldsymbol{g}_{\rm gri,-}, \tag{3.10}$$

$$\frac{\partial (f_{\rm cr}/c^2)}{\partial t} + \boldsymbol{\nabla}\cdot\left(\boldsymbol{u} f_{\rm cr}/c^2\right) + \boldsymbol{b}\cdot\boldsymbol{\nabla}P_{\rm cr} = -(\boldsymbol{b}\cdot\boldsymbol{\nabla}\boldsymbol{u})\cdot(\boldsymbol{b} f_{\rm cr}/c^2) - \boldsymbol{b}\cdot\left(\boldsymbol{g}_{\rm gri,+} + \boldsymbol{g}_{\rm gri,-}\right), \tag{3.11}$$

$$\frac{\partial \varepsilon_{\rm a,\pm}}{\partial t} + \boldsymbol{\nabla}\cdot[\boldsymbol{u}(\varepsilon_{\rm a,\pm}+P_{\rm a,\pm}) \pm v_{\rm a}\boldsymbol{b}\varepsilon_{\rm a,\pm}] = \boldsymbol{u}\cdot\boldsymbol{\nabla}P_{\rm a,\pm} \pm \boldsymbol{v}_{\rm a}\cdot\boldsymbol{g}_{\rm gri,\pm} - Q_{\pm}. \tag{3.12}$$

Here, c is the light speed (corresponding to *intrinsic* CR velocity in the ultra-relativistic approximation), $\boldsymbol{v}_{\rm a} = \boldsymbol{B}/\sqrt{\rho}$ is the Alfvén velocity, $B = \sqrt{\boldsymbol{B}^2}$ is the magnetic field strength, and $\boldsymbol{b} = \boldsymbol{B}/B$ the direction of the mean magnetic field. The exerted forces between CRs, Alfvén waves and the thermal gas are given by:

$$\boldsymbol{g} = \boldsymbol{g}_{\rm Lorentz} + \boldsymbol{g}_{\rm ponder} + \boldsymbol{g}_{\rm gri,+} + \boldsymbol{g}_{\rm gri,-}, \tag{3.13}$$

$$\boldsymbol{g}_{\rm Lorentz} = -\boldsymbol{\nabla}_{\perp}P_{\rm cr}, \tag{3.14}$$

$$\boldsymbol{g}_{\rm ponder} = -\boldsymbol{\nabla}(P_{\rm a,+} + P_{\rm a,-}), \tag{3.15}$$

$$\boldsymbol{g}_{\rm gri,\pm} = \frac{\boldsymbol{b}}{3K_{\pm}}[f_{\rm cr} \mp v_{\rm a}(\varepsilon_{\rm cr} + P_{\rm cr})], \tag{3.16}$$

where $\boldsymbol{g}_{\rm Lorentz}$ is the Lorentz force due the large-scale magnetic field, $\boldsymbol{g}_{\rm ponder}$ is the ponderomotive force, $\boldsymbol{g}_{\rm gri,\pm}$ are the Lorentz forces due to small-scale magnetic field fluctuations of Alfvén waves that affect CRs, and the perpendicular gradient is given by $\boldsymbol{\nabla}_{\perp} = (\mathbf{1} - \boldsymbol{bb})\cdot\boldsymbol{\nabla}$.

The CR energy equation (3.10) contains source terms on the right-hand side that arise as a result of adiabatic changes and resonant scattering off of Alfvén waves via the gyroresonant instability (gri). We refrain from including additional CR source and sink terms, as we focus solely on transport processes of CRs. Equations (3.10) and (3.11) fully describe CR diffusion and CR streaming in the self-confinement picture. The right-hand side of the Alfvén-wave equation (3.12) shows loss terms $Q_{\pm}$ due to damping processes.

The CR-Alfvénic subsystem is closed by the grey approximation for the CR diffusion coefficient:

$$\frac{1}{\kappa_\pm} = \frac{9\pi}{8}\frac{\Omega}{c^2}\frac{\varepsilon_{\mathrm{a},\pm}/2}{\varepsilon_B}\left(1 + \frac{2v_\mathrm{a}^2}{c^2}\right). \tag{3.17}$$

Here, $\Omega = ZeB/(\gamma mc)$ is the relativistic gyrofrequency of a CR population with charge Ze and characteristic Lorentz factor γ, e is the elementary charge, and m is the particle rest mass. This equation links the transported CR energy density directly to the Alfvénic turbulence, described by its energy density $\varepsilon_{\mathrm{a},\pm}$.

The total pressure and energy density of thermal gas, magnetic fields, CRs, and Alfvén waves are given by

$$P_\mathrm{tot} = P_\mathrm{th} + \frac{\boldsymbol{B}^2}{2} + P_\mathrm{cr} + P_{\mathrm{a},+} + P_{\mathrm{a},-}, \tag{3.18}$$

$$\varepsilon_\mathrm{tot} = \frac{\rho\boldsymbol{u}^2}{2} + \varepsilon_\mathrm{th} + \varepsilon_B + \varepsilon_\mathrm{cr} + \varepsilon_{\mathrm{a},+} + \varepsilon_{\mathrm{a},-}. \tag{3.19}$$

Even in the absence of explicit gain and loss terms, it is not possible to conserve the total energy and momentum in terms of the preceding quantities in every frame. Only the total energy and momentum as measured in an inertial frame (i.e., the 'lab' frame) can be manifestly conserved. The CR energy and momentum densities defined above are measured in the comoving frame and their evolution equations are expressed in the semi-relativistic limit. This semi-relativistic limit prohibits a meaningful Lorentz transformation between both frames so that contributions from pseudo forces do not vanish after a transformation from the comoving frame into the lab frame. Consequently, total momentum and energy are altered by these pseudo forces even in lab frame. However, if CRs move with non-relativistic bulk velocities, their inertia is negligible and no formal degeneracy between the two frames occurs. In addition, the erroneously transformed pseudo forces vanish. In this case, the total energy $E_\mathrm{tot} = \int \mathrm{d}^3x\, \varepsilon_\mathrm{tot}$ (where $\boldsymbol{x}$ denotes the spatial coordinate) is a conserved quantity so that

$$\frac{\partial\varepsilon_\mathrm{tot}}{\partial t} + \boldsymbol{\nabla}\cdot[\boldsymbol{u}(\varepsilon_\mathrm{tot} + P_\mathrm{tot}) + f_\mathrm{tot}\boldsymbol{b}] = 0, \tag{3.20}$$

where the total energy flux density along the magnetic field lines is given by

$$f_\mathrm{tot} = f_\mathrm{cr} + v_\mathrm{a}\varepsilon_{\mathrm{a},+} - v_\mathrm{a}\varepsilon_{\mathrm{a},-} - B\,(\boldsymbol{u}\cdot\boldsymbol{B}). \tag{3.21}$$

Likewise, the total momentum is solely given by the mean gas momentum

$$\boldsymbol{m}_\mathrm{tot} = \rho\boldsymbol{u}, \tag{3.22}$$

and is a conserved quantity, which follows from the conservation law

$$\frac{\partial \boldsymbol{m}_{\rm tot}}{\partial t} + \boldsymbol{\nabla} \cdot (\boldsymbol{u}\boldsymbol{m}_{\rm tot} + P_{\rm tot}\mathbf{1} - \boldsymbol{B}\boldsymbol{B}) = 0. \tag{3.23}$$

There is no contribution by either large-scale or small-scale electromagnetic fields because their momenta are assumed to be vanishingly small in the non-relativistic MHD approximation.

3.3 CR Phase Space Dynamics

After summarizing the full set of equations for CR hydrodynamics, we will now derive them. Starting with the Vlasov equation, we discuss the Eddington approximation to the transport of the CR distribution function. In the next step, we will derive the CR fluid equations.

3.3.1 Focused CR transport equation

The CR distribution lives in phase space that is spanned by the momentum and spatial coordinates $\boldsymbol{p}$ and $\boldsymbol{x}$, respectively, and is defined as

$$f \equiv f(\boldsymbol{x}, \boldsymbol{p}, t) = \frac{d^6 N}{\mathrm{d}x^3\, \mathrm{d}p^3}. \tag{3.24}$$

It evolves according to the comoving Vlasov equation in the semi-relativistic limit,

$$\frac{\partial f}{\partial t} + (\boldsymbol{u} + \boldsymbol{v}) \cdot \boldsymbol{\nabla}_{\boldsymbol{x}} f + \boldsymbol{F} \cdot \boldsymbol{\nabla}_{\boldsymbol{p}} f = 0, \tag{3.25}$$

where the mean gas velocity $\boldsymbol{u}$ and time t are measured in the lab frame, the CR velocity v and momentum p are measured in the comoving frame, and $\boldsymbol{F}$ denotes the total force. The description in the comoving frame introduces pseudo forces (denoted by $\boldsymbol{F}_{\rm pseudo}$) since the momentum measured by an observer in the comoving frame changes for each change of the reference velocity $\boldsymbol{u}$. Furthermore, CRs as charged particles are subject to the Lorentz force, which we split into contributions by large-scale and small-scale electromagnetic fields, $\boldsymbol{F}_{\rm macro}$ and $\boldsymbol{F}_{\rm micro}$, respectively:

$$\boldsymbol{F} = \boldsymbol{F}_{\rm pseudo} + \boldsymbol{F}_{\rm macro} + \boldsymbol{F}_{\rm micro} \tag{3.26}$$

$$= -m\frac{\mathrm{d}\boldsymbol{u}}{\mathrm{d}t} - (\boldsymbol{p} \cdot \boldsymbol{\nabla})\boldsymbol{u} + Ze\frac{\boldsymbol{v} \times \boldsymbol{B}}{c} + Ze\left(\delta\boldsymbol{E} + \frac{\boldsymbol{v} \times \delta\boldsymbol{B}}{c}\right), \tag{3.27}$$

see equation (5.18) in Zank (2014) or Appendix 3.12 for a covariant derivation. Here, the Lagrangian time derivative is denoted by $\mathrm{d}/\mathrm{d}t = \partial/\partial t + \boldsymbol{u} \cdot \boldsymbol{\nabla}$ and $\delta\boldsymbol{E}$ and $\delta\boldsymbol{B}$ are electric and magnetic fluctuations, respectively.

The pseudo forces appear in the Vlasov equation because $\boldsymbol{u}$ acts as a reference velocity linking lab and comoving velocities and is itself a dynamical quantity. Both pseudo forces in equation (3.27) have slightly different interpretations: the first pseudo force is the result of an acceleration of the comoving frame itself. A CR at rest in the lab frame is perceived to be accelerated from the point of view of a comoving observer. The second pseudo force is due to spatial inhomogeneities of the flow field. If the CR moves in the lab frame, then a change of its position also causes the reference velocity to change because the comoving frame is now linked by a different velocity to the lab frame. From the perspective of a comoving observer this change in comoving CR velocity is perceived as an acceleration. Dimensional analysis suggests that the first pseudo force corresponds to an acceleration that is smaller by a factor of $O(u/v)$ in comparison to the second pseudo force (i.e., $O(u/c)$ for relativistic CRs). In the following, we thus neglect the contribution from the first pseudo force.

The small-scale field fluctuations are provided by MHD waves, in particularly by Alfvén waves, which are generated by the CR-driven gyroresonant instability. Since these waves are the source of CR scattering, we denote their contribution to the Vlasov equation as:

$$\left.\frac{\partial f}{\partial t}\right|_{\text{scatt}} = \boldsymbol{F}_{\text{micro}} \cdot \boldsymbol{\nabla}_p f. \tag{3.28}$$

We leave this term unspecified for now and return to it in Section 3.4.

CRs gyrate around large-scale magnetic fields on spatial and temporal scales that are small in comparison to any MHD scale. We can thus project out the full phase dynamics of CRs by taking the gyroaverage. Calculating this average of equation (3.25) results in the so called *focused* transport equation, which describes the gyroaveraged evolution of CRs. While Skilling (1971) performs this calculation in the Alfvén-wave frame, $\boldsymbol{u} + v_{\text{a}}\boldsymbol{b}$, the identical result is obtained in the frame comoving with the mean gas velocity $\boldsymbol{u}$ (Zank, 2014). Using the latter result of the focused transport equation, we arrive at:

$$\begin{aligned}
&\frac{\partial f}{\partial t} + (\boldsymbol{u} + \mu v \boldsymbol{b}) \cdot \boldsymbol{\nabla} f \\
&\quad + \left[\frac{1-3\mu^2}{2}(\boldsymbol{b}\cdot\boldsymbol{\nabla}\boldsymbol{u}\cdot\boldsymbol{b}) - \frac{1-\mu^2}{2}\boldsymbol{\nabla}\cdot\boldsymbol{u}\right] p\frac{\partial f}{\partial p} \\
&\quad + \left[v\boldsymbol{\nabla}\cdot\boldsymbol{b} + \mu\boldsymbol{\nabla}\cdot\boldsymbol{u} - 3\mu(\boldsymbol{b}\cdot\boldsymbol{\nabla}\boldsymbol{u}\cdot\boldsymbol{b})\right]\frac{1-\mu^2}{2}\frac{\partial f}{\partial \mu} = \left.\frac{\partial f}{\partial t}\right|_{\text{scatt}}.
\end{aligned} \tag{3.29}$$

Here, we use the conventional mixed coordinate system for phase space. While the ambient gas velocity $\boldsymbol{u}$ and the direction of the large scale magnetic field $\boldsymbol{b} = \boldsymbol{B}/B$ are measured in the lab frame, the particle velocity v, momentum p and the cosine of the pitch angle $\mu = \boldsymbol{v}\cdot\boldsymbol{b}/v$ are given with respect to the comoving frame. A general discussion of the adiabatic terms and other pseudo forces of this equation is given in le Roux and Webb (2012).

The complexity of transport terms in equation (3.29) alone precludes a general solution and we have to resort to approximations. In the following, we use a procedure which preserves the large-scale dynamics of the entire distribution in terms of thermodynamical quantities. To this end, we take moments of the momentum space variables μ and p and describe the energy content in CRs and their transport properties in terms of an energy flux that is coupled to the Alfvén-wave dynamics.

3.3.2 Eddington approximation

A similarly complex problem is the radiative transfer (RT) equation with its two phase space coordinates photon propagation direction $\boldsymbol{n}$ and photon frequency. Powerful methods describing the transport of comoving radiation energy were pioneered by Mihalas and Weibel Mihalas (1984) and Castor (2007).

In the case of an optically thick medium, the Eddington approximation is a valuable tool to model the transport of radiation energy. In this approximation, the RT equation is expanded up to first order in $\boldsymbol{n}$ while assuming that the contribution from higher-order moments of the radiation distribution can be neglected. This assumption is justified in the optically thick medium because rapid scattering quickly damps any anisotropy.

A more accurate approximation of RT problems with a preferred direction is the assumption of plane-parallel or slab geometry. In this case, all quantities of the medium are taken to be constant on planes perpendicular to this particular direction $\boldsymbol{n}$. The RT equation can then be expressed in terms of the coordinate along $\boldsymbol{n}$ and the direction cosine μ between the orientation of a ray and $\boldsymbol{n}$. In this setting, the Eddington approximation for the radiation intensity I simplifies to

$$I(\mu) = I_0 + I_1\mu, \tag{3.30}$$

where we suppress the spatial dependence of the first- and second-order moments I_0 and I_1 in our notation. However, this simplified slab geometry is of limited use because it often does not apply to astrophysical problems at hand.

This is different for CR transport where the mean magnetic field is a priori known as a preferred direction of (gyrophase averaged) motion. Thus, CR transport is locally akin to plane-parallel RT. To model CR transport with such an RT methodology, we have to account for the spatially and temporarily varying plane and translate the corresponding terminologies.

The direction cosine μ in RT is equivalent to the pitch-angle cosine μ in CR transport. Thus, we expand equation (3.29) in moments of the pitch angle. This expansion has a long history in

CR transport and is frequently revisited (see e.g. Klimas and Sandri, 1971; Earl, 1973; Webb, 1987; Zank et al., 2000; Snodin et al., 2006; Litvinenko and Noble, 2013; Rodrigues et al., 2018). For completeness, we recall the derivation to introduce our notation.

In general, any complete basis of functions could be used to expand f in pitch-angle. Particularly useful are the Legendre polynomials, because of their geometric relationship to the pitch angle.[1] Carrying out the complete expansion using these basis functions results in an infinite set of coupled differential equations. Even though this system captures the full dynamics of equation (3.29), it is not practicable because of the high degree of coupling between the transport terms (Zank et al., 2000).

Similar to RT, we circumvent problems arising from this coupling by truncating the expansion. Because CRs are subject to rapid scattering, anisotropies of their distribution are efficiently damped. We can thus assume that all moments larger than the first are negligibly small and proceed with

$$f = f_0 + 3\mu f_1, \tag{3.31}$$

while requiring that $f_0 \gg f_1$. Otherwise, higher-order moments could become dynamically important as a result of coupling and the truncated expansion would not converge. This quasi-linear approximation is valid in cases of self-confined CR transport, where sufficiently energetic Alfvén waves are generated by CRs. We will explicitly show this later on in Section 3.4.2.

Inserting the expansion (3.31) into equation (3.29) and taking the pitch-angle average results in

$$\frac{\partial f_0}{\partial t} + \boldsymbol{u}\cdot\boldsymbol{\nabla} f_0 + \boldsymbol{\nabla}\cdot(v\boldsymbol{b} f_1) - \frac{1}{3}(\boldsymbol{\nabla}\cdot\boldsymbol{u})p\frac{\partial f_0}{\partial p} = \left.\frac{\partial f_0}{\partial t}\right|_{\text{scatt}}. \tag{3.32}$$

Analogously, taking the μ-moment of equation (3.29) yields:

$$\begin{aligned}\frac{\partial f_1}{\partial t} + \frac{v}{3}\boldsymbol{b}\cdot\boldsymbol{\nabla} f_0 + \boldsymbol{u}\cdot\boldsymbol{\nabla} f_1 + \left[-\frac{2}{5}(\boldsymbol{b}\cdot\boldsymbol{\nabla}\boldsymbol{u}\cdot\boldsymbol{b}) - \frac{1}{5}\boldsymbol{\nabla}\cdot\boldsymbol{u}\right]p\frac{\partial f_1}{\partial p} \\ + \left[\frac{1}{5}\boldsymbol{\nabla}\cdot\boldsymbol{u} - \frac{3}{5}(\boldsymbol{b}\cdot\nabla\boldsymbol{u}\cdot\boldsymbol{b})\right]f_1 = \left.\frac{\partial f_1}{\partial t}\right|_{\text{scatt}}.\end{aligned} \tag{3.33}$$

The scattering terms on the right-hand side of equations (3.32) and (3.33) are calculated in Section 3.4.2.

A more complex expansion would use eigenfunctions of the scattering operator with a pitch-angle dependent scattering rate $\nu(\mu)$. These eigenfunctions exist and form a orthogonal set of functions by virtue of the Sturm-Liouville theory. In general, this would yield a different set of

[1] The Legendre polynomials are eigenfunctions of the pitch-angle Laplace operator $\partial_t f|_{\text{scatt}} = \partial_\mu[\nu(1-\mu^2)/2\,\partial_\mu f]$. This operator describes pitch-angle diffusion and ν denotes the scattering frequency. Note that this simple Laplacian resembles the actual scattering operator as discussed in equation (3.51).

basis functions that differ from the Legendre polynomials. While this approach would render pitch-angle averaging of the scattering coefficient unnecessary, this more rigorous treatment would obfuscate the derivation and make our results inherently dependent on the actual form of $\nu(\mu)$. Since we truncate the expansion after the first order and assume small anisotropies, we do not expect any change of the presented theory. Hence, our choice of a pitch-angle-averaged scattering rate represents a compromise between physical clarity and mathematical rigour.

3.3.3 Fluid equations

The CR energy density is given by

$$\varepsilon_{\rm cr} = \int \mathrm{d}^3 p \; E(p) f(p,\mu) = \int_0^\infty \mathrm{d}p \, 4\pi p^2 E(p) f_0(p). \tag{3.34}$$

where $E(p) = \sqrt{p^2c^2 + m^2c^4}$ is the total energy of CR particles. Combining the truncation in the pitch-angle expansion and assuming approximate gyrotropy of the CR distribution yields an isotropic CR pressure tensor:

$$\mathbf{P}_{\rm cr} = \int \mathrm{d}^3 p \; \boldsymbol{vp} f(p,\mu) = \int \mathrm{d}^3 p \; \boldsymbol{vp} f_0(p) = P_{\rm cr}\mathbf{1}. \tag{3.35}$$

where the isotropic CR pressure is given by:

$$P_{\rm cr} = \int \mathrm{d}^3 p \; \frac{pv}{3} f(p,\mu) = \int_0^\infty \mathrm{d}p \, 4\pi p^2 \frac{pv}{3} f_0(p). \tag{3.36}$$

Only the isotropic component f_0 of the CR distribution contributes to both quantities because any anisotropy vanishes as a result of pitch-angle integration and higher moments are neglected in our approximation. Pressure and energy density are coupled via the equation of state

$$P_{\rm cr} = (\gamma_{\rm cr} - 1)\varepsilon_{\rm cr}, \tag{3.37}$$

where the adiabatic index $\gamma_{\rm cr} = 4/3$ holds in the ultra-relativistic regime that we are focusing on.

Similarly, we define the CR energy flux density ($\boldsymbol{f}_{\rm cr}$) and the CR pressure flux ($\boldsymbol{K}_{\rm cr}$):

$$\boldsymbol{f}_{\rm cr} = c^2 \int \mathrm{d}^3 p \, \boldsymbol{p} f(p,\mu) = \int \mathrm{d}^3 p \, E(p) \boldsymbol{v} f(p,\mu), \tag{3.38}$$

$$\boldsymbol{K}_{\rm cr} = \int \mathrm{d}^3 p \, \frac{pv}{3} \boldsymbol{v} f(p,\mu). \tag{3.39}$$

Due to the assumed gyrotropy, both vectors point along the mean magnetic field. This allows us to use the magnitude of $\boldsymbol{f}_{\rm cr}$ and $\boldsymbol{K}_{\rm cr}$ instead of vector quantities to track the energy flux density

and pressure anisotropy. We define

$$f_{\rm cr} = \boldsymbol{b} \cdot \boldsymbol{f}_{\rm cr} = \int_0^\infty \mathrm{d}p\, 4\pi p^2 E(p) v f_1(p), \tag{3.40}$$

$$K_{\rm cr} = \boldsymbol{b} \cdot \boldsymbol{K}_{\rm cr} = \int_0^\infty \mathrm{d}p\, 4\pi p^2 \frac{pv}{3} v f_1(p), \tag{3.41}$$

where we adopted the truncation in the pitch-angle expansion in the last step. Algebraically, the same equation of state holds as for the CR energy density and pressure:

$$K_{\rm cr} = (\gamma_{\rm cr} - 1) f_{\rm cr}. \tag{3.42}$$

The interpretation of $f_{\rm cr}$ becomes apparent after multiplying equation (3.32) by $E(p)$ and successively integrating the equation over momentum space, which yields

$$\frac{\partial \varepsilon_{\rm cr}}{\partial t} + \boldsymbol{\nabla} \cdot (\boldsymbol{u}(\varepsilon_{\rm cr} + P_{\rm cr}) + \boldsymbol{b} f_{\rm cr}) = \boldsymbol{u} \cdot \boldsymbol{\nabla} P_{\rm cr} + \left.\frac{\partial \varepsilon_{\rm cr}}{\partial t}\right|_{\rm scatt}. \tag{3.43}$$

Hence, $f_{\rm cr}$ is the flux density of CR energy along the magnetic field. By analogy, $K_{\rm cr}$ is the corresponding (anisotropic) flux of CR pressure. The interpretation of the remaining terms in equation (3.43) is straightforward: the CR energy density is advected with the gas at velocity $\boldsymbol{u}$ and subject to adiabatic changes.

We derive the transport equation for the flux density of CR energy, $f_{\rm cr}$, in the ultra-relativistic limit ($v \to c$) and show in Section 3.7.2 how to generalize this simplification to account for the transport of CR energy across the full momentum spectrum. Multiplying equation (3.33) by $vE(p)$ and integrating over momentum space yields

$$\frac{\partial f_{\rm cr}}{\partial t} + \boldsymbol{\nabla} \cdot (\boldsymbol{u} f_{\rm cr}) + \frac{c^2}{3} \boldsymbol{b} \cdot \nabla \varepsilon_{\rm cr} = -(\boldsymbol{b} \cdot \boldsymbol{\nabla} \boldsymbol{u}) \cdot (\boldsymbol{b} f_{\rm cr}) + \left.\frac{\partial f_{\rm cr}}{\partial t}\right|_{\rm scatt}. \tag{3.44}$$

Here, we use equation (3.42) to cast the result in this compact form. The third term on the left-hand side corresponds to the Eddington term in RT. However, it differs from its original appearance since it is projected onto the magnetic field that guides the anisotropic CR transport. This term can be interpreted as a source term: any spatial anisotropy as manifested by a gradient in $\varepsilon_{\rm cr}$ gives rise to a change of the local anisotropy and hence to a flux of CR energy. The first term on the right-hand side accounts for the change of the local direction of reference and is thus equivalent to a pseudo force term. This is explicitly demonstrated by deriving the evolution equations (3.43) and (3.44) for $\varepsilon_{\rm cr}$ and $f_{\rm cr}$ in the semi-relativistic limit of the fully covariant conservation equations in Appendix 3.13.

Both equations fully describe the evolution of $\varepsilon_{\rm cr}$ and $f_{\rm cr}$ in our chosen geometry, i.e. along the local direction of the magnetic field. However, these equations are incomplete without specifying the scattering terms on the right-hand side.

3.4 CR scattering by magnetic turbulence

In this section, we compute the scattering terms for the CR energy density and flux density while accounting for the Fokker-Planck coefficients of pitch-angle and momentum diffusion.

3.4.1 Pitch-angle scattering

In our derivation so far, we adopted the essential assumption of rapid CR scattering with Alfvén waves. In general this interaction is described by a non-linear stochastic process. If the magnetic perturbations δB in the magnetic turbulence are small, $\delta B/B \sim 10^{-3}$ or less, this stochastic scattering process can be simplified and treated analytically. This is conventionally adopted within quasi-linear theory (QLT), where Boltzmann's and Maxwell's equation are evaluated up to linear order (Kulsrud, 2004).

The wave-particle scattering can be provided by self-generated Alfvén waves through the gyroresonant instability (Kulsrud and Pearce, 1969): any residual anisotropy of the CR distribution can excite resonant Alfvén waves as a collective interaction. In turn, these Alfvén waves scatter wave-generating CRs in pitch angle, eventually leading to (partial) isotropization of the distribution function as we will see. This mechanism is thought to be the principle contributor to all scattering processes and affects CRs at low to intermediate energies ($E \lesssim 200$ GeV, Lazarian and Beresnyak, 2006).

CRs scatter resonantly off of Alfvén waves when, in the wave frame, they gyrate around the mean magnetic field in the same direction as the magnetic field of the circularly polarized Alfvén waves. Formally, this requirement is captured by the resonance condition:

$$\omega - k_{\parallel} v \mu + \sigma \Omega = 0, \qquad \sigma \in \{+1, -1\} \tag{3.45}$$

where ω is the wave frequency of the wave, $\sigma = +1$ if CRs scatter with a right-hand polarized wave, and $\sigma = -1$ for scattering with a left-hand polarized wave. Provided that the dielectric contribution to the dispersion relation of Alfvén waves is small, the wave frequency is given by

$$\omega = \begin{cases} +k_{\parallel} v_{\mathrm{a}} & \text{for co-propagating waves, and} \\ -k_{\parallel} v_{\mathrm{a}} & \text{for counter-propagating waves.} \end{cases} \tag{3.46}$$

A CR particle can always interact with two types of Alfvén waves: if the CR co-propagates with the wave, the mode needs to be right-handedly polarized, if it counter-propagates, the wave mode needs to be left-handedly polarized. From now on, we identify $k \equiv k_{\parallel}$, i.e., we drop the subscript on the wave number but retain its meaning. Combining the dispersion relation (3.46)

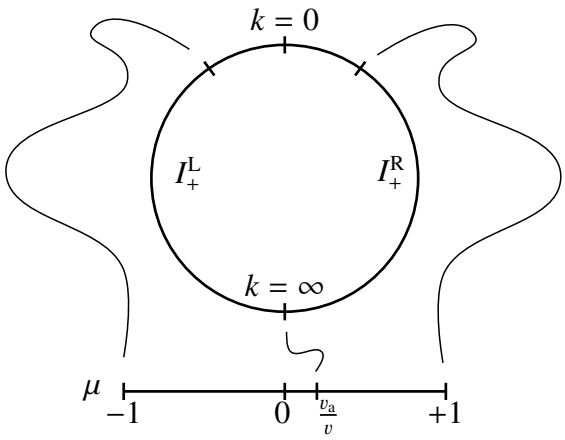

Figure 3.1: The resonance condition for co-propagating Alfvén waves. For any given μ there is only one resonant wave polarization state of left-(L) or right-(R) handedness. At $\mu = v_\mathrm{a}/v$ the resonant wave number $k_{\mathrm{res},+}$ becomes infinite and switches sign. This corresponds to a pitch angle of 90° in the wave frame. By moving the pitch angle across this point, the type of wave polarization state that a CR can resonate with also changes. Thus, the point $k = \infty$ connects both wave spectra in terms of their resonant property of CR scattering. This connection enables us to compactify k-space to a circle onto which the μ-axis can be mapped (via an Alexandroff compactification).

and the resonance condition (3.45), we can derive a wave number for CRs that resonantly interact with Alfvén waves:

$$k_{\mathrm{res},\pm} = \frac{\Omega}{\mu v \mp v_\mathrm{a}}, \tag{3.47}$$

where we suppress the polarization sign that we encapsulate in the next definition: the energy contained in waves at this wave number is given by the resonant wave power spectrum:

$$R_\pm(k_{\mathrm{res},\pm}) = I_\pm^{\mathrm{L}}(-k_{\mathrm{res},\pm}) + I_\pm^{\mathrm{R}}(k_{\mathrm{res},\pm}). \tag{3.48}$$

Here, $I_\pm^{\mathrm{L,R}}$ are the intensities of co-/counter-propagating Alfvén waves of each polarization state. The resonant wave intensity $I_\pm^{\mathrm{L,R}}(k_{\mathrm{res},\pm}) = 0$ for negative arguments, $k_{\mathrm{res},\pm} < 0$. In Fig. 3.1, we illustrate this definition together with the resonance condition. Through this definition $R_\pm$ identifies the correct polarization state of Alfvén waves that are resonant with a particular wave number $k_{\mathrm{res},\pm}$ of our CR particle.

We define a total wave power spectrum that contains all power carried by co- and counter-propagating waves:

$$E_\pm(k) = I_\pm^{\mathrm{L}}(k) + I_\pm^{\mathrm{R}}(k). \tag{3.49}$$

This enables us to define the total Alfvén wave energy density:

$$\varepsilon_{\mathrm{a},\pm} = \int_0^\infty \mathrm{d}k\, E_\pm(k). \tag{3.50}$$

Because Alfvén waves are purely magnetic perturbations, there are no electric fields in their own frames. Hence, the interaction between Alfvén waves and CRs preserves their kinetic energies but changes their pitch angles. Mathematically, this scattering can be described as a diffusion process in phase space (for the general case, see Schlickeiser (1989); and Teufel and Schlickeiser (2002) for our specific case). Thus, we have for pure pitch-angle scattering (Skilling, 1971):

$$\left.\frac{\partial f}{\partial t}\right|_{\mathrm{scatt,wave}} = \frac{\partial}{\partial \mu}\left(\frac{1-\mu^2}{2}\nu(p,\mu)\frac{\partial f}{\partial \mu}\right)\bigg|_{\mathrm{wave}} \tag{3.51}$$

where time and pitch angle derivatives have to be evaluated in the wave frame. The scattering frequencies for forward and backward propagating Alfvén waves are given by Schlickeiser (1989):

$$\nu_\pm(p,\mu) = \pi\Omega\frac{|k_{\mathrm{res},\pm}|\,R_\pm(k_{\mathrm{res},\pm})}{\varepsilon_B}. \tag{3.52}$$

Pitch-angle scattering thus damps the CR anisotropy in the wave frame.

In the comoving frame, propagating waves excite magnetic and electric fields. Accordingly, a scattering event implies an energy transfer between CRs and waves. Schlickeiser (1989) accounted for both pitch-angle and momentum diffusion in slab Alfvénic turbulence and found:

$$\left.\frac{\partial f}{\partial t}\right|_{\mathrm{scatt}} = \frac{\partial}{\partial \mu}\left(D_{\mu\mu}\frac{\partial f}{\partial \mu} + D_{\mu p}\frac{\partial f}{\partial p}\right) + \frac{1}{p^2}\frac{\partial}{\partial p}p^2\left(D_{\mu p}\frac{\partial f}{\partial \mu} + D_{pp}\frac{\partial f}{\partial p}\right). \tag{3.53}$$

The diffusion coefficients are given by (Schlickeiser, 1989; Dung and Schlickeiser, 1990):

$$D_{\mu\mu} = \frac{1-\mu^2}{2}\left[\left(1-\mu\frac{v_\mathrm{a}}{v}\right)^2\nu_+ + \left(1+\mu\frac{v_\mathrm{a}}{v}\right)^2\nu_-\right], \tag{3.54}$$

$$D_{\mu p} = \frac{1-\mu^2}{2}p\frac{v_\mathrm{a}}{v}\left[\left(1-\mu\frac{v_\mathrm{a}}{v}\right)\nu_+ - \left(1+\mu\frac{v_\mathrm{a}}{v}\right)\nu_-\right], \tag{3.55}$$

$$D_{pp} = \frac{1-\mu^2}{2}p^2\frac{v_\mathrm{a}^2}{v^2}(\nu_+ + \nu_-), \tag{3.56}$$

where $D_{\mu\mu}$ is the pitch-angle diffusion coefficient provided by magnetic fluctuations and D_{pp} is the momentum diffusion coefficient as a result of particle acceleration by fluctuating electric fields. The mixed coefficient $D_{\mu p}$ contains elements of both scattering processes and formally derives as a result of cross-correlations between electric and magnetic turbulence.

All coefficients are correct to any order in $O(v_\mathrm{a}/v)$ and completely describe the phase-space diffusion of CRs induced by scattering with parallel propagating Alfvén waves in the QLT approximation (Schlickeiser, 1989).

3.4.2 CR streaming

Evaluating equation (3.53) in terms of its moments is difficult, even in the ultra-relativistic limit. The fact that the scattering frequency is unknown precludes a direct calculation of the corresponding scattering terms.

This situation is reminiscent of RT. The analogue to the scattering by waves is the absorption and scattering of radiation by the gas. Our wave-scattering frequency is related to the absorption coefficient in RT. This coefficient has an intrinsic dependence on the photon frequency, as different absorption processes (i) operate in different frequency regimes and (ii) have a frequency dependence due to the underlying physical processes. In the context of RT, the absorption coefficient is often assumed to be constant. This strong assumption can be practically justified in cases where the dynamically interesting frequencies are confined to narrow bands. The resulting theory is called *grey* RT.

Here, we use a related approximation for CRs and define a reference energy E' of *typical* CRs. These CRs resonate with Alfvén waves of wave numbers larger than $k'_{\mathrm{min},\pm} = \Omega'/(v' \pm v_\mathrm{a})$, where Ω' and v' are the reference gyrofrequency and velocity at energy E'. In the following argument, we identify all occurring gyrofrequencies with Ω'.

We further confine our analysis to isospectral Alfvén-wave intensities:

$$I^L_\pm(k) = H(k - k'_{\mathrm{min},\pm})\, C_\pm \frac{1}{k^q}, \tag{3.57}$$

$$I^R_\pm(k) = H(k - k'_{\mathrm{min},\mp})\, C_\pm \frac{1}{k^q}, \tag{3.58}$$

where $C_\pm$ are normalisation constants, q is the spectral index and H is the Heaviside function. Using equation (3.50), we determine these constants to

$$C_\pm = (q-1)\frac{\varepsilon_{\mathrm{a},\pm}\Omega'^{q-1}}{(v'+v_\mathrm{a})^{q-1} + (v'-v_\mathrm{a})^{q-1}}. \tag{3.59}$$

Inserting this into equation (3.52) yields

$$\nu_\pm = \pi\Omega' \frac{\varepsilon_{\mathrm{a},\pm}}{\varepsilon_B}(q-1)\frac{|\mu v' \mp v_\mathrm{a}|^{q-1}}{(v'+v_\mathrm{a})^{q-1} + (v'-v_a)^{q-1}}. \tag{3.60}$$

This equation shows that it is impossible to fully embrace the idea of a grey transport theory that becomes trivially independent of pitch angle cosine μ. This would correspond to the case $q = 1$, for which the wave spectra $I^{\mathrm{L,R}}_\pm \propto k^{-1}$ become degenerate as equation (3.50) diverges. For $q > 1$, the isospectral scattering rate $\nu_\pm$ is physically well defined and converges. However, in general different moments of the scattering rate of equation (3.53) cannot be solved in closed form except for the algebraically convenient choice of $q = 2$, which we adopt here. It coincides

with the upper limit of theoretically inferred spectral indices of 0.8 to 2.0 for the bulk of resonant wave numbers (Lazarian and Beresnyak, 2006; Yan and Lazarian, 2011). Assuming $q = 2$ in equation (3.60), the pitch-angle averaged scattering frequencies are given by:

$$\bar{\nu}_{\pm} = \frac{3}{2}\int_{-1}^{1} \mathrm{d}\mu \frac{1-\mu^2}{2}\,\nu_{\pm} = \frac{3\pi}{8}\Omega' \frac{\varepsilon_{\mathrm{a},\pm}/2}{\varepsilon_B}\left(1+\frac{2v_{\mathrm{a}}^2}{v'^2}\right). \tag{3.61}$$

Here, $(1-\mu^2)/2$ is geometric factor connected to the pitch-angle gradient of equation (3.53). We checked that any different choice for $1 < q \leq 2$ yields the exact same result for the different moments up to order $O(\bar{\nu}v_{\mathrm{a}}^2/v'^2)$.

With every choice $q \neq 1$ we encounter a well-known problem of QLT: for CRs with $\mu = \pm v_{\mathrm{a}}/v'$ the scattering coefficient vanishes identically. Formally, these CRs cannot resonate with any wave. As this μ corresponds to gyration nearly perpendicular to the large-scale magnetic field, this absence of scattering is commonly referred to as the 90°-problem. This problem can be resolved by two different arguments: (i) in the presence of dielectric effects the sharp resonance is broadened and CRs with wave vectors $k_{\mathrm{res}} = \infty$ in our definition are able to resonate with waves of finite wave number and (ii) a second-order treatment of the particle trajectories in small-scale turbulence, which includes a description of perturbed trajectories, introduces further resonance broadening.

As shown by theory and checked by simulations, diffusion coefficients in QLT underestimate their correct values even for μ near $\pm v_{\mathrm{a}}/v'$ (Shalchi, 2005). Nevertheless the bulk of CRs are scattered with diffusion coefficients in accordance with expectation of QLT. Hence, we expect the impact of second-order QLT to only marginally change the presented result (if at all).

Equipped with this approximation, we now evaluate moments of equation (3.53). Multiplying this equation by $E(p)$ and $\mu E(p)$, respectively, and integrating over momentum space results in

$$\left.\frac{\partial \varepsilon_{\mathrm{cr}}}{\partial t}\right|_{\mathrm{scatt}} = -3\frac{v_{\mathrm{a}}}{c^2}(\bar{\nu}_+ - \bar{\nu}_-)K_{\mathrm{cr}} + 4\frac{v_{\mathrm{a}}^2}{c^2}(\bar{\nu}_+ + \bar{\nu}_-)P_{\mathrm{cr}}, \tag{3.62}$$

$$\left.\frac{\partial f_{\mathrm{cr}}}{\partial t}\right|_{\mathrm{scatt}} = -(\bar{\nu}_+ + \bar{\nu}_-)f_{\mathrm{cr}} + v_{\mathrm{a}}(\bar{\nu}_+ - \bar{\nu}_-)(\varepsilon_{\mathrm{cr}} + P_{\mathrm{cr}}), \tag{3.63}$$

where we used the ultra-relativistic approximation $v \to c$ again. The symmetry in those terms can be restored by using the equations of state linking energy density and pressure as well as their corresponding anisotropic fluxes. Thus, eliminating the CR pressure via equation (3.37) and the corresponding flux via equation (3.42), we arrive at

$$\left.\frac{\partial \varepsilon_{\mathrm{cr}}}{\partial t}\right|_{\mathrm{scatt}} = -\frac{v_{\mathrm{a}}}{3\kappa_+}\left[f_{\mathrm{cr}} - v_{\mathrm{a}}(\varepsilon_{\mathrm{cr}} + P_{\mathrm{cr}})\right] + \frac{v_{\mathrm{a}}}{3\kappa_-}\left[f_{\mathrm{cr}} + v_{\mathrm{a}}(\varepsilon_{\mathrm{cr}} + P_{\mathrm{cr}})\right], \tag{3.64}$$

$$\left.\frac{\partial f_{\mathrm{cr}}}{\partial t}\right|_{\mathrm{scatt}} = -\frac{c^2}{3\kappa_+}\left[f_{\mathrm{cr}} - v_{\mathrm{a}}(\varepsilon_{\mathrm{cr}} + P_{\mathrm{cr}})\right] - \frac{c^2}{3\kappa_-}\left[f_{\mathrm{cr}} + v_{\mathrm{a}}(\varepsilon_{\mathrm{cr}} + P_{\mathrm{cr}})\right], \tag{3.65}$$

where the diffusion coefficients associated with either wave are given by (see also Appendix 3.10)

$$\kappa_{\pm} = \frac{c^2}{3\bar{\nu}_{\pm}}. \tag{3.66}$$

The derivation of these equations concludes the proof of equations (3.10) and (3.11).

In deriving equations (3.64) and (3.65) we neglected every boundary term resulting from partial integrations in p. Formally, this imposes mathematical constraints on the functional form of the CR proton distribution function that we locally approximate with a power law in momentum, $f \propto p^{\alpha_\mathrm{p}}$. To justify the neglect of boundary terms at low momenta, we require a low-momentum spectral index $\alpha_\mathrm{p} > -1$, as the phase space volume element scales as $p^2 \mathrm{d}p\mathrm{d}\mu\mathrm{d}\varphi$. In practice, a realistic CR distribution fulfills this constraint since at low particle energies, CRs suffer fast Coulomb interactions with the thermal plasma. Hence, the CR population quickly establishes a nearly constant low-momentum spectral index $\alpha_\mathrm{p} \to 0$ (Enßlin et al., 2007). On the opposite side, our regularization constraint translates to a requirement for the high-momentum spectral index of $\alpha_\mathrm{p} < -4$. Diffusive shock acceleration at strong shocks generates CRs with a spectral slope of $\alpha_\mathrm{p} \approx -4.1$ and weaker shocks inject progressively softer spectra, thus meeting our requirement also holds in the high-energy regime (Amato and Blasi, 2006). Moreover, the CR distribution exhibits an exponential cut-off at the maximum proton energy ($\sim 10^{15}$ eV for supernova remnants and $\sim 10^{20}$ eV for ultra high-energy CRs), which implies that there is no restricting mathematical precondition of our theory due to the spectral form of the CR distribution.

3.4.3 Galilean-invariant CR streaming

This form of equations (3.64) and (3.65) highlights the limit of purely Alfvénic transport: if one of both waves dominates, CRs constantly lose energy and get scattered until their flux approaches the Alfvénic limit:

$$f_\mathrm{cr} \to \pm v_\mathrm{a}(\varepsilon_\mathrm{cr} + P_\mathrm{cr}). \tag{3.67}$$

We can understand this process in the wave frame: if the dominant wave scatters CRs, it isotropizes the CRs in its own frame. After the distribution reaches isotropy in the wave frame, the flux density of CR energy vanishes there by definition. A Galilean transformation into the comoving frame demonstrates that the CR flux density is given by the limit (3.67). Hence CRs and their energy are transported with $\pm v_a$ with respect to the gas velocity. This transport mode is called *streaming* of CRs and is enforced in modern transport theories through a steady-state assumption (Zweibel, 2013; Pfrommer et al., 2017a).

The above calculation had to be carried out to order $O(\bar{\nu}v_a^2/c^2)$ in order to obtain a consistent result, namely a Galilean invariant expression for scattering. As can be inferred from equations (3.64) and (3.65), efficient scattering in the wave frame is necessary for a vanishing CR energy transfer and flux, which is the case of an isotropic CR distribution in one of the wave frames.

Calculations to lower order in the scattering terms fail to correctly account for the frame change and are thus incompatible with any Galilean invariant theory of CR transport. In Appendix 3.10 we explicitly demonstrate why a lower-order calculation up to $O(\bar{\nu})$, which describes pure CR diffusion, is inconsistent.

In Appendix 3.11, we provide an alternative derivation of the scattering terms, which clarifies the physical origin of the high accuracy order $O(\bar{\nu}v_a^2/c^2)$ that is needed to fully account for Galilean invariant transport. We start by evaluating pure CR pitch-angle scattering in the wave frame, which is free of electric fields. The resulting space-like component of the four-force density that is oriented along the magnetic field is given by $-\bar{\nu}_{\pm}f_{cr}/c$ and is formally of order $O(v_a/c)$. Performing a Lorentz transformation to lowest order $O(v_a/c)$ into the comoving frame picks up another factor of v_a/c, thus explaining the puzzling result.

3.4.4 Flux-limited transport

In moment-based RT, there exists a simple physical constraint for the energy flux. Since photons travel with the speed of light c, the speed of the entire photon population is also limited to c:

$$\left|\frac{f_{rad}}{c(\varepsilon_{rad}+P_{rad})}\right| \leq 1, \tag{3.68}$$

where ε_{rad}, P_{rad} and f_{rad} are the radiation energy density, pressure and energy flux density. Both quantities are defined by analogy with their corresponding CR quantities.

A similar constraint must also hold for CRs. Consider an isolated population of CRs that carries a super-Alfvénic flux, $|f_{cr}| > v_a\varepsilon_{cr}$. By means of equation (3.64) this flux density induces a strong energy transfer from CRs to Alfvén waves via the gyroresonant instability. This possible mode of CR transport is unstable and rapidly decays to the Alfvénic streaming limit on the growth timescale of the gyroresonant instability (see Section 3.5.4). More formally, the presented argument states that CRs drift according to

$$\left|\frac{f_{cr}}{v_a(\varepsilon_{cr}+P_{cr})}\right| \lesssim 1. \tag{3.69}$$

This is a posterior justification of our initial assumption that $f_1/f_0 \ll 1$ as equation (3.69) implies

$$\left|\frac{f_1}{f_0}\right| \lesssim \frac{v_\mathrm{a}}{v} \ll 1. \tag{3.70}$$

Note that both constraints are not enforced by physical limitations, as in the case of radiation, but due to the assumed self-confinement of CRs.

From the microscopic point of view, this argument holds for CRs at low to intermediate energies, which are indeed self-confined. For externally-confined CRs at energies $E \gtrsim 200$ GeV, this Alfvénic constraint needs to be replaced by equation (3.68). Since low- and intermediate-energy CRs dominate the CR energy density for normal momentum spectral indexes $\alpha_\mathrm{p} \lesssim -4.2$ (assuming that the distribution function scales as $f \propto p^{\alpha_\mathrm{p}}$), we conclude that equation (3.69) is valid for momentum-integrated quantities.

If the Alfvén-wave energy is rapidly damped so that the damping overcomes the growth of waves, then the premise of this argument does not hold. In this situation CRs are insufficiently scattered and can indeed move with bulk velocities that exceed v_a. None the less, the energy transfer of the streaming instability increases by a factor $f_\mathrm{cr}/v_\mathrm{a}(\varepsilon_\mathrm{cr} + P_\mathrm{cr})$ provided that the bulk velocities are greater than v_a. This increased growth rate is still able to balance the larger damping rate and a dynamical equilibrium emerges. The complexity of this case prohibits a general discussion and the question whether an equilibrium state can be reached on hydrodynamical or on kinetic time-scales needs to be addressed for the specific scenario at hand.

3.5 Alfvén wave dynamics

In this section, we embrace the connection between CR and Alfvén-wave transport by deriving the energy equation for Alfvén waves in our framework. So far, there is only a limited literature on coupled transport of CRs and Alfvén waves available (e.g., Ko, 1992; Jones, 1993; Recchia et al., 2016; Zweibel, 2017). Hence, we discuss different damping mechanisms and calculate the corresponding energy moments, to cast our treatment of the waves into a hydrodynamical picture. We furthermore show that the gyroresonant instability acts as a source or sink of wave energy.

3.5.1 Alfvén waves as a fluid

To use Alfvén waves as a mediator between the thermal and the CR fluid, we seek to describe them by their mean energy and momentum content. Such a hydrodynamical description is

justified provided the oscillations characterizing the waves do not affect the large-scale hydrodynamics directly but only their spatial and temporal mean properties, implying that the time-scale of Alfvén-wave oscillations has to be much shorter than any hydrodynamical time-scale. This is observed by Alfvén waves with typical wavelengths that are equal to the gyroradii of (pressure-carrying GeV to TeV) CRs. Indeed, those wavelengths are much smaller and wave-frequencies are much larger than the corresponding characteristic scales of their embedding medium such as the ISM or the ICM.

Each Alfvén wave consists of two principle components: a perturbation in the mean motion of the thermal gas and one of the electromagnetic field. Both components contribute to the energy density contained in Alfvén waves at a certain wavenumber k, which amounts to the sum of kinetic energy and magnetic field density:

$$I_{\pm}^{\mathrm{L,R}}(k) = \rho \frac{\left\langle \delta \boldsymbol{u}_{\pm}^{\mathrm{L,R}}(k)^2 \right\rangle}{2} + \frac{\left\langle \delta \boldsymbol{B}_{\pm}^{\mathrm{L,R}}(k)^2 \right\rangle}{2}, \tag{3.71}$$

as the incompressibility condition of shear (or pseudo) Alfvén waves guarantees that no thermal energy is carried by Alfvén waves. The perturbations in the velocity and magnetic fields are linked by the MHD relation for Alfvén waves:

$$\delta \boldsymbol{u}_{\pm}^{\mathrm{L,R}} = \mp \frac{v_{\mathrm{a}}}{\boldsymbol{B}} \delta \boldsymbol{B}_{\pm}^{\mathrm{L,R}}. \tag{3.72}$$

Thus, the kinetic and magnetic energy of an Alfvén wave are in equipartition and the total energy density is:

$$I_{\pm}^{\mathrm{L,R}}(k) = \left\langle \delta \boldsymbol{B}_{\pm}^{\mathrm{L,R}}(k)^2 \right\rangle. \tag{3.73}$$

The mean momentum of the waves is solely given by the electromagnetic component: the perturbation in the gas momentum $\rho \boldsymbol{u}$ oscillates rapidly in space/time and thus has a zero mean over hydrodynamical scales. Contrary, the electromagnetic momentum given by the Poynting vector $\delta \boldsymbol{E}_{\pm}^{\mathrm{L,R}} \times \delta \boldsymbol{B}_{\pm}^{\mathrm{L,R}}/c$ does not oscillate and thus has a non-zero average. For Alfvén waves, the mean momentum density in a single wavemode as measured by an observer in the comoving frame is given by

$$\frac{\left\langle \delta \boldsymbol{E}_{\pm}^{\mathrm{L,R}}(k) \times \delta \boldsymbol{B}_{\pm}^{\mathrm{L,R}}(k) \right\rangle}{c} = \mp \frac{I_{\pm}^{\mathrm{L,R}}(k)}{c} \frac{\boldsymbol{v}_{\mathrm{a}}}{c}, \tag{3.74}$$

since the electric field of an Alfvén wave is $\delta \boldsymbol{E}_{\pm}^{\mathrm{L,R}}(k) = \mp \boldsymbol{v}_{\mathrm{a}} \times \delta \boldsymbol{B}_{\pm}^{\mathrm{L,R}}(k)/c$. In the non-relativistic MHD approximation, this electromagnetic momentum is neglected as it is assumed to be vanishingly small to order $O(v_{\mathrm{a}}/c)$. However, the result above is instructive because Alfvén waves do not carry kinetic momentum, which needs to be considered during the discussion of the acting forces.

We now discuss a minor and rather subtle discrepancy between the ideal MHD assumption and our treatment of CRs. In order to fully describe the interaction between CRs and Alfvén waves, we arrived at the momentum diffusion terms of Schlickeiser (1989). The moment expansion of those terms as manifest in equations (3.64) and (3.65) include the full effects of magnetic and electric fields and are formally accurate up to oder $O(v_\mathrm{a}^2/c^2)$. Here, the first and second order terms derive from the correlations $\langle \delta \boldsymbol{E}_\pm^{\mathrm{L,R}} \delta \boldsymbol{B}_\pm^{\mathrm{L,R}} \rangle$ and $\langle \delta \boldsymbol{E}_\pm^{\mathrm{L,R}} \delta \boldsymbol{E}_\pm^{\mathrm{L,R}} \rangle$ with $\delta E \sim v_\mathrm{a} \delta B/c$. Consequently, our description of the transfer of momentum and energy between Alfvén waves and CRs exhibits an accuracy with a comparable order, at least up to $O(v_\mathrm{a}/c)$. Contrarily, the formulation of ideal MHD in a non-relativistic setting disregards contributions of order $O(v_\mathrm{a}/c)$ and thus neglects contributions of the electric fields to any energy balance. Hence, there is a contradiction: electric fields do work on CRs while we neglect their energy density in equation (3.71).

To resolve this contradiction, we could account for the Poynting flux and energy density of the electric fields in the unperturbed MHD equations in a semi-relativistic approximation (Boris, 1970; Gombosi et al., 2002). This would restore the missing energy density of the electric field of the Alfvén waves to equation (3.71) but would simultaneously change the momentum equation of MHD, too. The latter step alters the dispersion relation of Alfvén waves to $\omega(k) = \pm k v_\mathrm{a}/\sqrt{1 + v_a^2/c^2}$ and we would need to reevaluate the right-hand side of equation (3.71). However, due to cancellations of Lorentz factors, expressing the total energy density $I_\pm^{\mathrm{L,R}}(k)$ in terms of $\langle \delta \boldsymbol{B}_\pm^{\mathrm{L,R}}(k)^2 \rangle$ again results in equation (3.73). In the end, the equipartition between kinetic and electromagnetic energy of an Alfvén wave remains unchanged.

3.5.2 Alfvén waves on an inhomogeneous background

To account for the inhomogeneous background of Alfvén waves, we perform a WKB (Wentzel-Kramers-Brillouin) approximation for the defining properties of Alfvén waves. In the following, we suppress the super- and sub-scripts of perturbations indicating their propagation directions and polarization states (± respectively L, R) for simplicity. We shall therefore assume that the subsequent arguments only hold for a distinct wave of given propagation direction and polarization state. For example, we decompose the magnetic field into plain waves:

$$\delta \boldsymbol{B}(\boldsymbol{x}) = \int \mathrm{d}k \, \delta \boldsymbol{B}(k, \boldsymbol{x}) \exp\left[i(k\boldsymbol{b} \cdot \boldsymbol{x} - \omega(\boldsymbol{k})t)\right], \tag{3.75}$$

where $\delta \boldsymbol{B}(k, \boldsymbol{x})$ is slowly varying in space and time. The quantity $\delta \boldsymbol{B}(k, \boldsymbol{x})$ can be interpreted as the perturbation of a single Alfvén wave with kinetic wavelength $\boldsymbol{k} = k\boldsymbol{b}$ located at $\boldsymbol{x}$. On hydrodynamical timescales the turbulent motions of these waves can be described by a few

statistical parameters which are defined as time averages over the high-frequency wave oscillations. We can exchange this time average by an ensemble average assuming the validity of the ergodic theorem. For parallel propagating Alfvén waves in slab turbulence the wave statistics is given by the mean and second-order correlation (Schlickeiser, 2002; Zank, 2014):

$$\langle \delta \boldsymbol{B}(k, \boldsymbol{x}) \rangle = 0, \tag{3.76}$$

$$\langle \delta \boldsymbol{B}(k, \boldsymbol{x})\, \delta \boldsymbol{B}(k', \boldsymbol{x}')^* \rangle = \frac{I_{\pm}^{\mathrm{L,R}}(k)}{2}\, \delta_{\mathrm{d}}(\boldsymbol{x} - \boldsymbol{x}')\, \delta_{\mathrm{d}}(k - k')\, (\mathbf{1} - \boldsymbol{bb}), \tag{3.77}$$

where δ_{d} is Dirac's delta distribution. Both delta distributions reflect that two different Alfvén waves at different localizations in configuration and wave-number space are uncorrelated. The tensor $\mathbf{1} - \boldsymbol{bb}$ accounts for the specific directions of the magnetic perturbations: they must be perpendicular to the mean magnetic field for parallelly propagating Alfvén waves.

The inhomogeneous wave background has further consequences: as the waves exert both magnetic and kinetic pressure (here in the form of ram pressure) on their surroundings, a spatially varying distribution of Alfvén waves induces a current that counteracts these imbalances. This slightly changes Ampère's law which reads in the MHD approximation as:

$$\boldsymbol{\nabla} \times \delta \boldsymbol{B} = \frac{1}{c} \delta \boldsymbol{j} \tag{3.78}$$

where $\delta \boldsymbol{j} = \delta \boldsymbol{j}_{\mathrm{gas}} + \delta \boldsymbol{j}_{\mathrm{cr}}$ denotes the total current induced by Alfvén waves, which is carried by the thermal gas (Achterberg, 1981b). Inserting equation (3.75) into Ampère's law yields:

$$\boldsymbol{\nabla} \times \delta \boldsymbol{B}(k, \boldsymbol{x}) + i\boldsymbol{k} \times \delta \boldsymbol{B}(k, \boldsymbol{x}) = \frac{1}{c} \delta \boldsymbol{j}(k, \boldsymbol{x}). \tag{3.79}$$

We assume that the gas current can be decomposed into two contributions: one that is inherent to the oscillatory motion of the waves, $\delta \boldsymbol{j}_{\mathrm{a}}$, and one that is a direct consequence of the inhomogeneities, $\delta \boldsymbol{j}_{\mathrm{inh}}$, with $\delta \boldsymbol{j}_{\mathrm{inh}} = \boldsymbol{0}$ if the background is homogeneous. Thus we find in the absence of such inhomogeneities

$$i\boldsymbol{k} \times \delta \boldsymbol{B}(k, \boldsymbol{x}) = \frac{1}{c} [\delta \boldsymbol{j}_{\mathrm{a}}(k, \boldsymbol{x}) + \delta \boldsymbol{j}_{\mathrm{cr}}(k, \boldsymbol{x})]. \tag{3.80}$$

This is in accordance to the usual expression of Ampère's law for Fourier-components in plasma physics. This decomposition allows us to directly use the results obtained in our local analysis where the WKB approximation is not applied and hence the Fourier components are assumed to be spatially invariant. This is particularly useful, since plasma kinetic effects are usually investigated on a homogeneous background.

3.5.3 Macroscopic energy transport

The transport equations for MHD waves can be derived with the action principle and Whitham's (1961) transport theory for waves (Dewar, 1970; Jacques, 1977). Here, we rederive their results for parallel propagating Alfvén waves following a different approach. This allows us to accurately identify the exerted forces and their associated work done on thermal and CR fluids.

We start with the Euler equation in the lab frame, which describes the thermal gas subject to a Lorentz force in its Lagrangian form ($\mathrm{d}/\mathrm{d}t = \partial/\partial t + \boldsymbol{u}\cdot\boldsymbol{\nabla}$):

$$\rho\frac{\mathrm{d}\boldsymbol{u}}{\mathrm{d}t} = -\boldsymbol{\nabla}P_{\mathrm{th}} + \frac{\boldsymbol{j}_{\mathrm{gas}}\times\boldsymbol{B}}{c}. \tag{3.81}$$

Introducing perturbations $q \to q + \delta q$ where $q \in \{\boldsymbol{u}, \boldsymbol{B}, \boldsymbol{j}\}$ in a Reynolds decomposition results in

$$\begin{aligned}\rho\left[\frac{\mathrm{d}\boldsymbol{u}}{\mathrm{d}t} + \frac{\mathrm{d}\delta\boldsymbol{u}}{\mathrm{d}t} + (\delta\boldsymbol{u}\cdot\boldsymbol{\nabla})\boldsymbol{u} + (\delta\boldsymbol{u}\cdot\boldsymbol{\nabla})\delta\boldsymbol{u}\right] &= -\boldsymbol{\nabla}P_{\mathrm{th}} \\ &+ \frac{1}{c}\left(\boldsymbol{j}_{\mathrm{gas}}\times\boldsymbol{B} + \delta\boldsymbol{j}_{\mathrm{gas}}\times\delta\boldsymbol{B} + \delta\boldsymbol{j}_{\mathrm{gas}}\times\boldsymbol{B} + \boldsymbol{j}_{\mathrm{gas}}\times\delta\boldsymbol{B}\right).\end{aligned} \tag{3.82}$$

We separate mean and fluctuating components by taking the ensemble average with $\langle\delta q\rangle$ and subtract the averaged from the unaveraged equations to arrive at:

$$\rho\frac{\mathrm{d}\boldsymbol{u}}{\mathrm{d}t} = -\boldsymbol{\nabla}P_{\mathrm{th}} + \frac{\boldsymbol{j}_{\mathrm{gas}}\times\boldsymbol{B}}{c} + \left\langle\frac{\delta\boldsymbol{j}_{\mathrm{gas}}\times\delta\boldsymbol{B}}{c} - (\rho\delta\boldsymbol{u}\cdot\boldsymbol{\nabla})\delta\boldsymbol{u}\right\rangle \tag{3.83}$$

$$\begin{aligned}\rho\frac{\mathrm{d}\delta\boldsymbol{u}}{\mathrm{d}t} &= -(\rho\delta\boldsymbol{u}\cdot\boldsymbol{\nabla})\boldsymbol{u} + \frac{\delta\boldsymbol{j}_{\mathrm{gas}}\times\boldsymbol{B}}{c} + \frac{\boldsymbol{j}_{\mathrm{gas}}\times\delta\boldsymbol{B}}{c} \\ &+ \left[\left\langle\frac{\delta\boldsymbol{j}_{\mathrm{gas}}\times\delta\boldsymbol{B}}{c} - (\rho\delta\boldsymbol{u}\cdot\boldsymbol{\nabla})\delta\boldsymbol{u}\right\rangle\right],\end{aligned} \tag{3.84}$$

where we introduced the abbreviation $[\langle q\rangle] = q - \langle q\rangle$. We identify the forces acting on the mean motion as the Reynolds stress and the pondermotive Lorentz force. Multiplying equation (3.84) by $\delta\boldsymbol{u}$, adding the continuity equation times $\boldsymbol{u}^2/2$, and ignoring terms that are third order in fluctuations results in an evolution equation for the kinetic energy in Alfvén waves:

$$\frac{\partial}{\partial t}\left(\rho\frac{\delta\boldsymbol{u}^2}{2}\right) + \boldsymbol{\nabla}\cdot\left(\boldsymbol{u}\rho\frac{\delta\boldsymbol{u}^2}{2}\right) + (\rho\delta\boldsymbol{u}\delta\boldsymbol{u}) : \boldsymbol{\nabla}\boldsymbol{u} = \pm\boldsymbol{v}_{\mathrm{a}}\cdot\frac{\delta\boldsymbol{j}_{\mathrm{gas}}\times\delta\boldsymbol{B}}{c}. \tag{3.85}$$

The same procedure results in Poynting's theorem for magnetic energy in fluctuations:

$$\begin{aligned}\frac{\partial}{\partial t}\left(\frac{\delta\boldsymbol{B}^2}{2}\right) + \boldsymbol{\nabla}\cdot\left[(\boldsymbol{u}\pm\boldsymbol{v}_{\mathrm{a}})\delta\boldsymbol{B}^2\right] - (\delta\boldsymbol{B}\delta\boldsymbol{B}) : \boldsymbol{\nabla}\boldsymbol{u} = \\ (\delta\boldsymbol{B}\boldsymbol{u}) : \boldsymbol{\nabla}\delta\boldsymbol{B} - (\boldsymbol{u}\pm\boldsymbol{v}_{\mathrm{a}})\cdot\frac{\delta\boldsymbol{j}\times\delta\boldsymbol{B}}{c}.\end{aligned} \tag{3.86}$$

Here, we used the MHD relation for Alfvén waves in the lab frame, $\delta\boldsymbol{E} = -(\boldsymbol{u} \pm \boldsymbol{v}_\mathrm{a}) \times \delta\boldsymbol{B}/c$, and the relation $\delta\boldsymbol{B} \cdot \boldsymbol{v}_\mathrm{a} = 0$ for parallel propagating Alfvén waves. Adding both equations for magnetic and kinetic energy of both polarizations states together with equations (3.75) and (3.77), we obtain a conservation law for the energy contained in Alfvén waves:

$$\frac{\partial E_\pm(k)}{\partial t} + \boldsymbol{\nabla} \cdot [(\boldsymbol{u} \pm v_\mathrm{a}\boldsymbol{b})\, E_\pm(k)] + \frac{1}{2}(\boldsymbol{\nabla} \cdot \boldsymbol{u})E_\pm(k) = \mp\, \boldsymbol{v}_\mathrm{a} \cdot \frac{\langle \delta\boldsymbol{j}_\mathrm{cr}(k) \times [\delta\boldsymbol{B}^\mathrm{L}_\pm(k) + \delta\boldsymbol{B}^\mathrm{R}_\pm(k)]\rangle}{c}, \tag{3.87}$$

which coincides with the result obtained by Dewar (1970) except for the work done by CRs. Following the arguments of Achterberg (1981b) we express this work using the growth rate Alfvén waves by:

$$\mp\boldsymbol{v}_\mathrm{a} \cdot \frac{\langle \delta\boldsymbol{j}_\mathrm{cr}(k) \times [\delta\boldsymbol{B}^\mathrm{L}_\pm(k) + \delta\boldsymbol{B}^\mathrm{R}_\pm(k)]\rangle}{c} = \Gamma_{\mathrm{gri},\pm}(k)R_\pm(k), \tag{3.88}$$

where $\Gamma_{\mathrm{gri},\pm}(k)$ is the growth rate of Alfvén waves caused by the gyroresonant instability (*gri* for short). There are additional physical loss-processes that act on Alfvén waves and convert kinetic and magnetic energy into heat. We model those processes by effective growth rates $\Gamma_{\mathrm{loss},\pm}(k)$, such that we finally obtain

$$\frac{\partial E_\pm(k)}{\partial t} + \boldsymbol{\nabla} \cdot [(\boldsymbol{u} \pm v_\mathrm{a}\boldsymbol{b})\, E_\pm(k)] + \frac{1}{2}(\boldsymbol{\nabla} \cdot \boldsymbol{u})E_\pm(k) = \Gamma_{\mathrm{gri},\pm}(k)R_\pm(k) - \Gamma_{\mathrm{loss},\pm}(k)E_\pm(k). \tag{3.89}$$

The interpretation of the left-hand side is straightforward: wave energy is transported with the Alfvén speed relative to the gas and experiences adiabatic changes due to the spectral wave pressure $E_\pm(k)/2$. The total energy contained in Alfvén waves is

$$\varepsilon_{\mathrm{a},\pm} = \int_0^\infty \mathrm{d}k\, E_\pm(k). \tag{3.90}$$

The total wave pressure obeys the equation of state

$$P_{\mathrm{a},\pm} = (\gamma_\mathrm{a} - 1)\varepsilon_{\mathrm{a},\pm}, \tag{3.91}$$

with an adiabatic index of $\gamma_\mathrm{a} = 3/2$. We can readily integrate equation (3.89) over wave number space to obtain

$$\frac{\partial \varepsilon_{\mathrm{a},\pm}}{\partial t} + \boldsymbol{\nabla} \cdot [(\boldsymbol{u} \pm v_\mathrm{a}\boldsymbol{b})\, \varepsilon_{\mathrm{a},\pm}] + \frac{1}{2}(\boldsymbol{\nabla} \cdot \boldsymbol{u})\varepsilon_{\mathrm{a},\pm} = S_{\mathrm{gri},\pm} - Q_\pm, \tag{3.92}$$

where the Fourier integrated source terms for energy gains and losses are given by

$$S_{\mathrm{gri},\pm} = \int_0^\infty \mathrm{d}k\, \Gamma_{\mathrm{gri},\pm}(k)R_\pm(k), \text{ and} \tag{3.93}$$

$$Q_\pm = \int_0^\infty \mathrm{d}k\, \Gamma_{\mathrm{loss},\pm}(k)E_\pm(k). \tag{3.94}$$

In the following, we discuss different wave creation and annihilation processes, which are known to operate in ISM or ICM conditions and provide expressions for $Q_\pm$.

3.5.4 Gyroresonant instability

As CRs drift with an anisotropy in the Alfvén frame and gyrate around the mean magnetic field, collectively they excite Alfvén waves in resonance with their gyromotion. This effect is intimately related to CR scattering: any CR distribution with a residual anisotropy of pitch angles transfers energy to or extracts energy from the waves via scattering. For instance, if CRs are moving in the same direction as an Alfvén wave packet, but the CR streaming velocity $f_{\rm cr}/(\varepsilon_{\rm cr} + P_{\rm cr})$ exceeds the Alfvén velocity $v_{\rm a}$, then these waves gain energy while the CR distribution loses energy. The growth rate of this process is (Zweibel, 2017; Kulsrud and Pearce, 1969):[2]

$$\Gamma_{\rm gri,\pm} = \pm \int {\rm d}^3 p \, \frac{\pi \Omega^2 v_{\rm a}}{\varepsilon_B} \frac{1-\mu^2}{2} p \left[\left(1 \mp \mu \frac{v_{\rm a}}{v}\right) \frac{\partial f}{\partial \mu} \pm \frac{v_{\rm a}}{v} p \frac{\partial f}{\partial p} \right] \delta_{\rm d} \left((\mu v \mp v_{\rm a}) k - \Omega \right) . \tag{3.95}$$

Dirac's δ distribution is the formal consequence of the gyroresonance condition of equation (3.47). Again, we account for the polarization dependence of the resonance by the definition of the resonant energy in equation (3.48). If we directly evaluate the ${\rm d}^3 p$-integral of equation (3.95), this definition and Dirac's δ distribution select the correct CR momenta and pitch angles, which are scattered by waves with a given k.

To obtain the source function of Alfvén wave energy in equation (3.93), we integrate over k-space and evaluate $R_\pm(k)$ at the zero of the argument of the δ distribution. Accounting for the approximation of isospectral wave intensities as discussed in Section 3.4.2, we find in the ultra-relativistic limit:

$$S_{\rm gri,\pm} = \pm \frac{v_{\rm a}}{3\kappa_\pm} \left[f_{\rm cr} \mp v_{\rm a} (\varepsilon_{\rm cr} + P_{\rm cr}) \right] . \tag{3.96}$$

Comparing this result to the CR energy loss term on the right-hand side of equation (3.64) we find that the sum of CR and wave energy is exactly conserved during gyroresonant scattering.

We can directly infer the acting forces from the growth and decay of Alfvén wave energy by integrating both sides of equation (3.88):

$$S_{\rm gri,\pm} = \pm \boldsymbol{v}_{\rm a} \cdot \boldsymbol{g}_{\rm gri,\pm}, \tag{3.97}$$

where $\boldsymbol{g}_{\rm gri,\pm}$ is the corresponding force density. Because the momentum of an Alfvén wave is aligned with the propagation direction of the Alfvén wave itself, each exerted force on or by Alfvén waves must be aligned with $\boldsymbol{b}$, too. We can finally conclude that

$$\boldsymbol{g}_{\rm gri,\pm} = \pm \frac{S_{\rm gri,\pm}}{v_{\rm a}} \boldsymbol{b} = \frac{\boldsymbol{b}}{3\kappa_\pm} [f_{\rm cr} \mp (\varepsilon_{\rm cr} + P_{\rm cr})]. \tag{3.98}$$

The derivation of equations (3.92) and (3.98) concludes the proof of equation (3.12).

[2] We multiply equation (4) of Zweibel (2017) by a factor of 2 to make it consistent with our definition of the resonant wave energy in equation (3.93).

3.5.5 Ion-neutral damping

One of the first damping mechanisms considered was the indirect damping of waves by the friction between ions and neutrals in a partially ionized medium (see Appendix C of Kulsrud and Pearce, 1969). The process can be understood as follows: collisions between ions and neutrals maintain near equilibrium so that they share a similar temperature and mean velocity (modified by the square root of the mass ratio). The ions are additionally accelerated by the Lorenz force generated by the Alfvén waves. As before, the waves lose energy due to this acceleration, while the ions gain this as kinetic energy. However, this force can be cancelled by friction between both particle species. In the end, the energy lost by waves is thermalised and heats both ions and neutrals.

We here account for the friction between ions (i), neutral hydrogen (H) and neutral helium (He). The damping rate for this three-component fluid was derived by Soler et al. (2016), whom we closely follow here. First, we consider the definition of the friction coefficient for collisions between ions and neutrals with small relative drift velocities:

$$\alpha_{\beta\beta'} = n_\beta \, n_{\beta'} \, m_{\beta\beta'} \, \sigma_{\beta\beta'} \frac{4}{3} \sqrt{\frac{8 k_\mathrm{b} T_\mathrm{th}}{\pi m_{\beta\beta'}}}, \tag{3.99}$$

where $\beta, \beta' \in \{\mathrm{i}, \mathrm{H}, \mathrm{He}\}$, $m_{\beta\beta'} = m_\beta \, m_{\beta'} / (m_\beta + m_{\beta'})$ is the reduced mass of either two species, n_β and m_β are the number density and mass of species β, T_th and k_B are temperature and Boltzmann's constant, respectively. We implicitly assume that all plasma components share the same temperature. The momentum-transfer cross sections of interest are $\sigma_\mathrm{iH} = 10^{-18}$ m^{-2} and $\sigma_\mathrm{iHe} = 3 \times 10^{-19}$ m^{-2}. The resulting damping rate is given by

$$\Gamma_\mathrm{in} = \frac{1}{2} \left(\frac{\alpha_\mathrm{iH}}{\rho_\mathrm{i}} + \frac{\alpha_\mathrm{iHe}}{\rho_\mathrm{i}} \right), \tag{3.100}$$

where we neglect terms, which are second order in the collision frequencies $\alpha_{\beta\beta'}/\rho_\mathrm{i}$ and ρ_i is the mass density of ions.

Since Γ_in is independent of wave number, we conclude that the total loss term of Alfvén waves by ion-neutral damping is given by

$$Q_{\mathrm{in},\pm} = \Gamma_\mathrm{in} \, \varepsilon_{\mathrm{a},\pm}. \tag{3.101}$$

3.5.6 Non-linear Landau damping

The thermal gas can be directly heated via another mechanism. Consider two waves 1 and 2 with wave numbers k_i and wave frequencies ω_i ($i \in \{1, 2\}$) that interact to form a beat wave,

which propagates at the group velocity

$$v_{\rm beat} = \frac{\omega_1 - \omega_2}{k_1 - k_2}. \tag{3.102}$$

Associated with this beat wave is a second-order electric field, which accelerates thermal particles travelling at similar velocities. More formally, the two waves 1 and 2 interact through their beat wave at the Landau resonance with particles around the thermal speed $v_{\rm th}$:

$$v_{\rm beat} - v_{\rm th} = 0. \tag{3.103}$$

In a linear perturbation analysis, Lee and Völk (1973) calculated the resulting damping of waves in a general setting. In a high-β plasma ($\beta_{\rm plasma} = v_{\rm th}^2/v_{\rm a}^2$), where thermal electrons and protons share the same temperature, the non-linear Landau (nll) damping rate can be approximated by (Völk and McKenzie, 1981; Miller, 1991)

$$\Gamma_{\rm nll,\pm}(k) = \frac{\sqrt{\pi}}{8}\frac{v_{\rm th}}{\varepsilon_B}k\int_0^k {\rm d}k'\, E_\pm(k'). \tag{3.104}$$

While this damping rate strictly only applies to waves of the same propagation direction, there can also be non-linear Landau damping between counter-propagating waves. However, this effect is smaller by an order of magnitude for high-β plasmas compared to the case of non-linear Landau of co-propagating waves (Achterberg, 1981a; Miller, 1991), hence we neglected this case here.

We can introduce a suitably averaged wave number $\langle k\rangle$ (as in McKenzie and Bond, 1983) so that the hydrodynamic version of equation (3.104) can be written as:

$$Q_{\rm nll,\pm} = \alpha\varepsilon_{\rm a,\pm}^2, \tag{3.105}$$

where the interaction coefficient is given by

$$\alpha = \frac{\sqrt{\pi}}{8}\frac{v_{\rm th}}{\varepsilon_B}\langle k\rangle, \tag{3.106}$$

with an averaged wave number (Völk and McKenzie, 1981):

$$\langle k\rangle = \frac{1}{\varepsilon_{\rm a,\pm}^2}\int_0^\infty {\rm d}k\, kE_\pm(k)\int_0^k {\rm d}k'\, E_\pm(k'), \tag{3.107}$$

which, to order of magnitude, corresponds to the resonant wave number of CRs. Please note that our particular choice of the algebraic form of $E_\pm(k) \propto k^{-2}$ formally gives raise to an ultraviolet divergence ($k \to \infty$) of wave energy loss by virtue of equations (3.104) and (3.94). We remind the reader that this profile was an appropriate choice for intermediate wave numbers

($k \sim c/\Omega$), where the turbulence is driven by the bulk of CRs. At larger wave numbers, i.e., in the inertial range and in the dissipation regime of the CR-driven turbulence, this spectrum is not applicable and would have to be modified to account for turbulent cascading and dissipation. This modification also cures the apparent ultra-violet divergence of the integral.

3.5.7 Turbulent and linear Landau damping

Magnetic turbulence becomes anisotropic through the elongation of wave packets along the mean magnetic field on scales much smaller than the injection scale (Goldreich and Sridhar, 1995). Two interacting wave packets shear each other and cause field-line wandering. As the two counter-propagating wave packets follow the perturbed field lines of their corresponding collision partner, they are distorted transverse to the mean magnetic field (Lithwick and Goldreich, 2001). This process operates on the eddy turnover time and results in a cascade of energy to higher wave numbers $k_\parallel$ (Farmer and Goldreich, 2004).

It also acts as a damping process because it removes energy from scales where it was injected. The damping rate is minimized at the largest scale where waves are driven that obey the gyroresonance condition $\lambda_{\parallel,\mathrm{max}} \sim k_{\parallel,\mathrm{min}}^{-1} \sim r_\mathrm{L}$, and can be estimated as (Farmer and Goldreich, 2004; Zweibel, 2013):

$$\Gamma_\mathrm{turb} \approx v_\mathrm{a} k_{\parallel,\mathrm{min}} \sqrt{\frac{k_\mathrm{mhd,turb}}{k_{\parallel,\mathrm{min}}}}, \tag{3.108}$$

where $k_\mathrm{mhd,turb}$ is the wave number at which the large scale MHD turbulence is driven.

A related process is linear Landau damping of oblique waves (Zweibel, 2017). Here the electric field of a single wave can interact with the gas through the Landau resonance. Since Alfvén waves constantly change their propagation angle relative to the mean magnetic field, this effect is directly linked to large-scale magnetic turbulence and the anisotropic cascade. The corresponding damping rate can be estimated as

$$\Gamma_\mathrm{ll} \approx v_\mathrm{a} \frac{\sqrt{\pi}}{4} k_{\parallel,\mathrm{min}} \sqrt{\beta_\mathrm{plasma} \frac{k_\mathrm{MHD,turb}}{k_{\parallel,\mathrm{min}}}}. \tag{3.109}$$

Combining both damping rates, the loss of total energy density by processes related to turbulence is

$$Q_\mathrm{turb+ll,\pm} = (\Gamma_\mathrm{turb} + \Gamma_\mathrm{ll}) \varepsilon_\mathrm{a,\pm}. \tag{3.110}$$

3.6 Coupling to the thermal gas

After deriving the CR-Alfvénic subsystem, which describes the hydrodynamics of Alfvén wave-mediated CR transport, we are now coupling the forces and work done by this subsystem to the MHD equations and address energy and momentum conservation of this new theory. First, we review the evolution equations of kinetic, thermal, and magnetic energy.

In the preceding section we have derived the Euler equation (3.83) for the mean motion of the thermal gas, which can be written in its conservation form as:

$$\frac{\partial(\rho \boldsymbol{u})}{\partial t} + \boldsymbol{\nabla} \cdot (\rho \boldsymbol{u}\boldsymbol{u} + \mathbf{1} P_{\mathrm{th}}) = \frac{\boldsymbol{j}_{\mathrm{gas}} \times \boldsymbol{B}}{c} + \left\langle \frac{\delta \boldsymbol{j}_{\mathrm{gas}} \times \delta \boldsymbol{B}}{c} - (\rho \delta \boldsymbol{u} \cdot \boldsymbol{\nabla}) \delta \boldsymbol{u} \right\rangle . \tag{3.111}$$

To derive the evolution equation for the mean kinetic energy, we multiply equation (3.83) with $\boldsymbol{u}$, the continuity equation with $\boldsymbol{u}^2/2$ and add both results to obtain:

$$\frac{\partial \varepsilon_{\mathrm{kin}}}{\partial t} + \boldsymbol{\nabla} \cdot (\boldsymbol{u} \varepsilon_{\mathrm{kin}}) = -\boldsymbol{u} \cdot \boldsymbol{\nabla} P_{\mathrm{th}} + \boldsymbol{u} \cdot \frac{\boldsymbol{j}_{\mathrm{gas}} \times \boldsymbol{B}}{c} + \boldsymbol{u} \cdot \left\langle \frac{\delta \boldsymbol{j}_{\mathrm{gas}} \times \delta \boldsymbol{B}}{c} - (\rho \delta \boldsymbol{u} \cdot \boldsymbol{\nabla}) \delta \boldsymbol{u} \right\rangle , \tag{3.112}$$

where $\varepsilon_{\mathrm{kin}} = \rho \boldsymbol{u}^2/2$ is the mean kinetic energy density. The thermal or internal energy equation for a gas with the equation of state $P_{\mathrm{th}} = (\gamma_{\mathrm{th}} - 1)\varepsilon_{\mathrm{th}}$, is given by

$$\frac{\partial \varepsilon_{\mathrm{th}}}{\partial t} + \boldsymbol{\nabla} \cdot [\boldsymbol{u}(\varepsilon_{\mathrm{th}} + P_{\mathrm{th}})] = \boldsymbol{u} \cdot \boldsymbol{\nabla} P_{\mathrm{th}} + Q_+ + Q_- , \tag{3.113}$$

where we added the heating contributions of the Alfvén wave damping processes. The magnetic energy of the large-scale fields is given in the MHD-approximation by

$$\frac{\partial \varepsilon_{\mathrm{mag}}}{\partial t} + \boldsymbol{\nabla} \cdot [\boldsymbol{u}(\varepsilon_{\mathrm{mag}} + \boldsymbol{B}^2/2) - \boldsymbol{u} \cdot \boldsymbol{B}\boldsymbol{B}] = -\boldsymbol{j} \cdot \boldsymbol{E} \tag{3.114}$$

$$= -\boldsymbol{u} \cdot \frac{\boldsymbol{j} \times \boldsymbol{B}}{c} , \tag{3.115}$$

where $\varepsilon_{\mathrm{mag}} = \boldsymbol{B}^2/2$. We are now going to discuss the forces and their associated works exerted by the large- and small-scale electromagnetic fields.

3.6.1 Perpendicular forces

We first focus on the large-scale Lorentz force. The mean current $\boldsymbol{j}_{\mathrm{gas}}$ is composed of electron and ion currents. It is an unknown quantity of the gas and cannot be expressed in terms of ρ, $\boldsymbol{u}$ and $\varepsilon_{\mathrm{th}}$ in general. In the framework of ideal MHD the dependence of the Euler equation on $\boldsymbol{j}_{\mathrm{gas}}$ can be directly removed using Ampère's law. This is not possible in the presence of CRs,

because the mean motion of CRs also drives a current and hence affects the magnetic field. Accounting for both currents, we obtain for Ampère's law:

$$\boldsymbol{\nabla} \times \boldsymbol{B} = \frac{\boldsymbol{j}_{\mathrm{gas}} + \boldsymbol{j}_{\mathrm{cr}}}{c}. \tag{3.116}$$

Again, the CR current is an unknown quantity but can be inferred by reversing our arguments above for the thermal gas.

By definition CRs gyrate around the mean magnetic field, and thus on time-scales that are short in comparison to those of hydrodynamics. Furthermore, we expect CRs to be nearly gyrotropic, where deviations from purely parallel motions are induced by the macroscopic motions and the pressure of CRs. This inertia of CRs counteracts the Lorentz force and we expect that both reach dynamical equilibrium on time-scales of a few gyro-orbits, which is much shorter than the hydrodynamical time-scales. We can use this fact for a Chapman–Enskog expansion of the perpendicular components of the total momentum balance to infer a gyroaveraged expression for the large-scale Lorentz force. For this, we integrate equation (3.25) multiplied with $\boldsymbol{p}$ over momentum space, neglect the respective inertial terms that act on gyration time-scales, and project the result perpendicular to the mean magnetic field to obtain (see also equation 3.204):[3]

$$\frac{\boldsymbol{j}_{\mathrm{cr}} \times \boldsymbol{B}}{c} = \boldsymbol{\nabla}_{\perp} P_{\mathrm{cr}}. \tag{3.117}$$

This implies that any Lorentz force originating from a large-scale CR current is identically balanced by the pressure of CRs. Combining this equation with Ampère's law (3.116) yields an expression for the Lorentz force exerted on the gas,

$$\frac{\boldsymbol{j}_{\mathrm{gas}} \times \boldsymbol{B}}{c} = (\boldsymbol{\nabla} \times \boldsymbol{B}) \times \boldsymbol{B} - \frac{\boldsymbol{j}_{\mathrm{cr}} \times \boldsymbol{B}}{c} \tag{3.118}$$

$$= -\boldsymbol{\nabla} \cdot \left(\frac{\boldsymbol{B}^2}{2} \mathbf{1} - \boldsymbol{B}\boldsymbol{B} \right) - \boldsymbol{\nabla}_{\perp} P_{\mathrm{cr}}. \tag{3.119}$$

One consequence of the MHD assumption is that the electromagnetic field does not carry momentum. Consequently, equation (3.119) is already the momentum balance of the electromagnetic field, where the individual Lorentz forces are identically balanced by the magnetic pressure and stress. We arrive at a combined momentum balance of the thermal gas and electromagnetic fields by inserting equation (3.119) into equation (3.111). This would be the form of

[3] This argument can be easily seen for non-relativistic/low-energy CRs in the lab frame: for those, we can neglect all velocity components of the CR mean velocity $\boldsymbol{u}_{\mathrm{cr}}$ that are perpendicular after a gyroaverage for an approximately gyrotropic CR distribution and directly deduce equation (3.117) from the CR Euler equation $\partial_t(\rho_{\mathrm{cr}}\boldsymbol{u}_{\mathrm{cr}}) + \boldsymbol{\nabla} \cdot (\rho_{\mathrm{cr}}\boldsymbol{u}_{\mathrm{cr}}\boldsymbol{u}_{\mathrm{cr}} + P_{\mathrm{cr}}\mathbf{1}) = (\boldsymbol{j}_{\mathrm{cr}} \times \boldsymbol{B})/c + \boldsymbol{g}_{\mathrm{gri},+} + \boldsymbol{g}_{\mathrm{gri},-}$.

the momentum equation known from textbooks when the contributions of CRs would vanish. But equation (3.119) introduces the perpendicular CR pressure gradient into the Euler equation as an additional term that apparently acts as an additional force.

3.6.2 Parallel forces

CRs do not directly interact with the thermal gas in the direction parallel to the mean magnetic field. Their influence is indirect, with the Alfvén waves acting as a mediator. Once the streaming instability causes a substantial growth of Alfvén waves, CRs lose energy and momentum. Various damping mechanisms subsequently transfer this energy and momentum from the waves to the thermal gas. Only in this scenario all three participants are tightly coupled. We have already discussed the tight correspondence between the energy loss rate of Alfvén waves and the momentum transfer through the associated forces in Section 3.5.3. Using similar steps as presented therein, we will derive a relation for the ponderomotive force acting on the thermal gas. Taking the cross-product of Ampère's law for Alfvén waves with $\delta\boldsymbol{B}$ results in (see equation 3.119):

$$\frac{\delta\boldsymbol{j}_{\mathrm{gas}} \times \delta\boldsymbol{B}}{c} = (\boldsymbol{\nabla} \times \delta\boldsymbol{B}) \times \delta\boldsymbol{B} - \frac{\delta\boldsymbol{j}_{\mathrm{cr}} \times \delta\boldsymbol{B}}{c} \tag{3.120}$$

$$= -\boldsymbol{\nabla} \cdot \left(\frac{\delta\boldsymbol{B}^2}{2}\mathbf{1} - \delta\boldsymbol{B}\delta\boldsymbol{B} \right) - \frac{\delta\boldsymbol{j}_{\mathrm{cr}} \times \delta\boldsymbol{B}}{c}. \tag{3.121}$$

Combining this result with the perturbed continuity equation in the comoving frame, $\boldsymbol{\nabla}\cdot(\delta\boldsymbol{u}\rho) = 0$, and equation (3.72), we can simplify the ensemble average of the perturbed quantities on the right-hand side of Euler's equation (3.111):

$$\left\langle \frac{\delta\boldsymbol{j}_{\mathrm{gas}} \times \delta\boldsymbol{B}}{c} - (\rho\delta\boldsymbol{u} \cdot \boldsymbol{\nabla})\delta\boldsymbol{u} \right\rangle = -\boldsymbol{\nabla} \cdot \left(\frac{\left\langle \delta\boldsymbol{B}^2 \right\rangle}{2}\mathbf{1} \right) - \left\langle \frac{\delta\boldsymbol{j}_{\mathrm{cr}} \times \delta\boldsymbol{B}}{c} \right\rangle \tag{3.122}$$

$$= -\boldsymbol{\nabla}(P_{\mathrm{a},+} + P_{\mathrm{a},-}) + \boldsymbol{g}_{\mathrm{gri},+} + \boldsymbol{g}_{\mathrm{gri},-}, \tag{3.123}$$

after inserting $\delta\boldsymbol{B} = \delta\boldsymbol{B}^L_+ + \delta\boldsymbol{B}^R_+ + \delta\boldsymbol{B}^L_- + \delta\boldsymbol{B}^R_-$ and separating the different contributions of co- and counter-propagating waves. Again, CR-associated forces appear in the mean momentum equation solely through the assumption of vanishing electromagnetic momenta of Alfvén waves.

We can combine those results to obtain our final equations for the mean gas momentum in equation (3.2) by inserting equations (3.119) and (3.123) into equation (3.83). Similarly, we obtain the evolution equation for the combined kinetic and thermal gas energies and large scale electromagnetic fields in equation (3.4) by inserting equations (3.119) and (3.123) into equation (3.112) and adding the three equations (3.112), (3.113) and (3.115). This completes

our derivation of the MHD equations augmented by the presence of CRs and small-scale Alfvén waves and finally our full CR–MHD system.

3.6.3 Conservation laws

We now discuss the conservation of the total energy and momentum of the MHD-CR system. Formally, the total energy and the momentum vector as measured by an observer residing in an inertial frame has to be conserved in the Newtonian limit. Mathematically, this requirement implies that the total momentum and energy densities obey a conservation equation of the type:

$$\frac{\partial q}{\partial t} + \boldsymbol{\nabla} \cdot \boldsymbol{f} = 0, \tag{3.124}$$

where q is the volume density of the conserved quantity and $\boldsymbol{f}$ is its flux. The relativistic generalization of energy and momentum conservation requires the covariant derivative of the energy-momentum tensor to identically vanish, $T^{\alpha\beta}{}_{;\alpha} \equiv 0$ (assuming Einstein's sum convention). Because the total momentum and energy contains contributions from (relativistic) CRs, we have to derive their conservation laws in the relativistic framework, taking appropriate approximations that are aligned with the non-relativistic formulation of ideal MHD. To proceed, we need to transform the CR energy and momentum densities from the comoving frame to the lab frame. To first order, the Lorentz-transformation of these quantities is given by (Mihalas and Weibel Mihalas 1984, see also Appendix 3.14):

$$\varepsilon_{\rm cr}|_{\rm lab} = \varepsilon_{\rm cr} + 2\frac{\boldsymbol{u} \cdot (f_{\rm cr}\boldsymbol{b})}{c^2} + O\left(u^2/c^2\right), \tag{3.125}$$

$$\boldsymbol{f}_{\rm cr}\Big|_{\rm lab} = f_{\rm cr}\boldsymbol{b} + \boldsymbol{u}(\varepsilon_{\rm cr} + P_{\rm cr}) + O\left(u^2/c^2\right). \tag{3.126}$$

The truncation of the Lorentz transformation after terms of order $O(u/c)$ can lead to non-conservation of energy and momentum: the evolution equations of $\varepsilon_{\rm cr}|_{\rm lab}$ and $f_{\rm cr}|_{\rm lab}$ contain terms that cannot be expressed as pure flux terms. This can be seen by taking the time derivative of equations (3.125) and (3.126) and by inserting the respective evolution equations for the comoving quantities. In principle, we could circumvent this problem by including increasingly higher-order terms. However, we would have to simultaneously increase the order of the Lorentz-transformation and the evolution equations for $\varepsilon_{\rm cr}$ and $f_{\rm cr}$ to obtain a consistent result.

Nevertheless, the underlying problem of the above procedure is our initial semi-relativistic approximation of ideal MHD and macroscopic CR transport, which in general do not satisfy the fully relativistic conservation equations. We instead downgrade our approximations to the Newtonian limit and demonstrate energy and momentum conservation therein. In the Newtonian limit, the relativistic CR population can only be transported with a non-relativistic mean

velocity. Such a situation is realized, e.g., when CRs are streaming with $|f_{\rm cr}/(\varepsilon_{\rm cr}+P_{\rm cr})|\sim v_{\rm a} \ll c$. In this case, the CR momentum density is negligible, $f_{\rm cr}/c^2 \sim 0$, and the introduced degeneracy between the two frames vanishes. Neglecting terms containing the CR momentum, equation (3.11) reduces to

$$\boldsymbol{\nabla}_{\parallel} P_{\rm cr} = -\boldsymbol{g}_{\rm gri,+} - \boldsymbol{g}_{\rm gri,-}, \tag{3.127}$$

where $\boldsymbol{g}_{\rm gri,\pm}$ is defined in equation (3.98). Combining equations (3.119) and (3.127) implies that all acting external forces are identically balanced by the CR pressure or vice versa when their momentum is negligible.

In this Newtonian case, equation (3.125) shows that the CR energy density in lab and the comoving frame coincide. We can hence derive a total energy equation by adding the energy equations of the thermal gas, CRs and Alfvén waves of equations (3.4), (3.10), and (3.12), which results in

$$\frac{\partial \varepsilon_{\rm tot}}{\partial t} + \boldsymbol{\nabla}\cdot\boldsymbol{f}_{\rm tot} = \boldsymbol{u}\cdot\left(\boldsymbol{\nabla}_{\parallel} P_{\rm cr} + \boldsymbol{g}_{\rm gri,+} + \boldsymbol{g}_{\rm gri,-}\right) \tag{3.128}$$

$$= 0, \tag{3.129}$$

where the right-hand side vanishes by equation (3.127). Furthermore, in the Newtonian limit neither CRs nor the electromagnetic field carry momentum, which leaves the mean motion of the thermal gas as the sole contributor to the total momentum balance. Thus, by inserting equation (3.127) into the Euler equation (3.2), we arrive at the total momentum balance in the Newtonian limit,

$$\frac{\partial \rho \boldsymbol{u}}{\partial t} + \boldsymbol{\nabla}\cdot(\rho \boldsymbol{u}\boldsymbol{u} + P_{\rm tot}\mathbf{1} - \boldsymbol{B}\boldsymbol{B}) = \boldsymbol{0}. \tag{3.130}$$

To summarize, in the Newtonian limit the total momentum and energy is conserved, while our semi-relativistic approximation prohibits such a statement in the relativistic case in the comoving frame. In contrast to this, we can ensure energy and momentum conservation in the semi-relativistic limit if we formulate all CRs transport equation in the lab frame from the beginning. However, this comes with the serious drawback that we would need to resolve the gyroscale dynamics of our CR distribution, which is impossible for astrophysical simulations on the macroscale, see Appendix 3.14 for details.

3.7 Discussion

After the derivation of the Alfvén wave-mediated CR transport equation, here we show how it relates to the classical streaming-diffusion equation that was previously used to model CR

transport. We close by showing how to generalize our simplified picture of grey CR transport to include spectral information of CR momentum space and Alfvén wave-number space.

3.7.1 Relation to the streaming-diffusion equation

The Newtonian limit in the preceding section can be realized for rapid scattering. In this case the scattering times of CRs are fast compared to the slow time-scales of the macroscopic evolution of the CR–gas fluid and terms associated with the fast time-scale can be evaluated in their steady state limit. This argument is similar to the Chapman–Enskog expansion previously applied at the kinetic level (Skilling, 1975; Schlickeiser, 1989), but here adapted for the macroscopic description. The only terms in the CR transport equations that are assumed to be small in this expansion are those containing the CR mean momentum density $f_{\rm cr}/c^2$ in equation (3.11). Interestingly, exactly these terms have also been neglected in the Newtonian limit to derive equation (3.127). Thus, the results obtained in the Newtonian limit are indistinguishable to the Chapman–Enskog expansion of the CR equations. Indeed, by rearranging and expanding equation (3.127) using the definition of $\boldsymbol{g}_{\rm gri,\pm}$ of equation (3.98), we obtain Fick's law for CRs:

$$\boldsymbol{b}\cdot\boldsymbol{\nabla}\varepsilon_{\rm cr} = -\frac{1}{\kappa}\left[f_{\rm cr} - u_{\rm st}(\varepsilon_{\rm cr}+P_{\rm cr})\right], \tag{3.131}$$

where the streaming velocity with respect to the fluid is given by

$$u_{\rm st} = v_{\rm a}\frac{\bar{\nu}_+ - \bar{\nu}_-}{\bar{\nu}_+ + \bar{\nu}_-} \tag{3.132}$$

and the total diffusion coefficient is

$$\kappa = \frac{c^2}{3(\bar{\nu}_+ + \bar{\nu}_-)}. \tag{3.133}$$

Comparing equation (3.131) to its original and complete evolution equation (3.11), it becomes clear that the Chapman–Enskog expansion approximates the flux in steady state. Inserting equation (3.131) into equation (3.10) results in:

$$\begin{aligned}\frac{\partial\varepsilon_{\rm cr}}{\partial t} + \boldsymbol{\nabla}\cdot[(\boldsymbol{u}+u_{\rm st}\boldsymbol{b})(\varepsilon_{\rm cr}+P_{\rm cr}) - \kappa\boldsymbol{b}\boldsymbol{b}\cdot\boldsymbol{\nabla}\varepsilon_{\rm cr}] = \\ +(\boldsymbol{u}+u_{\rm st}\boldsymbol{b})\cdot\boldsymbol{\nabla}P_{\rm cr} + 4\frac{\bar{\nu}_+\bar{\nu}_-}{\bar{\nu}_+ + \bar{\nu}_-}\frac{v_{\rm a}^2}{c^2}(\varepsilon_{\rm cr}+P_{\rm cr}),\end{aligned} \tag{3.134}$$

which coincides with the streaming-diffusion equation, modified by the inclusion of last the term (Ko, 1992; Zweibel, 2017; Pfrommer et al., 2017a). This term represents the second-order Fermi process, which accelerates CRs via electro-magnetic interactions with Alfvén waves. Since both $\bar{\nu}_+$ and $\bar{\nu}_-$ are positive, this process always transfers energy from Alfvén waves to

CRs. Note that this term only takes this simple form if one assumes that the collision frequencies $\nu_\pm$ are independent of CR momentum. If this were not the case, we would obtain a formal integral over momentum space of the CR distribution.

To correctly account for the second-order Fermi process to order $O(\bar{v}v_a^2/c^2)$, two parts of our derivation are necessary. First, the Galilean invariance of the scattering terms. Second, the inclusion of Alfvén waves to accurately estimate the scattering coefficient. It further guarantees that the total energy, $E_{\rm tot}$, in the system is conserved by this process.

Skilling (1975) derives similar expressions for the streaming velocity $u_{\rm st}$, the total diffusion coefficient κ and the time-scale of the second-order Fermi process, as given by equation (3.134), see the expressions below his equation (9). His results are formulated and valid in the kinetic framework. Our results for these 3 quantities can be obtained by replacing the scattering frequencies $\nu_\pm$ with their pitch-angle averaged counterparts $\bar{\nu}_\pm$ and moving into the fluid picture by taking the energy moment of his equation (9).

3.7.2 Spectral CR hydrodynamics

Here, we outline how to extend the presented theory to model the propagation of the CR momentum spectrum from the non-relativistic to the ultra-relativistic regime, which would be equivalent to dropping our grey approximation of CR transport. This extension would provide a more accurate description of CR transport at the expense of being more complicated algebraically and numerically.

The fundamental assumption when evaluating moments of the focused transport equation (3.29) is the validity of the ultra-relativistic limit for the intrinsic CR speed. While this is certainly true for high-energy CRs, it fails for CR protons with a kinetic energy around their rest mass energy. This issue could be addressed by describing CR transport in a multi-spectral approach: instead of using the total energy of the entire CR population as the fundamental quantity, we could define spectral CR energy densities, i.e., integrated over a finite momentum range instead of the full momentum space. This would enable us to define a typical CR velocity of that spectral momentum range (thereafter called *bin*), which could be used instead of c in the transport equation.

The spectral bins could also be used to better account for the inherent momentum dependence of CR scattering. We adopted the approximation of replacing the momentum-dependent gyrofrequency by a typical value in order to obtain very compact expressions. Instead of choosing a reference gyrofrequency, we would be able to more accurately capture the typical momenta and associated gyrofrequencies in the multi-spectral approach.

So far, we adopted an isospectral ansatz for the Alfvén wave intensities to account for their inherent scale dependence. As discussed, this assumption has some drawbacks. In conjunction to or separate from the multi-spectral description for the CRs, it would be possible to also drop this approximation. The overall procedure would be the same: first, we would define wave number bins for the Alfvén-wave intensities and describe the emerging dynamics in those bins. This directly enables a more accurate description of the gyroresonant scattering process and non-linear Landau damping, as both strongly depend on wave number.

However, this extension would come with a price: all of our derivations rely on partial integrations and each spectral bin introduces new boundary terms for every partial integration. This inevitably would expand our evolution equations. Aiming for transparency in this work, we decided in favour of describing the CR distribution by only two independent thermodynamical quantities, namely an energy density and its corresponding flux. For this choice every boundary term vanishes identically and we obtain our compact results.

3.8 Numerical demonstration

In this section, we demonstrate the feasibility of our presented approach in one dimension that is oriented along a magnetic flux tube. We showcase the interplay of CR transport mediated by Alfvén wave dynamics in a few selected idealized cases and discuss the strengths and weaknesses of our approach in comparison to other approaches used in the literature.

3.8.1 Methods

Here, we solely focus our attention to the dynamics of the new CR-Alfvén wave subsystem of the full set of hydrodynamical equations and leave a three-dimensional implementation and study of the dynamical impact of CRs to future work. Hence, we assume that the background gas is at rest and all MHD quantities are constant ($\rho, B_0 = \text{const.}, \boldsymbol{B} = B_0 \boldsymbol{e}_x, \boldsymbol{u} = \boldsymbol{0}$). With this reduction, the CR transport and Alfvén wave equations (3.10), (3.11), and (3.12) simplify to the numerical standard form:

$$\frac{\partial \boldsymbol{Q}}{\partial t} + \frac{\partial \boldsymbol{F}(\boldsymbol{Q})}{\partial x} = \boldsymbol{S}(\boldsymbol{Q}), \tag{3.135}$$

where the state and flux vectors are

$$\boldsymbol{Q} = \begin{bmatrix} \varepsilon_{\rm cr} \\ f_{\rm cr} \\ \varepsilon_{\rm a,+} \\ \varepsilon_{\rm a,-} \end{bmatrix}, \quad \boldsymbol{F}(\boldsymbol{Q}) = \begin{bmatrix} f_{\rm cr} \\ c^2\varepsilon_{\rm cr}/3 \\ +v_{\rm a}\varepsilon_{\rm a,+} \\ -v_{\rm a}\varepsilon_{\rm a,-} \end{bmatrix}, \tag{3.136}$$

while the sources are given by

$$\boldsymbol{S}(\boldsymbol{Q}) = \begin{bmatrix} -\frac{v_{\rm a}}{3\kappa_+}\left(f_{\rm cr} - v_{\rm a}\gamma_{\rm cr}\varepsilon_{\rm cr}\right) + \frac{v_{\rm a}}{3\kappa_-}\left(f_{\rm cr} + v_{\rm a}\gamma_{\rm cr}\varepsilon_{\rm cr}\right) \\ -\frac{c^2}{3\kappa_+}\left(f_{\rm cr} - v_{\rm a}\gamma_{\rm cr}\varepsilon_{\rm cr}\right) - \frac{c^2}{3\kappa_-}\left(f_{\rm cr} + v_{\rm a}\gamma_{\rm cr}\varepsilon_{\rm cr}\right) \\ +\frac{v_{\rm a}}{3\kappa_+}\left(f_{\rm cr} - v_{\rm a}\gamma_{\rm cr}\varepsilon_{\rm cr}\right) - \alpha\varepsilon_{\rm a,+}^2 + S_{\rm inj} \\ -\frac{v_{\rm a}}{3\kappa_-}\left(f_{\rm cr} + v_{\rm a}\gamma_{\rm cr}\varepsilon_{\rm cr}\right) - \alpha\varepsilon_{\rm a,-}^2 + S_{\rm inj} \end{bmatrix}, \tag{3.137}$$

where $S_{\rm inj}$ accounts for unresolved sources of Alfvén-wave energy. We only account for non-linear Landau damping (Section 3.5.6) and neglect other damping processes. Throughout this section we use internal code units ($v_{\rm a} = 1$) and write for the diffusion coefficients:

$$\frac{1}{3\kappa_\pm} = \chi\varepsilon_{\rm a,\pm}, \tag{3.138}$$

using equation (3.61).

We solve this equation with a finite volume scheme, which is second order by design. The hyperbolic eigenvalues of equation (3.135) have characteristic velocities $\pm c/\sqrt{3}$ and $\pm v_{\rm a}$. To avoid excessive numerical diffusion we separately calculate numerical fluxes for the CR subsystem ($\varepsilon_{\rm cr}$, $f_{\rm cr}$) and for the Alfvén-wave system ($\varepsilon_{\rm a,+}$, $\varepsilon_{\rm a,-}$) respectively. The fluxes at the cell boundaries are determined via the localized Lax-Friedrichs approximate Riemann solver, which calculates fluxes for the left and right states (LeVeque, 1992). For these states we use a space-time predictor, which approximates the left and right boundary values at a half-step akin to the MUSCL-Hancock method, which implicitly includes source terms (van Leer, 1979). This predictor uses reconstructed state gradients, which are limited in characteristic variables by a minmod limiter (Toro, 2009). The full time-step results from the divergence of the flux and a calculation of the source term. To resolve the small time-scales of scattering, we subcycle the source terms and implicitly update the state-vector in each cycle. A necessary condition for numerical convergence of a hyperbolic partial differential equation is a Courant-Friedrichs-Lewy (CFL) number less than unity; we adopt 0.3. Whether our scheme achieves its convergence order in practice remains to be seen. No analytic solution of the full set of equations is known to the authors, which precludes a formal convergence study.

In astrophysical environments under our consideration (ISM, CGM, ICM) and thus in simulations of those systems the light speed is 10^2 to 10^4 times larger than any MHD velocity. Thus, in order to follow CR dynamics that propagates information with the light speed, the resulting timestep is 3×10^2 to 3×10^4 times smaller by virtue of the CFL condition. Furthermore, this high signal velocity entails larger numerical diffusion for any Riemann solver of the same order. To reduce the diffusivity of the solution, we are either forced to increase the numerical order of our scheme or increase the spatial resolution, which would render most simulations unfeasible due to the increase in computational time.

Both problems can be addressed simultaneously by the reduced-speed-of-light approximation, which replaces the physical speed of light by an ad-hoc choice of a reduced value:

$$c \rightarrow c_{\mathrm{red}} < c. \tag{3.139}$$

However, to ensure physical validity of this approximation, the characteristic signal speed $c_{\mathrm{red}}/\sqrt{3}$ of the CR subsystem has to be larger than any MHD velocity, which guarantees the correct propagation of information when coupled to MHD. This can be motivated by looking at the opposite case: if the CR signal speed is equal or smaller than the largest MHD velocity, then CRs are unable to outrun advection by the gas and hence, information contained in the CR distribution is transported differently in the numerical scheme in comparison to Nature.

3.8.2 Set-up and simulations

To demonstrate the emerging CR dynamics, we simulate three different cases, each of which probes a specific characteristics of CR transport. In Table 3.1 we summarize the adopted numerical parameters for our method.

We always choose the source term for Alfvén-wave energy S_{inj} in such a way that $\varepsilon_{\mathrm{a},\pm} = 4 \times 10^{-10} \ldots 7 \times 10^{-9}$ would be the equilibrium wave energy density if only injection and nonlinear Landau damping changed the wave energy. At this level of wave energy, CR scattering by the waves would have no effect on the time-scales considered here. Gyroresonant scattering introduces an additional source or sink term in the balance of wave energy. Hence, the injection of waves via S_{inj} serves as a dynamical process to avoid numerically degenerate solutions. The values of χ and α are chosen so that the typical wave energy $\varepsilon_{\mathrm{a},\pm} \sim 10^{-6}$ in the regime of CRs streaming with Alfvén velocity. We use 1024 grid cells that are uniformly distributed in the computational domain, which we state together with the initial conditions. We use outflowing boundary conditions after Thompson (1990).

Table 3.1: Adopted numerical parameters for simulations with our method.

name	ICs	c_{red}	χ	α	S_{inj}
`tp_A_c100`	A	100	5×10^{7}	5×10^{10}	1×10^{-8}
`tp_A_c100_ld`	A	100	1×10^{6}	1×10^{11}	5×10^{-6}
`tp_A_c100_id`	A	100	1×10^{6}	5×10^{11}	5×10^{-6}
`tp_A_c100_hd`	A	100	1×10^{6}	1×10^{12}	5×10^{-6}
`tp_A_c10`	A	10	5×10^{7}	5×10^{10}	1×10^{-8}
`tp_B_c100`	B	100	5×10^{7}	5×10^{10}	1×10^{-8}
`tp_C_c10`	C	10	5×10^{7}	5×10^{10}	1×10^{-8}
`tp_C_c100`	C	100	5×10^{7}	5×10^{10}	1×10^{-8}

(i) We employ three different initial conditions (ICs).
(ii) Here, c_{red} the reduce speed of light, χ is a numerical factor that describes the diffusion coefficient (see equations (3.138) and (3.61)), α is the wave damping coefficient due to non-linear Landau damping for which we distinguish three cases: low, intermediate and high damping rates (labelled with `ld`, `id` and `hd`, respectively); S_{inj} accounts for unresolved sources of Alfvén-wave energy.

All these models are chosen to highlight different aspects of CR dynamics and to emphasize differences between the methods. They are all pathological, as we assume some functional forms of the physical quantities $\varepsilon_{\mathrm{cr}}$, f_{cr} and $\varepsilon_{\mathrm{a},\pm}$ which may not have a realization in reality. Now, we successively introduce the initial conditions for the simulations shown in this work.

Initial conditions A: isolated Gaussian

Our canonical example is a Gaussian distribution of CR energy density. We set up the energy flux density so that CRs stream initially with at the Alfvén velocity down their gradient. We also assume that there is a constant pool of Alfvén waves of both propagation directions initially present while the Gaussian contains additional wave energy. The specific initial conditions are

given by

$$g(x) = \exp(-40x^2), \tag{3.140}$$

$$\varepsilon_{\rm cr}(x) = g(x), \tag{3.141}$$

$$f_{\rm cr}(x) = \gamma_{\rm cr}\,\mathrm{sgn}(x)\varepsilon_{\rm cr}(x), \tag{3.142}$$

$$\varepsilon_{\rm a,\pm}(x) = (1 + g(x)) \times 10^{-6}. \tag{3.143}$$

We use $[-1, 1]$ as our simulation domain.

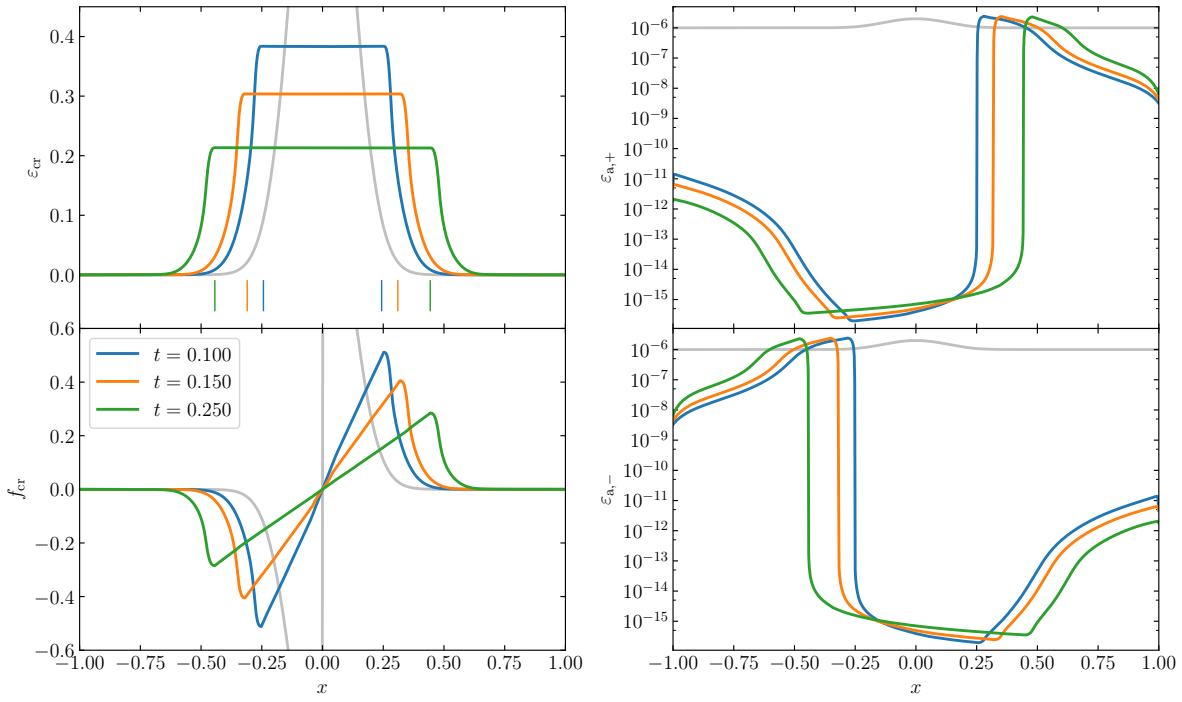

Figure 3.2: Temporal evolution of the Gaussian model `tp_A_c100` using our new description for Alfvén-wave-mediated CR transport. We show the CR energy density $\varepsilon_{\rm cr}$ and its flux $f_{\rm cr}$ (left-hand panels) as well as the energy density of co- and counter propagating Alfvén waves (right-hand panels) at three different times. The grey graphs show the initial conditions of each quantity, respectively. Vertical coloured lines in the top-left panel indicate the spatial extent of the Alfvénic characteristics of the initial Gaussian standard deviation that expand with velocity $\gamma_{\rm cr} v_{\rm a}$ in both directions.

Initial conditions B: Gaussian with background

The second set of initial conditions are given by

$$g(x) = \exp(-40x^2) \tag{3.144}$$

$$\varepsilon_{\mathrm{cr}}(x) = 10 + g(x) \tag{3.145}$$

$$f_{\mathrm{cr}}(x) = \gamma_{\mathrm{cr}}\mathrm{sgn}(x)g(x)\varepsilon_{\mathrm{cr}}(x) \tag{3.146}$$

$$\varepsilon_{\mathrm{a},\pm}(x) = (1 + g(x)) \times 10^{-6} \tag{3.147}$$

and follow the same reasoning as for initial conditions A, except that we place the Gaussian CRs distribution on top of a constant background of CR energy density, which has a 10 times larger amplitude in comparison to the Gaussian distribution. Setting up the flux this way ensures that only the Gaussian is streaming in the beginning while the background is kept at rest. Using this example, we can asses how the different numerical methods react to CR energy sources in the presence of an existing CR background. Here we simulate the domain $[-4, 4]$.

Initial conditions C: isolated box

The last set of initial conditions considered here is an isolated compact box of CR energy density, which is defined by

$$g(x) = 1_{[-1/4,1/4]}(x), \tag{3.148}$$

$$\varepsilon_{\mathrm{cr}}(x) = g(x), \tag{3.149}$$

$$f_{\mathrm{cr}}(x) = \gamma_{\mathrm{cr}}\mathrm{sgn}(x)\varepsilon_{\mathrm{cr}}(x), \tag{3.150}$$

$$\varepsilon_{\mathrm{a},\pm}(x) = (1 + g(x)) \times 10^{-6}, \tag{3.151}$$

where 1_A is the characteristic function of a set A. Again, we add an initial background of Alfvén waves which is enhanced in the region containing CRs. Here, the computational domain is given by $[-1, 1]$.

These initial conditions serve as a formal example to investigate the characteristics of the hyperbolic part of our differential equations. It is unlikely that this extremely sharp transition between the CR plateau and the region outside is realized in nature as the flat plateau would have to be communicated instantaneously and initial CR confinement would have to be perfect.

3.8.3 CR streaming and diffusion

In Fig. 3.2 we show the temporal evolution of the isolated Gaussian initial conditions for $\varepsilon_{\mathrm{cr}}$ (model `tp_A_c100`). We adopt a reduced speed of light of $c_{\mathrm{red}} = 100$ and thus begin with one

of the more natural set-ups.

The most prominent feature of the solution is the expanding plateau in the CR distribution, which propagates with the adiabatic Alfvén velocity $\pm\gamma_{\rm cr}v_{\rm a} = \pm 4/3$. The effective CR streaming velocity $u_{\rm st} \equiv f_{\rm cr}/(\varepsilon_{\rm cr} + P_{\rm cr})$ is sub-Alfvénic in the plateau region, as can be inferred from the bottom-left panel of Fig. 3.2. The plateau is flat since the CR energy density flux approximately scales as $f_{\rm cr} \sim x$ in this region, which yields $\partial f_{\rm cr}/\partial x \sim$ const. Hence, there is a coherent local CR energy loss which results in a decreasing energy level of the entire plateau. Co- and counter-propagating wave energy densities, $\varepsilon_{\rm a,\pm}$, are strongly damped as sub-Alfvénic streaming corresponds to a transfer of both wave energies to CRs because both wave types attempt to scatter CRs into their propagation direction. The injection of wave energy balances wave loses due to non-linear Landau damping and second-order Fermi processes at a low level of $\varepsilon_{\rm a,\pm} \sim 10^{-16}$.

The outer wings of the initial Gaussian CR population are spread out by CR diffusion because there is less wave energy available to efficiently scatter CRs. In these regions, the gyroresonant instability decelerates CRs and transfers their kinetic energy to Alfvén waves. This results in an increase of wave energy of the outwards propagating mode. Exactly at the transition between plateau and wings, there are spikes in $\varepsilon_{\rm a,\pm}$. These correspond to fronts at which CRs are scattered most efficiently and hence, stream almost perfectly with $f_{\rm cr} \approx \pm v_{\rm a}(\varepsilon_{\rm cr} + P_{\rm cr})$ so that residual growth of wave energy prevails over non-linear Landau damping.

As described, in the plateau region a large fraction of wave energy is damped. Hypothetical CR perturbations introduced there would not be efficiently scattered, because in order to do so, the waves would have to grow for approximately ten e-folding times to a level where the wave energy density would be large enough to affect the CR evolution. Hence these CR perturbations would propagate ballistically, an effect which we investigate now.

Using Fig. 3.3 we investigate how the reduced-speed-of-light approximation affects the overall solution. We accomplish this by simulating the time evolution of the idealized initial box and Gaussian CR distributions, each with two values of $c_{\rm red}$ (models `tp_A_c100` and `tp_A_c10` for the Gaussian as well as `tp_C_c100` and `tp_C_c10` for the box simulations, see Table 3.1). Because the numerical scattering time scales as $3\kappa/c_{\rm red}^2$, lowering $c_{\rm red}$ from 100 to 10 enables us to gain information about processes that usually happen at very small time-scales.

In the left column of Fig. 3.3 we display our solution for the box initial conditions in an $x - t$ diagram. In this plot every straight line corresponds to a characteristic velocity $u_{\rm char}$, as $x = u_{\rm char}t$. The most prominent characteristics is the adiabatic Alfvén velocity $\pm\gamma_{\rm cr}v_{\rm a}$, which encloses the extent of the evolved box. Visually, the true velocity appears to be somewhat

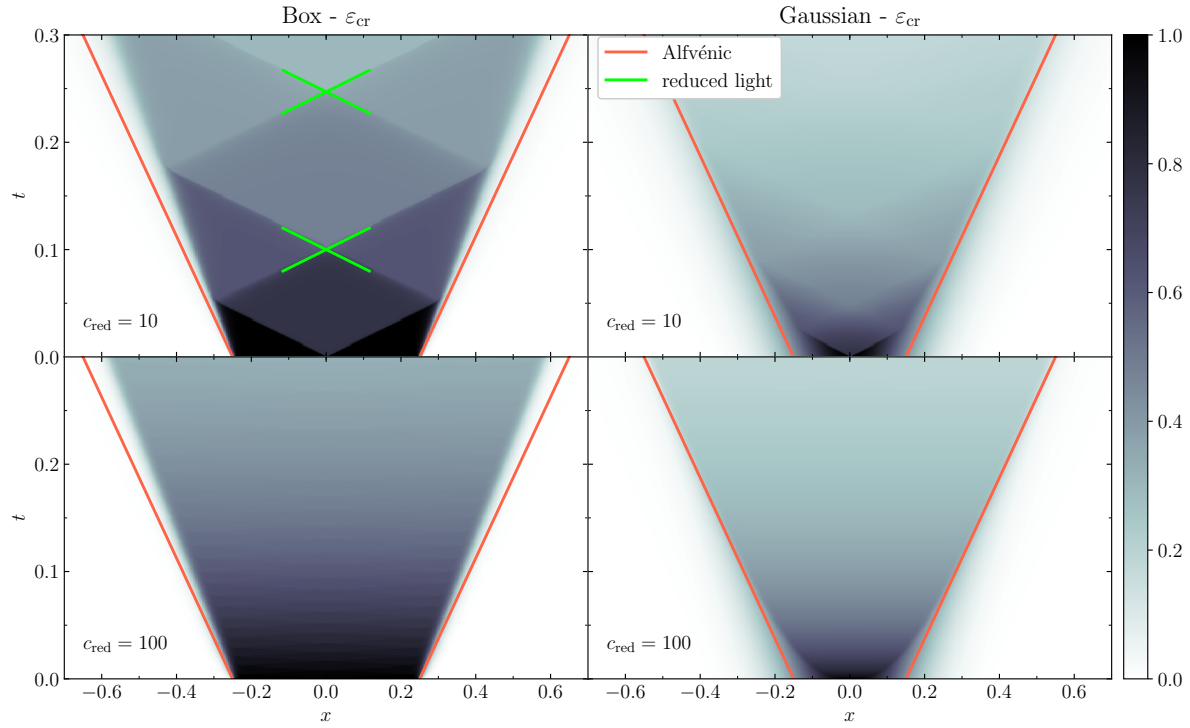

Figure 3.3: Time evolution of initial box (left column, models `tp_A_c10` and `tp_A_c100`) and Gaussian (right column, models `tp_C_c10` and `tp_C_c100`) CR distributions at different reduced speeds of light, c_{red}. While light-like characteristics are clearly visible for the evolving box distribution at low values of c_{red}, those disappear for larger values ($c_{red} = 100$) or for more realistic smooth initial CR distributions. These bird's-eye views of the evolving CR distributions show that CRs are self-confined in all cases and stream at the adiabatic Alfvén speed $\pm\gamma_{cr} v_a = \pm 4/3$. We colour-code the corresponding *Alfvénic* characteristics, which enclose the spatial extent of the CR distribution.

smaller, which results from the onset of diffusion at the box edges, causing them to spread apart.

In the pathological case of $c_{red} = 10$ (box initial conditions) we observe strong light-like characteristics propagating with velocity $\pm c_{red}/\sqrt{3}$. The initial sharp transition between the CR plateau and the region outside rapidly introduces an anisotropy via the geometric contribution of the Eddington term. As most of the initial wave energy has been used up to accelerate CRs via the second-order Fermi process, there is only a small amount of waves available to scatter CRs. Thus the anisotropically moving CRs cannot be efficiently scattered into one of the wave frames.

Furthermore, even though the CR gradient introduces anisotropy and should promote wave growth via the Eddington term, the growth rate is too small in order to efficiently reproduce waves. There are waves generated, but since the characteristics is a feature of small spatial extent travelling at large velocity its transition time is smaller than the wave growth time. The combination of both effects leads to incomplete scattering of these light-like characteristics, so that they propagate ballistically until they encounter one of the Alfvén characteristics. However, wave energy deposited by the light-like characteristics smoothes its wake. As the light-like characteristics interacts with the Alfvén characteristics, there is an evanescent wave transmitted and a reflected wave generated. While the evanescent wave damps instantaneously (the Alfvén mode prevails in presence of sufficiently energetic scattering waves), the reflected light-like characteristics propagates with a smaller amplitude in opposite direction.

The corresponding time-evolution of an isolated Gaussian for $c_{\rm red} = 10$ and $c_{\rm red} = 100$ is displayed in the right column of Fig. 3.3. Again, the entire CR population is enclosed by adiabatic *Alfvénic* characteristics that propagate at speed $\pm\gamma_{\rm cr} v_{\rm a} = \pm 4/3$. Here, the light-like characteristics are only present in the case $c_{\rm red} = 10$ for an initial transient after which they quickly diffuse and vanish almost entirely. In the case of $c_{\rm red} = 100$ there are no residual light-like characteristics visible and the evolution is completely smooth.

3.8.4 Impact of damping

In Fig. 3.4 we compare the influence of the damping coefficient α on the solution of isolated Gaussian simulations (initial conditions A). We show the results for simulations with $\alpha = 1\times10^{11}, 5\times10^{11}$ and 1×10^{12} at $t = 0.04$ and $c_{\rm red} = 100$ (models `tp_A_c100_ld`, `tp_A_c100_id` and `tp_A_c100_hd`). Here, we use a smaller CR-Alfvén wave coupling constant $\chi = 10^6$ to increase the relative impact of damping.

Corresponding to the notion of stronger damping, the maximum wave energy decreases for increasing damping coefficients. The overall shape of $\varepsilon_{\rm cr}$ remains similar while increasing damping coefficients yield broadened solutions of $\varepsilon_{\rm cr}$. This behaviour is expected: as less wave energy is available to scatter the CRs into their frame, the mode of ballistic transport starts to influence the solution. Hence, CRs get less efficiently scattered in the direction opposing their current propagation direction. As a result, an increasing damping rate yields an increasing CR flux density and consequently a broader, more diffusive solution of $\varepsilon_{\rm cr}$.

The particular numerical solutions presented here are clearly influenced by our choice of non-linear Landau damping. However, the overall trend remains the same for all damping processes. Consider two situations that start with the same CR distribution but exhibit varying

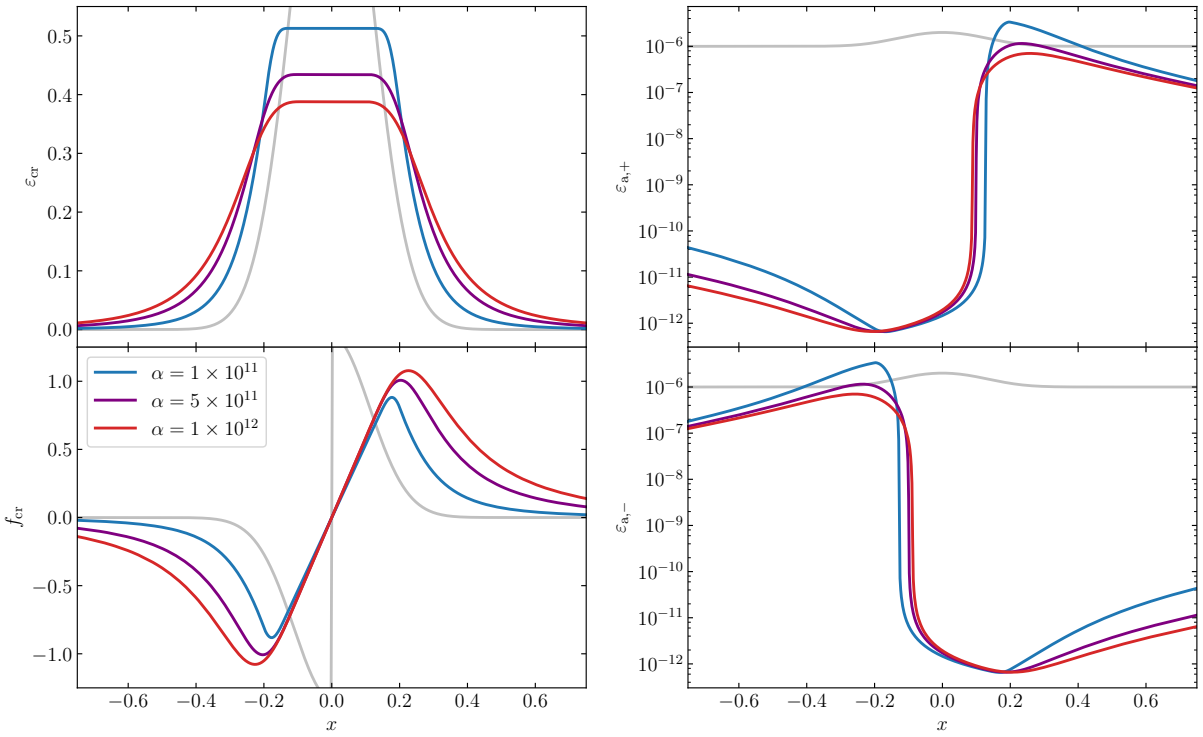

Figure 3.4: Effects of increasing the wave damping coefficient due to non-linear Landau damping, α. As α increases, the initial Gaussian becomes broader due to lack of efficient scattering, which is accompanied by an increasing CR energy flux density $f_{\rm cr}$. We use the same initial conditions for all three displayed values of α (shown in grey), adopt a reduced speed of light of $c_{\rm red} = 100$, and choose a snapshot at $t = 0.04$.

damping strengths. The case of stronger damping implies a more evolved CR distribution with a larger spatial support in comparison to the situation with the weaker damping process.

Lowering the imposed dynamical Alfvén wave energy threshold by altering the injection rate does not change the presented qualitative results in terms of $\varepsilon_{\rm cr}$ and $f_{\rm cr}$. Doing so results in lower overall levels of wave energy density.

3.8.5 Comparison to previous approaches

Here, we compare our approach to two other approaches for CR transport in the literature: Sharma et al. (2010) model equilibrium CR streaming that is augmented with numerical diffusion to ensure numerical stability and Jiang and Oh (2018) employ an ansatz inspired by RT. In Table 3.2 we summarize the adopted numerical parameters for each of their methods.

We compare simulations of two set-ups: the evolution of an isolated Gaussian of $\varepsilon_{\rm cr}$ (initial

Table 3.2: Adopted numerical parameters for simulations with the methods of Sharma et al. (2010) and Jiang and Oh (2018).

Method of Sharma et al. (2010):					
name	ICs	δ	$c_{\rm red}$	χ	α
`sc_A`	A	100		5×10^7	5×10^{10}
`sc_B`	B	100		5×10^7	5×10^{10}
Method of Jiang and Oh (2018):					
name	ICs	δ	$c_{\rm red}$	χ	α
`jo_A`	A		100	5×10^7	5×10^{10}
`jo_B`	B		100	5×10^7	5×10^{10}

(i) We employ two different initial conditions (ICs).
(ii) Here, δ is the regularization parameter of the streaming velocity in equation (3.154), $c_{\rm red}$ the reduced speed of light that enters equation (3.161), χ is a numerical factor that describes the diffusion coefficient, and α is the wave damping coefficient due to non-linear Landau damping.

conditions A, see Fig. 3.5) and of a Gaussian CR distribution on a homogeneous background (initial conditions B, see Fig. 3.6). While we have discussed the evolution of an isolated Gaussian with our theory in Section 3.8.3, here we briefly comment on the additional features that the solution assumes when we consider the Gaussian on a homogeneous background.

As CRs are streaming away from the extremum, the wings of the Gaussian expand and the central extremum decreases. As a result, the background $\varepsilon_{\rm cr}$ needs to respond to this change because the available volume for background CRs decreases since CRs cannot stream upwards their gradient. If this change were communicated with infinite signal speed, the level of CR background would steadily rise by analogy with the water level of a basin in which the walls are moving together. However, in reality this change needs to be communicated with the fastest signal speed. Indeed, our numerical solution shows two propagating bow waves ahead of the streaming Gaussian wings into the background medium that travel with the fastest characteristics $\pm c/\sqrt{3}$ (see Fig. 3.6). The wave front induces a small anisotropy which distorts the local equilibrium. With this anisotropy, a local preferred direction exists and CRs are scattered with different strengths by co- and counter-propagating waves. Due to this imbalance, the CRs begin to stream with the Alfvén speed in the preferred direction (see bottom-left panel of Fig. 3.6).

Method of Sharma et al. (2010)

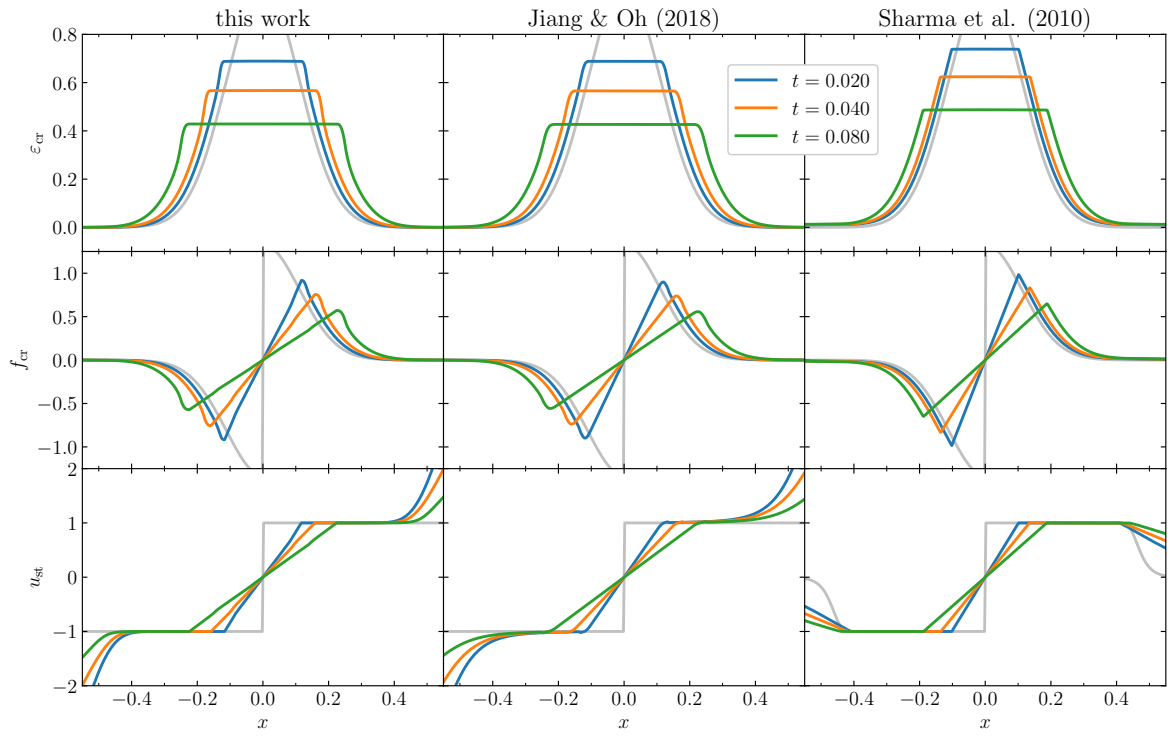

Figure 3.5: Comparison of the time evolution of an isolated Gaussian of $\varepsilon_{\rm cr}$ using three numerical methods. From left to right we compare the models `tp_A_c100`, `jo_A`, and `sc_A`. From top to bottom, we show CR energy density $\varepsilon_{\rm cr}$, its flux density $f_{\rm cr}$ and the CR streaming velocity $u_{\rm cr}$ at three different times (colour-coded). In the model of Sharma et al. (2010), we use the regularized streaming velocity of equation (3.154), regularized CR energy flux of equation (3.155) and define $u_{\rm st} \equiv f_{\rm cr}/(\varepsilon_{\rm cr} + P_{\rm cr})$ for the other two approaches.

Neglecting contributions from second-order Fermi processes, the steady-state version of the streaming-diffusion equation (3.134) reads in our simplified setting:

$$\frac{\partial \varepsilon_{\rm cr}}{\partial t} + \frac{\partial}{\partial x}\left[u_{\rm st}(\varepsilon_{\rm cr} + P_{\rm cr}) - \kappa_0 \frac{\partial \varepsilon_{\rm cr}}{\partial x}\right] = u_{\rm st}\frac{\partial P_{\rm cr}}{\partial x}, \tag{3.152}$$

where the streaming velocity is given by

$$u_{\rm st} = -v_{\rm a}\,{\rm sgn}\left(\frac{\partial \varepsilon_{\rm cr}}{\partial x}\right), \tag{3.153}$$

and κ_0 is a diffusion coefficient valid in equilibrium, where gains of Alfvén-wave energy via the gyroresonant instability are exactly canceled by wave-loss processes.

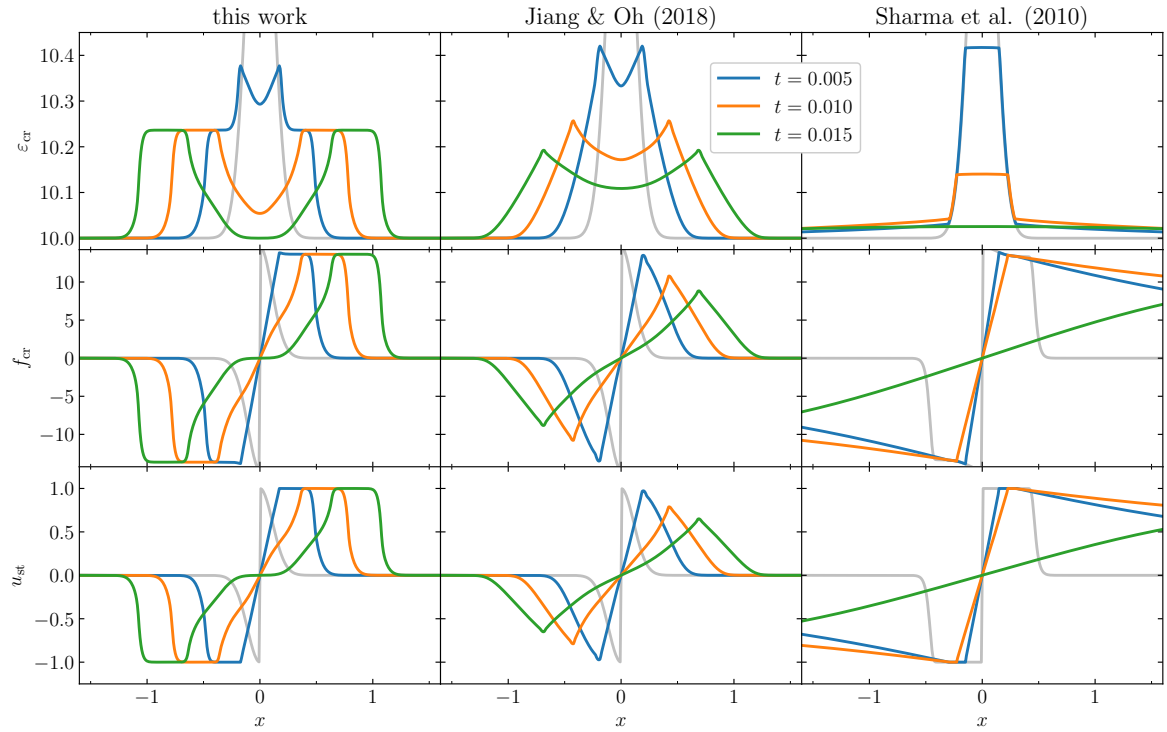

Figure 3.6: Same as in Fig. 3.5, but for the Gaussian on top of a homogeneous distribution of CR energy density. From left to right we compare the models `tp_B_c100`, `jo_B`, and `sc_B`.

This equation cannot be integrated using conventional finite-volume numerical methods because the functional form of this streaming velocity implies that the equation is a highly nonlinear diffusion equation. This problem was first analysed by Sharma et al. (2010), who suggested to regularize the streaming velocity of equation (3.153) via

$$\tilde{u}_{\rm st} = -v_{\rm a} \tanh\left(\frac{1}{\delta}\frac{\partial \varepsilon_{\rm cr}}{\partial x}\right), \tag{3.154}$$

where δ = const. is a (small) regularization parameter. By analogy with our theory applied to steady state, we define the regularized CR energy flux density:

$$\tilde{f}_{\rm cr} = \tilde{u}_{\rm st}(\varepsilon_{\rm cr} + P_{\rm cr}). \tag{3.155}$$

For $\delta \to 0$ the regularized streaming velocity matches its analytic counterpart. Inserting expression (3.154) for $\tilde{u}_{\rm st}$ into equation (3.152) yields for the advection term

$$\frac{\partial}{\partial x}\left[\tilde{u}_{\rm st}(\varepsilon_{\rm cr} + P_{\rm cr})\right] = \tilde{u}_{\rm st}\frac{\partial}{\partial x}(\varepsilon_{\rm cr} + P_{\rm cr}) - \kappa_{\rm reg}\frac{\partial^2 \varepsilon_{\rm cr}}{\partial x^2}, \tag{3.156}$$

with

$$\kappa_{\rm reg} = v_{\rm a}\gamma_{\rm cr}\varepsilon_{\rm cr}\frac{1}{\delta}\mathrm{sech}^2\left(\frac{1}{\delta}\frac{\partial\varepsilon_{\rm cr}}{\partial x}\right). \tag{3.157}$$

Here, $\kappa_{\rm reg}$ is a numerical diffusion coefficient that depends on the regularization parameter δ, the CR energy density, and its gradient. For weak CR energy gradients ($\partial\varepsilon_{\rm cr}/\partial x \ll \delta$) numerical diffusion dominates the solution while steady-state CR streaming emerges for steep CR energy density gradients ($\partial\varepsilon_{\rm cr}/\partial x \gg \delta$).

With this choice, the streaming-diffusion equation is classified as a non-linear diffusion equation, even in the limit of negligible physical diffusion ($\kappa_0 = 0$), and can be numerically integrated. In practical terms, this regularization attempts to emulate the steady state by reconstructing local CR streaming based on the energy gradient. The extension of equation (3.153) to values in between $\pm v_{\rm a}$ is justified, as this corresponds to a smooth transition between the two limiting stationary cases. The fact that we observe this behaviour in simulations of our new non-equilibrium CR transport model provides additional physical justification for this regularization.

To compare the results of this method to ours, we include the effects of finite physical diffusion modelled by κ_0. Performing a simultaneous Chapman–Enskog expansion of the equations for wave energy and CR energy flux (equation 3.135) we can estimate the energy density of the dominant wave species as:

$$\varepsilon_{\rm a} = \sqrt{\frac{v_{\rm a}}{3\alpha}\left|\frac{\partial\varepsilon_{\rm cr}}{\partial x}\right|}. \tag{3.158}$$

The associated diffusion coefficient κ_0 is given by

$$\frac{1}{\kappa_0} = \chi\sqrt{\frac{3v_{\rm a}}{\alpha}\left|\frac{\partial\varepsilon_{\rm cr}}{\partial x}\right|} \tag{3.159}$$

using the closure relation of equation (3.138). This argument for the evaluation of the diffusion coefficient κ_0 corresponds to that given before by Völk and McKenzie (1981); Jiang and Oh (2018) and numerically implemented by Wiener et al. (2013).

We implement this regularized scheme by evaluating the gradient in equation (3.154) on cell faces while all gradients in equation (3.152) are discretized using central differences. We integrate the time derivative using an explicit super-timestepping Runge-Kutta method (Meyer et al., 2012), which permits us to treat the non-linear parabolic terms robustly and with large, second-order accurate time-steps, thereby circumventing the restrictive parabolic von-Neumann criterion. In particular, we adopt a regularization parameter of $\delta = 0.005$ and use 120 super-timesteps.

In the right column of Fig. 3.5 we show the time evolution of the isolated Gaussian of $\varepsilon_{\rm cr}$ for the model by Sharma et al. (2010) (using model `sc_A`) and compare it to our numerical method. Both wings of the Gaussian are correctly transported with $\pm\gamma_{\rm cr} v_{\rm a} = \pm 4/3$. In this regime, the CRs transfer a sufficient amount of energy to resonant Alfvén waves in order to balance the damping of this wave type. In the assumed steady-state limit this corresponds to the regime in which one (i.e., the resonant) wave type dominates. Furthermore, the steady-state assumption implies that the CR distribution is isotropic in the frame of the dominant wave. As CRs stream away from the maximum, the spatial support of the Gaussian broadens. Energy conversion smoothes out the initial maximum in $\varepsilon_{\rm cr}$ so that it converges onto a plateau distribution. The residual gradient on the plateau continuously connects both wings in terms of energy flux density. This arises as a result of the diffusive nature of the regularization scheme, which would smooth any strong gradient of the energy flux.

In Fig. 3.6 we add a constant background of CR energy density (corresponding to the model `sc_B`). Now, the initial Gaussian is a small addition to the background, which is quickly erased by the diffusive nature of the regularization scheme. As a result, the CR energy converges to a constant value, losing any information about the initial conditions. Thus, in the picture of Sharma et al. (2010), the solution of this problem depends entirely on numerical diffusion and the specific choice of the regularization parameter.

Method of Jiang and Oh (2018):

The fundamental idea of Jiang and Oh (2018) was to describe CR transport with the equations of RT while modifying the scattering terms in order to restore the strongly-coupled limit of CR transport. For a medium at rest their one-dimensional equations read:

$$\frac{\partial \varepsilon_{\rm cr}}{\partial t} + \frac{\partial f_{\rm cr}}{\partial x} = u_{\rm st} \frac{\partial P_{\rm cr}}{\partial x}, \text{ and} \tag{3.160}$$

$$\frac{1}{c_{\rm red}^2} \frac{\partial f_{\rm cr}}{\partial t} + \frac{\partial P_{\rm cr}}{\partial x} = -\frac{1}{\kappa} f_{\rm cr}, \tag{3.161}$$

where all quantities retain the same meaning as in the preceding sections. The resemblance to the transport part of our equations (3.43) and (3.44) is not incidental since both descriptions root in the same ideas that originate from RT. In multiple dimension, however, both transport theories differ fundamentally as Jiang and Oh (2018) model the transport of CR energy in terms of a three-dimensional flux while our theory is based on its projection onto the direction of the

local magnetic field. The system of equations (3.160) and (3.161) is closed by

$$u_{\rm st} = -v_{\rm a}\,\mathrm{sgn}\left(\frac{\partial P_{\rm cr}}{\partial x}\right), \text{ and} \tag{3.162}$$

$$\kappa = \kappa_0 + \left|\frac{\partial P_{\rm cr}}{\partial x}\right|^{-1} v_{\rm a}\,(\varepsilon_{\rm cr} + P_{\rm cr})\,, \tag{3.163}$$

where the first equation encodes the steady-state limit of the streaming velocity. The second equation contains a diffusion coefficient κ_0 and a second term that is proportional to the Alfvén speed times the CR gradient length. We adopt the same approximation for the physical diffusion as laid down in equation (3.159). Taking the steady state limit with $\kappa_0 \to 0$ of equation (3.161) results in

$$f_{\rm cr} = u_{\rm st}(\varepsilon_{\rm cr} + P_{\rm cr}), \tag{3.164}$$

which corresponds to the correct energy flux in the limit of streaming CRs. Thus, the equations of Jiang and Oh (2018) can be regarded as a compromise between our theory and that of Sharma et al. (2010).

This closure of the diffusion coefficient in equation (3.163) is the distinguishing feature of the formalism by Jiang and Oh (2018), as it aims at reconstructing an effective diffusion coefficient from local information of $\varepsilon_{\rm cr}$ only. Its particular choice roots in the idea that any CR pressure gradient excites Alfvén waves, which efficiently scatter CRs so that they are primarily transported via streaming. Because the scattering coefficient scales as $\bar{\nu} \propto \varepsilon_{\rm a} \propto \kappa^{-1}$, a large gradient of $\varepsilon_{\rm cr}$ and consequently of steady-state wave energy implies a small diffusion coefficient. Conversely, CRs experience a large diffusion coefficient if the wave energy and hence the CR pressure gradient is negligible.

The numerical problems arising when evaluating the derivative of the discontinuity of the streaming velocity (i.e., $\mathrm{sgn}(\partial\varepsilon_{\rm cr}/\partial x)$) are naturally circumvented here, as the problematic term in equation (3.152) is replaced by the flux density $f_{\rm cr}$. Nevertheless, equation (3.161) depends non-linearly on $\partial P_{\rm cr}/\partial x$ through equation (3.163) and is thus classified as a Hamilton-Jacobi equation.[4] As a consequence of this model, the closure alters the signal propagation speed of the entire system.

We implement a numerical solver similar to that described by Jiang and Oh (2018). To this end we use the modified two-stage Runge-Kutta scheme to advance all quantities. The hyperbolic part of the equations is calculated using slope-limited piece-wise linear extrapolation to

[4] A Hamilton Jacobi equation in the theory of partial differential equations has the form $\partial q/\partial t = H(x, q, p = \partial q/\partial x)$, where in general q is a state vector and $H(x, q, p)$ is the Hamiltonian. Matching our physical intuition, the signal velocity s of the system is given by $s = \partial H(x, q, p)/\partial p$.

cell faces and the Lax–Friedrichs Riemann solver while the sources terms are treated implicitly. We calculate the diffusion coefficient of equation (3.163) before each stage as the mean of the left and right gradients of a cell. For this method, we use the same values of χ and α as for our method.

We show the results of this scheme for the isolated Gaussian (defined by model `jo_A`) in the middle column of Fig. 3.5. All displayed schemes show a flattening of the initial maximum of the CR pressure to a plateau where the gradient of $P_{\rm cr}$ approaches zero. This implies a large CR diffusion coefficient according to equation (3.163). The wings of the Gaussian are characterized by a sizeable CR gradient, which limits the diffusivity onto the diffusion coefficient κ_0. Here, the advective aspect of the scheme dominates, which results in a streaming CR distribution. In the transition zone CRs stream with Alfvén speed because the scattering coefficient is increased so that the flux rapidly converges towards $f_{\rm cr} = \pm v_{\rm a}(\varepsilon_{\rm cr} + P_{\rm cr})$. This corresponds to the equilibrium flux in equation (3.161) for a negligible diffusion mediated by κ_0. Overall the results with the method of Jiang and Oh (2018) for this test problem are almost identical to those obtained with our theory.

If we add a constant background to the Gaussian (model `jo_B`) and evolve the equations of Jiang and Oh (2018), the results are qualitatively comparable to that obtained by our new formulation but there are notable quantitative differences. The Gaussian is broadened, while maintaining a clear spatial separation to the background, which responds to the expanding enhancement of CR energy density. This scheme captures the undershoot at the position of the initial maximum of $\varepsilon_{\rm cr}$, however not to its full extent in comparison to the results of our new theory. The travelling plateaus seen in the evolution with our method are erased in the scheme of Jiang and Oh (2018) so that only a spike remains, which marks the transition between the moving wings and undershoot.

In conclusion, the transport equations by Jiang and Oh (2018) qualitatively agree better with our results and also show clear differences to the regularization approach of Sharma et al. (2010). This is the result of the adopted closure of Jiang and Oh (2018) for the diffusion coefficient, which emulates the actual CR dynamics more accurately.

3.9 Conclusions

We succeeded in developing a new macroscopic transport theory for CR transport, which includes both CR diffusion and streaming along magnetic field lines in the self-confinement picture: as CRs stream super-Alfvénically along the magnetic field, they resonantly excite Alfvén

waves through the gyroresonant instability. Scattering off of this wave field modulates the macroscopic mode of CR transport in interesting and non-trivial ways.

For the first time, we provide a mathematically rigorous derivation of the equations of CR hydrodynamics that are coupled to the evolution of Alfvén waves in the Eddington approximation of RT. We accomplish this by evaluating the zeroth- and first-order CR pitch-angle moment of the gyro-averaged CR transport equation and successive integration over CR-momentum space. As a result, we obtain two coupled evolution equations for the CR energy density $\varepsilon_{\rm cr}$ and its flux density $f_{\rm cr}$, which resemble the equations of classical radiation hydrodynamics.

However, both equations depend on CR scattering terms, which need to be specified to close this set of equations. Our key insight for evaluating CR scattering at magnetic turbulence consists in considering a reference energy of typical CRs, similar to the grey approximation of RT. This yields a pitch-angle-averaged scattering frequency that depends on the energy level of co- and counter-propagating waves, $\bar{\nu}_{\pm} \propto \varepsilon_{\rm a,\pm}$, and is not a constant value as often assumed in the literature. We explicitly demonstrate that CR-wave scattering terms to order $O(\bar{\nu} v_{\rm a}^2/c^2)$ need to be considered in order to provide a Galilean invariant and flux-limited CR transport. A Chapman–Enskog expansion of this new set of equations (i.e., filtering out fast time-scales associated with non-equilibrium transients) or equivalently the Newtonian limit enables us to recover the classical streaming-diffusion equation of CR transport in the steady-state flux limit.

The dependence of the scattering rate on $\varepsilon_{\rm a,\pm}$ immediately exemplifies the need to dynamically also evolve the Alfvén wave equations for self-consistency. To this end, we derive the transport of wave energy and cast it into our new picture. We provide a complete review of all available wave damping processes such as sub-Alfvénically streaming CRs, non-linear Landau damping, ion-neutral damping, turbulent and linear Landau damping, and show how their contributions change $\varepsilon_{\rm a,\pm}$. Most importantly, we explicitly demonstrate that the energy lost by CRs owing to the gyroresonant instability exactly matches the energy gained by Alfvén waves only if the calculation is done at least to order $O(\bar{\nu} v_{\rm a}^2/c^2)$.

We couple the new CR-Alfvénic subsystem to ideal MHD, ensuring energy and momentum conservation in the non-relativistic limit of MHD. A covariant derivation of our CR hydrodynamical equations in the semi-relativistic limit in the Appendix demonstrates the validity of these conservation laws. In particular, this calculation reveals that the adiabatic CR source term in the Newtonian limit can be understood as a non-vanishing metric connection (Christoffel symbol), i.e., it has the meaning of a geometric term that results from the transformation into the non-inertial comoving frame and is not equivalent to the work associated with a force.

We finally show numerical solutions of our new CR-Alfvén wave subsystem in one dimen-

sion that is oriented along a magnetic flux tube. Our first-principle approach significantly advances over previous steady-state approaches because it enables us for the first time to include non-equilibrium kinetic effects such as non-linear Landau damping, second-order Fermi acceleration or energy transfer via the gyroresonant instability in hydrodynamical settings. In particular, our numerical implementation enables to quantify the relative impact of these kinetic effects on CR transport and on how CR and wave-pressure gradients impact the dynamics of thermal plasma.

We provide a first parameter study of our CR transport theory and asses how it reacts to variations in

- the reduced speed of light, $c_{\rm red}$: smaller values give access to processes that act on faster time-scales but also promote (unphysical) ballistic CR transport;
- the wave damping coefficient α (due to the non-linear Landau process): larger values damp the peak wave energy, increase the CR flux density, and make CR transport more diffusive;
- the unresolved sources of Alfvén-wave energy, $S_{\rm inj}$: as long as there is some initial wave energy, the solution for the peak wave energy (that determines the mode of CR transport) is independent on the exact wave amplitude.

We emphasize that our theory has no tunable free parameters: $c_{\rm red}$ is chosen so that the solution does not depend on its specific value; the wave damping coefficient α and the inverse CR diffusion coefficient χ are given by MHD quantities and the characteristic gyrofrequency of our CR population in the grey approximation; and $S_{\rm inj}$ does not impact on the solution as long as it does not become dynamically important. This should enable us to accurately capture momentum and energy deposition of propagating CRs in future simulations of galaxy formation.

Our numerical simulations recover CR streaming and diffusion at self-generated waves. Comparing our solutions to two previously suggested approaches, we highlight similarities and differences. Our approach recovers the equation of Sharma et al. (2010) in the physical steady-state limit (i.e., in the presence of sufficient Alfvén wave energy). However, their approach has the weakness of excessive numerical diffusion for small CR gradients. This problem is reinforced in the presence of highly stratified CR energy densities, which are inevitably encountered in simulations of galaxies and galaxy clusters. This renders the solution problematic if CRs are injected into an already pre-existing CR background as this represents the weak-gradient regime.

Jiang and Oh (2018) describe CR transport with the equations of RT while modifying the scattering terms. Overall, the results obtained with their method are almost identical to those

obtained with our theory for the problems studied here. This is due to a similar two-moment treatment of CR transport in those approaches.

Summarizing, our novel derivations of CR hydrodynamics holds the promise to provide a sustainable framework to assess the importance of CR momentum and energy feedback for galaxy formation and the cosmological evolution of cool core galaxy clusters.

3.10 Appendix: CR diffusion

Following up on our discussion in Section 3.7.1 we saw that the diffusion term in the streaming-diffusion equation is a combination of $O(\bar{\nu}_\pm)$ terms in the Taylor expansion with respect to the small variable v_a/v. Hence, the diffusion term is present in any expansion. As we will show in the following, against common belief a purely diffusing CR population is physically inconsistent in case of self-confined CRs.

We start by expanding equation (3.53) to order $O(\nu_\pm)$ in v_a/v, which yields

$$\left.\frac{\partial f}{\partial t}\right|_\mathrm{scatt} = \frac{\partial}{\partial \mu}\left[\frac{1-\mu^2}{2}(\nu_+ + \nu_-)\frac{\partial f}{\partial \mu}\right]. \tag{3.165}$$

In physical terms this expansion neglects any contribution from electric fields. Consequently, the interaction between waves and CRs is fully described by pitch-angle scattering (even in the comoving frame). Taking the appropriate moments as in Section 3.4.2 results in

$$\left.\frac{\partial \varepsilon_\mathrm{cr}}{\partial t}\right|_\mathrm{scatt} = 0, \tag{3.166}$$

$$\left.\frac{\partial f_\mathrm{cr}}{\partial t}\right|_\mathrm{scatt} = -(\bar{\nu}_+ + \bar{\nu}_-) f_\mathrm{cr}. \tag{3.167}$$

The physical interpretation is straightforward: as CRs scatter solely off of magnetic fields, there is no energy transfer between waves and CRs. Furthermore, according to this equation, the CR population will evolve towards an isotropic distribution in the comoving frame because the scattering term of equation (3.53) is formulated in the comoving frame. This is in direct contrast to our finding that the appropriate frame of isotropization is the frame moving with Alfvén waves, which precludes an accurate formulation of CR transport to lowest (zeroth) order in the expansion variable v_a/v. In fact, in order to account for the Doppler-shift between gas and propagating waves, terms of order v_a/v are necessary.

Inserting these scattering terms in our fluid equations (3.43) and (3.44), we obtain a compact

set of transport equations:

$$\frac{\partial \varepsilon_{\rm cr}}{\partial t} + \boldsymbol{\nabla} \cdot [\boldsymbol{u}(\varepsilon_{\rm cr} + P_{\rm cr}) + \boldsymbol{b} f_{\rm cr}] = \boldsymbol{u} \cdot \boldsymbol{\nabla} P_{\rm cr} \tag{3.168}$$

$$\frac{\partial f_{\rm cr}}{\partial t} + \boldsymbol{\nabla} \cdot (\boldsymbol{u} f_{\rm cr}) + \frac{c^2}{3} \boldsymbol{b} \cdot \boldsymbol{\nabla} \varepsilon_{\rm cr} = -(\boldsymbol{b} \cdot \boldsymbol{\nabla} \boldsymbol{u}) \cdot (\boldsymbol{b} f_{\rm cr}) - (\bar{\nu}_+ + \bar{\nu}_-) f_{\rm cr} \tag{3.169}$$

In the following, we restrict ourselves to the special case of a background gas at rest and a homogeneous magnetic field (i.e., $\boldsymbol{u} = \boldsymbol{0}$ and $\boldsymbol{b} = \text{const.}$). Differentiating equation (3.168) with respect to t, taking the gradient along the magnetic field direction of equation (3.169), and combining the resulting equations, we obtain the *telegraph equation*:

$$\frac{1}{\bar{\nu}} \frac{\partial^2 \varepsilon_{\rm cr}}{\partial t^2} + \frac{\partial \varepsilon_{\rm cr}}{\partial t} = \boldsymbol{\nabla} \cdot (\kappa \boldsymbol{b}\boldsymbol{b} \cdot \boldsymbol{\nabla} \varepsilon_{\rm cr}) \,, \tag{3.170}$$

where again $\bar{\nu} = \bar{\nu}_+ + \bar{\nu}_-$ and $\kappa = c^2/(3\bar{\nu})$. This equation is a hyperbolic expansion of the usual (parabolic) diffusion equation, which is obtained by dropping the first term in the Chapman–Enskog expansion.

There has been a longstanding discussion concerning the validity of the telegraph equation to describe a diffusion process. The earliest work known to the authors which addresses this problem discusses the related process of heat transfer (Vernotte, 1958). The same discussion has recently resurfaced in the context of CRs.

The fundamental solution of equation (3.170) contains two singular wave fronts travelling at signal speed $\pm c/\sqrt{3}$ which decay at a typical rate of $\bar{\nu}/2$ (Malkov and Sagdeev, 2015). The existence of these characteristics casts doubt on the validity of the telegraph equation because direct numerical solutions of the underlying Boltzmann equation do not show these wave solutions (Litvinenko and Noble, 2013, 2016) not even at early times. At times greater at $2/\bar{\nu}$ the solutions to both, the telegraph and diffusion equation qualitatively match those of the Boltzmann equation. Thus, at times $t \lesssim 2/\bar{\nu}$ in the ballistic regime of transport, the telegraph and the diffusion equation fail to correctly describe CR transport, while at later times, both equations reproduce the *physical* diffusion of CRs.

The telegraph equation has the mathematical appeal that it is a hyperbolic equation that contains a finite signal speed, whereas the diffusion equation *apparently* has an infinitely fast signal speed. Moreover, if a physical system has an intrinsic anisotropy, the telegraph equation preserves these anisotropic properties. On the contrary, those features are smeared out in the diffusive solution (Litvinenko and Noble, 2016; Tautz and Lerche, 2016).

In conclusion, *physical* diffusion can be well described by the *mathematical* diffusion equation as well as the telegraph equation after a few scattering times, while the latter preserves

more physical properties. However, either equation is not suited to model CR transport in the self-confinement picture.

3.11 Appendix: Alternative derivation of the scattering terms

The derivation of the scattering terms in Section 3.4.2 includes all effects up to the order $O(v_\mathrm{a}^2/c^2)$ and hence includes terms that should be negligible as $v_\mathrm{a}/c \sim 10^{-5}$ to 10^{-3}. Here, we present an alternative derivation that is accurate to order $O(v_\mathrm{a}/c)$ which yields essentially equivalent results and discuss the origin of this apparent contradiction.

We consider the CRs to be represented by a non-degenerate relativistic gas in Minkowski space with a metric tensor $\eta_{\alpha\beta} = \mathrm{diag}(-1,1,1,1)$, where a CR of rest mass m is characterized by the space-time coordinates $(x^\alpha) = (x^0 = ct, \boldsymbol{x})$ and by the particle momentum four-vector $(p^\alpha) = (p^0, \boldsymbol{p})$. The momentum four-vector has a constant length $p^\alpha p_\alpha = -m^2c^2$, which implies that the total particle energy $E = cp^0$ can be expressed in terms of $\boldsymbol{p}$ by $E(p) = \sqrt{\boldsymbol{p}^2 + m^2c^2}$. Accounting for the Lorentz invariant d^3p/p^0, the energy-momentum tensor is given in terms of the CR distribution function $f(\boldsymbol{x}, \boldsymbol{p}, t)$ by

$$T_\mathrm{cr}^{\alpha\beta} = c \int \frac{\mathrm{d}^3p}{p^0}\, p^\alpha p^\beta f(\boldsymbol{x}, \boldsymbol{p}, t). \tag{3.171}$$

Evaluating the momentum integral yields

$$\left(T_\mathrm{cr}^{\alpha\beta}\right) = \begin{pmatrix} \varepsilon_\mathrm{cr} & \frac{1}{c} f_\mathrm{cr} \boldsymbol{b} \\ \frac{1}{c} f_\mathrm{cr} \boldsymbol{b} & P_\mathrm{cr} \mathbf{1} \end{pmatrix}. \tag{3.172}$$

The force density four-vector G^α is defined to be the covariant divergence of the energy-momentum tensor (implying Einstein's sum convention),

$$\nabla_\beta T_\mathrm{cr}^{\alpha\beta} \equiv G^\alpha. \tag{3.173}$$

This equation holds in any coordinate system, which becomes evident through its covariant notation.

Because we solely focus on the interaction of CRs with Alfvén waves, this momentum and energy exchange is modelled via CR scattering in equation (3.53). We can separate the contributions of the co- and counter-propagating Alfvén waves to this interaction and thus to the force density G^α. In their own frame these waves are purely magnetic and thus only scatter CRs

in pitch angle. We already calculated the appropriate energy and flux moments of pure pitch-angle scattering in Appendix 3.10. The result for co- and counterpropagating Alfvén waves is

$$(G_{\pm}{}^{\alpha})_{\mathrm{wave},\pm} = \begin{pmatrix} 0 \\ -\frac{\bar{\nu}}{c^2} f_{\mathrm{cr}}\Big|_{\mathrm{wave},\pm} \boldsymbol{b} \end{pmatrix}, \tag{3.174}$$

where $\bar{\nu}|_{\mathrm{wave},\pm}$ is the mean scattering coefficient evaluated in the Alfvén wave frame.

In order to obtain an expression for this force density in the comoving frame, we apply the Lorentz transformation

$$G^{\alpha}|_{\mathrm{cmf}} = \Lambda_{+}{}^{\alpha}{}_{\beta}\, G_{+}{}^{\beta}\Big|_{\mathrm{wave},+} + \Lambda_{-}{}^{\alpha}{}_{\beta}\, G_{-}{}^{\beta}\Big|_{\mathrm{wave},-} \tag{3.175}$$

in the $O(v_{\mathrm{a}}/c)$ limit

$$(\Lambda_{\pm}{}^{\alpha}{}_{\sigma}) = \begin{pmatrix} \gamma & \pm\gamma\boldsymbol{\beta} \\ \pm\gamma\boldsymbol{\beta} & \mathbf{1} + (\gamma-1)\frac{\boldsymbol{\beta}\boldsymbol{\beta}}{\beta^2} \end{pmatrix}_{\mathrm{wave}\to\mathrm{cmf}} = \begin{pmatrix} 1 & \pm\frac{\boldsymbol{v}_{\mathrm{a}}}{c} \\ \pm\frac{\boldsymbol{v}_{\mathrm{a}}}{c} & \mathbf{1} \end{pmatrix} + O\left(v_{\mathrm{a}}^2/c^2\right), \tag{3.176}$$

which yields for the four-force density in the comoving frame:

$$(G^{\alpha})_{\mathrm{cmf}} = \begin{pmatrix} -\frac{\bar{\nu} v_{\mathrm{a}}}{c^3} f_{\mathrm{cr}}\Big|_{\mathrm{wave},+} & + \frac{\bar{\nu} v_{\mathrm{a}}}{c^3} f_{\mathrm{cr}}\Big|_{\mathrm{wave},-} \\ -\frac{\bar{\nu}}{c^2} f_{\mathrm{cr}}\Big|_{\mathrm{wave},+} \boldsymbol{b} & -\frac{\bar{\nu}}{c^2} f_{\mathrm{cr}}\Big|_{\mathrm{wave},-} \boldsymbol{b} \end{pmatrix}. \tag{3.177}$$

This result corresponds to Fermi's (1949) original idea: while energy is conserved during the interaction between electromagnetic 'clouds' and CRs in the the 'cloud' frame, energy is transferred between the two in any other frame.

The CR energy flux evaluated in the wave frame is

$$f_{\mathrm{cr}}|_{\mathrm{wave},\pm} = f_{\mathrm{cr}} \mp v_{\mathrm{a}}(\varepsilon_{\mathrm{cr}} + P_{\mathrm{cr}}), \tag{3.178}$$

which can be derived from the Lorentz-transformed momentum four-vector to order $O(v_{\mathrm{a}}/c)$ or simply seen as the Galilean boost of the CR flux. Inserting this into the force density in equation (3.177) results in the scattering terms

$$\left.\frac{\partial \varepsilon_{\mathrm{cr}}}{\partial t}\right|_{\mathrm{scatt}} = -\bar{\nu}_{\mathrm{wave},+}\frac{v_{\mathrm{a}}}{c^2}\left[f_{\mathrm{cr}} - v_{\mathrm{a}}(\varepsilon_{\mathrm{cr}} + P_{\mathrm{cr}})\right] + \bar{\nu}_{\mathrm{wave},-}\frac{v_{\mathrm{a}}}{c^2}\left[f_{\mathrm{cr}} + v_{\mathrm{a}}(\varepsilon_{\mathrm{cr}} + P_{\mathrm{cr}})\right], \tag{3.179}$$

$$\left.\frac{\partial f_{\mathrm{cr}}}{\partial t}\right|_{\mathrm{scatt}} = -\bar{\nu}_{\mathrm{wave},+}\left[f_{\mathrm{cr}} - v_{\mathrm{a}}(\varepsilon_{\mathrm{cr}} + P_{\mathrm{cr}})\right] - \bar{\nu}_{\mathrm{wave},-}\left[f_{\mathrm{cr}} + v_{\mathrm{a}}(\varepsilon_{\mathrm{cr}} + P_{\mathrm{cr}})\right], \tag{3.180}$$

which coincide with our scattering terms associated with co- and counterpropagating waves in equations (3.64) and (3.65) upto the different definitions for the scattering frequencies.

Why do the two derivations that are accurate to different orders in v_a/c yield the same expression? To answer this question, we first recall the different orders of fundamental quantities appearing in our theory. The thermodynamic quantities ε_cr and f_cr share the same $O(1)$ in v_a/c since $f_\mathrm{cr} \sim v_\mathrm{a}(\varepsilon_\mathrm{cr} + P_\mathrm{cr})$ in a self-confinement scenario. However, the CR energy flux density enters the energy-momentum tensor in equation (3.172) in the relativistically appropriate form as f_cr/c, which is of order $O(v_\mathrm{a}/c)$. Transforming this quantity via a semi-relativistic Lorentz-transformation of order $O(v_\mathrm{a}/c)$ and retaining all terms may then introduce terms of order $O(v_\mathrm{a}^2/c^2)$ into the transformed equations. This is exactly the case for the Lorentz-transformed four-force above: the time-like component of equation (3.177) is a transformed space-like component of the Lorentz-force, which contains a factor f_cr/c, and is of order $O(v_\mathrm{a}^2/c^2)$.

At first sight, the terms of order $O(v_\mathrm{a}^2/c^2)$ could be regarded vanishingly small in a formally rigorous treatment, which aims to be correct up to order $O(v_\mathrm{a}^2/c^2)$. On the other side, there is a practical argument that underlines the importance of the $O(v_\mathrm{a}^2/c^2)$ terms. All terms in equation (3.179) are of this order. Neglecting them would correspond to a vanishing energy transfer between CRs and Alfvén waves. In consequence, there would be no amplified Alfvén waves and we would only account for damping processes, which left the CR essentially unscattered. Hence, any theory that builds upon the idea of CR self-confinement has to include scattering processes up to order $O(v_\mathrm{a}^2/c^2)$ to be consistent.

3.12 Appendix: Comoving Vlasov equation

Here, we present two different derivations of the Vlasov equation (3.25). The first and formally correct derivation yields Vlasov's equation for relativistic particles in the comoving frame. To capture all relevant pseudo forces, we need to evaluate the equations of motion in the semi-relativistic limit up to order $O(u^2/c^2)$. Surprisingly, the resulting Vlasov equation can also be derived in Newtonian mechanics without any relativistic corrections.

3.12.1 Semi-relativistic derivation

We first recall definitions of special relativity and the geometry of Minikoski space to find approximate expressions in the semi-relativistic limit. The Lorentz transformation from the comoving frame into the lab frame is given by

$$(\Lambda^{\alpha}{}_{\hat{\alpha}}) = \begin{pmatrix} \gamma & \gamma\boldsymbol{\beta} \\ \gamma\boldsymbol{\beta} & \mathbf{1} + (\gamma - 1)\dfrac{\boldsymbol{\beta}\boldsymbol{\beta}}{\boldsymbol{\beta}^2} \end{pmatrix}_{\mathrm{cmf}\to\mathrm{lab}} = \begin{pmatrix} 1 & \dfrac{\boldsymbol{u}}{c} \\ \dfrac{\boldsymbol{u}}{c} & \mathbf{1} \end{pmatrix} + O\left(u^2/c^2\right), \tag{3.181}$$

where $\boldsymbol{\beta} = \boldsymbol{u}/c$ and we approximated the transformation in the semi-relativistic limit. The motivation for choosing this approximation are our equations of CR hydrodynamics, which derive from the focused transport equation of CRs – a semi-relativistically transformed variant of the comoving Vlasov equation. The metric connection (Christoffel symbols) associated with this Lorentz transformation can be calculated in an otherwise flat space-time by (Misner et al., 2017)

$$\Gamma^{\hat{\alpha}}_{\hat{\nu}\hat{\mu}} = \Lambda^{\hat{\alpha}}{}_{\alpha}\Lambda^{\mu}{}_{\hat{\mu}}\frac{\partial\Lambda^{\alpha}{}_{\hat{\nu}}}{\partial x^{\mu}}, \tag{3.182}$$

where we use Greek letters with hats to denote quantities evaluated in the comoving frame, i.e., $\Lambda^{\mu}{}_{\hat{\mu}}$ transforms a contravariant vector from the comoving into the lab frame. The connection symbol is not symmetric in its lower indices owing to the torsion introduced by a non-vanishing curl of the flow. The only non-vanishing components of $\Gamma^{\hat{\alpha}}_{\hat{\nu}\hat{\mu}}$ in the semi-relativistic limit are given by

$$\Gamma^{\hat{0}}_{\hat{\imath}\hat{\jmath}} = \Gamma^{\hat{\imath}}_{\hat{0}\hat{\jmath}} = \frac{\nabla_{\hat{\jmath}}u_{\hat{\imath}}}{c}, \tag{3.183}$$

$$\Gamma^{\hat{\imath}}_{\hat{0}\hat{0}} = \Gamma^{\hat{0}}_{\hat{\imath}\hat{0}} = \frac{1}{c^2}\frac{\mathrm{d}u_{\hat{\imath}}}{\mathrm{d}t}, \tag{3.184}$$

where Roman indices denote space-like components, $\hat{\imath}, \hat{\jmath} \in \{1, 2, 3\}$. The second set of Christoffel symbols, which are of order $O(u^2/c^2)$, is necessary to restore the Newtonian limit even though the symbols are formally small. This will become apparent at the end of Section 3.12.2. We first consider a particle at position $x^{\hat{\alpha}}$ and velocity $v^{\hat{\alpha}}$. Its equations of motion generalise in Minkowski space to

$$\frac{\mathrm{d}x^{\hat{\alpha}}}{\mathrm{d}\tau} = v^{\hat{\alpha}}, \tag{3.185}$$

$$\frac{\mathrm{d}p^{\hat{\alpha}}}{\mathrm{d}\tau} + \Gamma^{\hat{\alpha}}_{\hat{\sigma}\hat{\nu}}v^{\hat{\sigma}}p^{\hat{\nu}} = F^{\hat{\alpha}}, \tag{3.186}$$

where the connection symbols account for local changes of the defining velocity of the comoving frame that occur during the motion of the particle, τ is the proper time and $(F^{\hat{\alpha}}) = \gamma(\boldsymbol{v}\cdot\boldsymbol{F}/c, \boldsymbol{F})$ is the Minkowski four-force representing the generalised electromagnetic force. The momentum equation can be simplified using the approximations in equation (3.183) and (3.184) to yield

$$\frac{\mathrm{d}p^{\hat{\imath}}}{\mathrm{d}\tau} + m\frac{\mathrm{d}u^{\hat{\imath}}}{\mathrm{d}t} + \boldsymbol{p}\cdot\boldsymbol{\nabla}u^{\hat{\imath}} = F^{\hat{\imath}}. \tag{3.187}$$

In absence of any particle creation or annihilation processes, the number of CRs is a conserved quantity along any path that is described by the equations of motion. Thus, we have

$$0 = \frac{\mathrm{d}f}{\mathrm{d}\tau} = \frac{\mathrm{d}x^{\hat{\alpha}}}{\mathrm{d}\tau}\frac{\partial f}{\partial x^{\hat{\alpha}}} + \frac{\mathrm{d}p^{\hat{\alpha}}}{\mathrm{d}\tau}\frac{\partial f}{\partial p^{\hat{\alpha}}}, \tag{3.188}$$

which describes the full phase-space evolution of CRs to any order. The covariant derivative in the semi-relativistic limit is given by

$$\left(\partial_{\hat{\beta}}\right) = \left(\Lambda^{\beta}{}_{\hat{\beta}}\,\partial_{\beta}\right) = \left(\frac{\partial}{c\partial t} + \frac{\boldsymbol{u}}{c}\cdot\boldsymbol{\nabla}, \boldsymbol{\nabla}\right) + O\left(u^2/c^2\right). \tag{3.189}$$

Here, the derivative in the comoving frame is expressed by quantities that are measured in the lab frame, $\boldsymbol{u}$ and t. This is in preparation of the conventional mixed coordinate system for the transport equation of CR energy density: while the ambient gas velocity $\boldsymbol{u}$ and the direction of the large scale magnetic field $\boldsymbol{b} = \boldsymbol{B}/B$ are measured in the lab frame, the CR energy and momentum densities, $\varepsilon_{\rm cr}$ and $f_{\rm cr}/c$ as well as the generalised force densities are given with respect to the comoving frame.

The on-shell condition $p^{\hat{\alpha}}p_{\hat{\alpha}} = -m^2c^2$ is a constraint equation that reduces the set of four independent momentum variables by one. We choose the space-like components $p^{\hat{\imath}}$ as the independent variables so that we have $f \equiv f(x^{\hat{\alpha}}, p^{\hat{\imath}})$. Adopting this definition, inserting the covariant derivative of equation (3.189) and the equations of motion (3.185) and (3.187) into equation (3.188) yields

$$0 = \frac{\mathrm{d}x^{\hat{\alpha}}}{\mathrm{d}\tau}\frac{\partial f}{\partial x^{\hat{\alpha}}} + \frac{\mathrm{d}p^{\hat{\imath}}}{\mathrm{d}\tau}\frac{\partial f}{\partial p^{\hat{\imath}}} = v^{\hat{\alpha}}\frac{\partial f}{\partial x^{\hat{\alpha}}} + \left(F^{\hat{\imath}} - \Gamma^{\hat{\imath}}_{\hat{\sigma}\hat{\gamma}}v^{\hat{\sigma}}p^{\hat{\gamma}}\right)\frac{\partial f}{\partial p^{\hat{\imath}}} \tag{3.190}$$

$$= \frac{\partial f}{\partial t} + (\boldsymbol{u}+\boldsymbol{v})\cdot\frac{\partial f}{\partial \boldsymbol{x}} + \left(\boldsymbol{F} - m\frac{\mathrm{d}\boldsymbol{u}}{\mathrm{d}t} - (\boldsymbol{p}\cdot\boldsymbol{\nabla})\boldsymbol{u}\right)\cdot\frac{\partial f}{\partial \boldsymbol{p}}, \tag{3.191}$$

which coincides with the Vlasov equation (3.25).

3.12.2 Newtonian derivation

Here, we derive the same result with similar arguments but solely within the framework of Newtonian mechanics. Consider a non-relativistic particle with velocity $\boldsymbol{v}_{\rm lab}$ that is measured in the lab frame. Its velocity in the comoving frame $\boldsymbol{v}$ is defined by

$$\boldsymbol{v}_{\rm lab} = \boldsymbol{v} + \boldsymbol{u}(\boldsymbol{x}(t), t), \tag{3.192}$$

where the background velocity $\boldsymbol{u}$ is evaluated at the position of the particle itself. Expressing Newton's equations of motion in comoving quantities yields

$$m\frac{\mathrm{d}\boldsymbol{v}_{\rm lab}}{\mathrm{d}t} = m\frac{\mathrm{d}\boldsymbol{v}}{\mathrm{d}t} + m\frac{\mathrm{d}}{\mathrm{d}t}\boldsymbol{u}(\boldsymbol{x}(t), t) = m\frac{\mathrm{d}\boldsymbol{v}}{\mathrm{d}t} + m\left(\frac{\mathrm{d}\boldsymbol{x}}{\mathrm{d}t}\cdot\boldsymbol{\nabla}\right)\boldsymbol{u} + m\frac{\partial \boldsymbol{u}}{\partial t} = \boldsymbol{F}, \tag{3.193}$$

where $\boldsymbol{F}$ is the electromagnetic force. This force is the same in all frames, as long as the Newtonian limit holds. We rearrange this equation to obtain

$$\frac{\mathrm{d}\boldsymbol{p}}{\mathrm{d}t} = \boldsymbol{F} - m\frac{\mathrm{d}\boldsymbol{u}}{\mathrm{d}t} - (\boldsymbol{p}\cdot\boldsymbol{\nabla})\boldsymbol{u}, \tag{3.194}$$

which coincides with the semi-relativistic equation (3.187). Note our different usages of $\mathrm{d}/\mathrm{d}t$: while the left-hand side is the time derivative of the particle momentum, the time derivative of $\boldsymbol{u}$ on the right-hand side of this equation is the convective derivative of the mean gas velocity. Although this derivation is valid only for a non-relatvistic gas, it allows us to interpret the result and further highlights the following two points: (i) the comoving velocity can either change due to spatial inhomogeneities or due to acceleration of the background velocity $\boldsymbol{u}$. This insight is the basis of our discussion in Section 3.3.1. (ii) Obviously, the pseudo forces arise from the boost into a non-inertial frame. One can show that the total kinetic energy and momentum are conserved based on the equations of comoving momentum and kinetic energy evolution if and only if all terms in the transformation from the comoving frame into the lab frame are retained.

To derive the Vlasov equation, we had to include factors of order $O(u^2/c^2)$ in the semi-relativistic derivation while our Newtonian derivation is only accurate to order $O(1)$ in u/c. This apparent contradiction is alleviated by inspection of equation (3.186) in connection with the Christoffel symbols of equation (3.184). Multiplying the Christoffel symbols by $v^{\hat{0}}$ and $p^{\hat{0}}$ yields another factor of c^2 that increases the accuracy in the final Vlasov equation from $O(u^2/c^2)$ to $O(1)$.

3.13 Appendix: Semi-Relativistic derivation of the CR hydrodynamics equations

Here, we present an alternative derivation of our hydrodynamical equations for CRs based on the conservation of the energy-momentum tensor in special relativity. Those equations include the contribution by Lorentz forces associated with large-scale fields and Alfvén waves and read in their covariant form:

$$\nabla_\beta T_{\mathrm{cr}}^{\alpha\beta} = j_{\mathrm{cr}}^{\beta} F^{\alpha}{}_{\beta} + \left\langle \delta j_{\mathrm{cr}}^{\beta} \left(\delta F^{\alpha}_{+\beta} + \delta F^{\alpha}_{-\beta} \right) \right\rangle , \tag{3.195}$$

where the CR energy-momentum tensor $T_{\mathrm{cr}}^{\alpha\beta}$ is given by equation (3.172), $F^{\alpha\beta}$ and $\delta F_{\pm}^{\alpha\beta}$ are the contravariant components of the electromagnetic field tensors for the large-scale and small-scale fields, and j_{cr}^{α} and $\delta j_{\mathrm{cr}}^{\alpha}$ are the CR four-currents induced by large-scale fields and Alfvén waves, respectively. Note that $F^{\alpha\beta}$ is linear in $\boldsymbol{E}$ and $\boldsymbol{B}$ such that a Reynolds decomposition in the mean and fluctuating components is straightforward. We identify the small-scale Lorentz forces by extending the result of our discussion in Section 3.6 to the relativistic case according to:

$$G_{\pm}^{\alpha} = \left\langle \delta j_{\mathrm{cr}}^{\beta} \, \delta F^{\alpha}_{\pm\beta} \right\rangle , \tag{3.196}$$

and write the large-scale Lorentz force as

$$G^{\alpha}_{\mathrm{Lorentz}} = j^{\beta}_{\mathrm{cr}} F^{\alpha}{}_{\beta}. \tag{3.197}$$

We derive the two-moment CR equations in Section 3.3.1 for $\varepsilon_{\mathrm{cr}}$ and f_{cr} as measured by an observer in the comoving frame. The equations of momentum and energy conservation are transformed as

$$\nabla_{\hat{\beta}} T^{\hat{\alpha}\hat{\beta}}_{\mathrm{cr}} = \partial_{\hat{\beta}} T^{\hat{\alpha}\hat{\beta}}_{\mathrm{cr}} + \Gamma^{\hat{\alpha}}_{\hat{\sigma}\hat{\beta}} T^{\hat{\sigma}\hat{\beta}}_{\mathrm{cr}} + \Gamma^{\hat{\beta}}_{\hat{\sigma}\hat{\beta}} T^{\hat{\alpha}\hat{\sigma}}_{\mathrm{cr}}. \tag{3.198}$$

During the following evaluation of equation (3.198), we assume that the CR mean momentum density is described by the general vector $\boldsymbol{f}_{\mathrm{cr}}/c^2$. We will insert $\boldsymbol{f}_{\mathrm{cr}} = f_{\mathrm{cr}}\boldsymbol{b}$ after the calculation of the space-like and time-like components of this equation. With the connection symbols from equations (3.183)-(3.184) and the derivative from equation (3.189) in place, the time-like component of equation (3.198) reads

$$\nabla_{\hat{\beta}} T^{\hat{0}\hat{\beta}}_{\mathrm{cr}} = \partial_{\hat{\beta}} T^{\hat{0}\hat{\beta}}_{\mathrm{cr}} + \Gamma^{\hat{0}}_{\hat{\imath}\hat{0}} T^{\hat{\imath}\hat{0}}_{\mathrm{cr}} + \Gamma^{\hat{0}}_{\hat{\imath}\hat{\jmath}} T^{\hat{\imath}\hat{\jmath}}_{\mathrm{cr}} + \Gamma^{\hat{0}}_{\hat{\imath}\hat{0}} T^{\hat{0}\hat{\imath}}_{\mathrm{cr}} + + \Gamma^{\hat{\jmath}}_{\hat{0}\hat{\jmath}} T^{\hat{0}\hat{0}}_{\mathrm{cr}} \tag{3.199}$$

$$= \frac{1}{c}\frac{\partial \varepsilon_{\mathrm{cr}}}{\partial t} + \frac{\boldsymbol{u}}{c}\cdot\boldsymbol{\nabla}\varepsilon_{\mathrm{cr}} + \boldsymbol{\nabla}\cdot\frac{\boldsymbol{f}_{\mathrm{cr}}}{c} + \frac{\boldsymbol{\nabla}\boldsymbol{u}}{c} : (P_{\mathrm{cr}}\mathbf{1}) + \frac{\boldsymbol{\nabla}\cdot\boldsymbol{u}}{c}\varepsilon_{\mathrm{cr}} + \frac{2}{c^2}\frac{\mathrm{d}\boldsymbol{u}}{\mathrm{d}t}\cdot\frac{\boldsymbol{f}_{\mathrm{cr}}}{c} \tag{3.200}$$

$$= \frac{1}{c}\left\{\frac{\partial \varepsilon_{\mathrm{cr}}}{\partial t} + \boldsymbol{\nabla}\cdot[\boldsymbol{u}(\varepsilon_{\mathrm{cr}} + P_{\mathrm{cr}}) + f_{\mathrm{cr}}\boldsymbol{b}] - \boldsymbol{u}\cdot\boldsymbol{\nabla}P_{\mathrm{cr}}\right\} = G^{\hat{0}}_{+} + G^{\hat{0}}_{-}, \tag{3.201}$$

which coincides with the combined equations (3.43) and (3.64) after inserting the scattering terms from equation (3.177). There is no energy exchange due to the large-scale Lorentz force because the corresponding electric field vanishes identically due to infinite-conductivity assumption of ideal MHD. In the final step in equation (3.201), we neglect the work done by the pseudo force containing the factor $\mathrm{d}\boldsymbol{u}/\mathrm{d}t$ because it is of order $\mathcal{O}(u^2/c^2)$.

Equivalently, we insert the connection symbols into the space-like components of equation (3.198) and obtain:

$$\nabla_{\hat{\beta}} T^{\hat{\imath}\hat{\beta}}_{\mathrm{cr}} = \partial_{\hat{\beta}} T^{\hat{\imath}\hat{\beta}}_{\mathrm{cr}} + \Gamma^{\hat{\imath}}_{\hat{0}\hat{0}} T^{\hat{0}\hat{0}}_{\mathrm{cr}} + \Gamma^{\hat{\imath}}_{\hat{0}\hat{\jmath}} T^{\hat{0}\hat{\jmath}}_{\mathrm{cr}} + \Gamma^{\hat{0}}_{\hat{\jmath}\hat{0}} T^{\hat{\imath}\hat{\jmath}}_{\mathrm{cr}} + \Gamma^{\hat{\jmath}}_{\hat{0}\hat{\jmath}} T^{\hat{\imath}\hat{0}}_{\mathrm{cr}} \tag{3.202}$$

$$= \left[\frac{\partial \boldsymbol{f}_{\mathrm{cr}}/c^2}{\partial t} + \boldsymbol{\nabla}\cdot\left(\boldsymbol{u}\boldsymbol{f}_{\mathrm{cr}}/c^2 + P_{\mathrm{cr}}\mathbf{1}\right) + \left(\boldsymbol{f}_{\mathrm{cr}}/c^2\cdot\boldsymbol{\nabla}\right)\boldsymbol{u} + \frac{1}{c^2}\frac{\mathrm{d}\boldsymbol{u}}{\mathrm{d}t}(\varepsilon_{\mathrm{cr}} + P_{\mathrm{cr}})\right]^{\hat{\imath}} \tag{3.203}$$

$$= \left[\frac{\partial \boldsymbol{f}_{\mathrm{cr}}/c^2}{\partial t} + \boldsymbol{\nabla}\cdot\left(\boldsymbol{u}\boldsymbol{f}_{\mathrm{cr}}/c^2 + P_{\mathrm{cr}}\mathbf{1}\right) + \left(\boldsymbol{f}_{\mathrm{cr}}/c^2\cdot\boldsymbol{\nabla}\right)\boldsymbol{u}\right]^{\hat{\imath}} = G^{\hat{\imath}}_{\mathrm{Lorentz}} + G^{\hat{\imath}}_{+} + G^{\hat{\imath}}_{-}. \tag{3.204}$$

Again, we neglect the vanishingly small contribution from the pseudo force containing the factor $\mathrm{d}\boldsymbol{u}/\mathrm{d}t$ in our semi-relativistic limit. If we included that pseudo force, the CR momentum and

energy equations would coincide with those obtained by Buchler (1979) for the respective radiation quantities except for the different scattering processes of CRs and radiation, respectively, cf. equations (29) and (30) of Buchler (1979).

After taking the dot product of equation (3.204) with $\boldsymbol{b}$, using $\mathrm{d}(\boldsymbol{b}\cdot\boldsymbol{b}) = 0$ where d is some differential and realizing that the Lorentz-force only acts perpendicular to the magnetic field, we arrive at the combined equations (3.44) and (3.65). Again the scattering terms $G^{\hat{i}}_{\pm}$ are given by equation (3.177).

Thus, we can rederive our hydrodynamical CR equations if we treat CRs as a relativistic fluid and approximate its evolution equations in the semi-relativistic limit. An interesting aspect of this alternative derivation is the clear separation between pseudo forces and the acting pressure and Lorentz forces. For example, the term $\boldsymbol{u}\cdot\boldsymbol{\nabla}P_{\mathrm{cr}}$ in equation (3.201) is commonly attributed to $P\mathrm{d}V$ work done on the thermal gas, which is associated with a pressure force $\boldsymbol{\nabla}P_{\mathrm{cr}}$ acting in the Newtonian limit (see Section 3.6). This is clearly not the case in the semi-relativistic limit for two reasons: (i) the formal origin of the $\boldsymbol{u}\cdot\boldsymbol{\nabla}P_{\mathrm{cr}}$ term is the fictitious energy source term $\Gamma^{\hat{0}}_{\hat{i}\hat{j}}T^{\hat{i}\hat{j}}_{\mathrm{cr}}$ in equation (3.199). Thus, this term is solely introduced by the transformation into the non-inertial comoving frame and not due to mechanical work associated with a force. (ii) equation (3.204) shows that the kinematic CR pressure acts on the CRs themselves and not on the thermal gas. Only if CRs carry no mean momentum ($\boldsymbol{f}_{\mathrm{cr}}/c^2 = 0$), this pressure acts formally on the MHD background because in this case $\boldsymbol{\nabla}P_{\mathrm{cr}} = \boldsymbol{g}_{\mathrm{Lorentz}} + \boldsymbol{g}_{\mathrm{gri},+} + \boldsymbol{g}_{\mathrm{gri},-}$ according to equation (3.204). Only in this case the $P\mathrm{d}V$ work done by CRs equals $\boldsymbol{u}\cdot\boldsymbol{\nabla}P_{\mathrm{cr}}$. Furthermore, we can understand why the term $\boldsymbol{u}\cdot\boldsymbol{\nabla}P_{\mathrm{cr}}$ in equation (3.201) does not describe mechanical work by examining the situation as seen by a observer comoving with the thermal gas: in the comoving frame we have $\boldsymbol{u} = \boldsymbol{0}$ by definition, which implies vanishing kinetic energy $\rho\boldsymbol{u}^2/2$. Consequently, there is (i) no kinectic energy that could be changed by the Lorentz force and (ii) for any force $\boldsymbol{g}$ there is no work done in this frame, $\boldsymbol{u}\cdot\boldsymbol{g} = 0$.

3.14 Appendix: Lab-frame equations and energy and momentum conservation

We use the results of the previous appendices to derive the evolution equations for CR energy and momentum density in the lab frame, expressed in their comoving quantities. This enables us to discuss energy and momentum conservation in the semi-relativistic limit and to point out problems arising in this formulation. To this end, we assume that CRs are not gyrotropic and

further define the vectorial form of the CR energy flux as

$$\boldsymbol{f}_{\rm cr} = \int \mathrm{d}^3 p\, E(p)\, \boldsymbol{v} f(p), \tag{3.205}$$

which coincides with our definition in equation (3.40) if we project this vector onto the direction of the mean magnetic field, i.e., if we require $\boldsymbol{f}_{\rm cr} \parallel \boldsymbol{b}$. We thus allow for CR mean motions that are oblique to the mean magnetic field as seen from an observer in the comoving frame. We postpone the discussion of the necessity of this more general definition to a later time, after the derivation of the evolution equations.

First, we transform the thermodynamical quantities $\varepsilon_{\rm cr}$, $f_{\rm cr}$ and $P_{\rm cr}$ into the lab frame. This can be accomplished by applying a Lorentz transformation to the rank-2 tensor in equation (3.171). The results are straightforwardly calculated and can be found in Mihalas and Weibel Mihalas (1984) in their equations (91.10) to (91.12). For completeness, we list the fully relativistic result and a semi-relativistic approximation. For the energy density, we find

$$\varepsilon_{\rm cr}|_{\rm lab} = \gamma^2 \varepsilon_{\rm cr} + 2\gamma^2 \frac{\boldsymbol{u}\cdot\boldsymbol{f}_{\rm cr}}{c^2} + \gamma^2 P_{\rm cr}\frac{\boldsymbol{u}^2}{c^2} = \varepsilon_{\rm cr} + 2\frac{\boldsymbol{u}\cdot\boldsymbol{f}_{\rm cr}}{c^2} + O(u^2/c^2), \tag{3.206}$$

which contains a non-trivial correction even in the semi-relativistic limit. Transforming the comoving CR momentum density (times c^2) into the lab frame yields

$$\boldsymbol{f}_{\rm cr}\big|_{\rm lab} = \gamma \boldsymbol{f}_{\rm cr} + \gamma^2 \varepsilon_{\rm cr}\boldsymbol{u} + \gamma P_{\rm cr}\boldsymbol{u} + \gamma(\gamma-1)P_{\rm cr}\boldsymbol{u} + \left(\gamma^2\frac{\boldsymbol{u}\boldsymbol{u}}{c^2} + \gamma(\gamma-1)\frac{\boldsymbol{u}\boldsymbol{u}}{\boldsymbol{u}^2}\right)\cdot\boldsymbol{f}_{\rm cr} \tag{3.207}$$

$$= \boldsymbol{f}_{\rm cr} + \boldsymbol{u}(\varepsilon_{\rm cr} + P_{\rm cr}) + O(u^2/c^2). \tag{3.208}$$

Similarly, the CR pressure transforms as

$$\mathbf{P}_{\rm cr}|_{\rm lab} = P_{\rm cr}\mathbf{1} + \gamma\frac{\boldsymbol{f}_{\rm cr}\boldsymbol{u} + \boldsymbol{u}\boldsymbol{f}_{\rm cr}}{c^2} + \gamma^2\varepsilon_{\rm cr}\frac{\boldsymbol{u}\boldsymbol{u}}{c^2} + 2\frac{\gamma(\gamma-1)\boldsymbol{u}\cdot\boldsymbol{f}_{\rm cr}}{c^2}\frac{\boldsymbol{u}\boldsymbol{u}}{\boldsymbol{u}^2} + (\gamma-1)^2\frac{\boldsymbol{u}\boldsymbol{u}}{\boldsymbol{u}^2}P_{\rm cr} + 2(\gamma-1)P_{\rm cr}\frac{\boldsymbol{u}\boldsymbol{u}}{\boldsymbol{u}^2}, \tag{3.209}$$

$$= P_{\rm cr}\mathbf{1} + \frac{\boldsymbol{f}_{\rm cr}\boldsymbol{u} + \boldsymbol{u}\boldsymbol{f}_{\rm cr}}{c^2} + O(u^2/c^2), \tag{3.210}$$

which is now a (non-trivial) symmetric rank-two tensor.

Because the (generalised) CR mean momentum can have components that are perpendicular to the mean magnetic field, the equilibrium argument from Section 3.6 does not hold any longer and we have to take the associated Lorentz force into account. With our definition of the CR mean momentum in terms of the CR energy flux density, we multiply the Lorentz force term in the Vlasov equation (3.25) by $E(p)\boldsymbol{v}$ and integrate the result over momentum space to obtain

$$c^2\boldsymbol{g}_{\rm Lorentz} = \int \mathrm{d}^3 p E(p)\boldsymbol{v}Ze\,\frac{\boldsymbol{v}\times\boldsymbol{B}}{c}\cdot\frac{\partial f}{\partial \boldsymbol{p}} = -\boldsymbol{\Omega}'\times\boldsymbol{f}_{\rm cr}, \tag{3.211}$$

where we have used the ultra-relativistic limit, $\Omega' = \Omega' \boldsymbol{b}$ and Ω' is defined in Section 3.4.2. This expression was previously derived by Forman et al. (1974), see their equation (A10). Note that the gyromotion happens on kinetic time-scales and is thus fast compared to any hydrodynamical time-scale. While this expression is valid for any non-equilibrium motion perpendicular to the mean magnetic field, the CRs can be considered to be in equilibrium after averaging over a longer time that extends over multiple gyro-orbits. This argument was used in our discussion in Section 3.6 that eventually resulted in equation (3.117), justifying the approximation used.

Accounting for perpendicular CR mean momenta also complicates their interaction with Alfvén waves, because the small-scale Lorentz forces do not need to be aligned with the magnetic field as in equation (3.180) for a gyrotropic CR distribution. The treatment by Schlickeiser (1989) of this interaction, which is the basis for our theory in Section 3.4, formally only holds for a gyrotropic CR distribution and thus only for the case of $\boldsymbol{f}_{\rm cr} \parallel \boldsymbol{b}$. None the less, following the preceding discussion, gyrotropy can be assumed on hydrodynamical time-scales so that we can extent the validity of equation (3.180) to nearly gyrotropic CR distributions with non-vanishing perpendicular CR mean momenta. We proceed with the Lorentz forces due to small-scale magnetic field fluctuations,

$$c^2 \boldsymbol{g}_{\rm gri,\pm} = \bar{\nu}_{\rm wave,\pm} \boldsymbol{b}\boldsymbol{b} \cdot \left[\boldsymbol{f}_{\rm cr} \mp \boldsymbol{v}_{\rm a}(\varepsilon_{\rm cr} + P_{\rm cr})\right], \tag{3.212}$$

which are equivalent to equation (3.180) for the assumption of a gyrotropic CR distribution with $\boldsymbol{f}_{\rm cr} = f_{\rm cr}\boldsymbol{b}$.

With those equations in place, we can finally turn to the evolution equations for lab-frame quantities. Inserting the semi-relativistic limits of $\varepsilon_{\rm cr}$, $f_{\rm cr}$, and $P_{\rm cr}$ of equations (3.206), (3.208), and (3.210) into the conservation equation (3.195) and evaluating the time-like and space-like components of that equation results in:

$$\frac{\partial}{\partial t}\left(\varepsilon_{\rm cr} + 2\frac{\boldsymbol{u}\cdot\boldsymbol{f}_{\rm cr}}{c^2}\right) + \boldsymbol{\nabla}\cdot\left[\boldsymbol{f}_{\rm cr} + \boldsymbol{u}(\varepsilon_{\rm cr} + P_{\rm cr})\right] = -\left[\boldsymbol{u}\cdot\boldsymbol{g}_{\rm Lorentz} + (\boldsymbol{u}+\boldsymbol{v}_{\rm a})\cdot\boldsymbol{g}_{\rm gri,+} + (\boldsymbol{u}-\boldsymbol{v}_{\rm a})\cdot\boldsymbol{g}_{\rm gri,-}\right], \tag{3.213}$$

$$\frac{1}{c^2}\frac{\partial}{\partial t}\left[\boldsymbol{f}_{\rm cr} + \boldsymbol{u}(\varepsilon_{\rm cr} + P_{\rm cr})\right] + \boldsymbol{\nabla}\cdot\left(P_{\rm cr}\mathbf{1} + \frac{\boldsymbol{f}_{\rm cr}\boldsymbol{u} + \boldsymbol{u}\boldsymbol{f}_{\rm cr}}{c^2}\right) = -\left(\boldsymbol{g}_{\rm Lorentz} + \boldsymbol{g}_{\rm gri,+} + \boldsymbol{g}_{\rm gri,-}\right). \tag{3.214}$$

This result directly enables us to demonstrate energy and momentum conservation of our equations in the semi-relativistic limit. Adding equations (3.4), (3.12) and (3.213) yields energy conservation and adding equations (3.2) and (3.214) results in momentum conservation in the

lab frame, respectively:

$$\frac{\partial}{\partial t}\left(\varepsilon_{\rm tot}+2\frac{\boldsymbol{u}\cdot\boldsymbol{f}_{\rm cr}}{c^2}\right)+\boldsymbol{\nabla}\cdot\left[\boldsymbol{u}(\varepsilon_{\rm tot}+P_{\rm tot})+\boldsymbol{f}_{\rm cr}+\boldsymbol{v}_{\rm a}(\varepsilon_{\rm a,+}-\varepsilon_{\rm a,-})-\boldsymbol{B}\,(\boldsymbol{u}\cdot\boldsymbol{B})\right]=0, \tag{3.215}$$

$$\frac{1}{c^2}\frac{\partial}{\partial t}\left[\boldsymbol{f}_{\rm cr}+\boldsymbol{u}(\rho c^2+\varepsilon_{\rm cr}+P_{\rm cr})\right]+\boldsymbol{\nabla}\cdot\left(P_{\rm tot}\mathbf{1}+\rho\boldsymbol{u}\boldsymbol{u}-\boldsymbol{B}\boldsymbol{B}+\frac{\boldsymbol{f}_{\rm cr}\boldsymbol{u}+\boldsymbol{u}\boldsymbol{f}_{\rm cr}}{c^2}\right)=\boldsymbol{0}, \tag{3.216}$$

where $\varepsilon_{\rm tot}$ and $P_{\rm tot}$ are given by equations (3.19) and (3.18), respectively.

To simplify the discussion on the applicability of the lab-frame equations, we neglect the relativistic corrections to the CR energy and pressure on the left-hand sides of equations (3.206) and (3.208) and obtain:

$$\frac{\partial\varepsilon_{\rm cr}}{\partial t}+\boldsymbol{\nabla}\cdot\left[\boldsymbol{f}_{\rm cr}+\boldsymbol{u}(\varepsilon_{\rm cr}+P_{\rm cr})\right]=-\left[\boldsymbol{u}\cdot\boldsymbol{g}_{\rm Lorentz}+(\boldsymbol{u}+\boldsymbol{v}_{\rm a})\cdot\boldsymbol{g}_{\rm gri,+}+(\boldsymbol{u}-\boldsymbol{v}_{\rm a})\cdot\boldsymbol{g}_{\rm gri,-}\right], \tag{3.217}$$

$$\frac{1}{c^2}\frac{\partial}{\partial t}\left[\boldsymbol{f}_{\rm cr}+\boldsymbol{u}(\varepsilon_{\rm cr}+P_{\rm cr})\right]+\boldsymbol{\nabla}\cdot(P_{\rm cr}\mathbf{1})=-\left(\boldsymbol{g}_{\rm Lorentz}+\boldsymbol{g}_{\rm gri,+}+\boldsymbol{g}_{\rm gri,-}\right). \tag{3.218}$$

As outlined above, the Lorentz force in this equation introduces a kinetic time-scale which is challenging to resolve in numerical simulations of macroscopic systems. To remedy the situation for numerical simulations we could use the near-equilibrium assumption and remove the kinetic time-scale by averaging over it. We adopted this approach in the comoving frame by using the gyroaveraged Fokker-Planck equation in Section 3.3.1 and consequently neglected any perpendicular inertia of CRs in Section 3.6 to infer the time-averaged large-scale Lorentz force. This procedure proves to be difficult in the lab frame: here, the momentum equation carries all the information about the energy transport perpendicular to the mean magnetic field.

This is in contrast to its comoving counterpart, where the momentum equation only describes the motion relative to the gas frame, which solves a few conceptional problems of the lab frame. This additional complication precludes a clear separation of motions perpendicular and parallel to the mean magnetic field. A Chapman–Enskog expansion, which was used in Section 3.6.1, yields the same result for the Lorentz force as in the comoving frame, namely equation (3.119). But this expansion neglects any perpendicular contributions in the time-derivative terms in the momentum equation (3.218). This equation states that CRs are not transported perpendicular to the mean magnetic field with the gas in the lab frame or $[\boldsymbol{f}_{\rm cr}+\boldsymbol{u}(\varepsilon_{\rm cr}+P_{\rm cr})]_\perp=\boldsymbol{0}$. This contradicts the idea of gyroaveraged evolution where CRs are rapidly gyrating along field lines and are thus transported perpendicular to $\boldsymbol{B}$ with the gas by definition. Hence, we cannot use the Chapman–Enskog expansion in the lab frame the same way as we did in the comoving frame.

Attempting to circumvent this expansion by directly assuming $\boldsymbol{f}_{\rm cr}=f_{\rm cr}\boldsymbol{b}$ leads to difficulties, too. Using this assumption in equation (3.218) leaves terms in the time derivative that are

perpendicular to $\boldsymbol{B}$. This perpendicular component balances the term $\boldsymbol{\nabla}_{\perp} P_{\rm cr}$ and the Lorentz-force term. It thus acts on kinetic time-scales at worst – a property that we tried to avoid at all costs when deriving a CR hydrodynamics theory for macroscopic astrophysical scales. We thus conclude that it is difficult to treat the Lorentz force in the lab frame on hydrodynamical time-scales. Contrarily, this can be easily achieved in the comoving frame via a straightforward projection operation that is followed by gyroaveraging the CR distribution function.

4 Comparing Different Closure Relations for Cosmic Ray Hydrodynamics

This chapter is based on the published paper by Thomas, T. ; Pfrommer, C.:
Monthly Notices of the Royal Astronomical Society, Volume 509, Issue 4, pp.4803-4816

Cosmic ray (CR) hydrodynamics is a (re-)emerging field of high interest due to the importance of CRs for the dynamical evolution of the interstellar, the circumgalactic, and the intracluster medium. In these environments, CRs with GeV energies can influence large-scale dynamics by regulating star formation, driving galactic winds or by altering the pressure balance of galactic halos. Recent efforts have moved the focus of the community from a one-moment description of CR transport towards a two-moment model as this allows for a more accurate description of the microphysics impacting the CR population. Like all hydrodynamical theories, these two-moment methods require a closure relation for a consistent and closed set of evolution equations. The goal of this paper is to quantify the impact of different closure relations on the resulting solutions. To this end, we review the common P1 and M1 closure relations, derive a new four-moment H1 description for CR transport and describe how to incorporate CR scattering by Alfvén waves into these three hydrodynamical models. While there are significant differences in the transport properties of radiation in the P1 and M1 approximations in comparison to more accurate radiative transfer simulations using the discrete ordinates approximation, we only find small differences between the three hydrodynamical CR transport models in the free streaming limit when we neglect CR scattering. Most importantly, for realistic applications in the interstellar, circumgalactic or intracluster medium where CR scattering is frequent, these differences vanish and all presented hydrodynamical models produce the same results.

4.1 Introduction

CRs are a diverse population of energetic particles with energies ranging from MeV to PeV (Zweibel, 2013). While low-energy CRs are responsible for (some of) the ionisation of gas in molecular clouds (Padovani et al., 2009) and high energy CRs with energies $\gtrsim$ TeV provide a window into the dynamics of CRs through observations with imaging air/water Cherenkov telescopes (Strong et al., 2007), the bulk energy-carrying GeV CRs influence the kinematics and thermodynamics of various astrophysical environments (Zweibel, 2017). CRs injected into the interstellar medium at the shocks of supernovae can leave their injection site, lift gas out of a galactic disk, and drive mass-loaded galactic scale winds (Breitschwerdt et al., 1991; Uhlig et al., 2012; Recchia et al., 2016; Dashyan and Dubois, 2020; Rathjen et al., 2021). Because this gas is removed momentarily or completely out of the galaxy it cannot participate in subsequent star formation processes (Girichidis et al., 2016; Simpson et al., 2016b; Pfrommer et al., 2017a; Farber et al., 2018; Semenov et al., 2021). Furthermore, the ejected gas in combination with the CRs provides an additional pressure in the circumgalactic medium, which alters the accretion of fresh gas out of the intergalactic medium (Buck et al., 2020). To correctly model these astrophysical processes, it is important to describe the physics of CRs correctly. This is a difficult task because CRs only rarely interact with their surroundings through particle-particle collisions while they primarily interact indirectly with the gas through scatterings at electromagnetic fields (Zweibel, 2017). If the surrounding gas can be described in terms of magneto-hydrodynamics (MHD), CRs provide a pressure that is directed perpendicular to the MHD magnetic field (Zweibel, 2013). Parallel to this magnetic field, CR transport is governed by their interactions with small-scale perturbations with typical length scales comparable to the gyroradius of CRs. On these length scales MHD is not applicable and kinetic plasma physics dictates the evolution of CRs (Kulsrud, 2004). Various plasma processes such as the gyroresonant (Kulsrud and Pearce, 1969), the intermediate scale (Shalaby et al., 2021), or Bell's instability (Bell, 2004) can strongly influence the propagation of CRs.

To model the transport of CRs on scales significantly larger than their gyroradius, we need to adopt drastic approximations. These require the development of theoretical models and numerically tractable algorithms that are efficient enough so that the resulting model is able to bridge the separation in length scales from small-scale micro physics to the large-scale astrophysical environment. These requirements are rather challenging to achieve with a kinetic description but can be readily provided by hydrodynamical approximations. The clear downside of hydrodynamical models is that they coarse-grain kinetic physics, thus possibly losing some of the important plasma-kinetic effects. Yet, the emergence of large-scale simulations employing

CR hydrodynamics (Girichidis et al., 2016; Pfrommer et al., 2017a; Chan et al., 2019) and their ability to approximately model CR microphysics (Thomas and Pfrommer, 2019; Hopkins et al., 2021b) rather than completely neglecting CRs at all proves the success of CR hydrodynamics.

The first CR hydrodynamical theories were one-moment hydrodynamical models in which one scalar quantity (either the CR energy or number density) is used to describe the entire CR population and its propagation properties (Breitschwerdt et al., 1991). The resulting transport phenomena can be categorised into (i) *CR advection*, which describes CR confinement by a large scale magnetic field to the gas so that CRs follow the bulk movement of the gas, (ii) *CR streaming*, which assumes frequent CRs scatterings with small-scale electromagnetic waves so that CRs are confined to move with these waves along a magnetic field line, and (iii) *CR diffusion*, which applies to infrequent CR scatterings that are not able to maintain bulk kinetic motions of CRs but strong enough so that the remaining transport can be expressed through a diffusion process (Thomas et al., 2020). While the theoretical description of all these processes is well established, only CR advection and diffusion can be numerically described by standard methods with small modifications to account, e.g., for the anisotropic nature of CR transport (Hanasz and Lesch, 2003; Sharma and Hammett, 2011; Yang et al., 2012; Girichidis et al., 2014; Pakmor et al., 2016b; Butsky and Quinn, 2018; Dubois et al., 2019). Finding a stable and accurate numerical discretisation of CR streaming in the one-moment picture proves to be difficult (Sharma et al., 2009). This prompted the (re-)development of two-moment hydrodynamical models, which also include the flux of the scalar quantity as an independent and evolved quantity (Webb, 1985; Jiang and Oh, 2018; Thomas and Pfrommer, 2019). These second-order models solve the problem of how to numerically discretise the CR streaming effect but come with the increased demand for effective theoretical descriptions of the CR microphysics to get a self-consistent evolution of the CR flux. Additionally, they provide convenient tools that can describe CR diffusion more accurately and do not completely break down if CR scattering is less frequent.

Like all hydrodynamical models, these two-moment models suffer from a closure problem: an n-th moment hydrodynamical model depends on the $(n + 1)$-th moment or, in other words, every hydrodynamical model requires a closure for the next-higher order moment in terms of the moments it is evolving. Thus, two-moment models, which evolve only the zeroth and first moment, require information about the second moment of the CR distribution for a consistent set of closed evolution equations. This problem was implicitly circumvented in the theories of Jiang and Oh (2018) and Thomas and Pfrommer (2019) by using a Taylor (or Legendre) expansion of the CR distribution up to first order while assuming that any higher-order expansion

coefficients vanish. This enables them to calculate the required second moment in terms of the zeroth and first moment directly without additional information or physical insight. This procedure is also known in the theory of radiation transport and called the P1 approximation. In this context the P1 approximation has been shown to exhibit some shortcomings: the P1 approximation implicitly assumes that scattering is frequent and removes any higher-order expansion coefficients. This leads to some problematic properties of the P1 approximation: (i) while the maximum propagation speed of radiation is the speed of light c, it is artificially reduced to $c/\sqrt{3}$ in the P1 approximation (Olson et al., 2000) and (ii) if scattering is infrequent, contrary to the assumption, the P1 approximation can produce negative number or energy densities (Kershaw, 1976). Both shortcomings can be avoided by using an M1 approximation which employs other means to calculate the second moment (Levermore, 1984). Recently, this idea originally developed for radiation hydrodynamics was translated to the case of CR transport (Hopkins et al., 2021c).

In this paper, we compare the P1 and M1 approximations for CR transport in terms of the resulting evolution for a given CR or radiation distribution. We quantity the differences with the goal to judge which of the two approximations yields the most accurate solution. To this end, we discuss and review the derivations of the P1 and M1 approximations for CRs and radiation in Section 4.2. We additionally develop a new four-moment approximation named the H1 approximation for CR-transport and present simplified models of CR scatterings with Alfvén waves for all three hydrodynamic models. In Section 4.3, we illustrate the differences of the closures with a set of numerical simulations where we use the same simulation setup but alter the used transportation model to evolve radiation, CR hydrodynamics without and with scatterings. In Section 4.4, we present an additional simulation that quantifies the differences of the transport model in the case of CR scattering. We close this paper with a discussion in Section 4.5. The goal-oriented reader may want to directly jump to Section 4.3 for the main results of this study. We use $\boldsymbol{ab}$ to denote the dyadic product of the two vectors $\boldsymbol{a}$ and $\boldsymbol{b}$.

4.2 CR and Radiation Hydrodynamics

In this section, we present the theoretical foundations required to understand our numerical experiments. We review the derivations of the two-moment P1 and M1 hydrodynamical closure relations and derive a new four-moment H1 approximation for the case of CR transport. This will enable us to judge whether it is worth to further explore this route and to derive even higher-order closure relations to capture more detailed dynamics of CRs.

In our discussion, we focus on a mono-energetic ultra-relativistic population of CRs. In this limit, the Boltzmann transport equation for a distribution of particles f can be written as:

$$\frac{1}{c}\frac{\partial f}{\partial t} + \boldsymbol{d}\cdot\boldsymbol{\nabla} f = \left.\frac{1}{c}\frac{\partial f}{\partial t}\right|_{\rm scatt}, \tag{4.1}$$

where c is the speed of light and $\boldsymbol{d} = \boldsymbol{v}/c$ is the direction of the CR velocity $\boldsymbol{v}$. We place all terms describing the interaction of CRs with electro-magnetic fields on the right-hand side and use this term as a placeholder, which will be specified in Section 4.2.6 (this also includes all forces acting on the particles). In this notation, the Boltzmann equation is formally equivalent to the radiative transfer equation when f is interpreted as the specific intensity of radiation and $\boldsymbol{d}$ is the propagation direction of radiation. This degeneracy is broken once we account for CRs gyrating around the magnetic field. Assuming that the population of CRs is equally distributed in terms of the gyration phase angle, Eq. (4.1) can be simplified to the *focused* transport equation (Zank, 2014) for the simplified case studied here that assumes that the gas is at rest:

$$\frac{1}{c}\frac{\partial f}{\partial t} + \mu\boldsymbol{b}\cdot\boldsymbol{\nabla} f + (\boldsymbol{\nabla}\cdot\boldsymbol{b})\frac{1-\mu^2}{2}\frac{\partial f}{\partial \mu} = \left.\frac{1}{c}\frac{\partial f}{\partial t}\right|_{\rm scatt}, \tag{4.2}$$

where $\boldsymbol{b} = \boldsymbol{B}/B$ is the direction of the magnetic field, $B = \sqrt{\boldsymbol{B}^2}$ is the magnitude of the magnetic field, and $\mu = \boldsymbol{b}\cdot\boldsymbol{d}$ is the pitch angle cosine of the CRs so that the mono-energetic, gyrotropic CR distribution attains the following dependence: $f = f(\boldsymbol{x}, \mu)$, where $\boldsymbol{x}$ is the space coordinate. The second term states that this equation solely describes transport of CRs through space along magnetic field lines. The third term is the magnetic focusing term and describes the change of a particle's pitch angle caused by a spatially varying magnetic field through the $\boldsymbol{\nabla}\cdot\boldsymbol{b}$ factor. This term has a simple physical interpretation: if $\boldsymbol{\nabla}\cdot\boldsymbol{b} > 0$ then magnetic field lines diverge and CRs are beamed in the direction of the magnetic field. In the opposite situation, when magnetic field lines converge or $\boldsymbol{\nabla}\cdot\boldsymbol{b} < 0$, CRs are beamed in the opposite direction of the magnetic vector field. Another useful way to write this equation is given by:

$$\frac{1}{c}\frac{\partial f}{\partial t} + (\boldsymbol{b}\boldsymbol{\nabla}) : \left[\mu f\mathbf{1} + \frac{1-\mu^2}{2}\frac{\partial f}{\partial \mu}(\boldsymbol{b}\boldsymbol{b} - \mathbf{1})\right] = \left.\frac{1}{c}\frac{\partial f}{\partial t}\right|_{\rm scatt}. \tag{4.3}$$

This result can be derived by realising that $\boldsymbol{b}\cdot\boldsymbol{b} = 1$ and $(\boldsymbol{b}\boldsymbol{b}) : \boldsymbol{\nabla}\boldsymbol{b} = \boldsymbol{b}\cdot\boldsymbol{\nabla}(\boldsymbol{b}\cdot\boldsymbol{b})/2 = 0$. The advantage of this formulation is that it only contains one spatial derivative and eliminates the $\boldsymbol{\nabla}\cdot\boldsymbol{b}$ term which is numerically challenging to model.

We assume that the magnetic field is static and that the underlying MHD fluid is at rest. Theories for CR hydrodynamics differ in the reference frame they are formulated in. There are two choices for the reference frame that are commonly used: (i) The laboratory frame is

the frame in which the MHD equations are formulated and thus provides an obvious choice and (ii) the comoving frame (which moves with the MHD fluid) simplifies the derivation of the fluid interaction terms. Because the comoving frame is a non-inertial frame this also introduces pseudo-forces into the CR equations which complicates the interpretation of the resulting equations. As we assume that the MHD fluid is at rest, the laboratory and the comoving frames coincide and no pseudo-forces appear in Eq. (4.3). This starting point of the derivation of CR transport differs from the one presented in Thomas and Pfrommer (2019), were we assumed a dynamic MHD fluid. Our assumptions allow us to focus this work on the anisotropic transport of CRs along magnetic fields allows without the need to disentangle the transport of CRs itself from the motion of their hosting magnetic field lines in a dynamic MHD fluid. We note that the presented derivations and conclusions in this work carry over to the case of a dynamic MHD fluid, where the dynamics adds yet another degree of complexity.

4.2.1 Two-moment hydrodynamics and the closure problem

We first derive a two-moment hydrodynamical approximation for CR transport as described by Eq. (4.2) in a general setting. Such a theory aims to find evolution equations for the first two moments of f, which are defined by

$$f_0 = \frac{1}{2}\int_{-1}^{1} \mathrm{d}\mu\, f(\mu), \tag{4.4}$$

$$f_1 = \frac{1}{2}\int_{-1}^{1} \mathrm{d}\mu\, \mu f(\mu), \tag{4.5}$$

in such a way that their evolution depends on each other while f_0 and f_1 remain independent quantities. In such a two-moment approximation, the information about the μ-structure of f is encoded in the moments f_0 and f_1, which in general implies a loss of information because not all the potential structure of f can be mapped onto the first two moments. However, if the higher-order moments (representing a larger degree of anisotropy in phase space) are maintained at a small level by some physical (scattering) process, it is sufficient to evolve f_0 and f_1 and to capture the essentials of the physics.

The individual evolution equations can be extracted from Eq. (4.2) by multiplying both sides of Eq. (4.2) with 1 and μ, respectively, and averaging the result over μ space to arrive at

$$\frac{1}{c}\frac{\partial f_0}{\partial t} + \boldsymbol{\nabla}\cdot(\boldsymbol{b} f_1) = \left.\frac{1}{c}\frac{\partial f_0}{\partial t}\right|_{\mathrm{scatt}}, \tag{4.6}$$

$$\frac{1}{c}\frac{\partial f_1}{\partial t} + \boldsymbol{b}\cdot\boldsymbol{\nabla} f_2 + (\boldsymbol{\nabla}\cdot\boldsymbol{b})\frac{3f_2 - f_0}{2} = \left.\frac{1}{c}\frac{\partial f_1}{\partial t}\right|_{\mathrm{scatt}}, \tag{4.7}$$

where we define the second moment f_2 by [1]

$$f_2 = \frac{1}{2}\int_{-1}^{1} \mathrm{d}\mu\, \mu^2 f(\mu). \tag{4.8}$$

With these equations at hand, the first moment f_1 can also be interpreted as the flux of f_0. The evolution of f_0 depends on f_1 according to Eq. (4.6) and the evolution of f_1 depends itself on f_2 (Eq. 4.7), which is an unknown quantity. Consequently, Eqs. (4.6) and (4.7) do not form a closed set of equations and cannot be solved without additional information on f_2.

This is the so called *closure problem* that has the obvious solution to choose a *closure relation* for f_2 in form of a closed expression that depends on f_0 and f_1. We now present the P1 and M1 closure relations for CR two-moment hydrodynamics which originate from radiation hydrodynamics.

4.2.2 The P1 approximation

The P1 approximation is the simplest hydrodynamical approximation of Eq. (4.2) and results in a simple closure relation for the second moment. This approximation adopts a linear function in pitch-angle for the distribution f. We use the notation of Thomas and Pfrommer (2019) and define

$$f_{\mathrm{P1}} = f_0 + 3\mu f_1, \tag{4.9}$$

which complies with the definitions of the first two moments in Eqs. (4.4) and (4.5). All other moments in the Taylor expansion of f are assumed to be vanishingly small so that their contribution to the resulting dynamics of f can be neglected. The second moment in this approximation as calculated by the integral in Eq. (4.8) using f_{P1} from Eq. (4.9) is given by:

$$f_2 = \frac{1}{3} f_0, \tag{4.10}$$

which forms the closure relation for the P1-approximation. The evolution equations in Eqs. (4.6) and (4.7) simplify to:

$$\frac{1}{c}\frac{\partial f_0}{\partial t} + \boldsymbol{\nabla}\cdot(\boldsymbol{b} f_1) = \left.\frac{1}{c}\frac{\partial f_0}{\partial t}\right|_{\mathrm{scatt}}, \tag{4.11}$$

$$\frac{1}{c}\frac{\partial f_1}{\partial t} + \frac{1}{3}\boldsymbol{b}\cdot\boldsymbol{\nabla} f_0 = \left.\frac{1}{c}\frac{\partial f_1}{\partial t}\right|_{\mathrm{scatt}}. \tag{4.12}$$

The second term in Eq. (4.12), $\boldsymbol{b}\cdot\boldsymbol{\nabla} f_0/3$, can be interpreted as a pressure term for an isothermal fluid with sound speed $c/\sqrt{3}$. In a constant magnetic field these equations are a set of linear

[1] We define f_n to be the n-th monomial moment of f instead of the moment of the n-th Legrendre polynomial.

hyperbolic differential equations whose characteristics travel with velocities $\pm c/\sqrt{3}$. Building upon this insight, we can construct an alternative distribution function that yields the same moments as f_{P1} in Eq. (4.9) and an identical evolution of f_0 and f_1 as described by Eqs. (4.11) and (4.12) but highlights the two-stream property:

$$f_{\text{2-stream}} = \left(f_0 - \sqrt{3} f_1\right) \delta\left(\mu + \frac{1}{\sqrt{3}}\right) + \left(f_0 + \sqrt{3} f_1\right) \delta\left(\mu - \frac{1}{\sqrt{3}}\right), \tag{4.13}$$

where δ denotes Dirac's δ distribution. Thus, the P1 approximation coincides with a two-stream approximation. Consequently, it can not capture beam-like CR transport where all CRs are travelling with velocities $\boldsymbol{v}$ projected onto magnetic field that have $|\boldsymbol{v} \cdot \boldsymbol{b}| \sim c$ or $|\mu| \sim 1$ on average. A further shortcoming of the P1 approximation is that information is only propagated at $\pm c/\sqrt{3}$ but not at any smaller or higher velocity. Both points are serious problems of the P1 approximation as those propagation modes are included in Eq. (4.2) where the fastest velocity is equal to $\pm c$ but information is also propagated at any velocity in between $-c$ and $+c$. The reason for this shortcoming is the linear approximation in Eq. (4.9): the distribution f must be peaked toward $\mu \sim \pm 1$ in order to realise a beam transport mode. This anisotropic pitch-angle distribution cannot be captured by any combination of f_0 and f_1. However, the clear advantage of the P1 approximation is its simplicity and correctness when CR scattering as described by $\partial f/\partial t|_{\mathrm{scatt}}$ is strong and damps all higher-order moments in the pitch-angle distribution.

The distribution f correspond to a probability density and has to be non-negative if it describes a physical population of particles. A natural question to ask is whether we can find such a non-negative distribution for a given set of moments. Kershaw (1976) derived general conditions on the first three moments that—provided they are fulfilled—guarantee the existence of such a non-negative distribution f. In our notation, the first three conditions are

$$0 \leq f_0, \tag{4.14}$$

$$|f_1| \leq f_0, \tag{4.15}$$

$$\left(\frac{f_1}{f_0}\right)^2 \leq \frac{f_2}{f_0} \leq 1. \tag{4.16}$$

These conditions provide a mathematical explanation for the failure of the P1 approximation: in this model, we have $f_2 = f_0/3$ and the third condition is violated if $|f_1| > f_0/\sqrt{3}$. This is in accordance with a non-negativity constraint for each of the terms in Eq. (4.13). Note that this corollary provides a more stringent constraint than the second of Kershaw's conditions (Eq. 4.15).

4.2.3 The M1 approximation

To avoid the non-negativity problem of the distribution by construction, it is necessary to formulate an evolution equation for f_1 that always respects the bounds of Eqs. (4.15) and (4.16). The M1 family of closure relations accomplishes this while simultaneously capturing the beam mode of radiation/CR transport without the addition of another evolution equation. This is accomplished by deriving theories that result in second moments that entirely depend on f_0 and f_1 while simultaneously fulfilling Kershaw's conditions in Eqs. (4.14) to (4.16). In the M1 approximation, the zeroth and second moment are related by the Eddington factor D via

$$f_2 = D f_0. \tag{4.17}$$

D depends on f_0 and f_1 in such a way so that the beam transportation mode and the P1 approximation are realised in the appropriate limits. With this definition, the evolution equations for the first two moments in Eqs. (4.6) and (4.7) read as:

$$\frac{1}{c}\frac{\partial f_0}{\partial t} + \boldsymbol{\nabla} \cdot (\boldsymbol{b} f_1) = \frac{1}{c}\frac{\partial f_0}{\partial t}\bigg|_{\text{scatt}}, \tag{4.18}$$

$$\frac{1}{c}\frac{\partial f_1}{\partial t} + \boldsymbol{b} \cdot \boldsymbol{\nabla}(D f_0) + (\boldsymbol{\nabla} \cdot \boldsymbol{b})\frac{3D-1}{2} f_0 = \frac{1}{c}\frac{\partial f_1}{\partial t}\bigg|_{\text{scatt}}. \tag{4.19}$$

The f_1 equation of this approximation and thus the full evolution of the two-moment system is equal to it's P1 analogue if $D = 1/3$, which is assumed in the P1 approximation. A similar result is derived by Hopkins et al. (2021c).

Kershaw's closure

The most accessible route to derive an M1-like approximation is given by the Kershaw (1976) closure. In our presentation of this closure we follow the derivation of Schneider (2016) who presents a theory for radiative transfer in slab geometry. Due to the similarity of the CR and radiative transfer problems, we can follow their derivation and apply it to the CR case studied here. The general idea of Kershaw's closure is to blend between a P1-type approximation and a beam approximation, which only depends on the ratio f_1/f_0 and thus on the anisotropy of radiation/CR transport. In the limit $|f_1/f_0| \ll 1$, the P1 approximation should be recovered while the beam representation should be used for $|f_1/f_0| \sim 1$. This behaviour is realised by the

following distribution:

$$f_{\rm Kershaw} = \frac{1}{3} f_{\rm sym} + \frac{2}{3} f_{\rm beam}, \tag{4.20}$$

where

$$f_{\rm sym} = (f_0 - f_1)\,\delta(\mu + 1) + (f_0 + f_1)\,\delta(\mu - 1), \tag{4.21}$$

$$f_{\rm beam} = f_0\,\delta(\mu - f_1/f_0). \tag{4.22}$$

The Eddington factor is readily calculated to be:

$$D = \frac{1}{3} + \frac{2}{3}\left(\frac{f_1}{f_0}\right)^2. \tag{4.23}$$

If the Eddington factor $D = 1/3$ then transport is nearly isotropic ($|f_1/f_0| \sim 0$), and vice versa, restoring the P1 limit. If, instead, there is an anisotropy ($|f_1/f_0| > 0 \rightarrow D > 1/3$) the evolution of the P1 and Kershaw's approximation for CRs will noticeably differ due the influence of the focusing term in Eq. (4.19). The beam transportation mode is realised for a high degree of anisotropy ($|f_1/f_0| \sim 1 \rightarrow D \sim 1$). In this limit, CRs are transported with characteristic speeds $\pm c$ as expected for CRs that are beamed.

Levermore's closure

Others means and arguments can be used to infer Eddington factors for radiation hydrodynamics that provide the same limits as Kershaw's closure. One possible choice of D is obtained by assuming an isotropic distribution in the frame comoving with velocity f_1/f_0 and employing the covariant transformation laws of energy, momentum, and pressure to get (Levermore, 1984; Hanawa and Audit, 2014):

$$D = \frac{1}{3} + \frac{2(f_1/f_0)^2}{2 + \sqrt{4 - 3(f_1/f_0)^2}}. \tag{4.24}$$

We see that the required limits are realised in the Levermore closure:

$$|f_1/f_0| \rightarrow 0 \quad \text{results in} \quad D \rightarrow 1/3, \tag{4.25}$$

$$|f_1/f_0| \rightarrow 1 \quad \text{results in} \quad D \rightarrow 1. \tag{4.26}$$

Again, using the correspondence between radiative and CR transport, we can apply Levermore's closure also to the CR case. In the remainder of this paper we will exclusively use Levermore's closure in Eq. (4.24) for the M1 approximation due to it's popularity in the literature and because its derivation is based on physics arguments, i.e., we solve the CR moment equations Eqs. (4.18) and (4.19) complemented by Eq. (4.24) for D.

4.2.4 The H1 approximation

A shortcoming of both, the P1 and M1 approximation, is their inability to capture two interpenetrating beams of CRs. This can be easily seen by counting the number of independent variables: each beam is defined by the number of CRs and their average velocity. For two beams this amounts to four independent quantities, which cannot be described in the P1 or M1 approximation because both models are characterised by only two independent quantities. The obvious way to cure this shortcoming is to generalise the P1 or M1 approximations by including more independent variables. Let N denote an arbitrary integer that states the order of the considered polynomial, then the PN approximation for the focused transport equation is given in Zank (2014). Increasing the number of degrees of freedom and thus the number of moments makes the task to find a positive distribution f that complies with these moments more challenging.

Instead of using the PN approximation as a generalisation, here we present a new H1 approximation. Instead of increasing the order of the considered polynomial, the H1 approximation is characterised by an improved discretisation in pitch-angle space. In particular we split the μ-domain in two equal parts (where the 'H' in H1 denotes the half space in pitch angle) and assume that f is given by a linear function in each subdomain:

$$f_{\mathrm{H1}} = \begin{cases} f_0^- + 12 f_1^- (\mu + 1/2) & \text{for} \quad \mu < 0, \\ f_0^+ + 12 f_1^+ (\mu - 1/2) & \text{for} \quad \mu > 0. \end{cases} \tag{4.27}$$

Taking the 1 and $\mu \pm 1/2$ moments of Eq. (4.2) in the range of $\mu \in [-1, 0]$ and $\mu \in [0, 1]$ yields the following evolution equations for the four quantities $f_0^\pm$ and $f_1^\pm$:

$$\begin{aligned} &\frac{1}{c}\frac{\partial f_0^\pm}{\partial t} + (\boldsymbol{b}\cdot\boldsymbol{\nabla})\left(\pm\frac{f_0^\pm}{2} + f_1^\pm\right) \\ &\qquad + (\boldsymbol{\nabla}\cdot\boldsymbol{b})\left(\mp\frac{1}{2}f(0) \pm \frac{f_0^\pm}{2} + f_1^\pm\right) = \frac{1}{c}\left.\frac{\partial f_0^\pm}{\partial t}\right|_{\mathrm{scatt}}, \end{aligned} \tag{4.28}$$

$$\begin{aligned} &\frac{1}{c}\frac{\partial f_1^\pm}{\partial t} + (\boldsymbol{b}\cdot\boldsymbol{\nabla})\left(\frac{f_0^\pm}{12} \pm \frac{f_1^\pm}{2}\right) \\ &\qquad + (\boldsymbol{\nabla}\cdot\boldsymbol{b})\left(\frac{1}{4}f(0) - \frac{f_0^\pm}{4} \pm f_1^\pm\right) = \frac{1}{c}\left.\frac{\partial f_1^\pm}{\partial t}\right|_{\mathrm{scatt}}, \end{aligned} \tag{4.29}$$

where the value of $f(0)$ is introduced through integration by part. Formally, f is not defined at $\mu = 0$. We continue by adopting the arithmetic average of the limiting values to the left and right of 0:

$$f(0) = \frac{1}{2}(f_0^+ + f_0^-) - 3(f_1^+ - f_1^-). \tag{4.30}$$

Information for this set of equations is propagated with velocities $c(-1/2 \pm \sqrt{1/12})$ (associated with the fields f_0^- and f_1^-) or $c(+1/2 \pm \sqrt{1/12})$ (associated with the fields f_0^+ and f_1^+). The fastest propagation speeds in this approximation are $(\pm 1/2 \pm \sqrt{1/12})c \approx \pm 0.78c$. Consequently, the H1 model can be interpreted as two ultra-relativistic fluids that move with mean speeds $\pm c/2$ along the magnetic field and each experiencing a pressure with an isothermal sound speed of $\sqrt{1/12}c \approx 0.28c$. This confirms that the H1 approximation can describe two interpenetrating streams of CRs.

By defining $f_0 = f_0^- + f_0^+$ and $\Delta f_0 = f_0^+ - f_0^-$ we can derive a conservation law for f_0 and a non-conservative hyperbolic differential equation for Δf_0 in the form of Eq. (4.3):

$$\frac{1}{c}\frac{\partial f_0}{\partial t} + \boldsymbol{\nabla} \cdot \left[\boldsymbol{b}\left(\frac{\Delta f_0}{2} + f_1^+ + f_1^-\right)\right] = \frac{1}{c}\left.\frac{\partial f_0}{\partial t}\right|_{\text{scatt}}, \tag{4.31}$$

$$\begin{aligned}\frac{1}{c}\frac{\partial \Delta f_0}{\partial t} + (\boldsymbol{b}\boldsymbol{\nabla}) : \Bigg[&\left(\frac{f_0}{2} + f_1^+ - f_1^-\right)\mathbf{1} \\ &+ \left(-f(0) + \frac{f_0}{2} + f_1^+ - f_1^-\right)(\boldsymbol{bb} - \mathbf{1})\Bigg] = \frac{1}{c}\left.\frac{\partial \Delta f_0}{\partial t}\right|_{\text{scatt}}.\end{aligned} \tag{4.32}$$

The equations for $f_1^\pm$ can be put in the same form resulting in:

$$\begin{aligned}\frac{1}{c}\frac{\partial f_1^\pm}{\partial t} + (\boldsymbol{b}\boldsymbol{\nabla}) : \Bigg[&\left(\frac{f_0^\pm}{12} \pm \frac{f_1^\pm}{2}\right)\mathbf{1} \\ &+ \left(\frac{f(0)}{4} - \frac{f_0^\pm}{4} \pm f_1^\pm\right)(\boldsymbol{bb} - \mathbf{1})\Bigg] = \frac{1}{c}\left.\frac{f_1^\pm}{\partial t}\right|_{\text{scatt}}.\end{aligned} \tag{4.33}$$

We use Eqs. (4.31) to (4.33) in our simulations employing the H1 approximation. The non-negativity of f in this approximation is guaranteed in all cases if

$$|f_1^-| < f_0^-/6 \quad \text{and} \quad |f_1^+| < f_0^+/6. \tag{4.34}$$

4.2.5 Radiation hydrodynamics

For completeness, we now review the basic aspects of radiation hydrodynamics. The fundamental difference of CR and radiative transport is the treatment of the direction of transport. For CR transport, this direction is fixed to be the direction of the local magnetic field. By contrast, the direction of radiation transport cannot be determined a priori but is an evolving quantity. This is reflected in the way we define moments of f in radiation hydrodynamics: instead of only using pitch-angle moments (scalar quantities), the three-dimensional nature of the general radiative transport equation requires us to use full directional moments (tensor quantities) with

$$\boldsymbol{f}_n = \frac{1}{4\pi}\int_{S^2} \mathrm{d}^2\Omega\, \boldsymbol{d}^{(n)} f(\boldsymbol{d}), \tag{4.35}$$

where $\mathrm{d}^2\Omega$ is the differential solid angle, $\boldsymbol{d}$ is the propagation direction of radiation, $\boldsymbol{d}^{(n)}$ is the n-th order tensor product of $\boldsymbol{d}$ with itself, and $\boldsymbol{f}_n$ is the n-th moment of f and a rank-n tensor. The P1 approximation for radiation hydrodynamics is readily derived by considering the distribution

$$f = f_0 + 3\boldsymbol{d} \cdot \boldsymbol{f}_1, \tag{4.36}$$

taking the 1 and $\boldsymbol{d}$ averages of the radiative transfer equation yields:[2]

$$\frac{1}{c}\frac{\partial f_0}{\partial t} + \boldsymbol{\nabla} \cdot \boldsymbol{f}_1 = 0 \tag{4.37}$$

$$\frac{1}{c}\frac{\partial \boldsymbol{f}_1}{\partial t} + \boldsymbol{\nabla} \cdot (\mathbf{D} f_0) = 0, \tag{4.38}$$

where the P1 Eddington tensor is given by:

$$\mathbf{D} = \frac{1}{3}\mathbf{1}. \tag{4.39}$$

The M1 approximation for radiation hydrodynamics replaces this tensor with (Levermore, 1984):

$$\mathbf{D} = \frac{3D-1}{2}\frac{\boldsymbol{f}_1}{f_1}\frac{\boldsymbol{f}_1}{f_1} + \frac{1-D}{2}\mathbf{1}. \tag{4.40}$$

where D is given by Eq. (4.24).

4.2.6 CR scattering

So far we only accounted for the interaction of CRs with a large scale mean magnetic field but there are several mechanisms, which produce magnetic field fluctuations with typical length scales comparable to the gyroradius of CRs. Here, we focus on the interaction of CRs with small-scale gyroresonant Alfvén waves mediated by pitch-angle scattering. Other mechanisms such as external confinement of CRs by MHD turbulence (Lazarian and Beresnyak, 2006) or scattering of CRs by the intermediate scale instability (Shalaby et al., 2021) are not considered but could be included in an extension of the presented theory. The phase-space diffusion coefficients for pitch-angle scattering in our mono-energetic approximation can be derived from Schlickeiser (1989) in the first-order limit in v_a/c so that the scattering term reads:

$$\left.\frac{\partial f}{\partial t}\right|_\mathrm{scatt} = \frac{\partial}{\partial \mu}\left\{\frac{1-\mu^2}{2}\nu_\pm\left[\left(1 \mp 2\mu\frac{v_\mathrm{a}}{c}\right)\frac{\partial f}{\partial \mu} \mp 3\frac{v_\mathrm{a}}{c}f\right]\right\}, \tag{4.41}$$

where $\nu_\pm = \nu_\pm(\mu)$ is the scattering rate of CRs with gyroresonant Alfvén waves that travel in the direction of (+) or against (−) the magnetic field with Alfvén velocity v_a. This first-order limit in v_a/c is sufficient because accounting for second-order terms is only necessary

[2] Here we omit radiation-matter interactions.

to ensure energy conservation (Thomas and Pfrommer, 2019). Energy is naturally conserved in our mono-energetic approximation and thus this low-order approximation can be used to simplify the calculations. The actual value of the scattering coefficient is set by the energy balance of magnetic fluctuations of gyroresonant Alfvén waves. In general, this scattering term is actually a sum over the scattering contributions from both types of Alfvén waves. We suppress this sum for readability and in our, yet to be presented, simplified model where at most one type of Alfvén waves provides the scattering.

One of the main sources of energy is the CR streaming instability (Kulsrud and Pearce, 1969) that is active once CRs stream faster than Alfvén waves (approximately when $|\partial_\mu f| > (v_\mathrm{a}/c)f$). This converts kinetic energy from CRs to energy contained in Alfvén waves which in turn provide the scattering agents of CRs. Damping of Alfvén waves is provided by various mechanisms (Zweibel, 2013) and thermalises this energy. Typically, the growth rate of Alfvén wave energy and the total damping rate balance each other to reach a quasi-steady state.

We are not able to follow this energy balance in our idealised model for CR transport here. This is mostly due to our assumption that CRs are mono-energetic and thus cannot lose energy. Nevertheless, to mimic the behaviour of CR losses, we assume that the scattering frequency is non-vanishing if we were to model the energy transfer in a more complete description and energy would be transferred from the CRs to the gyroresonant Alfvén waves. Thomas and Pfrommer (2019) observed that for the gyroresonant interaction, we have

$$\text{CR energy loss} \sim v_\mathrm{a} \times \text{ CR momentum loss}, \tag{4.42}$$

which is positive once CRs travel faster (defined in by some average) than Alfvén waves and are decelerated towards the Alfvén velocity. Because CR energy loss equals the gain of Alfvén wave energy, we assume that gyroresonant Alfvén waves are present and scatter CRs once CRs have been decelerated by Alfvén waves.

By applying our model for CR scattering we are losing some aspects of the general setting such as a possibly spatio-temporal varying scattering coefficient that might impact the evolution of the CRs. However, by using our mono-energetic approach and our model for the inclusion of CR scattering we achieve clarity through simplicity. Using the full description for CR scattering that also contains the evolution of CR energies would complicate the following derivation of the corresponding hydrodynamic interaction terms tremendously. Further, we would need to follow the detailed energy balance of the gyroresonant Alfvén waves. This would shift our attention away from the transport of CRs along magnetic field as realised by different closure schemes towards a discussion of the dynamical interplay of CRs and gyroresonant Alfvén waves. We

refrain from introducing these additional conceptional degrees of freedom and leave it for future work.

CR scattering in the P1 and M1 approximation

A discussion of gyroresonant pitch-angle scattering in a fully energy-dependent setting using the P1 approximation is presented by Thomas and Pfrommer (2019). Here, we use a more simplified model for the P1 and M1 approximation. We assume that the scattering rates are independent of pitch angle:

$$\nu_{\pm}(\mu) = \nu_{\pm} = \text{const.} \tag{4.43}$$

Taking the 1 and μ moments in the P1 approximation yields the following expressions for the scattering terms in Eqs. (4.11) and (4.12):

$$\left.\frac{1}{c}\frac{\partial f_0}{\partial t}\right|_{\text{scatt}} = 0, \tag{4.44}$$

$$\left.\frac{1}{c}\frac{\partial f_1}{\partial t}\right|_{\text{scatt}} = -\frac{\nu_{\pm}}{c}\left(f_1 \mp \frac{v_\text{a}}{c} f_0\right), \tag{4.45}$$

while the result for the M1 approximation in Eqs. (4.18) and (4.19) is given by:

$$\left.\frac{1}{c}\frac{\partial f_0}{\partial t}\right|_{\text{scatt}} = 0, \tag{4.46}$$

$$\left.\frac{1}{c}\frac{\partial f_1}{\partial t}\right|_{\text{scatt}} = -\frac{\nu_{\pm}}{c}\left(f_1 \mp \frac{v_\text{a}}{c}\frac{1+3D}{2} f_0\right). \tag{4.47}$$

Because $D = 1/3 + O\left((f_1/f_0)^2\right)$, the scattering terms of the P1 and M1 approximation only differ if the flow of CRs is highly anisotropic. Thus, Eq. (4.47) reduces to its P1 counterpart if $|f_1/f_0| \to 0$, as expected. For comparability and simplicity, we assume that the same expressions for the activation of the scattering holds true for the P1 and M1 approximations. For both approximations, CRs are decelerated once $|f_1| > (v_\text{a}/c) f_0$ and thus we use

$$\nu_{\pm} \begin{cases} > 0 & \text{if } f_1 \gtrless \pm(v_\text{a}/c) f_0, \\ = 0 & \text{else.} \end{cases} \tag{4.48}$$

This procedure only describes the activation of scattering. The actual value used for the scattering frequency (once it is activated) is assumed to be a constant and given for our numerical experiment in Section 4.3.

CR scattering in the H1 approximation

For the H1 approximation, we include a dependence of scattering coefficients on μ and assume that they have the following form:

$$\nu_{\pm} = \begin{cases} \nu_{\pm}^{\mathrm{L}} & \text{for} \quad \mu < 0, \\ \nu_{\pm}^{0} & \text{for} \quad \mu = 0, \\ \nu_{\pm}^{\mathrm{R}} & \text{for} \quad \mu > 0. \end{cases} \tag{4.49}$$

The reasoning for this splitting is apparent once the four scattering source terms are calculated: to derive these terms for f_0 and Δf_0, we calculate the 1-moments on the intervals $[-1, 0]$ and $[0, 1]$ to get:

$$\left.\frac{1}{c}\frac{\partial f_0}{\partial t}\right|_{\mathrm{scatt}} = 0, \tag{4.50}$$

$$\left.\frac{1}{c}\frac{\partial \Delta f_0}{\partial t}\right|_{\mathrm{scatt}} = -\frac{\nu_{\pm}(0)}{c}\left(\frac{\partial f}{\partial \mu}(0) \mp 3\frac{v_{\mathrm{a}}}{c} f(0)\right). \tag{4.51}$$

The scattering rate $\nu_{\pm}^{0}(0)$ thus mediates the scattering of CRs through the $\mu = 0$ point. Without this term, CRs would not be able to scatter through this point, which is a problem commonly referred to as the 90° problem. Numerical studies (Bai et al., 2019) and more detailed theoretical models for pitch-angle scattering (Shalchi and Schlickeiser, 2005) indicate that while scattering at $\mu = 0$ is reduced, it is sufficiently frequent and scatters CRs between the two hemispheres. Moving on, we calculate the μ moments on the intervals $[-1, 0]$ and $[0, 1]$ to get:

$$\begin{aligned} \left.\frac{1}{c}\frac{\partial f_1^-}{\partial t}\right|_{\mathrm{scatt}} &= \frac{\nu_{\pm}(0)}{4c}\left(\frac{\partial f}{\partial \mu}(0) \mp 3\frac{v_{\mathrm{a}}}{c} f(0)\right) \\ &\quad - \frac{\nu_{\pm}^{\mathrm{L}}}{c}\left[4 f_1^- \mp \frac{v_{\mathrm{a}}}{c}\left(f_0^- - \frac{3}{2} f_1^-\right)\right], \end{aligned} \tag{4.52}$$

$$\begin{aligned} \left.\frac{1}{c}\frac{\partial f_1^+}{\partial t}\right|_{\mathrm{scatt}} &= \frac{\nu_{\pm}(0)}{4c}\left(\frac{\partial f}{\partial \mu}(0) \mp 3\frac{v_{\mathrm{a}}}{c} f(0)\right) \\ &\quad - \frac{\nu_{\pm}^{\mathrm{R}}}{c}\left[4 f_1^+ \mp \frac{v_{\mathrm{a}}}{c}\left(f_0^+ + \frac{3}{2} f_1^+\right)\right]. \end{aligned} \tag{4.53}$$

Thus, $\nu_{\pm}^{\mathrm{L}}$ describes the scattering of f_1^- while $\nu_{\pm}^{\mathrm{R}}$ describes the scattering of f_1^+. These expressions contain f and $\partial_\mu f$ evaluated at $\mu = 0$, which is formally not well defined. We follow the approach of van Leer and Nomura (2005), who consider discontinuous Galerkin discretisations of diffusion equations, and derive:

$$f(0) = \frac{1}{2}(f_0^+ + f_0^-) - \frac{1}{2}(f_1^+ - f_1^-), \tag{4.54}$$

$$\frac{\partial f}{\partial \mu}(0) = \frac{9}{4}(f_0^+ - f_0^-) - \frac{15}{2}(f_1^+ + f_1^-) \tag{4.55}$$

by fitting a forth-order polynomial through the four independent variables. While this approach has been derived for a numerical method, it is appropriate here because the presented H1-approximation can be interpreted as a discontinuous Galerkin approximation on two computational cells with linear basis functions. Again, we consider scattering, described by one of the three rates, to be active once their scattering induces a momentum loss of CRs:

$$\nu_{\pm}^{\mathrm{L}} \begin{cases} > 0 & \text{if } 4f_1^- \gtrless \pm\frac{v_\mathrm{a}}{c}\left(f_0^- - \frac{3}{2}f_1^-\right), \\ = 0 & \text{else,} \end{cases} \tag{4.56}$$

$$\nu_{\pm}^{0} \begin{cases} > 0 & \text{if } \partial_\mu f(0) \gtrless \pm 3\frac{v_\mathrm{a}}{c} f(0), \\ = 0 & \text{else,} \end{cases} \tag{4.57}$$

$$\nu_{\pm}^{\mathrm{R}} \begin{cases} > 0 & \text{if } 4f_1^+ \gtrless \pm\frac{v_\mathrm{a}}{c}\left(f_0^+ + \frac{3}{2}f_1^+\right), \\ = 0 & \text{else.} \end{cases} \tag{4.58}$$

This concludes our derivation of the theoretical models.

4.3 Numerical Example

We continue by describing our numerical discretisation and simulation setup. We present a suite of simulations that all use the same initial conditions and parameters but employ different transport methods. We start by considering radiation transport and compare the P1 and M1 fluid approximations to a more accurate discrete ordinates solution. By allowing transport solely along magnetic fields in the same numerical setup, we compare the P1, M1 and H1 fluid models for CR transport. In particular, we compare simulations with and without CR scattering to study the differences between the fluid approximations.

4.3.1 Numerical method and setup

In our simulations we use a two-dimensional Cartesian grid in the computational domain $x, y \in [0, 1]^2$ with 1024^2 equally spaced resolution elements. We employ a standard finite volume method to evolve the initial conditions until $t = 2$ or two light crossing times (with $c = 1$). The time integration is accomplished using Heun's second-accurate Runge-Kutta method where the length of each timestep is given by $\Delta t = 0.2\Delta x/c$ and Δx denotes the side length of the resolution elements. The finite volume scheme uses a piecewise linear reconstruction of the primitive variables f_0, f_1/f_0, $\boldsymbol{f}_1/f_0$, $f_0^\pm$ and $f_1^\pm/f_0^\pm$ (where applicable) onto the

center of interfaces between resolution elements using the monotonised central slope limiter (van Leer, 1979). At the interface we use approximate Riemann solvers to calculate the fluxes exchanged between neighbouring resolution elements. For simulation of radiation hydrodynamics using the P1 closure we use the Lax-Friedrichs Riemann solver; for simulations with the M1 closure we use the HLLC Riemann solver of Berthon et al. (2007). We also include a simulation with a discrete ordinates approximation of the radiative transfer equation (4.1) where we simulate 200 discrete rays, equally spaced in all directions of the plane, per computational cell and call this solution S200. Radiation in each ray is upwinded at interfaces. For simulations of CR hydrodynamics using the P1 closure we use the localised Lax-Friedrichs Riemann solver presented in Thomas et al. (2021); for simulations with the M1 or H1 closure we use a straightforward extension of the aforementioned Riemann solver that accounts for the varying Eddington factor in the M1 case or for the four independent quantities in the H1 case. All boundaries of the computational domain are periodic.

Radiation or CRs are set up using a random population of cloudlets. We place 30 circular cloudlets with random radii r uniformly distributed in $[0, 0.1]$. The center of the cloudlets are distributed uniformly throughout the computational domain. We add for each cloudlet a cloud contribution of

$$f_{0,\mathrm{cloudlet}} = \begin{cases} 0.1 & \text{if } \|\boldsymbol{x} - \boldsymbol{x}_\mathrm{c}\| < r, \\ 0 & \text{otherwise,} \end{cases} \tag{4.59}$$

where $\boldsymbol{x}_\mathrm{c}$ is the center of the cloudlet and adopt a background of radiation or CRs given by $f_{0,\mathrm{background}} = 10^{-3}$. Every other moment, e.g. f_1, $\boldsymbol{f}_1$, $f_1^\pm$ and Δf_0 are initially set to zero if the transport model follows their evolution. For the S200 simulation, radiation is distributed equally among all rays.

We use random instead of handpicked initial conditions to demonstrate the different behaviours of the respective transport models and to highlight their differences while reducing possible biases introduced by the initial conditions. These are chosen to trigger the interaction between radiation or CRs emerging from different cloudlets so that the resulting evolution is non-trivial.

Our CR hydrodynamics simulations contain a magnetic field that we initialize with a magnetic vector potential $\boldsymbol{A}$ so that we obtain a divergence-free magnetic field via $\boldsymbol{B} = \boldsymbol{\nabla} \times \boldsymbol{A}$ using second-order finite differences. We set the in-plane components of the vector potential to zero: $A_x = 0$ and $A_y = 0$. The out-of-plane component A_z is initialized in a similar fashion as f_0: we

place 100 magnetic loops randomly in the whole domain whereby each loop is set up via:

$$A_{z,\mathrm{loop}} = \begin{cases} 0.2 - ||\boldsymbol{x} - \boldsymbol{x}_\mathrm{c}|| & \text{if } ||\boldsymbol{x} - \boldsymbol{x}_\mathrm{c}|| < 0.2, \\ 0 & \text{otherwise,} \end{cases} \tag{4.60}$$

where $\boldsymbol{x}_\mathrm{c}$ is the center of the magnetic field loop. The resulting vector potential is given by the sum of the individual contributions $A_{z,\mathrm{loop}}$ of all magnetic loops. The high number of magnetic loops is required to guarantee a complete covering of the computational domain with magnetic loops and to get a resulting irregular topology in the magnetic field.

The remaining free parameters in our setup are c, v_a/c and the scattering frequencies. We chose $c = 1$ for all simulations and $v_\mathrm{a}/c = 0.1$ for simulations with CR scattering. This is a conservative high value as in the interstellar, the circumgalactic, and the intracluster medium typical values have $v_\mathrm{a} < 1000$ km s^{-1}. We use this high value to place an upper bound on the differences between the different transport methods. In addition, most numerical codes with two-moment CR hydrodynamics capabilities also employ a reduced speed of light approximation where c is artificially lowered to reduce numerical diffusion and computational cost (Jiang and Oh, 2018; Thomas et al., 2021). If CR scattering is activated, we adopt $\nu = 1000$ with ν representing $\nu_\pm$, $\nu_\pm^\mathrm{L}$, $\nu_\pm^0$ or $\nu_\pm^\mathrm{R}$. This value is based on the following consideration: for interstellar and circumgalactic medium applications the light crossing time across 1 kpc is $t_\mathrm{cross} \sim \mathrm{kpc}/c = 10^{11}$ s while the typical timescale of CR scattering is $t_\mathrm{scatt} \sim 3\kappa/c^2 = 10^8$ s where we assume that the diffusion coefficient of GeV CRs is $\kappa = 3 \times 10^{28}$ cm^2 s^{-1}. Fixing the ratio $t_\mathrm{cross}/t_\mathrm{scatt}$ yields for $t_\mathrm{cross} = 1$ in our simulations $t_\mathrm{scatt} = 1/\nu = 1/1000$.

We explicitly enforce the positivity bounds $|f_1| < f_0/\sqrt{3}$ for the P1 model and $|f_1^\pm| < f_0^\pm/6$ for the H1 model by clipping f_1 or $f_1^\pm$ to the maximum allowed value if they violate this limit at the beginning of a timestep in the simulation. The same is done for $\boldsymbol{f}_1$ in the radiation P1 model where we change only the magnitude of f_1 but not its direction. We checked for numerical convergence of the presented simulations by running each simulations at half the resolution and found no significant differences between the results at both resolutions. To check for numerical convergence of the discrete ordinate S200 simulation with respect to the number of radiation rays used, we increased the number of rays from 200 to 400 and found no significant differences of the results.

4.3.2 Radiation hydrodynamics

In our first set of simulations, we compare the evolution of radiation cloudlets. As we do not account for any radiation-matter interaction in our simulations, transport of radiation is

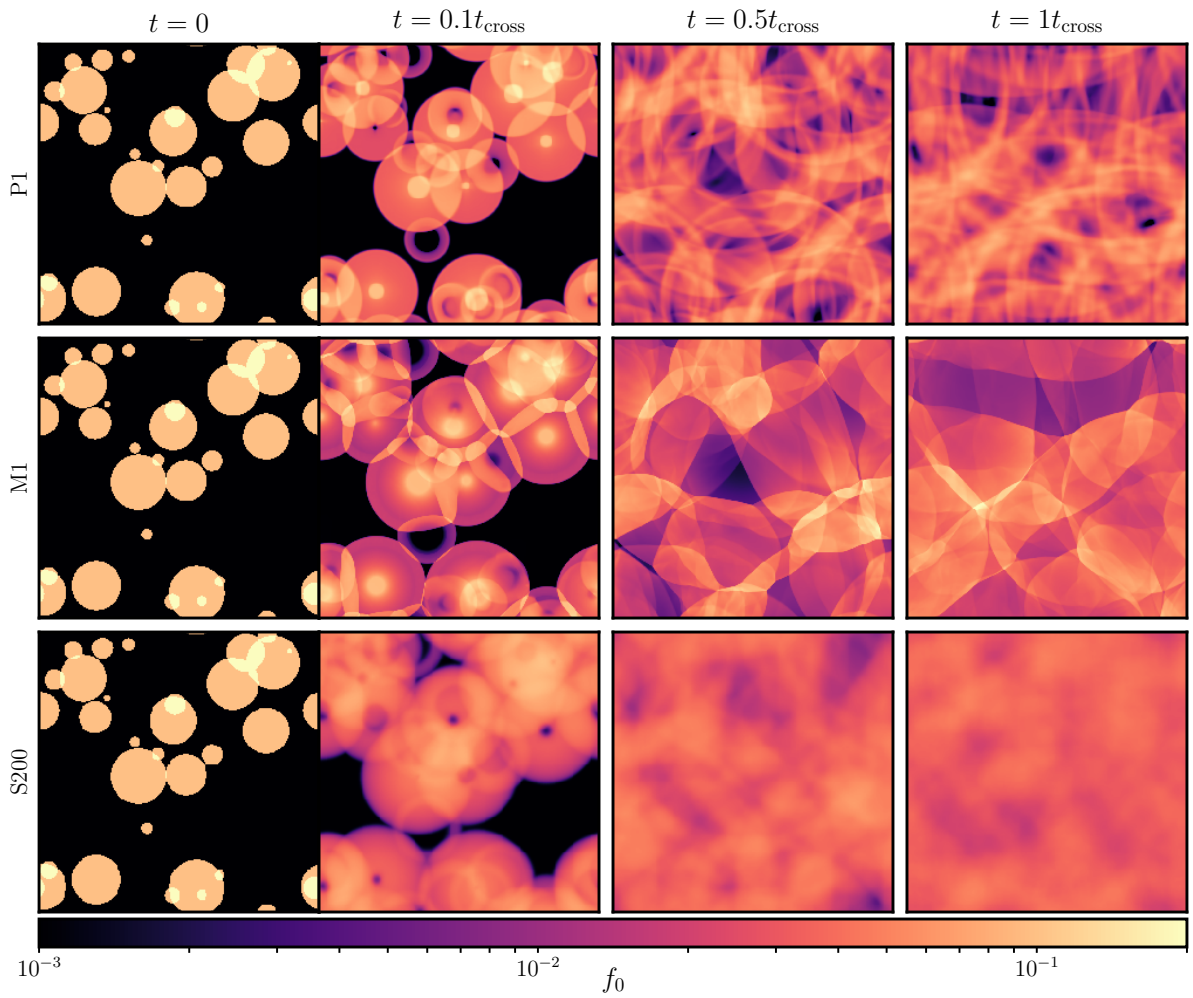

Figure 4.1: The first moment f_0 (or photon number density) at different times as calculated with the P1 and M1 fluid models and the S200 discrete ordinates solution. We display the entire simulation box.

always in the free-streaming regime and radiation should be transport at its maximum velocity c freely without any interactions at all. Formally, no hydrodynamic description for radiation should be applied to these simulations at all because this approximation is expected to break down. Nevertheless, the results of these simulations are instructive as they enable us to gauge the maximum influence of closure relations in a worst-case scenario. This demonstrates the wide-ranging implications that the choice of a transport model can have.

The results are presented in Fig. 4.1. At early times ($t = 0.1t_{\text{cross}}$), the differences between the P1 and M1 approximations appear to be minor. The cloudlets expand mostly radially. The major difference between the two approximations is how the radial expansion shapes a cloudlet. In the P1 approximation, the expansion of each cloudlet is uniform inside an annulus that starts

at the edge of the cloudlet and extents into is interior via an expansion front. The radiation inside this annulus is expanding uniformly as can be seen in the homogeneous brightness of such annuli. For the M1 approximation, the propagation model is different. Here, the cloudlets are not uniformly expanding but are rarefied and develop smooth gradients from the central brightness towards the edge of these expanding cloudlets. For both transport models, the expansion of a cloudlet changes its morphology into a ring-like structure for isolated cloudlets. Large cloudlets have a brightness maximum at their geometric centre. This is not caused by a built-up of radiation but is due to a lag in expansion. The centre of those cloudlets was not hit by the expansion wave and is, consequently, not expanding.

For cloudlets with nearby neighbours an additional difference can be observed between the P1 and M1 closure relations. At points where the expansion fronts of two cloudlet overlap, the radiation density in the P1 model results in a superposition of photon packages while in the M1 model shock fronts emerge and change the propagation direction of the radiation flux into non-radial directions. Because of the rarefactions of radiation and the developing shock fronts, the M1 closure model exhibits characteristics of *fluidisation* of radiation. This self-interaction of radiation is not induced by any physical process but a manifestation of the fluid approximation and must be regarded as a short-coming of this method.

Both, the P1 and the M1 approximations compare poorly to the discrete ordinates solution. In this model, expanding cloudlets show smoother outer edges and no central brightness enhancement. The smoothness of the evolution can be attributed to the local non-radial propagation of radiation that is possible in the S200 model. Nevertheless, the global radial expansion of a cloudlet is caused by the overlap of radiation propagating into different, non-radial directions. Furthermore, we do not observe central brightness maxima in the S200 model because this model does not feature any expansion fronts that first need to travel inside a cloudlet in order to trigger an expanding motion. Instead, the entire cloudlets starts to expand with the beginning of the simulation.

The expansion velocity of the cloudlets is different for the various transport models. For every model this velocity is equal to the fastest information propagation velocity. Hence, the expansion velocity is $c/\sqrt{3} \approx 0.57c$ for the P1 approximation while it is c for the M1 and S200 approximations. This leads to smaller expanding cloudlets in the P1 case in comparison to the expanding cloudlets in the M1 and S200 cases, which share the same spatial extent.

At later times, at $t = 0.5t_{\mathrm{cross}}$ and $t = 1t_{\mathrm{cross}}$, we do not find similarities between the presented transport methods. The mechanisms driving the differences at earlier times are more pronounced because the radiation that originates from multiple individual cloudlets interacts

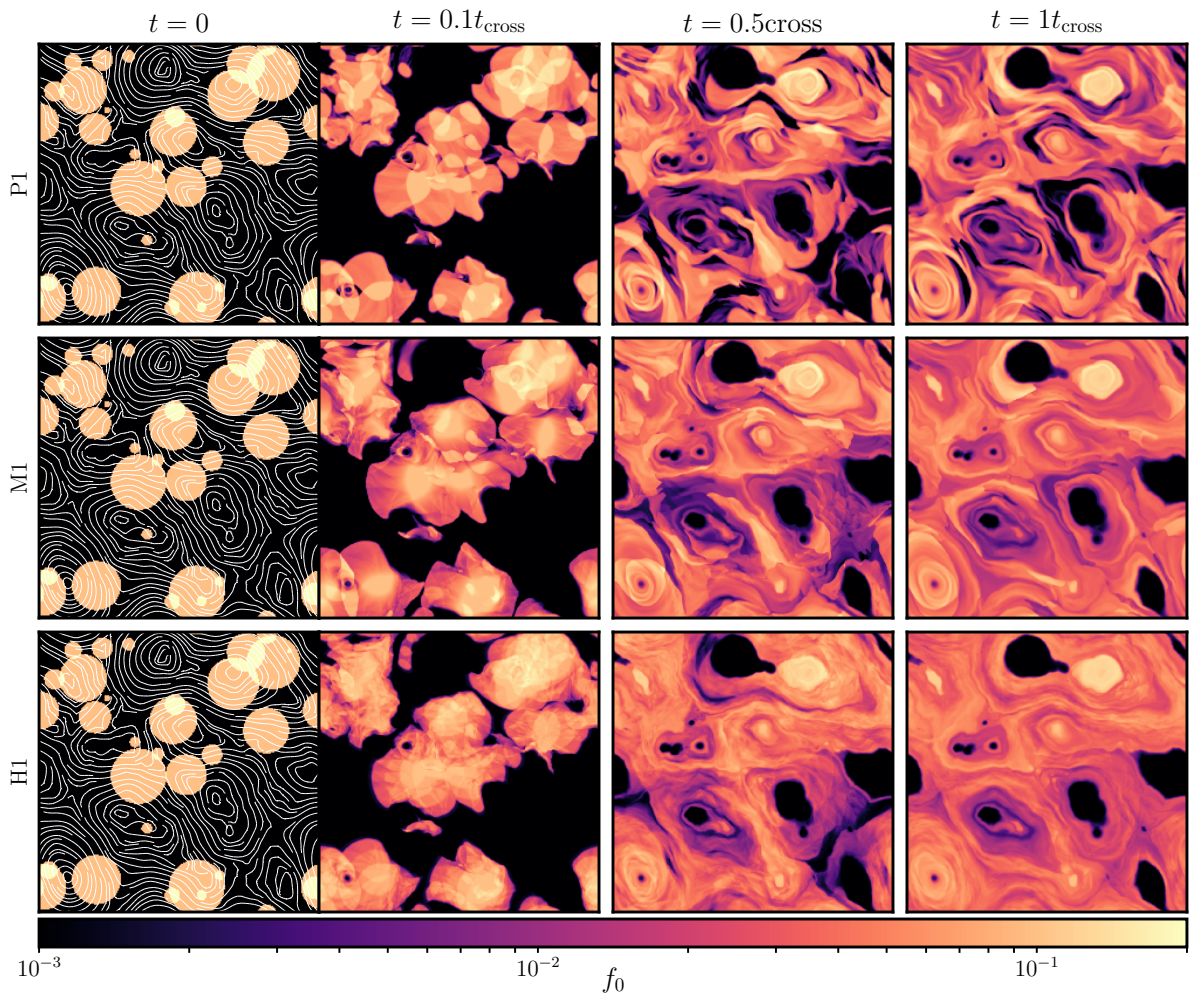

Figure 4.2: The first moment f_0 (or CR number density) at different times as calculated with the P1, M1 and H1 fluid models *without* CR scattering. We display the entire simulation box. The white lines in the left-most panels trace the magnetic field.

so that there is no cloudlet evolving in isolation any more. The simulations with the P1 closure shows a complex network of overlapping radiation rings resembling caustics. By contrast, streams of radiation frequently collide in the M1 simulations developing a pattern that is reminiscent of super-sonic turbulence with multiple and connected shock fronts travelling through the simulation domain. Radiation in the S200 model is diluted to the point that the computational domain is filled by a diffusive fog of radiation with no distinctive morphology.

4.3.3 CR hydrodynamics

For our next set of simulations, we restrict the transport of radiation solely along magnetic fields and thus switch our attention to CR transport. In this case, no discrete ordinates solution is available as a reference solution and we need to compare the three fluid approximations (P1, M1, H1) to each other. The reason for the development of our new H1 approximation in Section 4.2 is that it provides a more accurate representation of CR transport and enables us to evaluate the performance of the P1 and M1 methods. Like the previous set of simulations, here we neither account for interactions of CRs with the surrounding plasma nor with electromagnetic waves but only allow for their anisotropic transport along magnetic fields. Consequently, CRs are in the free-streaming limit at all times. We present the results of these simulations in Fig. 4.2.

The structure of the P1 solution is dominated by cloudlets that are stretched and distorted while CRs are transported along the magnetic field. This leads to a patchy morphology of f_0 visible at $t = 0.1t_{\mathrm{cross}}$ and $t = 0.5t_{\mathrm{cross}}$. At later times at $t = 1t_{\mathrm{cross}}$, the cloudlets are stretched to wrap around magnetic loops and overlap with themselves or with neighbouring cloudlets. We can understand the reason for this evolution, by realising that each cloudlet in the radiation simulation in Section 4.3.2 developed into an expanding annulus. In the present simulation, these annuli can only expand and move along magnetic field lines. Therefore, every cloudlet will split into two parts: one moving along and the other one moving opposite to the direction of the magnetic field permeating the cloudlet. In each of these two parts, f_0 is rather uniform so that overlapping parts from different cloudlets create the observed patchy structure where f_0 increases stepwise towards local brightness maxima. This is different for the M1 model. Radiation cloudlets in the M1 model are rarefying. This is also the case for CRs transported with the M1 model: there are fewer patches with $f_0 \sim$ const. present in the M1 solution in comparison to its P1 counterpart but instead more regions in which f_0 shows smooth gradients. The same holds true for the simulation with the H1 approximation. In the M1 and H1 models, the simulations contain regions with multiple wavefronts that cross through each other. Most importantly, in all methods, CRs are confined to magnetic islands, which we identify with closed magnetic loops with a small spatial extent, and which fill their hosting island mostly homogeneously. Regions which are not connected to a cloudlet through a magnetic field line do not contain CRs that any time. This creates the dark magnetically insulated islands in Fig. 4.2 whose surroundings get populated by CRs over time while no CR enters the magnetic island itself.

The differences between the results of the P1 and M1 approximations are smaller for anisotropic

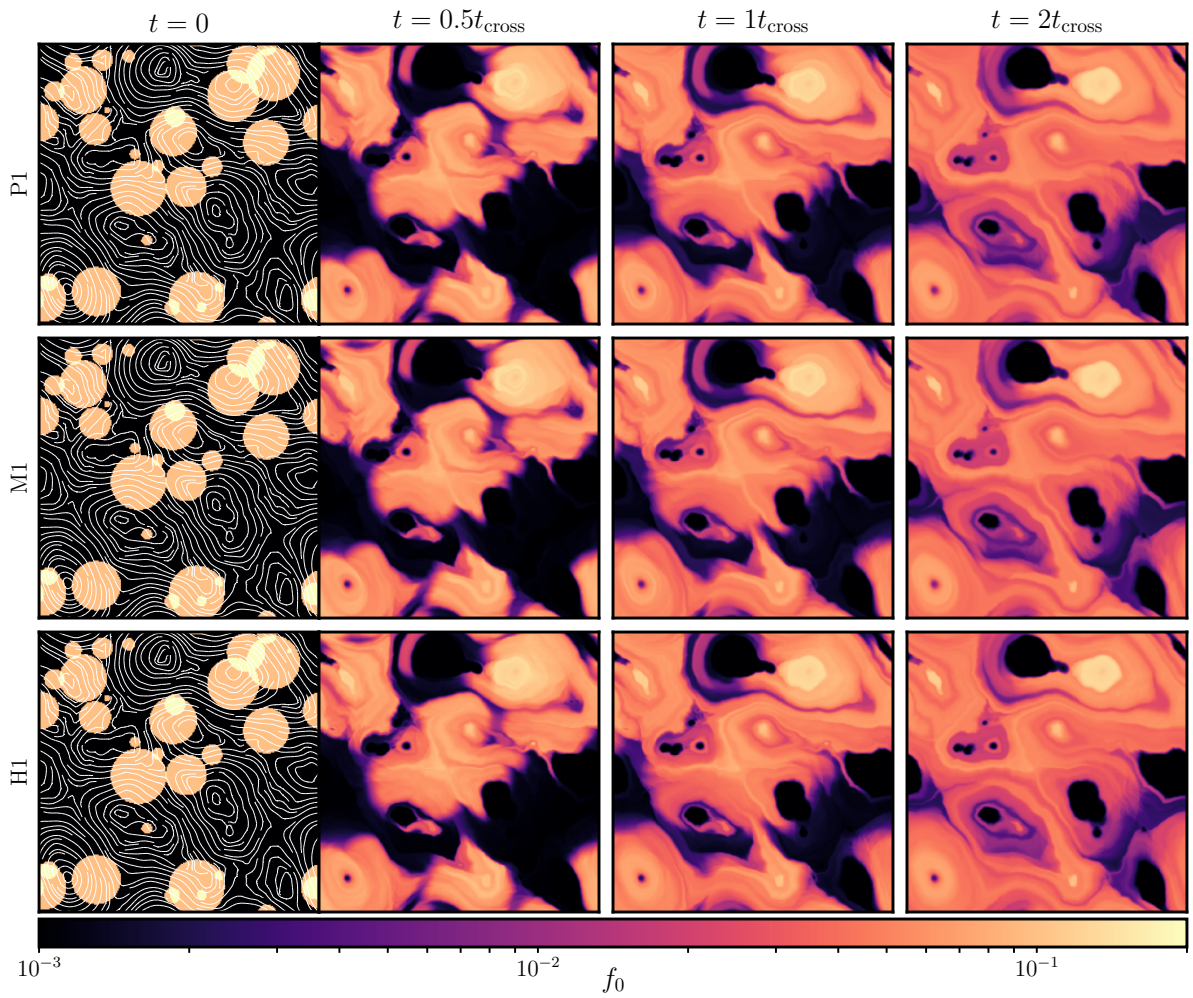

Figure 4.3: The first moment f_0 (or CR number density) at different times as calculated with the P1, M1 and H1 fluid models *with* CR scattering. We display the entire simulation box. The white lines in the left most panels trace the magnetic field.

CR transport in comparison to radiation transport (cf. Fig. 4.1 vs. Fig. 4.2): in the case of radiation transport, both approximations lead to fundamentally different solutions while we can identify the most prominent features in both approximations if the transport is restricted to be along magnetic field lines. This is because CRs trace the magnetic field topology and thus features contained in the magnetic field will be inevitably present also in the global CR distribution. Only if we compare the P1 and M1 approximations along a single magnetic field line, we are able to quantify differences.

CR cloudlets expand with the same velocity as their radiation counterparts. Like in the radiation case, the M1 cloudlets expand initially with velocity c along magnetic field lines while CRs in the P1 case travel at maximum speeds of $c/\sqrt{3} \approx 0.57c$. The expansion velocity

of CR cloudlets in the H1 approximation is placed in between the P1 and M1 case with a maximum velocity of $(1/2 + \sqrt{1/12})c \approx 0.78c$. The spherical bright spots observed at the centres of radiation cloudlets in the P1 and M1 approximations are still present for the CR case. Here, cloudlets do not radially expand with respect to a cloudlet centre but propagate along the magnetic field lines permeating the cloudlet. Because these magnetic field lines are non-uniform, the bright spots of the cloudlets develop irregular shapes.

Morphologically, we find more structure in the P1 results, which are smoothed out in case of the M1 or H1 solutions, the latter of which shows the most diffusive appearance. This is due to the increasing dynamical flexibility of the M1 approximation or the two additional degrees of freedom in the H1 approximation in comparison to P1. Overall, the M1 and H1 results resemble each other while the P1 morphology shows the largest contrast to that of the two other methods (see also Hopkins et al., 2021c, for a P1-M1 comparison).

In the case of the M1 and H1 methods, the magnetic focusing term provides a source of indirect scattering that can explain the similarity of both approximations. The reason why magnetic focusing can act as a scattering agent is particular easy to understand for the M1 model; in this case, the magnetic focusing term in the f_1-equation is given by

$$\left.\frac{\partial f_1}{\partial t}\right|_{\text{focusing}} = (\boldsymbol{\nabla}\cdot\boldsymbol{b})\frac{3D-1}{2} \tag{4.61}$$

and $3D - 1 > 0$ for $|f_1/f_0| > 0$. For a given magnetic field line, CRs will be transported through regions where $\boldsymbol{\nabla}\cdot\boldsymbol{b} > 0$ and further down this field line through regions where $\boldsymbol{\nabla}\cdot\boldsymbol{b} < 0$ provided the magnetic field topology is sufficiently irregular. Depending on this sign the focusing term switches its behaviour, i.e. the CR flux f_1 increases or decreases. If the sign of $\boldsymbol{\nabla}\cdot\boldsymbol{b}$ is permanently changing, the evolution of f_1 will become more random. On the other hand, if $\boldsymbol{\nabla}\cdot\boldsymbol{b}$ does not change its sign, f_1 might evolve towards a state where Kershaw's condition in Eq. (4.15) is violated. Whether it is possible to construct such magnetic field topologies will be left as an open question for future studies. Further, we note that the magnetic focusing discussed here is different from the effects of magnetic focusing in the context of the CGL (Chew-Goldberger-Low) equations (Chew et al., 1956). There magnetic focusing influences the balance between gas pressure components parallel and perpendicular to the direction magnetic field while in our case it influences the evolution of the momentum or heat flux densities (as encoded in f_1). Both effects originate micro-physically in the same $\boldsymbol{\nabla}\cdot\boldsymbol{b}$ term of Eq. (4.2).

Clearly this scattering effect is only important if it is the most dominant source of scattering which is the case in the presented idealised simulations in which we explicitly do not account for any other source of scattering. We also note that the resulting effect of this scattering might be further exaggerated by our fluid models. The magnetic focusing terms originates in the

corresponding term in Eq. (4.2) that is clearly not describing a scattering process but advection of f through pitch-angle space. By its nature, advection is localised in pitch-angle space and transfers information contained in f from μ to some neighbouring $\mu + \mathrm{d}\mu$. Because pitch-angle moments involve integrals over μ space, low-order fluid models lost most of their memory about localised information of f and only retain information of the global moment structure of f. Consequently, fluid models cannot accurately describe the magnetic focusing process in all details. Yet, because we account for the focusing term in deriving the evolution equations for the moments f_n, we simultaneously account for its global effect on f which thus retains some indirect memory through the scattering process as explained above.

4.3.4 CR hydrodynamics with scattering

For our last set of simulations, we include CR scattering through the models described in Section 4.2.6. They are accurate to first order in v_a/c and as such, they are comparable to each other and consistently formulated so that our results are not influenced by any differences between them. This allows us to quantify the impact of the different transport models in the case of effective CR scattering. The results of the simulations are presented in Fig. 4.3.

By including CR scattering in our simulations, the local flux of CRs is reduced, which results in a slower transport of CRs through the simulation domain. For this reason we show f_0 in Fig. 4.3 at later times in comparison to the previous Figs. 4.1 and 4.2. The CR dynamics slightly differs in comparison to the case without CR scattering: cloudlets smoothly spread along magnetic field lines. Sharp transitions as observed in the simulations without CR scattering are not visible. Structures with a larger contrast are caused by neighbouring magnetic fields where one field line is connected to a cloudlet and can be populated by CRs while the other is not connected and remains devoid of CRs. Neither patchiness nor rarefied structures, which are a characteristics for the P1 and M1 method of CR transport without scattering are present in this case. At late times, cloudlets dissolve into each other and build up a rather homogeneous sea of CRs. There are smooth transitions between regions filled with abundant CRs and those that contain fewer CRs (or which have not yet been reached by any) if they are connected through a magnetic field line.

There are no visible differences between the results calculated with the P1 and M1 approximations at any time. The reason for this is that the difference between both models is the way they treat CR fluxes that are mildly to fully anisotropic, i.e., $f_1 \sim f_0$. In such situations, the M1 Eddington factor $D \neq 1/3$ and differs from its P1 counterpart. However, in the presented scenario, CR scattering is effective and leads to low anisotropies in the CR distribution with

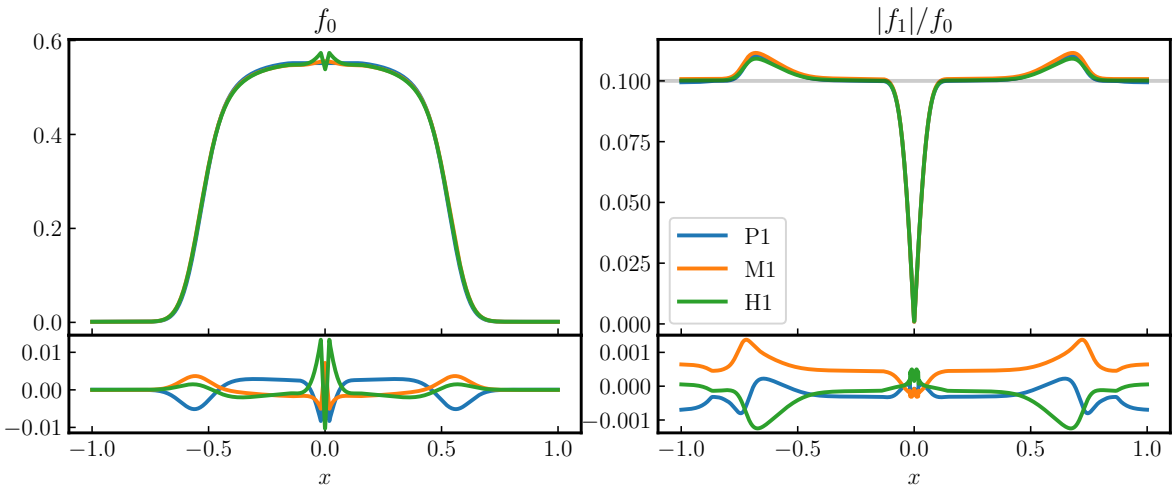

Figure 4.4: The first moment f_0 (or CR number density) and the transport velocity f_1/f_0 calculated with the P1, M1 and H1 fluid models *with* CR scattering for the one-dimensional example. Both top panels show the of f_0 and f_1/f_0 directly while the bottom panels show the deviations of these quantities from their common average (calculated as the mean result of all three transport methods). The thin grey line in the top-right panel marks $|f_1|/f_0 = v_a/c = 0.1$.

$f_1 \sim (v_a/c)f_0 = 0.1 f_0$ and thus $D \sim 1/3$ even in the M1 case. The M1 approximation is effectively reduced (by removing the main difference) to the P1 approximation if scattering removes anisotropy or, in other words, is reducing the flux of CRs to non-relativistic values.

All major features observed in the two-moment approximations (P1 and M1) can be readily found in the simulations with the H1 approximation. However, there are minor differences between the P1/M1 and H1 results. In particular, the H1 simulation exhibits small details that are absent in the P1 and M1 cases. These are best observed in regions into which CR have just entered, i.e., where f_0 is small. The reason for this is that the H1 approximation provides four degrees of freedom and thus allows for more hydrodynamical waves to travel inside the simulation which then create the observed fine-grained structure.

4.4 Quantifying the differences

The previous section demonstrated visually that the difference between the three presented transport descriptions vanishes once we accounted for the scattering of CRs. We use this section to quantify this result. To this end, we run an additional set of one-dimensional simulations with the same numerical method, parameters and scattering prescription as used in the previous

section. The simulation domain spans $x \in [-1, 1]$ and is resolved by 2048 computational cells. The CRs are initialized with a constant density $f_0 = 10^{-2}$ and are assumed to be stationary $\Delta f_0 = f_1 = f_1^- = f_1^+ = 0$. The magnetic field is pointing along the direction of the simulation domain and $v_a/c = 0.1$. To trigger the dynamics in the simulation, we inject CRs with a rate $\dot{f}_0 = \exp\left(-250\, x^2\right)$.

The results of the simulations are presented in Fig. 4.4 at $t = 5$. All three transport models yield similar results. The injection of CRs gradually creates an overdensity of CRs in the centre of the simulation domain. Their inertia leads to the grow of their transport velocity on both sides and moves CRs towards the boundaries resulting in a rather flat central plateau of CRs. The location of the fastest CR transport roughly coincides with the location of the steepest number density gradient (where the CR plateau transitions into the background CRs), which is the region where the effect of CR inertia is maximised. At this point, the CR transport speeds slightly exceed the Alfvén speed $|f_1|/f_0 \lesssim 1.1 v_a/c$. Inside the injection region ($|x| < 0.1$) CR scattering is unable to accelerate the freshly injected CRs to be transported with Alfvén speed. Outside these two regions CRs stream with speeds comparable to the Alfvén speed $|f_1|/f_0 \sim v_a/c$. We compare the first moment f_0 and the transport velocity (in units of the light speed) f_1/f_0 for all three transport models by computing the individual differences to the average taken over the results of all three transport models. The differences are largest (i) at the largest value of the f_0 gradient where the transport velocities differ the most and (ii) at the centre of the simulation domain where f_0 for the H1 model shows some additional spike-like features. The relative differences of f_0 stay at or below 1 per cent while differences in the transport velocity are approximately ten times smaller.

Because f_1 is a proxy for the momentum density of the CR population, we infer that the momentum transferred from the CRs to the background MHD gas would be similar for all three models due to the similar evolution of f_1. Because the dynamics of CRs, the MHD gas, and their interactions are similar for all three transport models, the total evolution of a more complete model of a composite CR and MHD gas (in comparison to the simplified model presented here) is expected to similar for all three models provided the coupling of CRs is strong.

4.5 Discussion and Conclusion

In order to investigate the differences between closure relations for CR hydrodynamics, we (i) reviewed the derivation of the P1 and M1 fluid approximations starting from the general fo-

cused transport equation, (ii) discussed how a simplified model for CR scattering with Alfvén waves can be implemented and (iii) presented a set of numerical simulations that highlight the deviations of the different approximations. In order to check the correctness of these approximations, we develop and present the new H1 fluid approximation which evolves four moments of the CR pitch-angle distribution instead of the two moments used by the P1 and M1 approximations. Because the P1 and M1 models were originally developed in the context of radiation hydrodynamics we also include simulations and derivations of both models in this limit and compare simulation results to a more correct radiation transfer simulation using the discrete ordinates approximation. Because (GeV or higher-energy) CRs and radiation are both relativistic (particle) species with a negligible rest mass energy density, any insight gained from the radiation case can be used to understand the CR transport.

As we advance to ever-increasing details and include more CR physics, we observe that the differences between the presented hydrodynamical models get smaller. While the P1 and M1 approximations generate large differences in the evolution of radiation, including a large-scale magnetic field for CR transport already results in a more similar spatial CR distribution in the P1 and M1 approximations because CRs are necessarily confined to and transported along magnetic field lines. The large scale structure of the resulting CR distribution is now set by the magnetic field topology, which effectively reduces the degrees of freedom for the transport and thus the dimensionality of the solution space. Nevertheless, if we compare the CR evolution along an individual magnetic field line in both approximations, we still observe differences.

This situation changes once we include the effects of CR scattering. In this more realistic case the differences between the approximations are significantly reduced to the point where they are merely of academic interest. This is an expected result because scattering reduces the local flux so that the bulk of CRs is transported with non-relativistic velocities and the relativistic corrections of the M1 method become ineffectual. As a result, simulations with the M1 approximation are effectively indistinguishable from their P1 counterpart. Even if we consider the higher-order accurate H1 approximation, the differences between the results of the P1, M1 and H1 models are very small and have negligible astrophysical consequences. This is because CR scattering is a pitch-angle diffusion process that reduces the amount of information encoded in the pitch-angle distribution of CRs. Higher-order methods such as the H1 approximation strive to encode more information in the CR pitch-angle distribution. However, because there is very little additional fine-structure contained in the pitch-angle distribution (at timescales comparable or longer than a light crossing time) modelling these degrees of freedom does not significantly improve the accuracy of the solution.

The advantage of the M1 approximation in comparison to the P1 approximation is that it allows for the beam transport mode in a two-moment fluid description. The beam mode is characterised by a high degree of anisotropy in the CR distribution. However, if this anisotropy is large enough, additional micro-scale plasma processes such as the non-resonant hybrid instability (Bell, 2004) and the intermediate-scale instability (Shalaby et al., 2021) start to dominate and influence the CR evolution. Therefore, to provide a consistent description of CR dynamics these additional kinetic processes need to be incorporated in the fluid description through the scattering terms. Note that both instabilities act in such a way that they drive the CR distribution towards isotropy and thus towards the applicability of the regime of the P1 approximation. Lastly, we want to stress that this discussion and hydrodynamical models in general are only valid on scales significantly larger than the CR gyroradius and mean free path. On scales comparable to the CR gyroradius only kinetic descriptions provide useful tools for investigations.

Using a more detailed description of CR transport is clearly worthwhile from a theoretical standpoint but whether this is also the case for numerical simulations of marco-scale astrophysical environments is debatable. Modern day simulations are not only limited by the computational power available but also by the amount of physical processes modelled within them. Focusing more on micro-scale kinetic CR physical processes and how these can be coarse-grained and incorporated into a large-scale fluid model may lead to more correct solutions with higher physical credibility in comparison to higher-order CR fluid models. As CR transport is tightly linked to the magnetic field topology, using an accurate numerical method to calculate the evolution of the magnetic field will have a positive impact on the accuracy of the simulated CRs. Note that we can only observe minor differences in the simulations with CR scattering because of our high-resolution idealised setup. In resolution-starved simulations of realistic astrophysical scenarios, motions of the plasma and the magnetic field introduce another source of scattering via numerical diffusion. This additional but artificial scattering will further decrease the differences between the considered hydrodynamical models.

In summary, we find that the P1 approximation produces equally accurate solutions in comparison to the M1 approximation of CR transport *if CR scattering is efficient* while there are small differences if scattering is inefficient. However, the applicability of the M1 approximation is questionable in the case of inefficient scattering and higher-order fluid models such as the presented H1 model or fluid-kinetic models provide a better approximation, allow for more degrees of freedom to be evolved, and retain more information of the underlying CR distribution.

5 A Finite-Volume Method for Two-Moment Cosmic-Ray Hydrodynamics on a Moving Mesh

This chapter is based on the published paper by Thomas, T. ; Pfrommer, C. ; Pakmor, R.: Monthly Notices of the Royal Astronomical Society, Volume 503, Issue 2, pp.2242-2264

We present a new numerical algorithm to solve the recently derived equations of two-moment cosmic ray hydrodynamics (CRHD). The algorithm is implemented as a module in the moving mesh Arepo code. Therein, the anisotropic transport of cosmic rays (CRs) along magnetic field lines is discretised using a path-conservative finite volume method on the unstructured time-dependent Voronoi mesh of Arepo. The interaction of CRs and gyroresonant Alfvén waves is described by short-timescale source terms in the CRHD equations. We employ a custom-made semi-implicit adaptive time stepping source term integrator to accurately integrate this interaction on the small light-crossing time of the anisotropic transport step. Both the transport and the source term integration step are separated from the evolution of the magneto-hydrodynamical equations using an operator split approach. The new algorithm is tested with a variety of test problems, including shock tubes, a perpendicular magnetised discontinuity, the hydrodynamic response to a CR overpressure, CR acceleration of a warm cloud, and a CR blast wave, which demonstrate that the coupling between CR and magneto-hydrodynamics is robust and accurate. We demonstrate the numerical convergence of the presented scheme using new linear and non-linear analytic solutions.

5.1 Introduction

CRs are highly energetic particles that pervade most astrophysical plasmas. While CR electrons are important agents that shape the non-thermal emission seen in radio, X-ray and γ-ray observations, CR protons in the Milky Way's mid-plane contain on average 100 times more energy than CR electrons and dominate the total energy budget of CRs (Zweibel, 2013). Similar to our Milky Way, in many astrophysical environments the energy contained in CRs is sufficiently large that their dynamics is affecting the thermal gas (Boulares and Cox, 1990; Zweibel, 2017). Notable examples of such a situation are winds of star-forming galaxies. Inside these winds CRs have energy densities comparable to those of magnetic fields and thermal energy densities (Breitschwerdt et al., 1991; Buck et al., 2020). In the interstellar medium (ISM) the major source of CRs are expanding supernova shocks where the diffusive shock acceleration mechanism accelerates thermal low-energy particles to relativistic energies (Blandford and Eichler, 1987; Caprioli and Spitkovsky, 2014). After they leave their acceleration side and are escaping into the ISM, CRs start to accelerate its ambient medium out of the disc and launch mass-loaded galactic size outflows (Heckman and Thompson, 2017). The dynamics of CR driven winds are investigated using one-dimensional flux tube models (Breitschwerdt et al., 1991; Everett et al., 2008; Recchia et al., 2017; Schmidt et al., 2019), stratified box simulations targeting the scales of several parsecs (Girichidis et al., 2016; Simpson et al., 2016b; Farber et al., 2018), idealized simulations of isolated disks (Hanasz and Lesch, 2003; Uhlig et al., 2012; Hanasz et al., 2013; Salem and Bryan, 2014; Pakmor et al., 2016b; Ruszkowski et al., 2017; Wiener et al., 2017b; Jacob et al., 2018; Butsky and Quinn, 2018; Chan et al., 2019; Dashyan and Dubois, 2020), and cosmological simulations (Jubelgas et al., 2008; Salem et al., 2014, 2016; Hopkins et al., 2021b; Buck et al., 2020). All of these methods assume different modes of CR propagation and interactions.

CRs with energies $\gtrsim$ GeV are nearly collisionless and interact with their environment by scattering off of magnetic irregularities (Schlickeiser, 2002). Proposed candidates for these irregularities are turbulent magnetosonic waves (Lee and Voelk, 1975; Yan and Lazarian, 2002; Vukcevic, 2013) and Alfvén waves on scales comparable to the gyroradius of the CR (Kulsrud and Pearce, 1969; Skilling, 1975). Depending on the frequency of this scattering, the microphysical transport of CRs drastically changes. If the scattering is infrequent but existing then CRs start to diffusive along magnetic field lines. In addition to this diffusion, a population of CRs might drift with some non-negligible average velocity. If this drift is faster than the local speed of Alfvén waves then CRs excite gyroresonant Alfvén waves through the gyroresonant instability (Kulsrud and Pearce, 1969). These waves are in turn able to scatter CRs more fre-

quently which further amplifies the instability. This self-amplifying feedback loop stops when the average velocity coincides with the Alfvén speed, i.e. when the CRs start to stream with the Alfvén waves. Recent particle-in-cell simulations support this picture (Lebiga et al., 2018; Holcomb and Spitkovsky, 2019; Bai et al., 2019; Haggerty and Caprioli, 2019; Shalaby et al., 2021). On a macroscopic level, diffusing or streaming CRs spatially redistribute their energy more independently of the gas flow compared to the internal energy of the gas which seeds a plethora of new dynamics (Skilling, 1971; Salem and Bryan, 2014; Wiener et al., 2017b).

CR transport is commonly described by one of three different theories. The kinetic description directly uses the Maxwell-Newton system of equations to investigate the trajectories and electromagnetic interactions of individual charged particles (Pohl et al., 2020). Fokker-Planck-type theories describe an ensemble of CRs in the full six dimensional phase space with a statistical approach (Schlickeiser, 2002; Malkov, 2018). Hydrodynamical models only describe the spatial transport while encoding the phase space information in a moment hierarchy of the distribution function (McKenzie and Webb, 1984; Breitschwerdt et al., 1991; Ko, 1992; Zweibel, 2017). The hydrodynamic description of CRs is commonly employed in simulations that model large scale astrophysical applications that are not reachable with kinetic simulations. The majority of the published numerical studies uses the one-moment model where CRs are described only by the time evolution of their energy density (Hanasz and Lesch, 2003; Wagner et al., 2006; Pfrommer et al., 2006, 2007; Enßlin et al., 2007; Jubelgas et al., 2008; Yang et al., 2012; Hanasz et al., 2013; Girichidis et al., 2014; Salem and Bryan, 2014; Pfrommer et al., 2017a; Dubois et al., 2019).

While this approach is successful in describing the advective and diffusive transport of CRs, streaming of CRs imposes another challenge. Sharma et al. (2010) observe that a standard finite difference or finite volume discretisation of CR streaming seeds a strong numerical instability that quickly leads to unphysical results. They propose a regularization that adds numerical diffusion and tames the numerical instability. Jiang and Oh (2018) recently proposed to use a second moment of the CR distribution function to simultaneously evolve the energy and flux of CRs which automatically cures the numerical instabilities of the one-moment approach.

Inspired by their idea, Thomas and Pfrommer (2019) derived equations for the CR energy and momentum flux starting from the quasi-linear Fokker-Planck theory of Schlickeiser (2002). Including equations for the energy of gyroresonant Alfvén waves allows for a description of CR streaming and diffusion based on their gyroresonant interactions and various (collisionless or collisional) damping processes. Thomas and Pfrommer (2019) showed that an effective description including the formal order $O(\bar{\nu} v_\mathrm{a}^2/c^2)$ of the scattering between CRs and Alfvén waves

is necessary in order to achieve momentum and energy conservation while complying with the first law of thermodynamics (here, $\bar{\nu}$ is the pitch-angle averaged CR scattering frequency, v_a is the Alfvén velocity and c is the light speed). Furthermore, the derived theory is only Galilean invariant to this order. The resulting two-moment CR-fluid theory reduces in the limit of strong scattering to previously presented one-moment theories. The emerging dynamics of CRHD was shown to be consistent with the theoretical expectation and free of the numerical instability. Applying CRHD to observations with the MeerKAT radio telescope, which discovered a unique population of faint non-thermal filaments pervading the central molecular zone close to the Galactic center, revealed compelling evidence that GeV CRs are mainly streaming with the local Alfvén speed (Thomas et al., 2020).

Thomas and Pfrommer (2019) present one-dimensional and highly idealised simulations. In this paper we present a numerical algorithm that can be used to simulate CRHD with the moving mesh code Arepo in three dimensions and for a variety of applications that range from simulating supernova remnant explosions to jets from active galactic nuclei to galaxies and galaxy clusters in cosmological environments. The basis of our algorithm is a path-conservative finite volume method to accurately simulate the anisotropic transport of CRs combined with a custom-made adaptive time stepping integrator to model their gyroresonant interaction with Alfvén waves.

Our paper is structured as follows. In Section 5.2 we review the CRHD equations and briefly describe the modelled physics. In Section 5.3 we detail our numerical descritization of the CRHD equations on a moving mesh and test the algorithm with various problems in Section 5.4. We present a formulation of CRHD in cosmological comoving coordinates in App. 5.6. As path-conservative schemes are not common in computational astrophysics, we present a derivation of those schemes in App. 5.7. In App. 5.8 we present a mathematical and numerical convergence proof of our source term integrator. Throughout the paper we use Heaviside-Lorentz units and write $\boldsymbol{ab}$ for the tensor product of $\boldsymbol{a}$ and $\boldsymbol{b}$.

5.2 Equations of Cosmic Ray Hydrodynamics

We use the two-fluid approximation to describe the CR-gas composite fluid which allows separate transport of the non-relativistic thermal particle population and high-energy CRs. While the thermal gas is modelled with the MHD approximation, the CRs are assumed to be ultra-relativistic with a particle speed equal to the speed of light c. Additionally, CRs are described using a two-moment approach where the CR energy density and its flux density are evolved

independently. We use a grey approach for the CRs that only tracks the total CR energy and flux densities and does not account for their energy-dependence (see Girichidis et al., 2020 for an energy dependent fluid theory of diffusing CRs). In this scenario Thomas and Pfrommer (2019) derived a new set of equation for CRHD based on the Fokker-Planck theory of CRs in its quasi-linear limit. The theory accounts for the anisotropic transport of CRs along magnetic field lines, the gyro-resonant interaction of CRs and Alfvén waves, and the coupling of Alfvén waves and CRs to the thermal gas. The complete set of equations is:

$$\frac{\partial \rho}{\partial t} + \boldsymbol{\nabla} \cdot [\rho \boldsymbol{u}] = 0, \tag{5.1}$$

$$\frac{\partial \rho \boldsymbol{u}}{\partial t} + \boldsymbol{\nabla} \cdot [\rho \boldsymbol{u}\boldsymbol{u} + P_{\rm tot}\mathbf{1} - \boldsymbol{B}\boldsymbol{B}] = \boldsymbol{b}\boldsymbol{\nabla}_{\parallel} P_{\rm cr} + \boldsymbol{g}_{\rm gri,+} + \boldsymbol{g}_{\rm gri,-}, \tag{5.2}$$

$$\frac{\partial \boldsymbol{B}}{\partial t} + \boldsymbol{\nabla} \cdot [\boldsymbol{B}\boldsymbol{u} - \boldsymbol{u}\boldsymbol{B}] = \mathbf{0}, \tag{5.3}$$

$$\begin{aligned}\frac{\partial \varepsilon}{\partial t} + \boldsymbol{\nabla} \cdot [\boldsymbol{u}(\varepsilon + P_{\rm tot}) - (\boldsymbol{u}\cdot\boldsymbol{B})\boldsymbol{B}] &= (P_{\rm cr} + P_{\rm a,+} + P_{\rm a,-})\boldsymbol{\nabla}\cdot\boldsymbol{u} \\ &+ \boldsymbol{u}\cdot(\boldsymbol{b}\boldsymbol{\nabla}_{\parallel}P_{\rm cr} + \boldsymbol{g}_{\rm gri,+} + \boldsymbol{g}_{\rm gri,-}) + Q_+ + Q_-,\end{aligned} \tag{5.4}$$

$$\frac{\partial \varepsilon_{\rm cr}}{\partial t} + \boldsymbol{\nabla} \cdot [\boldsymbol{u}\varepsilon_{\rm cr} + \boldsymbol{b} f_{\rm cr}] = -P_{\rm cr}\boldsymbol{\nabla}\cdot\boldsymbol{u} - v_{\rm a}\boldsymbol{b}\cdot\left(\boldsymbol{g}_{\rm gri,+} - \boldsymbol{g}_{\rm gri,-}\right), \tag{5.5}$$

$$\frac{\partial f_{\rm cr}}{\partial t} + \boldsymbol{\nabla} \cdot [\boldsymbol{u} f_{\rm cr}] + c_{\rm red}^2 \boldsymbol{\nabla}_{\parallel} P_{\rm cr} = -f_{\rm cr}(\boldsymbol{b}\boldsymbol{b}) : \boldsymbol{\nabla}\boldsymbol{u} - c_{\rm red}^2 \boldsymbol{b}\cdot\left(\boldsymbol{g}_{\rm gri,+} + \boldsymbol{g}_{\rm gri,-}\right), \tag{5.6}$$

$$\frac{\partial \varepsilon_{\rm a,\pm}}{\partial t} + \boldsymbol{\nabla} \cdot [\boldsymbol{u}\varepsilon_{\rm a,\pm} \pm v_{\rm a}\boldsymbol{b}\varepsilon_{\rm a,\pm}] = -P_{\rm a,\pm}\boldsymbol{\nabla}\cdot\boldsymbol{u} \pm v_{\rm a}\boldsymbol{b}\cdot\boldsymbol{g}_{\rm gri,\pm} - Q_\pm, \tag{5.7}$$

where ρ is the mass density of the thermal gas, $\rho\boldsymbol{u}$ its momentum density, $\boldsymbol{B}$ the magnetic field, $\boldsymbol{b}$ the unit direction of the magnetic field, $\boldsymbol{\nabla}_{\parallel}$ the gradient along this direction, $\varepsilon_{\rm cr}$ is the energy density of CRs, $f_{\rm cr}$ is the energy flux density of CRs along the direction of the magnetic field, $\varepsilon_{\rm a,\pm}$ is the energy density of gyroresonant Alfvén waves, and $v_{\rm a} = B/\sqrt{\rho}$ is the Alfvén velocity. The total MHD energy density is given by

$$\varepsilon = \frac{1}{2}\rho u^2 + \varepsilon_{\rm th} + \frac{1}{2}B^2, \tag{5.8}$$

where $\varepsilon_{\rm th}$ is the thermal energy density. The total pressure of the composite fluid of MHD, CRs, and Alfvén waves is,

$$P_{\rm tot} = P_{\rm th} + \frac{1}{2}B^2 + P_{\rm cr} + P_{\rm a,+} + P_{\rm a,-}, \tag{5.9}$$

where the thermal, CR, and Alfvén wave pressures obey the following equations of state:

$$P_{\rm th} = (\gamma_{\rm th} - 1)\varepsilon_{\rm th}, \tag{5.10}$$

$$P_{\rm cr} = (\gamma_{\rm cr} - 1)\varepsilon_{\rm cr}, \tag{5.11}$$

$$P_{\rm a,\pm} = (\gamma_{\rm a} - 1)\varepsilon_{\rm a,\pm}, \tag{5.12}$$

where the individual adiabatic indices are given by:

$$[\gamma_{\rm th}, \gamma_{\rm cr}, \gamma_{\rm a}] = \left[\frac{5}{3}, \frac{4}{3}, \frac{3}{2}\right]. \tag{5.13}$$

The gyroresonant interaction between Alfvén waves and CRs is described by

$$\boldsymbol{g}_{\rm gri,\pm} = \frac{\boldsymbol{b}}{3\kappa_\pm}[f_{\rm cr} \mp v_{\rm a}(\varepsilon_{\rm cr} + P_{\rm cr})] \tag{5.14}$$

$$= \frac{3\pi}{8}\frac{eB}{\gamma mc^3}\frac{\varepsilon_{\rm a,\pm}}{B^2}\boldsymbol{b}[f_{\rm cr} \mp v_{\rm a}(\varepsilon_{\rm cr} + P_{\rm cr})], \tag{5.15}$$

where $\kappa_\pm$ is the CR diffusion coefficient in the grey approximation, e is the elementary charge, m is the rest mass of the CR particle, c is the speed of light, and γ is defined as the Lorentz factor of a typical CR. We use $\gamma = 2$ to simulate a population that is dominated by GeV CR protons. The diffusion coefficients $\kappa_\pm$ are calculated based on the local scattering rate with Alfvén waves. Thus, CRHD includes diffusion that is not assuming a fixed diffusion coefficient but follows elements of the unresolved microphysics to calculate spatially and temporally varying diffusion coefficients. The terms $\boldsymbol{g}_{\rm gri,\pm}$ have the units of a force density and are strictly aligned with the direction of the magnetic field. We allow the energy of gyroresonant Alfvén waves to be damped by including the damping terms $Q_\pm$ in Eq. (5.7). Damping by ion-neutral collisions, interaction with turbulence, and various plasma-kinetic processes including non-linear Landau damping have been proposed to be important (Zweibel, 2017). While our code can be easily expanded to include all of effects, we here focus solely on non-linear Landau damping:

$$Q_\pm = \alpha\varepsilon_{\rm a,\pm}^2 \tag{5.16}$$

$$= \frac{\sqrt{\pi}}{8B^2}\frac{2eB}{\gamma mc^2}\sqrt{\frac{(\gamma_{\rm th}-1)\varepsilon_{\rm th}}{\rho}}\varepsilon_{\rm a,\pm}^2, \tag{5.17}$$

where α is the self-coupling constant of Alfvén waves. These $Q_\pm$ are quadratic in $\varepsilon_{\rm a,\pm}$ and their numerical discretization is more difficult in comparison to damping terms for ion-neutral or turbulent damping.

Direct collisions between CR particles themselves or CR and thermal particles occur rarely. They interact via Lorentz-forces provided by large-scale (MHD) electromagnetic fields $\boldsymbol{B}$ or by scatterings on small scales provided by the energy contained in gyroresonant Alfvén waves $\varepsilon_{\rm a,\pm}$.

Perpendicular to the magnetic field CRs interact with the thermal gas indirectly through Lorentz forces. The Lorentz force acting on the CRs in the perpendicular direction is balanced by the perpendicular CR pressure gradient. This pressure gradient would alter the momentum of the electromagnetic field if we were not using the MHD approximation. Therein

the magnetic field lines are frozen in and their dynamics follows the motion of the thermal gas. For this approximation to hold true the perpendicular CR pressure gradient must exert a force on the thermal gas itself and not on the electromagnetic field. This gives rise to the $\boldsymbol{\nabla}_\perp P_{\rm cr} = \boldsymbol{\nabla} P_{\rm cr} - \boldsymbol{b}\nabla_\parallel P_{\rm cr} = (\mathbf{1} - \boldsymbol{bb}) \cdot \boldsymbol{\nabla} P_{\rm cr}$ terms in the gas momentum and energy equations in Eqs. (5.2) and (5.4).

In our model, CRs interact with their surroundings parallel to the magnetic field only through the gyroresonant scatterings. To lowest order the force balance parallel to the magnetic field is dominated by pitch angle scattering. In this process gyroresonant Alfvén waves stochastically scatter CRs by changing their pitch angle. For an ensemble of gyrotropic CRs this alters only the component of the mean momentum that is aligned with the magnetic field. This momentum is transferred to the gyroresonant Alfvén waves, which changes the momentum of the thermal particles that support the hydromagnetic Alfvén wave on the microscopic level, and cumulatively, this leads to acceleration of the mean gas momentum on the macroscopic level (Achterberg, 1981b; Thomas and Pfrommer, 2019). This process is encoded in the $\boldsymbol{g}_{\rm gri}$ terms in Eqs. (5.2) and (5.4). In addition to a change in momentum, the gyroresonant interaction also transfers energy between CRs and Alfvén waves. This is described by the $\pm v_{\rm a} \boldsymbol{b} \cdot \boldsymbol{g}_{\rm gri}$ terms in Eqs. (5.5) and (5.7). If this transfer is such that CRs lose energy while Alfvén waves gain energy then this process is called gyroresonant instability. This is the case when the streaming speed of CRs exceeds the Alfvén speed, i.e., forward propagating Alfvén waves gain energy when

$$v_{\rm cr} = \frac{f_{\rm cr}}{\varepsilon_{\rm cr} + P_{\rm cr}} > v_{\rm a} \tag{5.18}$$

while backward propagating Alfvén waves gain energy when $v_{\rm cr} < -v_{\rm a}$.

The propagation of CRs in this hydrodynamic model exhibits two extremes. The first one is ballistic transport, which is realised when CRs are not scattered frequently. In this case the $\boldsymbol{g}_{\rm gri,\pm}$ terms can be neglected and the $\boldsymbol{\nabla}_\parallel P_{\rm cr}$ term dominates the flux evolution in Eq. (5.6). CRs propagate with a characteristic light like velocity $c/\sqrt{3}$ and do not couple to the thermal gas along the magnetic field direction. The second extreme is the streaming of CRs with Alfvén waves when scattering by those waves dominates. In this case the $\boldsymbol{\nabla}_\parallel P_{\rm cr}$ term in the flux equation is negligibly small and the $\boldsymbol{g}_{\rm gri,\pm}$ terms of Eq. (5.6) dictate the dynamics. In this regime, CR and thermal fluids are tightly coupled. If the scattering by either forward or backward propagating gyroresonant Alfvén waves is strong enough, the steady state of CR streaming can be reached where $\boldsymbol{g}_{\rm gri,\pm} = 0$ or equivalently, $v_{\rm cr} = \pm v_{\rm a}$ for one of the wave types. If none of these two extremes is an adequate approximation, CRs diffuse along the magnetic field lines. Both the CR pressure gradient and gyroresonant interaction terms contribute to Eq. (5.6). If a

considerable CR flux is built up by the CR gradient term then the gyroresonant instability may operate and amplify Alfvén waves at the expense of the CRs. This increases the scattering rate as $\boldsymbol{g}_{\mathrm{gri},\pm} \propto \varepsilon_{\mathrm{a},\pm}$ and subsequently decreases f_{cr} until it finds itself in the streaming regime.

The speed of light c is larger than any other velocity in the CRHD equations (since we assume the non-relativistic limit of MHD). For applications it is beneficial to use a reduced speed of light c_{red} that is smaller than the actual speed of light but larger than any other relevant velocity. In this way the hierarchy of the dynamics is preserved and physical implications of the reduced speed of light are minimised. Originally, the reduced speed of light approximation has been used in the context of radiative transfer. Therein, the approximation was introduced to speed up simulations that solve the time-dependent radiative transfer equation or one of it's descendants (see i.e., Gnedin, 2016). We replace the factors of c^2 with their reduced values in Eq. (5.6). This replacement is chosen such that the steady state value of the CR energy flux obtained via a Chapman-Enskog expansion of Eq. (5.6) is independent of the actual value of c_{red} and coincides with Eq. (138) of Thomas and Pfrommer (2019) given by

$$f_{\mathrm{cr}} = -\kappa \boldsymbol{b} \cdot \nabla \varepsilon_{\mathrm{cr}} + v_{\mathrm{a}} \frac{\varepsilon_{\mathrm{a},+} - \varepsilon_{\mathrm{a},-}}{\varepsilon_{\mathrm{a},+} + \varepsilon_{\mathrm{a},-}} (\varepsilon_{\mathrm{cr}} + P_{\mathrm{cr}}), \tag{5.19}$$

where κ is the total diffusion coefficient defined by $\kappa^{-1} = \kappa_+^{-1} + \kappa_-^{-1}$. Furthermore, the definition and the value of the diffusion coefficients are unaltered by the choice of the c_{red}. By contrast, the scattering rate

$$\nu_{\pm} = \frac{c_{\mathrm{red}}^2}{3\kappa_{\pm}} \tag{5.20}$$

is affected by the reduced speed of light approximation and is generally lower in simulations in comparison to its actual, physical value.

The steady state defined by Eq. (5.19) will be realised provided that c_{red} is by far the fastest transport velocity in the system and scattering of CRs by Alfvén waves is frequent. If this limit cannot be reached, the reduced speed of light approximation changes the velocity at which information contained in $\varepsilon_{\mathrm{cr}}$ and f_{cr} is transported. Because our primary interest and envisioned applications of the present numerical method are situations where the coupling between CRs and the gas are important, this steady state should be reachable. Employing this approximation heavily reduces the computational cost because it relaxes the time step constraint for a numerically stable simulation. Nevertheless, any results produced on the basis of the reduced speed of light approximation have to be additionally checked for convergence with respect to the value of c_{red}.

5.3 Numerical Algorithm

In this section we present a finite volume method that solves a descretized version of Eqs. (5.1) to (5.7) on the moving mesh of Arepo (Springel, 2010). The majority of terms in Eqs. (5.1) to (5.7) depend on the flow velocity $\boldsymbol{u}$ and describe adiabatic processes. The remaining gradient or divergence terms are derivatives along the magnetic field lines and represent the anisotropic transport of CRs. Instead of developing a unified finite volume method for both categories, we apply two different finite volume schemes: one for the adiabatic terms which use the advantageous properties of the moving mesh code and another one for the anisotropic transport. In addition to gradient and divergence terms, Eqs. (5.1) to (5.7) also contain source terms that describe the fast micro-scale dynamics of CRs and Alfvén waves. We develop a special implicit integrator that manages the stiffness of those terms. The two finite volume methods and the source term integrator are combined in an operator-split approach to yield the full evolution for a single time step. We now describe each of those integration steps separately.

5.3.1 Adiabatic CRHD in Arepo

During this first step we solve the parts of the CRHD equations that contain all adiabatic processes:

$$\frac{\partial \rho}{\partial t} + \boldsymbol{\nabla} \cdot [\rho \boldsymbol{u}] = 0, \tag{5.21}$$

$$\frac{\partial \rho \boldsymbol{u}}{\partial t} + \boldsymbol{\nabla} \cdot [\rho \boldsymbol{u}\boldsymbol{u} + P_{\mathrm{tot}} \mathbf{1} - \boldsymbol{B}\boldsymbol{B}] = \mathbf{0}, \tag{5.22}$$

$$\frac{\partial \boldsymbol{B}}{\partial t} + \boldsymbol{\nabla} \cdot [\boldsymbol{B}\boldsymbol{u} - \boldsymbol{u}\boldsymbol{B}] = \mathbf{0}, \tag{5.23}$$

$$\frac{\partial \varepsilon}{\partial t} + \boldsymbol{\nabla} \cdot [\boldsymbol{u}(\varepsilon + P_{\mathrm{tot}}) - (\boldsymbol{u} \cdot \boldsymbol{B})\boldsymbol{B}] = (P_{\mathrm{cr}} + P_{\mathrm{a},+} + P_{\mathrm{a},-}) \boldsymbol{\nabla} \cdot \boldsymbol{u}, \tag{5.24}$$

$$\frac{\partial \varepsilon_{\mathrm{cr}}}{\partial t} + \boldsymbol{\nabla} \cdot [\boldsymbol{u} \varepsilon_{\mathrm{cr}}] = -P_{\mathrm{cr}} \boldsymbol{\nabla} \cdot \boldsymbol{u}, \tag{5.25}$$

$$\frac{\partial f_{\mathrm{cr}}}{\partial t} + \boldsymbol{\nabla} \cdot [\boldsymbol{u} f_{\mathrm{cr}}] = -f_{\mathrm{cr}} (\boldsymbol{b}\boldsymbol{b}) : \boldsymbol{\nabla} \boldsymbol{u}, \tag{5.26}$$

$$\frac{\partial \varepsilon_{\mathrm{a},\pm}}{\partial t} + \boldsymbol{\nabla} \cdot [\boldsymbol{u} \varepsilon_{\mathrm{a},\pm}] = -P_{\mathrm{a},\pm} \boldsymbol{\nabla} \cdot \boldsymbol{u}. \tag{5.27}$$

These equations mostly resemble those solved in Pfrommer et al. (2017a) but additionally include the Lagrangian transport of f_{cr} and $\varepsilon_{\mathrm{a},\pm}$.

The equations are solved on the moving mesh of Arepo. We use the second-order accurate time integration and gradient reconstruction scheme (Pakmor et al., 2016c) and extent the algorithm of Pfrommer et al. (2017a): The finite volume scheme uses an extension of the

HLLD (Miyoshi and Kusano, 2005a) approximate Riemann solver that takes the additional pressures and increased signal velocities into account. As an input state for the HLLD we use the interface-interpolated primitive variables ρ, $\boldsymbol{u}$, $\boldsymbol{B}$, $P_{\rm th}$, $P_{\rm cr}$ and $P_{\rm a,\pm}$. The divergence terms on the left-hand side of Eqs. (5.25) to (5.27) are upwinded based on the direction of the mass flow at a given interface. The velocity gradient and divergence terms on the right-hand side of Eqs. (5.24) to (5.27) are discretised using Gauss' theorem. The velocities needed to evaluate the surface integral are taken to be those velocities of the HLLD Riemann solver that lay on a given interface. We use the Powell scheme for divergence control (Powell et al., 1999; Pakmor and Springel, 2013). The inclusion of the CR dynamics does not interfere with the Powell scheme.

The quasi-Lagrangian nature of Arepo allows us to evaluate the Riemann solver in a frame that is approximately comoving with the interfaces. This drastically lowers the applied numerical dissipation (Springel, 2010; Pakmor et al., 2011). Reynold's transport theorem states that we need to account for the mesh motion with an additional geometric flux in the finite volume scheme. We fully account for this flux during the current, adiabatic, step. As a consequence, we do not need to account for the mesh motion in all subsequent integration steps of this time step. While this choice has the advantage that it simplifies the algorithmic complexity of the upcoming integration steps, it comes at a cost: neglecting the mesh motion corresponds to an operator splitting between adiabatic and parallel transport, which induces an additional numerical error.

5.3.2 Path-conservative scheme for anisotropic transport

The gradient and divergence terms in Eqs. (5.1) to (5.7) that are aligned with the magnetic field are:

$$\frac{\partial \varepsilon_{\rm cr}}{\partial t} + \nabla \cdot (\boldsymbol{b} f_{\rm cr}) = 0, \tag{5.28}$$

$$\frac{\partial f_{\rm cr}}{\partial t} + c_{\rm red}^2 \boldsymbol{b} \cdot \nabla P_{\rm cr} = 0, \tag{5.29}$$

$$\frac{\partial \rho \boldsymbol{u}}{\partial t} - \boldsymbol{b}\boldsymbol{b} \cdot \nabla P_{\rm cr} = \boldsymbol{0}, \tag{5.30}$$

$$\frac{\partial \varepsilon_{\rm a,\pm}}{\partial t} + \nabla \cdot (\pm \boldsymbol{b} v_{\rm a} \varepsilon_{\rm a,\pm}) = 0. \tag{5.31}$$

We omitted the gas energy equation and defer its discussion to the end of this subsection. These equations can be conveniently written into the more compact form

$$\frac{\partial \boldsymbol{U}}{\partial t} + \nabla \cdot \boldsymbol{F}(\boldsymbol{U}) + \mathbf{H}(\boldsymbol{U}) : \nabla \boldsymbol{U} = \boldsymbol{0}, \tag{5.32}$$

where[1]

$$\boldsymbol{U} = \left(\varepsilon_{\rm cr}, f_{\rm cr}, \rho\boldsymbol{u}, \varepsilon_{a,+}, \varepsilon_{a,-}\right)^T, \tag{5.33}$$

$$\boldsymbol{F} = \left(\boldsymbol{b} f_{\rm cr}, \boldsymbol{0}, \boldsymbol{0}, +\boldsymbol{b} v_{\rm a} \varepsilon_{\rm a,+}, -\boldsymbol{b} v_{\rm a} \varepsilon_{\rm a,-}\right)^T, \tag{5.34}$$

$$\mathsf{H} = (\gamma_{\rm cr} - 1) \begin{bmatrix} 0 & 0 & \dots \\ c_{\rm red}^2 \boldsymbol{b} & 0 & \dots \\ -\boldsymbol{b}\boldsymbol{b} & 0 & \dots \\ 0 & 0 & \dots \\ 0 & 0 & \dots \end{bmatrix}, \tag{5.35}$$

where $\boldsymbol{U}$ is the state vector, $\boldsymbol{F}$ is the flux vector, and $\mathsf{H}(\boldsymbol{U}) : \nabla \boldsymbol{U}$ is the so called non-conservative product. This non-conservative product poses a conceptional challenge. Commonly employed Godunov-like finite volume methods can be readily applied to equations that only contain a flux divergence but no non-conservative product. Path-conservative finite volume methods generalize the well-established theory and methods of finite volume schemes to equations with non-conservative products (Parés, 2006). We provide an introduction to path-conservative schemes in App. 5.7. We use such a path-conservative scheme and describe its implementation on the Voronoi mesh provided by Arepo.

We describe this discretization for a cell with label i that has a volume V_i and shares an interface with an adjacent cell j. This interface has a label ij and a vector area $\boldsymbol{A}_{ij}$ that points from the inside of i towards j. The situation is shown in Fig. 5.1. The path-conservative finite volume scheme as generalized for this mesh configuration for a purely non-conservative equation reads

$$V_i \frac{\mathrm{d}\boldsymbol{U}_i}{\mathrm{d}t} + V_i \mathsf{H}(\boldsymbol{U}_i) : \nabla_{\rm recon} \boldsymbol{U}_i + \sum_j \boldsymbol{A}_{ij} \cdot \boldsymbol{D}_{L,ij} = \boldsymbol{0}, \tag{5.36}$$

whereas the classical Godunov-like finite volume scheme reads

$$V_i \frac{\mathrm{d}\boldsymbol{U}_i}{\mathrm{d}t} + \sum_j \boldsymbol{A}_{ij} \cdot \boldsymbol{F}_{ij} = \boldsymbol{0}. \tag{5.37}$$

The corresponding equation of the path-conservative scheme for the cell j reads

$$V_j \frac{\mathrm{d}\boldsymbol{U}_j}{\mathrm{d}t} + V_j \mathsf{H}(\boldsymbol{U}_j) : \nabla_{\rm recon} \boldsymbol{U}_j + \sum_i (-\boldsymbol{A}_{ij}) \cdot \boldsymbol{D}_{R,ij} = \boldsymbol{0}. \tag{5.38}$$

The individual terms have the following meaning:

[1] The rows in the matrix $\boldsymbol{F}$ and the rank-3 tensor H correspond to entries in the rows of $\boldsymbol{U}$. The scalar product and the double contraction in Eq. (5.32) have to be applied to the columns of $\boldsymbol{F}$ and H.

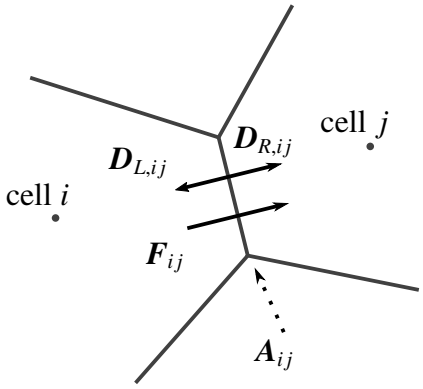

Figure 5.1: Assignment of the flux $\boldsymbol{F}_{ij}$ and linear fluctuations $\boldsymbol{D}_{LR,ij}$ for the interface $\boldsymbol{A}_{ij}$ as used in the path-conservative finite volume scheme.

- The interface flux $\boldsymbol{F}_{ij}$ is the flux $\boldsymbol{F}$ exchanged between neighbouring cells. This flux enters only in Godunov-like finite volume schemes and is calculated with an exact or approximate Riemann solver.
- The factors $\boldsymbol{D}_{L,R,ij}$ are called linear fluctuations and are introduced to incorporate the non-conservative product into the finite volume scheme. They ensure numerical stability and consistency of the numerical solution at discontinuities by adding numerical dissipation (see also App. 5.7). These fluctuations are calculated by an approximate Riemann solver. We add non-zero linear fluctuations only for those equations that contain a non-conservative product, i.e., for f_{cr} and $\rho\boldsymbol{u}$.
- The term $\mathbf{H}(\boldsymbol{U}_i) : \nabla_{\text{recon}}\boldsymbol{U}_i$ is the non-conservative product evaluated within the cell. This term accounts for the non-conservative product in smooth parts of the flow. The gradient $\nabla_{\text{recon}}\boldsymbol{U}_i$ is the gradient of the linear reconstruction of $\boldsymbol{U}$ inside the cell i. We use the least-square gradient estimate of Pakmor et al. (2016c).

For purely conservative equations the flux $\boldsymbol{F}_{ij}$ can be interpreted as a physical flux, i.e. it tells us the flow rate of $\boldsymbol{U}$ through the interface A_{ij}. This flux is naturally the same for the right and left adjacent cell of the interface. Such an interpretation is not possible for the linear fluctuations. Here, $\boldsymbol{D}_{L,ij} \neq \boldsymbol{D}_{R,ij}$ holds in general.

Equations (5.28) to (5.31) contain either a flux divergence or a non-conservative product such that either Eq. (5.36) or Eq. (5.37) is sufficient to describe their evolution in the finite volume framework. It is possible to describe both a flux divergence and a non-conservative product simultaneously in the same finite volume discretization with minor modifications in the combined version of Eqs. (5.36) and (5.37) (Dumbser and Balsara, 2016).

We now describe the Riemann solver that we use to calculate the interface flux and linear fluctuations. The Riemann solver takes the states left (L) and right (R) of an interface in order to calculate the flux and linear fluctuations based on the input states. For a second-order accurate scheme these states need to be interpolated onto the interface. To this end, we assume that $\boldsymbol{U}$ is a linear function inside the cell and use the least-square gradient estimate of Pakmor et al. (2016c) for the interpolation. Our Riemann solver is based on the generalization of the HLLE Riemann solver for path-conservative scheme as derived in Dumbser and Balsara (2016). The classical form (for a zero non-conservative product) of this Riemann solver assumes that the solution to the Riemann problem at the interface can be approximated by a constant intermediate value, denoted by $\boldsymbol{U}_*$. The region of influence of the Riemann problem is assumed to be bounded by a leftwards-travelling wave with speed S_L and a rightwards-travelling wave with speed S_R. This idea can be generalized to adopt the HLLE for hyperbolic equations with non-conservative products (see Dumbser and Balsara, 2016, or App. 5.7). We use this Riemann solver in its localized Lax-Friedrichs (LF) limit where we set $S_L = -S$ and $S_R = +S$ where S denotes the absolute value of the fastest wave speed.

The individual fluxes and linear fluctuations are calculated as follows. Equation (5.28) describes the evolution of $\varepsilon_{\rm cr}$ in conservative form. Consequently, the usual LF flux is

$$F_{ij}^{\varepsilon_{\rm cr}} = \frac{(bf_{\rm cr})_L + (bf_{\rm cr})_R}{2} - \frac{S}{2}\left(\varepsilon_{{\rm cr},R} - \varepsilon_{{\rm cr},L}\right), \tag{5.39}$$

and the value of the intermediate state is given by

$$\varepsilon^*_{{\rm cr},ij} = \frac{\varepsilon_{{\rm cr},L} + \varepsilon_{{\rm cr},R}}{2} + \frac{(bf_{\rm cr})_L + (bf_{\rm cr})_R}{2S}. \tag{5.40}$$

Here, $b_{L,R} = \boldsymbol{A}_{ij} \cdot \boldsymbol{B}_{L,R}/(A_{ij}B_{L,R})$ are the projections of the magnetic field onto the interface normal. We use a notation where q^*_{ij}, F^q_{ij}, $D^q_{ij,L}$, and $D^q_{ij,R}$ denote the intermediate state, the flux, and linear fluctuations as projected on the interface normal of a quantity q.

Equation (5.29) for $f_{\rm cr}$ is purely non-conservative. To calculate the intermediate value of $f_{\rm cr}$ we evaluate equation (14) of Dumbser and Balsara (2016) and obtain

$$\begin{aligned} f^*_{{\rm cr},ij} = \frac{f_{cr,L} + f_{cr,R}}{2} &+ c^2_{\rm red}\frac{\bar{b}_L}{2S}\left(P^*_{{\rm cr},ij} - P_{{\rm cr},L}\right) \\ &- c^2_{\rm red}\frac{\bar{b}_R}{2S}\left(P^*_{{\rm cr},ij} - P_{{\rm cr},R}\right), \end{aligned} \tag{5.41}$$

where $P^*_{{\rm cr},ij} = (\gamma_{cr} - 1)\varepsilon^*_{{\rm cr},ij}$, and

$$\bar{b}_L = \frac{3b_L + b_R}{4}, \tag{5.42}$$

$$\bar{b}_R = \frac{3b_R + b_L}{4}, \tag{5.43}$$

are directional biased averages of the magnetic field projections. After calculating this value, the linear fluctuations for $f_{\rm cr}$ are given by

$$D^{f_{\rm cr}}_{ij,L} = +S\,(f_{{\rm cr},L} - f^{*}_{{\rm cr},ij}), \tag{5.44}$$

$$D^{f_{\rm cr}}_{ij,R} = -S\,(f_{{\rm cr},R} - f^{*}_{{\rm cr},ij}). \tag{5.45}$$

The description above lacks a value for the speed of the fastest wave of the Riemann problem at the interface. Physically, the fastest wave is formed by ballistically propagating CRs. The speed of this wave is light-like and given by $c_{\rm red}\sqrt{\gamma_{\rm cr}-1}$ (Thomas and Pfrommer, 2019). Because CRs are transported along magnetic fields, we weight this wave speed with the local projection of the magnetic field at the interface to get:

$$S = c_{\rm red}\sqrt{\gamma_{\rm cr}-1}\,\max\{b_L, b_R\}\,. \tag{5.46}$$

The equation for the gas momentum density $\rho\boldsymbol{u}$ in Eq. (5.30) is non-conservative. We use the algebraic similarity between the non-conservative product of $f_{\rm cr}$ and $\rho\boldsymbol{u}$ and define the linear fluctuations via:

$$D^{\rho\boldsymbol{u}}_{ij,L} = -\frac{\boldsymbol{b}_L}{c^2_{\rm red}} D^{f_{\rm cr}}_{ij,L}, \tag{5.47}$$

$$D^{\rho\boldsymbol{u}}_{ij,R} = -\frac{\boldsymbol{b}_R}{c^2_{\rm red}} D^{f_{\rm cr}}_{ij,R}, \tag{5.48}$$

where $\boldsymbol{b}_{L,R} = \boldsymbol{B}_{L,R}/B_{L,R}$ are the unit vectors along the direction of the magnetic field to the left and right of the interface.

The remaining equation for $\varepsilon_{\rm a,\pm}$ in Eq. (5.31) is conservative. This equation is independent of the light speed and if we used S in Eq. (5.46) as the signal velocity of $\varepsilon_{\rm a,\pm}$, this would introduce an unnecessary level of numerical dissipation. Hence, we use the classical LF flux:

$$F^{\varepsilon_{\rm a,\pm}}_{ij} = \frac{(bv_{\rm a}\varepsilon_{\rm a,\pm})_L + (bv_{\rm a}\varepsilon_{\rm a,\pm})_R}{2} - \frac{S_a}{2}\,(\varepsilon_{{\rm a,\pm},R} - \varepsilon_{{\rm a,\pm},L}) \tag{5.49}$$

with an alfvénic signal velocity given by:

$$S_a = \max\{(bv_{\rm a})_L, (bv_{\rm a})_R\}. \tag{5.50}$$

Finally, the kinetic energy changed during the momentum update. We account for this change in a conservative way by setting:

$$\Delta(\varepsilon_{\rm kin}) = \Delta(\varepsilon_{\rm tot}) = \varepsilon^{n+1}_{\rm kin} - \varepsilon^{n}_{\rm kin} = \frac{(\rho\boldsymbol{u}^{n+1})^2}{2\rho} - \frac{(\rho\boldsymbol{u}^{n})^2}{2\rho}. \tag{5.51}$$

Writing the update of the kinetic and thus the total energy in this form does not alter the thermal energy but avoids artificial heating/cooling.

To ensure the stability of this transport step a Courant-Friedrichs-Levy (CFL) criterion on the time step must be fulfilled. We use

$$\Delta t_{\mathrm{cr,req}} = \mathrm{CFL} \times \min_{\mathrm{cells}} \frac{\Delta x}{c_{\mathrm{red}} \sqrt{\gamma_{\mathrm{cr}} - 1}}, \tag{5.52}$$

where CFL ~ 0.3 is the CFL-number, Δx is a measure for the cell size, $\Delta t_{\mathrm{cr,req}}$ is the maximum allowed time step for the parallel transport step, and the minimum is taken over all active cells. The maximum allowed time step for the adiabatic CRHD step Δt_{mhd} is larger than $\Delta t_{\mathrm{cr,req}}$ even if a reduced speed of light is used. Conversely, a single parallel transport step is computationally less expensive than a single iteration of the adiabatic CRHD. It is beneficial to execute multiple iterations of the parallel transport step for one iteration of the adiabatic CRHD step to lower the total computational cost of the algorithm. This can be achieved by subcycling of the parallel transport step. Subcycling also relaxes the effectively required time step criterion for the parallel transport step. We implement subcycling for the path-conservative scheme of this section with a total of N_{cr} subcycles. The subcycles are added in an operator-split fashion. To this end, we execute $N_{\mathrm{cr}}/2$ subcycles before and after the adiabatic CRHD update is calculated. The overall algorithm (adiabtic CRHD + subcycled parallel transport) is executed with a time step

$$\Delta t = \min(N_{\mathrm{cr}}\, \Delta t_{\mathrm{cr,req}}, \Delta t_{\mathrm{mhd}}) \tag{5.53}$$

while the time step for a single parallel transport subcycle is given by

$$\Delta t_{\mathrm{cr}} = \frac{\Delta t}{N_{\mathrm{cr}}}. \tag{5.54}$$

The downside of this procedure is that it induces some numerical errors. This is because the numerical splitting ignores the interdependence of the adiabatic and parallel transport steps. We found, however, that the errors caused by subcycling are quite small for the presented test problems provided a modest number of subcycles is used. To avoid any numerical errors altogether, we recommend to use the smallest affordable number of subcycles for a given application.

5.3.3 Gyroresonant interaction and wave damping

So far we have dealt with all terms that contain spatial gradients and need a finite volume approach for their numerical modelling. The remaining terms fall into the category of source

terms. They describe the gyroresonant interaction of CRs with Alfvén waves and the subsequent damping of Alfvén waves. For the state vector

$$\boldsymbol{U} = \left(\varepsilon_{\mathrm{cr}}, f_{\mathrm{cr}}, \varepsilon_{a,+}, \varepsilon_{a,-}\right)^T, \tag{5.55}$$

the source terms in Eqs. (5.1) to (5.7) take the form of

$$\frac{\partial \boldsymbol{U}}{\partial t} = \mathbf{R}(\boldsymbol{U})\boldsymbol{U}, \tag{5.56}$$

where the rate matrix $\mathbf{R}$ is given by:

$$\mathbf{R}\left(\boldsymbol{U}\right) = \begin{pmatrix} v_{\mathrm{a}}^2 \chi \gamma_{\mathrm{cr}} T & -v_{\mathrm{a}} \chi D & 0 & 0 \\ c_{\mathrm{red}}^2 v_{\mathrm{a}} \chi \gamma_{\mathrm{cr}} D & -c_{\mathrm{red}}^2 \chi T & 0 & 0 \\ -v_{\mathrm{a}}^2 \chi \gamma_{\mathrm{cr}} \varepsilon_{a,+} & +v_{\mathrm{a}} \chi \varepsilon_{a,+} & -\alpha \varepsilon_{a,+} & 0 \\ -v_{\mathrm{a}}^2 \chi \gamma_{\mathrm{cr}} \varepsilon_{a,-} & -v_{\mathrm{a}} \chi \varepsilon_{a,-} & 0 & -\alpha \varepsilon_{a,-} \end{pmatrix}. \tag{5.57}$$

We use abbreviations for the sum and the directional difference of the two Alfvén wave energies:

$$T = \varepsilon_{a,+} + \varepsilon_{a,-}, \tag{5.58}$$

$$D = \varepsilon_{a,+} - \varepsilon_{a,-}, \tag{5.59}$$

and define

$$\chi = \frac{3\pi}{8} \frac{3}{\gamma m c^3 B}. \tag{5.60}$$

The characteristic timescales of the gyroresonant interaction and wave damping, encoded in the rate matrix, are typically short in comparison to the time scale of the MHD dynamics. To bridge the difference of these timescales, we integrate Eq. (5.56) using an adaptive time step method. Although a variety of such methods exists, we opt for a custom-made method that takes the special structure of Eq. (5.56) into account. There is an algorithm at the heart of any adaptive time step method that (i) calculates a suitable source integration time step Δt_{src} so that the final numerical error is small and (ii) performs the ODE intergration during a subcycle. With the adapative time stepping method the parallel transport time step $\Delta t_{\mathrm{cr}} \geq \Delta t_{\mathrm{src}}$ is separated into possibly smaller source integration subcycles. The source intergration is executed after every single parallel transport subcycle.

The integration extends from a given state $\boldsymbol{U}^n$ to the state at the next time step $\boldsymbol{U}^{n+1}$ using the

following semi-implicit method:

$$\boldsymbol{U}^p = \boldsymbol{U}^n + \Delta t \mathbf{R}\left(\boldsymbol{U}^n\right) \boldsymbol{U}^p, \tag{5.61}$$

$$\boldsymbol{U}^r = \frac{1}{2}(\boldsymbol{U}^n + \boldsymbol{U}^p), \tag{5.62}$$

$$\boldsymbol{U}^* = \boldsymbol{U}^n + \gamma \Delta t \mathbf{R}\left(\boldsymbol{U}^r\right) \boldsymbol{U}^*, \tag{5.63}$$

$$\boldsymbol{U}^{n+1} = \boldsymbol{U}^n + (1-\gamma)\, \Delta t \mathbf{R}\left(\boldsymbol{U}^r\right) \boldsymbol{U}^* + \gamma \Delta t \mathbf{R}\left(\boldsymbol{U}^r\right) \boldsymbol{U}^{n+1}, \tag{5.64}$$

where $\gamma = 1 - 2^{-1/2}$. The first step in Eqs. (5.61) and (5.62) returns a first-order prediction of the Alfvén wave energy densities at the middle of the current time step which is used in Eqs. (5.63) and (5.64) to calculate a second-order accurate update of the state. We prove these statements in App. 5.8. If the rate matrix R would be a constant, the final update in Eqs. (5.63) and (5.64) would coincide with the implicit Runge-Kutta method of Pareschi and Russo (2005).

Due to the block-structured lower-triangular form of R, the linear equation systems in Eqs. (5.61) to (5.64) can be solved efficiently by direct backsubstitution instead of inverting the matrix R. For this we perform a 2x2 inversion of the $(\varepsilon_{\rm cr}, f_{\rm cr})$ equations followed by two trivial 1x1 inversions of the $(\varepsilon_{\rm a,+}, \varepsilon_{\rm a,-})$ equations.

The source integration time step is chosen to keep the numerical error small. We use the already calculated first-order accurate solution from the predictor step Eq. (5.63) as a comparison solution and estimate the (non-dimensional) numerical error by:

$$\texttt{Err} = \max_i \left\{ \frac{|\boldsymbol{U}_i^p - \boldsymbol{U}_i^{n+1}|}{\texttt{Atol} + \texttt{Rtol} \max\left(|\boldsymbol{U}_i^p|, |\boldsymbol{U}_i^{n+1}|\right)} \right\}, \tag{5.65}$$

where the maximum is taken over all components $\boldsymbol{U}_i$ of the state vector $\boldsymbol{U}$. Here, `Rtol` and `Atol` are the desired relative and absolute errors. We start the adaptive time stepping with $\Delta t_{\rm src} = \Delta t_{\rm cr}$ and chose the time step for the next subcycle $\Delta t_{\rm src,next}$ as

$$\Delta t_{\rm src,next} = \Delta t_{\rm src} \min\left(5, 0.9\, \texttt{Err}^{-1/2}\right), \tag{5.66}$$

where the numerical factors 5 and 0.9 prevent rapid changes in $\Delta t_{\rm src}$. If $\texttt{Err} > 1$ the current subcycle is rejected and restarted. Otherwise, if $\texttt{Err} \leq 1$ then the current subcycle is accepted, the state vector updated, and the time advanced by $\Delta t_{\rm src}$. The subcycling is stopped after the sum of $\Delta t_{\rm src}$ from all accepted subcycles equals $\Delta t_{\rm cr}$. The typical number of source term subcycles does not exceed 10 for the test problems presented in the next section.

Once the source term integration for the CR variables is completed, we update the gas state. To do so, we calculate the momentum and energy lost by CRs and Alfvén waves, and add it to

gas via:

$$\Delta\left(U_{\mathrm{th}}\right) = \frac{\Delta\left(\varepsilon_{\mathrm{th}}\right)}{\rho} = -\frac{\Delta\left(\varepsilon_{\mathrm{cr}} + \varepsilon_{\mathrm{a},+} + \varepsilon_{\mathrm{a},-}\right)}{\rho}, \tag{5.67}$$

$$\Delta\left(\rho\boldsymbol{u}\right) = -\frac{\Delta\left(\boldsymbol{b} f_{\mathrm{cr}}\right)}{c_{\mathrm{red}}^2}, \tag{5.68}$$

$$\Delta\left(\varepsilon_{\mathrm{kin}}\right) = -\frac{[\rho\boldsymbol{u}^n + \Delta(\rho\boldsymbol{u})]^2}{2\rho} - \frac{[\rho\boldsymbol{u}^n]^2}{2\rho}, \tag{5.69}$$

where U_{th} is the internal energy per unit mass and $\Delta(q) = q^{n+1} - q^n$ is the total change of q during the source term integration. Simply adding the corresponding work as $\Delta t_{\mathrm{cr}} \boldsymbol{u} \cdot \boldsymbol{g}_{\mathrm{gri}} = -\boldsymbol{u} \cdot \Delta(\boldsymbol{b} f_{\mathrm{cr}})/c_{\mathrm{red}}^2$ to the total energy would cause artificial cooling and heating. Instead we do not directly update the total energy but instead update the internal energy and recalculate the kinetic energy to prevent this problem. Although the temperature increases due to wave damping, we calculate the affected coefficients in Eq. (5.57) using the temperature at the start of the integration.

5.4 Test Problems

In this section we test our algorithm with various simplified and complex problem setups. We do not only describe the performance of the algorithm in our discussions but also aim to understand the emerging physical dynamics.

5.4.1 CR-Alfvén wave interaction

In this first problem we test whether the source term integrator from Section 5.3.3 correctly captures the interactions between CRs and Alfvén waves. To this end we perform two simulations with homogeneous initial conditions such that all gradient terms vanish and only the source terms remain. We initialize the thermal gas with $\rho = m_{\mathrm{p}}\,\mathrm{cm}^{-3}$, $\boldsymbol{u} = \boldsymbol{0}$, $P_{\mathrm{th}} = (10^4\ \mathrm{K}) k_{\mathrm{B}}\,\mathrm{cm}^{-3}$ and $v_{\mathrm{a}} = 10\,\mathrm{km\,s}^{-1}$. We employ a speed of light with $c_{\mathrm{red}} = 1000\,\mathrm{km\,s}^{-1}$. We use two setups for CRs and Alfvén waves to highlight different behaviours in their dynamics.

Super-alfvénic streaming. Here we investigate CRs streaming with superalfvénic velocities. We initialize the CRs with $\varepsilon_{\mathrm{cr}} = 2\varepsilon_B$ and $f_{\mathrm{cr}} = 4 v_{\mathrm{a}}(\varepsilon_{\mathrm{cr}} + P_{\mathrm{cr}})$ while the Alfvén waves are initialized with $\varepsilon_{\mathrm{a},+} = 10^{-8}\varepsilon_{\mathrm{cr}}$ and $\varepsilon_{\mathrm{a},-} = 0$. We run the simulation until $t = 40\mathrm{kyr}$ with $\Delta t = 10$ yr. The results are displayed in Fig. 5.2.

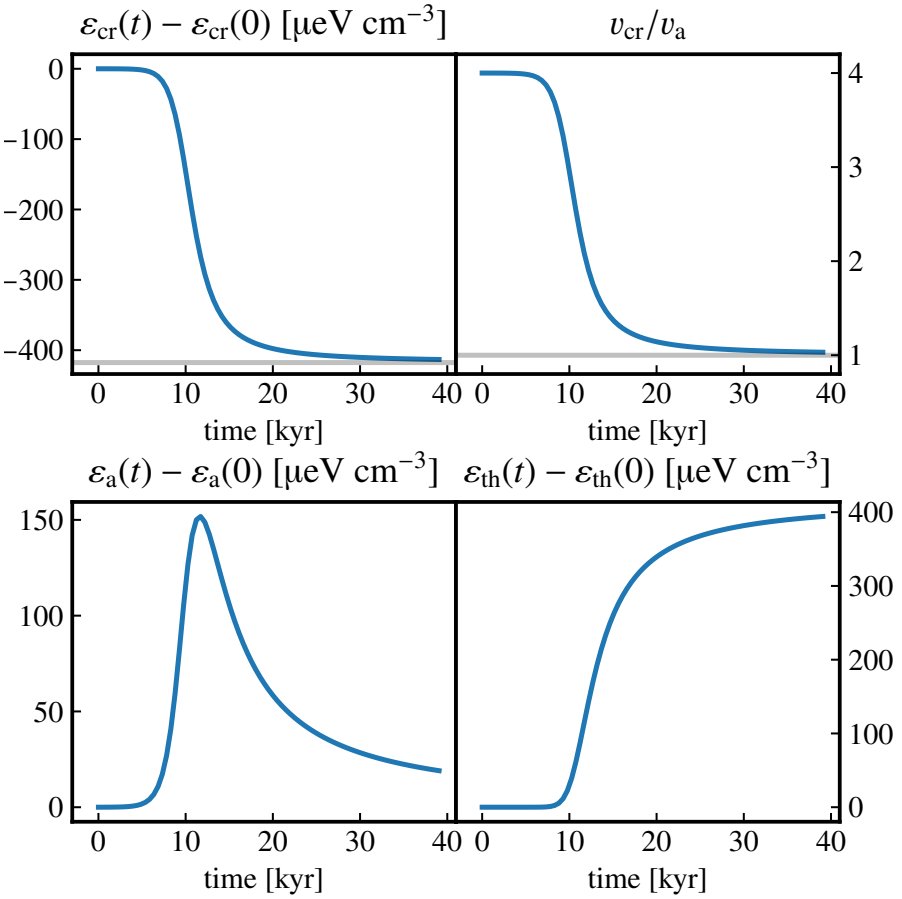

Figure 5.2: Time evolution of the CR, Alfvén wave, thermal energy density, and the streaming speed for the test with initially super-alfvénic streaming speeds. The grey line displays the analytic estimate for the asymptotic change in CR energy density and streaming speed.

The scattering rate of CRs in the initial conditions is given by

$$\nu_+ = \frac{c_{\rm red}^2}{3\kappa_+} = \frac{3\pi}{16}\Omega\frac{\varepsilon_{a,+}}{\varepsilon_B}\frac{c_{\rm red}^2}{c^2} \tag{5.70}$$

$$= \frac{1}{39\ \mathrm{Myr}}, \tag{5.71}$$

where $\Omega = eB/(\gamma mc)$ is the relativistic gyrofrequency of a CR proton population with charge e and characteristic Lorentz factor $\gamma = 2$, and we adopted a magnetic field strength of $B = v_a\sqrt{\rho} = 1.29\ \mu$G. The reason for scattering to be a slow process are the comparably small values of $\varepsilon_{a,+}$ and $c_{\rm red}$. In contrast, the growth rate of the energy density of gyroresonant Alfvén

waves is fast with[2]

$$\Gamma_{\mathrm{gri},+} = \frac{v_\mathrm{a}\boldsymbol{b}\cdot\boldsymbol{g}_{\mathrm{gri},+}}{\varepsilon_{\mathrm{a},+}} = \frac{3\pi}{16}\Omega\frac{v_\mathrm{a}[f_\mathrm{cr} - v_\mathrm{a}(\varepsilon_\mathrm{cr} + P_\mathrm{cr})]}{c^2\varepsilon_B} \tag{5.72}$$

$$= \frac{1}{0.97\ \mathrm{kyr}}. \tag{5.73}$$

Because nonlinear Landau damping is a wave-wave interaction, the corresponding damping rate

$$\Gamma_{\mathrm{nlld},+} = \alpha\varepsilon_{\mathrm{a},+} = \frac{\sqrt{\pi}}{8B^2}\frac{2eB}{\gamma mc^2}\sqrt{\frac{(\gamma_\mathrm{th}-1)\varepsilon_\mathrm{th}}{\rho}}\varepsilon_{\mathrm{a},\pm} \tag{5.74}$$

$$= \frac{1}{46\ \mathrm{Myr}}. \tag{5.75}$$

for the given initial conditions is also slow.

Initially the gyroresonant instability operates, as $\Gamma_{\mathrm{gri},+} > \Gamma_{\mathrm{nlld},+}$, and transfers energy from CRs to Alfvén waves, which decelerates the CRs. With increasing Alfvén wave energy the growth rate of the gyroresonant instability also increases. This results in a faster deceleration and an energy transfer. Non-linear Landau damping becomes important at $t \sim 10$ kyr when Alfvén waves have accumulated sufficient energy. This damping thermalizes Alfvén waves and in consequence, leads to an increase of thermal energy. At $t \gtrsim 15$kyr, CRs are reaching the streaming speed $v_\mathrm{cr} = v_\mathrm{a}$, the gyroresonant instability is weaker, and the deceleration of and energy transfer from CRs is slower. The instability cannot overcome the wave damping and Alfvén wave energy is decreasing. At later times the simulation approaches the asymptotic regime where the dynamics is unaltered.

For $t \to \infty$, CRs start to stream with the Alfvén waves $v_\mathrm{cr} = f_\mathrm{cr}/(\varepsilon_\mathrm{cr}+P_\mathrm{cr}) = v_\mathrm{a}$ or $f_\mathrm{cr} = v_\mathrm{a}(\varepsilon_\mathrm{cr}+P_\mathrm{cr})$. From $t = 0$ to $t \to \infty$ the CRs lose a momentum density $\Delta f_\mathrm{cr} c_\mathrm{red}^{-2} = -3v_\mathrm{a}c_\mathrm{red}^{-2}(\varepsilon_\mathrm{cr} + P_\mathrm{cr})$. The corresponding decrease (increase) in CR (Alfvén) energy density is $\Delta\varepsilon_\mathrm{cr} = -3{v_\mathrm{a}}^2c^{-2}(\varepsilon_\mathrm{cr} + P_\mathrm{cr})$. As $\Delta\varepsilon_\mathrm{cr}/\varepsilon_\mathrm{cr} < 1$ the initial value of ε_cr can be used to evaluate the previous expressions. The values for $\Delta\varepsilon_\mathrm{cr}$ and Δf_cr are reached in the asymptotic limit as indicated by the grey lines in Fig. 5.2.

Second-order Fermi process. For this problem, we initialise a reservoir of Alfvén waves and CRs that are streaming with sub-alfvénic velocities. This triggers an energy transfer from Alfvén waves to CRs which is referred to as the second-order Fermi process (Ko, 1992). The CRs are initialized with $\varepsilon_\mathrm{cr} = 2\varepsilon_B$ and $f_\mathrm{cr} = 0.5v_\mathrm{a}(\varepsilon_\mathrm{cr} + P_\mathrm{cr})$ whereas both Alfvén wave energy

[2]Note that the definition of $\Gamma_{\mathrm{gri},+}$ adopted here differs from the definition of the wave-number dependent growth rate $\Gamma_{\mathrm{gri},\pm}$ used in Thomas and Pfrommer (2019).

densities are set to $\varepsilon_{a,+} = \varepsilon_{a,-} = 10^{-4}\varepsilon_{cr}$. We simulate until $t = 30$kyr with a time step of $\Delta t = 10$ yr . The results are displayed in Fig. 5.3.

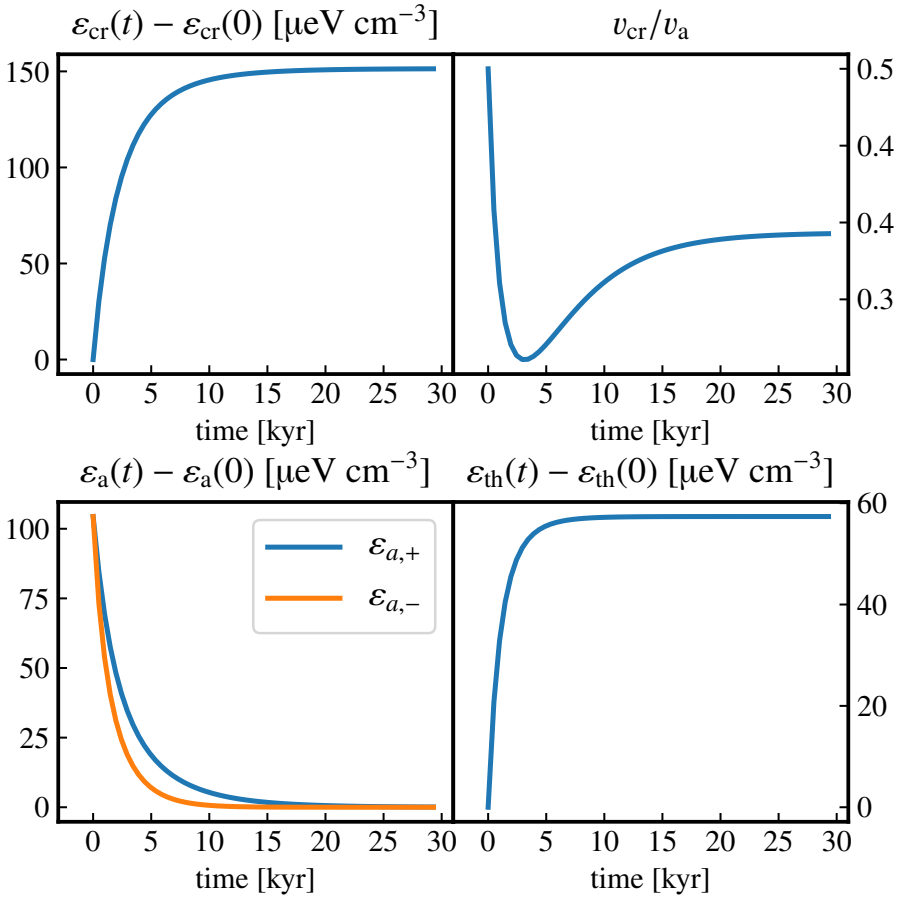

Figure 5.3: Time evolution of the CR, Alfvén wave, thermal energy density, and the streaming speed for the test with an initially operating second-order Fermi process.

Due to the high level of energy contained in gyroresonant Alfvén waves, the scattering rate of CRs for the present initial conditions is fast with

$$\nu = \nu_+ + \nu_- = \frac{1}{1.9\ \text{kyr}}. \tag{5.76}$$

The growth rate of Alfvén waves

$$\Gamma_{\text{gri},+} = -\frac{1}{5.8\ \text{kyr}} \qquad \text{while} \qquad \Gamma_{\text{gri},-} = -\frac{1}{1.9\ \text{kyr}} \tag{5.77}$$

is also fast but negative, indicating a damping of Alfvén wave energy, caused by the subalfvénic velocity of CRs. The nonlinear Landau damping rate has a similar timescale with

$$\Gamma_{\text{nlld},+} = \Gamma_{\text{nlld},-} = \frac{1}{4.6\ \text{kyr}}. \tag{5.78}$$

Thus, nonlinear Landau damping and the loss of Alfvén wave energy due to the gyroresonant interaction are equally important for the initial evolution of the energy in gyroresonant Alfvén waves.

During the entire simulation Alfvén waves lose energy by accelerating CRs and due to nonlinear Landau damping. In turn, the CRs and thermal energy densities are monotonically increasing for all times. The gyroresonant instability cannot be active as CRs are unable to reach super-alfvénic velocities in this setup. Both backward and forward propagating resonant Alfvén waves accelerate the CRs to their respective wave frame. The timescale for these are acceleration are similar as both wave types almost identical energy densities. The situation would be symmetrical if the initial streaming velocity of CRs wouldn't be biased towards the direction of forward propagating Alfvén waves.

The forces exerted by gyroresonant Alfvén waves on the CRs in Eq. (5.6) can be rewritten in terms of difference between CR streaming velocity and the Alfvén speed:

$$\boldsymbol{b} \cdot \left(\boldsymbol{g}_{\mathrm{gri},+} + \boldsymbol{g}_{\mathrm{gri},-} \right) \propto \varepsilon_{\mathrm{a},+} \left(v_{\mathrm{cr}} - v_{\mathrm{a}} \right) + \varepsilon_{\mathrm{a},-} \left(v_{\mathrm{cr}} + v_{\mathrm{a}} \right) \tag{5.79}$$

Initially, $\boldsymbol{b} \cdot \boldsymbol{g}_{\mathrm{gri},-} > \boldsymbol{b} \cdot \boldsymbol{g}_{\mathrm{gri},+}$ or $\Gamma_{\mathrm{gri},-} > \Gamma_{\mathrm{gri},+}$ as the velocity difference between CRs and backward propagating Alfvén waves is larger compared to difference between CRs and forward propagating Alfvén waves. Thus in the beginning the CRs experience a net acceleration towards $-v_{\mathrm{a}}$ which causes the initial decrease in the streaming speed. The accompanying energy transfer from Alfvén waves to CRs is also stronger which explains the faster depletion of energy in backward propagating Alfvén waves. At $t \sim 5\mathrm{kyr}$, the remaining backward propagating Alfvén waves are unable to overcome the acceleration by the forward propagating Alfvén waves. From this point on CRs are accelerated towards $+v_{\mathrm{a}}$, which gives rise to an increase in streaming speed. At later times, there is no energy in Alfvén waves left and the acceleration of CRs slows down to eventually come to a halt.

5.4.2 Shock tubes with CR streaming

Shock tubes are decisive numerical tests for the robustness and accuracy of a given numerical scheme that solves hyperbolic conservation laws. In particular, one-dimensional shock tubes unveil problems during the reconstruction stage or shortcomings of the Riemann solver. The analytic solutions to shock tube problems of hyperbolic conservation laws are self-similar and consist of sequences of rarefactions, shocks and contact discontinuities. The jumps in the conserved variables at those discontinuities are provided by the Rankine-Hugoniot jump conditions.

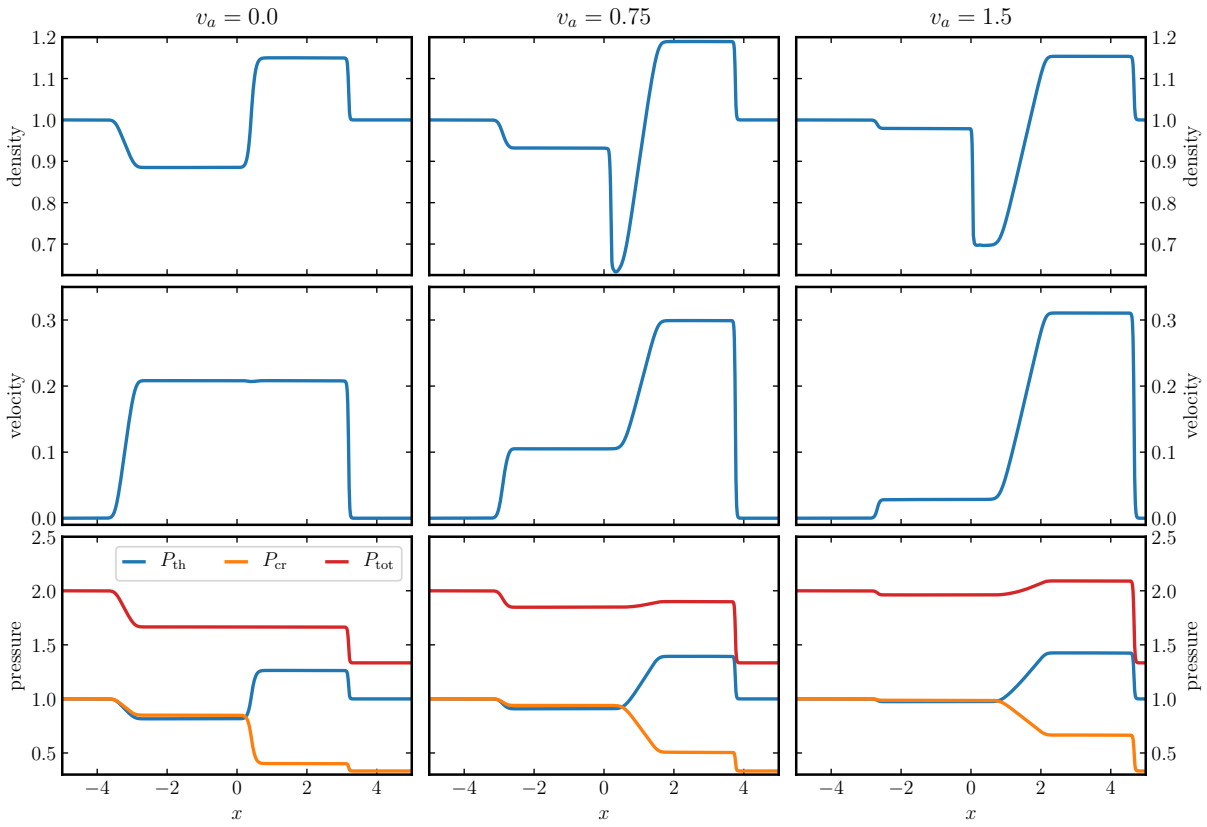

Figure 5.4: Density, velocity and pressure profiles for shock tubes with different values of the fixed Alfvén speed.

However, all aspects of this mature theory for hyperbolic conservation laws do not apply to our equations due the existence of and the strong dependence of the dynamics on the source terms in Eqs. (5.1) to (5.7). Nevertheless, we can reinterpret the equations for small $\kappa_{\pm}$ and large c as a relaxation approximation to the streaming-diffusion equations of Pfrommer et al. (2017a) in the sense of Parés (2006). In this limit shock tubes solved with our equations have the same shock structure as the streaming-diffusion equations. To guarantee that this limit applies, we do not evolve $\varepsilon_{\rm a,\pm}$ but fix the values of $\kappa_{\pm}$.

We setup a shock tube with initial conditions given by: $\rho = 1$, $\boldsymbol{u} = \boldsymbol{0}$, $\boldsymbol{B} = 10^{-13}\boldsymbol{e}_x$, $P_{\rm th} = 1$, $f_{\rm cr} = v_{\rm a}(\varepsilon_{\rm cr} + P_{\rm cr})$,

$$P_{\rm cr} = \begin{cases} 1, & x < 0, \\ 0.3333, & x > 0. \end{cases} \tag{5.80}$$

We fix the value of $v_{\rm a}$ independently of ρ and $\boldsymbol{B}$. Otherwise $v_{\rm a}$ would jump together with the density across any discontinuity which would make the interpretation of the results overly complicated. We use a moving one-dimensional mesh with initially 1024 equidistant cells in

the domain $x \in [-5, +5]$ but we note that we get similar results for a fixed mesh. We show in Fig. 5.4 the result of simulations with $v_a = 0, 0.75, 1.5$ at $t = 2$ with $c_{red} = 10$, $\kappa_+ = 1/300$, $\kappa_- = 0$, and $N_{cr} = 4$.

We use the case with $v_a = 0$ as a reference for the discussion of the two other shocks. This case is identical to the purely adiabatic two-fluid cosmic-ray hydrodynamics with additional diffusion (Pfrommer et al., 2017a). The final state of the simulation shown on the left-hand side of Fig. 5.4 consists of a rarefaction that is travelling to the left, a shock that travels to the right, and a central contact discontinuity over which thermal and CR pressures experience a jump but the total pressure stays constant. The contact discontinuity is characterised by a jump in density and a constant total pressure and velocity across. The gas needs to be accelerated to reach this velocity. This is accomplished by the pressure gradients at the rarefaction and shock. Both accelerations are such that the gas velocities behind the rarefaction and shock exactly match.

This is in contrast to the cases of $v_a \neq 0$ (middle and right-hand side of Fig. 5.4): here additional CR's stream across the rarefaction and decrease the total pressure gradient. This weakens the acceleration by the rarefaction and leads to a slower gas velocity behind it (i.e., to the right of the rarefaction). This would be sufficient to create a velocity mismatch at the former contact discontinuity. However, the shock on the right is also stronger with streaming CR's. Here the jump in total pressure is larger owning to a increased jump in CR pressure that have streamed across the former contact discontinuity. Consequently, the acceleration of gas at the shock is also increased which implies faster gas downstream of the shock. To compensate for the weaker acceleration to the left and stronger acceleration to the right of the former contact discontinuity, an additional rarefaction forms. This new rarefaction is moving to the right and is stronger than the already present rarefaction. It dilutes the gas efficiently, which can be seen in the $v_a = 0.75$ case by the variation in gas density at the position of the former contact discontinuity.

Interestingly, the contact discontinuity still exists: it is located to the left of the new rarefaction but the density jump has switched its sign. In the $v_a = 0.75$ case, the central rarefaction seems to be attached to the contact discontinuity forming a compound wave as observed in the density profile. Contrarily, both rarefaction and contact discontinuity are properly separated in the $v_a = 1.5$ case. We argue that the observed connection in the $v_a = 0.75$ case is due to numerical and physical diffusion. Overall the numerical solutions are well behaved.

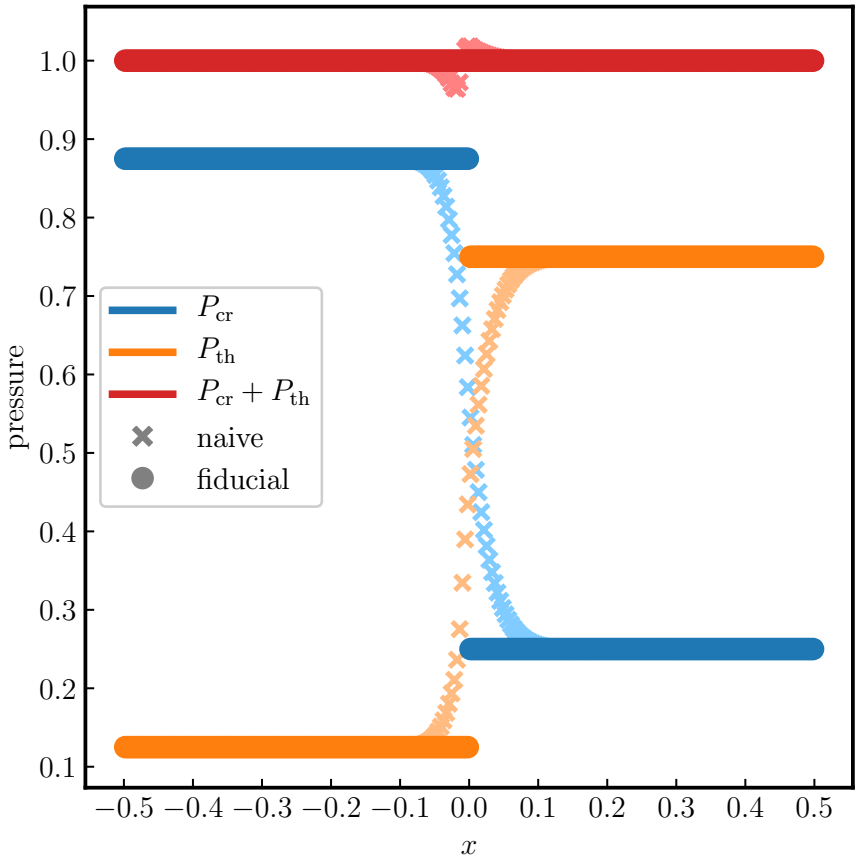

Figure 5.5: CR and thermal pressures of the perpendicular contact discontinuity problem. The profiles calculated with our fiducial Riemann solver are displayed with circles in opaque colours. In addition we show the profiles for the naive diffusive Riemann solver with crosses in semi-transparent colours.

5.4.3 Perpendicular magnetised contact discontinuity

In the direction perpendicular to the magnetic field interactions between Alfvén waves and CRs are unimportant. In this direction, only the CR pressure is able to alter the momentum of the gas, meditated by the Lorentz force (Thomas and Pfrommer, 2019). In a one-dimensional setting, where the magnetic field is perpendicular to the axis, the CR dynamics becomes adiabatic. The combined CR and gas system is, at its core, a two temperature fluid. A contact discontinuity in the two temperature fluid is not only characterised by a density jump, but there can also be a discontinuity in both partial pressures as long as the total pressure remains constant. We now demonstrate that the Riemann solver described in Section 5.3.2 is able to accurately capture these contact discontinuities. We use a static numerical grid with 256 mesh points that

are placed uniformly in the domain $x \in [-0.5, +0.5]$. The initial fluid velocity and CR flux are zero: $\boldsymbol{u} = \boldsymbol{0}$ and $f_{\rm cr} = 0$. The gas density is initialised with $\rho = 1$. The actual contact discontinuity is created by keeping the total pressure constant but adopting a jump in both, the CR and thermal pressure. We chose

$$[P_{\rm th}, P_{\rm cr}] = \begin{cases} \left[\frac{1}{8}, \frac{7}{8}\right] & x < 0, \\ \left[\frac{3}{4}, \frac{1}{4}\right] & x > 0. \end{cases} \tag{5.81}$$

The magnetic field $\boldsymbol{B} = \boldsymbol{e}_y$ is perpendicular to the normal of the contact discontinuity and, consequently, is also perpendicular to the cell interfaces. The light speed is set to $c_{\rm red} = 10$. The number of subcycles is $N_{\rm cr} = 2$.

The pressure profiles at $t = 1$ are displayed in Fig. 5.5. The results coincide with the initial conditions up to machine precision. This is by construction. The finite volume scheme of Pfrommer et al. (2017a) used in Section 5.3.1 to solve the adiabatic interactions uses an extension of the HLLD Riemann solver. This Riemann solver was designed to resolve the contact discontinuity without additional numerical dissipation. The finite volume scheme from Section 5.3.2 describes the dynamics parallel to the magnetic field and should not have any impact in the present test. This is ensured by the implicit weighting of all numerical fluxes in Section 5.3.2 with the projection of the magnetic field to the cell interface normal. This is a necessity for physical flux terms but not for terms that add artificial diffusion. Especially the weighting in the wave speed estimate in Eq. (5.46) is important here. For cell interfaces where the magnetic field is perpendicular to the cell interface normal the wave speed is $S = 0$ due to the weighting. This is the case for the present contact discontinuity. As the wave speed is zero, the artificial diffusion term in Eq. (5.39) is zero and no numerical diffusion is applied.

To demonstrate this, we compare our Riemann solver to an alternative that does not have this feature. Only the weighting with the projections on the magnetic field needs to be removed to accomplish this. We define a 'naive' Riemann solver that uses the wave speed estimate

$$S_{\rm naive} = c_{\rm red} \sqrt{\gamma_{\rm cr} - 1}. \tag{5.82}$$

We rerun a simulation with the same settings but replace S from Eq. (5.46) with $S_{\rm naive}$. In Fig. 5.5, the thermal and CR pressure profiles calculated with the naive Riemann solver show the expected additional diffusivity around the discontinuity. It causes an increase of pressure in the low-pressure region for both, the gas and CRs. This destroys the total pressure balance at the contact discontinuity and induces perpendicular fluid motion.

We note that the presented test only demonstrates that numerical diffusion vanishes for a local magnetic field that is perpendicular to a given cell interface. In multidimensional simulations

with arbitrary magnetic field- and mesh geometries this is rarely the case. Nevertheless, in the general situation where the projection of the direction of the magnetic field on the cell interface is non-zero, the weighting of the wave speed in Eq. (5.46) with the same projection guarantees that only a minimal yet necessary amount of numerical diffusion is added.

To conclude, we showed that the finite volume scheme of Section 5.3.2 avoids unnecessary interference with the dynamics perpendicular to the magnetic field when the proposed wave speed estimate in Eq. (5.46) is used.

5.4.4 Anisotropic transport of a wedge

The transport of a wedge along a ring magnetic field is one of the standard tests for anisotropic transport. It was used in Sharma and Hammett (2007) to highlight problems of standard methods that show non-physical transport perpendicular to the magnetic field. If not treated correctly, numerical discretisation effects can lead to the loss of monotonicity in diffusion problems or to a violation of the second law of thermodynamics in the context of thermal conduction. We use this test to show that our method is able to transport CRs anisotropically without any of those problems.

We simulate a wedge of CR energy density on a two-dimensional hexagonal, static mesh with 128^2, 256^2, and 512^2 generating points in the domain $x, y \in [-500, 500]$ pc. We set $\rho = m_p$ cm^{-3}, $P_{\mathrm{th}} = c_{\mathrm{sd}}^2 \rho / \gamma_{\mathrm{th}}$, where $c_{\mathrm{sd}} = 30$ km s^{-1} is the thermal sound speed, $\boldsymbol{u} = \boldsymbol{0}$, and the magnetic field to be $\boldsymbol{B} = v_{\mathrm{a}} \sqrt{\rho} \boldsymbol{e}_\varphi$ where $v_{\mathrm{a}} = 30$ km s^{-1} and $\boldsymbol{e}_\varphi$ is the unit vector in polar direction. These MHD quantities are kept fixed for the simulations in this section. The CR are initialised with

$$\varepsilon_{\mathrm{cr}} = \begin{cases} 10 \text{ eV cm}^{-3} & \text{for } |\varphi| < \frac{\pi}{12} \ \wedge \ \frac{r}{500 \text{ pc}} \in [0.5, 0.7], \\ 10^{-3} \text{ eV cm}^{-3} & \text{else,} \end{cases} \tag{5.83}$$

where $r^2 = x^2 + y^2$ and φ is the polar angle. In addition, we set $f_{\mathrm{cr}} = 0$, $\varepsilon_{\mathrm{a},\pm} = 10^{-4} \varepsilon_{\mathrm{cr}}$, and adopt $c_{\mathrm{red}} = 500, 1000, 2000$ km s^{-1}.

The resulting CR energy density at $t = 5$ Myr for all nine combinations of c_{red} and number of mesh points is shown in Fig. 5.6. The situation along the magnetic field is reminiscent of the simulation of a rectangular CR population in Thomas and Pfrommer (2019). The CR wedge has expanded along the magnetic field with approximately Alfvén velocity. The two lines in each panel display the theoretical position of the edges of the wedge in the case if the CRs were streaming with exactly the Alfvén velocity. In between those two lines $\varepsilon_{\mathrm{cr}}$ is mostly flat along φ coordinate. The value of $\varepsilon_{\mathrm{cr}}$ increases for fixed ϕ along the radial coordinate from

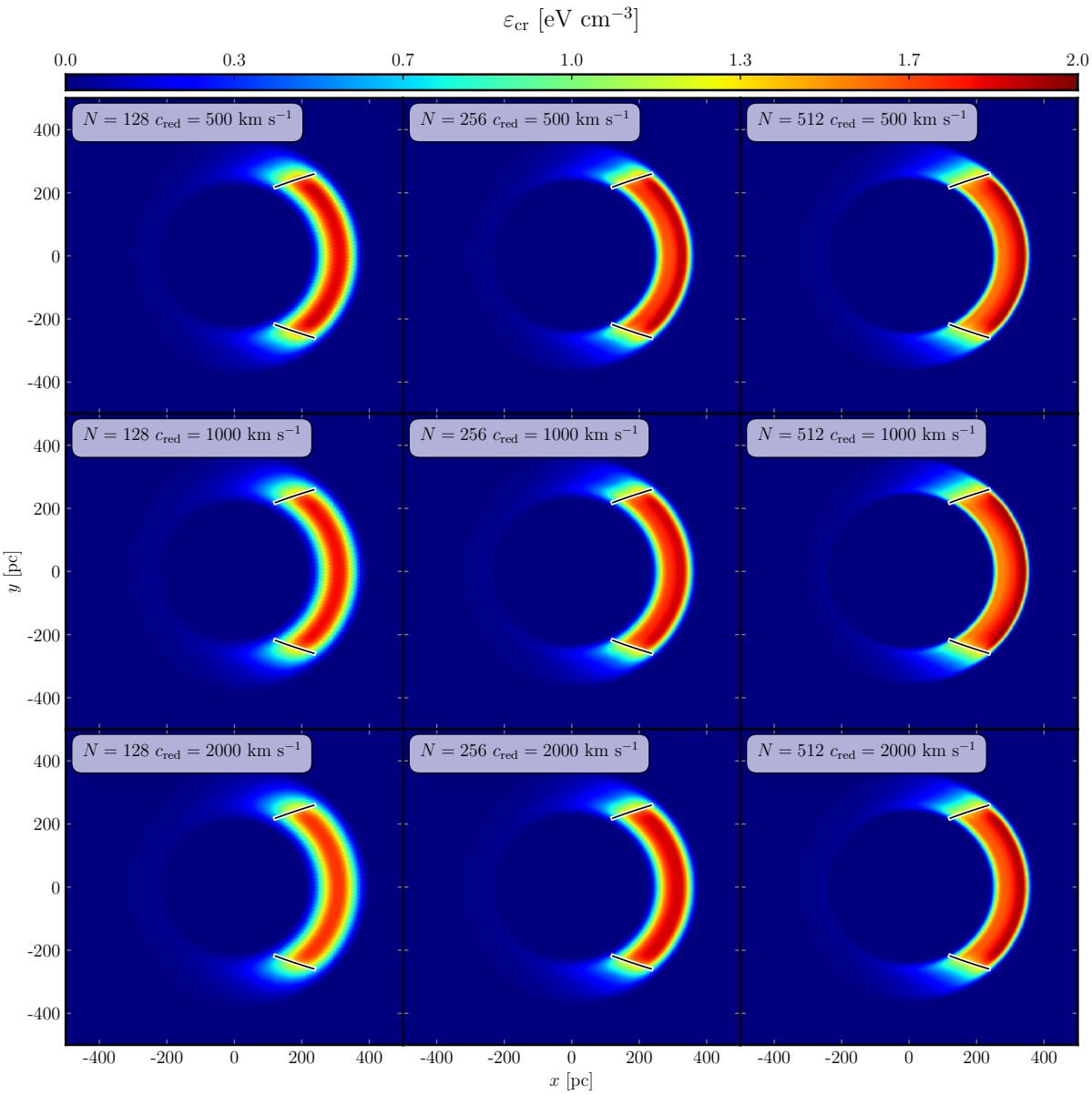

Figure 5.6: The anisotropic CR transport of a wedge test for a grid of varying mesh-points N and light speeds $c_{\rm red}$ at $t = 5$ Myr. The black-and-white lines indicate the position of the wedge fronts if CRs were streaming exactly with the Alfvén speed.

the inner edge to the outer edge due to the increasing CR energy content available at each r as given by the initial conditions. At the outer edge, numerical diffusion causes a decrease of $\varepsilon_{\rm cr}$ in the radial direction. The radial extent of this numerical feature shrinks with increasing resolution. Additionally, CRs diffusive ahead of the wedge and start to fill the ring. We observe no artificial oscillation and monotonicity is preserved. We conclude that our scheme is able to correctly model anisotropic transport.

Increasing the speed of light also increases the applied numerical diffusion. The numerical diffusion affects the large-r edge of the wedge more strongly because in this region, the $\varepsilon_{\rm cr}$ gradient between wedge and background is strongest. This can be best observed by comparing the three panels of the first column in Fig. 5.6: while the maximum of $\varepsilon_{\rm cr}$ is located at the centre of the wedge for $c_{\rm red} = 2000$ km s^{-1}, it moves to larger radii for $c_{\rm red} = 500$ km s^{-1}. Increasing the resolution of the simulation has the expected effect: the numerical diffusion decreases if more mesh generating points are used.

5.4.5 Telegrapher's equation

Linear perturbation analysis and simulations of linear waves provide another useful tool for understanding the mathematical character of equations and for code testing. In its simplest form small perturbation are introduced to a constant state that is a stable solution of the underlying equations. While no meaningful and stable state exists for our full CRHD equations, we can readily derive such a state in the telegrapher's limit of the equations.

In this limit, terms of higher order than $O(1)$ in $v_{\rm a}/c$ are ignored. We assume that the scattering of CRs is provided by a source other than Alfvén waves and set $\kappa_{\pm}$ to a fixed value, i.e., we only account for scattering centres moving in one direction. In this scenario, Eqs. (5.5) and (5.6) form the telegrapher's equations. This set of equations describes a non-Fickian diffusive transport of CRs (Malkov and Sagdeev, 2015; Litvinenko and Noble, 2016; Rodrigues et al., 2019). With these assumptions we lost the physical interpretation of the equations (see App. A of Thomas and Pfrommer 2019) but can nevertheless test the numerical performance of our code.

We linearly perturb Eqs. (5.1) to (5.7) in a one-dimensional setting by replacing every quantity q by $q + \delta q$, adopt $q = $ const., and neglect all second and higher-order terms in δq. The magnetic field is aligned with the axis. We neglect the transverse components of $\boldsymbol{u}$ and $\boldsymbol{B}$, and assume $\boldsymbol{u} = \boldsymbol{0}$ and $f_{\rm cr} = 0$ for a stable background state. The result of this perturbation

procedure is:

$$\frac{\partial \delta\rho}{\partial t} + \rho \frac{\partial \delta u}{\partial x} = 0, \tag{5.84}$$

$$\frac{\partial \delta u}{\partial t} + \frac{1}{\rho}\frac{\partial \delta P_{\rm th}}{\partial x} = +\frac{1}{3\rho\kappa}\delta f_{\rm cr}, \tag{5.85}$$

$$\frac{\partial \delta P_{\rm th}}{\partial t} + \rho c_{\rm sd}^2 \frac{\partial \delta u}{\partial x} = 0, \tag{5.86}$$

$$\frac{\partial \delta P_{\rm cr}}{\partial t} + \rho c_{\rm cr}^2 \frac{\partial \delta u}{\partial x} + (\gamma_{\rm cr} - 1)\frac{\partial \delta f_{\rm cr}}{\partial x} = 0, \tag{5.87}$$

$$\frac{\partial \delta f_{\rm cr}}{\partial t} + c_{\rm red}^2 \frac{\partial \delta P_{\rm cr}}{\partial x} = -\frac{c^2}{3\kappa}\delta f_{\rm cr}, \tag{5.88}$$

where $c_{\rm cr}^2 = \gamma_{\rm cr} P_{\rm cr}/\rho$.

Solutions to those equations can be found by using the Fourier transformation of the perturbations. We use the convention $\delta q(x,t) = \delta q(k)\exp(\mathrm{i}kx - \mathrm{i}\omega t)$ for $\delta q \in [\delta\rho, \delta u, \delta P_{\rm th}, \delta P_{\rm cr}, \delta f_{\rm cr}]$ and find the dispersion relation by solving

$$\det \begin{bmatrix} -\omega & \rho k & 0 & 0 & 0 \\ 0 & -\omega & k/\rho & 0 & \mathrm{i}/(3\rho\kappa) \\ 0 & \rho c_{\rm sd}^2 k & -\omega & 0 & 0 \\ 0 & \rho c_{\rm cr}^2 k & 0 & -\omega & (\gamma_{\rm cr}-1)k \\ 0 & 0 & 0 & c^2 k & -\omega - \mathrm{i}c^2/(3\kappa) \end{bmatrix} = 0, \tag{5.89}$$

and find

$$\begin{aligned} 0 = \omega \Bigg\{ & \omega^2 \left(k^2 c_{\rm sd}^2 - \omega^2\right) \\ & + \frac{c_{\rm red}^2}{3\kappa}\left[\mathrm{i}k^2\omega c_{\rm cr}^2 + \left(k^2 c_{\rm sd}^2 - \omega^2\right)\left(\mathrm{i}\omega - 3k^2\kappa(\gamma_{\rm cr}-1)\right)\right]\Bigg\}. \end{aligned} \tag{5.90}$$

The $\omega = 0$ solution is the entropy mode known from ordinary adiabatic hydrodynamics. The remaining four solutions can be identified in the $\kappa \to \infty$ limit where gas and CR hydrodynamics are decoupled. Two solutions are sound waves waves that are modified by the presence of CRs when κ is finite. We refer to them as 'modified sound waves'. The last two waves are associated with CR dynamics. We call them 'CR waves' in the following.

All simulations conducted in this section use $\rho = 1$, $P_{\rm th} = 0.01\gamma_{\rm th}^{-1}$, $P_{\rm cr} = 0.01\gamma_{\rm cr}^{-1}$, $c_{\rm red} = 1$ and $N_{\rm cr} = 4$.

Dispersion relation

In Fig. 5.7 we display the damping coefficient $-\mathrm{Im}(\omega)$ and the phase velocity $v_{\rm ph} = \mathrm{Re}(\omega/k)$ for all four waves and $\kappa = 1/3$. All solutions have different behaviours below and above a

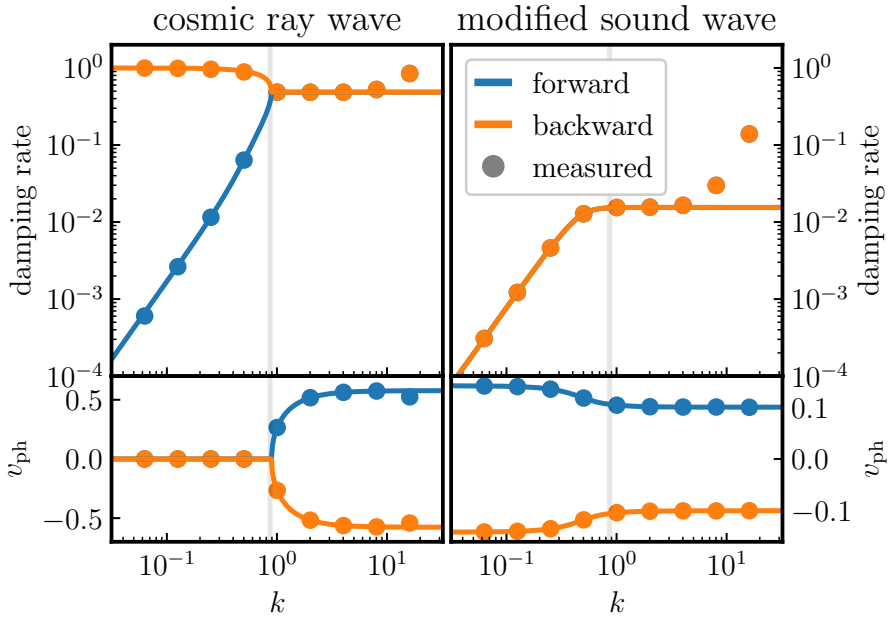

Figure 5.7: The dispersion relation of the hydrodynamic telegrapher's equation. We show the damping rate $-\mathrm{Im}(\omega)$ (top row) and phase velocity $v_{\rm ph} = \mathrm{Re}(\omega/k)$ (bottom row) of the CR wave (left panels) and the modified sound wave (right panels) for different wavenumbers k. In positive x-direction (forward) propagating waves are shown in blue while in negative x-direction (backward) propagating waves are shown in orange. The dots represent the values measured in our simulations.

certain wave number $k \sim 1$. By dropping the first term in the second line of Eq. (5.90), we find a branching point in the CR wave solutions that is approximately located at

$$k_{\rm mfp} = \frac{c_{\rm red}}{2\sqrt{3}\kappa}, \tag{5.91}$$

which has the physical meaning of an inverse mean free path. For $k < k_{\rm mpf}$, the wave length is above the mean free path of CRs and the dynamics is dominated by CR scattering. The two CR wave modes are standing waves. One of them is damped at a rate ~ 1 while the other solution shows a diffusive-like wave frequency $\omega \sim -\mathrm{i}\kappa k^2$. The latter is a feature of the telegrapher's equations, as they are a non-Fickian description for physical diffusion. Furthermore, CRs and the thermal gas are tightly coupled as scattering is frequent. The modified sound waves are slightly damped and travel with phase speeds larger than adiabatic sound speed. For $k > k_{\rm mpf}$, CR scattering is inefficient and the CR and gas dynamics are decoupled. Consequently, the sound waves are travelling with the adiabatic sound velocity $c_{\rm sd}$. The CR waves are travelling at speeds $\sim c/\sqrt{3} \sim 0.57c$. This velocity is expected in the Eddington limit adopted in the derivation of the CRHD equations (Thomas and Pfrommer, 2019).

Equipped with these analytical results, we can test whether our numerical algorithm is able to reproduce them. The simulation box has length 1 and is filled with 4096 equally spaced static mesh points. We setup 9 linear plane waves with wave numbers ranging from $k = 2\pi$ to $k = 2\pi \times 512$ in powers of 2. We run simulations for both wave types and both propagation directions. The CR waves are initialised by setting $\delta f_{\rm cr}(k) = 10^{-6}$ and calculating the remaining components by solving Eqs. (5.84) to (5.88) using the respective wave frequency $\omega = \omega(k, \kappa)$ for a given k and κ. The setup for the modified sound waves is similar: here we set $\delta u(k) = 10^{-6}$ and calculate the other Fourier components in terms of the velocity perturbation. After this, the real part of each component is added to the background state. This procedure ensures that the initial conditions are eigensolutions to the underlying differential equations. The simulation are run until $t = 10$.

Damping rates are derived by fitting an exponential function to the amplitude of the Fourier component of δu at the respective wave number. The real part of the wave frequency $\mathrm{Re}(\omega)$ is calculated using the average derivative of the argument of the same Fourier component. The inferred damping rates and phase velocities are also plotted in Fig. 5.7. They agree with the analytical prediction for low to intermediate wave numbers. For higher wave numbers the wave trains of the plain wave are resolved by fewer grid cells and numerical diffusion starts to affect the evolution. This can be seen in the damping rates. They are altered by a contribution originating from numerical diffusion with $\omega \rightarrow \omega + \omega_{\rm num} \sim \omega - \mathrm{i}(c_{\rm red}/\sqrt{3})\Delta x k^2$ where Δx is the grid spacing and $\omega_{\rm num} \sim -\mathrm{i}(c_{\rm red}/\sqrt{3})\Delta x k^2$ is an upper limit.

Parameter study

The wave number k and the diffusion coefficient κ are independent parameters in Eq. (5.90) and cannot be factored into a joint parameter. Thus the dependence of the wave frequency on κ is different in comparison to the dependence on k. In Fig. 5.8 we keep $k = 2\pi \times 2$ fixed but vary κ and show the damping rates and phase velocities of both wave types. For larger κ scattering is inefficient and the CR and gas dynamics become decoupled. In this case, the modified sound waves are moving with the adiabatic sound speed $c_{\rm sd}$ while the CR waves are travelling at $c_{\rm red}/\sqrt{3}$. The scattering rate $c_{\rm red}^2/(3\kappa)$ is increased for a smaller κ and CRs are efficiently coupled to the gas. This yields standing CR waves with two distinct damping rates and an increased effective sound speed of the modified sound waves. The damping rates of the modified sound waves achieve their maximum values at $\kappa \sim k_{\rm mpf}$ where the transition between coupled and decoupled CRHD dynamics occurs.

To see whether our code can reproduce these results, we run 7 simulations with κ increasing

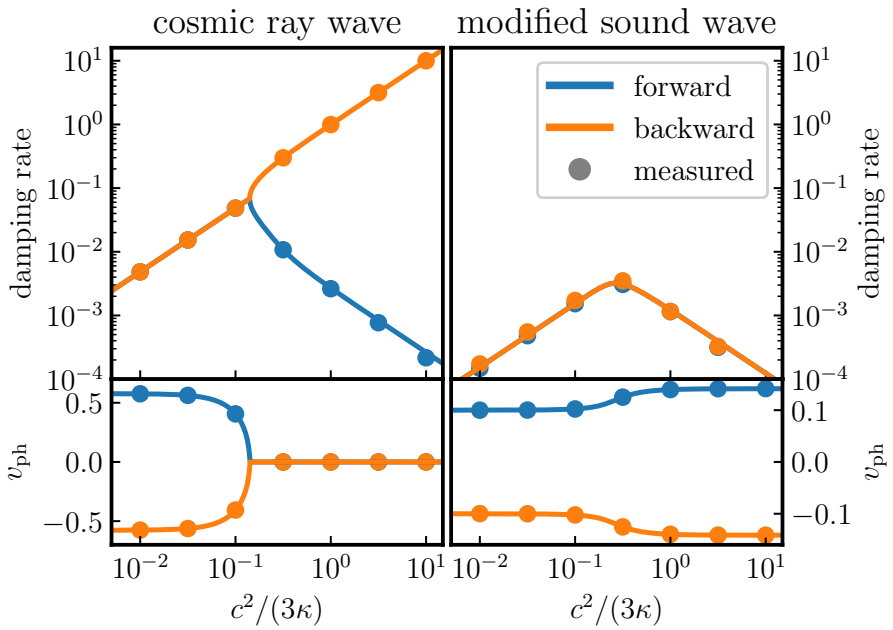

Figure 5.8: Same as Fig. 5.7 but this time with a fixed k but variable scattering rates $c^2/(3\kappa)$.

from 1/30 to 30 in logarithmic steps for each wave type. The numerical grid consist of 4096 equally spaced points in a domain of length 1. Damping rates and phase velocities are calculated the same way as in the previous subsection and the results are shown in Fig. 5.8. The inferred numerical damping rates and phase velocities agree with the analytical predictions and show negligibly small deviations.

Convergence study

As a last application of our linear wave analysis, we test for numerical convergence of our code. We set up an eigensolution of the forward travelling CR wave as initial condition and increase the number of cells $N_{\rm cells}$ from 64 to 16384 in factors of 2. The average L1-difference of the simulated δu and the corresponding analytical eigensolution at $t = 10$ is used as error measurement. This L1-error is calculated for each resolution and displayed in Fig. 5.9. The convergence order is 1.72 and thus somewhat below second order. Although both, the CRHD and MHD modules are individually second-order accurate, we expect only a first-order convergence owing to the operator splitting of both modules. The numerical convergence rate is exceeding first order, which suggests that the measured total error is still in a regime where the error is dominated by the errors of the individual modules and not by error originating from the operator splitting.

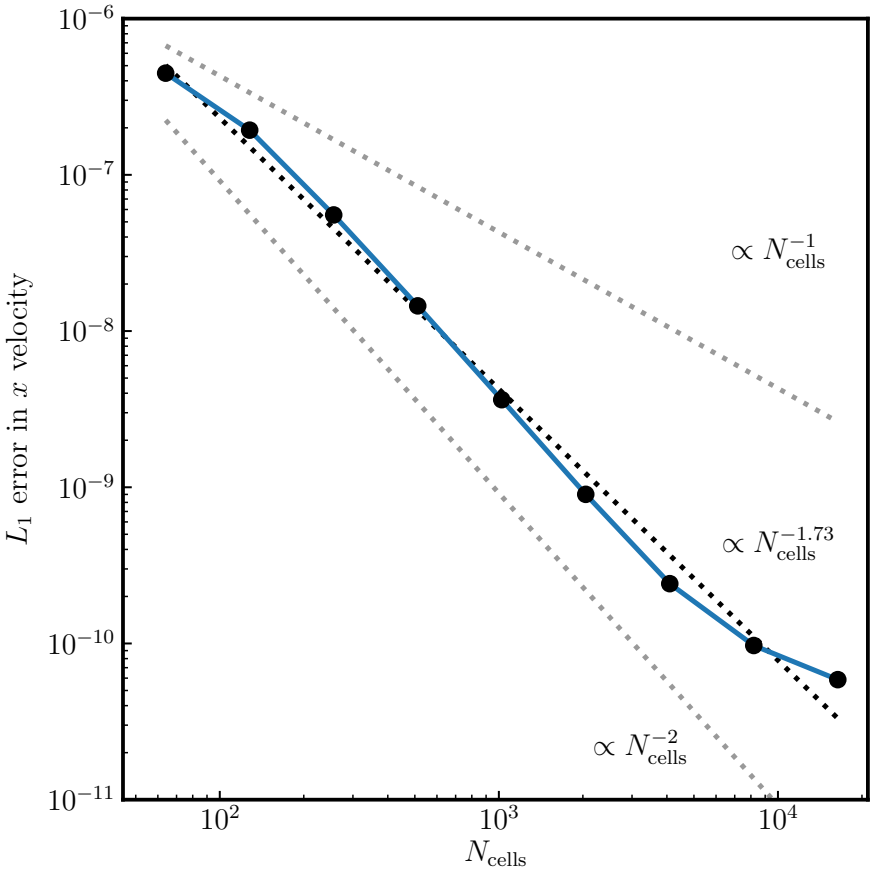

Figure 5.9: Convergence test for a linear forward-travelling CR wave of the telegrapher's equation.

5.4.6 Hydrodynamic response to a Gaussian CR distribution

We now move on to simulating the influence of a local CR overpressure on an otherwise homogeneous ambient gas distribution. The pressure-gradient of the CRs will set the gas into motion. This enables us to test the coupling between the CR and MHD modules. Our one-dimensional setup closely follows Wiener et al. (2017b). The thermal MHD fluid is initialised with a mass density $\rho_0 = 1.204 \times 10^{-24}$ g cm^{-3}, sound speed $c_{\mathrm{sd}} = 100$ km s^{-1}, and Alfvén speed $v_{\mathrm{a}} = 100$ km s^{-1}. The fluid is at rest while the magnetic field points along the simulation axis. The CR flux is chosen such that the CRs stream with Alfvén speed down their gradient. We simulate both a broad CR distribution with

$$P_{\mathrm{cr}} = 10^{-4} P_{\mathrm{th}} + P_{\mathrm{th}} \exp\left(\frac{x^2}{2\mathrm{kpc}^2}\right), \tag{5.92}$$

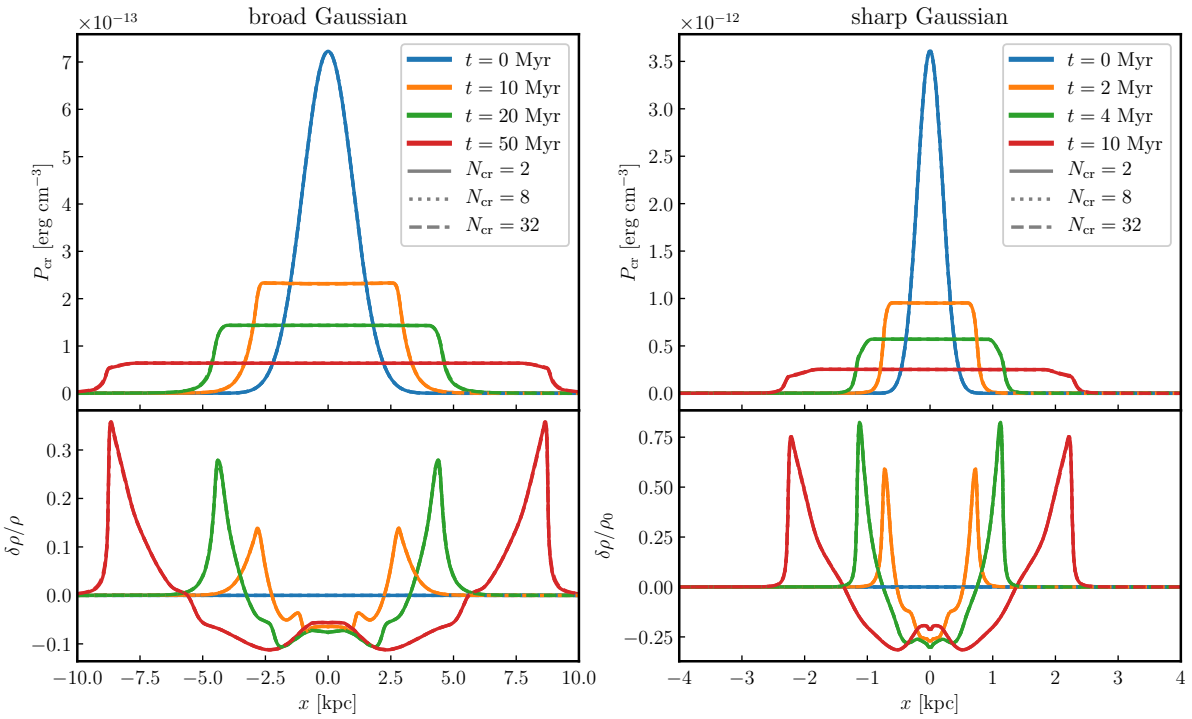

Figure 5.10: CR pressure (top row) and mass density fluctuation (bottom row) for a broad (left column) and a narrow Gaussian (right column) initial distribution of CRs on an otherwise homogeneous background. Note the different scales of both panels. This Figure is comparable to figure 7 in Wiener et al. (2017b).

and a sharp CR distribution with

$$P_{\rm cr} = 10^{-4} P_{\rm th} + 5 \times P_{\rm th} \exp\left(\frac{x^2}{2(200\ {\rm pc})^2}\right). \tag{5.93}$$

Initially, both Alfvén wave energy densities are given by $\varepsilon_{\rm a,\pm} = 10^{-6}\varepsilon_{\rm cr}$. The simulation domain $x \in [-50, +50]$ kpc is sampled by 4096 mesh-generating points that move quasi Lagrangian. We use $c_{\rm red} = 3000$ km s^{-1} and $N_{\rm cr} = 2, 8, 32$.

In Fig. 5.10 we display $P_{\rm cr}$ and the fractional change of the mass density for both distributions. The evolution of $P_{\rm cr}$ is similar to those of the Gaussians described in Thomas and Pfrommer (2019): both wings of the Gaussian CR distribution propagate in opposite directions while creating a flat plateau in between. At the wings the gyroresonant instability creates sufficient Alfvén waves such that CRs and the gas are well coupled. This converts CR to gas momentum and pushes the gas away from the center. The gas reacts to this acceleration by creating a central underdensity and swept-up shells at the position of the CR gradient. The gas is rarefied between both shells.

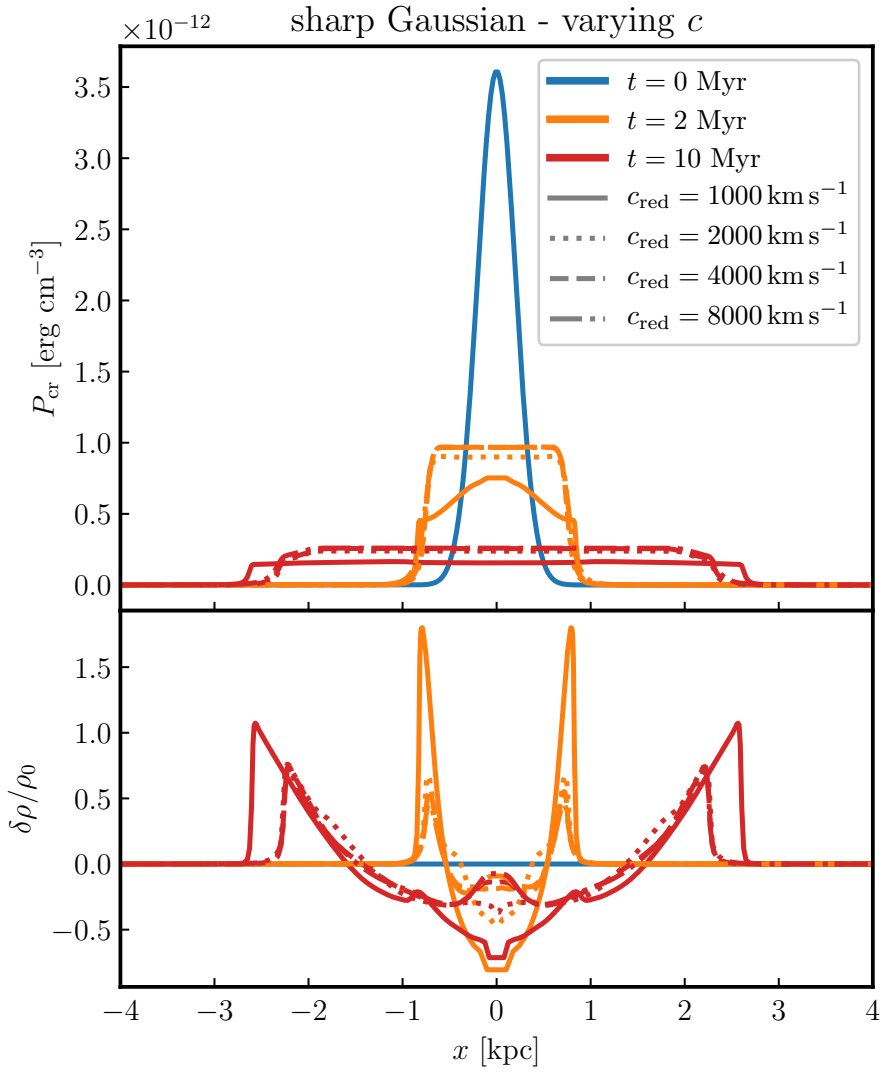

Figure 5.11: CR pressure (top row) and mass density fluctuation (bottom row) for a narrow Gaussian initial distribution of CRs (right column of Fig. 5.10) and different choices for the reduced speed of light c_{red}.

Before we compare our results to Wiener et al. (2017b), a few technical details need to be recalled: Wiener et al. (2017b) uses the implementation of Uhlig et al. (2012) to simulate the streaming of CRs in the SPH-code Gadget-2. In this method the streaming terms of the advection-diffusion equation for the CR energy are discretised using a parabolic SPH operator. This introduces additional numerical diffusion that damps the otherwise occurring and dominating numerical noise. By comparing figure 7 in Wiener et al. (2017b) to our Fig. 5.10, we find good overall agreement between both methods and only small differences that we will comment on in the following. We notice that the plateaus calculated with our presented method are flatter

which might be caused by our smaller numerical diffusion. In consequence, our gradients in $P_{\rm cr}$ at the wings of the Gaussian are steeper. Furthermore, the kinks in ρ inside the central region are more pronounced in our solution albeit they are recognisable in their solutions. We attribute this to the deficiency of SPH for subsonic flows.

We broadly vary the number of CR module subcycles $N_{\rm cr}$ for this test to quantify its influence on the solution. The profiles of $P_{\rm cr}$ for different $N_{\rm cr}$ look identical while minor differences in the density are noticeable. Their origin is likely the application and subsequent subtraction of the parallel $P_{\rm cr}$ gradient forces: we first add the $\nabla_\parallel P_{\rm cr}$ during the adiabatic step described in Section 5.3.1 and subtract it during the parallel transport step as described in Section 5.3.2. During the second step $P_{\rm cr}$ changes which prevents an exact cancellation. Only if the CRs are well coupled and $\boldsymbol{b} \cdot (\boldsymbol{g}_{\rm gri,+} + \boldsymbol{g}_{\rm gri,-}) \sim \nabla_\parallel P_{\rm cr}$ then the force exerted by the gyroresonsant interaction adds the lost parallel momentum back to the gas neglecting the previous subtraction. The observed small deviations in $\delta\rho/\rho_0$ indicate that this process is mostly independent of $N_{\rm cr}$.

In Fig. 5.11 we show the results of simulations with the sharp CR distribution that use $N_{\rm cr} = 8$ subcycles and different values for the reduced speed of light of $c_{\rm red} \in [1000, 2000, 4000, 8000]$ km s^{-1}. This tests the impact and the convergence of our simulations in Fig. 5.10 with respect to the reduced speed of light approximation. The simulations using $c_{\rm red} \in [2000, 4000, 8000]$ km s^{-1} show a similar behaviour in their $P_{\rm cr}$ profiles for all times while the $c_{\rm red} = 1000$ km s^{-1} has generally a lower value of $P_{\rm cr}$ at a given point in space in time. This is caused by the increased extent of the region bounded by the swept-up shells in this simulation. The same trend can be observed in the mass density. Here the simulations with higher values for $c_{\rm red}$ have similar profiles while the results for $c_{\rm red} = 1000$ km s^{-1} is off. For this value of $c_{\rm red}$, the swept-up shells feature higher values of ρ whereas the central underdensity has even been more diluted in comparison to the other simulations. We conclude that simulations with $c_{\rm red} \lesssim 2000$ km s^{-1} are not converged with respect to the speed of light and recommend to use $c_{\rm red} \gtrsim 3000$ km s^{-1} for this particular test problem. The maximum sound speed $c_{\rm sd}$ in any of the 4 simulations in this parameter study is 220 km s^{-1} while the maximum Alfvén velocity $v_{\rm a}$ and bulk velocity v_x are 45 and 271 km s^{-1}, respectively. We thus recommend a reduced speed of light that is $\gtrsim 10$ faster than any other signal speed in the simulation.

5.4.7 Acceleration of a warm cloud

Observations employing absorption line spectroscopy of the CGM show that the CGM is multiphase medium and consists of hot 10^6 K, low-density gas with embedded high-density, warm 10^4 K clouds, some of which reach velocities exceeding hundreds of km s^{-1} (Tumlinson et al.,

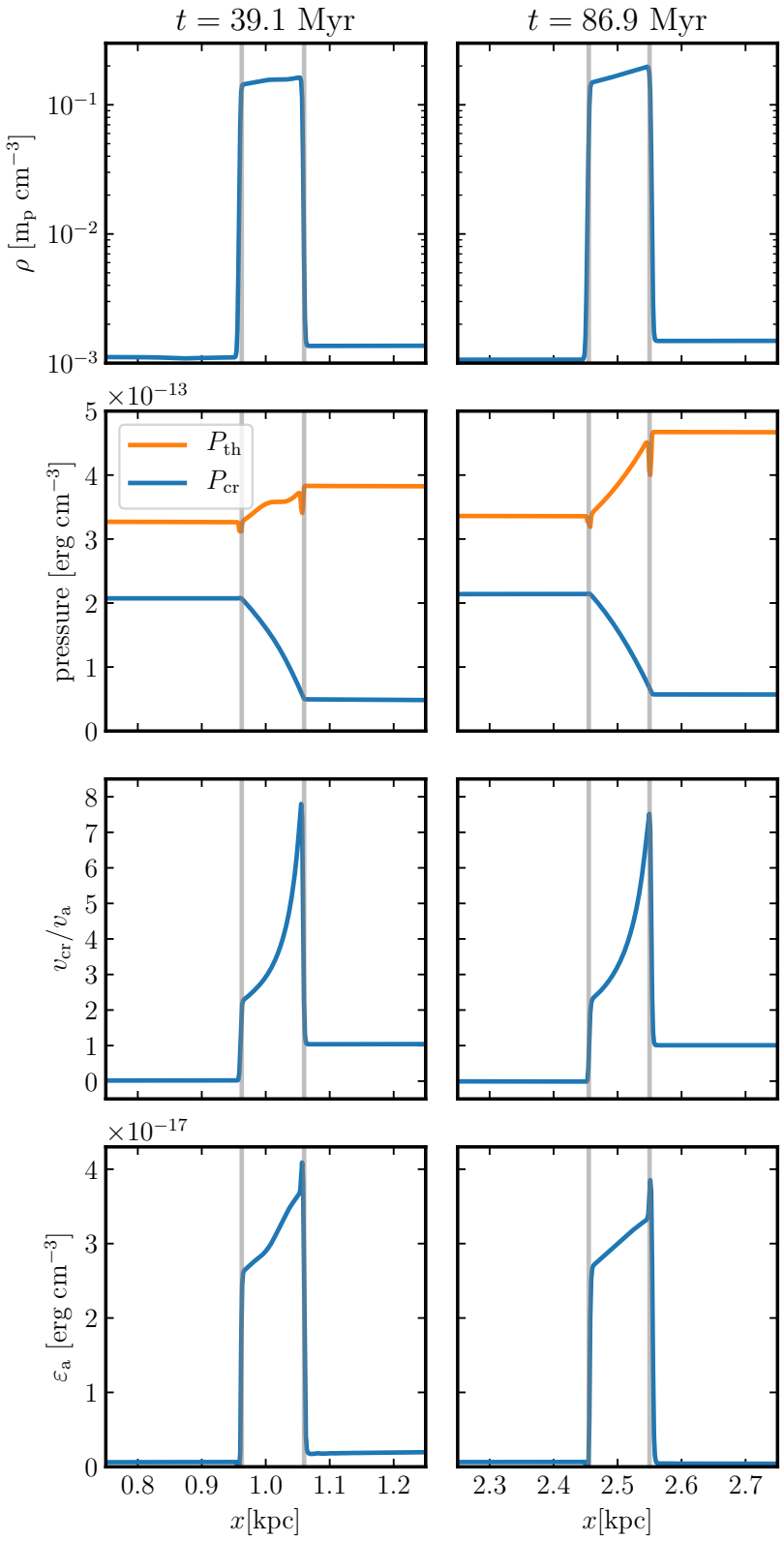

Figure 5.12: Profiles of density, pressure, CR streaming speed in units of the local Alfvén speed, and energy density of forward propagating Alfvén waves for the warm cloud test problem at two different times. Grey lines indicate the extent of the cloud.

2017). One of the proposed mechanisms to accelerate these clouds are CRs (Wiener et al., 2017a, 2019). A flux of CRs impinging on a cloud causes the cloud to be accelerated. A reservoir of standing CRs builds up in front of the cloud and the decreasing Alfvén speed inside the cloud causes the CRs to leave the cloud at a lower pressure but with a larger streaming speed. This effect is called the bottleneck effect (Skilling, 1971; Wiener et al., 2017b). The 'potential difference' of CR pressure between the front and the back of the cloud leads to its acceleration. We test our numerical method with a simulation of this scenario and note that other methods for two-moment CR transport have already been tested the same way (Jiang and Oh, 2018).

We simulate the cloud in a one-dimensional setting and mostly follow Wiener et al. (2019). We initialise the cloud centred at 500 pc with mass density $\rho = 2.35 \times 10^{-25}$ g cm^{-3} and width 100 pc. The mass density of the ambient medium is $\rho = 2.26 \times 10^{-21}$ g cm^{-3}. The magnetic field is aligned with the axis of the simulation and has a strength of 1 μG. The thermal gas is initially at rest. The gas pressure $P_{\mathrm{th}} = \rho k_B T/(\mu\, m_{\mathrm{p}})$ is uniform and set to 3.42 erg cm^{-3}. The mean molecular weight μ in units of the proton mass m_{p} is assumed to be 0.6. This pressure corresponds to a temperature T of 10^4 K inside the warm cloud and 1.1×10^6 K in the hot medium. Initially, only a negligible amount of CR and Alfvén wave energy is present.

We include optically thin cooling of the thermal gas by additionally evolving the temperature via

$$\frac{\partial T}{\partial t} = \frac{\mu}{\mu_{\mathrm{H}}} \frac{\gamma_{\mathrm{th}} - 1}{k_{\mathrm{B}}} (\Gamma - n_{\mathrm{H}} \Lambda)\,, \tag{5.94}$$

where Λ is the cooling function, $\Gamma = 10^{-25}$ erg s^{-1} represents a uniform heating rate, and $\mu_{\mathrm{H}} = 1.63$ is the mass fraction of hydrogen atoms. We use the fit to the Cloudy cooling function assuming collisional ionisation equilibrium as given in Appendix A of Schneider and Robertson (2018). Cooling is implemented in an operator-split manner. The temperature is evolved in time using a subcycled Euler method. The updated temperature is allowed to vary by 1 per cent from its old value during a single cycle. We impose a temperature floor of 10^4 K. Inclusion of the heating rate in addition to the gas cooling makes the hot phase, as given by the initial condition, stable.

We use constant-extrapolation boundary conditions for all quantities on the right side of the domain. The boundary conditions on the left side are set as follows: all MHD quantities are extrapolated with their constant values, the CR energy density is $\varepsilon_{\mathrm{cr}} = 6.488 \times 10^{-13}$ erg cm^{-3}, the forward-propagating Alfvén wave energy density is $\varepsilon_{\mathrm{a},+} = 10^{-6} \varepsilon_{\mathrm{cr}}$, and f_{cr} is set to be reflective by copying the value in the first cell but switching its sign. The CR module uses $c_{\mathrm{red}} = 500$ km s^{-1} and $N_{\mathrm{cr}} = 4$. The numerical grid range is $x \in [0, 3]$ kpc and consists of 2048 equally spaced mesh generating points. Because the fluid motion is mostly subsonic we keep

the grid static.

The numerical solution is displayed in Fig. 5.12 at $t = 39.1$ Myr and $t = 86.9$ Myr. The solution reaches a quasi-steady state where profiles have the same characteristic form over a long time while the values of individual quantities show small variations.

The bottleneck effect of CRs can be observed in the CR pressure profile: to the left of the cloud the CR pressure is higher than to its right and smoothly transitions between the two values inside the cloud. The pile-up of CRs causes them to stream with sub-alfvénic velocities ahead of the cloud (i.e., to the left of it). Because the Alfvén speed is reduced by a factor ~ 10 inside the warm cloud, this gives rise to super-alfvénic CR streaming speeds inside the cloud. This triggers an energy transfer from CRs to Alfvén waves via the gyroresonant instability and an effective growth of Alfvén waves. Interestingly, the streaming speed increases as the CRs flow through the cloud. This may seem counter-intuitive as the streaming speed should decrease to the Alfvén speed if there is sufficient energy in Alfvén waves present. Here, the $P_{\rm cr}$ gradient term and the term that describes the interaction between CRs and forward propagating Alfvén waves are both relevant for the evolution. The CR flux decreases from $v_{\rm cr} > v_{\rm a}$ to $v_{\rm cr} \sim v_{\rm a}$ only if the CR-Alfvén wave interaction dominates. But inside the cloud the $P_{\rm cr}$ gradient term is dominant. As a result, the CR flux increases in the cloud because the $P_{\rm cr}$ gradient is positive. The CR pressure profiles of Wiener et al. (2017a) show a shallow gradient inside the cloud and jump at the right edge of the cloud. This jump is not present in our simulation.

The acceleration by CRs is almost uniform in space so that the density only slightly increases towards the leading edge. Over the course of the simulation the cloud is not fragmented but experiences a compression by 30 per cent to 70 pc when the initial front of CR's makes contact with it at $t \sim 10$ Myr. After that event, the cloud quickly expands again to its original side length ~ 100 pc and approximately maintains this size for the rest of the simulation. In Fig. 5.12 the grey lines trace the interface between the cloud and the ambient medium. For the displayed times at $t = 39.1$ Myr and $t = 86.9$ Myr the cloud is 95pc and 97pc wide.

The thermal pressure to the right of the cloud is steadily increasing over time once the quasi-steady state is reached. While the CR pressure gradient dominates the overall pressure balance inside the cloud, the rising thermal pressure and its associated gradient slows down the acceleration of the cloud. The increase in $P_{\rm th}$ is caused by adiabatic compression of the gas, which is the result of the acceleration of the cloud and a pile-up of gas to the right of the cloud. We confirmed this by verifying that the entropy measure $P_{\rm th}\rho^{-\gamma_{\rm th}}$ to the right of the cloud remains nearly constant in the course of the simulation. This effect is particularly strong in our one dimensional simulation. In two or three dimensions the pile-up will likely be weaker as the

flow will be able to escape in the other dimensions.

The numerical solution is well behaved and the transition between hot and warm media is sharp because we do not take into account thermal conduction in these simulations. The blips in the thermal pressure are caused by mixing the warm and hot phases which causes an overcooling at the interface. This seeds some small amplitude sound waves that travel inside the warm cloud.

5.4.8 CRHD vortex

To quantitatively assess the accuracy of our algorithm to anisotropically transport CR and to couple them to the gas, we simulate a steady state analytic vortex. Analytical solutions for isodensity vortices already exist for hydrodynamics and MHD (Yee et al., 1999; Balsara, 2004). The principle idea in the derivation of the hydrodynamic/MHD solutions is that centrifugal force induced by the rotation of the vortex can be balanced by pressure forces or shear. This idea can be readily extended to CRHD where CRs are moving in a circular magnetic field and exert a Lorentz force with the $\nabla_\perp P_{\rm cr}$ term in the momentum equation, Eq. (5.2), that counteracts the centrifugal force.

Assuming an equilibrium in two-dimensional polar (R, φ) coordinates, the radial component of the Euler equation reads

$$\frac{\partial (T_{RR} + P_{\rm cr})}{\partial R} = \frac{1}{R}\left(T_{\varphi\varphi} - T_{RR}\right), \tag{5.95}$$

where the RR and $\varphi\varphi$ components of the pressure-stress tensor for a circular magnetic field are given by:

$$T_{RR} = \left(\rho \boldsymbol{u}\boldsymbol{u} + P_{\rm th}\mathbf{1} + P_{\rm mag}\mathbf{1} - \boldsymbol{B}\boldsymbol{B}\right)_{RR} \tag{5.96}$$

$$= P_{\rm th} + \frac{B_\varphi^2}{2}, \tag{5.97}$$

$$T_{\varphi\varphi} = \left(\rho \boldsymbol{u}\boldsymbol{u} + P_{\rm th}\mathbf{1} + P_{\rm mag}\mathbf{1} - \boldsymbol{B}\boldsymbol{B}\right)_{\varphi\varphi} \tag{5.98}$$

$$= \rho u_\varphi^2 + P_{\rm th} - \frac{B_\varphi^2}{2}, \tag{5.99}$$

where $P_{\rm mag} = B^2/2$, u_R, B_R are the components of $\boldsymbol{u}$ and $\boldsymbol{B}$ in R direction, and u_φ, B_φ are the corresponding components in φ direction. We can solve Eq. (5.95) by integrating the pressures after inserting a given rotation curve and a magnetic field profile. In our case there is a degeneracy in the solutions as the pressure can be provided either by the thermal gas or the CRs. We chose to keep the thermal pressure constant and integrate the CR pressure. Our initial

conditions and steady state solutions for this setup are given by:

$$\rho = m_\mathrm{p}\ \mathrm{cm}^{-3}, \tag{5.100}$$

$$\boldsymbol{u} = u_0 \exp\left(\frac{1-\hat{R}^2}{2}\right)\boldsymbol{e}_\varphi, \tag{5.101}$$

$$\boldsymbol{B} = u_0 \sqrt{\rho} \exp\left(\frac{1-\hat{R}^2}{2}\right)\boldsymbol{e}_\varphi, \tag{5.102}$$

$$P_\mathrm{th} = \frac{\rho u_0^2}{\gamma_\mathrm{th}}, \tag{5.103}$$

$$P_\mathrm{cr} = \rho u_0^2 \left[\frac{1}{\gamma_\mathrm{th}} - \frac{\hat{R}^2}{2}\exp\left(1-\hat{R}^2\right)\right], \tag{5.104}$$

$$f_\mathrm{cr} = \varepsilon_{\mathrm{a},\pm} = 0, \tag{5.105}$$

where $u_0 = 30\ \mathrm{km\ s^{-1}}$ and

$$\boldsymbol{e}_\varphi = \frac{[-y, +x, 0]^T}{100\mathrm{pc}}, \tag{5.106}$$

$$\hat{R} = \frac{R}{100\ \mathrm{pc}}. \tag{5.107}$$

A shortcoming of this solution is that it does not contain any Alfvén wave dynamics. This is due to two technical reasons. First, wave damping converts Alfvén wave energy to thermal energy. Because these two components have different adiabatic indices, this would cause a pressure imbalance. Second, the gyroresonant interaction would transfer momentum from CRs to the gas along the magnetic field which would cause a additional azimuthal acceleration. In both cases the balance between the pressure gradient forces and the centrifugal force would cease to exist and the dynamical equilibrium would be lost. We set up simulations of the vortex initial conditions on a two-dimensional hexagonal mesh in a computational domain of $x, y \in [-1, +1]$ kpc. We use $c_\mathrm{red} = 1000\ \mathrm{km\ s^{-1}}$, $N_\mathrm{cr} = 10$, and constant-extrapolation boundary conditions.

Although the initial conditions correspond to an analytical solution of this problem, numerical errors build up after the simulations has started. These errors are caused by the misalignment of mesh interfaces with the polar coordinate axes but allows us to test the convergence of our method. To perform the convergence test, we increase the number of mesh generating points from 64^2 to 2048^2 in powers of 2 for each dimension. We use two different mesh types to perform the simulations. At any given resolution we use a regular hexagonal mesh and an irregular mesh, which was created from it's regular counterpart but features a randomised offset of the mesh generating points. These offsets have a random direction and a random magnitude

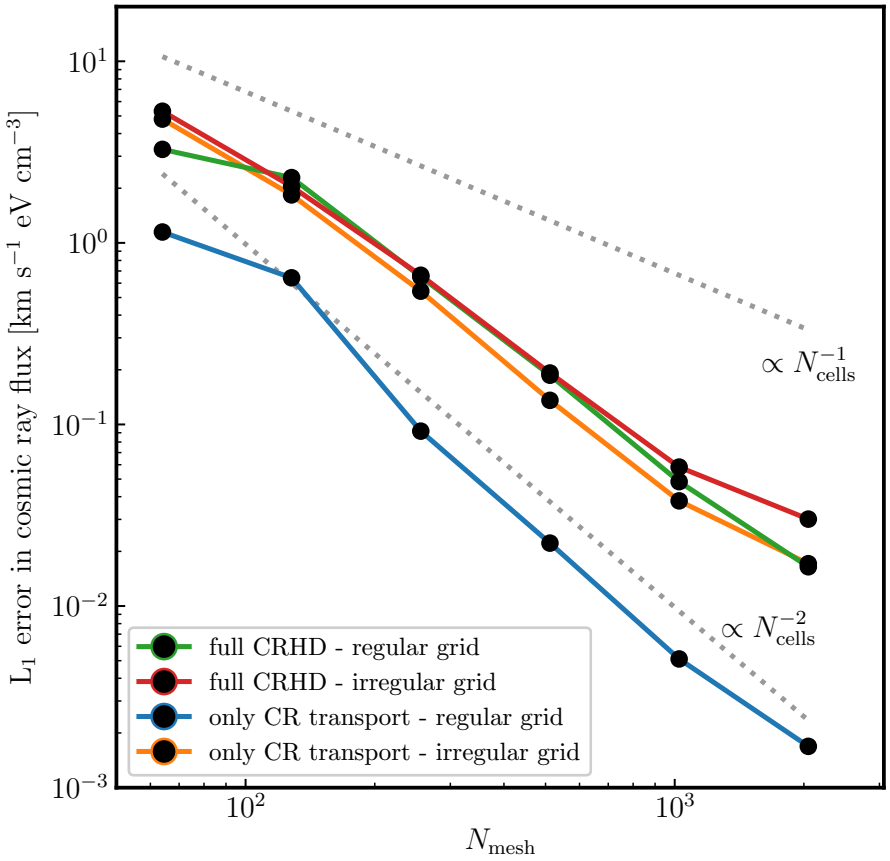

Figure 5.13: Convergence test for the two-dimensional isodensity vortex for the two tested modes of CRHD physics and each simulated with two different mesh types, respectively.

of up to 20 per cent of the cell radius of the regular mesh. With increasing mesh resolution the deviations from the analytic solution should decrease for both mesh types, which allows us to test convergence of our scheme with a non-linear problem. We run this test with two different transport modes for the CRs.

1. **Full CRHD.** Here we integrate the full set of CRHD equations on a moving mesh. This tests the code's capability to maintain the dynamical equilibrium of the analytical solution. For these simulations, we use the moving-mesh capability.
2. **Only CR transport.** Here we use the same setup, as described above, but update only $\varepsilon_{\mathrm{cr}}$ and f_{cr} on a static mesh. Even with this additional restriction, the analytical solution remains valid. The resolution study tests whether the code can accurately transport CRs anisotropically and keep $f_{\mathrm{cr}} = 0$.

We measure the numerical error by calculating the L1 error norm of f_{cr} at $t = 1$ Myr. The

results are shown in Fig. 5.13. Our method converges for both transport modes. In the *full CRHD* case the convergence order is ~ 1.6 (1.62 for the regular mesh and 1.56 for the irregular mesh) which is similar to the result found for the telegrapher's test in Section 5.4.5. This result is unexpectedly good because the formal convergence order is still 1 due to the operator splitting. This suggests that the error introduced by the operator splitting is lower than the error of the individual transport modules. The convergence order for the *CR transport-only* case is 1.95 for the regular mesh which corresponds to second-order convergence. We measure a convergence order of 1.69 for *CR transport-only* for the irregular mesh which is consistent with the convergence of our scheme in the *full CRHD* case. This result is expected because the anisotropic transport of CRs is solely described by the parallel transport step and the order-reducing operator splitting for the coupling between CRs and gas is absent.

5.4.9 Blast wave

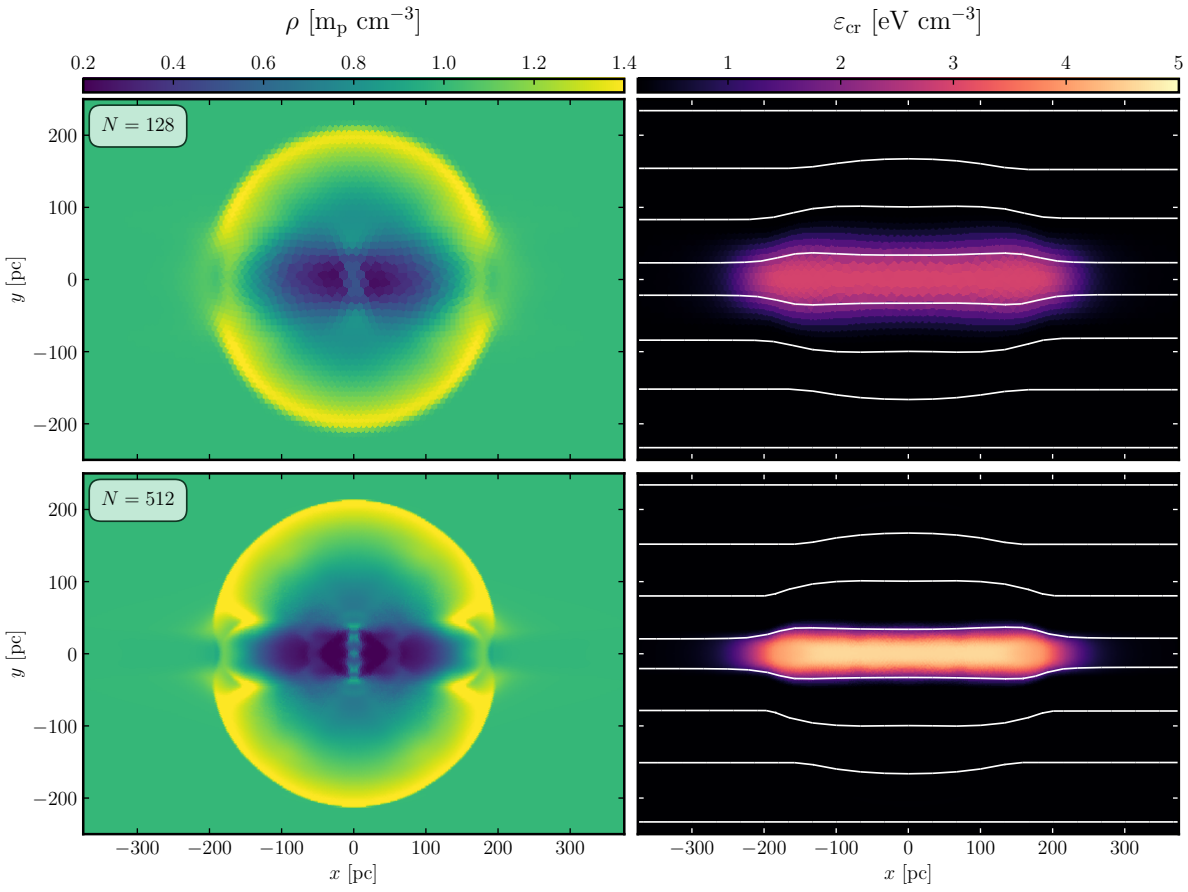

Figure 5.14: Mass density and CR energy density for the blast wave test problem with two different mesh resolutions. White lines trace the magnetic field.

In this simulation we test our algorithm with a blast-wave problem triggered by a CR overpressure. We expect interesting deviations caused by the anisotropic transport of CRs in comparison to the purely spherical morphology of a Sedov-like blast wave that has been launched by a thermal overpressure. Similar tests have already been conducted for streaming and diffusing CRs (Pakmor et al., 2016a; Jiang and Oh, 2018). Our initial conditions are as follows: the MHD quantities are set to $\rho = 1\mathrm{m_p cm^{-3}}$, $\boldsymbol{u} = \boldsymbol{0}$, $P_{\mathrm{th}} = c_{\mathrm{sd}}^2 \rho/\gamma_{\mathrm{th}}$, and $\boldsymbol{B} = v_{\mathrm{a}} \sqrt{\rho} \boldsymbol{e}_x$ where sound- and Alfvén speeds are $c_{\mathrm{sd}} = 10$ km s^{-1} and $v_{\mathrm{a}} = 20$ km s^{-1}. The CR energy density in the background is set to $P_{\mathrm{cr}} = 0.1 P_{\mathrm{th}}$ and $P_{\mathrm{cr}} = 100 P_{\mathrm{th}}$ inside the overpressured region. This region is centred at $(x, y) = (0, 0)$ and has a radius of 20 pc. Initially, we adopt $f_{\mathrm{cr}} = 0$ and $\varepsilon_{\mathrm{a},\pm} = 10^{-4} \varepsilon_{\mathrm{cr}}$. We use $c_{\mathrm{red}} = 1000$ km s^{-1} and $N_{\mathrm{cr}} = 8$ to simulate our CR dynamics. The simulations have been conducted with 128^2 and 512^2 moving mesh-generating points for an initially hexagonal mesh in the domain $x, y \in [-500, +500]$ pc.

The results are displayed in Fig. 5.14. Perpendicular and oblique to the direction of the magnetic field the evolution is adiabatic and the resulting density profile is mostly spherical. Along the magnetic field lines the evolution deviates from spherical symmetry. There the CRs start to stream away from the central overpressured region and form a mostly flat bar. This alters the shock structure and causes the density shell to break up into two discontinuities. At the inner discontinuity both the CR energy density and mass density jump while the outer discontinuity is the continuation of the spherical shell where negligible CRs are present but a density jump occurs. CRs diffuse ahead of the shock and push a small amount of gas alongside. Additionally, a central and two smaller ridges at $x \sim \pm 50$ pc are observable in ρ. Those same ridges are also visible in figure 12 of Jiang and Oh (2018). The y-motion of the blast waves carries magnetic field lines along. This rarefies the CRs in the vertical direction. The perturbed magnetic field lines traces the extent of the CR distribution in Fig. 5.14.

By comparing the lower to the high resolution simulation, we observe that both results look similar and show the same general features. The decreased resolution for the 128^2 simulations implies a higher numerical diffusivity which leads to a broader CR distribution and a lower maximum value of $\varepsilon_{\mathrm{cr}}$.

5.5 Summary

In this paper we presented a new finite volume method that enables us to simulate CRHD on the moving mesh of the Arepo code. We extend the CRHD equations of Thomas and Pfrommer (2019) to cosmological, comoving coordinates so that the presented scheme can be applied to

study CR feedback in galaxies and galaxy clusters.

Our algorithm consist of three distinct integration steps that model different parts of the included CR physics. The first step integrates the adiabatic dynamics of MHD and CR quantities and accounts for the quasi-Lagrangian motion of the mesh. To this end, the previously available CR module (Pfrommer et al., 2017a) was extended to include the evolution of the CR flux and gyroresonant Alfvén waves. In the next step a path-conservative finite volume scheme is employed to describe the anisotropic transport of CRs along magnetic field lines. We use a Lax-Friedrichs-type Riemann solver that is able to resolve contact discontinuities. This anisotropic transport step can be subcycled and uses the reduced speed of light approximation to reduce the total computational cost of the algorithm, thus enabling large-scale cosmological simulations. In the last step, the gyroresonant interaction and wave damping mechanisms are modelled in our algorithm using a source term integration step. We developed a custom-made adaptive time step semi-implicit ODE integrator to solve this short-timescale effects numerically. All three integration steps are combined in an operator-split manner. We tested the algorithm and our implementation using multiple tests that simulate problems of varying complexity and target different aspects of the algorithm. We verified that

1. multi-dimensional simulations show the expected CR streaming and diffusion modes of anisotropic CRs transport,
2. the algorithm is accurate by comparing the results of our simulations against solutions of the linearised and full set of CRHD equations. We showed that our implementation reaches a convergence order that ranges between first and second order, and that
3. coupling between CR and thermal gas is correctly accounted for with simulations of shocks, blast waves, the expansion of a smooth CR distribution, and the acceleration of a warm cloud.

The excellent performance of our method leaves us confident that the presented algorithm is versatile and allows for accurate and stable simulations of complex astrophysical environments. The combination all methods enables us to simulate the impact of CRs on the global evolution of the investigated system with little compromises on the included CR transport mechanisms.

5.6 Appendix: Cosmological Equations

The CRHD equations laid down in Eqs. (5.1) to (5.7) are valid for a static space time. Arepo has the capability to run simulations in an expanding universe. To facilitate simulations of CRHD in an expanding universe the CRHD equations have to be adapted to eliminate the homoge-

neous Hubble expansion via comoving coordinates. To this end, we assume that the expansion can be described by a time-dependent scale factor $a(t)$ that obeys Friedmann's equations. We parameterise space using the comoving coordinate $\boldsymbol{x}$ and eliminate the physical coordinate $\boldsymbol{r}$ from the CRHD equations. We also define comoving analogues to previous used quantities (denoted by a subscript c) to simplify the algebraic complexity and to transform the comoving equations into a form similar to their static counterparts. We use

$$\boldsymbol{r} = a\boldsymbol{x}, \qquad \boldsymbol{u}_\mathrm{c} = \boldsymbol{u} - \dot{a}\boldsymbol{x}, \tag{5.108}$$

$$\rho = \rho_\mathrm{c} a^{-3}, \qquad \boldsymbol{B} = \boldsymbol{B}_\mathrm{c} a^{-2}, \tag{5.109}$$

$$\varepsilon_\mathrm{th} = \varepsilon_\mathrm{th,c} a^{-3}, \qquad \varepsilon_\mathrm{cr} = \varepsilon_\mathrm{cr,c} a^{-4}, \tag{5.110}$$

$$\varepsilon_\mathrm{a,\pm} = \varepsilon_\mathrm{a,\pm,c} a^{-9/2} \qquad f_\mathrm{cr} = f_\mathrm{cr,c} a^{-4}, \tag{5.111}$$

where $\boldsymbol{u}_\mathrm{c}$ is the peculiar velocity. The ideal gas laws for the thermal gas, CRs, and Alfvén waves remain the same and define their corresponding comoving pressures via

$$P_\mathrm{th,c} = (\gamma_\mathrm{th} - 1)\varepsilon_\mathrm{th,c}, \tag{5.112}$$

$$P_\mathrm{cr,c} = (\gamma_\mathrm{cr} - 1)\varepsilon_\mathrm{cr,c}, \tag{5.113}$$

$$P_\mathrm{a,\pm,c} = (\gamma_\mathrm{a} - 1)\,\varepsilon_\mathrm{a,\pm,c}. \tag{5.114}$$

The total comoving energy density contained in the MHD fluid is defined as:

$$\varepsilon_\mathrm{c} = \frac{\rho_\mathrm{c}\boldsymbol{u}_\mathrm{c}^2}{2} + \varepsilon_\mathrm{th,c} + \frac{\boldsymbol{B}_\mathrm{c}^2}{2a} \tag{5.115}$$

while the total comoving pressure is:

$$P_\mathrm{tot,c} = P_\mathrm{th,c} + \frac{\boldsymbol{B}_\mathrm{c}^2}{2a} + \frac{1}{a}P_\mathrm{cr,c} + \frac{1}{a^{3/2}}\left(P_\mathrm{a,+} + P_\mathrm{a,-}\right). \tag{5.116}$$

With those definitions the continuity equation can be written as

$$\frac{\partial \rho_\mathrm{c}}{\partial t} + \frac{1}{a}\boldsymbol{\nabla}_{\boldsymbol{x}} \cdot (\rho_\mathrm{c}\boldsymbol{u}_\mathrm{c}) = 0, \tag{5.117}$$

where $\nabla_{\boldsymbol{x}}$ is the gradient with respect to the comoving coordinate $\boldsymbol{x}$. Euler's equation takes the form:

$$\begin{aligned}\frac{\partial(a\rho_\mathrm{c}\boldsymbol{u}_\mathrm{c})}{\partial t} + \frac{1}{a}\boldsymbol{\nabla}_{\boldsymbol{x}} \cdot \left[a\left(\rho_\mathrm{c}\boldsymbol{u}_\mathrm{c}\boldsymbol{u}_\mathrm{c} + P_\mathrm{tot,c}\mathbf{1} - \frac{1}{a}\boldsymbol{B}_\mathrm{c}\boldsymbol{B}_\mathrm{c}\right)\right] = \\ + \frac{1}{a}\boldsymbol{b}_\mathrm{c}\boldsymbol{\nabla}_{\boldsymbol{x},\parallel}P_\mathrm{cr,c} + a^4\left(\boldsymbol{g}_\mathrm{gri,+} + \boldsymbol{g}_\mathrm{gri,-}\right),\end{aligned} \tag{5.118}$$

where $\boldsymbol{\nabla}_{\boldsymbol{x},\parallel} = \boldsymbol{b}_\mathrm{c} \cdot \nabla_{\boldsymbol{x}}$ is the gradient in comoving coordinates projected onto the direction of the magnetic field $\boldsymbol{b}_\mathrm{c} = \boldsymbol{B}_\mathrm{c}/B_\mathrm{c}$. The comoving magnetic field is evolved using Faraday's law:

$$\frac{\partial \boldsymbol{B}_\mathrm{c}}{\partial t} + \frac{1}{a}\boldsymbol{\nabla}_{\boldsymbol{x}} \cdot [\boldsymbol{B}_\mathrm{c}\boldsymbol{u}_\mathrm{c} - \boldsymbol{u}_\mathrm{c}\boldsymbol{B}_\mathrm{c}] = \boldsymbol{0}. \tag{5.119}$$

Using the Hubble function $H = \dot{a}/a$, the MHD energy equation can be written as:

$$\begin{aligned}\frac{\partial (a^2\varepsilon_\mathrm{c})}{\partial t} + \frac{1}{a}\boldsymbol{\nabla}_{\boldsymbol{x}} \cdot \left\{ a^2 \left[\boldsymbol{u}_\mathrm{c}(\varepsilon_\mathrm{c} + P_\mathrm{tot,c}) - \frac{1}{a}(\boldsymbol{u}_\mathrm{c} \cdot \boldsymbol{B}_\mathrm{c})\boldsymbol{B}_\mathrm{c} \right] \right\} = \\ + \left(P_\mathrm{cr,c} + \frac{1}{a^{1/2}} P_\mathrm{a,+,c} + \frac{1}{a^{1/2}} P_\mathrm{a,-,c} \right) \boldsymbol{\nabla}_{\boldsymbol{x}} \cdot \boldsymbol{u}_\mathrm{c} \\ + \boldsymbol{u}_\mathrm{c} \cdot \left[a^2 \boldsymbol{b}_\mathrm{c} \boldsymbol{\nabla}_{\boldsymbol{x},\parallel} P_\mathrm{cr,c} + a^5 \left(\boldsymbol{g}_\mathrm{gri,+} + \boldsymbol{g}_\mathrm{gri,-} \right) \right] \\ - a^5 Q_\pm + \frac{aH}{2}\boldsymbol{B}_\mathrm{c}^2,\end{aligned} \tag{5.120}$$

while the CR energy equation becomes (assuming $\gamma_\mathrm{cr} = 4/3$):

$$\begin{aligned}\frac{\partial \varepsilon_\mathrm{cr,c}}{\partial t} + \frac{1}{a}\boldsymbol{\nabla}_{\boldsymbol{x}} \cdot [\boldsymbol{u}_\mathrm{c}\varepsilon_\mathrm{cr,c} + \boldsymbol{b}_\mathrm{c} f_\mathrm{cr,c}] = -P_\mathrm{cr,c}\frac{1}{a}\boldsymbol{\nabla}_{\boldsymbol{x}} \cdot \boldsymbol{u}_\mathrm{c} \\ - a^4 v_\mathrm{a} \boldsymbol{b}_\mathrm{c} \cdot \left(\boldsymbol{g}_\mathrm{gri,+} - \boldsymbol{g}_\mathrm{gri,-} \right).\end{aligned} \tag{5.121}$$

The CR energy flux equations in comoving coordinates is:

$$\begin{aligned}\frac{\partial f_\mathrm{cr,c}}{\partial t} + \frac{1}{a}\boldsymbol{\nabla}_{\boldsymbol{x}} \cdot [\boldsymbol{u}_\mathrm{c} f_\mathrm{cr,c}] + \frac{c^2}{a}\boldsymbol{\nabla}_{\boldsymbol{x},\parallel} P_\mathrm{cr,c} = \\ - \frac{1}{a} f_\mathrm{cr,c}(\boldsymbol{b}_\mathrm{c}\boldsymbol{b}_\mathrm{c}) : \boldsymbol{\nabla}_{\boldsymbol{x}}\boldsymbol{u}_\mathrm{c} - a^4 c^2 \boldsymbol{b}_\mathrm{c} \cdot \left(\boldsymbol{g}_\mathrm{gri,+} + \boldsymbol{g}_\mathrm{gri,-} \right).\end{aligned} \tag{5.122}$$

Finally, the equation for the energy contained in gyroresonant Alfvén waves is given by:

$$\begin{aligned}\frac{\partial \varepsilon_\mathrm{a,\pm,c}}{\partial t} + \frac{1}{a}\boldsymbol{\nabla}_{\boldsymbol{x}} \cdot [\boldsymbol{u}_\mathrm{c}\varepsilon_\mathrm{a,\pm,c} \pm v_\mathrm{a}\boldsymbol{b}\varepsilon_\mathrm{a,\pm,c}] = \\ - P_\mathrm{a,\pm,c}\frac{1}{a}\boldsymbol{\nabla}_{\boldsymbol{x}} \cdot \boldsymbol{u}_\mathrm{c} + a^{9/2}\left(\pm v_\mathrm{a}\boldsymbol{b} \cdot \boldsymbol{g}_\mathrm{gri,\pm} - Q_\pm \right).\end{aligned} \tag{5.123}$$

We use the Alfvén speed with the variables $\boldsymbol{B}$ and ρ instead of their comoving counterparts because it simplifies the equation above. The Alfvén speed can be conveniently calculated using the comoving variables via

$$v_\mathrm{a} = B_\mathrm{c}\rho_\mathrm{c}^{-1/2}a^{-1/2}. \tag{5.124}$$

These equations reduce to Eqs. (5.1) to (5.7) in the case of a static universe, i.e. when $a = 1$ and $H = 0$.

5.7 Appendix: Path-Conservative Schemes

In this appendix we provide a short introduction to path-conservative schemes. Because path-conservative schemes share many properties and generalise Godunov-type finite-volume schemes for conservation laws, we first recall the derivation of the latter to explain the former.

The solution to the one-dimensional conservation law

$$\frac{\partial \boldsymbol{U}}{\partial t} + \frac{\partial \boldsymbol{F}(\boldsymbol{U})}{\partial x} = \boldsymbol{0} \tag{5.125}$$

is described in the finite volume framework using cell averages $\ldots, \boldsymbol{U}_{i-1}, \boldsymbol{U}_i, \boldsymbol{U}_{i+1}, \ldots$ of the state vector $\boldsymbol{U}$. The time evolution of those is described by

$$\boldsymbol{0} = \frac{\mathrm{d}\boldsymbol{U}_i}{\mathrm{d}t} + \frac{1}{\Delta x}\int_i \mathrm{d}x \frac{\partial \boldsymbol{F}}{\partial x}, \tag{5.126}$$

$$= \frac{\mathrm{d}\boldsymbol{U}_i}{\mathrm{d}t} + \frac{1}{\Delta x}\left(\boldsymbol{F}_{*,i+1/2} - \boldsymbol{F}_{*,i-1/2}\right), \tag{5.127}$$

where we used the divergence theorem to evaluate the integral and $\boldsymbol{F}_{*,i\pm1/2}$ are the fluxes evaluated at the interfaces $i \pm 1/2$. Let us concentrate the discussion on one of those interfaces. At the interface itself the state vector may be discontinuous and may have different values to its left and right side denoted by $\boldsymbol{U}_{L,R}$. Formally, this situation is similar to the initial conditions of a Riemann problem that is centred on the interface. Riemann solvers calculate a full or approximate solution to the Riemann problem to obtain the value for the flux $\boldsymbol{F}_*$ through this interface using the given information. One of the most popular and simplest Riemann solvers is the HLLE Riemann solver (Harten et al., 1983). This Riemann solver approximates the solution to the Riemann problem with a single constant intermediate state $\boldsymbol{U}_*$. The region where $\boldsymbol{U}_*$ is realized is separated from the $\boldsymbol{U}_{L,R}$ regions by one left- and one rightwards travelling discontinuity. We denote the speed of those discontinuities by S_L and S_R, respectively. The intermediate state $\boldsymbol{U}_*$ can be calculated using the Rankine-Hugoniot jump conditions for these discontinuities:

$$S_L(\boldsymbol{U}_* - \boldsymbol{U}_L) = \boldsymbol{F}_* - \boldsymbol{F}_L \tag{5.128}$$

$$S_R(\boldsymbol{U}_* - \boldsymbol{U}_R) = \boldsymbol{F}_* - \boldsymbol{F}_R. \tag{5.129}$$

Both equations can be readily solved for $\boldsymbol{U}_*$ and $\boldsymbol{F}_*$. A trivial modification of those equations is:

$$\boldsymbol{F}_* = \boldsymbol{F}_L + S_L(\boldsymbol{U}_* - \boldsymbol{U}_L) \tag{5.130}$$

$$= \boldsymbol{F}_R + S_R(\boldsymbol{U}_* - \boldsymbol{U}_R), \tag{5.131}$$

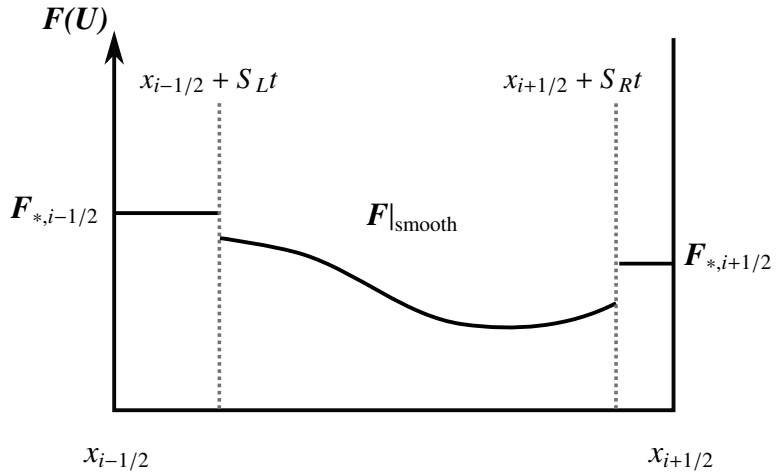

Figure 5.15: Structure of the flux $\boldsymbol{F}(x)$ inside the cell i that consists of a smooth inner part $\boldsymbol{F}|_{\text{smooth}}$ and two constant interface fluxes $\boldsymbol{F}_{*,i\pm1/2}$. Gray dashed lines represent characteristics that travel with S_L and S_R away from the interfaces.

which states that the HLL flux can be expressed in terms of left- or right-handed fluxes and states once $\boldsymbol{U}_*$ is known. Inserting Eqs. (5.130) and (5.131) into Eq. (5.127) gives:

$$\begin{aligned}\frac{\mathrm{d}\boldsymbol{U}^i}{\mathrm{d}t} &+ \frac{1}{\Delta x}\left(\boldsymbol{F}_{i,R} - \boldsymbol{F}_{i,L}\right) \\ &+ \frac{S_R}{\Delta x}\left(\boldsymbol{U}_{*,R} - \boldsymbol{U}_{i,R}\right) - \frac{S_L}{\Delta x}\left(\boldsymbol{U}_{*,L} - \boldsymbol{U}_{i,L}\right) = \boldsymbol{0}\end{aligned} \tag{5.132}$$

where we switched from the face-centred back to the cell-centred meaning of left (L) and right (R). This equation can be interpreted in a mathematical, distributional sense with the help of the integral form of the finite volume method in Eq. (5.126) and Fig. 5.15. In Fig. 5.15 we display $\boldsymbol{F}(x)$ inside the cell. At the cell interface the otherwise smooth flux jumps from its value 'inside' the cell to the HLL flux. The derivative of this profile inside the cell is given by:

$$\begin{aligned}\frac{\partial \boldsymbol{F}}{\partial x} = \left.\frac{\partial \boldsymbol{F}}{\partial x}\right|_{\text{smooth}} &+ \delta(x - x_{i+1/2} - S_R t)\, S_R \left(\boldsymbol{U}_{*,R} - \boldsymbol{U}_{i,R}\right) \\ &- \delta(x - x_{i-1/2} - S_L t)\, S_L \left(\boldsymbol{U}_{*,L} - \boldsymbol{U}_{i,L}\right),\end{aligned} \tag{5.133}$$

where the Dirac δ-distributions account for interface jumps, which result from the waves that travel from the interface into the cell. Inserting this expression into Eq. (5.126) and evaluating the integral at positive but infinitely small t yields Eq. (5.132). The first term can be interpreted as the contribution of the smooth component to the total flux while the last two terms are the singular contributions of the jumps of $\boldsymbol{F}$ at the cell interface.

Now, the finite volume method for non-conservative equations of the form

$$\frac{\partial \boldsymbol{U}}{\partial t} + \mathbf{H}\frac{\partial \boldsymbol{U}}{\partial x} = \boldsymbol{0} \tag{5.134}$$

reads in the finite volume framework as

$$\frac{\mathrm{d}\boldsymbol{U}_i}{\mathrm{d}t} + \frac{1}{\Delta x}\int_i \mathrm{d}x\, \mathbf{H}\frac{\partial \boldsymbol{U}}{\partial x} = \mathbf{0}. \tag{5.135}$$

The divergence theorem cannot be applied directly and above's methods for conservation laws cannot be used without modification. The central idea of how to solve this integral with path-conservative schemes is to impose a strict analogy in each discretisation and calculation step to conservative equations despite their formal differences. A justification for this procedure is that the path-conservative scheme should reduce to an ordinary Godunov-scheme for $\mathbf{H} = \partial_{\boldsymbol{U}}\boldsymbol{F}$, i.e., when the non-conservative equation coincides with a conservation law.

We assume that $\partial_x \boldsymbol{U}$ has the same functional form as $\partial_x \boldsymbol{F}$ in Eq. (5.133), namely, that it is composed of an inner smooth gradient and singular contributions travelling away from the interfaces. If we adopt a linear approximation for $\boldsymbol{U}$ inside the cell then the integral can be easily solved to yield the path-conservative scheme for Eq. (5.134):

$$\begin{aligned}\frac{\mathrm{d}\boldsymbol{U}_i}{\mathrm{d}t} + \mathbf{H}_i \left.\frac{\partial \boldsymbol{U}}{\partial x}\right|_{\text{smooth}} \\ + \frac{S_R}{\Delta x}\left(\boldsymbol{U}_{*,R} - \boldsymbol{U}_{i,R}\right) - \frac{S_L}{\Delta x}\left(\boldsymbol{U}_{*,L} - \boldsymbol{U}_{i,L}\right) = \mathbf{0},\end{aligned} \tag{5.136}$$

where $\mathbf{H}_i$ is the cell-average of $\mathbf{H}$. It is sufficient to use the midpoint value $\mathbf{H}_i$ for $\mathbf{H}(x)$ and the gradient of $\boldsymbol{U}$ as calculated via the standard piecewise-linear approximation to get an $O(\Delta x^2)$ accurate scheme. The singular contributions are the principle components of path conservative schemes that allow for stable and shock-capturing numerical simulations. We define

$$\boldsymbol{D}_L = S_L(\boldsymbol{U}_L - \boldsymbol{U}_*), \tag{5.137}$$

$$\boldsymbol{D}_R = S_R(\boldsymbol{U}_R - \boldsymbol{U}_*), \tag{5.138}$$

and call the $\boldsymbol{D}_{L,R}$ linear fluctuations. With this definition the path-conservative scheme reduces to

$$\begin{aligned}\frac{\mathrm{d}\boldsymbol{U}_i}{\mathrm{d}t} + \mathbf{H}_i \left.\frac{\partial \boldsymbol{U}}{\partial x}\right|_{\text{smooth}} \\ + \frac{1}{\Delta x}\left(\boldsymbol{D}_{i+1/2,L} - \boldsymbol{D}_{i-1/2,R}\right) = \mathbf{0},\end{aligned} \tag{5.139}$$

which is the one-dimensional form of the more general Eq.(5.36).

The fluctuation terms are still unspecified as we do not have an expression for $\boldsymbol{U}_*$. In the case of conservation laws we use Rankine-Hugoniot jump conditions at the cell interface to calculate $\boldsymbol{U}_*$. These jump conditions are not applicable for non-conservative equations. Yet, a

permitted generalization for the jump conditions is presented in Dal Maso et al. (1995). These conditions read for our case:

$$S_L(\boldsymbol{U}_* - \boldsymbol{U}_L) = \int_0^1 \mathrm{d}s\, \mathbf{H}(\boldsymbol{U}_L(s)) \frac{\partial \boldsymbol{U}_L(s)}{\partial s}, \tag{5.140}$$

$$S_R(\boldsymbol{U}_* - \boldsymbol{U}_R) = \int_0^1 \mathrm{d}s\, \mathbf{H}(\boldsymbol{U}_R(s)) \frac{\partial \boldsymbol{U}_R(s)}{\partial s}, \tag{5.141}$$

where $\boldsymbol{U}_{L,R}(s)$ with $s \in [0, 1]$ are *paths* connecting all states at the interface. We impose boundary conditions for these paths with

$$\boldsymbol{U}_L(0) = \boldsymbol{U}_L \text{ and } \boldsymbol{U}_L(1) = \boldsymbol{U}_*, \tag{5.142}$$

$$\boldsymbol{U}_R(0) = \boldsymbol{U}_R \text{ and } \boldsymbol{U}_R(1) = \boldsymbol{U}_*. \tag{5.143}$$

These jump conditions are true generalisations as they reduce to the usual Rankine-Hugoniot conditions for $\mathbf{H} = \partial_{\boldsymbol{U}} \boldsymbol{F}$. In this case both integrals can be solved independently of the chosen path. The results are the usual jump conditions for conservation laws in Eqs. (5.130) and (5.131). The required consistency between conservative and non-conservative schemes is achieved.

For a path-conservative scheme to converge, almost arbitrary paths can be chosen. However, the realised numerical solutions for different paths will differ at shocks. The choice of a path dictates the jump conditions and thus the solution at the shock (Parés and Muñoz-Ruiz, 2009). A well-motivated path can be chosen if the underlying physical model can be expanded to include physical viscosity. The paths describing the solutions in the inviscid case can then be calculated as the limit of vanishing viscosity of a steady state solution of the viscous equation. The construction of those paths is cumbersome and rarely carried out. A more simplistic yet tractable choice is to assume linear paths:

$$\boldsymbol{U}_L(s) = \boldsymbol{U}_L + (\boldsymbol{U}_* - \boldsymbol{U}_L)\, s, \tag{5.144}$$

$$\boldsymbol{U}_R(s) = \boldsymbol{U}_R + (\boldsymbol{U}_* - \boldsymbol{U}_R)\, s. \tag{5.145}$$

For those paths the generalised Rankine-Hugoniot jump conditions read:

$$S_L(\boldsymbol{U}_* - \boldsymbol{U}_L) = \mathbf{H}_L(\boldsymbol{U}_* - \boldsymbol{U}_L), \tag{5.146}$$

$$S_R(\boldsymbol{U}_* - \boldsymbol{U}_R) = \mathbf{H}_R(\boldsymbol{U}_* - \boldsymbol{U}_R), \tag{5.147}$$

where

$$\mathbf{H}_L = \int_0^1 \mathrm{d}s\, \mathbf{H}(\boldsymbol{U}_R(s)), \tag{5.148}$$

$$\mathbf{H}_R = \int_0^1 \mathrm{d}s\, \mathbf{H}(\boldsymbol{U}_L(s)). \tag{5.149}$$

Note that also here, the intermediate state $\boldsymbol{U}_*$ implicitly enters these equations through $\boldsymbol{U}_{L,R}(s)$. An iterative procedure to calculate $\boldsymbol{U}_*$ based on the Newton-Raphson method is proposed in Dumbser and Balsara (2016).

We apply the path-conservative scheme to model the transport of CRs along the magnetic field. In this case the fastest wave at any given interface is the light-like wave that travels with velocity $\sim c/\sqrt{3}(\boldsymbol{b}\cdot\boldsymbol{n})$, where $\boldsymbol{n}$ is the interface normal. The magnitude of this velocity hardly differs between the left and right states and both values can be assumed to be equal. We continue by assuming that S_L and S_R have the same magnitude but different signs, i.e.

$$S_L = -S, \tag{5.150}$$

$$S_R = +S, \tag{5.151}$$

where S is given by Eq. (5.46). In this case, the solution for $\boldsymbol{U}_*$ is given by:

$$\begin{aligned}\boldsymbol{U}_* = \frac{\boldsymbol{U}_L + \boldsymbol{U}_R}{2} + \frac{\mathbf{H}_R}{2S}(\boldsymbol{U}_* - \boldsymbol{U}_R) \\ - \frac{\mathbf{H}_L}{2S}(\boldsymbol{U}_* - \boldsymbol{U}_L).\end{aligned} \tag{5.152}$$

The expression for $f^*_{\rm cr}$ in Eq. (5.41) is derived using this equation. For our application, $\mathbf{H}$ only depends on the direction of the magnetic field. For our assumed operator-splitting, this is a constant during the parallel transport step. Thus we can readily calculate the $\mathbf{H}_L$ and $\mathbf{H}_R$ without any iterative solution. The expression for b_L and b_R in Eqs. (5.42) and (5.43) are $\mathbf{H}_L$ and $\mathbf{H}_R$ terms evaluated for $f_{\rm cr}$. They can be derived by solving the corresponding integrals assuming that

$$(\boldsymbol{b}\cdot\boldsymbol{n})_* = \frac{1}{2}\left[(\boldsymbol{b}\cdot\boldsymbol{n})_L + (\boldsymbol{b}\cdot\boldsymbol{n})_R\right]. \tag{5.153}$$

5.8 Appendix: ODE-integrator Convergence Proofs

Numerical solutions of an ordinary differential equation (ODE) converge to an analytical solution provided the integrator satisfies the *consistency conditions* for the ODE. The consistency conditions are derived by Taylor expanding $\boldsymbol{U}^{n+1} = \boldsymbol{U}(t^n + \Delta t)$ for small Δt and by subsequently substituting derivatives by the ODE itself. The consistency conditions up to third-order in Δt of the ODE in Eq. (5.56) read:

$$\boldsymbol{U}^{n+1} = \left[\mathbf{1} + \Delta t\mathbf{R} + \frac{\Delta t^2}{2}\left(\mathbf{R}^2 + \mathbf{R}_U\mathbf{R}\boldsymbol{U}^n\right) + O\left(\Delta t^3\right)\right]\boldsymbol{U}^n, \tag{5.154}$$

where $\mathbf{R} = \mathbf{R}(\boldsymbol{U}^n)$ and $\mathbf{R}_{\boldsymbol{U}} = \mathrm{grad}_{\boldsymbol{U}}\mathbf{R}(\boldsymbol{U}^n)$. We prove that our integrator in Eqs. (5.61) to (5.64) fulfils the consistency conditions by Taylor expanding every integrator stage for small Δt. We obtain for the stared stage:

$$\begin{aligned}\boldsymbol{U}^* &= [\mathbf{1} - \gamma\Delta t\mathbf{R}(\boldsymbol{U}^r)]^{-1}\boldsymbol{U}^n \\ &= \left[\mathbf{1} + \gamma\Delta t\mathbf{R}(\boldsymbol{U}^r) + \gamma^2\frac{\Delta t^2}{2}\mathbf{R}_r^2 + \mathcal{O}\left(\Delta t^3\right)\right]\boldsymbol{U}^n,\end{aligned} \tag{5.155}$$

while the result for the final stage is:

$$\begin{aligned}\boldsymbol{U}^{n+1} &= [\mathbf{1} - \gamma\Delta t\mathbf{R}(\boldsymbol{U}^r)]^{-1}\left[\boldsymbol{U}^n + (1-\gamma)\boldsymbol{U}^*\right] \\ &= [\mathbf{1} - \gamma\Delta t\mathbf{R}(\boldsymbol{U}^r)]^{-2}\left[\mathbf{1} + (1-2\gamma)\Delta t\mathbf{R}(\boldsymbol{U}^r)\right]\boldsymbol{U}^n \\ &= \left[\mathbf{1} + \Delta t\mathbf{R}(\boldsymbol{U}^r) + \left(2\gamma - \gamma^2\right)\Delta t^2\mathbf{R}(\boldsymbol{U}^r)^2 + \mathcal{O}\left(\Delta t^3\right)\right]\boldsymbol{U}^n.\end{aligned} \tag{5.156}$$

It is sufficient to expand the predicted rate matrix $\mathbf{R}(\boldsymbol{U}^r)$ up to $\mathcal{O}\left(\Delta t^2\right)$ to reach the desired overall third-order accuracy because it always enters Eqs. (5.156) and (5.155) together with an additional factor of Δt. We get:

$$\begin{aligned}\mathbf{R}(\boldsymbol{U}^r) &= \mathbf{R}\left(\boldsymbol{U}^n + \frac{\Delta t}{2}\mathbf{R}\boldsymbol{U}^p\right) \\ &= \mathbf{R}\left(\boldsymbol{U}^n + \frac{\Delta t}{2}\mathbf{R}\boldsymbol{U}^n + \mathcal{O}(\Delta t^2)\right) \\ &= \mathbf{R} + \frac{\Delta t}{2}\mathbf{R}_{\boldsymbol{U}}\mathbf{R}\boldsymbol{U}^n + \mathcal{O}\left(\Delta t^2\right).\end{aligned} \tag{5.157}$$

We conclude that the integrator is second-order consistent if and only if

$$\gamma_\pm = 1 \pm \frac{1}{\sqrt{2}} \tag{5.158}$$

after substituting Eq. (5.157) into Eq. (5.156) and comparing the result to Eq. (5.154). We discarded the '+'-solution because in this case the star stage would predict a solution at $t^* = t^n + \gamma_+\Delta t > t^n + \Delta t$ which would limit the overall stability of the integrator.

We numerically test our integrator by applying it to the initial value problem:

$$\frac{\mathrm{d}y}{\mathrm{d}t} = y - y^2, \tag{5.159}$$

$$y(0) = 2, \tag{5.160}$$

which has the analytical solution:

$$y(t) = \frac{\exp(t)}{\left(\frac{1}{2} - 1\right) + \exp(t)}. \tag{5.161}$$

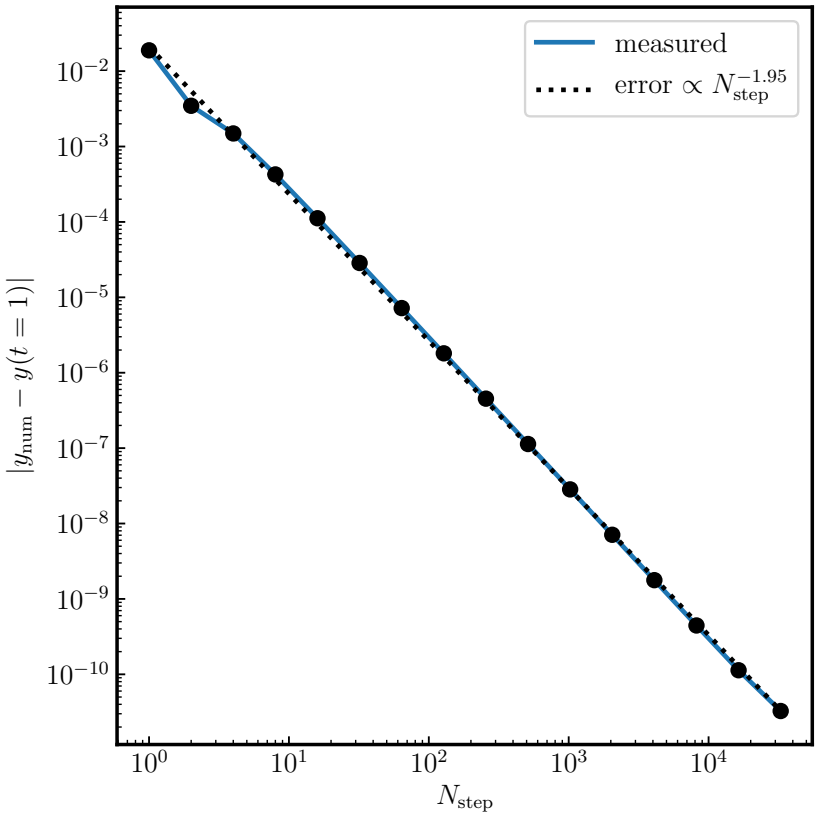

Figure 5.16: Convergence test for our ODE integrator applied to the initial value problem provided in Eq. (5.159). We display the absolute error of the numerical solution using a blue line and black dots for different $\Delta t = 1/N_{\mathrm{step}}$. The black dotted line shows a power law fit to these errors.

This differential equation is a scaled version of the equation for Alfvén wave energy density for fixed values of $\varepsilon_{\mathrm{cr}}$ and f_{cr}. The performance of the integrator for this reduced problem is thus indicative of its accuracy for the entire system of equations.

We numerically integrate y to $t = 1$ using $\Delta t = 1/N_{\mathrm{step}}$ and vary N_{step} from 1 to 32768. In Fig. 5.16 we show the absolute difference of the numerical solution and analytical solution of Eq. (5.161). The numerical errors behave slightly worse than expected and scale with $\Delta t^{1.95}$.

6 Cosmic Ray-Driven Galactic Winds: Transport Modes of Cosmic Rays and Alfvén-Wave Dark Regions

This chapter is based on a manuscript by Thomas, T. ; Pfrommer, C. ; Pakmor, R. and was submitted to the Monthly Notices of the Royal Astronomical Society.

Feedback mediated by cosmic rays (CRs) is an important process in galaxy formation. Because CRs are long-lived and because they are transported along magnetic field lines independently of any gas flow, they can efficiently distribute their feedback energy within the galaxy. We present an in-depth investigation of (i) how CRs launch galactic winds from a disc that is forming in a $10^{11}\mathrm{M}_{\odot}$ halo and (ii) how CR transport affects the dynamics in a galactic outflow. To this end, we use the Arepo moving-mesh code and model CR transport with the two-moment description of CR hydrodynamics. This model includes the CR interaction with gyroresonant Alfvén waves that enables us to self-consistently calculate the CR diffusion coefficient and CR transport speeds based on coarse-grained models for plasma physical effects. This delivers insight into key questions such as whether the effective CR transport is streaming-like or diffusive-like, how the CR diffusion coefficient and transport speed change inside the circumgalactic medium (CGM), and to what degree the two-moment approximation is needed to faithfully capture these effects. We find that the CR-diffusion coefficient reaches a steady-state in most environments with the notable exception of our newly discovered Alfvén-wave dark regions where the toroidal wind magnetic field is nearly perpendicular to the CR pressure gradient so that CRs are unable to excite gyroresonant Alfvén waves. However, CR transport itself cannot reach a steady-state and is not well described by either the CR streaming paradigm, the CR diffusion paradigm or a combination of both.

6.1 Introduction

CRs are charged particles that reach from non-relativistic to fully relativistic energies and span more than twelve orders of magnitude in energy. They constitute an important component inside the interstellar medium (ISM) because their energy density is comparable to that provided by turbulence, thermal pressure or magnetic pressure, respectively (Boulares and Cox, 1990; Cox, 2005; Naab and Ostriker, 2017). This already implies that CRs can impact the dynamics of the ISM in a significant way. CRs with energies $\gtrsim$ GeV are nearly collisionless and interact with their environment by scattering off of gyroresonant electro-magnetic waves (Schlickeiser, 2002), which couples CRs to the thermal plasma and enables them to exchange momentum and energy.

Indeed, because of their ability to accelerate gas, CRs can launch, shape or alter galactic winds that influence the evolution of a galaxy (Uhlig et al., 2012; Pakmor et al., 2016b; Ruszkowski et al., 2017; Girichidis et al., 2018; Farber et al., 2018; Jacob et al., 2018; Butsky and Quinn, 2018; Dashyan and Dubois, 2020; Quataert et al., 2022b; Farcy et al., 2022). Equally important, CRs with approximately MeV energies that pervade the neutral gaseous phase of the ISM provide an important channel of ionisation contributing significantly to the molecular chemistry of the ISM (Dalgarno, 2006; Padovani et al., 2020). After they are expelled into the CGM, CRs build up a pressure support against infalling gas whilst maintaining galactic outflows (Salem et al., 2016; Buck et al., 2020; Li et al., 2020). Models that account for CR acceleration within the jets of an active galactic nucleus (AGN) show a modified jet morphology and distribute the AGN feedback energy differently into the intracluster medium of the central regions of the cool core cluster (Jacob and Pfrommer, 2017b; Yang et al., 2019; Ehlert et al., 2018). High-energy CR ions are able to participate in hadronic interactions with the ambient gas, which produces e.g., gamma rays and radio-emitting electrons and positrons. Hence, improving our understanding of the spatial CR distribution is crucial for interpreting observations (Evoli et al., 2008; Gabici, 2009; Werhahn et al., 2021b,c,a).

Owing to their quasi-collisionless nature, CRs show a distinct transport behaviour in every medium they are pervading. Magnetic fields are mainly mediating the dynamics and the transport of CRs. CR protons with GeV energies dominate the total energy budget of the CR population and interact with the magnetic field in the following way: (i) CRs propagate along the large-scale magnetic field because the CR gyroradius is small compared to typical astrophysical scales in galaxies and in the ISM (Zweibel, 2013, 2017; Hanasz et al., 2021), (ii) CRs interact with magnetic fluctuations of the turbulent cascade through resonant and non-resonant interactions (Yan and Lazarian, 2004, 2011; Lazarian and Xu, 2022), and (iii) CRs themselves

can drive small-scale magnetic perturbations by means of plasma physical processes and then interact with those magnetic fluctuations later on (Kulsrud and Pearce, 1969; Shalaby et al., 2021, 2022).

Modelling CR dynamics is a difficult task because of the myriad of contributing physical processes, the large range of CR energies, and the large separation between length- and time-scales relevant for CRs and the astrophysical environment of interest. With the first advent of hydrodynamical theories for CR transport it was possible to show that CRs are able to drive galactic winds and can influence the structure of shocks (Ipavich, 1975; Drury and Falle, 1986; Breitschwerdt et al., 1991; Dorfi and Breitschwerdt, 2012). These hydrodynamical theories use a 'one-moment' approximation for CR transport where the CR energy or number density is the only quantity that describes the entire CR population. These one-moment descriptions are frequently and successfully used in many applications. CR transport along magnetic fields in this approximation can be categorised using the CR diffusion or CR streaming pictures (Wiener et al., 2013, 2017b). If CRs are streaming, their interactions and momentum exchange with small-scale magnetic perturbations are sufficiently frequent so that the CRs are effectively co-moving with the magnetic perturbations – in the case of CRs scattering with Alfvén waves, the CRs population travels with the Alfvén speed. If scattering is less frequent, then CRs are not well coupled to magnetic perturbations and perform a random walk along magnetic field lines, which results in CR diffusion (Skilling, 1971).

While the numerical modelling of CR diffusion is possible with only few modifications to standard numerical schemes, integrating CR streaming poses a challenge (Sharma et al., 2009; Sharma and Hammett, 2011). The requirement of a stable and accurate numerical scheme that is able to integrate the CR streaming equation resulted in the development of a second generation of hydrodynamical theories for CR transport that employ a two-moment approximation (Jiang and Oh, 2018; Thomas and Pfrommer, 2019). Therein, the momentum or flux density of CRs is additionally taken into account and provides a second moment of the CR population. This approach supersedes the previous one-moment description of CR transport as it does not any more rely on a predefined paradigm such as CR streaming or diffusion, but instead allows the emerging CR dynamics to freely adjust to changes, depending on the environmental properties. It is possible to improve the fidelity of spatial CR transport further by including higher-order moments but Thomas and Pfrommer (2022) showed that if scattering by magnetic perturbations is the dominant driver of CR transport, the two-moment description is sufficiently accurate in describing the resulting dynamics.

In Thomas et al. (2020) the authors show that the combined CR streaming and diffusion

transport model provided by a two-moment approximation, is in fact required to match the observed CR distribution of a class of non-thermal (radio harp) filaments located in the central molecular zone of our Galaxy that have been observed by the MeerKAT radio telescope (Heywood et al., 2022). A shortcoming of these two-moment hydrodynamical descriptions is their marginalisation over the entire CR energy spectrum so that they only provide a "grey" picture of CR hydrodynamics (CRHD). This neglects inherent differences between CR transport at different energies and different cooling processes acting on different parts of the CR energy spectrum. Transport descriptions that resolve the CR spectrum have been derived (Girichidis et al., 2020; Ogrodnik et al., 2021; Hopkins et al., 2022) and show that e.g., galactic winds are launched differently in models employing either a grey or an energy-resolved description of CR transport (Girichidis et al., 2022).

In this work we use the grey two-moment method for CRHD of Thomas and Pfrommer (2019) that accounts for the CR interaction with self-generated Alfvén waves and evolves the energy densities of those Alfvén waves in addition to the energy and flux densities of CRs. The entire hydrodynamic subsystem of CR and Alfvén-wave equations is coupled to the thermal gas, which is described by the equations of magneto-hydrodynamics (MHD). We apply this model in the context of a CR-driven outflow of a disc galaxy, which forms inside a $M_{200} = 10^{11}\mathrm{M}_{\odot}$ halo. We focus our discussion on how CRs and the galactic wind influence each other by examining (i) the exact wind launching mechanism that the CRs provide at the disc-halo interface and (ii) how CRs are transported in terms of their diffusion coefficients and realised streaming speeds. We demonstrate that neither CR diffusion nor CR streaming are appropriate descriptions for the resulting transport in our simulation. In addition, we study a new phenomenon called "Alfvén wave dark regions" within the galactic wind, which describes regions devoid of CR-generated Alfvén waves, and discuss the physical processes that lead to their formation.

Our paper is structured as follows. In Section 6.2 we briefly recall those aspects of the CRHD model of Thomas and Pfrommer (2019) and the resulting CR transport dynamics that are relevant for this work. In Section 6.3 we detail our simulation setup and the used numerical parameters. We devote Section 6.4 to a discussion of the properties and launching mechanism of a CR-driven galactic outflow. In Section 6.5, we investigate how CR energy is transported in the galactic outflow and study the emergent CR diffusion coefficient. Afterwards, we discuss the physical origin of Alfvén-wave dark regions in Section 6.6. We close this paper with a discussion of our results and possible caveats in Section 6.7 and present our conclusion in Section 6.8. We use the Heaviside-Lorentz system of units throughout this paper.

6.2 Primer on CR Hydrodynamics

In this section, we discuss aspects of CR hydrodynamics that will later on become important to understand the results of our simulation.

6.2.1 Reduced equations of CR hydrodynamics

Instead of recalling the full set of CR hydrodynamical equations, here we focus our discussion on the transport of CRs along the magnetic field direction as well as the source terms due to gyroresonant CR interactions with Alfvén waves and their prevalent damping process, and refer to Thomas and Pfrommer (2019) for a discussion of all aspects of CR hydrodynamics. Their two-moment description for CR hydrodynamics follows the dynamics of CRs in terms of the energy density $\varepsilon_{\rm cr}$, its energy flux $f_{\rm cr}$ and the energy densities $\varepsilon_{\rm a,\pm}$ of gyroresonant Alfvén waves. These waves interact via gyroresonant CR scatterings as a result of the Lorentz force that is induced by plasma-scale magnetic perturbations of gyroresonant Alfvén waves. In Thomas and Pfrommer (2019) we self-consistently account for these scattering processes in terms of those four hydrodynamical quantities. In deriving the fundamental equations, we use the quasi-linear theory for the CR-Alfvén wave interactions and couple the CR fluid to the underlying thermal gas in an MHD approximation. In reduced form, which is sufficient for our discussion, these equations read:

$$\begin{aligned}\frac{\partial \varepsilon_{\rm cr}}{\partial t} + \boldsymbol{\nabla}\cdot(f_{\rm cr}\boldsymbol{b}) &= -\frac{v_{\rm a}}{3\kappa_+}[f_{\rm cr} - v_{\rm a}(\varepsilon_{\rm cr}+P_{\rm cr})] \\ &\quad + \frac{v_{\rm a}}{3\kappa_-}[f_{\rm cr} + v_{\rm a}(\varepsilon_{\rm cr}+P_{\rm cr})] + \ldots, \qquad (6.1)\\ \frac{\partial f_{\rm cr}}{\partial t} + c_{\rm red}^2\boldsymbol{b}\cdot\boldsymbol{\nabla}P_{\rm cr} &= -\frac{c_{\rm red}^2}{3\kappa_+}[f_{\rm cr} - v_{\rm a}(\varepsilon_{\rm cr}+P_{\rm cr})] \\ &\quad - \frac{c_{\rm red}^2}{3\kappa_-}[f_{\rm cr} + v_{\rm a}(\varepsilon_{\rm cr}+P_{\rm cr})] + \ldots, \qquad (6.2)\\ \frac{\partial \varepsilon_{\rm a,+}}{\partial t} + \boldsymbol{\nabla}\cdot(\varepsilon_{\rm a,+}v_{\rm a}\boldsymbol{b}) &= +\frac{v_{\rm a}}{3\kappa_+}[f_{\rm cr} - v_{\rm a}(\varepsilon_{\rm cr}+P_{\rm cr})] \\ &\quad - \alpha\varepsilon_{\rm a,+}^2 + \ldots, \qquad (6.3)\\ \frac{\partial \varepsilon_{\rm a,-}}{\partial t} + \boldsymbol{\nabla}\cdot(\varepsilon_{\rm a,-}v_{\rm a}\boldsymbol{b}) &= -\frac{v_{\rm a}}{3\kappa_-}[f_{\rm cr} + v_{\rm a}(\varepsilon_{\rm cr}+P_{\rm cr})] \\ &\quad - \alpha\varepsilon_{\rm a,-}^2 + \ldots, \qquad (6.4)\end{aligned}$$

where we intentionally omit the (advective and adiabatic) terms responsible for transport of CRs and gyroresonant Alfvén waves with the flow of the underlying gas, which is symbolised by the dots.

The following quantities have been used: $\boldsymbol{b} = \boldsymbol{B}/B$ is the direction of the magnetic field $\boldsymbol{B}$, which has a field strength B, $v_\mathrm{a} = B/\sqrt{\rho}$ is the Alfvén speed supported by the MHD fluid with a mass density ρ, and c_red is the reduced speed of light, that is decreased from the physical value c because of numerical efficiency reasons. However, we require c_red to be much faster than the fastest MHD signal speed in the problem. The CR pressure is

$$P_\mathrm{cr} = (\gamma_\mathrm{cr} - 1)\varepsilon_\mathrm{cr} \qquad \text{where} \qquad \gamma_\mathrm{cr} = \frac{4}{3}, \tag{6.5}$$

and ε_cr denotes the CR energy density. The diffusion coefficients of CRs, $\kappa_\pm$, are defined by

$$\frac{1}{3\kappa_\pm} = \frac{3\pi}{8}\frac{eB}{\gamma mc^3}\frac{\varepsilon_{\mathrm{a},\pm}}{B^2}, \tag{6.6}$$

where e is the elementary charge and γ is the typical Lorentz factor of the CR protons of rest mass m. The diffusion coefficients are a measure for the coupling strength between CRs and gyroresonant Alfvén waves, and scale as $\kappa_\pm^{-1} \propto \nu_\pm \propto \varepsilon_{\mathrm{a},\pm}$, where $\nu_\pm$ is the CR particle-wave scattering rate. We also include non-linear Landau damping of Alfvén waves, which enters Eqs. (6.3) and (6.4) trough the terms $\alpha\varepsilon_{\mathrm{a},\pm}^2$. The coupling constant for this process is given by

$$\alpha = \frac{\sqrt{\pi}}{8B^2}\frac{2eB}{\gamma mc^2}\sqrt{\frac{P_\mathrm{th}}{\rho}}, \tag{6.7}$$

where P_th is the pressure of the thermal gas.

In Thomas and Pfrommer (2019), we assume that the CRs are an ultra-relativistic fluid, which creates an interesting relationship between the CR energy flux density f_cr and the mean momentum density of the CR population: because ultra-relativistic particles have energies $E = \gamma mc^2$ and momenta $p \simeq \gamma mc$, we can interpret f_cr/c^2 as the mean momentum density which simplifies the interpretation of our results.

6.2.2 CR pressure and inertia

We start by discussing the influence of the CR pressure term on the left-hand side of Eq. (6.2). Due to the correspondence between CR energy flux and CR momentum density, this pressure term corresponds to a force. It is not a body force acting on the CR particles but a collective effect affecting a population of CRs. In the context of ideal thermal gases, the thermodynamic pressure is sustained by the molecular motion of individual gas particles in combination with collisions between gas particles. These particle-particle collisions are negligible for CRs. Here, the CR pressure term is purely sustained by the inertia of CRs. This inertia can collectively induce macroscopic fluxes of CRs in situations where CRs have an inhomogeneous distribution

in space. We illustrate this with the following example: consider an isolated region of CRs without any initial CR flux. This situation can be realised by an equal amount of CRs travelling with and against the direction of the magnetic field. As CRs at both boundaries start to leave the region, this implies a non-zero flux of CRs outside the initial confinement region. In this scenario, there is no force acting on the CRs responsible for the resulting CR flux but simply the inertia of CRs in combination with an inhomogeneous CR distribution.

In our simulations this CR inertia acts as a jump-start for the CR dynamics: there are more CRs inside a galactic disc in comparison to its galactic halo, which implies a CR pressure gradient that increases toward the disc. Hence, more CRs travel from the galactic disc towards the halo along a magnetic field line rather than the opposite way. This creates an initial flux of CRs pointing from the galactic disc to the halo. Once this flux exceeds the Alfvén speed, CRs start to excite gyroresonant Alfvén waves and their mutual interaction becomes important as we will discuss now.

6.2.3 Gyroresonant interaction – gas acceleration

The gyroresonant interaction between CRs and small-scale Alfvén waves is described through the source terms on the right-hand sides of Eqs. (6.1) and (6.2). Microphysically, this process takes place if the gyromotion of CRs coincides with the gyration of the magnetic perturbation of small-scale Alfvén waves – hence this is a resonant process. To discuss how energy is transferred by this process, we focus on CR interactions with Alfvén waves that are propagating in the direction of the magnetic field. The first term on the right-hand side of Eq. (6.1) implies that if the velocity at which CR energy is transported,

$$v_{\rm cr} = \frac{f_{\rm cr}}{\varepsilon_{\rm cr} + P_{\rm cr}} \tag{6.8}$$

is larger in magnitude than the Alfvén speed, $v_{\rm cr} > v_{\rm a}$, and hence, is faster than Alfvén waves, CRs start to lose energy. As a result, the energy in forward travelling gyroresonant Alfvén waves increases at the same rate according to Eq. (6.3). The opposite process happens for $v_{\rm cr} < v_{\rm a}$, which implies CR energy gain by damping the energy contained in forward travelling gyroresonant Alfvén waves. The interaction between CRs and backward propagating Alfvén waves follows the same general idea. In summary, CRs lose energy to gyroresonant Alfvén waves by growing them once $|v_{\rm cr}| > v_{\rm a}$ and extract energy from them if $|v_{\rm cr}| < v_{\rm a}$.

The CR flux density $f_{\rm cr}$ changes during this process so that it is increased (or decreased) towards $f_{\rm cr} = \pm v_{\rm a}(\varepsilon_{\rm cr} + P_{\rm cr})$ or $v_{\rm cr} = \pm v_{\rm a}$ as described by the source terms on the right-hand sides of Eq. (6.2). This change corresponds to a mean force acting on the CR population because

$f_{\rm cr}$ is an equivalent measure for the mean CR momenta. This force needs to be balanced by an opposing force to ensure momentum conservation. Because Alfvén waves are supported by the thermal plasma and because they are the source of gyroresonant interactions, they mediate this opposing force to the thermal gas. It is this process that enables CRs to accelerate the gas. In case of super-alfvénic CRs with $v_{\rm cr} > v_{\rm a}$, the interaction with forward travelling gyroresonant Alfvén waves effectively decelerates CRs (reduces $v_{\rm cr}$ or $f_{\rm cr}$), which in turn accelerates the thermal gas in the direction of the magnetic field.

6.2.4 Damping of Alfvén waves – gas heating

CR-excited Alfvén waves can be damped by various processes such as collisionless non-linear Landau damping that we focus our attention on here. In this process two Alfvén waves with different wavenumbers non-linearly interact to create a beatwave, which in turn leads to small-scale pressure perturbations at the scale of the beatwave (Lee and Völk, 1973; Miller, 1991). This beatwave is subsequently Landau-damped and thus heats the gas. Thus, this process dissipates the energy contained in gyroresonant Alfvén waves by heating the underlying thermal gas. As CRs transfer energy to Alfvén waves and Alfvén waves dissipate their electromagnetic energy into heat, the combination of this damping process and the gyroresonant interaction opens up a channel for CRs to inject energy into their surrounding medium and to influence the thermodynamics therein.

6.2.5 Steady state CR transport

If the dynamical processes governing the transport of the CR fluid are sufficiently fast in comparison to any other relevant process, CR transport approaches a steady state which can be determined from Eq. (6.2) and which is characterised by the steady state flux:

$$f_{\rm cr,steady} = v_{\rm st}(\varepsilon_{\rm cr} + P_{\rm cr}) - \kappa \boldsymbol{b} \cdot \boldsymbol{\nabla} \varepsilon_{\rm cr}, \tag{6.9}$$

where

$$\kappa^{-1} = \kappa_+^{-1} + \kappa_-^{-1} \tag{6.10}$$

is the total diffusion coefficient and the CR streaming velocity is given by

$$v_{\rm st} = v_{\rm a} \frac{\kappa_+^{-1} - \kappa_-^{-1}}{\kappa_+^{-1} + \kappa_-^{-1}}. \tag{6.11}$$

Whether it is possible to establish this steady state depends on the initial CR flux or velocity: the CRs must be faster than Alfvén waves, $|v_{\rm cr}| > v_{\rm a}$ because only in this case, the CRs themselves are able to continuously drive gyroresonant Alfvén waves that are required to maintain frequent particle-wave scatterings and to eventually approach this steady state. In the other case, $|v_{\rm cr}| < v_{\rm a}$, the CRs damp gyroresonant Alfvén waves and diminish residual Alfvén wave energy, which reduces the scattering rate, and consequently increases the dynamical timescale of CRs. Because the Alfvén wave energy is drained exponentially fast, it is not possible to reach the steady state without an external source of gyroresonant Alfvén waves.

Provided CR energy is transported faster than Alfvén waves, $|v_{\rm cr}| > v_{\rm a}$, only one of the two types of gyroresonant Alfvén waves can be excited: because CRs are faster than one type of Alfvén waves, they are automatically slower than the other wave type. In this case $v_{\rm st} = \pm v_{\rm a}$ and the velocity difference between CRs and Alfvén waves in Eq. (6.9) is given by the diffusion term. The sign of this velocity difference determines which type of gyroresonant Alfvén wave is excited: e.g., if we assume $\boldsymbol{b}\cdot\boldsymbol{\nabla}P_{\rm cr} < 0$, then CR inertia accelerates the CR population so that they are faster than those Alfvén waves that propagate along the direction of the magnetic field, i.e., $v_{\rm cr} > v_{\rm a}$ and enables those waves to grow, implying $\varepsilon_{\rm a,+} \neq 0$ and $\kappa_+ < \infty$. For $\boldsymbol{b}\cdot\boldsymbol{\nabla}P_{\rm cr} > 0$, we obtain $\varepsilon_{\rm a,-} \neq 0$ and $\kappa_- < \infty$. If one of the wave types is being damped, only one diffusion coefficient is not infinite, and the expression in Eq. (6.11) simplifies to the negative sign of the CR energy gradient or

$$v_{\rm st,steady} = -v_{\rm a}\,\mathrm{sign}\left(\boldsymbol{b}\cdot\boldsymbol{\nabla}\varepsilon_{\rm cr}\right). \tag{6.12}$$

Thus, in steady state CRs preferentially "stream down their gradient".

6.3 Simulation Setup

We perform a CRHD simulation of an isolated disc galaxy with the moving-mesh code Arepo (Springel, 2010). The galaxy is initialized in a $M_{200} = 10^{11}\mathrm{M}_\odot$ halo with 10^6 equal-mass gas particles particles that are in hydrostatic equilibrium with the dark matter halo. The setup up is similar to those used in previous works (Pakmor et al., 2016b; Pfrommer et al., 2017c, 2021; Werhahn et al., 2021b). The dark matter halo is static and follows the analytic form of an NFW halo with concentration parameter $c = 7$ (Navarro et al., 1997). Using dark matter particles to simulate a dynamically evolving dark matter halo has little impact on the overall galaxy evolution in this setup (Jacob et al., 2018). Gas cells are initialised following the same spherically symmetric NFW profile with a baryon mass fraction of $\Omega_{\rm b}/\Omega_{\rm m} = 0.155$. Halo masses and

length scales are measured in units of $h^{-1}\mathrm{M}_\odot$ and h^{-1}kpc, where $H_0 = 100\,h$ km s^{-1} Mpc^{-1}is today's value of the Hubble constant. Initially, the gaseous halo slowly rotates with a total angular momentum of $J = \lambda G M_{200}^{5/2} / \sqrt{E_{200}}$ where G is Newton's constant, E_{200} is the energy contained in the system, defined by equation (22) in Mo et al. (1998), and $\lambda = 0.05$ is the dimensionless spin-parameter. The initial magnetic field is pointing along the x axis with a uniform magnetic field strength of 10^{-10}G. Neither CRs nor gyroresonant Alfvén waves are present in the initial conditions.

The equations of two-moment CRHD are discretised with the finite volume scheme as described in Thomas et al. (2021), which is an extension of the existing and well-tested CR and MHD modules of Arepo (Pakmor and Springel, 2013; Pfrommer et al., 2017a) and which uses the second-order time integrator and reconstruction algorithms of Pakmor et al. (2016c). The CRHD equations of Thomas et al. (2021) use the P1 Eddington approximation as the closure relation that was shown to provide robust and converged results in comparison to higher order closure schemes (Thomas and Pfrommer, 2022). Optically thin gas cooling, star formation, and the adopted effective equation of state used to model the ISM are described in Springel and Hernquist (2003).

CRs are accelerated at the shocks of supernova (SN) remnants and escape later into the ISM. In order to model this process, we inject CR energy

$$E_{\mathrm{CR,inj}} = \zeta e_{\mathrm{SN}} m_\star \tag{6.13}$$

into the neighbouring 32 ± 1 computational cells weighted with a spline kernel (as employed in smoothed particle hydrodynamics) instantaneously after a star particle with mass $m_\star$ was created. The parameter $\zeta = 0.05$ defines the fraction of kinetic SN energy that is converted into CR energy. The specific energy $e_{\mathrm{SN}} = 10^{49}\mathrm{erg}\,\mathrm{M}_\odot^{-1}$ is the approximate average energy that is released by core-collapse SNe per solar mass of newly formed stars assuming a Kroupa initial mass function and 10^{51}erg per supernova (Kroupa, 2001; Pfrommer et al., 2017a). Note that we do not directly inject thermal or kinetic SN energy into the ISM because this process is already modeled by the effective equation of state. In addition to CRs, SN shocks also amplify the magnetic field in their surroundings. Instabilities driven by CRs in the precursor of these shocks such as the Bell or smaller-scale instabilities (Bell, 2004; Shalaby et al., 2021, 2022) create small-scale turbulent magnetic fields that are able to scatter CRs. The creation of these magnetic fields can be described by a local gain of $\varepsilon_{\mathrm{a},\pm}$ around SN remnants. Because (i) the fraction of energy contained in the Alfvénic mode of MHD turbulence in those precursors and (ii) the fraction of Alfvén waves that are able to effectively escape the SNe site are two

unknowns, we inject a conservative amount of energy in gyroresonant Alfvén waves,

$$E_{\mathrm{a},+,\mathrm{inj}} = 10^{-5} E_{\mathrm{CR,inj}}, \quad \text{and} \tag{6.14}$$

$$E_{\mathrm{a},-,\mathrm{inj}} = 10^{-5} E_{\mathrm{CR,inj}} \tag{6.15}$$

together and in the same fashion as CRs for every newly created star particle.

Arepo provides the ability to refine and derefine computational cells based on arbitrary user-defined criteria. While the standard Lagrangian refinement scheme keeps the mass enclosed by a computational cell nearly constant, super-Lagrangian refinement schemes can be used to increase the resolution of the simulation in regions of interest (Suresh et al., 2019; Hummels et al., 2019; van de Voort et al., 2019). Here, we focus our attention on the dynamics and the launching of the galactic outflow and thus apply a super-Lagrangian refinement to gas cells situated in the (inner) CGM. We define the following mass and volume targets for computational cells:

- Cells should have a target mass $M_{\mathrm{cell,target}} = 1.55 \times 10^4 \mathrm{M}_\odot$,
- Cells at galactocentric radii $r < 60$ kpc should have a target volume $V_{\mathrm{cell,target}} = 4\pi r^3_{\mathrm{cell,target}}/3$ with a maximum equivalent radius $r_{\mathrm{cell,target}} = 600\mathrm{pc}$,
- Cells at galactocentric radii $r < 30$ kpc should have a maximum equivalent radius $r_{\mathrm{cell,target}} = 200\mathrm{pc}$,
- Cells at galactocentric radii $r < 2.5$ kpc should have a maximum equivalent radius $r_{\mathrm{cell,target}} = 50\mathrm{pc}$.

If either cell mass or volume do not match their target values within a factor of two, the cell is either refined or de-refined in order to again fulfil the criteria. Furthermore, to avoid large volume deviations of adjacent cells we refine a computational cell if one of its Voronoi neighbours has a 10 times smaller volume.

For the CR transport we use a reduced speed of light of $c_{\mathrm{red}} = 8000\ \mathrm{km\,s^{-1}}$ and subcycle the CR transport along the magnetic field lines 8 times for each invocation of the MHD solver. Because typical sound and Alfvén speeds reach at maximum of $1000\ \mathrm{km\,s^{-1}}$, our choice of the reduced speed of light leads to well separated light-like and MHD characteristics. CR cooling is implemented such that $f_{\mathrm{cr}}/\varepsilon_{\mathrm{cr}}$ and thus the effective CR transport velocity is kept constant during CR cooling. We use the CR Coulomb and hadronic cooling rates provided by Pfrommer et al. (2017a).

6.4 CR-driven Outflows

In this section, we first assess the general properties of CR driven outflows using our two-moment method of CRHD and then focus on the exact driving mechanism of the galactic wind in our simulation.

6.4.1 Outflow properties

The initial evolution of the simulation follows those of other simulations of isolated disc galaxies: the gas loses pressure support by radiative cooling and starts to fall towards the centre of the halo. While conserving the total angular momentum, a gaseous disc starts to form inside out. As the first gas cells start to exceed the star formation threshold, their gas mass is converted into star particles, which inject their feedback energy into their surroundings. Initially, there is no outflow for the first Gyr and the disc is only able to launch an bipolar galactic wind once the injected CR energy provides enough pressure in the central regions. This behaviour is similar to other simulations that use a collapsing gaseous halo setup, which are discussed in detail in previous works (Pakmor et al., 2016b; Pfrommer et al., 2017c; Jacob et al., 2018). In this section we discuss general properties of this outflow and the hydrodynamical processes that lead to its launching.

The emerging outflow is bipolar, has gas velocities $\sim$ 100 km s^{-1} and is launched in the central kpc of the galactic disc as can be inferred from Fig. 6.1 at t = 4 Gyr. The morphology of this outflow resembles the structure of AGN jets as it consist of an inner fast and underdense outflow (the spine in the AGN jet terminology) and an outer, slower-moving cylindrical shell that shears the stationary CGM at larger radii (the sheath in AGN jet terminology).

The inner outflow is generally characterised by a high Alfvén velocity that reaches $v_\mathrm{a} \sim$ 1000 km s^{-1} near the galactic plane. This high Alfvén velocity is due to the interplay of two processes: (i) the wind ejects gas from the galactic plane and carries along magnetic field lines which were amplified by the magnetic dynamo to high magnetic field strengths and (ii) the inner outflow has a low density. Both properties are required to explain the high Alfvén velocity in the inner outflow (bottom-right panel of Fig. 6.1) because the magnetic energy density and thus in the magnetic field strength does not show the spine-sheath structure and instead shows a smoothly declining strength in the CGM towards larger cylindrical radii (bottom-middle panel).

The inner wind also shows a depression in CR energy density (central panel of Fig. 6.1) and a slight enhancement of thermal energy density (top middle panel). The central outflow is dominated by thermal energy, which can be inferred from the map of $X_\mathrm{cr} = P_\mathrm{cr}/P_\mathrm{th}$ (centre

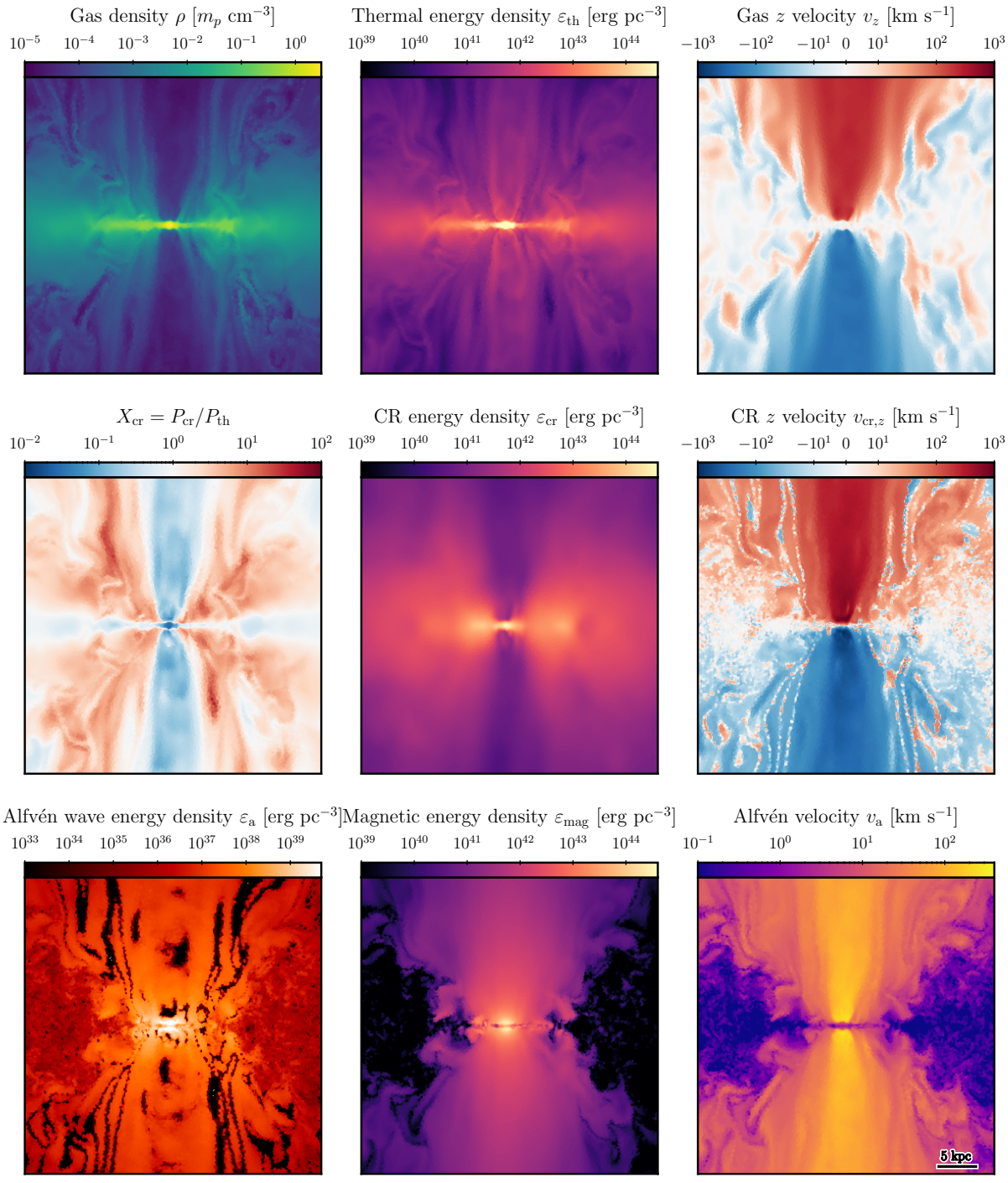

Figure 6.1: Gallery showing various quantities of the galactic outflow in quadratic slices with 40 kpc side length laying in the x–z plane centred on the centre of the simulation box at $t = 4$ Gyr. The panels for the thermal, CR, and magnetic energy densities share the same dynamic range while the panel for the Alfvén wave energy density uses a different scale.

right panel). This quantity prominently changes from $X_{\rm cr} > 1$ (CR pressure dominated) in the outer CGM to $X_{\rm cr} < 1$ in the inner outflow. CRs are generally transported away from the disc with speeds comparable to the Alfvén velocity, which is visible in the projected z component of the CR velocity defined by $v_{{\rm cr},z} = v_{\rm cr}\boldsymbol{b} \cdot \boldsymbol{e}_z$, where $\boldsymbol{e}_z$ is the unit vector pointing in z direction.

The outer wind is CR pressure dominated and has a more structured morphology in gas density, thermal and Alfvén wave energy densities, as well as in all three velocity variables shown in Fig. 6.1 (Alfvén velocity, z components of the gas and CR velocities, right column). The outermost boundary of the outflow is traced by the sharp transition in the CGM material that is enriched by magnetic fields with energy densities $\varepsilon_{\rm mag} \gtrsim 10^{40}$ erg pc^{-3} and CGM material that only shows spurious enhancements of the magnetic field strength. This transition region is also characterised by a patchy structure in the vertical component of the gas velocity: some of the gas is currently falling towards the disc while in other places, gas is moving away from the mid plane. Gas in the outer wind can shear in this transition region via Kelvin-Helmholtz type instabilities and mix with the rest of the CGM. As a result, this creates the more diverse morphology of the outer wind in comparison to the seemingly laminar inner outflow.

The bottom-left panel of Fig. 6.1 shows the total energy density contained in Alfvén waves, $\varepsilon_{\rm a} = \varepsilon_{{\rm a},+} + \varepsilon_{{\rm a},-}$. This quantity also follows the morphology of the wind: $\varepsilon_{\rm a}$ has high values (10^{39} erg pc^{-3}) immediately above and below the galactic disc, strongly decreases in the galactic outflow (10^{37} erg pc^{-3}) and attains its lowest values (10^{36} erg pc^{-3}) in the rest of the CGM. Furthermore, there are distinctive filamentary structures where $\varepsilon_{\rm a} \sim 0$ in isolated regions, so called "Alfvén-wave dark regions". While these regions are patchy within the inner wind, they are vertically elongated in the outer wind. These regions in the inner wind do not correlate with any other displayed quantity. By contrast, the elongated dark regions in the outer wind can also be found at places where the z-component of the CR velocity $v_{{\rm cr},z}$ changes sign. Because the wind is otherwise filled with Alfvén waves, the most likely reason for the absence of Alfvén wave in these regions are localised damping processes: the sign-reversal of $v_{{\rm cr},z}$ points towards low CR velocities themselves, indicating more slowly moving CRs in comparison to the fast Alfvén waves, which would then be effectively damped through the Fermi-II process. We further discuss the origin of these "Alfvén-wave dark regions" in Section 6.6.

6.4.2 Wind launching

The outflow is launched by CRs at the disc-halo interface. One of our super-Lagrangian refinement requirements imposes an upper limit on the effective cell radii of 50 pc to properly resolve this region in our simulation. The aim of such a high-resolution region is to ensure a large number of computational cells that provide a sufficiently good statistics to accurately investigate the wind launching mechanism. In Fig. 6.2, we display relevant quantities in slices of cylindrical region defined by $|z| < 3.5$ kpc and $R = \sqrt{x^2 + y^2} < 1$ kpc which encloses the wind launching site. In the top-left panel, we display the Alfvén and CR velocity (for energy transport), as well as the z component of the gas velocity. Within the galactic disc, for $|z| < 0.5$ kpc, CRs move faster than the local Alfvén speed. Both start to share similar velocities once the wind is launched. This happens at $|z| \sim 0.6$ kpc, the height at which the gas is accelerated to move away from the galactic disc. We formally define the wind launching site to be $|z| = 0.6$kpc and mark this galactic height in all panels of Fig. 6.2. This acceleration continues up to a galactic height $|z| \sim 1$ kpc where $|v_z| \sim 150$ km s^{-1}. At larger galactic heights the acceleration becomes weaker until the maximum outflow velocity, $|v_z| \sim 200$ km s^{-1} is reached at $|z| \sim 2$ kpc.

Figure 6.2: Quantities relevant for the discussion of the wind-launching mechanism measured in a cylindrical region defined by $|z| < 3.5$ kpc and $R < 1$ kpc at $t = 4$ Gyr. We sample this region with 50 equally spaced vertical bins and display the median (coloured lines) and the 20$^{\text{th}}$-to-80$^{\text{th}}$ percentiles (shaded regions) of each volume-weighted quantity inside each bin. The top-left panel shows the Alfvén and CR velocity (for energy transport), as well as the z component of the gas velocity. The middle left panel shows the dimensionless Alfvén defect $(|v_{\text{cr}}| - v_{\text{a}})/v_{\text{a}}$, which is discussed in the main-text. The lower left panel shows the CR, thermal, magnetic and Alfvén wave pressures while the upper right panel shows the force densities exerted on the gas by the magnetic field, CRs, gravity, and the thermal pressure. The force densities of the magnetic field are separated into contributions from the magnetic tension and pressure forces in the middle-right panel. The lower right panel shows the gas cooling and heating rates originating from optically thin cooling processes and Alfvén wave heating. The grey vertical line marks $|z| = 0.6$ kpc, the wind launching site.

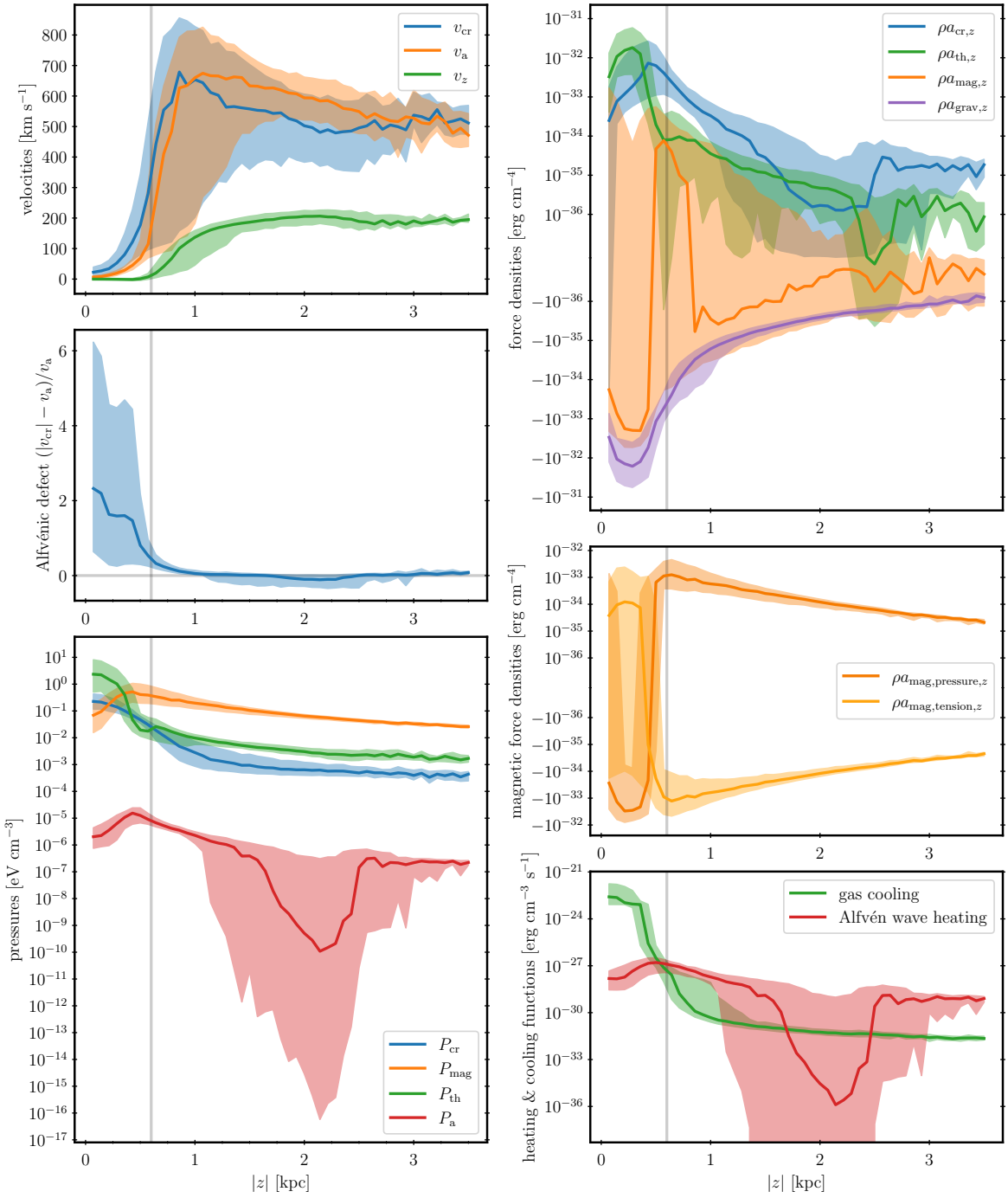
velocities [km s^{-1}]
$v_{\rm cr}$
$v_{\rm a}$
v_z
Alfvénic defect $(|v_{\rm cr}| - v_{\rm a})/v_{\rm a}$
pressures [eV cm^{-3}]
$P_{\rm cr}$
$P_{\rm mag}$
$P_{\rm th}$
$P_{\rm a}$
$|z|$ [kpc]
force densities [erg cm^{-4}]
$\rho a_{{\rm cr},z}$
$\rho a_{{\rm th},z}$
$\rho a_{{\rm mag},z}$
$\rho a_{{\rm grav},z}$
magnetic force densities [erg cm^{-4}]
$\rho a_{{\rm mag,pressure},z}$
$\rho a_{{\rm mag,tension},z}$
heating & cooling functions [erg cm^{-3} s^{-1}]
gas cooling
Alfvén wave heating
$|z|$ [kpc]

Using the Alfvénic transport defect $(|v_{\rm cr}| - v_{\rm a})/v_{\rm a}$ (middle-left panel of Fig. 6.2) we can understand how this outflow is launched. This quantity is equal to zero if the CR energy is transported with the local Alfvén velocity and larger if the CR energy is transported faster than the Alfvén velocity. As discussed in Section 6.2, CRs have the potential to accelerate the ambient gas if this Alfvénic defect is larger than zero. If the Alfvénic defect is zero, CRs and Alfvén waves are tightly coupled and CRs are exerting a pressure force on the ambient gas. Below the wind launching side, CR energy is transported with approximately two times the Alfvén velocity which decreases for increasing z indicating that CRs and Alfvén waves start to couple. Both velocities start to converge just at the wind launching site, leaving CRs and the gas tightly coupled. Thus, at the wind launching site CRs are able to accelerate the ambient gas. Note that also the statistical scatter (displayed by the 20th to 80th volume-weighted percentiles) of the Alfvénic defect is low around the wind launching side which points towards a coherent process at this location.

The ability of CRs to accelerate the gas does not imply that CRs are actually responsible for the wind launching. Magnetic or thermal pressures could also lift the gas into an outflow. To discuss this possibility we show the relevant pressures in the bottom-left panel of Fig. 6.2. A steep pressure gradient in $P_{\rm th}$ or $P_{\rm mag}$ at the wind launching site would indicate that the wind could also be pressure driven. The thermal pressure profile shows two turning points in the vicinity of the wind launching site whereas both, the CR and magnetic pressure profiles have gradients that can lead to an effective vertical acceleration. To quantify the overall contribution of the forces caused by magnetic fields, CRs, thermal pressure, and gravity to the final acceleration of the gas, we display the vertical components of

$$\rho \boldsymbol{a}_{\rm mag} = \rho \boldsymbol{a}_{\rm mag,pressure} + \rho \boldsymbol{a}_{\rm mag,tension} \tag{6.16}$$

$$= -\boldsymbol{\nabla} \cdot \left(\frac{B^2}{2} \mathbf{1} - \boldsymbol{B}\boldsymbol{B} \right), \tag{6.17}$$

$$\rho \boldsymbol{a}_{\rm cr} = -\boldsymbol{\nabla}_{\perp} P_{\rm cr} + \frac{\boldsymbol{b}}{3\kappa_{+}} [f_{\rm cr} - v_{\rm a}(\varepsilon_{\rm cr} + P_{\rm cr})] + \frac{\boldsymbol{b}}{3\kappa_{-}} [f_{\rm cr} + v_{\rm a}(\varepsilon_{\rm cr} + P_{\rm cr})], \tag{6.18}$$

$$\rho \boldsymbol{a}_{\rm th} = -\boldsymbol{\nabla} P_{\rm th}, \tag{6.19}$$

in the top-right panel of Fig. 6.2 together with the vertical force density caused by gravity, $\rho \boldsymbol{a}_{\rm grav}$ (that includes the external gravitational potential and self-gravity of the gas). CRs clearly dominate the outward-pointing force near the wind launching site. The force exerted by the thermal pressure comes second while it is nearly two orders of magnitude weaker than the force attributed to CRs. The total force exerted by the magnetic field shows alternating acceleration

directions. It accelerates the gas away from the discs only at the wind launching side. Otherwise the median force points towards the galactic disc and counteracts the outflow. This may seem counter-intuitive because the magnetic pressure gradient in the top-left panel of Fig. 6.2 shows that the magnetic pressure force is accelerating gas in the outflow direction at and above the wind launching side. To resolve this puzzle, we separately show the contribution from magnetic pressure and tension forces in the middle-right panel of Fig. 6.2. The magnetic pressure force profile follows our expectations from the median pressure profile: gas is accelerated away from disc right at and above the wind launching side. But the magnetic tension force accelerates the gas in the opposite direction in this region. Because the magnetic tension and pressure forces have comparable magnitudes but different signs, their combined net force shows a smaller magnitude. This cancellation effect is not perfect and the sign and magnitude of the residual net magnetic force varies spatially, which explains the alternating signs of the net magnetic force densities.

We display the heating and cooling rates that govern the thermodynamics of the gas in the wind in the bottom-right panel of Fig. 6.2. Gas heating is provided through damping of gyroresonant Alfvén waves. Consequently, this heating is strong at the wind launching site where CRs efficiently excite Alfvén waves through the streaming instability. Because Alfvén-wave heating exceeds gas cooling above the wind-launching site, the gas is effectively heated. This explains the increase of thermal pressure in this region and causes the generation of turning points (see bottom-left panel of Fig. 6.2). At heights 1 kpc $\lesssim |z| \lesssim$ 2.5 kpc, CRs propagate slower than Alfvén waves (see top- and middle-left panel) and the streaming instability ceases to transfer energy from CRs to Alfvén waves, which suffer unbalanced strong (non-linear Landau) damping. This leads to low values of the energy contained in Alfvén waves and the associated pressure in this region. Because of the decreasing level of Alfvén waves, there is less energy available for damping, which implies a lower heating rate in this region. Furthermore, we see a reduction of the CR mediated force because the availability of Alfvén waves influences the coupling strength between CRs and the gas. Gas with the lowest median Alfvén-wave heating rate at $|z| \sim 2$ kpc shows a reduced thermal pressure force possibly because in that region, the median gas cooling rate locally exceeds the Alfvén wave heating rate.

In Fig. 6.3, we display the median and the 20^{th}-to-80^{th} mass-weighted percentiles of the vertical gas velocity profile, which we compare to the escape velocity v_{esc} defined by

$$v_{\text{esc}}^2(z) = 2 \int_z^{R_{200}} \mathrm{d}\, r \frac{G M_{<r}}{r^2}, \tag{6.20}$$

where $M_{<r}$ is the mass contained in a sphere of radius r within the initial NFW halo and $R_{200} = 74.4$ kpc is the virial radius. To compute these velocity profiles, we only consider gas cells at

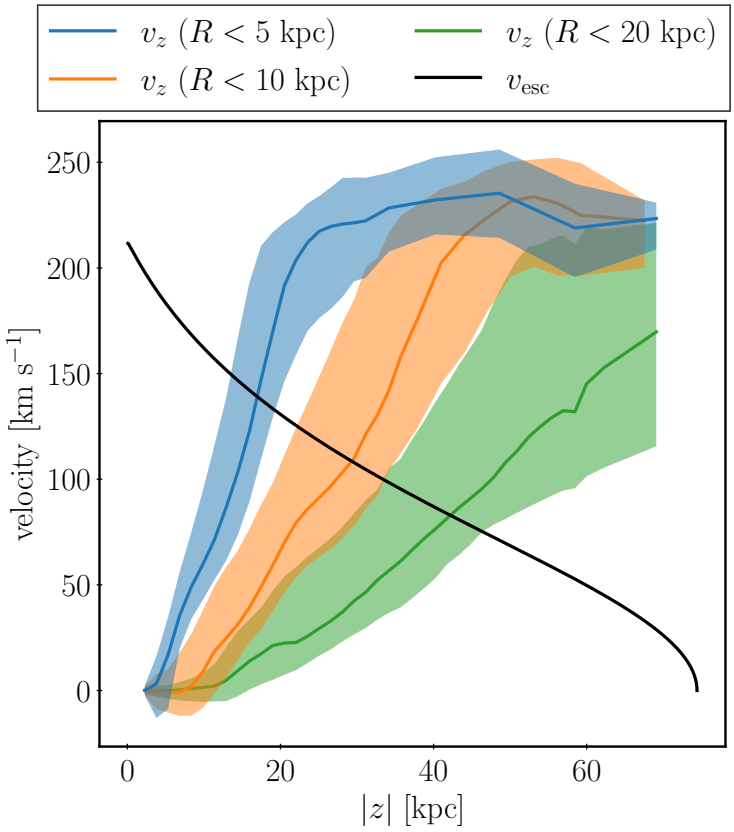

Figure 6.3: Median (coloured lines) and 20$^{\rm th}$-to-80$^{\rm th}$ mass-weighted percentiles (shaded regions) of the vertical velocity are compared to the escape velocity of the initial NFW halo as a function of vertical height at $t = 4$ Gyr. We sample v_z with 50 equally spaced bins from $z = 0$ kpc to $|z| = 70$ kpc and only consider cells with $R < 5$, 10, and 20 kpc, respectively. To increase our statistics, we merge neighbouring vertical bins until each bin contains a minimum of 1000 computational cells. Note that we flip the sign of v_z for gas particles with $z < 0$ so that the profiles shows outflow velocities with respect to the disc.

galactocentric (cylindrical) radii of $R < 5$, 10, and 20 kpc. We observe a continuous increase of the outflow velocity for all three cylinder radii. Note that both, the entrained halo gas of the wind and the gas that is part of the gaseous halo count toward the mass-weighted statistics. Consequently, a larger velocity value at a larger elevations does not necessary imply that all of the CGM at this height has been accelerated but instead means that the mass of the CGM that is not part of the outflow loses statistical weight. Furthermore, for larger cylindrical radii R, there is more halo gas included in the statistics, which causes shallower gradients in the outflow velocity profiles. Nevertheless, the outflow velocity exceeds the escape velocity of the halo in

all cases, indicating that CR feedback is in principle able to expel the ISM beyond the virial radius and to substantially reduce the amount of gas in the galaxy that is necessary for ongoing star formation.

6.5 CR Energy Transport

In this section, we discuss how the speed of CR energy transport, $v_{\rm cr}$, compares to other characteristic velocities and how its simulated value compares to values derived from the steady-state assumption. Second, we assess how well the CR diffusion coefficient, which is a measure of the CR scattering rate and directly related to the energy density of gyroresonant Alfvén waves, compares to the steady-state approximation. We emphasise that the transport velocity of the CR energy and the diffusion coefficient are different and complementary aspects of CR transport, which are not trivially related in the two-moment picture of CRHD. By contrast, the CR transport velocity respectively its flux and the CR diffusion coefficient are directly related in the case of the one-moment description of CRHD via Eq. (6.9).

6.5.1 CR transport velocity

In the one-moment approximation for CR transport the evolution of the CR energy is described by a convection-diffusion process, where the convection of CRs energy is realised by CRs streaming down their gradient. The characteristic speed for this process is given by the Alfvén speed. In Fig. 6.4, we display the $|v_{\rm cr}|$–$v_{\rm a}$ distribution for the whole simulation box with a CR-energy weighting. The most striking feature in this distribution is the prominent accumulation of energy on 1-to-1 relation. This shows that most of the CR energy is transported at velocities comparable to the Alfvén velocity. Deviation from the 1-to-1 relation are either created by the influence of CR diffusion or can be explained by a non steady-state transport of CRs. CR diffusion, the second cornerstone of the convection-diffusion picture, can increase $v_{\rm cr}$ and thus explain the fraction of CR energy above the 1-to-1 relation. One can notice that the 1-to-1 relation is indeed extended towards higher CR transport velocities in the range $v_{\rm a} \sim$ 300–600 km s^{-1} while it has a clear cutoff towards lower values of $v_{\rm cr}$. Thus CR diffusion can explain the deviations in this range.

CR energy that is transported slower than Alfvén waves, $v_{\rm cr} \lesssim v_{\rm a}$, cannot be explained in the convection-diffusion picture. A large amount of CR energy situated at $v_{\rm a} < 200$ km s^{-1} falls into this category and is mainly derived from the galactic disc where these low Alfvén velocities can be found in combination with a considerable amount of CR energy. The last noticeable feature

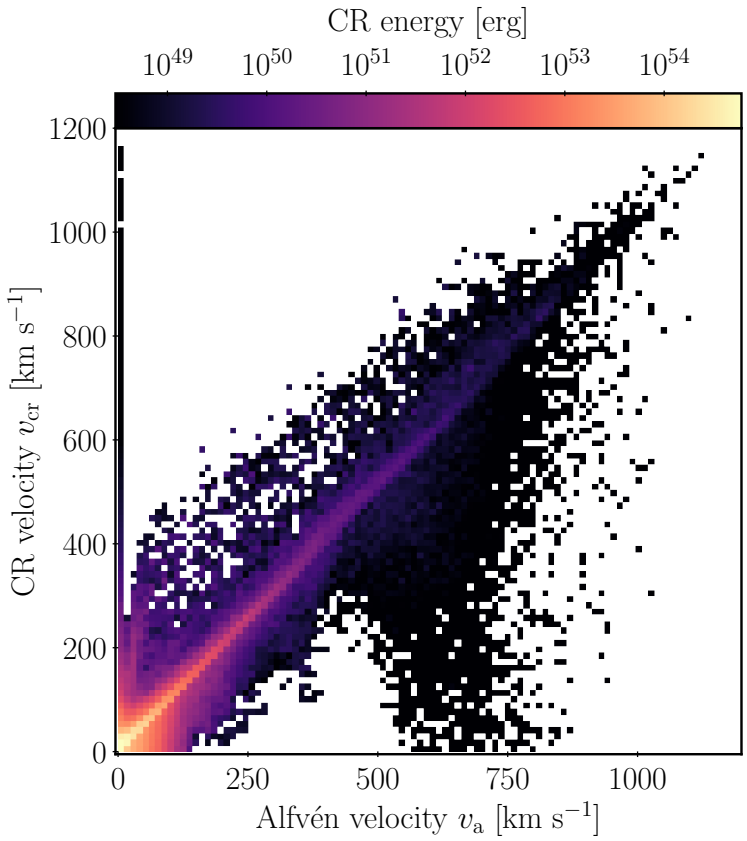

Figure 6.4: Two-dimensional histogram of the plane spanned by CR velocity and Alfvén speed at $t = 4$ Gyr where we weight each computational cell of the simulation with its CR energy. The correlation between both quantities shows that CR energy is mostly transported with the local Alfvén velocity.

is the extended region at $v_a \sim 500$–800 km s^{-1} where CR energy is transported slower than Alfvén waves. In this region, the Fermi-II process is able to operate and thus, we expect the corresponding spatial regions to have a small amount of Alfvén wave energy. Small values of $v_{cr}/v_a < 1$ and high Alfvén speeds can be found within the Alfvén wave dark regions in the galactic outflow (visible in the bottom-left panel of Fig. 6.1 as dark patches and filaments).
We further quantify the deviation of the simulated CR transport and the steady-state transport by comparing the steady-state velocity, defined by

$$v_{cr,steady} = \frac{f_{cr,steady}}{\varepsilon_{cr} + P_{cr}} = v_{st} - \kappa \frac{\boldsymbol{b} \cdot \boldsymbol{\nabla} \varepsilon_{cr}}{\varepsilon_{cr} + P_{cr}}, \tag{6.21}$$

with the simulated CR energy transport velocity using the Fickian defect

$$D_F = \frac{v_{cr} - v_{cr,steady}}{v_{cr}}. \tag{6.22}$$

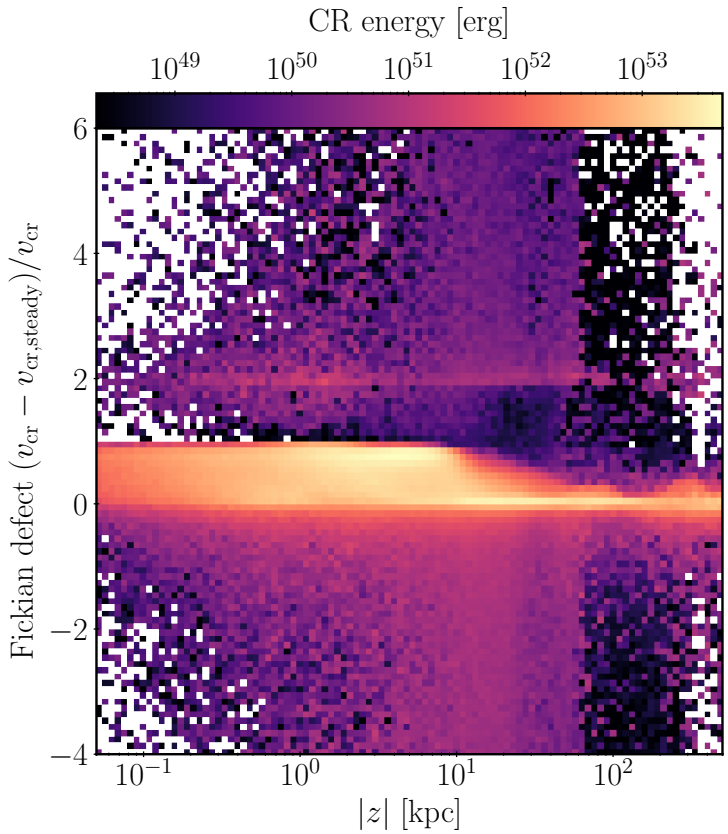

Figure 6.5: Two dimensional histogram of the Fickian defect $D_{\rm F} = (v_{\rm cr} - v_{\rm cr,steady})/v_{\rm cr}$, which represents the dimensionless deviation of the CR velocity to its predicted steady state value $v_{\rm cr,steady}$ in a streaming-diffusion approximation, at $t = 4$ Gyr. A zero value of $D_{\rm F}$ means that the CR energy is transported with its steady state velocity; a value of one means that CR energy is transported although the steady state assumption predicts no transport; a value of two means that CR energy is transported with the steady state velocity but opposite to its predicted direction. We weight each computational cell of the simulation with its CR energy before binning into this histogram.

We plot the CR-energy weighted distribution of this quantity with respect to the galactic height z in Fig. 6.5. We use the CR diffusion coefficient as calculated by Eq. (6.10) and hence based upon the local energy density of Alfvén waves. The Fickian defect can be interpreted as follows:

- If $D_{\rm F} = 0$ then the CR energy transport velocity coincides with its value from the steady-state approximation.
- If $D_{\rm F} = 1$ then the CR energy transport velocity in steady-state approximation is negligi-

ble compared to the realized velocity. Both values differ considerably.

- If $D_\mathrm{F} = 2$ then both the CR energy transport velocity in steady-state approximation and its simulated counterpart coincide in magnitude but have opposite signs. Both values differ considerably.
- If $D_\mathrm{F} < 0$ then the CR energy is transported slower than predicted by the steady-state approximation.

Because most of the CR energy is located in the galactic disc for galactic heights $|z| < 1\mathrm{kpc}$, we find no clear correlation of the simulated and steady-state CR transport velocity in the ISM. Most CRs in this region have a Fickian defect of $0 \lesssim D_\mathrm{F} \lesssim 1$ so that CR energy is transported with its steady-state velocity or faster. Because of these substantial deviations it is thus hard to argue in favour of the steady-state approximation, which appears not to be applicable in the ISM. The same holds true in the inner CGM defined here by $1 < |z| < 10$, where there is an even smaller fraction of CRs transported at the steady-state velocity. The galactic wind expels CRs into parts of the outer CGM with galactic heights $|z| > 10$. These regions dominate the statistics in the corresponding part of Fig. 6.5. There we mainly find $D_\mathrm{F} \approx 0$ implying that CRs transport their energy at the steady-state velocity which is a good approximation in the outflow region of the outer CGM.

Given that the streaming-diffusion picture is only valid in some parts of the simulation domain, we are going to quantify the CR transport into various categories. To this end, we compare the CR energy transport velocity as realised in our simulation to the steady-state prediction. We define the following categories using conditions that we apply to the computational cells in the simulation:

- a computational cell can be described by the pure streaming model if $|v_\mathrm{cr} - v_\mathrm{st}| < 0.1|v_\mathrm{cr}|$, which defines the 'streaming' category,
- a computational cell can be described by the pure diffusion model if $|v_\mathrm{cr} - \kappa(\boldsymbol{b}\cdot\boldsymbol{\nabla}\varepsilon_\mathrm{cr})/(\varepsilon_\mathrm{cr} + P_\mathrm{cr})| < 0.1|v_\mathrm{cr}|$, which defines the 'diffusion' category,
- a computational cell can be described by the mixed streaming-diffusion model if $|v_\mathrm{cr} - v_\mathrm{cr,steady}| < 0.1|v_\mathrm{cr}|$, which defines the 'streaming + diffusion' category,
- a computational cell can be described by the advection model if $|v_\mathrm{cr}| < 0.1|v_\mathrm{cr,steady}|$, which defines the 'advection' category, and
- if a computational cell does not match the criteria of any of the previous categories and thus CR transport cannot be described by a steady-state model, it is labelled by the 'non steady-state transport' category.

This categorisation requires some clarifications and discussions on possible overlapping cate-

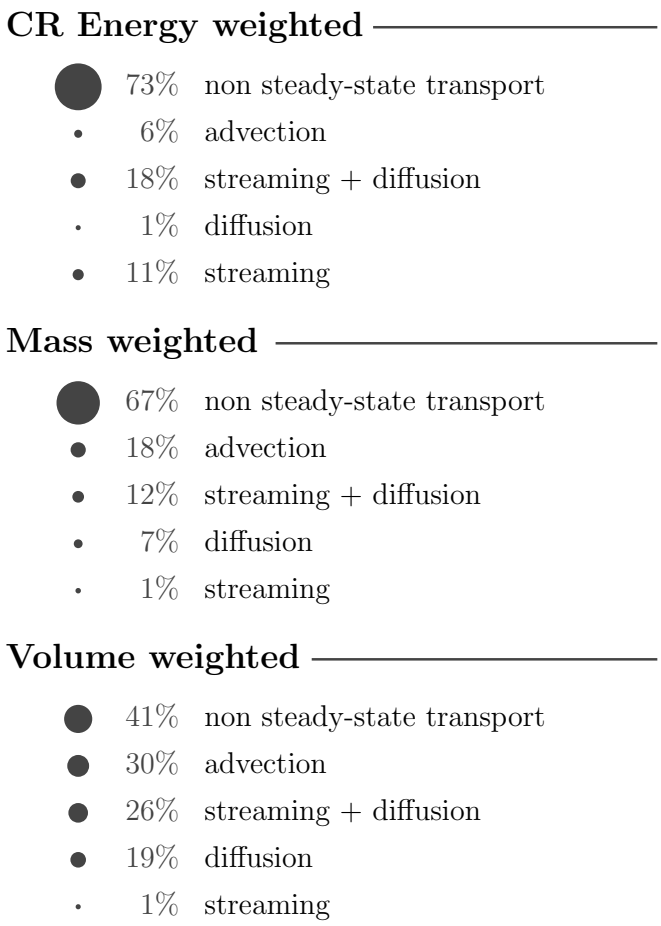

Figure 6.6: Classification of the realised CR transport mode into categories representing CR transport paradigms with different statistical weighting schemes. The categories are defined in the main text. Note that by our definitions the categories 'advection', 'streaming + diffusion', 'diffusion', and 'streaming' share some overlap in case the CR transport is slow. If a computational cell does not fulfil at least one of the criteria be to characterised by one of the steady-state transport modes then it counts towards the 'non steady-state transport' category.

gories. First, the 'streaming + diffusion' category overlaps with the 'streaming' and 'diffusion' categories but is not limited to the intersection of both categories. Second, a given computational cell can fall into multiple categories describing steady-state transport: (i) if the local Alfvén velocity or the velocity associated with CR diffusion is small, then the transport in these cells can also be described by CR advection, and (ii) if the Alfvén and CR diffusion velocities are comparable by coincidence, then this computational cell contributes to both the streaming

and diffusion categories. Third, the 'non steady-state transport' has, by definition, no overlap with any of the other categories. In conclusion, the categories represent the consistency of CR transport in our simulation with one or the other transport paradigm.

Figure 6.6 displays the result of this categorisation for different statistical weightings. The weighting is accomplished by summing up the statistical weights of the individual cells that contribute to a category and divide afterwards by the total weight of the whole simulation to get the quoted percentages. As noted above, because the categories are not mutually exclusive, the total sum of percentages in one weighting scheme necessarily exceeds the 100 per cent mark. For all weightings explored in Fig. 6.6, the non steady-state transport is the most populated category and thus, most of the time CR transport is inconsistent with any steady-state approximation. This highlights the importance of the two-moment approximation, which enables the description of CR transport beyond the steady-state paradigm. If we were to abandon the two-moment approximation and would like to describe CR transport with a steady-state approach, then the most important CR transport processes to be considered would be the 'advection' and 'streaming + diffusion' categories.

6.5.2 CR diffusion coefficient

Although we have just shown that the pure diffusion approximation is inconsistent with most of CR transport in our simulation, the concept of a CR diffusion coefficient is nevertheless relevant for this discussion: it is not only a measure for the transport speed in the diffusion approximation but is particularly a measure of the CRs scattering rate $\nu_{\pm} \propto \kappa_{\pm}^{-1}$ with gyroresonant Alfvén waves and as such, determines how tightly CRs are coupled to the thermal gas via Alfvén-wave scattering.

Figure 6.7 shows the total diffusion coefficient in the same slice through the simulation box as used in Fig. 6.1. Overall the diffusion coefficient ranges from $\kappa \sim 3 \times 10^{27}\mathrm{cm}^2\mathrm{s}^{-1}$ to $\sim 10^{29}\mathrm{cm}^2\mathrm{s}^{-1}$ in the inner CGM with the notable exceptions of the Alfvén wave dark regions in the outflow (where $\kappa \to \infty$). The values of κ show a general gradient that is aligned with the direction of the outflow. We find lower values of the diffusion coefficient within the galactic disc and larger values in the outflow. The low diffusion coefficient in the galactic disc is caused by the absence of strong damping – the non-linear Landau damping mechanism is efficient where the energy density of Alfvén waves and temperatures are high. While there are sufficient gyroresonant Alfvén waves in the disc, the ISM in our simulation is warm, which lowers the overall effectiveness of this damping mechanism. Note that ion-neutral damping, which we neglected in the present work, also plays an important role in setting the diffusion coefficient in

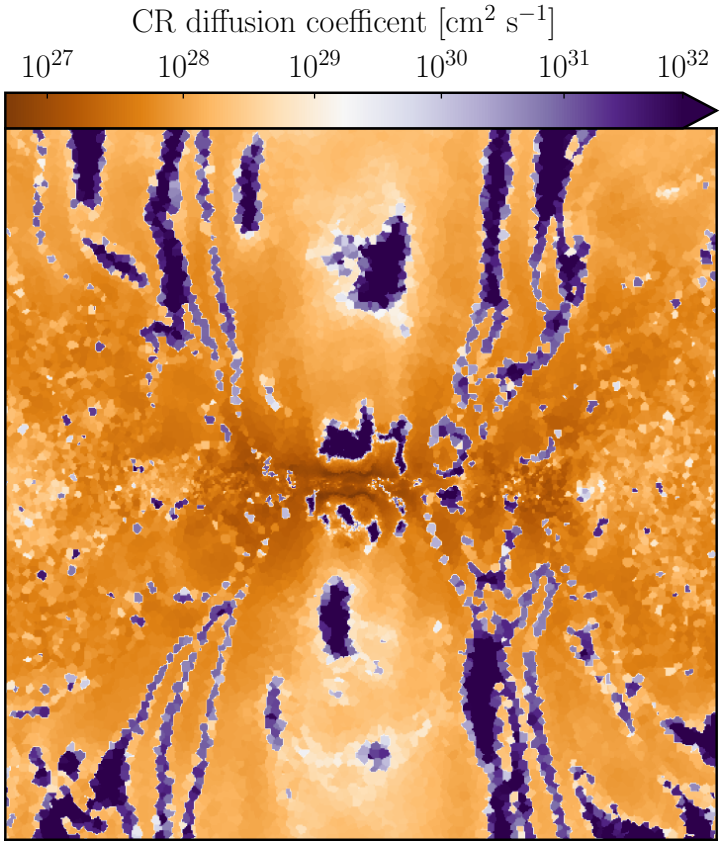

Figure 6.7: (Total) CR diffusion coefficient κ (as defined in Eq. 6.10) in a slice through the simulation domain at $t = 4$ Gyr. The figure extent and slice positioning are as in Fig. 6.1.

the ISM.

In the outflow, non-linear Landau damping is active due to high temperatures and the presence of Alfvén waves. Yet, we attribute the gradient of the diffusion coefficient not entirely to the damping of Alfvén waves but also to (i) the prevalent adiabatic losses that are stronger in comparison to the ISM and (ii) to the slower amplification of Alfvén waves at larger galactic heights. The increased rate of adiabatic losses are a direct consequence of the stratification of $\varepsilon_{\rm cr}$ and B in the outflow (see Fig. 6.1 and 6.2). The lower magnetic and CR energy densities imply a smaller driving of gyroresonant Alfvén waves because the self-confinement terms on the right-hand sides of Eqs. (6.3) and (6.4) scale as $\propto B\varepsilon_{\rm cr}(|v_{\rm cr}| - v_{\rm a})$. CRs have large diffusion coefficients in these Alfvén wave dark regions because $1/\kappa \propto (\epsilon_{\rm a,+} + \epsilon_{\rm a,-})$, which states that the absence of gyroresonant Alfvén waves implies a large diffusion coefficient.

Because we only account for Alfvén waves that are created through the streaming instability

and neglect other dynamical sources such as Alfvén waves that result from turbulent cascading, we underestimate the possibly available energy in form of magnetic fluctuations in Alfvén wave dark regions. Hence the derived values of the CR diffusion coefficient may overestimate the true value that results from CR-scattering with all forms of magnetic fluctuations. Consequently, the presented diffusion coefficient in Alfvén wave dark regions should be regarded as an upper limit.

Previous studies routinely assume that the CR diffusion coefficient can be approximated by a steady-state approximation where the growth and damping of gyroresonant Alfvén waves balance each other. We can check the validity of this approximation using our simulation. To calculate the steady state, we equate growth and damping terms of Alfvén wave energy in

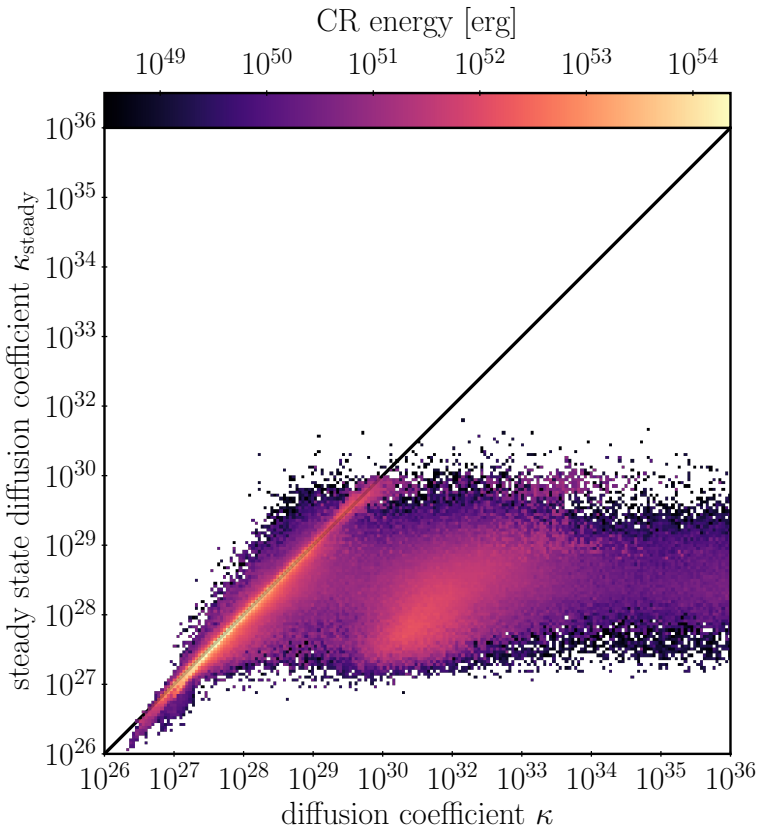

Figure 6.8: Comparison of the simulated diffusion coefficient (horizontal axis, defined in Eq. 6.10) and the steady state diffusion coefficient (vertical axis, defined in Eq. 6.25) at $t = 4$ Gyr. The steady state diffusion coefficient is calculated based on the assumed instantaneous balance between Alfvén wave growth and damping. We weight each computational cell of the simulation with its CR energy before binning into this histogram. The grey line corresponds to a 1-to-1 relation.

Eqs. (6.3) and (6.4) whilst assuming that CR energy is transported with $v_{\rm cr,steady}$. This leads to a steady state Alfvén wave energy of

$$\varepsilon_{\rm a,steady} = \sqrt{\frac{v_{\rm a}}{\alpha}|\boldsymbol{b}\cdot\boldsymbol{\nabla}P_{\rm cr}|} \tag{6.23}$$

which can be translated into an steady-state CR diffusion coefficient $\kappa_{\rm steady}$ using Eq. (6.6) to yield:

$$\kappa_{\rm steady} = \frac{4}{9\pi^{3/4}}\left(\frac{e^2}{\gamma m c^4 P_{\rm th}^{1/2}}\frac{P_{\rm cr}}{L_{\rm cr}}\right)^{-1/2} \tag{6.24}$$

$$\sim 9.2\times10^{27}{\rm cm}^2\ {\rm s}^{-1} \times\left(\frac{\varepsilon_{\rm th}}{10^{42}\,{\rm erg\,pc^{-3}}}\right)^{1/4}\left(\frac{P_{\rm cr}}{L_{\rm cr}}\frac{1\,{\rm kpc}}{10^{42}\,{\rm erg\,pc^{-3}}}\right)^{-1/2}, \tag{6.25}$$

where $L_{\rm cr} = P_{\rm cr}/|\boldsymbol{b}\cdot\boldsymbol{\nabla}P_{\rm cr}|$ is the gradient length scale of the CR pressure. We compare $\kappa_{\rm steady}$ to the simulated non-steady state diffusion coefficient κ in Fig. 6.8. Each bin in this histogram is weighted by the sum of CR energy over all computational cells that fall inside it. Thus, a brighter colouring corresponds to a larger CR energy. We observe that most CRs scatter at a rate that is well described by a steady-state diffusion coefficient, $\kappa \sim \kappa_{\rm steady}$. We emphasise that both of these diffusion coefficients derive from the streaming and diffusion picture of CR transport where the streaming process provides an additional convective process that transports CRs along magnetic field lines. Both descriptions are not comparable to an effective diffusion coefficient $\kappa_{\rm eff} = f_{\rm cr}/(\boldsymbol{b}\cdot\boldsymbol{\nabla}\varepsilon_{\rm cr})$ that describes the CR flux resulting from streaming and diffusion processes effectively in a diffusion-only approximation.

Both Alfvén wave growth and damping are fast processes with typical time scales of ~ 10 kyr. Hence, we would naively expect the diffusion coefficient to also reach the steady state on these time scales. However, near the steady state the typical and effective time scale of Alfvén wave dynamics can be slower when damping and growth are nearly balanced. This leaves the probability of Alfvén waves with associated diffusion coefficients that only fluctuate around the steady state.

In Fig. 6.8, we find an additional population of CRs with $\kappa \sim 10^3\kappa_{\rm steady}$ and a broad distribution of diffusion coefficients that have high $\kappa \gg \kappa_{\rm steady} \sim 10^{28}{\rm cm}^2\ {\rm s}^{-1}$. That particular sub-population of CRs and their associated Alfvén waves fail to reach a steady state. Inspecting Fig. 6.7 we find that the broad distribution of high κ values is caused by Alfvén wave dark regions and their vicinities where numerical diffusion causes a decrease of the surrounding Alfvén wave energy. This causes mixing of Alfvén-wave energies at the interfaces of dark regions and thus a broadened distribution of CR energy densities and the corresponding diffusion coefficients.

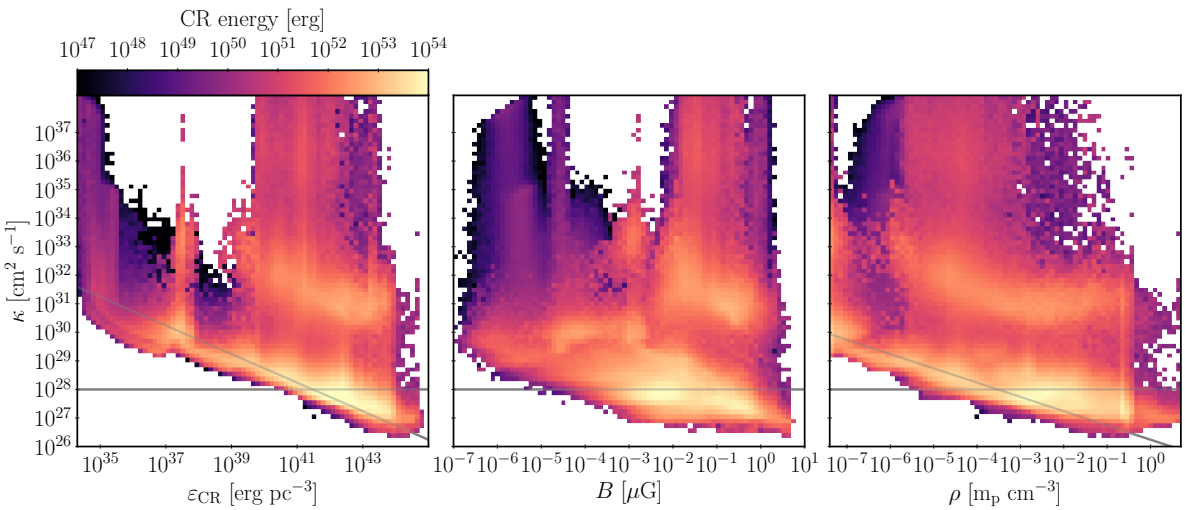

Figure 6.9: Scaling of the CR diffusion coefficient κ (defined in Eq. 6.10) with the CR energy density (left panel), the magnetic field strength (middle panel) and the gas density (right panel) at $t = 4$ Gyr. We weight each computational cell of the simulation with its CR energy before binning into those histogram. The thick horizontal grey line marks the canonical value of the CR diffusion coefficient, 10^{28}cm^2 s^{-1}. The thin oblique grey lines in the left and right panels display the correlations $\kappa \sim 10^{28}\mathrm{cm}^2\,\mathrm{s}^{-1}(\varepsilon_{\rm cr}/10^{42}\,\mathrm{erg\,pc}^{-3})^{-0.5}$ and $\kappa \sim 10^{28}\mathrm{cm}^2\,\mathrm{s}^{-1}(\rho/3\times10^{-4}\,\mathrm{m_p\,cm}^{-3})^{-0.5}$.

In Fig. 6.9 we correlate the simulated diffusion coefficient κ with various quantities using two-dimensional histograms. We again weight each bin of the histogram with the CR energy contained to highlight the relevance of each bin for the CR dynamics. In the left-hand panel of Fig. 6.9 we compare the diffusion coefficient with the local CR energy density and also find distinct diffusion coefficients that correspond to the discussed steady-state population and Alfvén wave dark regions. The steady state population contains most of the CRs and has $\kappa \sim 10^{27}$–10^{30}cm^2 s^{-1} for $\varepsilon_{\rm cr} \sim 10^{35}$–$10^{43}$erg pc^{-3}. We find a weak correlation of $\kappa \sim 10^{28}\mathrm{cm}^2\,\mathrm{s}^{-1}(\varepsilon_{\rm cr}/10^{42}\,\mathrm{erg\,pc}^{-3})^{-0.5}$ with a substantial scatter around the relation by approximately an order of magnitude. This scaling can be understood by assuming that the diffusion coefficient of these CRs is near its steady state value and thus can be described by Eq. (6.25) while the typical length scale of CRs in the halo does not show large variations. In this case, $\kappa \propto \varepsilon_{\rm cr}^{-0.5}$ directly follows from Eq. (6.25). The second population of CRs is characterised by CR energy densities in the range $\varepsilon_{\rm cr} \sim 10^{40}$–$10^{43}$erg pc^{-3} but with κ values that connect the steady-state diffusing CRs with $\kappa \to \infty$. CRs belonging to the second population reside in and around the Alfvén wave dark regions. Thus, steady-state diffusing CRs are not associated with

the Alfvén wave dark regions and are consequently the volume filling population.
Correlating κ with the magnetic field strength B in the middle panel of Fig. 6.9 reveals at most a very weak correlation between these quantities. Both, the volume filling CR population and the population associated with the Alfvén wave dark regions are visible. The magnetic field ranges four orders of magnitude for a given diffusion coefficient κ of the volume filling CR population and thus, we cannot deduce a clear relation between the two quantities. For the volume filling population, where $\kappa \sim \kappa_{\rm steady}$, this follows from Eq. (6.25) because $\kappa_{\rm steady}$ does not depend on B. The right panel of Fig. 6.9 shows the relation of the diffusion coefficient with the local mass density ρ. The two populations of CRs are also visible and separated from each other. The diffusion coefficient of the volume filling CR population shows a strong scatter around a weak correlation with mass density, $\kappa \sim 10^{28}\mathrm{cm}^2\,\mathrm{s}^{-1}(\rho/3\times10^{-4}\,\mathrm{m_p\,cm^{-3}})^{-0.5}$. This scaling is empirical because $\kappa_{\rm steady}$ from Eq. (6.25) does not directly depend on ρ. At mass densities that correspond to the disc-halo interface ($\rho \sim 10^{-3}$–$10^{-1}\mathrm{m_p\ cm^{-3}}$) the typical diffusion coefficient is $\kappa \sim 3\times10^{27}\mathrm{cm}^2\ \mathrm{s}^{-1}$.
We note that while the diffusion coefficient reaches a steady state most of the time, this is not the case for the CR flux as discussed in Section 6.5.1. This difference is not a contradiction because the two quantities describe two separate physical processes that have different associated timescales. The diffusion coefficient is a measure for how fast CRs are scattered and its steady state is set by the balance of wave growth and wave damping. Consequently, this steady state can be reached on the timescales of the contributing growth and damping processes. The CR flux or the CR transport velocity are measures of how fast CR energy is transported and its steady state is mediated by the interaction with Alfvén waves. This steady-state can only be reached on a much longer timescale that is not only characterised the CR scattering process but also by the hydrodynamic adjustments of the gradients in CR energy density, which appears to be the rate-limiting step (see Eq. 6.21).

6.6 Alfvén wave dark regions

In this section we discuss the origin of the Alfvén wave dark regions. They are characterised by a localised strong decrease of energy contained in gyroresonant Alfvén waves and a corresponding increase in the CR diffusion coefficient. We concluded in Section 6.5.2 that the volume filling CR population is approximately transported with a steady-state diffusion coefficient while CRs in the Alfvén wave dark regions scatter considerably less frequent, which implies $\kappa \gg \kappa_{\rm steady}$. The simplest explanation for this situation is that the steady state, which

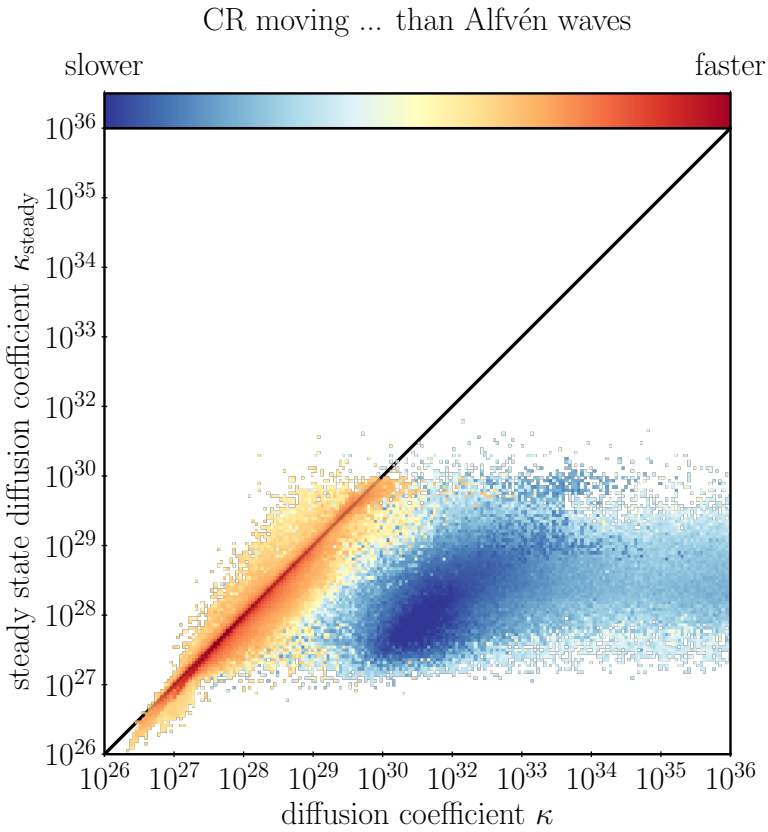

Figure 6.10: As Fig. 6.8 but here, the colour scheme distinguishes whether the CRs in a histogram bin preferentially move with a velocity v_{cr} that is slower (blue) or faster (red) than the Alfvén velocity. The shading of each colour (blue or red) is determined by the (logarithmic) amount of CR energy in that bin so that a more saturated colour indicates a larger average CR energy in that histogram bin.

is characterised by a balance of Alfvén-wave growth and damping, cannot be realised. Because the non-linear Landau damping damping rate scales linearly as $\Gamma_{\mathrm{nlld}} \propto \varepsilon_{\mathrm{a},\pm}$, any wave growth could be balanced by this damping process because $\varepsilon_{\mathrm{a},\pm}$ would adopt to match the corresponding wave growth rate. Thus, as long as CRs provide a positive growth rate through the gyroresonant instability, non-linear Landau damping should be able to balance wave growth and the Alfvén waves should settle into a steady state.

However, because a steady state cannot be reached for Alfvén wave dark regions, Alfvén wave growth is apparently prevented. This situation can be realised by CRs that move with $|v_{\mathrm{cr}}| < v_{\mathrm{a}}$. Those CRs drain energy from Alfvén waves through the gyroresonant interaction or, in other words, damp them. We can verify our conclusions by inspecting Fig. 6.10 which shows the same data as Fig. 6.8 and thus correlates the steady state diffusion coefficient to the diffusion

coefficient in our simulation. The difference between both figures is that Fig. 6.10 colour-codes two categories: CRs in red-shaded colours move preferentially faster than Alfvén waves ($v_{\rm cr} > v_{\rm a}$) while CRs in blue-shaded colours move preferentially slower than Alfvén waves ($v_{\rm cr} < v_{\rm a}$). CRs with $\kappa \gg \kappa_{\rm steady}$ fall into the second category and are thus in a regime where they damp Alfvén waves. Within each category, we weight the distribution with the CR energy so that the colour saturation level represents the CR energy at a certain diffusion coefficient. CRs and associated Alfvén waves that show approximately steady-state values of the diffusion coefficient are transported super-alfvénically while CRs in the Alfvén wave dark regions are transported sub-alfvénically.

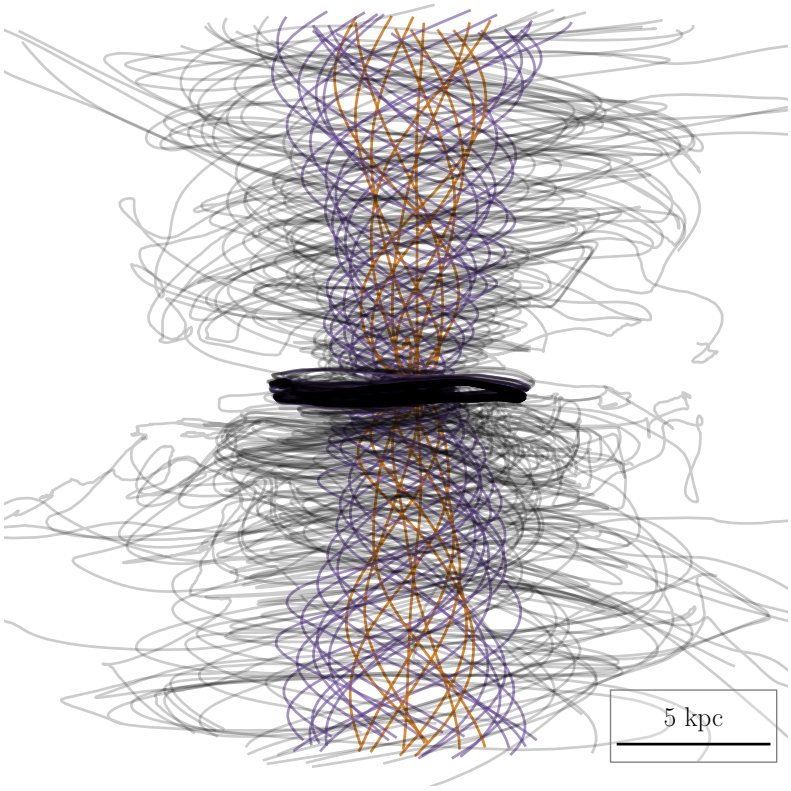

Figure 6.11: Individual magnetic field lines inside the inner CGM which anchor inside the galaxy and run through the inner galactic wind at $t = 4$ Gyr. The grey coloured field lines show the highly winded magnetic field lines in the outer wind, while the purple magnetic field lines separate the winded from the rather straight, orange-coloured field lines located in the inner wind.

Inspection of the bottom-left panel of Fig. 6.1 or of Fig. 6.7 reveals that the Alfvén wave dark regions are localised and isolated in the sense that there is no smooth transition between regions that are filled with or devoid of gyroresonant Alfvén waves along flowlines. These dark regions

also appear to be clustered in the outer wind. This clustering also coincides with a transition of the magnetic field topology and hence a change of CR transport geometry from the inner to the outer wind. In Fig. 6.11 we show magnetic field lines (generated by numerically integrating $\mathrm{d}\boldsymbol{x}/\mathrm{ds} = \boldsymbol{B}/B$, where s is the arc length along the magnetic field line) within the galactic outflow. The galaxy is visible as a dark accumulation of magnetic field lines in the centre of figure. Magnetic field lines are anchored in the disc but carried along with the galactic wind out of the ISM. This connects the galactic discs to the CGM by means of CR transport. The ratio of vertical-to-toroidal magnetic field component depends on the position inside the wind. Because the inner wind is faster, it is able to stretch the magnetic field lines in the vertical direction more easily. This leads to straighter appearance of magnetic field inside the inner wind. Contrarily, in the outer wind magnetic field lines are dominantly toroidal. As we move from the outer to the inner wind, there is a smooth transition from the toroidal to the dominantly vertical magnetic field. We highlight magnetic field lines in each of the three different regions (inner wind, outer wind, and transition region) in Fig. 6.11 with different colours.

In Fig. 6.12 we analyse the transport of CRs along two magnetic field lines. The blue magnetic field line was selected to pass through an Alfvén wave dark region (as indicated in the upper panel) while the green magnetic field line does not intersect an Alfvén wave dark region at the image layer. In the following, we call the points at which the field lines intersect the image panel *points of interest*. We interpolate the CR energy density $\varepsilon_{\mathrm{cr}}$ and the ratio $v_{\mathrm{cr}}/v_{\mathrm{a}}$ along the two magnetic field lines and display these quantities in the lower panels of Fig. 6.12. We show the actually interpolated data (which contains noise due to the interpolation from the Voronoi grid onto the field lines) and a filtered version of the data which removes some of the small-scale noise. The horizontal coordinate is the arc length along the magnetic field line and negative arc lengths correspond to regions closer to the galactic disc.

Figure 6.12: Top panel: same as the Alfvén wave energy density $\varepsilon_{\mathrm{a}} = \varepsilon_{\mathrm{a},+} + \varepsilon_{\mathrm{a},-}$ panel of Fig. 6.1 but overlaid are the projections of two magnetic field lines onto the image layer. Both magnetic field lines intersect with the image plane at the location marked with a cross in the image. The line plots show the interpolated CR energy density $\varepsilon_{\mathrm{cr}}$ (middle panel) and the CR transport velocity in units of the Alfvén velocity $v_{\mathrm{cr}}/v_{\mathrm{a}}$ (bottom panel) along the two magnetic field lines. The crosses mark the position along the magnetic field line that corresponds to the intersection with the image plane in the top panel. The blue magnetic field line passes through a Alfvén wave dark region at the image layer while the green one does not.

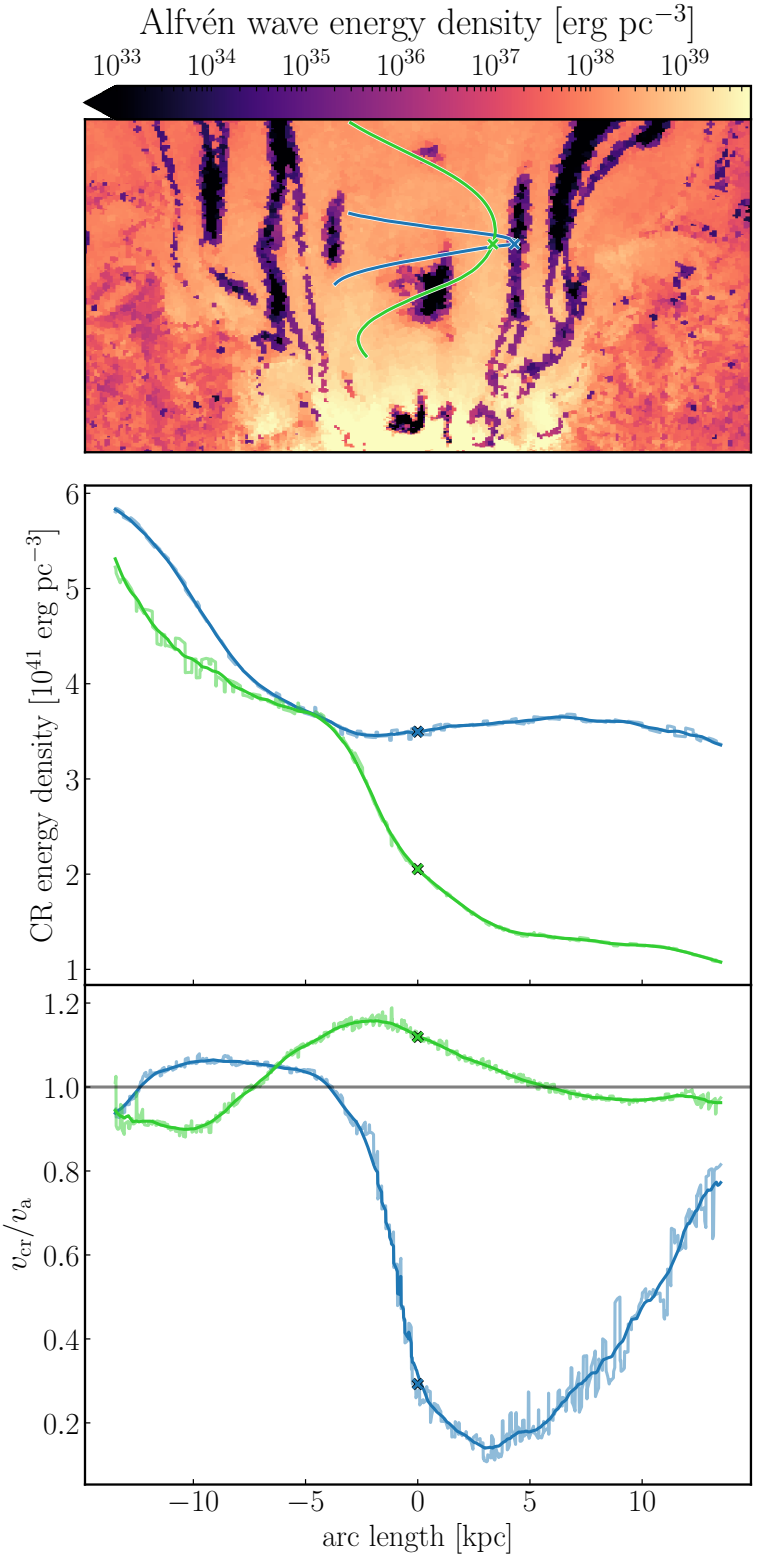
Alfvén wave energy density [erg pc^{-3}]
10^{33} 10^{34} 10^{35} 10^{36} 10^{37} 10^{38} 10^{39}
CR energy density [10^{41} erg pc^{-3}]
1 2 3 4 5 6
v_{cr}/v_a
0.2 0.4 0.6 0.8 1.0 1.2
−10 −5 0 5 10
arc length [kpc]

We first focus on the *green* magnetic field line. At its point of interest the CR energy density shows a monotonic, large gradient so that CR inertia is able to accelerate CRs beyond the Alfvénic point, $v_{\rm cr} \gtrsim v_{\rm a}$. This implies efficient driving of gyroresonant Alfvén waves, which leads to a sizeable Alfvén wave energy density as shown in the upper panel. The opposite happens along the *blue* magnetic field line. Here, we identify an inflection point in $\varepsilon_{\rm cr}$ in the vicinity of the point of interest. Thus, although both magnetic field lines are embedded in the same global gradient of $\varepsilon_{\rm cr}$ (see central panel of Fig. 6.1), locally the gradient along $\boldsymbol{B}$ is pointing in the opposite direction. Assuming that CRs are transported away from the galactic disc and towards the point of interest, the transport of CRs is rapidly decelerated at the point of interest due to CR inertia which results in $v_{\rm cr} < v_{\rm a}$. This in turn enables CRs to extract energy from gyroresonant Alfvén waves and leads to low levels of $\varepsilon_{\rm a}$ inside these regions.

6.7 Discussion and caveats

In this work we show that the extension of CR hydrodynamics towards a more realistic description using our two-moment approach and a model for the interactions of CRs and self-generated small-scale Alfvén waves impacts the transport of CRs in a galactic wind.

In our model we follow the CRs in the grey approximation and marginalise over the entire CR energy spectrum. This results in an effective description of CR transport with the overall CR energy budget being approximately dominated by GeV CRs (assuming typical CR spectral indices, Enßlin et al., 2007). While this is certainly a valid first-order approximation, an improved description will follow the CR energy spectrum and thus be able to account for the energy-dependent transport of CRs. For example, Girichidis et al. (2022) consider the transport of the CR momentum spectrum and account for the variation of the CR diffusion coefficient with energy using the same collapsing halo setup as we do. They show that the inclusion of an energy dependent transport has implications for the wind launching and the distribution of CRs in the CGM. This is because CRs at different energies cool on different timescales and deviate in their transport speed and mode which leads to an overall change in the CR dynamics. Furthermore, because CR transport is tightly linked to the gas dynamics through momentum exchange, they find that the morphologies of the galactic wind and disc differ when simulated with spectrally resolved CRs.

The CR transport velocity in our simulation is determined by CR interactions with gyroresonant Alfvén waves and consequently the processes that grow and damp these waves. Here, we only consider the gyroresonant interaction of CRs and non-linear Landau damping of Alfvén waves.

While these are considered to be the most important processes, a plethora of other relevant processes that are associated with CR transport are not accounted for. Examples of those processes that may impact the dynamics of CRs in galactic winds are turbulent damping of Alfvén waves (Farmer and Goldreich, 2004; Lazarian and Xu, 2022) but also additional scattering of CRs by magnetic fluctuations that are shifted into resonance through the turbulent cascade (Yan and Lazarian, 2011). Additionally, the scattering of CRs with small-scale ion-cyclotron waves through the intermediate scale instability (Shalaby et al., 2021) might be important as it is able to faster exchange energy between CRs and plasma-scale electromagnetic waves in comparison to interaction with gyroresonant Alfvén waves. This can provide more CR scattering and consequently smaller CR diffusion coefficients.

Under realistic ISM conditions, SNe launch structured fountain-type outflows where cold ($\sim$ 10 K) and warm ($\sim 10^4$ K) gas is entrained into a hot outflow. This is done in part by mixing hot halo gas with cold-warm gas to a thermally unstable phase that quickly cools and joins the warm phase so that there is a net growth of mass in this phase (Gronke and Oh, 2018; Li et al., 2020; Sparre et al., 2020) as well as through magnetic tension of magnetic field lines that are anchored in the outflowing hot wind and draped around cold clouds (Dursi and Pfrommer, 2008). Moreover, CRs that are accelerated at SN remnant shocks in the multiphase ISM and stream/diffuse away from the source regions into the CGM can also help to accelerate the wind and shape its properties (Girichidis et al., 2016; Simpson et al., 2016b; Farber et al., 2018; Girichidis et al., 2018).

The CR dynamics differs within cold-warm clumps in comparison to hot winds because nonlinear Landau damping becomes subdominant as ion-neutral damping starts to prevail due to the availability of neutral atoms that collisionally damp gyroresonant Alfvén waves (Armillotta et al., 2021). This is clearly not only true for the galactic wind but also for the ISM itself. Thus, more detailed investigations of the dynamical impact of CR-Alfvén wave interactions on those small scales are welcome. While the cited ISM models with CR physics are simulating stratified boxes of localised ISM patches, only recently it has become possible to simulate and investigate the impact of individual SNe on galactic scales (Hu et al., 2017; Gutcke et al., 2021), however limited to dwarf galaxies. An SN event in our simulations represents a population of SNe that inject CRs co-spatially and simultaneously into the ISM. For this reason and because we model the ISM through a modified equation of state that effectively describes the warm and hot phases with a single effective fluid, we are unable to locate the origin of the dynamics of CRs and accompanying Alfvén waves in spatially resolved, individual SNe. Because the diffusion coefficient is expected to strongly vary in space (Semenov et al., 2021; Armillotta

et al., 2021) and CRs impact the dynamics of the ISM, a thorough investigation of CR transport and their interplay with the surrounding environment in the multi-phase ISM is postponed to future work.

Our initial condition consists of a rotating gaseous halo. Due to cooling and gravity this halo collapses and forms a disc inside out owning to angular momentum conservation. Not all the gas directly collapses into the galactic disc but remains as a smooth and diffusive gaseous halo around the galaxy. The expelled galactic wind has to do volume work against the inertia of this halo gas. In a more realistic scenario where the galaxy is embedded in a cosmologically forming halo, the CGM is substantially more structured due to streams of accreting gas. A CR driven wind inevitably interacts with these gaseous streams, which alters gas flows inside the halo (Buck et al., 2020), the viral shock (Ji et al., 2021), and possibly observables of the CGM (Butsky et al., 2021). Applying our hydrodynamical scheme of non-equilibrium CR interactions with Alfvén waves in this setup would reveal whether the Alfvén wave dark regions we discovered percolate the entire galactic halo or whether they are only confined to the inner galactic wind.

6.8 Conclusions

Here, we study the formation and evolution of an isolated disc galaxy with halo mass 10^{11} $M_{\odot}$ that includes CR feedback through the injection of CR by SNe and CR transport based on the two moment description of Thomas and Pfrommer (2019). This allows us to self-consistently follow crucial aspects of the transport of CRs along magnetic fields such as CR diffusion and streaming. We model the interactions between CRs and gyroresonant Alfvén waves together with the non-linear Landau damping process of these waves in our hydrodynamical model. This enables us to self-consistently calculate the CR diffusion and scattering rates in a time and space resolved manner without the need to employ ad hoc choices for these coefficients. Our investigation focuses on the interaction of CRs with the galactic wind and the transport properties of CRs therein. Our results include:

- CRs injected into the ISM start to build up a stratified distribution above and below the disc and the bulk of CRs gets accelerated by means of the CR inertia to super-alfvénic velocities at the disc-halo interface. If these CRs are efficiently coupled to the gas through their interaction with gyroresonant Alfvén waves, their momentum is transferred to the surrounding gas. This causes the CRs to be decelerated and the ambient gas to be accelerated by means of momentum-conservation, which eventually launches a galactic wind

(see Figs. 6.1 and 6.2).

- The galactic outflow is bipolar, magnetised and is split into two characteristic regions. The inner wind is thermally dominated and underdense, which differs considerably from the outer wind, which is dominated by CR pressure. This outer wind interacts with the ambient CGM through shear motions and thus, turbulent mixing between the CGM and the wind leads to a more structured outflow morphology (see Fig. 6.1).
- CR transport inside the galactic winds does not follow either CR streaming, CR diffusion or the mixed streaming + diffusion paradigm in the steady-state approximation. We find that CRs are preferentially transported in a non-steady state mode, which we characterise by a deviation from Fickian transport (see Figs. 6.5 and 6.6). This transport mode ultimately cannot be described by the popular one-moment CR transport paradigm and can only be captured using higher-order descriptions such as our two-moment method, which self-consistently solves for the effective transport speed of CRs that itself results from the dynamics and gyro-resonant Alfvén-wave scattering of CRs.
- The CR diffusion coefficient is a measure for the inverse CR scattering rate, which depends on the amplitude of Alfvén waves. In contrast to the CR transport speed (which cannot be described by steady state transport), we find that the CR diffusion coefficient in our simulation is approximated well for most of the CRs by the steady state value that is derived from balancing the growth and damping rates of Alfvén waves (see Fig. 6.8). Correlating the CR diffusion coefficient with characteristic variables for CR transport reveals that κ scales as $\varepsilon_{\rm cr}^{-0.5}$ and $\rho^{-0.5}$ and shows no strong scaling with the local magnetic field strength (see Fig. 6.9).
- Unexpectedly, we discover CRs with diffusion coefficients orders of magnitudes larger than the expected steady-state value. Those CRs populate isolated regions in the transition zone between the inner and outer wind, which are devoid of gyroresonant Alfvén waves and which we name Alfvén wave dark regions (see Figs. 6.7 and 6.1). This phenomenon is caused by CRs with effective transport speeds smaller than the local Alfvén speed which implies that CRs are extracting energy from Alfvén waves inside these regions (see Figs. 6.10 and 6.12).

Our study of the plasma physics of CR transport in self-consistently driven galactic winds opens up the possibility for exploring how CR feedback impacts galaxy formation and evolution.

6.9 Appendix: Exponential Integrator

CR interactions with Alfvén waves are mediated through source terms in Eqs. (6.1) to (6.4), which can be brought into the following algebraic form:

$$\frac{\mathrm{d}\boldsymbol{U}}{\mathrm{d}t} = \mathbf{R}(\boldsymbol{U})\boldsymbol{U}, \tag{6.26}$$

where the state vector is

$$\boldsymbol{U} = \left(\varepsilon_{\mathrm{cr}}, f_{\mathrm{cr}}, \varepsilon_{a,+}, \varepsilon_{a,-}\right)^T, \tag{6.27}$$

and the rate matrix is given by

$$\mathbf{R}\left(\boldsymbol{U}\right) = \begin{pmatrix} v_{\mathrm{a}}^2\chi\gamma_{\mathrm{cr}}T & -v_{\mathrm{a}}\chi D & 0 & 0 \\ c_{\mathrm{red}}^2 v_{\mathrm{a}}\chi\gamma_{\mathrm{cr}}D & -c_{\mathrm{red}}^2\chi T & 0 & 0 \\ -v_{\mathrm{a}}^2\chi\gamma_{\mathrm{cr}}\varepsilon_{a,+} & +v_{\mathrm{a}}\chi\varepsilon_{a,+} & -\alpha\varepsilon_{a,+} & 0 \\ -v_{\mathrm{a}}^2\chi\gamma_{\mathrm{cr}}\varepsilon_{a,-} & -v_{\mathrm{a}}\chi\varepsilon_{a,-} & 0 & -\alpha\varepsilon_{a,-} \end{pmatrix}. \tag{6.28}$$

Here, we define the abbreviations

$$T = \varepsilon_{a,+} + \varepsilon_{a,-}, \tag{6.29}$$

$$D = \varepsilon_{a,+} - \varepsilon_{a,-}, \tag{6.30}$$

$$\chi = \frac{3\pi}{8}\frac{e}{\gamma m c^3 B}. \tag{6.31}$$

In Thomas et al. (2021) we present a semi-implicit second order Runge-Kutta like scheme that numerically solves Eq. (6.26) in combination with an adaptive timestepping algorithm to control the numerical error. The adaptive timestepping algorithm implements subcycling of the source term integration by dynamically increasing or the decreasing the integration timestep for a given subcycle until a given numerical error, which may be introduced through the numerical discretisation, is below an imposed limit.

We found that the semi-implicit integrator of Thomas et al. (2021) causes the adaptive timestepping algorithm to request an unnecessary large number of subcycles to meet the criterion if the Alfvén wave energy densities are exponentially damped. This is the case when $\mathbf{R}(\boldsymbol{U})$ is approximately constant and dominated by the entries in its lower-left corner. This behaviour is detrimental to the overall performance of the source term integration. In order to increase the performance of the algorithm, we developed a drop-in replacement for the source-term integrator of Thomas et al. (2021). The derivation is as follows: the analytic solution of Eq. (6.26) is

$$\boldsymbol{U}(t) = \exp\left\{\int_0^t \mathrm{d}t' \mathbf{R}\left[\boldsymbol{U}(t')\right]\right\}\boldsymbol{U}(0), \tag{6.32}$$

which is a recursive solution because the argument of the matrix exponential itself depends on the solution $\boldsymbol{U}(t)$. We can dissolve this recursive relation by applying a second-order Runge Kutta-like approximation to the integral in Eq. (6.32). The result of this procedure is

$$\boldsymbol{U}^* = \exp\left[\Delta t \mathbf{R}(\boldsymbol{U}^n)\right] \boldsymbol{U}^n \tag{6.33}$$

$$\boldsymbol{U}^{n+1} = \exp\left\{\frac{\Delta t}{2}\left[\mathbf{R}(\boldsymbol{U}^n) + \mathbf{R}(\boldsymbol{U}^*)\right]\right\}\boldsymbol{U}^n, \tag{6.34}$$

where Δt is the length of the timestep. This is a second-order numerical approximation to Eq. (6.26). We found that this integrator generally outperforms the original integrator of Thomas et al. (2021) in terms of the required computational resources to achieve a requested error tolerance in the adaptive timestepping algorithm. Hence, we use this new integrator for the simulation in this paper.

The advantage of the new integrator becomes apparent if we consider a situation that caused the problem of the old integrator in first place: if $\mathbf{R}(\boldsymbol{U})$ is approximately constant or slowly varying then Eq. (6.26) becomes a simple linear ordinary differential equation, which has an exponentially decaying or growing solution, depending on the sign of $\mathbf{R}(\boldsymbol{U})$. In this situation the first stage in Eq. (6.33) already provides a solution that is close to the analytical solution. If $\mathbf{R}(\boldsymbol{U}) \sim$ const., this first stage is already the exact analytical solution. If $\mathbf{R}(\boldsymbol{U}) \neq$ const. the second stage in Eq. (6.34) is improving the numerical solution according to the predictor-corrector scheme. The new integrator returns a well-behaved numerical solution if $\mathbf{R}(\boldsymbol{U})$ is slowly varying but encodes small physical timescales without triggering subcycling by the adaptive timestepping algorithm. This feature cannot be achieved with the old semi-implicit integrator.

7 Probing Cosmic Ray Transport with Radio Synchrotron Harps in the Galactic Center

This chapter is based on the published paper by Thomas, T. ; Pfrommer, C. ; Enßlin, T: The Astrophysical Journal Letters, Volume 890, Issue 2, id.L18, 6 pp. (2020)

Recent observations with the MeerKAT radio telescope reveal a unique population of faint non-thermal filaments pervading the central molecular zone (CMZ), a region rich in molecular gas near the Galactic center. Some of those filaments are organized into groups of almost parallel filaments, seemingly sorted by their length, so that their morphology resembles a harp with radio emitting "strings". We argue that the synchrotron emitting GeV electrons of these radio harps have been consecutively injected by the same source (a massive star or pulsar) into spatially intermittent magnetic fiber bundles within a magnetic flux tube or via time-dependent injection events. After escaping from this source, the propagation of cosmic ray (CR) electrons inside a flux tube is governed by the theory of CR transport. We propose to use observations of radio harp filaments to gain insight into the specifics of CR propagation along magnetic fields of which there are two principle modes: CRs could either stream with self-excited magneto-hydrodynamical waves or diffuse along the magnetic field. To disentangle these possibilities, we conduct hydrodynamical simulations of either purely diffusing or streaming CR electrons and compare the resulting brightness distributions to the observed synchrotron profiles of the radio harps. We find compelling evidence that CR streaming is the dominant propagation mode for GeV CRs in one of the radio harps. Observations at higher angular resolution should detect more radio harps and may help to disentangle projection effects of the possibly three-dimensional flux-tube structure of the other radio harps.

7.1 Introduction

Radio observations of the Galactic center region show many isolated, elongated filaments (Yusef-Zadeh et al., 1984; Lang et al., 1999; LaRosa et al., 2001; Nord et al., 2004; Yusef-Zadeh et al., 2004). Recent high-resolution observations with the MeerKAT radio telescope found that the filaments trace bipolar bubbles that are rising from the CMZ (Heywood et al., 2019). The filaments are characterised by a high aspect ratio, a filament-aligned magnetic field (Lang et al., 1999), strongly polarized emission (LaRosa et al., 2001), and a hard spectral index that steepens away from the geometric center of the filaments (Law et al., 2008). Hence, these non-thermal filaments (NTFs) are illuminated by synchrotron-emitting electrons.

Explanations for injecting relativistic electrons into NTFs include magnetic reconnection (Lesch and Reich, 1992; Bicknell and Li, 2001), acceleration in young stellar clusters (Yusef-Zadeh, 2003), magnetized wakes of molecular clouds (Shore and LaRosa, 1999; Dahlburg et al., 2002), pulsar wind nebula (Bykov et al., 2017; Barkov and Lyutikov, 2019), stellar winds of massive stars (Rosner and Bodo, 1996; Yusef-Zadeh and Wardle, 2019), and even annihilation of light dark matter (Linden et al., 2011). Whether the origin of the parsec-sized straight NTFs is causally linked to the electron source that powers them is unclear.

To explain the brightness of NTFs, we need to take a closer look at CR propagation. The Lorentz force ties CRs to any macroscopic magnetic field and causes the CRs to follow the field line motion. When magnetic fields are frozen into and move along with the fluid, CRs are bound to follow these fluid motions. This is called *CR advection* and shown in the left-hand panel of Fig. 7.1. We expect CR advection to be unimportant for NTFs as their straight morphology excludes large-scale gas motions perpendicular to the NTFs that change their appearance.

Of particular interest for NTFs is CR propagation along the mean magnetic field. It can be classified into two principle modes depending on the frequency of particle scatterings with magneto-hydrodynamic waves. (i) For frequent scatterings, the ensemble average of the particle distribution follows the motions of their non-relativistic scattering centers while individual particles move with their relativistic velocities. This is the basis for describing CRs as a hydrodynamical fluid on scales larger than the effective mean-free path. (ii) For infrequent CR-wave scatterings, CRs move ballistically and individual particle trajectories obey a kinetic description. Malkov (2017) showed that CRs leave the ballistic regime after three characteristic scattering times and enter a diffusive, fluid-like behaviour (middle panel of Fig. 7.1).

For CRs with energies below $\sim$ 200 GeV, magneto-hydrodynamical (MHD) waves are likely the dominant source of scattering (Yan and Lazarian, 2011; Blasi et al., 2012). CRs can provide their own scattering centers by exciting Alfvén waves on scales comparable to their gyroradii

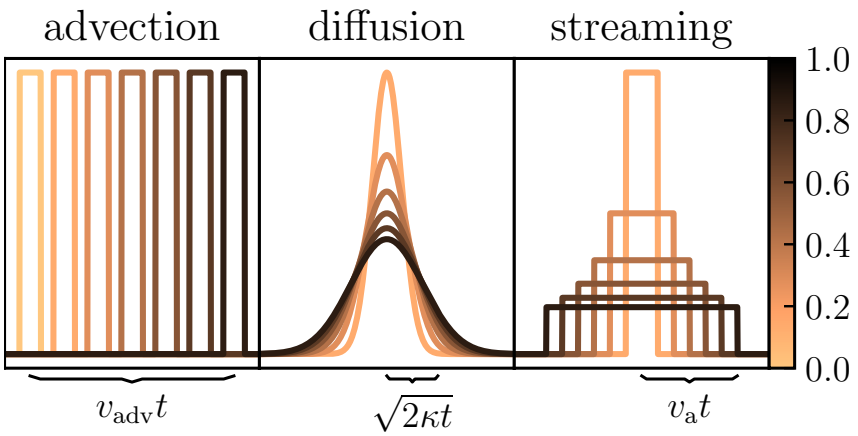

Figure 7.1: Archetypical transport modes of CR fluids. *Left:* CRs tied to frozen-in magnetic fields are advected with the bulk plasma velocity, $v_{\rm adv}$. *Middle:* when CRs are weakly scattered by Alfvén waves, they diffuse away from a given source (after an initial time) with a root-mean-square velocity of $\sqrt{2\kappa/t}$ (where t is the time and κ denotes the diffusion coefficient) along the magnetic field. *Right*: if CRs are effectively scattered, they stream with the Alfvén speed, v_a, along the magnetic field.

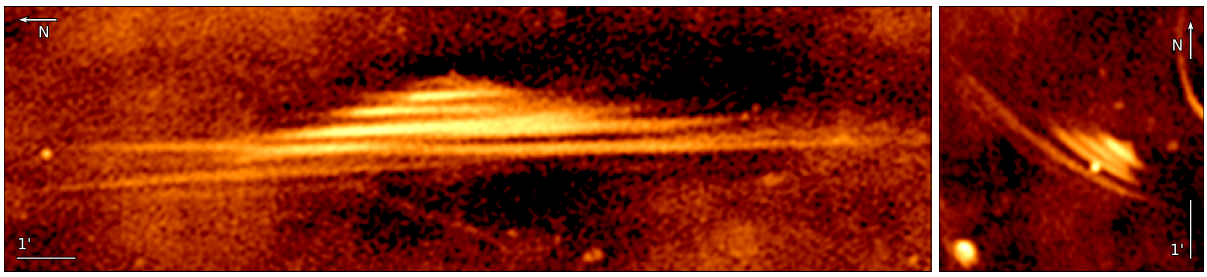

Figure 7.2: Two radio harps in the MeerKAT observation of the CMZ (Heywood et al., 2019). Left: the NTF G359.85+0.39 was discovered by LaRosa et al. (2001); also named N10 in Law et al. (2008). Right: G359.47+0.12 was first imaged by Heywood et al. (2019). Their names correspond to their position in Galactic coordinates.

through the gyroresonant instability (Kulsrud and Pearce, 1969). These Alfvén waves interact with CRs so that the effective CR drift velocity approaches the Alfvén velocity, v_a, which is referred to as *CR streaming*.

CRs injected by a compact source excite Alfvén waves while leaving their acceleration site. These Alfvén waves are travelling in opposite directions along the magnetic field away from the source. Both leading fronts of Alfvén waves span an expanding region populated by CRs. Due to their confinement into this region, the CR population rarefies. Assuming perfect confinement, there is a sharp transition between locations that are occupied by or free of injected CRs (see right panel of Fig. 7.1).

This fundamental difference between CR streaming and diffusion allows us to differentiate between the two modes by studying the radio synchrotron brightness along NTFs: (i) the synchrotron emission from diffusing CR electrons smoothly fades away from a compact source while streaming CR electron populations show a central constant brightness level and a sharp transition to any background emission and (ii) as indicated in Fig. 7.1, the root-mean-square distance of diffusing CR electrons increases as $\sqrt{2\kappa t}$ while in the CR streaming model, it increases linearly with time as $v_{\rm a}t$. If we were to observe equidistantly-spaced snapshots of the two propagation modes, then the envelope of the snapshots should either show a bell shape (for CR diffusion), a triangle (for pure CR streaming), or an inverse bell shape (for CR streaming + diffusion).

In this Letter we are studying a particular class of NTFs that we call *radio synchrotron harps* and of which we show two examples in Fig. 7.2. We will argue that those objects provide a rich avenue to study CR transport and propagation using radio observations.

7.2 Sources Powering Non-Thermal Filaments

A massive star or pulsar moving through the CMZ with velocity $v_* \sim v_{\rm a}$ can intersect and inject CRs into a magnetic flux tube that has been stretched by the bipolar outflow from the CMZ (Heywood et al., 2019).

We conjecture that the regular arrangement of the harp "strings" in Fig. 7.2 is created either by injecting CRs into spatially intermittent magnetic flux tubes or by a temporally intermittent injection process. Spatially intermittent magnetic fields are expected in magneto-turbulent environments such as the CMZ (Beresnyak and Lazarian, 2015). Turbulent dynamo action can locally amplify the diffuse magnetic field from $\sim$ 10 μG to the observed 100–1000 μG in NTFs (Boldyrev and Yusef-Zadeh, 2006). For temporally intermittent CR injection, CRs must

be actively impeded from passing through the interface between the continuously accelerating source and the ISM, possibly due to a temporarily missing magnetic connection through that interface, causing CR confinement.

In both cases, the different "string" lengths show a chronological sequence of CR injection events onto an NTF. After injection, the CRs propagate along the magnetic filament, which decreases their energy density and increases their spatial extent. Hence, NTFs with more recently injected CRs appear shorter and brighter while previously injected CRs form longer and fainter filaments. The resulting morphology is that of a filamentary isosceles triangle (or bell) with a bright apex and a fainter base, see Fig. 7.2.

Wind termination shocks of massive stars CR electrons generated at wind termination shocks or bow shocks of massive stars can illuminate NTFs (Rosner and Bodo, 1996; Yusef-Zadeh and Wardle, 2019). Massive stellar winds interact with their local interstellar medium (ISM) by building up an interaction layer between the wind interior and the ISM. This layer is confined by a bow shock that encompasses the shocked ISM and a wind termination shock. These shocked fluids are initially separated by a contact discontinuity, which becomes unstable to Rayleigh-Taylor instabilities that cause mixing of both fluids. At both shocks, electrons can be accelerated to relativistic energies via diffusive shock acceleration (e.g., del Valle and Pohl, 2018). Some bow shocks are luminous enough for observable synchrotron emission (Benaglia et al., 2010, for a runaway-O-star bow shock). The stand-off radius R between star and bow shock is given by the pressure balance between stellar wind and ISM:

$$R = \left(\frac{\dot{M} v_\infty}{4\pi(\rho_{\rm ISM} v_\star^2 + P_{\rm ISM} + B^2/8\pi)} \right)^{1/2} \sim 0.05 \text{ pc}, \tag{7.1}$$

where $\dot{M} \sim (10^{-8}\text{–}10^{-5}) \mathrm{M}_\odot \text{ yr}^{-1}$ is the mass loss rate, $v_\infty \sim (1000\text{–}2500)$ km s^{-1} is the terminal wind velocity, $v_\star \sim$ few $\times$ 10 km s^{-1} is the relative velocity of the star, $\rho_{\rm ISM}$ and $P_{\rm ISM}$ are the ambient ISM density and pressure, and B is the ISM magnetic field strength. At a distance of 8.2 kpc to the CMZ, this corresponds to an angular scale of 8″, close to the observational resolution of 6″ (Heywood et al., 2019). We assume that the NTFs are embedded in the warm CMZ phase with gas temperature $T = 10^4$ K and number density $n = 100$ cm^{-3}. This implies magnetically dominating NTFs with $B \sim 200$ μG and a plasma beta $\beta = P_{\rm ISM}/(B^2/8\pi) = 2c_s/v_{\rm a} \sim 0.1$, which explains the straight NTF morphology that is not affected by turbulent gas motions. The stellar wind kinetic luminosity is

$$L_{\rm wind} = \frac{1}{2} \dot{M} v_\infty^2 \sim 1 \times 10^{35} \text{ erg s}^{-1} \tag{7.2}$$

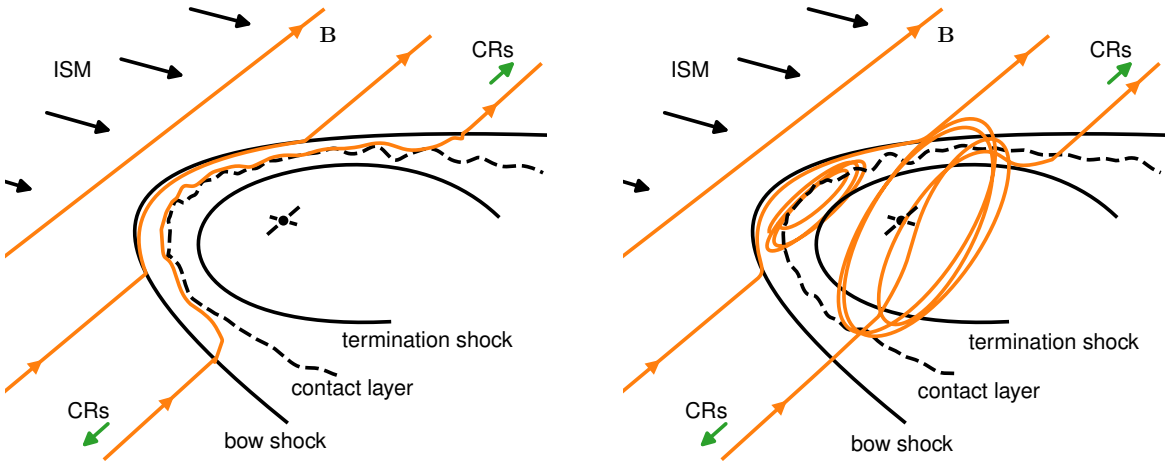

Figure 7.3: Sketches of possible scenarios that can inject CRs into NTFs. *Left*: a massive star located in the center drives a stellar wind that terminates at a shock. This shock accelerates CRs, which diffuse onto draped ISM magnetic fields, which experienced mixing with the shocked wind via Rayleigh-Taylor instabilities and escape into the ISM. *Right:* a pulsar drives the wind by accelerating electron-positron pairs towards the wind termination shock. Piled up field lines behind the wind termination shock can reconnect with the ISM magnetic field, allowing CRs to escape.

so that the wind termination shock is

$$\frac{L_{\rm wind}}{L_{\rm bow}} = \frac{\dot{M} v_\infty^2}{\rho_{\rm ISM} v_\star^3 2\pi R^2} \sim 10^2 \tag{7.3}$$

times more powerful than the bow shock, implying that the termination shock dominates the CR acceleration. Assuming that all kinetic wind energy is dissipated at the wind-termination shock and an electron acceleration efficiency of 0.1%, the total CR electron luminosity is

$$L_e = 1 \times 10^{-3}\, L_{\rm wind} \sim 1 \times 10^{32}\ {\rm erg\ s^{-1}}. \tag{7.4}$$

Magnetized winds of rotating stars result in perpendicular termination shocks that can accelerate electrons (Xu et al., 2019) but not protons (Caprioli and Spitkovsky, 2014).
While moving through the ISM, the stellar wind bubble piles up a magnetic draping layer at the contact discontinuity. Accelerated electrons diffuse onto these field lines and escape from their acceleration site. Subsequently, they move away from the star, emit synchrotron radiation in the strongly magnetized ISM flux tubes, and illuminate the NTFs (see left panel of Fig. 7.3).

Pulsar winds Another possible source of CR electrons for NTFs are pulsar wind nebulae (PWN, Barkov and Lyutikov, 2019). PWNs are fueled by a central pulsar with a spin-down luminosity $\dot{E} \sim 5 \times 10^{37}$ erg s^{-1}. The wind is launched at the light cylinder of the pulsar's magnetosphere, where electron-positron pairs leave the magnetosphere and are accelerated by the strong electromagnetic fields. Further acceleration can take place in reconnection layers of the striped pulsar wind. Similar to a stellar wind, the pulsar wind is separated from the ISM by a layer consisting of the wind termination shock, a contact discontinuity and a possible bow shock. An ISM magnetic field that is draped around the pulsar wind can reconnect at the contact discontinuity with the magnetic field originating from the wind interior (Barkov and Lyutikov, 2019; Barkov et al., 2019). This allows relativistic particles to escape from the PWN into the ISM, see the right-hand panel of Fig. 7.3. The stand-off distance of the pulsar wind is

$$R = \left(\frac{\dot{E}}{4\pi c(\rho_{\rm ISM} v_\star^2 + P_{\rm ISM} + B^2/8\pi)} \right)^{1/2} \sim 0.05 \text{ pc}. \tag{7.5}$$

Not all electrons leave the PWN so that the luminosity of NTF-injected electron-positron pairs is

$$L_e = 2.5 \times 10^{-4} \frac{\dot{E}}{\sigma} \sim 1 \times 10^{32} \text{ erg s}^{-1}, \tag{7.6}$$

where $\sigma \sim 100$ is the pulsar wind magnetization.

If this pulsar-scenario holds true, then the observed number of $> 10^2$ NTFs (Heywood et al., 2019) indicates a pulsar population in the CMZ. If every NTF hosts a pulsar and the produced CR electrons inverse-Compton scatter and radiate in γ-rays, then this can explain the Galactic Center excess seen with the *Fermi* γ-ray telescope (Bartels et al., 2016; Lee et al., 2016; Fermi-LAT Collaboration, 2017; Barkov and Lyutikov, 2019).

Radio emission from non-thermal filaments Both scenarios are comparable in terms of their energy budget and size of the acceleration site. Thus, the energy injected into a flux tube,

$$E_{\rm CR} = f_{\rm esc} \frac{R}{v_\star} L_e \sim 5 \times 10^{42} \text{ erg}, \tag{7.7}$$

is the same for both sources. Here, $f_{\rm esc} \sim 0.3 - 1$ is the time fraction during which CRs near the wind termination shock are injected into a flux tube. Furthermore, assuming that the injected electrons/pairs have a Lorentz factor $\gamma \sim 10^3$, they emit synchrotron radiation at

$$\nu = \frac{3eB\gamma^2}{2\pi m_e c} \sim 1.5 \text{ GHz} \tag{7.8}$$

with a total luminosity of

$$L_{\rm syn} = E_{\rm CR} \frac{\sigma_{\rm T} B^2 \gamma}{6\pi m_e c} \sim 2 \times 10^{29} \text{ erg s}^{-1}, \tag{7.9}$$

which corresponds to a spectral flux of

$$F_{\rm syn} = \frac{L_{\rm syn}}{2\pi d^2 \nu} \sim 2 \text{ mJy} \tag{7.10}$$

at a distance of $d = 8.2$ kpc. Within the uncertainties, this matches the radio harp flux. The associated synchrotron cooling time of $\sim 10^6$ yr is much longer than the CR propagation time of ~ 60 kyr so that we do not expect synchrotron fading (see Sect. 7.3).

7.3 Hydrodynamic Flux Tube Model for Radio Harps

Already the detection of radio harps is a strong argument in favor of CR propagation with $v_{\rm a}$: CRs leaving the source have individual trajectories that are preferentially aligned with the magnetic flux tube. As NTFs lay mostly perpendicular to the Galactic plane, the synchrotron radiation should be beamed away from the Galactic plane and undetectable for us. Thus, to explain the NTF detection, some mechanism is needed that effectively scatters CRs such that their beamed radiation is observable with radio telescopes. A likely possibility is pitch-angle scattering by gyroresonant Alfvén waves. CRs moving along a flux-tube can excite these Alfvén waves via the gyroresonant instability, which leads to CR streaming close to the Alfvén speed, $v_{\rm a}$ (see Sect. 7.1).

We model CR electron propagation inside NTFs with the following numerical setup: we assume self-similar evolution of the individual filaments in a harp and that the observation samples the NTF evolution at different times. Within a propagation model, this allows us to conduct a single simulation for all filaments. Filaments of different lengths correspond to different simulation times: longer filaments correspond to later times with a broadened CR distribution.

We assume an Alfvén speed of $v_{\rm a} = 40$ km s^{-1} and use ISM parameters as detailed in Sect. 7.2. The simulation domain is aligned with the magnetic flux tube, which is assumed to be straight and to have a constant cross section πR^2 during the simulation. The CR electrons are initialised by injecting $E_{\rm CR} = 5 \times 10^{42}$ erg into a Gaussian with width 0.05 pc to model CR injection at the bow shock of a massive star or pulsar.

1. The *diffusion* model assumes that the CRs diffuse along the magnetic flux tubes with a constant coefficient $\kappa = 3 \times 10^{25}$ cm^2 s^{-1}, which was chosen to match NTF sizes with a diffusion length scale $l = \sqrt{2\kappa t}$ and $t = 30$ kyr.[1] We include Alfvén wave cooling of CRs (see Pfrommer et al., 2017a).

[1] In the *diffusion* model, only the combination κt is constrained by the diffusion length; for simplicity, we use the time scale of the *streaming + diffusion* model.

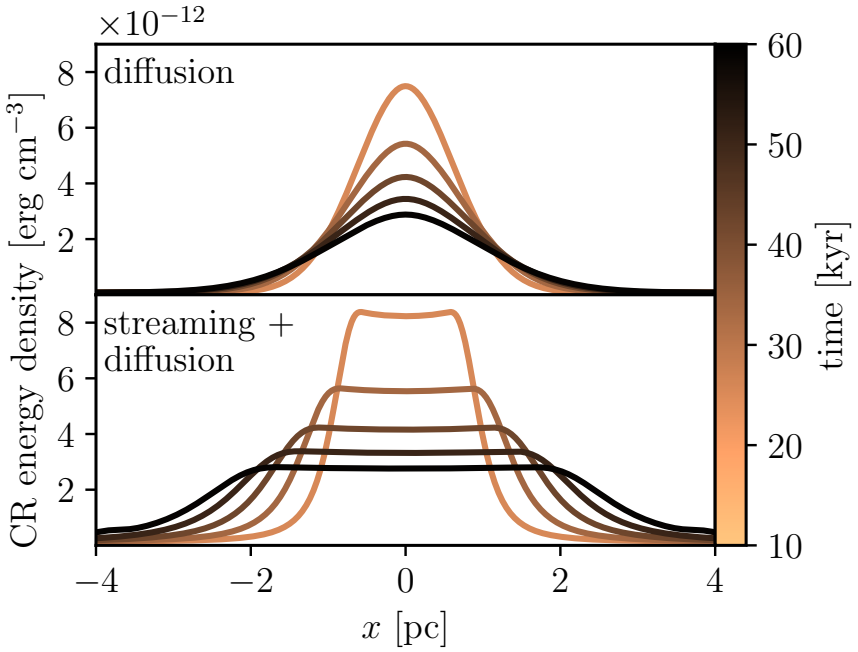

Figure 7.4: Evolution of the energy densities of CR electrons for the two propagation models over the course of 60 kyr.

2. The *streaming + diffusion* model uses the more accurate CR transport description of Thomas and Pfrommer (2019), which evolves the CR energy and momentum density. Additionally, the energy contained in gyroresonant Alfvén waves is evolved and coupled to CRs using quasi-linear theory of CR transport. We only consider non-linear Landau damping of Alfvén waves (see Thomas and Pfrommer, 2019). The initial CR energy flux is chosen so that CRs stream with v_a.

The *streaming + diffusion* model includes details of the microphysical CR-Alfvén-wave interactions that are absent in the pure *diffusion* model. In comparison to the *diffusion* model (where κ = const.) the diffusion coefficient in the *streaming + diffusion* model is calculated based on the local strength of Alfvén waves. We solve the equations of Thomas and Pfrommer (2019) using a finite volume method (Thomas et al. in prep.) in the moving mesh code `AREPO` (Springel, 2010) for both models (in the *diffusion* model we set κ = const). We use a one-dimensional grid with 4096 cells, a grid spacing of $\Delta x = 4 \times 10^{-3}$ pc, and outflowing boundary conditions. A reduced speed of light $\tilde{c} = 1000$ km s^{-1} is used and we confirmed that the presented results are robust for changes of $\tilde{c}$.

We present the CR electron energy density evolution in Fig. 7.4. The result for the *diffusion* model resembles the typical evolution of a diffusion process: the initial Gaussian approximately maintains its shape while increasing its physical extent. The deviations from a pure diffusion

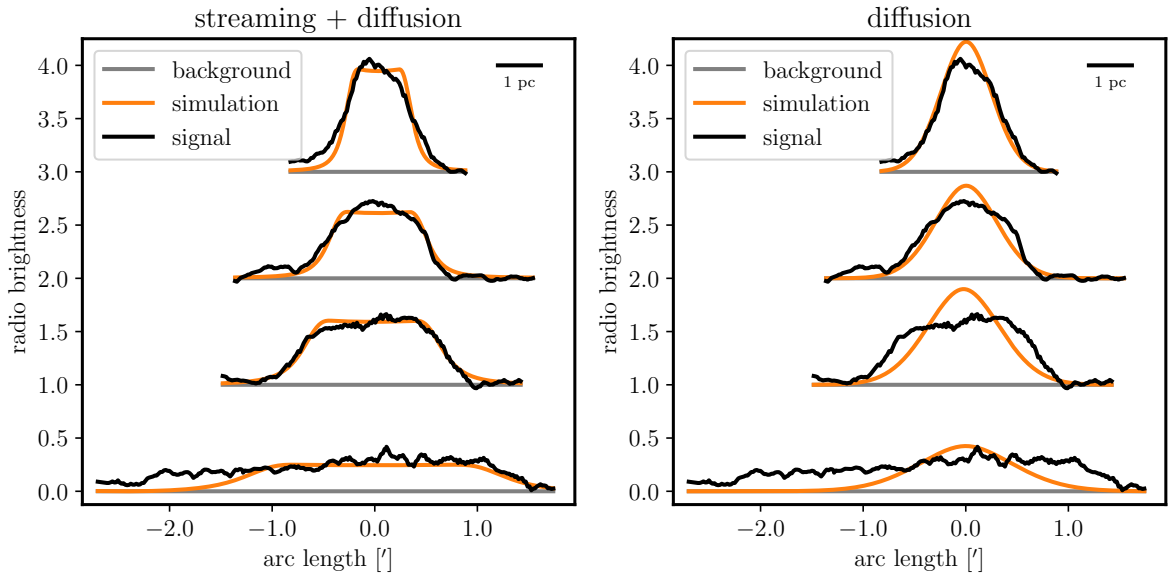

Figure 7.5: Comparison between the observed radio emission from the radio harp G359.47+0.12 (extracted from Heywood et al., 2019) and the simulated profiles. The simulated profiles are displayed at times 16, 26, 37, and 72 kyr (top to bottom) after CR injection. The filaments each have an offset of 1 in the y-direction. We convert physical distances in the simulation to angular sizes assuming a distance of 8.2 kpc to the CMZ. The *streaming + diffusion* model matches the MeerKAT radio data significantly better than the *diffusion* model.

profile are caused by CR-energy losses due to Alfvén-wave cooling.
Including CR-Alfvén-wave interactions allows CRs to enter the CR streaming regime. Therein the two Gaussian wings are traveling at speeds of $\sim \pm v_\mathrm{a}$ in opposite directions. In between the two wings the CRs are rarefied causing the development of an almost constant-energy-density plateau. At later times, the CRs are unable to maintain a high energy level of Alfvén waves. In consequence, CRs get less frequently scattered and enter the diffusive CR-transport regime.

7.4 Comparison to Observations

We extract radio brightness profiles of the MeerKAT filaments (Heywood et al., 2019) by taking cuts along individual filaments of the harp G359.47+0.12, shown in Fig. 7.2 on the right. We use one segment for the three brightest filaments, respectively, and four segments for the faintest filament to trace its curvature. In Fig. 7.5, we compare this to our simulations by scal-

ing the simulated CR energy density with a constant factor to match the observed radio flux. This factor is chosen so that the brightness in the first filament approximately agrees with the scaled simulated profiles. To match the brightness of the third and fourth filament in the *streaming + diffusion* model, we had to increase the scaling by 25% and 40%, respectively. For the *diffusion* model, we need to increase these factors by 50%. The displayed background noise level is calculated by averaging the diffuse background excluding resolved and bright sources. Only the *streaming + diffusion* model agrees with the observed profiles while the *diffusion* model is unable to reproduce the late-time central flat emission because the diffusion profile maintains its central maximum, causing there excess emission and underestimates the emission at larger distances. The gradients of the diffusion profile progressively flatten whereas the observations maintain sharp edges. Contrarily, the flat plateaus and sharp late-time gradients are well explained in the *streaming + diffusion* model. Therein, the plateau naturally corresponds to the rarefying CR energy density while the expanding CR fronts match the steep transition of the radio emission.

There are no primary beam corrections applied to the four pointings that make up the MeerKAT mosaic (Heywood et al., 2019). While this precludes accurate photometry of the large-scale emission, the small-scale radio-harp profiles should mostly be unaffected. We note that the image of G359.47+0.12 shows a circularly shaped area with reduced flux levels of filaments and background emission, which is centered just outside the image in the lower right part of Fig. 7.2. This reduced flux might be an artefact of the lacking primary beam corrections during imaging (Heywood et al., 2019) and could explain the asymmetric shape of the older synchrotron filaments in Fig. 7.5. If correct, the agreement of the *streaming + diffusion* model with the observation may improve even more after primary beam corrections and the *diffusion* model will become worse, strengthening our finding.

We attempted to apply the same analysis to the harp G359.85+0.39. However, its filaments appear to be overlapping in projection. Whether the overlap is caused by the projection of individual spatially separated or of braided flux tubes that divert away from the central bright emission is not obvious. This ambiguity precludes a simple emission modeling of the complex flux-tube structure. However, the morphological similarity of both harps, which exhibit the shape of an inverted bell curve, strongly suggests that CR streaming is responsible for the emission structure in both cases.

We predict a massive star or pulsar at the tip of each radio harp and encourage observers to search for them.

7.5 Conclusions

Here, we presented a model that explains the morphological appearance of the new phenomenon of radio harps observed within the bipolar outflows by MeerKAT. A careful modeling of two competing CR transport schemes (pure CR diffusion and a combination of CR streaming and diffusion in the self-confinement picture) demonstrates that only the CR *streaming* model is able to match the detailed brightness distributions of the individual NTFs of the harp G359.47+0.12. The intermittency of the harp emission either reveals details of the magnetic field structure or about the magnetic reconnection processes at the interface of the shocked stellar (or pulsar) wind with the surrounding interstellar magnetic field. We hope that future high-resolution observations enable us to disentangle the possibly three-dimensional structure of the other harp G359.85+0.39 and to detect more examples of this phenomenon. This will consolidate our conclusions that CR streaming is the relevant propagation mode for GeV CRs.

8 Blinc – a new AMR code for Radiation-Magnetohydrodynamics

In this chapter, we present the AMR code Blinc which solves the equations of radiation magnetohydrodynamics on a space and time adaptive mesh. The code is written in modern C++ and parallized using the MPI-3 library. It is composed out of two main building blocks: 1) the mesh framework that provides routines to create and manipulate uniform and adaptive meshes in a highly parallelized computing environments 2) a framework that provides a foundation for finite-volume methods to solve conservation laws and related equations on this mesh. In developing this code, we are inspired by other code projects that support the progress of computational astrophysics in the context of magnetohydrodynamics and radiation hydrodynamics such as (non-exhaustive list): Arepo (Springel, 2010; Pakmor et al., 2011; Pakmor and Springel, 2013), Athena/Athena++ (Stone et al., 2008, 2020), Enzo/Enzo-E (Bryan et al., 2014; Bordner and Norman, 2018), Nirvana (Ziegler, 2011), Pluto (Mignone et al., 2007, 2012), and Ramses (Teyssier, 2002; Fromang et al., 2006).

In Blinc, the mesh is composed out of logically rectangular patches and a block-structured / forest-of-octrees AMR approach is used to achieve spatial adaptivity. Most hydrodyanmical codes use a tree data structure to represent and organize this mesh in computer memory. Blinc uses a fundamentally different strategy and describes the mesh topology using a graph. Similar to Schornbaum and Rüde (2018), each patch in the simulation saves and maintains information about its immediate neighbouring patches which eliminates the need for a global tree structure from which this information can be inferred. We detail how the mesh is described in our graph-based approach and how spatial adaptivity is realized within the graph. The Hilbert space-filling curve is used for domain decomposition and to distribute the computational work on a parallel computers. We developed and describe an effective diffusive load balancer that employs an iterative algorithm that resembles the physical diffusion process on this curve. This load balancer is able to redistribute patches and achieve (almost) equal-share-of-work among participating MPI processes.

The mesh provides a foundation on which we build finite-volume schemes to solve equations that are similar to

$$\frac{\partial \boldsymbol{U}}{\partial t} + \boldsymbol{\nabla} \cdot \boldsymbol{F}(\boldsymbol{U}) = \boldsymbol{S}(\boldsymbol{U}), \tag{8.1}$$

where $\boldsymbol{U}$ is the state vector and is composed out of physical quantities those flux is $\boldsymbol{F}$ and $\boldsymbol{S}$ are explicit source terms. Methods to solve these equations in curvilinear coordinates such as Cartesian, spherical and cylindral coordinates in 1D, 2D, and 3D assuming the respective sym-

metries are implemented. We describe how the divergence operator in Eq. (8.1) is discretized in different coordinate systems and take special care that this discretization is consistent with the finite-volume idea. Directionally unsplit, shock-capturing higher order Godnuov methods are used in conjunction with Riemann solvers to discretize Eq. (8.1). This class of finite-volume schemes needs a time integration scheme to advance the state vector in time and reconstruction methods to interpolate cell-averaged quantities to cell interfaces as input variables for Riemann solvers. Multiple options are available for these methods and we detail how they are implemented in Blinc.

Each simulation starts after the initial conditions have been specified and is composed of a sequence of individual timesteps. Each timestep represents an iteration of the finite-volume scheme which advances time by some Δt which is either bound by an user-speficied value or the CFL condition

$$\Delta t = \mathrm{CFL} \min_{\mathrm{cells}} \left(\frac{v_{\mathrm{max,x}}}{\Delta x} + \frac{v_{\mathrm{max,y}}}{\Delta y} + \frac{v_{\mathrm{max,z}}}{\Delta z} \right)^{-1} , \tag{8.2}$$

where $\mathrm{CFL} \in [0, 1]$ is the well-known Courant-Friedrichs-Lewy number, $v_{\mathrm{max,x,y,z}}$ are the fastest characteristic speeds that are reached in the simulated hydrodynamical model, $\Delta x, y, z$ are the typical cell sizes, and the minimum is taken over all cells in the simulation.

We describe how we construct solvers for magnetohydrodyanmics and radiation hydrodynamics based of the M1-closure into this framework. The divergence constraint of the magnetic field in the equations of magnetohydrodynamics is taken care of using the constrained transport or the Powell method. In order to calculate the electric fields in the constrained transport method, we use the method of Gardiner and Stone (2005). No such well-established standard method exists for the Powell method which started our development of a novel discretization of the Powell terms based on path-conservative finite-volume schemes. Through various test problems, we demonstrate the robustness of our solvers and of the AMR framework. We also highlight that the constrained transport and Powell method give quantitatively different and yet qualitatively comparable results.

In the finite-volume paradigm, we evolve the cell-average of a quantity U inside a given cell with indicies ijk and volume V_{ijk}

$$U_{ijk} = \frac{1}{V_{ijk}} \int_{V_{ijk}} \mathrm{d}^3 r \, U(\boldsymbol{r}) \tag{8.3}$$

and associate this with the value of U at the cell centre. We use both the cell-average and cell-centred values interchangeably which limits the convergence order of the employed schemes to be at most 2nd order in space. Throughout this chapter, we may drop any of the indices ijk for readability if their presence is unnecessary and if no confusion arises in the given context.

A natural question to ask is why to write a completely new AMR framework or a solver for radiation-magnetohydrodynamics in the first place. The answer is: by accident. Blinc was originally a simple tool made and meant as a playground to learn about Godunov methods, Riemann solvers, and timestepping schemes. Accumulation of individual small extensions driven by feature creep lead to its current state.

8.1 Mesh Framework

The mesh framework is completely separated from all physical modules and is fundamental to Blinc. It provides data structures and methods to create and manipulate adaptive logically rectangular grids on which simulations are performed. It is further responsible to distribute and synchronize the associated physical data between MPI processes. In Blinc, we loosely follow a forest-of-octrees approach in our design choices and are influenced by Athena++ (Stone et al., 2020), Enzo-E/Cello (Bordner and Norman, 2018), p4est (Burstedde et al., 2011), and Schornbaum and Rüde (2018).

8.1.1 Grid Topology and Ghost Cells

We first describe how a uniform mesh is represented in our framework. The mesh itself covers the whole simulation domain and is composed out of $N_x \times N_y \times N_z$ cells in 3D and N_y and N_z might be one for simulations in lower dimensions. To create this mesh, we stitch patches with $N_{\text{patch},x} \times N_{\text{patch},y} \times N_{\text{patch},z}$ cells together. Each patch represents a rectangular sub-volume of the simulation domain. This stitching effectively decomposes the global mesh into a collection of sub-meshes.

We assign integer coordinates (i, j, k) to each patch such that we can identify them during the mesh creation process. We show a mesh composed out of 3×3 patches in Fig. 8.1. Patches are connected with each other to form the global mesh. This notion of connectivity is realized in most AMR codes through a tree data structure. In our mesh framework, we try not to use any tree structure. This is for the following reason: a global tree structure would require information about the whole mesh and the entirety of all patches in it. Each modification to the mesh itself will also result in a modification this global tree which needs to be synchronized between all participating MPI processes. Designing scalable algorithms which achieve this is non-trivial.

We use a graph-based approach to describe patch connectivity. Therein, each patch stores information that represents the connections to it is neighbouring patches. The patch holds onto this information for its whole lifetime and the mesh framework is responsible for consistently

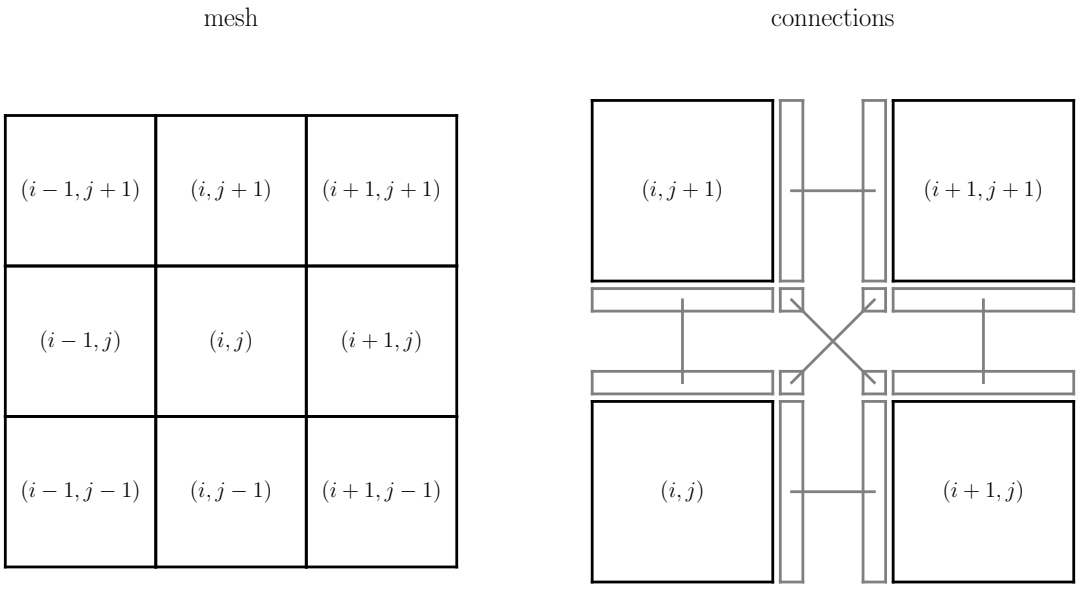

Figure 8.1: Left: Example of a uniform mesh which is composed out of handful rectangular patches. Right: We show four patches in black, grey regions that represent the ghost cell regions around those patches, and how these patches are connected through grey lines.

updating it every time the immediate neighbourhood of the patches changes in some way. The whole mesh is then implicitly given by the collection of patches and their connections. We show the patch topology and the connections inside a 2×2-patch mesh in Fig. 8.1. In graph-theory terminology, a patch is a vertex while connections are edges between vertices.
Because the mesh and patches are logically rectangular, we can categorize them based on geometrical terms: we call the connection between a patch (i, j, k) and a neighbouring patch with integer coordinates $(i + \mathrm{d}i, j + \mathrm{d}j, k + \mathrm{d}k)$:

$$\begin{aligned} \text{a (inter)face-connection} \quad & \text{if } |\mathrm{d}i| + |\mathrm{d}j| + |\mathrm{d}k| = 1, \\ \text{a edge-connection} \quad & \text{if } |\mathrm{d}i| + |\mathrm{d}j| + |\mathrm{d}k| = 2, \\ \text{a corner-connection} \quad & \text{if } |\mathrm{d}i| + |\mathrm{d}j| + |\mathrm{d}k| = 3. \end{aligned}$$

Connections are, by definition, symmetric which means that if patch A holds a connection to patch B then patch B also holds a connections to patch A. Once we also store information about the hosting MPI rank of each neighbour patch together with the connections, distribution of patches among MPI processes is straightforward because each patch knows about its neighbourhood and with which MPI process it needs to communicate in order to receive additional

information. In case a patch is transferred from one MPI rank to another one, only this localized information needs to be updated. This is different in AMR codes that curate an global tree to hold the mesh. Therein, the tree needs to be updated on all processors each time such an transfer takes place. In our graph-based approach, only the hosts of immediate neighbouring patches need to be informed.

In a finite-volume algorithm, fluxes are exchanged between cell interfaces. Some of these cell interfaces are located on patch interfaces. The data stored within the cells of a given patch might be insufficient to calculate how much flux needs to be exchanged. To circumvent this issue, ghost cell are attached on the outside of each patch which are buffer regions for the information that is logically located on a different patch. To fill the ghost cells, we must know the corresponding patch whose cells they are representing. Here the connections of a patch are used. Because connections store all the information about neighbouring patches, we can associate ghost cells that lay behind either a face, edge or corner of a patch with the corresponding connections. We display the ghost cell regions together with their associated connection in Fig. 8.1. Populating the ghost cells with required information is achieved through communication buffers. These buffers are located within the shared memory of a given computing node and are exchanged through one-sided communication routines (such as MPI_PUT of the MPI-3 library).

8.1.2 Adaptive Mesh Refinement

We provide the ability to locally refine or derefine patches to change the resolution of a simulation in certain regions. The user defines refinement and derefinement criteria to adapt the resolution in or away from regions of interest. During refinement, a given patch is replaced by 2^{N_D} patches where N_D is the number of dimensions. Because patches represent a group of computational cells, patch refinement also corresponds to a cell refinement where each cell is replaced by 2^{N_D} cells. Derefinement operates in the opposite way and replaces previously refined cells and patches by coarser counterparts.

Refinement and derefinement of patches modifies the local graph topology of our mesh. We assign integer coordinates to refined child patches of a given parent patch following:

$$i_\mathrm{child} = 2i_\mathrm{parent} + \mathrm{d}i, \tag{8.4}$$

$$j_\mathrm{child} = 2j_\mathrm{parent} + \mathrm{d}j, \tag{8.5}$$

$$k_\mathrm{child} = 2k_\mathrm{parent} + \mathrm{d}k, \tag{8.6}$$

where $\mathrm{d}i, \mathrm{d}j, \mathrm{d}k \in 0, 1$. The integer coordinates of the parent can be inferred by,

$$i_{\text{parent}} = i_{\text{child}} \,//\, 2, \tag{8.7}$$

$$j_{\text{parent}} = j_{\text{child}} \,//\, 2, \tag{8.8}$$

$$k_{\text{parent}} = k_{\text{child}} \,//\, 2, \tag{8.9}$$

where // denotes the integer division operator. This last operations can be used to deduce the connection category between neighbouring patches by applying it to the interger coordinates of finer patches. We save the AMR level as an additional property of the each patch - patches of the root mesh have an AMR level of 0 while refining increases the AMR level by one. Only the combination of AMR level and integer coordinates uniquely identifies a patch when AMR is used.

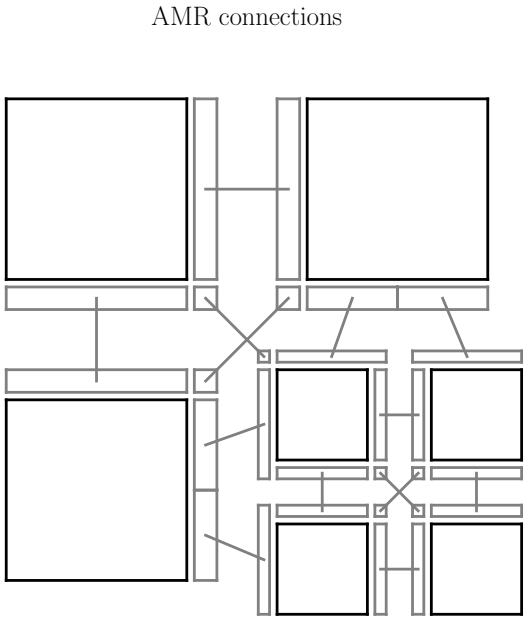

Figure 8.2: Extension of the right panel of Fig. 8.1 to an AMR mesh. The size of the black outlined patches indicates their AMR level.

In Fig. 8.2, we show how a refined patch is integrated in to the graph of a 2×2 patch mesh. Connections from neighbouring patches are removed from the parent patch, and neighbouring patches are reconnected to the refined patches. From the viewpoint of the neighbouring coarse patches, there are now multiple face connection in one direction. In order to decide how patches are connected, we require that each patch is connected to another neighbouring patch through exactly one connection. Following this rule, some corner connections of the refined patches are

missing and have been combined into the face connection. Face connections that point from a finer to coarser interface represent an expanded region of ghost cells.

Mesh Regularity through the 2:1 Ratio

We enforce the so called 2:1 ratio between neighbouring patches by requiring that they do not differ in their AMR level by more than one. Using the terminology of Isaac et al. (2012), we require that our mesh is *corner balanced* which means that all face-, edge-, and corner-neighbours do not have AMR level differences larger than one. The reason for this is twofold: 1) this allows us to make certain assumptions about this mesh topology that enables code optimisations, e.g. with this requirement we know that each patch has at most $2 \times N_\mathrm{D} \times 2^{N_\mathrm{D}-1}$ faces because there are two faces per dimension that can be split into $2^{N_\mathrm{D}-1}$ finer faces in an AMR scenario. We thus need to allocate memory for this specific number of faces at most. 2) neighbouring cells do not drastically differ in volume and thus in their typical cell size which is favourable to reduce numerical errors. To ensure that this requirement holds at any time, the refinement and derefinement operations are carried out in a specific way.

Refinement Patches are flagged for refinement from the finest level towards the root level. Moving in this direction, patches at each level that are flagged for refinement check whether neighbouring patches need to be refined to enforce the 2:1 ratio. Neighbouring patches at a coarser level would violate this requirement once the flagged patch would be refined - to avoid this situation they are also flagged for refinement. Once all refinement flagging operations are carried out, a hypothetical instantaneous refinement of all flagged patches would result in mesh with a 2:1 ratio between all patches. But on a serial or even parallel computer the patches-to-be-refined queue must be processed in some way which might not guarantee that the 2:1 ratio requirement is fulfilled at all times and hence also during the refinement process itself. To accomplish this, we refine patches level by level going from the root level down to the finest level. This strategy ensures that once the refinements at a given level have been completed the mesh still has the 2:1 ratio property. To understand the reason why, we start our argumentation by considering the situation at the root level first: there, patches can be refined in any case without violating the property at all. Patches at this level are refined such that patches at the next finer level can also be refined without a violation. Thus, once patches at the root level are refined, patches at the level 1 can be refined. These patches are also flagged for refinement such that the patches at the corresponding next level might be refined without a violation. At this point, refinement is a recursive operation where each step in the recursion ensures that the next

step can be executed with a violation of the 2:1 rule.

Derefinement The algorithm for derefinement proceeds in an inverse fashion. Patches can be flagged for derefinement only if all of its neighbouring patches are on the same level and are not flagged for refinement or if neighbouring patches that are on a finer level are flagged for derefinement. Derefinement itself is executed starting from the finest to the root level on a level by level basis. As for the refinement process, this ensures that once all patches on a given level are derefined then the patches on the next coarser level can be derefined without violating the 2:1 requirement.

Prolongation and Restriction

Each time patches and consequently their associated cells are (de-)refined, all physical fields that are defined on them need to be reapproximated on the new patches based on the information available on the progenitor patches. In the multigrid terminology, the refinement process is called prolongation while the derefinement of the field is called restriction. For fields that are defined on cell-centres, which represent average densities of conserved quantities such as mass, momentum, and energy, we employ a 2nd-order restriction operator,

$$U_{\text{fine}} = U_{\text{coarse}} + (\mathrm{d}_x U)(x_\mathrm{f} - x_\mathrm{c}) + (\mathrm{d}_y U)(y_\mathrm{f} - y_\mathrm{c}) + (\mathrm{d}_y U)(z_\mathrm{f} - z_\mathrm{c}) \quad \text{for all} \quad \text{fine} \in \text{childs} \tag{8.10}$$

where 'childs' is the set of refined cells that originate from the 'coarse' cell, U_{fine} is the prolongated value and represents the quantity averaged over the fine mesh cell, U_{coarse} is the quantity averaged over the coarse mesh cell, $x_\mathrm{f}, y_\mathrm{f}, z_\mathrm{f}$ are the cell centre coordinates of the fine cell, and $x_\mathrm{c}, y_\mathrm{c}, z_\mathrm{c}$ are the cell centre coordinates of the coarse cell. [1] The gradients are calculated by

$$\mathrm{d}_x U = \textsc{Minmod}\left(\frac{U_{\text{coarse},i+1} - U_{\text{coarse},i}}{x_{c,i+1} - x_{c,i}}, \frac{U_{\text{coarse},i} - U_{\text{coarse},i-1}}{x_{c,i} - x_{c,i-1}}\right), \tag{8.11}$$

$$\mathrm{d}_y U = \textsc{Minmod}\left(\frac{U_{\text{coarse},j+1} - U_{\text{coarse},j}}{y_{c,j+1} - y_{c,j}}, \frac{U_{\text{coarse},j} - U_{\text{coarse},j-1}}{y_{c,j} - y_{c,j-1}}\right), \tag{8.12}$$

$$\mathrm{d}_z U = \textsc{Minmod}\left(\frac{U_{\text{coarse},k+1} - U_{\text{coarse},k}}{z_{c,k+1} - z_{c,k}}, \frac{U_{\text{coarse},k} - U_{\text{coarse},k-1}}{z_{c,k} - z_{c,k-1}}\right), \tag{8.13}$$

where the minmod limiter is defined by

$$\textsc{Minmod}(a, b) = \frac{\operatorname{sign}(a) + \operatorname{sign}(b)}{2} \min\left(\operatorname{abs}(a), \operatorname{abs}(b)\right). \tag{8.14}$$

[1] We describe how the prolongation operator is implemented in Cartesian coordiantes for clarity. In curvilinear coordinates, the cell centres are defined in a finite-volume sense by their average coordinates $\boldsymbol{c}_{\text{center}} = V^{-1} \int_V \mathrm{d}^3 V \boldsymbol{c}$ where $\boldsymbol{c}$ is the coordinate vector and V is the volume of the cell at interest.

Additional limiters might be employed to enforce additional physical properties of the prolongated quantities such as positivity of energy and mass density. The restriction operator is less involved and given by:

$$U_{\text{coarse}} = \sum_{\text{fine} \in \text{childs}} \frac{V_{\text{fine}}}{V_{\text{coarse}}} U_{\text{fine}}, \tag{8.15}$$

where V_{fine} and V_{coarse} are the cell volume of the fine and coarse cells, respectively. These operators are also used to synchronise ghost cell values between patches on an AMR mesh.
For face-centred quantities, we employ a 1st-order prolongation where on interfaces that are shared between the coarse and fines cells

$$F_{\text{fine}} = F_{\text{coarse}} \quad \text{for all} \quad \text{fine} \in \text{childs} \tag{8.16}$$

holds, where F_{fine} is the interface averaged quantity on the fine cell interfaces, and F_{coarse} is the interface averaged quantity on the coarse cell interfaces. On fine cell interfaces that do not have a coarse counterpart, we employ the 1st order interpolation as described by Tóth and Roe (2002). The corresponding restriction operator reads as:

$$F_{\text{coarse}} = \sum_{\text{fine} \in \text{childs}} \frac{A_{\text{fine}}}{A_{\text{coarse}}} F_{\text{fine}}, \tag{8.17}$$

where A_{fine} and A_{coarse} are the respective interface areas of the fine and coarse cell interfaces. This operator is also used to synchronize the fluxes of the finite-volume scheme at cell interfaces that are shared between neighbouring patches on different AMR levels (Berger and Colella, 1989). This is a necessary step to ensure that conserved quantities are correctly transported in a conservative manner on an AMR grid. This synchronization takes place before any flux divergences are calculated which is different to the orginal refluxing strategy of Berger and Colella (1989).

Time Adaptivity

In our default configuration, all patches are advanced in time using the global timestep. In a simulation employing an adaptive mesh, the CFL condition can result in timestep requirements that strongly vary between patches because typical cell sizes also vary. If a short global timestep is caused by a small number of fine patches, it is beneficial and efficient to advance these patches using a shorter timestep. We implement a method that accomplish this and allow for individual timesteps of patches. Our algorithm broadly follows Berger and Oliger (1984), Berger and Colella (1989), Springel (2010), and Mignone et al. (2012).

We use a hierarchy-of-2 time binning system to group patches with similar timestep requirements into groups. We define the timestep of a timebin to be a power-of-2 fraction of some maximum timestep: $\Delta t_{\rm bin} = 2^{-\rm bin}\Delta t_{\rm max}$ where $\Delta t_{\rm max}$ is either chosen by the user or defaults to the duration of the simulation. Patches are grouped into the timebin with the largest timestep that is still smaller or equal to the timestep requirement of the patch. Neighbouring patches are allowed to have timebin differences of at most 1. If a patch has a neighbour on a finer AMR level then the timestep of the patch must be longer or equal to the timestep of the neighbouring patch. To enforce these conditions, we use a similar algorithm as we did to ensure the 2:1 ratio during the spatial refinement process.

Time integration is then accomplished by invoking the finite-volume algorithm on all patches with active timebins. To decide whether a timebin is active the following recursive definition is used: we say that a timebin i is active if two conditions are met: 1) the timebin $i + 1$ is also active 2) on the last iteration of the timebin $i + 1$, our timebin of interest i was not active. The timebin with the shortest timestep that has at least one patch grouped into it is always active.

All patches in active timebins will be synchronized in physical time after an iteration of this algorithm. In order to achieve a conservative update of physical quantities, fluxes between patches on slow and fast timebins need to be synchronized. This is done by replacing the fluxes at shared interfaces using:

$$F_{\rm slow}^{n\to n+1} = \frac{\Delta t^{n\to n+1/2} F_{\rm fast}^{n\to n+1/2} + \Delta t^{n+1/2\to n} F_{\rm fast}^{n+1/2\to n+1}}{\Delta t^{n\to n+1/2} + \Delta t^{n+1/2\to n+1}}, \tag{8.18}$$

where the $F_{\rm fast}^{n\to n+1/2}$ flux originates from the first iteration of patch on the fast timebin with a timestep $\Delta t^{n\to n+1/2}$, and the flux $F_{\rm fast}^{n+1/2\to n+1}$ flux originates from the second iteration of patch on the fast timebin with a timestep $\Delta t^{n+1/2\to n+1}$. This flux synchronization is carried out if both the fast and slow timebins are active.

Ghost cells are only communicated between patches that are synchronized. It is desirable to extrapolate the evolution in ghost-cells for patches on fast timebins in order to increase the consistency in the time integration. Currently, we do not implement a method for this and leave this for future work.

8.1.3 Load Balancing

For simulations with large number of patches, an efficient load balancing algorithm is needed to distribute the total amount of required computing power between all MPI processes. The basic task of this load balancing algorithm is to assign an equal amount of work to each process. In Blinc, we regard the patch as a quanta of work by which we assume that each patch

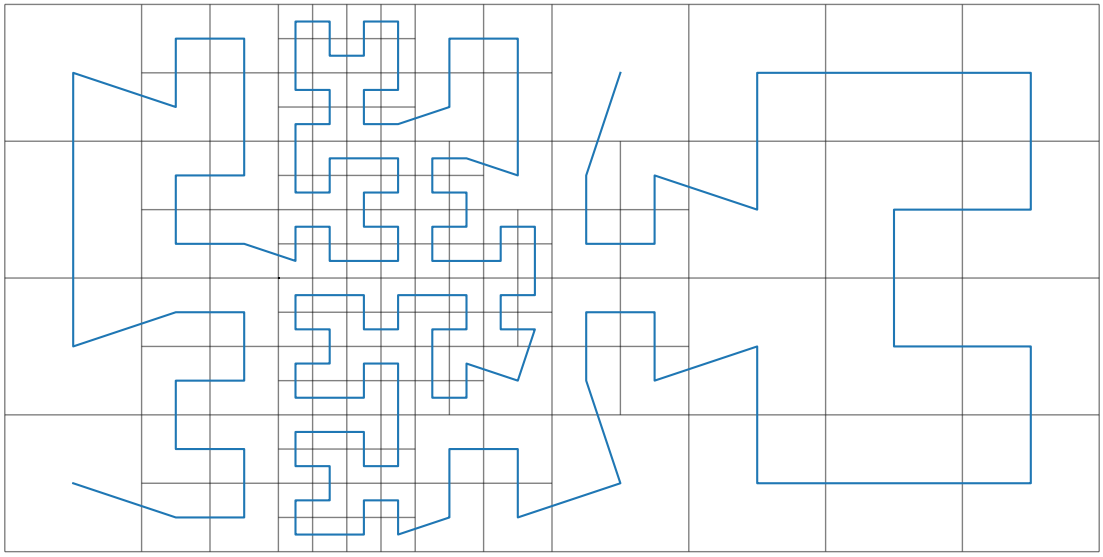

Figure 8.3: Hilbert space filling curve applied to an AMR simulation with 2 levels of refinement. Mesh patches are outlined using grey coloured lines and are connected by the blue space filling curve

needs roughly to same amount of computing time to complete a single timestep (which is not necessary true in general). The task of our load balancing algorithm is thus to balance the number of patches per process. We use two fundamentally different algorithms to (approximately) achieve load balancing. The first algorithm is a global load balancing method that establishes a near-perfect balance at a given time in the simulation while the second algorithm is a diffusive load balancing algorithm that achieves a balanced patch distribution after multiple invocations of this method.

The bookkeeping of the global load balancing method is done by a single process. It is only called once at the beginning of the simulation after the initial mesh has been constructed but before actual memory for the simulation data is allocated for the initial patches. This process gathers information about all patches that are present initially and then assigns an equal number of patches to each processor. It then communicates the information about the assigned patches together with the neighbourhood information of these patches to their assigned host processors. To establish a correlation of between spatial position of the patches with their location on different processors, we calculate a single and unique 1D number that acts as an identifier of patches. We use the Hilbert space-filling curve to calculate this number based on the integer coordinates of the patches. In particular, we employ the algorithm of Lawder and King (2001) to determine this Hilbert key. We can sort the list of patches using this Hilbert key and implicitly

connect all patches with a 1D space-filling curve. In Fig. 8.3, we show patches of an AMR mesh together with the associated Hilbert space-filling curve that connects them. Both of our load balancing algorithms use the Hilbert key to distribute patches such that neighbouring Hilbert keys are located on neighbouring processors (as defined by the MPI rank number). This is done in the global load balancing method by cutting the Hilbert curve in N_{procs} segments where N_{procs} is the total number of MPI processes such that each segment contains an (roughly) equal number of patches. Patches that are within these segments are then send to their assigned processor. This procedure is also used in other codes such as RAMSES and AREPO / GADGET2 (Springel, 2005) while ATHENA++ uses a similar approach but employs the z-curve as a space-filling curve (Stone et al., 2020).

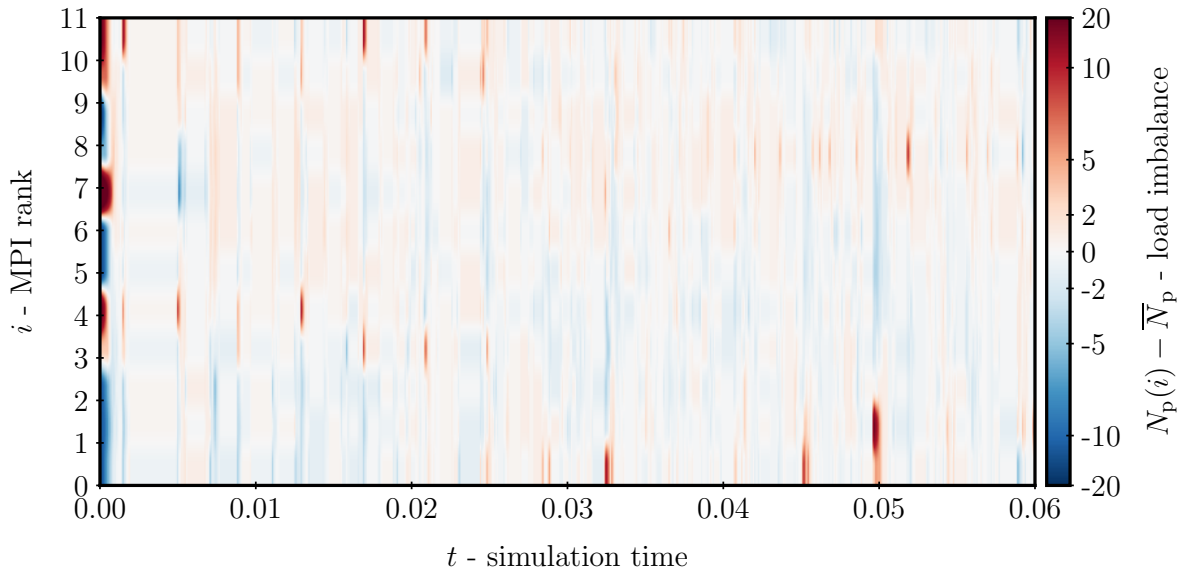

Figure 8.4: The load imbalance, calculated by $N_{\text{p}}(i) - \overline{N}_{\text{p}}$, is shown for the simulation in Sec. 8.4.4 with the CT method on a 12-core machine.

The basic idea of the diffusion load balancing algorithm is to accomplish the redistribution of patches towards a state of equal-share-of-work for all processors through a diffusion process. A similar idea for load balancing is used by Schornbaum and Rüde (2018) to demonstrate that their AMR code based on the WALBERLA framework has favourable scalability properties.

To motivate that diffusion load balancing might be advantageous over other algorithms, we need to consider how a load imbalance is create in our code. In AMR codes patches can be refined and derefined which alters the patch topology but also changes the number of patches on the processor where such an AMR event takes place. Assuming that these AMR events rarely happen and sparsely appear in space then each of these AMR events will also create

a load imbalance that is localized in space in time. We can further assume that each AMR event only corresponds to slight load imbalance because the number of patches on the affected processor changes by a maximum of seven in a 3D simulation (three in 2D and one in 1D). In such a situation, a global load balancer needs, by definition, information about the whole mesh to calculate a redistribution of the patches to reduce this small load imbalance. This requires a computational complex and communication intensive algorithm.

Instead, we use our diffusion load balancer whose imposed aim is to reduce the local load imbalance through a localized redistribution of patches. This process solely depends on local information about the mesh and is readily parallelizable. On each invocation of the diffusion load balancer, we aim to reduce the load imbalance by one or two patches on each processor. Successive invocations of the diffusion load balancer can reduce any load imbalance.

In our design of the actual algorithm that implements these ideas, we are guided by the physical diffusion process where some physical quantity flows from regions of high concentration to region with low concentration. We regard the number of patches on a processor as this physical quantity while the coordinate axis along which the diffusion operates is given by the MPI rank. We apply periodic boundary conditions to this axis. Some adaption to the original idea of physical diffusion need to be made in order to apply it to our situation mainly because physical diffusion is a continuous process that acts on real numbers while our process is discrete and acts on integer quantities. In order to decide whether we want to transfer from one processor to a processor with neighbouring MPI rank, we first define $N_\mathrm{p}(i)$ as the number of patches on the processor with rank i, calculate $\overline{N}_\mathrm{p} = N_\mathrm{procs}^{-1} \sum_i N_\mathrm{patches}(i)$ as the average number of patches, and then use the following algorithm (written in pseudo code):

If $N_\mathrm{p}(i-1) - N_\mathrm{p}(i) > 1$ then **send** (condition 1)
Else If $N_\mathrm{p}(i-1) - N_\mathrm{p}(i) = 1$
  If $N_\mathrm{p}(i-2) - N_\mathrm{p}(i-1) = 0$ and $\left(N_\mathrm{p}(i-1) < \overline{N}_\mathrm{p} \quad \text{or} \quad N_\mathrm{p}(i) > \overline{N}_\mathrm{p}\right)$ then **send** (condition 2)
  If $N_\mathrm{p}(i-2) - N_\mathrm{p}(i-1) > 0$ then **send** (condition 3)

where **send** indicates that one patch will be send from the processor with rank p to the process with rank $p-1$. To ensure that the segments of the Hilbert curve stay connected, the patch with the lowest Hilbert key is send. The symmetrical equivalent of this algorithm is used to decide whether a patch will be send from the processor p to the processor $p+1$.

Condition 1 checks whether the neighbouring patch counts differ by at least two which is an obvious case where we can locally reduce the load imbalance. The case where this difference is only one needs to be handled with care and turns out to be crucial to achieve global balance

through successive diffusive load balance: Condition 2 checks whether the local patch count gradient points towards the average patch count. We transfer patches in this case to allow the algorithm to establish balance in situations where the patch numbers on a processor are, e.g., given by ... 3 3 4 4 5 5 ... with $\overline{N}_{\text{patches}} < 4$. This condition is also necessary to avoid the development of staircase features in the $N_{\text{patches}}(p)$ function. Condition 3 recognises situations where the patch numbers on processor are, e.g., given by ... 4 5 6 7 8... where the direct-neighbour patch count information is insufficient to test for a local patch number gradient that requires balancing.

Just like the physical diffusion process, this algorithm effectively transports patches from processors with a high patch count to those processors that have low patch count. Perfect load balance may not be achieved as the total number of patches in the simulation might not be dividable by N_{procs}. Nevertheless, we observed that the diffusive load balancer convergences on a state where all processors hold an equal number of patches with ±one patch variance through various test simulations.

In Fig. 8.4, we show the load imbalance for an AMR simulation executed on a total of 12 MPI ranks. At the beginning of this simulation, many refinement operations are carried out in order to fulfil the refinement criteria of this simulation. This strong global load imbalance poses an problem for the load balancer and some time is needed to establish load balance. Otherwise, AMR events, especially those corresponding to patch refinements, are visible by saturated colours throughout the duration of the simulation. These localized load imbalances are quickly diffused away and local and global load balance is established over a short period of time.

8.2 Finite-Volume Algorithm

In this section, we are describing technical aspects of the finite-volume algorithm that are unrelated to the actual physics which we will discuss later. In particular, we detail how the divergence operator is discretized in different coordinate systems in Sec. 8.2.1, how cell averaged quantities are interpolated from the cell centre to the cell interfaces Sec. 8.2.2, and how the time integration is accomplished in Sec. 8.2.3.

8.2.1 Coordinate System

The coordinate system in Blinc provides a mapping between the logically rectangular patches and the actual physical space of the simulation domain. We provide the option to use either

Cartesian, cylindrical or spherical coordinate systems that the user has to choose at compile time using a configuration flag. These coordinate systems are implemented using C++-classes that share a common abstract interface. Additional coordinate systems can be implemented by using the same interface. One of the main tasks of a coordinate system in the finite-volume code Blinc is to provide a discretization and an implementation of the divergence operator in Eq. (8.1). While is this a straightforward operation in Cartesian coordinates, the divergence operator of a flux tensor $\boldsymbol{F}$ includes geometric source terms if it is evaluated in general curvilinear coordinates. Because $\nabla \cdot \boldsymbol{F} = 0$ for $\boldsymbol{F} = P\mathbf{1}$ with $P = \text{const}$, these geometrical source terms need to be properly discretized such that the resulting discretized divergence operator also vanishes is this case. This requirement is important for a physical situation where a medium has a uniform pressure: because we have from the Euler equation $\partial_t \rho \boldsymbol{u} = -\nabla \cdot (P\mathbf{1}) + \ldots$, if the requirement on the vector divergence is not met then the discretization of the pressure divergence itself will seed motions without an underlying physical reason.

Cartesian Coordinates

The directions defined by the three cell indices are mapped to Cartesian coordinates via:

$$(i, j, k) \longrightarrow (x, y, z) \tag{8.19}$$

Expanding the divergence operator in the conservation law of a scalar quantity u with flux $\boldsymbol{F} = (F_x, F_y, F_z)$ reads as:

$$\frac{\partial u}{\partial t} + \frac{\partial F_x}{\partial x_i} + \frac{\partial F_y}{\partial y_j} + \frac{\partial F_z}{\partial z_k} = 0, \tag{8.20}$$

where we augment the the spatial derivatives with their corresponding cell indices to indicate that these derivatives will be discretized numerically. In a finite-volume scheme, we are interested in the evolution of the mean-value of u inside a given cell. To find the corresponding evolution for the mean value, we calculate the average of Eq. (8.20) by stating how the spatial derivatives transform in it:

$$\frac{\partial q}{\partial x_i} \longrightarrow \frac{1}{\int_{\text{cell}\,ijk} \mathrm{d}V} \int_{\text{cell}\,ijk} \mathrm{d}V \frac{\partial q}{\partial x} = \frac{q_{i+1/2} - q_{i-1/2}}{x_{i+1/2} - x_{i-1/2}}, \tag{8.21}$$

$$\frac{\partial q}{\partial y_j} \longrightarrow \frac{1}{\int_{\text{cell}\,ijk} \mathrm{d}V} \int_{\text{cell}\,ijk} \mathrm{d}V \frac{\partial q}{\partial y} = \frac{q_{j+1/2} - q_{j-1/2}}{y_{j+1/2} - y_{j-1/2}}, \tag{8.22}$$

$$\frac{\partial q}{\partial z_k} \longrightarrow \frac{1}{\int_{\text{cell}\,ijk} \mathrm{d}V} \int_{\text{cell}\,ijk} \mathrm{d}V \frac{\partial q}{\partial z} = \frac{q_{k+1/2} - q_{k-1/2}}{z_{k+1/2} - z_{k-1/2}}, \tag{8.23}$$

where q is a placeholder function and $q_{i+1/2}$ is q evaluated at the interface between cells i and $i+1$. This interface has an associated coordinate $x_{i+1/2}$.

Expanding the divergence operator in the conservation law of a vector quantity $\boldsymbol{u} = (u_x, u_y, u_z)$ with tensor flux $\boldsymbol{F}$ reads as:

$$\frac{\partial u_x}{\partial t} + \frac{\partial F_{xx}}{\partial x_i} + \frac{\partial F_{xy}}{\partial y_j} + \frac{\partial F_{xz}}{\partial z_k} = 0, \tag{8.24}$$

$$\frac{\partial u_y}{\partial t} + \frac{\partial F_{yx}}{\partial x_i} + \frac{\partial F_{yy}}{\partial y_j} + \frac{\partial F_{yz}}{\partial z_k} = 0, \tag{8.25}$$

$$\frac{\partial u_z}{\partial t} + \frac{\partial F_{zx}}{\partial x_i} + \frac{\partial F_{zy}}{\partial y_j} + \frac{\partial F_{zz}}{\partial z_k} = 0, \tag{8.26}$$

where we use the following convention for indices of flux tensors: the first index tells us which vector component is associated with the flux component while the second index indicates the direction in which this flux component is pointing into. For Cartesian coordinates, no geometric source terms need to be discretized and we can reuse the same discretization of the scalar divergence for the vector divergence.

Cylindrical Coordinates

The directions defined by the three cell indices are mapped cylindrical coordinates via:

$$(i, j, k) \longrightarrow (R, z, \varphi) \tag{8.27}$$

and the position vector is calculated via

$$\boldsymbol{r} = \begin{bmatrix} R\cos(\varphi) \\ R\sin(\varphi) \\ z \end{bmatrix}. \tag{8.28}$$

Expanding the divergence operator in the conservation law of a scalar quantity u with flux $\boldsymbol{F} = (F_R, F_z, F_\varphi)$ reads as:

$$\frac{\partial u}{\partial t} + \frac{1}{R}\frac{\partial R F_R}{\partial R_i} + \frac{\partial F_z}{\partial z_j} + \frac{1}{R}\frac{\partial F_\varphi}{\partial \varphi_k} = 0, \tag{8.29}$$

while the vector divergence operator in the conservation law of a vector quantity $\boldsymbol{u} = (u_R, u_z, u_\varphi)$ with flux $\boldsymbol{F}$ reads as:

$$\frac{\partial u_R}{\partial t} + \frac{1}{R}\frac{\partial R F_{RR}}{\partial R_i} + \frac{\partial F_{Rz}}{\partial z_j} + \frac{1}{R}\frac{\partial F_{R\varphi}}{\partial \varphi_k} - \frac{1}{R}F_{\varphi\varphi} = 0, \tag{8.30}$$

$$\frac{\partial u_z}{\partial t} + \frac{1}{R}\frac{\partial R F_{zR}}{\partial R_i} + \frac{\partial F_{zz}}{\partial z_j} + \frac{1}{R}\frac{\partial F_{z\varphi}}{\partial \varphi_k} = 0, \tag{8.31}$$

$$\frac{\partial u_\varphi}{\partial t} + \frac{1}{R}\frac{\partial R F_{\varphi R}}{\partial R_i} + \frac{\partial F_{\varphi z}}{\partial z_j} + \frac{1}{R}\frac{\partial F_{\varphi\varphi}}{\partial \varphi_k} + \frac{1}{R}F_{R\varphi} = 0. \tag{8.32}$$

The geometric source terms can be interpreted as centrifugal forces in the context of the Euler equation. Using the same finite-volume averages as for discretization of the Cartesian divergence operator, we find that the discretized version of the derivatives read as:

$$\frac{1}{R}\frac{\partial Rq}{\partial R_i} \longrightarrow 2\frac{R_{i+1/2}q^{i+1/2} - R_{i-1/2}q^{i-1/2}}{R_{i+1/2}^2 - R_{i-1/2}^2}, \tag{8.33}$$

$$\frac{\partial q}{\partial z_j} \longrightarrow \frac{q_{j+1/2} - q_{j-1/2}}{z_{j+1/2} - z_{j-1/2}}, \tag{8.34}$$

$$\frac{\partial q}{\partial \varphi_k} \longrightarrow \frac{q_{k+1/2} - q_{k-1/2}}{\varphi_{k+1/2} - \varphi_{k-1/2}}, \tag{8.35}$$

while the remaining factors of $1/R$ are calculated to be:

$$\frac{1}{R} \longrightarrow \frac{1}{\int_{\text{cell}\,ijk} \mathrm{d}V} \int_{\text{cell}\,ijk} \mathrm{d}V \frac{1}{R} = \frac{1}{\int_{R_{i-1/2}}^{R_{i+1/2}} \mathrm{d}R\, R} \int_{R_{i-1/2}}^{R_{i+1/2}} \mathrm{d}R\, R \frac{1}{R} = 2\frac{R_{i+1/2} - R_{i-1/2}}{R_{i+1/2}^2 - R_{i-1/2}^2}. \tag{8.36}$$

The components of the flux tensor appearing in the geometrical source terms are evaluated depending on the dimensionality of the problem at hand. If the problem assumes symmetry in φ then we calculate $F_{\varphi\varphi} \rightarrow F_{\varphi\varphi}|_{ijk}$ and $F_{R\varphi} \rightarrow F_{R\varphi}|_{ijk}$ at the cell centre. Otherwise, in a fully three dimensional simulation, we calculate both flux components through an average of the flux returned from the Riemann solvers at the φ-interfaces:

$$F_{\varphi\varphi} \rightarrow \frac{1}{2}\left(F_{\varphi\varphi}\big|_{k+1/2} + F_{\varphi\varphi}\big|_{k-1/2}\right), \tag{8.37}$$

$$F_{R\varphi} \rightarrow \frac{1}{2}\left(F_{R\varphi}\big|_{k+1/2} + F_{R\varphi}\big|_{k-1/2}\right). \tag{8.38}$$

With these discretizations at hand, it is easy to show that no spurious forces are seeded in the R-momentum equations when $\boldsymbol{F} = P\mathbf{1}$ with $P = \text{const}$ because

$$\frac{1}{R}\frac{\partial RF_{RR}}{\partial R_i} - \frac{1}{R}F_{\varphi\varphi} \longrightarrow 2\frac{R_{i+1/2}P - R_{i-1/2}P}{R_{i+1/2}^2 - R_{i-1/2}^2} - 2P\frac{R_{i+1/2} - R_{i-1/2}}{R_{i+1/2}^2 - R_{i-1/2}^2} = 0. \tag{8.39}$$

Spherical Coordinates

The directions defined by the three cell indices to spherial coordinates via:

$$(i, j, k) \longrightarrow (r, \theta, \varphi) \tag{8.40}$$

and the position vector is calculated via

$$\boldsymbol{r} = \begin{bmatrix} r\sin(\theta)\cos(\varphi) \\ r\sin(\theta)\sin(\varphi) \\ r\cos(\theta) \end{bmatrix}. \tag{8.41}$$

Expanding the divergence operator in the conservation law of a scalar quantity u with flux $\boldsymbol{F} = (F_r, F_\theta, F_\varphi)$ reads as:

$$\frac{\partial u}{\partial t} + \frac{1}{r^2}\frac{\partial r^2 F_r}{\partial r_i} + \frac{1}{r\sin\theta}\frac{\partial \sin\theta F_\theta}{\partial \theta_j} + \frac{1}{r\sin\theta}\frac{\partial F_\varphi}{\partial \varphi_k} = 0, \tag{8.42}$$

while the vector divergence operator in the conservation law of a vector quantity $\boldsymbol{u} = (u_r, u_\theta, u_\varphi)$ with flux $\boldsymbol{F}$ reads as:

$$\frac{\partial u_r}{\partial t} + \frac{1}{r^2}\frac{\partial r^2 F_{rr}}{\partial r_i} + \frac{1}{r\sin\theta}\frac{\partial \sin\theta F_{r\theta}}{\partial \theta_j} + \frac{1}{r\sin\theta}\frac{\partial F_{r\varphi}}{\partial \varphi_k} - \frac{1}{r}\left(F_{\theta\theta} + F_{\varphi\varphi}\right) = 0, \tag{8.43}$$

$$\frac{\partial u_\theta}{\partial t} + \frac{1}{r^2}\frac{\partial r^2 F_{\theta r}}{\partial r_i} + \frac{1}{r\sin\theta}\frac{\partial \sin\theta F_{\theta\theta}}{\partial \theta_j} + \frac{1}{r\sin\theta}\frac{\partial F_{\theta\varphi}}{\partial \varphi_k} + \frac{1}{r}F_{r\theta} - \frac{\cot\theta}{r}F_{\varphi\varphi} = 0, \tag{8.44}$$

$$\frac{\partial u_\varphi}{\partial t} + \frac{1}{r^2}\frac{\partial r^2 F_{\varphi r}}{\partial r_i} + \frac{1}{r\sin\theta}\frac{\partial \sin\theta F_{\varphi\theta}}{\partial \theta_j} + \frac{1}{r\sin\theta}\frac{\partial F_{\varphi\varphi}}{\partial \varphi_k} + \frac{1}{r}F_{r\varphi} + \frac{\cot\theta}{r}F_{\theta\varphi} = 0. \tag{8.45}$$

We calculate the volume-averaged derivatives in the finite-volume setting using:

$$\frac{1}{r^2}\frac{\partial r^2 q}{\partial r_i} \longrightarrow 3\frac{r^2_{i+1/2}q^{i+1/2} - r^2_{i-1/2}q^{i-1/2}}{r^3_{i+1/2} - r^3_{i-1/2}}, \tag{8.46}$$

$$\frac{1}{\sin\theta}\frac{\partial \sin\theta q}{\partial \theta_j} \longrightarrow \frac{\sin\theta_{j+1/2}q^{j+1/2} - \sin\theta_{j-1/2}q^{j-1/2}}{-\cos\theta_{j+1/2} + \cos\theta_{j-1/2}}, \tag{8.47}$$

$$\frac{\partial q}{\partial \varphi_k} \longrightarrow \frac{q_{k+1/2} - q_{k-1/2}}{\varphi_{k+1/2} - \varphi_{k-1/2}}. \tag{8.48}$$

All other geometrical factors, which stand in front of the derivatives or appear in the geometrical source terms, are calculated via:

$$\frac{1}{r} \longrightarrow \frac{3}{2}\frac{r^2_{i+1/2} - r^2_{i-1/2}}{r^3_{i+1/2} - r^3_{i-1/2}}, \tag{8.49}$$

$$\frac{1}{\sin\theta} \longrightarrow \frac{\theta_{j+1/2} - \theta_{j-1/2}}{-\cos\theta_{j+1/2} + \cos\theta_{j-1/2}}, \tag{8.50}$$

$$\cot\theta \longrightarrow \frac{\sin\theta_{j+1/2} - \sin\theta_{j-1/2}}{-\cos\theta_{j+1/2} + \cos\theta_{j-1/2}}. \tag{8.51}$$

As for the cylindrical coordinate system, components of the flux tensor are either calculated at the cell centre or, if possible, by averaging results from the Riemann solvers at the associated coordinate interfaces. With these particular discretizations of the geometrical terms, no spurious motions are seeded in a uniform media with a constant pressure $\boldsymbol{F} = P\mathbf{1}$ with $P = \text{const}$ because all terms containing diagonal terms of $\boldsymbol{F}$ cancel each other in the r-momentum Eq. (8.43) and the θ-momentum Eq. (8.44).

8.2.2 Reconstruction

The Riemann solver used in Godunov-schemes expect values for state vectors to the left and to the right of a cell interface. Using the mean state vectors as the state vectors at the interface results in an overall diffusive numerical scheme. Using higher-order reconstruction of the mean state vectors to the interface can greatly reduce the diffusivity of the numerical scheme. We focus our discussion of different reconstruction procedures on the one-dimensional case. The reconstruction in multi-dimensions is carried out in a dimension-by-dimension fashion where we apply the one-dimensional algorithm on each dimension individually. Instead of using the state vector $\boldsymbol{U}$ directly, we use a set of primitive variables $\boldsymbol{W} = \boldsymbol{W}(\boldsymbol{U})$ for the reconstruction. The Riemann solver at a cell interface with label $i + 1/2$ is then invoked by

$$\boldsymbol{F}_{i+1/2} = \boldsymbol{F}_{i+1/2}(\boldsymbol{W}_{i+1/2,L}, \boldsymbol{W}_{i+1/2,R}), \tag{8.52}$$

where $\boldsymbol{W}_{i+1/2,L}$ and $\boldsymbol{W}_{i+1/2,R}$ are the left-handed and right-handed interpolated primitive state vectors of the interface. They are calculated by

$$\boldsymbol{W}_{i-1/2,R} = \boldsymbol{W}_i - \delta\boldsymbol{W}_{i\to i-1/2}, \tag{8.53}$$

$$\boldsymbol{W}_{i+1/2,L} = \boldsymbol{W}_i + \delta\boldsymbol{W}_{i\to i+1/2}, \tag{8.54}$$

where we define $\delta\boldsymbol{W}_{i\to i+1/2}$ and $\delta\boldsymbol{W}_{i\to i-1/2}$ as the interpolation gradients of the mean state vector $\boldsymbol{W}_i$. In practice, the components of the primitive vector $\boldsymbol{W}$ are reconstructed on a component-by-component basis. It is thus sufficient to describe how we reconstruct a single-valued quantity W.

There are multiple ways how to calculate these gradients. We implement the piecewise-constant, piecewise-linear, piecewise-parabolic interpolation schemes which we describe in this section. Additionally, we implemented various central weighted essentially non-oscillarty (CWENO) scheme such as the 3rd-order CWENO3 scheme (Levy et al., 1999; Cravero et al., 2018), a multi-dimensional CWENO2 scheme (Semplice et al., 2016), and a variant of the 5th-order CWENO5 scheme (Capdeville, 2008). We do not present or use these CWENO reconstruction methods in this work to increase the overall readability.

Also for readability, we present the piecewise limiter as implemented for uniform Cartesian grids. On curvilinear grids or on stretched Cartesian grids, we use the modifications of the piecewise-linear interpolation as presented in Mignone (2014). This makes the piecewise-linear interpolation as our default choice for simulations on curvilinear grids as the CWENO and piecewise-parabolic schemes have not been adapted to these coordinate systems yet.

Piecewise-constant Interpolation The simplest albeit most diffusive way to interpolate W to the interfaces is to not use any high-interpolation at all by using the cell average as the interface values. This donor-cell scheme sets

$$\delta W_{i\to i-1/2} = \delta W_{i\to i+1/2} = 0. \tag{8.55}$$

As a result, the spatial integration becomes 1st-order accurate and experience shows that this method is highly diffusive. It is implemented as a fallback option and exists in the code for debugging reasons. We strongly recommend to use a high-order interpolation scheme for any practical application.

Piecewise-linear Interpolation To construct a piecewise-linear interpolation inside a cell, we use a modified variant of the monotized-central limiter (van Leer, 1979) which sets both interpolation gradients to:

$$\delta W_{i\to i-1/2} = \delta W_{i\to i+1/2} = \frac{1}{2}\mathrm{MMC}(W_{i+1} - W_i, W_i - W_{i-1}), \tag{8.56}$$

where

$$\mathrm{MMC}(a,b) = \frac{\mathrm{sign}(a) + \mathrm{sign}(b)}{2} \min\left(1.5\mathrm{abs}(a), 1.5\mathrm{abs}(b), \frac{1}{2}\mathrm{abs}(a+b)\right). \tag{8.57}$$

The original monotized-central limiter is similar to the MMC and is defined by:

$$\mathrm{MC}(a,b) = \frac{\mathrm{sign}(a) + \mathrm{sign}(b)}{2} \min\left(2\mathrm{abs}(a), 2\mathrm{abs}(b), \frac{1}{2}\mathrm{abs}(a+b)\right). \tag{8.58}$$

Both the original and modified version of the monotized-central limiter impose less stringent bounds on the graditions as the minmod limiter from Eq. (8.14):

$$\textsc{Minmod}(a,b) = \frac{\mathrm{sign}(a) + \mathrm{sign}(b)}{2} \min\left(\mathrm{abs}(a), \mathrm{abs}(b)\right). \tag{8.59}$$

In all cases $|\mathrm{MC}| \geq |\mathrm{MMC}| \geq |\textsc{Minmod}|$ holds. The monotized-central limiter tends to produce rather non-monotonic interpolations which leads to simulation crashes frequently. Conversely, the minmod limiter produces numerical results that are too smooth. Our modifications to the monoticed-central limiter are made to balance between these two limiters. The MMC limiter provides additional stability in comparison to the MC-limiter and the resulting numerical diffusivity is reduced in comparison to the Minmod-limiter. Similar findings are reported in Gittings et al. (2008).

Piecewise-parabolic Interpolation The piecewise-parabolic interpolation provides 3rd-order accuracy in smooth-flows at the expense of a higher computational cost compared to the piecewise-linear interpolation. The original piecewise-parabolic method (PPM) is presented Colella and Woodward (1984), is extended to approximate smooth extrema without excessive limiting in Colella and Sekora (2008); Sekora and Colella (2009); McCorquodale et al. (2015), and is adapted to be applicable in spherical and cylindrical coordinates by Mignone (2014). The underlying idea of all of these methods is to calculate a higher-order approximation of the interface-value first and then to limit these values so that certain desired properties, such as stability, preservation of smooth extrema, and limiting at shocks, are achieved in a second step. We do not use one of the 'classical' limiting methods but adopt the general reconstruct-then-limit procedure of the PPM. In the first step, we calculate an unlimited interpolated values at the interfaces using

$$\delta W^{*}_{i\to i-1/2} = \frac{2(W_i - W_{i-1}) + (W_{i+1} - W_i)}{3}, \tag{8.60}$$

$$\delta W^{*}_{i\to i+1/2} = \frac{(W_i - W_{i-1}) + 2(W_{i+1} - W_i)}{3}, \tag{8.61}$$

where the $*$ indicates that these are unlimited values. The particular placement of parenthesis around the discrete differences is important and implemented as such in Blinc to ensure floating-point symmetry of this reconstruction step. To limit these values, we adapt the limiter of Moe et al. (2015), that was originally developed to limit discontinuous Galerkin methods, to our PPM variant. The gist of the Moe et al. (2015)-limiter is to compare the variation of W inside the cell (given by the unlimited reconstructed interface values) to the variation of W in the vicinity of a given cell (given by the values of W in neighbouring cells) in order to detect when additional limiting is needed. We calculate the variation of W in the vicinity of a cell using the minimal and maximal values of W in the face-neighbouring cells:

$$\mathrm{MaxValNeigh} = \max_{q\in[i,j,k]} \max(W_{q-1}, W_{q+1}), \tag{8.62}$$

$$\mathrm{MinValNeigh} = \min_{q\in[i,j,k]} \min(W_{q-1}, W_{q+1}). \tag{8.63}$$

With these values at hand, we calculate the external variation of W using:

$$\mathrm{ExtVar} = \min\Big(\mathrm{abs}(\mathrm{MaxValNeigh} - W_{i,j,k}), \mathrm{abs}(\mathrm{MaxValNeigh} - W_{i,j,k})\Big). \tag{8.64}$$

The internal variation is then given by

$$\mathrm{IntVar} = \frac{1}{2} \sum_{q\in[i,j,k]} \max(\delta W_{q\to q-1/2}, \delta W_{q\to q+1/2}), \tag{8.65}$$

which is the maximum variation of W inside the cell. This external variation sets an upper limit on the variation inside the cell such that the face-interpolated values do not exceed the minimum and maximum neighbouring values of W. The final limiting is accomplished by comparing these two variations and reducing the internal variation if it exceeds the external variation while keeping the unlimited reconstruction in the case that the internal variation is less than the external variation. For this, we define a smoothing factor

$$\alpha = \min\left(1, \frac{\mathrm{ExtVar}}{\mathrm{IntVar}}\right), \tag{8.66}$$

and the final and limited gradients are given by

$$\delta W_{i\to i-1/2} = \alpha\, \delta W^*_{i\to i-1/2}, \tag{8.67}$$

$$\delta W_{i\to i+1/2} = \alpha\, \delta W^*_{i\to i+1/2}. \tag{8.68}$$

We calculate MaxValNeigh, MinValNeigh, and IntVar while calculating the unlimited gradients and the final limiting is done is in an extra loop over all active cells.
This limiting procedure is quiet effective and cost efficient - yet it results in a more diffusive PPM variant because smooth extrema are clipped. One advantage of this limiting procedure is that it can be implemented without any code branches and is thus efficiently vectorized by modern code compilers. Currently, we have implemented this method only for uniform Cartesian grids. To extend our PPM variant to be applicable with curvilinear coordinates, the method of Mignone (2014) to calculate unlimited interface values might be used to replace Eqs. (8.60) and (8.61). No modifications of the limiting steps are needed to adapt our PPM variant to curvilinear grids.

8.2.3 Time integration

The time derivative in Eq. (8.1) is interpreted as a total derivative in the method of lines approach. This allows us to integrate the underlying partial differential equation using integration schemes derived for ordinary differential equations. To formally advance our numerical solution $\boldsymbol{U}^n$ from time t to time $t + \Delta t$, we need to evaluate the integral in

$$\boldsymbol{U}^{n+1} = \boldsymbol{U}^n + \int_{t^n}^{t^n+\Delta t} \mathrm{d}t\, \frac{\partial \boldsymbol{U}(t)}{\partial t} \tag{8.69}$$

to calculate the solution $\boldsymbol{U}^{n+1}$ at $t+\Delta t$. This integration can be accomplished using Runge-Kutta or related integrators. In Blinc we implemented the 1st-order (RK1), the 2nd-order (RK2), 3rd-order (RK3) Runge-Kutta schemes and additionally implemented the VL2 (Falle, 1991) and MUSCL (Van Leer, 1977) integrators. Details of these integrators are discussed in this section.

RK1 - Forward Euler The 1st-order Runge-Kutta scheme applied to Eqs. (8.1) and (8.69) integrates the differential equation in one step and reads as

$$\boldsymbol{U}^{n+1} = \boldsymbol{U}^{n} - \Delta t\, \boldsymbol{\nabla} \cdot \boldsymbol{F}(\boldsymbol{U}^{n}) + \Delta t\, \boldsymbol{S}(\boldsymbol{U}^{n}). \tag{8.70}$$

Experience shows that this method can only be used together with a piecewise-cosntant reconstruction of primitive variables. Higher-order reconstruction schemes tend to produce highly oscillatory solutions with this time integrator.

RK2 - Heun's Method The 2nd-order Runge-Kutta scheme applied to Eqs. (8.1) and (8.69) integrates the differential equation in two steps and reads as

$$\boldsymbol{U}^{n+1,*} = \boldsymbol{U}^{n} - \Delta t\, \nabla \cdot \boldsymbol{F}(\boldsymbol{U}^{n}) + \Delta t\, \boldsymbol{S}(\boldsymbol{U}^{n}), \tag{8.71}$$

$$\boldsymbol{U}^{n+1} = \boldsymbol{U}^{n} - \frac{\Delta t}{2} \boldsymbol{\nabla} \cdot \left[\boldsymbol{F}(\boldsymbol{U}^{n}) + \boldsymbol{F}(\boldsymbol{U}^{n+1,*})\right] + \frac{\Delta t}{2} \left[\boldsymbol{S}(\boldsymbol{U}^{n}) + \boldsymbol{S}(\boldsymbol{U}^{n+1,*})\right]. \tag{8.72}$$

By inserting the first substep of this integrator into the last substep, we can rewrite this last substep as:

$$\boldsymbol{U}^{n+1} = \frac{1}{2}\left(\boldsymbol{U}^{n} + \boldsymbol{U}^{n+1,*}\right) - \frac{\Delta t}{2} \boldsymbol{\nabla} \cdot \boldsymbol{F}(\boldsymbol{U}^{n+1,*}) + \frac{\Delta t}{2} \boldsymbol{S}(\boldsymbol{U}^{n+1,*}). \tag{8.73}$$

Note that this particular form both substeps of the 2st-order Runge-Kutta scheme individually resemble the 1st-order Runge-Kutta scheme. Thus, we can implement the 2nd-order Runge-Kutta as a sequence of two cycles of the form

$$\boldsymbol{U}^{\mathrm{t}} = \boldsymbol{U}^{\mathrm{c}} - \alpha \Delta t\, \boldsymbol{\nabla} \cdot \boldsymbol{F}(\boldsymbol{U}^{s}) + \alpha \Delta t\, \boldsymbol{S}(\boldsymbol{U}^{s}), \tag{8.74}$$

where $\boldsymbol{U}^{\mathrm{t}}$ is the target state vector, $\boldsymbol{U}^{\mathrm{s}}$ is the source state vector, $\boldsymbol{U}^{\mathrm{c}}$ is a convex combination of previous source state vector, and $\alpha \leq 1$ denotes the time fraction of the current cycle. If the states that contribute to $\boldsymbol{U}^{\mathrm{c}}$ share physically desirable properties such as positive mass- or energy density then their convex combination will also have these properties. This feature of the time integrator is shared by many strong stability-preserving Runge-Kutta schemes (Gottlieb et al., 2001).

RK3 The 3rd-order Runge-Kutta scheme applied to Eqs. (8.1) and (8.69) integrates the differential equation in three steps and reads as

$$\boldsymbol{U}^{n+1,*} = \boldsymbol{U}^n - \Delta t\, \nabla \cdot \boldsymbol{F}(\boldsymbol{U}^n) + \Delta t\, \boldsymbol{S}(\boldsymbol{U}^n), \tag{8.75}$$

$$\boldsymbol{U}^{n+1/2,*} = \boldsymbol{U}^n - \frac{\Delta t}{4}\boldsymbol{\nabla} \cdot \left[\boldsymbol{F}(\boldsymbol{U}^n) + \boldsymbol{F}(\boldsymbol{U}^{n+1,*})\right] + \frac{\Delta t}{4}\left[\boldsymbol{S}(\boldsymbol{U}^n) + \boldsymbol{S}(\boldsymbol{U}^{n+1,*})\right], \tag{8.76}$$

$$\begin{aligned}\boldsymbol{U}^{n+1} = \boldsymbol{U}^n &- \frac{\Delta t}{6}\boldsymbol{\nabla} \cdot \left[\boldsymbol{F}(\boldsymbol{U}^n) + \boldsymbol{F}(\boldsymbol{U}^{n+1,*}) + 4\boldsymbol{F}(\boldsymbol{U}^{n+1/2,*})\right] \\ &+ \frac{\Delta t}{6} \quad \left[\boldsymbol{S}(\boldsymbol{U}^n) + \boldsymbol{S}(\boldsymbol{U}^{n+1,*}) + 4\boldsymbol{S}(\boldsymbol{U}^{n+1/2,*})\right].\end{aligned} \tag{8.77}$$

We can use the same substitution procedure we used the 2nd-order Runge-Kutta on the last two substeps and cast them in form of Eq. (8.74):

$$\boldsymbol{U}^{n+1/2,*} = \frac{1}{4}\left(3\boldsymbol{U}^n + \boldsymbol{U}^{n+1,*}\right) - \frac{\Delta t}{4}\boldsymbol{\nabla} \cdot \boldsymbol{F}(\boldsymbol{U}^{n+1,*}) + \frac{\Delta t}{4}\boldsymbol{S}(\boldsymbol{U}^{n+1,*}), \tag{8.78}$$

$$\boldsymbol{U}^{n+1} = \frac{1}{3}\left(\boldsymbol{U}^n + 2\boldsymbol{U}^{n+1,*}\right) - \frac{4\Delta t}{6}\boldsymbol{\nabla} \cdot \boldsymbol{F}(\boldsymbol{U}^{n+1/2,*}) + \frac{4\Delta t}{6}\boldsymbol{S}(\boldsymbol{U}^{n+1/2,*}). \tag{8.79}$$

This method is also a strong stability-preserving Runge-Kutta scheme (Gottlieb et al., 2001).

VL2 - Van-Leer Integrator A compelling alternative to systematically derived Runge-Kutta methods is provided by integration methods that are based on insights gained from practice and ad-hoc derivations. One example is the predictor-corrector integrator of Falle (1991) with additional implementation details presented by Stone and Gardiner (2009). The integrator reads as:

$$\boldsymbol{U}^{n+1/2} = \boldsymbol{U}^n - \frac{\Delta t}{2}\boldsymbol{\nabla} \cdot \boldsymbol{F}_{\text{loworder}}(\boldsymbol{U}^n) + \frac{\Delta t}{2}S\,(\boldsymbol{U}^n), \tag{8.80}$$

$$\boldsymbol{U}^{n+1} = \boldsymbol{U}^n - \Delta t\boldsymbol{\nabla} \cdot \boldsymbol{F}(\boldsymbol{U}^{n+1/2}) + \Delta t S\,(\boldsymbol{U}^{n+1/2}), \tag{8.81}$$

where we calculate $\boldsymbol{F}_{\text{loworder}}$ as a 1st order flux approximation. We use the same Riemann solver, as in the default integration, for the low-order flux but do not apply a reconstruction method to primitive variables - we effectively use the piecewise-constant interpolation for this predictor step. In the corrector step, we use the higher-order reconstruction method. This reduces the overall cost of this integrator because only one, computationally expensive, call to the reconstruction method per timestep is needed. Nevertheless, this time-integrator is still 2nd-order in time because the integral in Eq. (8.69) is approximated using the midpoint rule, which is 2nd-order, and the 1st-order approximation $\boldsymbol{U}^{n+1/2}$ for $\boldsymbol{U}(t^n + \Delta t/2)$ does not degrade the overall convergence order.

MUSCL-Hancock Method The MUSCL-Hancock method (Van Leer, 1977) is similar to the VL2 method a predictor-corrector method. They differ in the design of the predictor step. The MUSCL-Hancock method first calculates a piecewise-linear reconstruction of the primitive variables and then advances them for a half-timestep using the evolution equation of the primitive variables:

$$\frac{\partial \boldsymbol{W}}{\partial t} + \boldsymbol{A} : \boldsymbol{\nabla} \boldsymbol{W} = \boldsymbol{0}, \tag{8.82}$$

where $\boldsymbol{A}$ is an advective matrix, which can be derived from the flux $\boldsymbol{F}$. The half-timestep advance is executed using:

$$\left.\frac{\partial \boldsymbol{W}}{\partial t}\right|_i = -\boldsymbol{A}_i : \boldsymbol{\nabla} \boldsymbol{W}_i^n, \tag{8.83}$$

where the gradients $\nabla \boldsymbol{W}_i^n$ are calculated using the gradients obtained from the reconstruction. The reconstruction is retained and the inputs for the Riemann solver are then calculated based on the half-step primitive variables. This can be written in terms of the left- and right-handed reconstructed primitive variables as:

$$\boldsymbol{W}_{i-1/2,R} = \left(\boldsymbol{W}_i + \frac{\Delta t}{2} \left.\frac{\partial \boldsymbol{W}}{\partial t}\right|_i\right) - \delta \boldsymbol{W}_{i \to i-1/2}, \tag{8.84}$$

$$\boldsymbol{W}_{i+1/2,L} = \left(\boldsymbol{W}_i + \frac{\Delta t}{2} \left.\frac{\partial \boldsymbol{W}}{\partial t}\right|_i\right) + \delta \boldsymbol{W}_{i \to i+1/2}. \tag{8.85}$$

This integrator is computationally cheap because only one call to the reconstruction procedure per timestep is needed. We implemented this integrator for Cartesian meshes only because the gradient operator $\nabla \boldsymbol{W}_i^n$ needs to be adapted to curvilinear coordinates which has not been done in Blinc. Furthermore, this integrator does not fit in our code-structure that handles the sourceterms. The sourceterm interface in Blinc expects conserved variables but this integrator advances primitive variables. Instead of providing the user with the ability to specify sourceterms in terms of primitive and conserved variables, we opted to not include the sourceterms during the predictor step. This simplifies the code tremendously but results in 1st-order in time convergence of the MUSCL-Hancock method when sourceterms are present. If curvilinear coordinates or an accurate integration of sourceterms are called for by the problem at hand, we recommend to use the VL2 integrator.

8.3 Physics Modules

In this section, we are describing two physics modules that are build on top of the finite-volume framework of Blinc. The first one is a module for magnetohydrodynamics which needs some modifications of the standard finite-volume paradigm to incorporate the divergence constraint

of the magnetic field. The second module integrates the equation of radiation hydrodynamics with the M1 closure.

8.3.1 Magnetohydrodynamics

The evolution equations of magnetohydrodynamics can be written in form of Eq. (8.1) if we define the state vector and fluxes via

$$\boldsymbol{U} = \begin{bmatrix} \rho \\ \rho\boldsymbol{u} \\ \boldsymbol{B} \\ \varepsilon_{\mathrm{tot}} \end{bmatrix} \quad \text{and} \quad \boldsymbol{F(U)} = \begin{bmatrix} \rho\boldsymbol{U} \\ \rho\boldsymbol{uu} + P_{\mathrm{tot}}\mathbf{1} - \boldsymbol{BB} \\ \boldsymbol{Bu} - \boldsymbol{uB} \\ \boldsymbol{u}(\varepsilon_{\mathrm{tot}} + P_{\mathrm{tot}}) - \boldsymbol{u}\cdot\boldsymbol{BB} \end{bmatrix}, \tag{8.86}$$

where the total energy and pressure are defined by

$$\varepsilon_{\mathrm{tot}} = \rho\frac{\boldsymbol{u}^2}{2} + \varepsilon_{\mathrm{th}} + \frac{\boldsymbol{B}^2}{2}, \tag{8.87}$$

$$P_{\mathrm{tot}} = P_{\mathrm{th}} + \frac{\boldsymbol{B}^2}{2}. \tag{8.88}$$

In Blinc we support both adiabatic MHD, where the equation of state takes the form of

$$P_{\mathrm{th}} = (\gamma_{\mathrm{th}} - 1)\varepsilon_{\mathrm{th}}, \tag{8.89}$$

with $\gamma_{\mathrm{th}} = 5/3$ by default, and isothermal MHD where $P_{\mathrm{th}} = c_{\mathrm{sd}}^2\rho$. We define the primitive variables of MHD using

$$\boldsymbol{W} = \begin{bmatrix} \rho \\ \boldsymbol{u} \\ \boldsymbol{B} \\ P_{\mathrm{th}} \end{bmatrix}. \tag{8.90}$$

To solve the Riemann problems at the interfaces between cells, we implemented the HLLE Riemann solver (Einfeldt, 1988), HLLC Riemann solver (Li, 2005), the HLLD Riemann solver for the adiabatic equation of state (Miyoshi and Kusano, 2005b), the HLLD Riemann solver for the isothermal equation of state (Mignone, 2007), the linearized Roe Riemann solver (Roe, 1981; Stone et al., 2008), and the general Osher Riemann solver with a 3rd-order accurate integration of the integral that connects left- and right-handed states (Dumbser and Toro, 2011). For all Riemann solvers, we use the wavespeed estimates of Davis (1988) and use the speed of

the fast magnetosonic wave as the extremal wavespeed. For the CFL condition in Eq. (8.2), we adopt the following approximation for the fastest wave speeds inside the cell:

$$v_{\mathrm{max,i}} = |u_i| + c_{\mathrm{sqr}} \qquad \text{for } i \in [x, y, z] \tag{8.91}$$

where $c_{\mathrm{sqr}}^2 = c_{\mathrm{sd}}^2 + c_{\mathrm{a}}^2$ and $c_{\mathrm{a}}^2 = B/\sqrt{\rho}$. These velocities are always larger then or equal to the fast magnetosonic wavespeed. We implemented a base finite-volume solver that integrates Eqs. (8.1) and (8.86) using the aforementioned methods respecting the general general conservation laws. This solver needs to be augmented with additional features to incorporate the divergence constraint on the magnetic field that is inherited from Maxwell's equations:

$$\boldsymbol{\nabla} \cdot \boldsymbol{B} = 0. \tag{8.92}$$

This equation poses a conceptional challenge to the finite-volume paradigm because 1) it is not an evolution equation but a constraint valid at any time and 2) the evolution equations for MHD do not guarantee that this equation holds once they have been discretized with standard finite-volume methods. Consequently, the base finite-volume scheme, which is not adapted to handle this constraint, will generate spurious magnetic monopoles even if there are no monopoles in the initial conditions. These monopoles are unphysical on their own but also negatively influence the evolution of the gas because the Lorentz-force exerted by the magnetic field might not act strictly perpendicular to the direction of the magnetic field. In order to circumvent this problem, the classical finite-volume algorithm has to be adapted in some form - see Tóth (2000) for a discussion of possible ways of how to accomplish this. In Blinc, we implement the constrained transport technique and the Powell method. In the constraint transport method, a staggered-mesh approach is used to evolve the magnetic fields that are now redefined on cell interfaces (Evans and Hawley, 1988). In the Powell method, terms that introduce unphysical behaviour through magnetic monopoles are explicitly removed from the MHD equations (Powell et al., 1999). We now describe how both methods are implemented.

Constrained Transport

To introduce the constrained transport method, we rewrite the induction equation in its natural form:

$$\frac{\partial \boldsymbol{B}}{\partial t} + c\boldsymbol{\nabla} \times \boldsymbol{\mathcal{E}} = \boldsymbol{0}, \tag{8.93}$$

where the electric field is given by $\boldsymbol{\mathcal{E}} = -(\boldsymbol{u} \times \boldsymbol{B})/c$ in the MHD approximation. We can use a staggered-mesh approach to discretize this equation and centre the magnetic field on the interfaces between cells (Evans and Hawley, 1988). Using this method, the three components

of the magnetic field are conceptually located on different interfaces: B_x is situated on an x-interface, B_y on a y-interface, B_z on a z-interface. By applying the Stokes' instead of Gauss' theorem, the induction equation can be readily discretized and we have in a 2nd-order-in-space approximation:

$$A_{x,i+1/2jk}\frac{\partial B_{x,i+1/2jk}}{\partial t} = -L_{z,i+1/2j+1/2k}(\boldsymbol{u}\times\boldsymbol{B})_{z,i+1/2j+1/2k} + L_{z,i+1/2j-1/2k}(\boldsymbol{u}\times\boldsymbol{B})_{z,i+1/2j-1/2k} + L_{y,i+1/2jk+1/2}(\boldsymbol{u}\times\boldsymbol{B})_{y,i+1/2jk+1/2} - L_{y,i+1/2jk-1/2}(\boldsymbol{u}\times\boldsymbol{B})_{y,i+1/2jk-1/2}, \tag{8.94}$$

where the evolution equations for the other components of the magnetic field can be inferred by cyclic permutation of the indices, $A_{x,i+1/2jk}$ is the surface area of the x-interface of between cell i and $i+1$, $L_{z,i+1/2j+1/2k}$ denotes the length of the corresponding cell edge, and $(\boldsymbol{u}\times\boldsymbol{B})_{z,i+1/2j+1/2k}/c$ is the z-component of the average electric-field on this cell edge. Here, we write the discretized induction equation in Cartesian coordinates for clarity. The extension to curvilinear coordinates is straightforward and can be accomplished by relabelling the magnetic and magnetic field components, interface areas and edge lengths correspondingly. Taking cylindrical coordinates as an example this relabelling is $(x, y, z) \rightarrow (R, \varphi, z)$. No geometric source terms appear in curvilinear coordinates for the induction equation. A cell centred approximation for the magnetic field vector can be calculated, again in a 2nd-order-in-space approximation, by:

$$B_{x,ijk} = \frac{1}{2}\left(B_{x,i+1/2\,jk} + B_{x,i-1/2\,jk}\right), \tag{8.95}$$

$$B_{y,ijk} = \frac{1}{2}\left(B_{y,ij+1/2\,k} + B_{y,ij-1/2\,k}\right), \tag{8.96}$$

$$B_{z,ijk} = \frac{1}{2}\left(B_{z,ijk+1/2} + B_{z,ijk-1/2}\right). \tag{8.97}$$

For consistency, we update the cell centred magnetic field energy density simultaneously as we update the cell-centred magnetic field. This is accomplished by first subtracting the magnetic field energy density from the total energy density before the cell-centred values of the magnetic field are updated and then adding the updated magnetic field energy density back to into the total energy density. Although this update corresponds to a loss of fundamental energy conservation in our algorithm, it provides more stability (Helzel et al., 2011).

The advantage of this formalism is that the discretized divergence of the magnetic field stays

constant in time:

$$\begin{aligned}\frac{\partial \nabla \cdot \boldsymbol{B}_{ijk}}{\partial t} = & A_{x,i+1/2jk}\frac{\partial B_{x,i+1/2jk}}{\partial t} - A_{x,i-1/2jk}\frac{\partial B_{x,i-1/2jk}}{\partial t} \\ & A_{y,ij+1/2k}\frac{\partial B_{y,ij+1/2k}}{\partial t} - A_{y,ij-1/2k}\frac{\partial B_{y,ij-1/2k}}{\partial t} \\ & A_{z,ijk+1/2}\frac{\partial B_{z,ijk+1/2}}{\partial t} - A_{z,ijk-1/2}\frac{\partial B_{z,ijk-1/2}}{\partial t} = 0,\end{aligned} \tag{8.98}$$

which means that if the divergence constraint is fulfilled by the initial conditions then it will be fulfilled for all times and no spurious magnetic monopoles are generated by the numerical scheme.

To calculate the edge-centred electric fields, we use the method of Gardiner and Stone (2005, 2008) which upwinds face-centred electric fields calculated by the Riemann solver with the help of cell-centred electric fields. This method is less computational expensive than other methods that achieve the same low level of numerical diffusion. See Mignone and Del Zanna (2021) for how face-centred Riemann solver can be extended to calculate edge-centred electric fields.

The major disadvantage of the constraint transport scheme is that all methods that handle AMR-related operations in the code need to be implemented twice: the first time for the cell-centred quantities and their fluxes of the standard finite-volume scheme and a second time for the face-centred magnetic field and their electric fields for the constrained transport method. Currently, we only implemented a 1st-order spatial prolongation of face-centred magnetic fields.

Powell Method

The Powell or 8-wave method (Powell et al., 1999) takes a completely different approach: instead of choosing numerical discretization that fundamentally adheres to the divergence constraint, the Powell method explicitly removes all terms from Eq. (8.1) that are proportional to $\nabla \cdot \boldsymbol{B}$. This results in a modified set of MHD equations:

$$\frac{\partial \boldsymbol{U}}{\partial t} + \nabla \cdot \boldsymbol{F} = -\begin{bmatrix} 0 \\ \boldsymbol{B} \\ \boldsymbol{u} \\ \boldsymbol{u} \cdot \boldsymbol{B} \end{bmatrix} \nabla \cdot \boldsymbol{B}. \tag{8.99}$$

Removing these terms is advantageous if the numerical solution contains magnetic monopoles: although present they cannot (formally) impact the evolution of the MHD quantities in an unphysical way. Another interesting property of the Powell method is that $\nabla \cdot \boldsymbol{B}$ is a conserved

quantity:

$$\frac{\partial \boldsymbol{\nabla} \cdot \boldsymbol{B}}{\partial t} + \boldsymbol{\nabla} \cdot (\boldsymbol{u} \boldsymbol{\nabla} \cdot \boldsymbol{B}) = 0, \tag{8.100}$$

which states that magnetic monopoles are advected with the gas flow (Powell et al., 1999). Consequently, the monopoles can then be diminished either by removal of gas and $\nabla \cdot \boldsymbol{B}$ with outflows through the simulation boundaries or by numerical mixing of regions with positive and negative magnetic divergence. A disadvantage, resulting from this property, is that magnetic monopoles accumulate in regions where the gas flow convergences.

No standard numerical scheme exists for the Powell method although there are modern Godunov/finite-volume based codes that implement this method (Waagan, 2009; Pakmor and Springel, 2013; Li et al., 2018). We presume that the reason for the absence of a standard is mainly because Eq. (8.99) is a non-conservative hyperbolic PDE. This special class of PDEs cannot be numerically discretized by standard Godunov finite-volume schemes. Extensions of the finite-volume idea exists that yield robust and accurate schemes such as the path-conservative finite-volume schemes (Parés, 2006). We provide an introduction to path-conservative finite-volume schemes in Sec. 5.7. In Díaz et al. (2019), the authors show that the standard HLL Riemann solver can be extended using minor modifications to account for non-conservative terms. We use their method for our discretization of the $\nabla \cdot \boldsymbol{B}$ terms of the Powell method.

In our context, we split the numerical flux at a cell interface in two separated but related numerical fluxes that take the Powell-source terms into account. These two fluxes are applied to the cells that are to the left and right of a given interface. These fluxes are denoted by $\boldsymbol{F}_{L,i+1/2}$ and $\boldsymbol{F}_{R,i+1/2}$ and are set to be

$$\boldsymbol{F}_{L,i+1/2} = \boldsymbol{F}_{i+1/2,\mathrm{RS}} - \frac{S_L}{S_R - S_L} \begin{bmatrix} 0 \\ \overline{\boldsymbol{B}} \\ \overline{\boldsymbol{u}} \\ \hline \overline{\boldsymbol{u} \cdot \boldsymbol{B}} \end{bmatrix} (B_{n,R} - B_{n,L}), \tag{8.101}$$

$$\boldsymbol{F}_{R,i+1/2} = \boldsymbol{F}_{i+1/2,\mathrm{RS}} - \frac{S_R}{S_R - S_L} \begin{bmatrix} 0 \\ \overline{\boldsymbol{B}} \\ \overline{\boldsymbol{u}} \\ \hline \overline{\boldsymbol{u} \cdot \boldsymbol{B}} \end{bmatrix} (B_{n,R} - B_{n,L}), \tag{8.102}$$

where $\boldsymbol{F}_{i+1/2,\mathrm{RS}}$ is the flux returned by the Riemann solver at this interface, $B_{n,L}$ and $B_{n,R}$ are the components normal to the interface that are reconstructed and interpolated onto the interface,

and various averaged quantities are given by

$$\begin{bmatrix} 0 \\ \overline{\boldsymbol{B}} \\ \overline{\boldsymbol{u}} \\ \overline{\boldsymbol{u} \cdot \boldsymbol{B}} \end{bmatrix} = \begin{bmatrix} 0 \\ \frac{1}{2}(\boldsymbol{B}_L + \boldsymbol{B}_R) \\ \frac{1}{2}(\boldsymbol{u}_L + \boldsymbol{u}_R) \\ \frac{1}{6}\boldsymbol{u}_L \cdot (2\boldsymbol{B}_L + \boldsymbol{B}_R) + \frac{1}{6}\boldsymbol{u}_R \cdot (\boldsymbol{B}_L + 2\boldsymbol{B}_R) \end{bmatrix}. \tag{8.103}$$

We extend the original implementations of all Riemann solvers to include terms that dissipate the normal component of the magnetic field:

$$\boldsymbol{F}_{i+1/2,\mathrm{RS},B_n} = \frac{S_L S_R}{S_R - S_L}(B_{n,R} - B_{n,L}). \tag{8.104}$$

Most Riemann solvers expect a single value for the normal component of the magnetic field. In this case, we use the average value $B_n = (B_{n,R} + B_{n,L})/2$ for this purpose. Otherwise no modification to the Riemann solvers are made. These interface and Riemann solver related additions to the finite-volume scheme account for fluctuations of the non-conservative terms in context of the path-conservative finite-volume scheme of the Powell-modified MHD equations at the cell interfaces. To account for the fluctuations of these terms inside the cell, we add a sourceterm

$$\boldsymbol{S}(\boldsymbol{U})|_{\mathrm{Powell}} = -\begin{bmatrix} 0 \\ \boldsymbol{B} \\ \boldsymbol{u} \\ \boldsymbol{u} \cdot \boldsymbol{B} \end{bmatrix}_{ijk} (\nabla \cdot \boldsymbol{B})|_{\mathrm{interior}}, \tag{8.105}$$

to our integrator, where $(\nabla \cdot \boldsymbol{B})|_{\mathrm{interior}}$ is evaluated using reconstructed and interpolated values of the normal component of the magnetic field at the interfaces. To integrate these Powell sourceterms, we use the same discretization of the divergence operator as the underlying finite-volume scheme and include them in the integration method as regular sourceterms - see Sec. 8.2.3. This completes our description of our implementation of the Powell method.

We want to stress that the analytical form of the Powell method in Eq. (8.99) removes any spurious and unphysical force that originates from magnetic monopoles. This is not necessarily the case for the presented discretized version because the Powell-terms are an addition on top of the existing MHD finite-volume solver and no fundamental modifications of, e.g., the Riemann solvers are made to remove the magnetic monopole forces entirely. Our implementation of the Powell terms removes the majority of the magnetic monopole forces but we cannot conduct a formal proof that all magnetic monopole forces are removed. Consequently, we expect that some residual numerical forces are still present. In practice, our scheme is stable and

accurate enough that these forces do not prohibit any serious MHD simulation which we will demonstrate with our test problems.

8.3.2 Radiation Hydrodynamics

In BLINC, we include radiation by solving the equation of radiation hydrodynamics (Mihalas and Weibel Mihalas, 1984). This set of equation is less general than equation of radiative transfer and describes how photons are transported in terms of their energy/number and flux density. We can write these equations in form of Eq. (8.1) via:

$$\boldsymbol{U} = \begin{bmatrix} \varepsilon_{\mathrm{rad}} \\ \boldsymbol{F}_{\mathrm{rad}} \end{bmatrix} \quad \text{and} \quad \boldsymbol{F(U)} = \begin{bmatrix} \boldsymbol{F}_{\mathrm{rad}} \\ c^2 \boldsymbol{P}_{\mathrm{rad}} \end{bmatrix}, \tag{8.106}$$

where $\varepsilon_{\mathrm{rad}}$ is the energy density, $\boldsymbol{F}_{\mathrm{rad}}$ is the energy flux density, and $\boldsymbol{P}_{\mathrm{rad}}$ is the pressure tensor of the radiation field. The sourceterms $\boldsymbol{S}(\boldsymbol{U})$ represent the radiation-matter interaction processes such as absorption, scattering, and emission of radiation. They are too complicated to be stated in all generality here. We will explicit state which processes are account for in the simulations of our test problems.

In order to be able to simulate multifrequency transport of radiation, we allow for multiple radiation fields. Each field is associated with a certain frequency range. Inside each band, interactions between radiation and matter is consider to be grey - absorption and scattering cross section, source functions, and emissivities are averaged over the frequency range with a suitable statistical weighting.

In general, the radiation tensor is an independent quantity and its evolution is different from the energy or flux densities. In a formally and generally accurate description of radiation transport, this tensor needs to be calculated from the solution of the radiation transfer equation itself. We make the approximation that the radiation pressure can be calculated based on the local values of energy and flux density alone via the M1 closure relation (Levermore, 1984). In this approximation, the radiation pressure tensor is given by:

$$\boldsymbol{P}_{\mathrm{rad}} = \left(\frac{1-\xi}{2} \mathbf{1} + \frac{3\xi - 1}{2} \frac{\boldsymbol{F}_{\mathrm{rad}}}{|\boldsymbol{F}_{\mathrm{rad}}|} \frac{\boldsymbol{F}_{\mathrm{rad}}}{|\boldsymbol{F}_{\mathrm{rad}}|} \right) \varepsilon_{\mathrm{rad}}, \tag{8.107}$$

where $\xi \in [1/3, 1]$ is given for the M1 closure by:

$$\xi = \frac{3 + 4f^2}{5 + 2\sqrt{4 - 3f^2}} \quad \text{with} \quad f = \frac{|\boldsymbol{F}_{\mathrm{rad}}|}{c\varepsilon_{\mathrm{rad}}}. \tag{8.108}$$

With this closure relation, the evolution of the radiation is completely determined by local quantities. Furthermore, radiation shows a fluid-like behaviour in this approximation: we can

rewrite the evolution equation for the flux density in a form that resembles the Euler equation of (gaseous) hydrodynamics because it contains both, an inertia term ($\propto \boldsymbol{F}_{\mathrm{rad}}\boldsymbol{F}_{\mathrm{rad}}$) and pressure term ($\propto \varepsilon_{\mathrm{rad}}\boldsymbol{I}$). In fact, it can be shown that the equations of radiation hydrodynamics correspond to the relativistic hydrodynamical energy equations of an ordinary fluid (Hanawa and Audit, 2014).

A variety of hydrodynamics codes that contain a numerical scheme to integrate these equations are described in the literature (non-exhaustive list): Arepo-RT (Kannan et al., 2019), Athena (Skinner and Ostriker, 2013), Aton (Aubert and Teyssier, 2008), Heracles (González et al., 2007), Pluto (Fuksman and Mignone, 2019), Quokka (Wibking and Krumholz, 2022), Ramses-RT (Rosdahl et al., 2013), SFUMATO-M1 (Fukushima and Yajima, 2021), SR-R2MHD (Takahashi and Ohsuga, 2013), and Swift (Chan et al., 2021). All of them differ in terms of the included physical processes and the details of the employed numerical methods.

In Blinc, we implement the equations of radiation hydrodynamics in our finite-volume framework using the HLLC Riemann solver of Fuksman and Mignone (2019) and the HLLE Riemann solver (Einfeldt, 1988; Skinner and Ostriker, 2013), use the wave speeds of the fastest eigenmodes of the system from Skinner and Ostriker (2013), use the primitive variables $\varepsilon_{\mathrm{rad}}$ and $\boldsymbol{F}_{\mathrm{rad}}/\varepsilon_{\mathrm{rad}}$ for the reconstruction, and use the speed of light c as the fastest wave speed in the CFL condition in Eq. (8.2) with $v_{\mathrm{max,x}} = v_{\mathrm{max,y}} = v_{\mathrm{max,z}} = c$. An earlier implementation of this module used the HLLC Riemann solver of Berthon et al. (2007) which we employed in Chapter 4. The speed of light is a parameter that needs to be specified at compile time. This allows the user to employ the reduced speed of light approximation.

We implement the chemistry network for hydrogen and helium together with a model for molecular hydrogen following Nickerson et al. (2018), see there for details and a definition of all sourceterms. This network is coupled to the radiation hydrodynamics and MHD solvers. The MHD solver advects the number densities of [H_2, HI, HII] and [HeI, HeII, HeIII] as passive scalars whereas the radiation hydrodynamics solver transports the photoionizing/photodissociating FUV-EUV radiation. The chemical reactions and the radiation matter interactions are integrated after the timestepping of the MHD and radiation hydrodynamics solvers completed their respective timestepping. The time integration of these processes is accomplished through a 1st-order semi-implicit update which is subcycled following the 10% rule of Rosdahl et al. (2013). Because MHD/radiation transport and photo-chemistry are treated separately, this coupling formally has a 1st-order convergence rate.

8.4 Test Problems

In this section, we present various test problems that demonstrate the robustness and accuracy of our solvers.

8.4.1 Standard MHD tests

Here, we compile a suite of standard test problems that we simulate with our CT and Powell solvers. All problems use by default $N^2 = 512^2$ cells, CFL = 0.4, the VL2 integrator, the HLLD Riemann solver, piecewise-parabolic reconstruction, and are carried out on a Cartesian grid with periodic boundary conditions. In Fig. 8.5, we show the results for simulations using the CT and the Powell methods and display a single quantity q. We additionally plot the normalized difference of both simulations via

$$\Delta = \frac{q_{\mathrm{CT}} - q_{\mathrm{Powell}}}{q_{\mathrm{CT}} + q_{\mathrm{Powell}}} \tag{8.109}$$

on a cell-by-cell basis.

Orszag Tang Vortex The classical Orszag and Tang (1979) test problem can be interpreted as a simulation of decaying MHD turbulence that uses a very simplified setup for the initial turbulence. The simulation domain is $(x, y) \in [0, 1]^2$ and the simulation is run until $t = 0.5$. The gas is set up using $\rho = 25/36\pi$, $P_{\mathrm{th}} = 5/12\pi$, $\boldsymbol{u} = [-\sin(2\pi y), \sin(2\pi x), 0]$, and $\boldsymbol{B} = [-\sin(2\pi y), \sin(4\pi x), 0]/\sqrt{4\pi}$. The flow first passes a quasi-linear episode of evolution until non-linear mode-mode coupling results in a very structured and fine-grained appearance of all MHD quantities. We follow the de-facto standard and show the gas mass density structure at $t = 0.5$. Visual comparison of the results obtained with the CT and Powell method shows no significant difference between the two simulations. Numerical differences are maximised at the various shock waves that travel through the simulation domain. Their density differences reach amplitudes of $\Delta \sim 15\%$.

Blast Wave In this test, we set off a blast wave in a magnetized ambient medium and adopt the (slightly modified) setup of Londrillo and Del Zanna (2000). The simulation domain is $(x, y) \in [-1, +1]^2$ and the simulation is run until $t = 0.35$. The ambient medium has $\rho = 1$, $\boldsymbol{u} = \boldsymbol{0}$, $\boldsymbol{B} = (\boldsymbol{e}_x + \boldsymbol{e}_y)/\sqrt{2}$, and $P_{\mathrm{th}} = 0.1$. The blast wave is injected by increasing the thermal pressure to $P_{\mathrm{th}} = 10$ in the central region where $R = \sqrt{x^2 + y^2} < 0.25$. The resulting density structure is highly anisotropic although the central overpressurized region was spherical. This

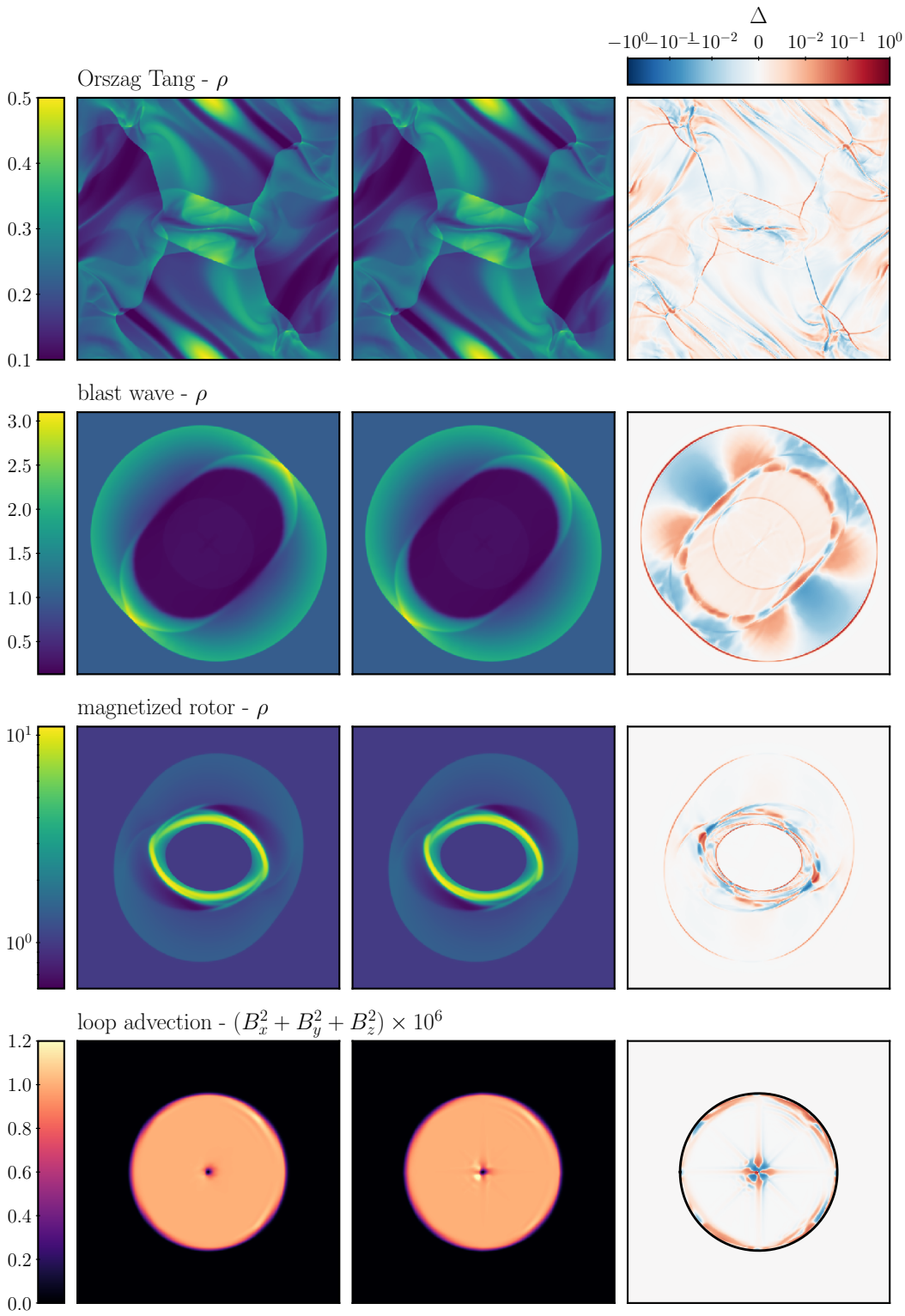

Figure 8.5: Gallery of various standard MHD test problems. For each problem, the left-handed panel shows the CT simulation while the central panel shows with the Powell method. The right-handed panel shows the normalized difference between the both. For the loop advection test, we plot the differences only for $r < 0.3$ which is indicated by a black outline.

is because the blast wave has to perform additional work to bend magnetic field lines. Both, the Powell and the CT method give similar results for this test problem with no clear visual difference in the density structure. Numerical differences are present with values of the density Δ reaching up to 20% at the shock wave.

Magnetized Rotor In the magnetized rotor test by Balsara and Spicer (1999), a spinning gaseous body is initially situated inside a low density magnetized ambient medium. The simulation domain is $(x, y) \in [-0.5, +0.5]^2$ and the simulation is run until $t = 0.15$. The initial condition for both the ambient medium and the central body are given by $\rho = 1 + 9f(R)$, the thermal pressure $P_{\text{th}} = 1$, the radial velocity $v_R = 0$, the tangential velocity $v_\varphi = 20f(R)$, the magnetic field is uniform with $\boldsymbol{B} = \boldsymbol{e}_x$. The transition function is given by $f(R) = \min(1, \max(0, (R_1 - R)/(R_1 - R_0)))$ with $R_0 = 1$ and $R_1 = 0.12$. We find no obvious visual differences between the results of the CT and the Powell simulations in the density structure. The largest numerical differences can be found in the density at discontinuities where $\Delta \sim 15\%$.

Loop Advection In our last standard MHD test, we simulate the advection of a low-amplitude magnetic field loop over an otherwise unmagnetized quiescent medium following the setup of Gardiner and Stone (2005). The simulation domain is $(x, y) \in [0, 2] \times [0, 1]$. We use $2N \times N$ cells to account for the aspect ratio of the simulation domain and the simulation is run until $t = 1$. The initial conditions are: $\rho = 1$, $P_{\text{th}} = 1$, $(u_x, u_y, u_z) = (2, 1, 0)$, and the magnetic field is set up using a magnetic vector potential with $(A_x, A_y, A_z) = (0, 0, 10^{-3}(R_0 - R))$ in a region where $R < R_0 = 0.3$ while $\boldsymbol{A} = \boldsymbol{0}$ outside of this region. Again, the Powell and CT simulations are comparable. The central region shows some artefacts that are grid-aligned in the simulation with the Powell method. There, the numerical differences in the magnetic energy density reach up to $\Delta \sim 40\%$. In Fig. 8.5, we plot Δ only for $R < R_0$ because outside this region the magnetic field strength is comparable to the epsilon of floating point precision and the differences are mostly dominated by floating point arithmetic errors and not by the differences in the integration method.

8.4.2 Alfvén Wave - Convergence Test

In order to test the convergence properties of our MHD solvers, we use the Alfvén wave example of Gardiner and Stone (2005). The setup initialises a travelling circularly-polarized Alfvén wave that propagates over the numerical grid in an oblique direction. This test is interesting because Alfvén waves are normal modes of MHD equations which are also solutions even if

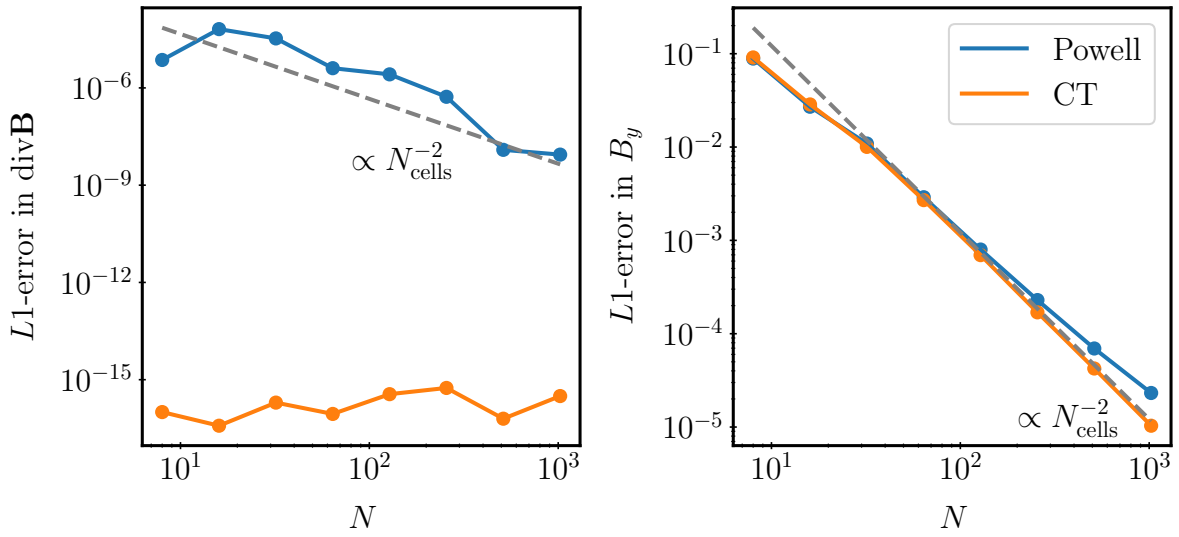

Figure 8.6: Travelling Alfvén wave convergence test of the MHD solvers. Left: L1-error in the divergence constraint of the magnetic field $\nabla \cdot \boldsymbol{B} = 0$ Right: L1-error in the in-plane component B_y of the magnetic field. The dashed lines in both panels indicating a 2nd-order error profile.

their associated perturbation amplitudes are non-linear. The two-dimensional periodic simulation domain is given by $(x, y) \in [-\sqrt{5}/2, +\sqrt{5}/2] \times [-\sqrt{5}/4, +\sqrt{5}/4]$ and is sampled by $2N \times N$ cells where we vary N from 8 to 1024 in steps of 2. We use Cartesian coordinates, CFL = 0.9, the VL2 integrator, the HLLD Riemann solver, and the piecewise-parabolic reconstruction method. We perform two resolution studies: one uses the Powell method and the other uses CT methods to handle the divergence constraint. The Alfvén wave is set up so that it travels at an angle of $\theta = \arctan(2)$. We state the initial conditions in a rotated coordinate system which is given by:

$$x_1 = +x\cos(\theta) + y\sin(\theta), \tag{8.110}$$

$$x_2 = -x\sin(\theta) + y\cos(\theta), \tag{8.111}$$

$$x_3 = z. \tag{8.112}$$

The magnetic and velocity fields are given by

$$\begin{bmatrix} B_1 \\ B_2 \\ B_3 \end{bmatrix} = \begin{bmatrix} 1 \\ 0.1\sin(2\pi x_1) \\ 0.1\cos(2\pi x_1) \end{bmatrix} \quad \text{and} \quad \begin{bmatrix} u_1 \\ u_2 \\ u_3 \end{bmatrix} = \begin{bmatrix} 0 \\ 0.1\sin(2\pi x_1) \\ 0.1\cos(2\pi x_1) \end{bmatrix}, \tag{8.113}$$

while $P = 0.1$ and $\rho = 1$. We set up the magnetic field of the Alfvén wave using the vector potential $[A_1, A_2, A_3] = [0, 0, 0.1\cos(2\pi x_1)/2\pi]$ for the CT method. We evaluate the results for both methods at $t = 1$ when the wave has crossed the box ones and the analytical solution is given by the initial conditions.

In Fig. 8.6, we show in the left-hand panel the L1-error of the divergence constraint $\nabla \cdot \boldsymbol{B} = 0$. This constraint is fulfilled in the CT method by construction and the resulting error is at machine precision of double precision floating point numbers $\sim 10^{-16}$. The Powell-method does not fulfill the constrained and magnetic monopoles are formally present but the deviation of the divergence constraint converge at 2nd-order in space. Hence for increasing resolution, the residual negative effects that magnetic monopoles might convey also decrease for the Powell-method. In the right panel of Fig. 8.6, we show the L1-error of the in-plane component B_y. Both integration methods show similar convergence profiles where the Powell method convergences slightly slower then the CT method. For low cell numbers, the errors decrease at a somewhat lower rate than 2nd-order. We suspect that the extrema-clipping properties of the reconstruction method might have a strong influence there because the cells that represent the extrema of the wave train represent a non-negligible fraction of all cells. For moderate to high resolutions, the L1-error convergences at 2nd-order in space.

8.4.3 Parker Wind - Convergence Test

Parker (1958) pointed out that an outflow launched by the sun itself provide the gas velocities which are required to explain the presence of comet tails. He considers a magnetised wind originating from the sun and found that the hydrostatic equations of motions of the gas in this scenario can be solved. Here, we use a more simplified model of an unmagnetised isothermal outflow with spherical-symmetry to test the convergence properties of our code in spherical coordinates. First, we derive the analytic solution for this problem. The continuity equation in this situation reads as:

$$\frac{1}{r^2}\frac{\partial}{\partial r} r^2 \rho v_\mathrm{r} = 0 \tag{8.114}$$

which can be integrated in radius and shows that the mass-loss rate

$$\dot{M} = 4\pi r^2 \rho v_\mathrm{r} \tag{8.115}$$

is a constant throughout the wind. The equation of motion including the gravitational force from the sun, of mass M, reads as:

$$\frac{1}{r^2}\frac{\partial}{\partial r} r^2 \rho v_\mathrm{r}^2 + \frac{\partial P_\mathrm{th}}{\partial r} = -\rho \frac{GM}{r^2}. \tag{8.116}$$

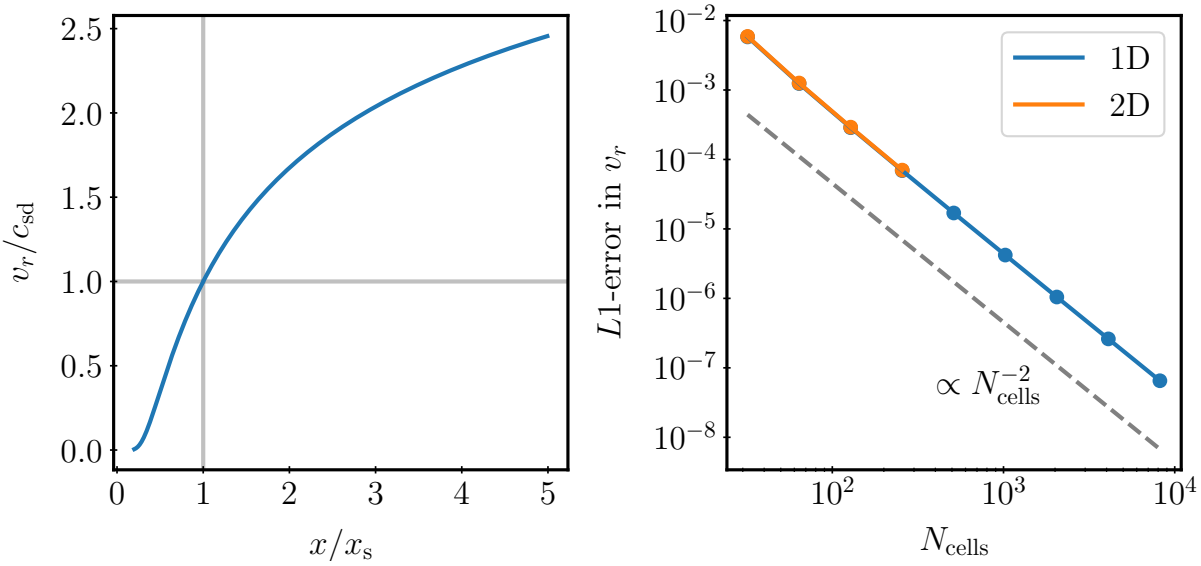

Figure 8.7: Left: Radial velocity v_r profile of the spherically-symmetric Parker wind for the 1D simulation with $N_{cells} = 1024$. The vertical grey line indicates the critical point while the horizontal grey line indicates the sound speed. Right: L1-error of v_r as calculated in our 1D and 2D simulations. The dotted line shows an error-profile for 2nd-order convergence.

Inserting the continuity equation and the equation of state $P_{th} = c_{sd}^2 \rho$ yields:

$$v_r \frac{\partial v_r}{\partial r} = -\frac{c_{sd}^2}{\rho}\frac{\partial \rho}{\partial r} - \frac{GM}{r^2} \tag{8.117}$$

or after some additional manipulations:

$$\left(v_r - \frac{c_{sd}^2}{v_r}\right)\frac{\partial v_r}{\partial r} = 2\frac{c_{sd}^2}{r^2}(r - r_{crit}), \tag{8.118}$$

where we defined the critical radius as $r_{crit} = GM/2c_{sd}^2$. The critical radius is the radius where the velocity derivative cannot be inferred from the equation of motion anymore because of algebraic reasons. The sonic point is a related point inside the flow and marks the point where $v_r = c_{sd}$. We infer from this form of the equation of motion that in our special case the critical and sonic points of the flow coincide. This equation can be integrated by moving the radial derivative on the left-hand side out to include the parenthesis and by introducing a radial derivative on the right-hand side. The result can be integrated to give:

$$\left(\frac{v_r}{c_{sd}}\right)^2 - 2\log\left(\frac{v_r}{c_{sd}}\right) = 4\log\left(\frac{r}{r_{crit}}\right) + 4\frac{r_{crit}}{r} + C, \tag{8.119}$$

where C is an integration constant. By requiring that the critical and the sonic point coincide, we get $C = -3$. Although this equation is transcendent, it is the complete solution to the equation of motion and is sufficient to calculate all required flow quantities. In practice, we apply the iterative Newton-Raphson algorithm to Eq. (8.119) in order to calculate v_r to machine precision for a given r and infer ρ from Eq. (8.115).

In the simulations, we use spherical coordinates, piece-linear interpolation, the VL2 timestepping, CFL = 0.4, and the HLLE Riemann solver for isothermal magnetohydrodynamics. We use $GM = 2$, $c_\mathrm{sd} = 1$, $\dot{M} = 1$ such that velocities are given in terms of the sound speed and radial coordinates are given in units of the critical radius. We use the analytic solution for the initial conditions. The numerical grid spans from $r = 0.2$ to $r = 5$ using a logarithmic spacing and includes $\theta \in [0, \pi]$ in 2D. We apply reflective boundary conditions at both θ-boundaries, at the outer r-boundary, we simply extrapolate the outflow, and at the lower boundary we relax the extrapolated radial velocity towards the analytical solution by $v_\mathrm{r,boundary} = 0.5(v_\mathrm{r,analytic} + v_\mathrm{r,extrapolated})$ and fix the density to its analytical solution. The velocity relaxation at the lower boundary is needed because there the flow is subsonic and needs to be able to adjust to the flow inside the simulation domain to be stable (see Thompson, 1990, for a proper implementation of subsonic boundary conditions). We use N_cells-cells in the radial direction with $N_\mathrm{cells} = 32 \ldots 8192$ in steps of 2 and $N_\mathrm{cells} = 32 \ldots 256$ in 2D; the θ-grid uses $2N_\mathrm{cells}$ cells.

In Fig. 8.7, we show the resulting radial velocity v_r profile for the 1D-simulation with $N_\mathrm{cells} = 1024$ at $t = 50$ which corresponds to ~ 10 crossing times. The flow is launched at the lower radial-boundary with highly subsonic velocities and steadily accelerated until it reaches $v_\mathrm{r} = c_\mathrm{sd}$ at $r = 1$, as expected. Above the sonic point, gas acceleration decreases and the radial velocity profile gets shallower. Also in Fig. 8.7, we display the $L1$-error of the simulated radial velocity compared to the analytical solution for both the 1D and 2D simulations. For both cases, our code converges at 2nd-order. Both the 1D- and 2D-errors nearly coincide for a given N_cells. This is a non-trivial result because the 2D-simulations can drift away from perfect spherical symmetry because of non-radial motions that might be seeded through the geometric source terms of the divergence operator in the momentum equation or by interactions with the lateral boundaries. Because we take special care to properly discretize the geometric source terms and correctly implemented the boundary conditions, the deviations from spherical-symmetry are minuscule.

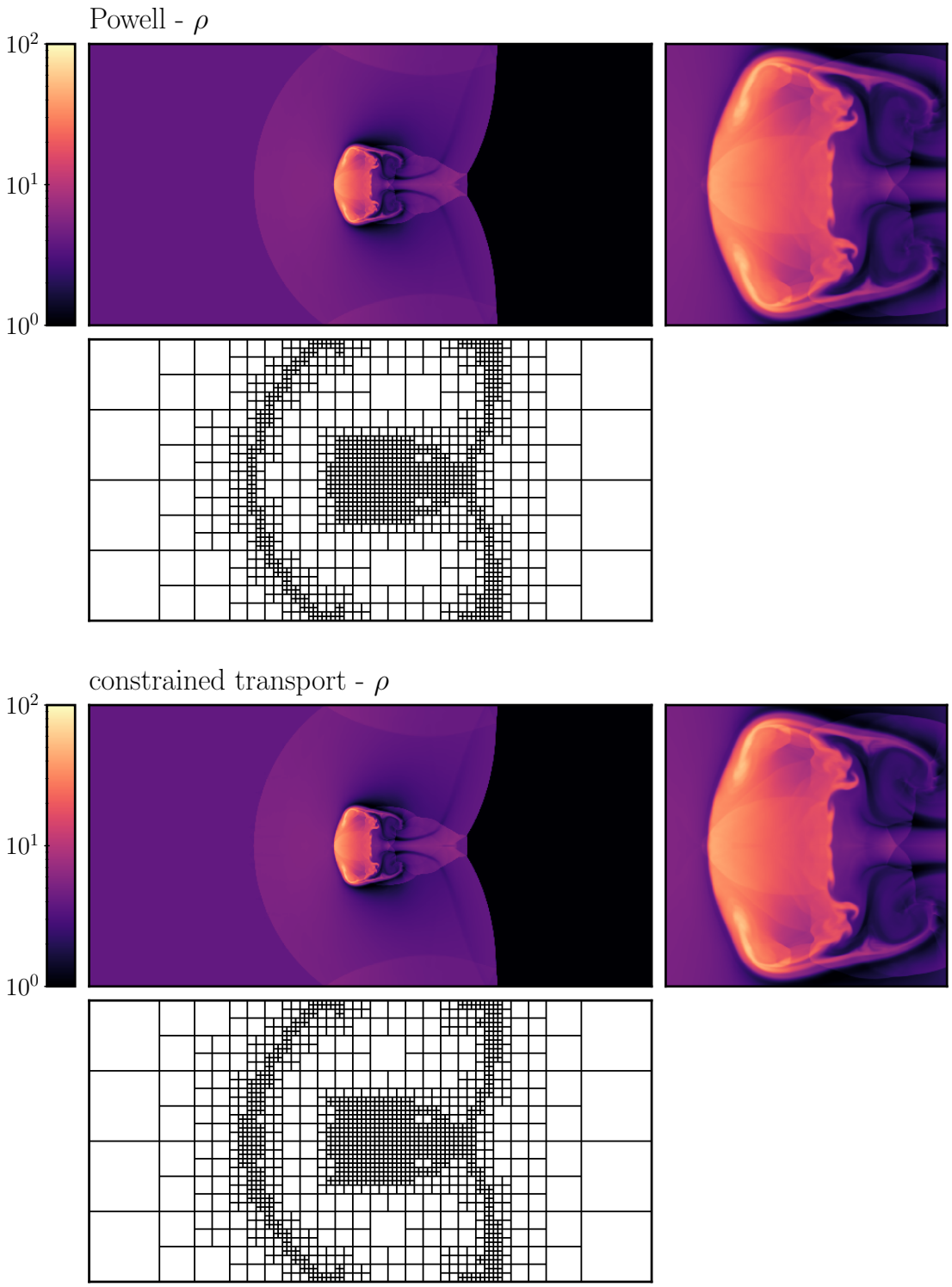

Figure 8.8: The results of the cloud shock interaction simulation for both the Powell (top) and CT (bottom) methods at $t = 0.06$. For each method, the large coloured panel shows ρ in the whole simulation domain while the small coloured panel shows a zoom-in onto the central region that encloses the cloud. The remaining panels show the patch outlines. Each rectangle corresponds to a patch with 32^2 cells.

8.4.4 Cloud Shock Interaction

In this example, we simulate the interaction of an incoming shock wave with an overdensity, named cloud in the following. We adopt the setup of Dai and Woodward (1998). We use this example to demonstrate the space and time AMR capabilities of BLINC. The ambient medium and the shock are initialized using

$$\begin{bmatrix} \rho \\ P_{\text{th}} \\ u_x \\ u_y \\ u_z \end{bmatrix} = \begin{bmatrix} 3.86859 \\ 167.345 \\ 11.2536 \\ 0 \\ 0 \end{bmatrix} \quad \text{and} \quad \begin{bmatrix} B_x \\ B_y \\ B_z \end{bmatrix} = \begin{bmatrix} 0 \\ 2.1826182 \\ 0 \end{bmatrix} \quad \text{for } x < 0.031, \tag{8.120}$$

and

$$\begin{bmatrix} \rho \\ P_{\text{th}} \\ u_x \\ u_y \\ u_z \end{bmatrix} = \begin{bmatrix} 1 \\ 1 \\ 0 \\ 0 \\ 0 \end{bmatrix} \quad \text{and} \quad \begin{bmatrix} B_x \\ B_y \\ B_z \end{bmatrix} = \begin{bmatrix} 0 \\ 0.56418956 \\ 0 \end{bmatrix} \quad \text{for } x >= 0.031. \tag{8.121}$$

The cloud is centred on $[x, y] = [0.25, 0]$, has a radius of $r = 0.15$, and is initialized with a density

$$\rho = 10. \tag{8.122}$$

No other quantity is changed inside the cloud radius. The simulation domain is $[x, y] \in [-0.5, 1.5] \times [-0.5, +0.5]$ in Cartesian coordinates and is initially sampled by 8×4 patches. Each patch holds 32^2 cells. We use the HLLD Riemann solver, the VL2 integrator, CFL = 0.4, and the piecewise-parabolic reconstruction. The simulation is carried out twice: once with the Powell method and once with the CT method. The y-boundaries are periodic while the x-boundaries have simple outflow boundary conditions. We use adaptive timestepping and AMR with the following criteria: we calculate for each patch the maximum absolute and normalized Laplacian of the density first:

$$\text{indicator} = \max\left(\frac{|\rho_{i+1j} - 2\rho_{ij} + \rho_{i-1j}| + |\rho_{ij+1} - 2\rho_{ij} + \rho_{ij-1}|}{\rho_{ij}}\right) \tag{8.123}$$

then decide whether a patch is refined or can be derefined based on

$$\text{indicator} > 10^{-1} \longrightarrow \text{refine.} \tag{8.124}$$

$$\text{indicator} < 10^{-2} \longrightarrow \text{derefine.} \tag{8.125}$$

This criterion tries to resolve density fluctuations and structures. We allow for a maximum of 4 additional levels of spatial refinement and 7 bins difference between the minimum and maximum occupied timebins. The resulting density structure of the cloud is displayed in Fig. 8.8 together with the patch topology as given by the patch outlines. Minor differences can be seen in the density structure of the clouds when comparing the results of the Powell and CT methods. The most notable differences can be found in the highly compressed parts of the cloud and in the central structure of the tails. The most obvious differences between the two simulations can be seen in the patch topology. For the CT simulation, a handful more patches are refined in the front of the cloud itself and on the bow shock that is driven away from the cloud.

8.4.5 Interstellar Medium

In this numerical experiment, we simulate a patch of the turbulent magnetized multiphase ISM under solar-neighbourhood conditions in a tallbox simulation domain. We account for the kinetic and thermal feedback provided by supernovae to regulate the ISM. Various studies use a similar setting to investigate the dynamics of the ISM (de Avillez and Breitschwerdt, 2005; Walch et al., 2015; Li et al., 2015; Kim and Ostriker, 2017). We do not explicitly model the chemical state of the ISM but use the tabulated cooling and heating functions of Ploeckinger and Schaye (2020). We adopt their *UVB_dust1_CR0_G0_shield0* model which includes molecule formation on dust grains, photoelectric heating of these, cooling by molecules and metal ions at low temperatures, as well as cooling by H, He, and metal lines at temperatures above 10^4 K.

Gravitational Potential and Initial Conditions We adopt the stellar gravitational potential of Walch et al. (2015) to represented a population of previously formed stars and model it using an isothermal sheet with:

$$\rho_\star(z) = \rho_\star(z=0)\,\mathrm{sech}^2(z/2z_\mathrm{d}) \tag{8.126}$$

where the midplane stellar density is $\rho_\star(z=0) = \Sigma_\star/4z_\mathrm{d}$, the stellar surface density is $\Sigma_\star = 30\mathrm{M}_\odot\,\mathrm{pc}^{-2}$, and the scaleheight of the stars is $z_\mathrm{d} = 100\,\mathrm{pc}$. Self-gravity of the gas is neglected. The total gravitational acceleration is given by:

$$g_{z,\mathrm{grav}}(z) = -8\pi G\rho_\star(0)z_\mathrm{d}\tanh(z/2z_\mathrm{d}). \tag{8.127}$$

To generate quiescent initial condition for our simulation, we iteratively solve the equation of

hydrostatic equilibrium

$$\frac{\partial P_{\rm th}}{\partial z} + \frac{\partial B^2/2}{\partial z} = \rho g_{z,\rm grav}(z). \tag{8.128}$$

We make a first guess on the initial density and pressure profile and then solve this equation by integrating $P_{\rm th}$ from the midplane out into the CGM on a fine grid in z. The new values of the thermal pressure are converted into a density field by calculating the equilibrium pressure at which heating and cooling of the gas are balanced [2]:

$$\mathcal{L}(P_{\rm th,eq}(\rho), \rho) = \mathcal{H}(P_{\rm th,eq}(\rho), \rho), \tag{8.129}$$

where $\mathcal{L}$ is the cooling function and $\mathcal{H}$ is the heating function. The density field is then given by the inverse of $P_{\rm th,eq}(\rho)$. The magnetic field is calculated by:

$$B(z) = B_x(z) = B(z=0)\sqrt{\rho(z)/\rho(z=0)}, \tag{8.130}$$

where the midplane magnetic field strength is $B(z=0) = 0.1\,\mu$G. With the new values of B and ρ, we integrate Eq.(8.128) again. The change in the density field needs to be damped to achieve convergence. We replace the new density field $\rho_{\rm new}$ with $\rho_{\rm new} \leftarrow (\rho_{\rm new} + 3\rho_{\rm old})/4$ where $\rho_{\rm old}$ is the density field from the last iteration. We impose a lower threshold density of $n_{\rm H} = 2\times10^{-6}\,{\rm cm}^{-3}$ inside the halo. This procedure is repeated until the maximum change in the ρ field drops below 10^{-7} from one to the next iteration. This whole algorithm is repeated with different choices for the initial midplane pressure until the gas surface density of the calculated density field is

$$\Sigma_{\rm gas} = 10\,{\rm M}_\odot\,{\rm pc}^{-2}. \tag{8.131}$$

The initial conditions are in thermal and hydrostatic equilibrium so that only small velocity perturbations are seeded during the initial phase of the simulation.

Supernova Feedback We model supernova feedback assuming that each supernova releases an energy amount of

$$E_{\rm SN} = 10^{51}\,{\rm erg}. \tag{8.132}$$

Supernovae are randomly distributed throughout the disk. We assume that they are uniformly distributed in x, y and normally distributed in z with a characteristic scale height of 50 pc which

[2] We use the metallicity $Z = Z_\odot$ and redshift $z = 0$ entries of the cooling and heating curves.

corresponds to the *random*-driving model of Walch et al. (2015). For the Chabrier (2001) initial mass function, approximately 1 supernova per 100 $M_\odot$ formed stellar mass exposes in form of a supernova type II. This translates for our gas surface density into an approximate supernova rate surface density of

$$\dot{N}_{\mathrm{SN}} = 60\,\mathrm{Myr}^{-1}\mathrm{kpc}^{-2} \tag{8.133}$$

when we convert the gas surface density into star formation surface density using the Kennicutt (1998)-Schmidt-Law. This value is again consistent with Walch et al. (2015).

In order to inject the feedback energy of the supernovae, we define a region with radius $r_{\mathrm{inj}} = 4\Delta x$ around the supernova position as the feedback region. Depending on the local mean density, this region may not resolve the Sedov-Taylor phase of the supernova and thus underestimate the momentum feedback of this supernovae. If this is the case, we do not inject energy in form of heat but in form of momentum into the feedback region. To interpolate between these two extremes, we define the factor

$$\chi = \min\left(1, \frac{M_{\mathrm{inj}}}{800\mathrm{M}_\odot}\right) \tag{8.134}$$

where M_{inj} is the mass contained in the feedback region. Once this factor is determined, we calculate how much (radial) momentum p_{inj} and thermal energy E_{inj} is injected into the feedback region by:

$$p_{\mathrm{inj}} = \min\left(p_{\mathrm{term}}, \sqrt{\frac{2\chi E_{\mathrm{SN}}}{M_{\mathrm{inj}}}}\right), \tag{8.135}$$

$$E_{\mathrm{inj}} = (1-\chi)E_{\mathrm{SN}}, \tag{8.136}$$

where the terminal momentum $p_{\mathrm{term}} = 3\times10^5\,\mathrm{M}_\odot\,\mathrm{km\,s}^{-1}$ acts as an upper bound for the momentum generated until the end of the Sedov-Taylor phase. This value for the terminal momentum is consistent with simulations focusing on the local feedback by individual or multiple supernovae (Cioffi et al., 1988; Kimm and Cen, 2014; Martizzi et al., 2015; Kim and Ostriker, 2015). In addition, we heat every cell that is inside the feedback region to $T = 10^4$ K if its current temperature falls below this value. Feedback is instantaneous and every supernova is a discrete event in time.

In each cell that is contained within the feedback region, we inject momentum and energy following

$$p_{\mathrm{inj,cell,lim}} = \min\left(350\,\mathrm{km\,s}^{-1}\rho V_{\mathrm{cell}}, p_{\mathrm{inj}} \times V_{\mathrm{cell}}/V_{\mathrm{inj}}\right), \tag{8.137}$$

$$E_{\mathrm{inj,cell,lim}} = \min\left(\left(350\,\mathrm{km\,s}^{-1}\right)^2\rho V_{\mathrm{cell}}, E_{\mathrm{inj}} \times V_{\mathrm{cell}}/V_{\mathrm{inj}}\right), \tag{8.138}$$

where we additionally limit both values to stabilize the simulation and to avoid small timesteps.

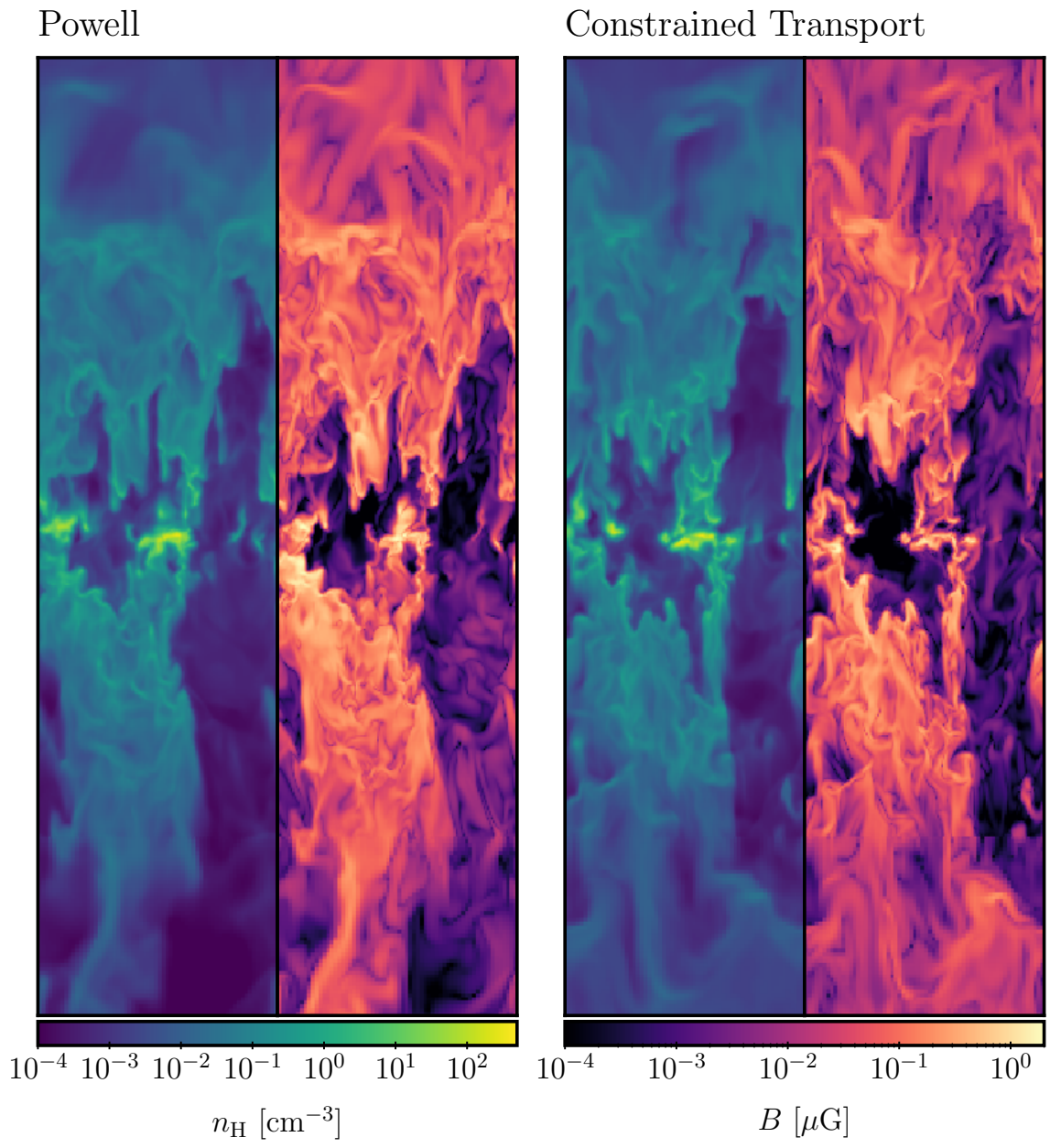

Figure 8.9: *xz*-slices through the simulation domain showing the hydrogen number density n_{H} and the magentic field strength B at $t = 150\,\mathrm{Myr}$. Each panel has a size of $1\,\mathrm{kpc} \times 2\,\mathrm{kpc}$.

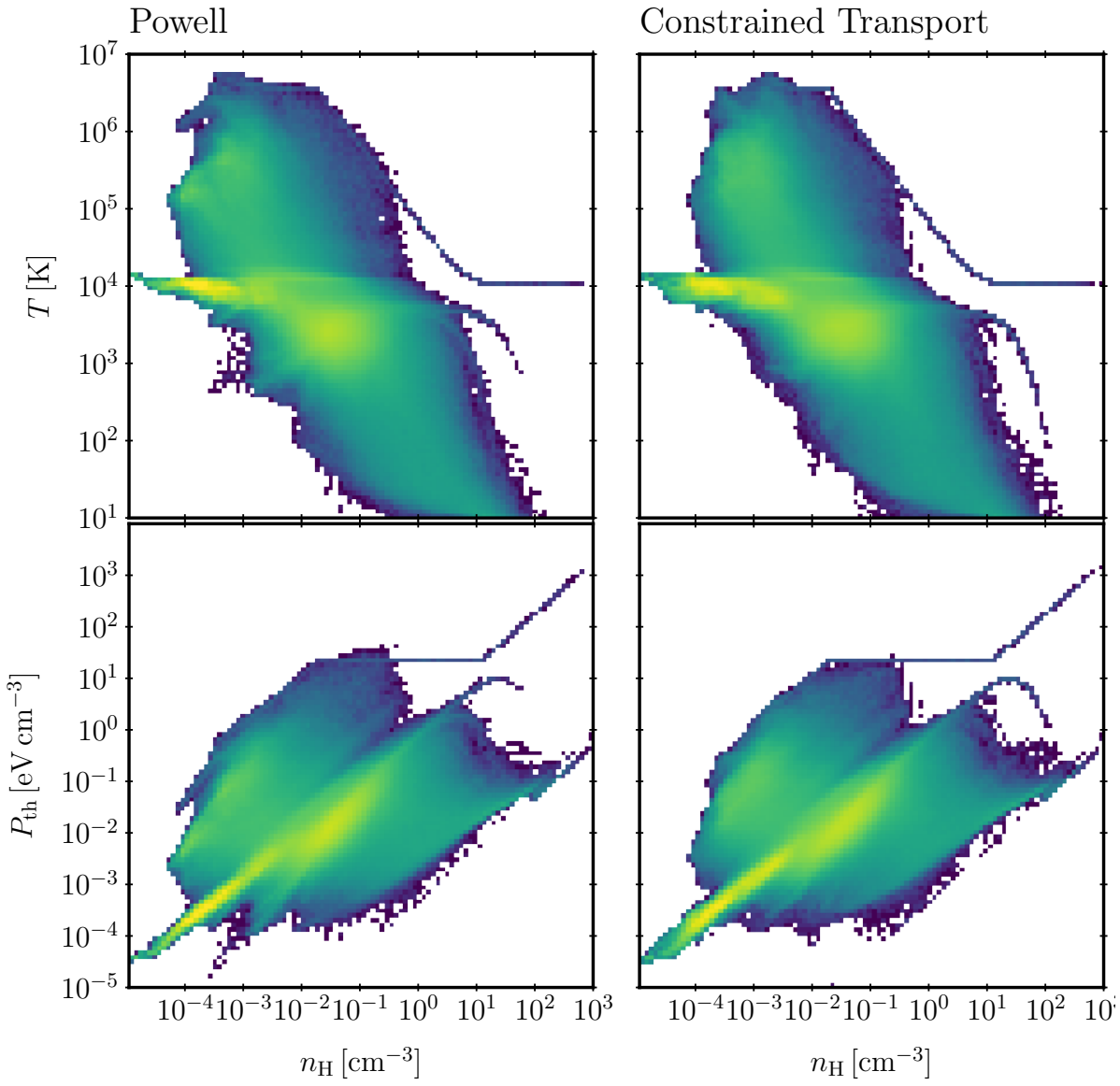

Figure 8.10: 2D histograms correlating the hydrogen number density $n_{\rm H}$, temperature T, and the thermal pressure at $t = 150\,\mathrm{Myr}$. Colours show the accumulated volume inside a bin in log-scale.

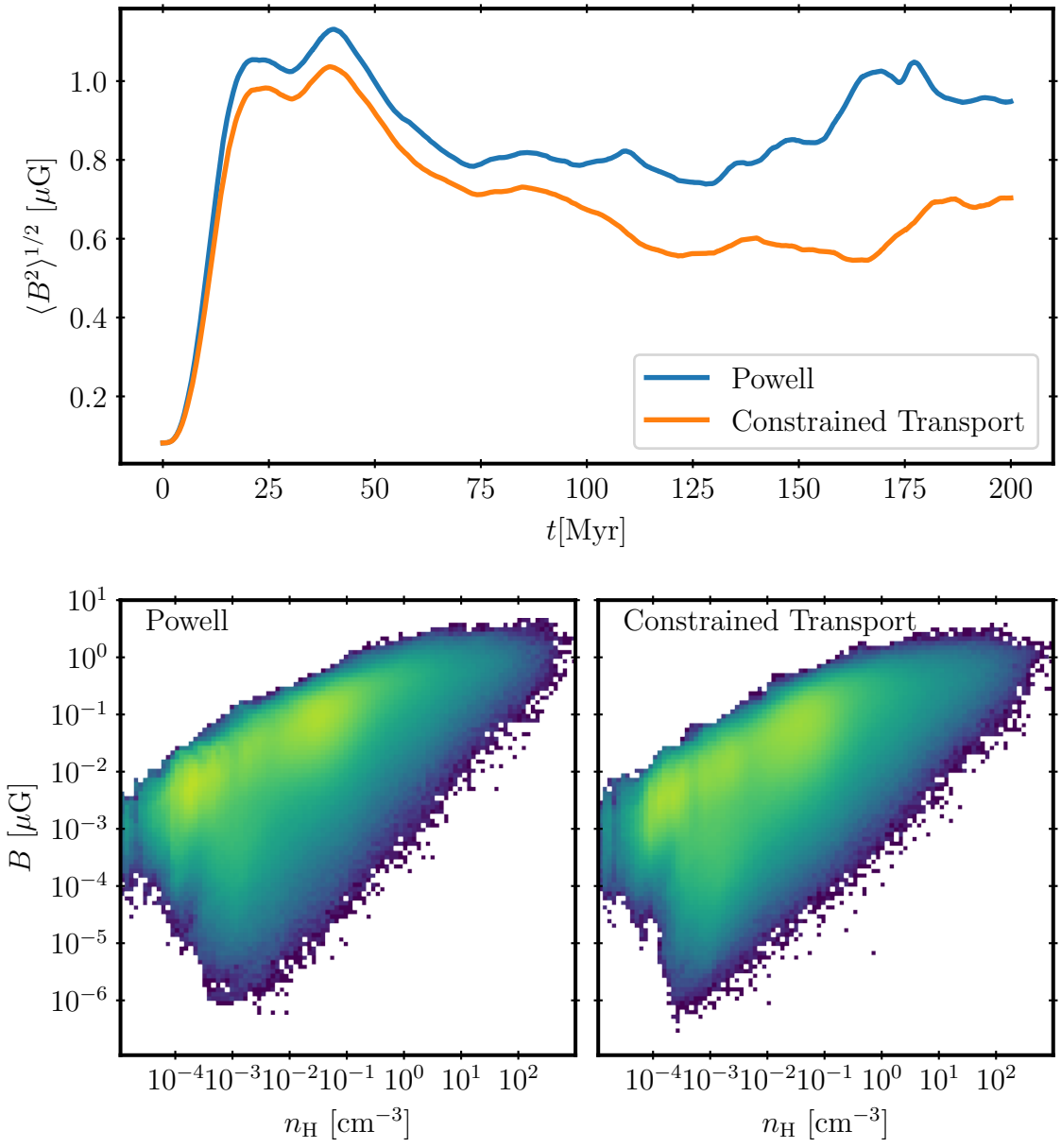

Figure 8.11: Top: Evolution of the mass-averaged root-mean-square magnetic field strength over the course of the simulation. Bottom: 2D histograms correlating the hydrogen number density n_H and the magnetic field strength B at $t = 150\,\mathrm{Myr}$. Colours show the accumulated volume inside a bin in log-scale.

Simulations and Results We simulate our model for the ISM in the domain $(x, y) \in [-0.5\,\mathrm{kpc}, 0.5\,\mathrm{kpc}]^2$ and $z \in [-5\,\mathrm{kpc}, +5\,\mathrm{kpc}]$ which is sampled by a $64 \times 64 \times 640$ root grid consisting of 16^3 patches. All patches of this root grid are refined in the $|z| < 1\,\mathrm{kpc}$ region by one additional AMR level. This results in an effective resolution of $\sim 8\,\mathrm{pc}$ inside the ISM. This resolution is identified in Kim and Ostriker (2017) as an upper bound for the applicability of the TIGRESS model. We apply periodic boundary conditions in the x- and y-directions and outflow boundary conditions for the z-directions. The simulations are performed with the HLLD Riemann solver, the RK2 time-integrator, the piecelinear reconstruction method, and CFL=0.3. The cooling and heating functions are integrated as sourceterms with a simple explicit integrator that subcycles the evolution of $U_{\mathrm{th}} = \varepsilon_{\mathrm{th}}/\rho$ such that this quantity changes by at most 10% in each subcycle. We perform two simulations: one with the constrained transport method and one with the Powell method. Supernovae explode every $\Delta t = 1/60\,\mathrm{Myr}$. They are placed at the same positions for both simulation such that a direct comparison is possible. A temperature floor of $T = 10\,\mathrm{K}$ is employed.

We show slices of the hydrogen number density n_{H} and of the magnetic field strength in Fig. 8.9 after 150 Myr of evolution. The quiescent initial conditions are quickly perturbed by the supernovae. A highly structured ISM develops. Neighbouring supernovae drive superbubbles into the ISM and compress gas to form high-density regions around the galactic midplane. The diffuse medium above the galactic midplane is highly turbulent and magnetised in both simulations. Two superbubbles can be seen in both simulations. At the time of the snapshot, the more elongated superbubble experiences a breakout in negative z-direction for the Powell method while this breakout cannot be seen in the constrained transport simulation. The vertical extent in positive z-direction is similar in both simulation. The smaller superbubble is situated between two cloud complexes. The positions of these two high-density cloud complexes are almost identical in both simulations: the cloud at the left boundary of the panel is situated above the midplane in both simulations while the central cloud is found right on the midplane. Both are in contact with the diffuse gas that reaches out to larger galactic heights.

In the top panels of Fig. 8.10, we show the n_{H}-T diagrams of both simulations. The temperatures are calculated by interpolating the tables provided by Ploeckinger and Schaye (2020). Temperatures range from $10^7\,\mathrm{K}$ to $10\,\mathrm{K}$. A cold, a warm, and a hot phase are present. Low temperature gas is preferentially found at high densities which are needed for molecular and low temperature metal line cooling to become effective. One striking isolated feature is present in both simulations at $T \sim 10^4\,\mathrm{K}$ to $10^5\,\mathrm{K}$ and densities $n_{\mathrm{H}} > 10^{-1}\,\mathrm{cm}^{-3}$. This is an imprint of our feedback implementation and originates from a supernova explosion. Both phase diagrams are

comparable. The most obvious difference can be observed in gas at densities $n_{\mathrm{H}} \sim 10^{-5} - 10^{-3}$. The coexistence of hot, warm, and cold phases at the same pressure can also seen in the n_{H}-P_{th} distribution which are also displayed in Fig. 8.10. Slight differences can be identified in this diagram around the structures at $n_{\mathrm{H}} \sim 10^{-5} - 10^{-3}$. Otherwise, these phase diagrams are also similar and no obvious difference between the simulations with the two methods is visible.
In Fig. 8.11, we show the evolution of the mass-averaged root-mean-square magnetic field strength. After a similar initial growth in both simulations, this quantity is systematically larger in the Powell simulation. We suspect that this might be caused because the two schemes apply different amounts of numerical resistivity in different ways. Further analysis accompanied by a resolution study is required to pinpoint the exact origin of this difference. Also in Fig. 8.11, the n_{H}-B distributions are shown. Both simulations show similar features at low densities and the general outline of both distributions are comparable.
We conclude from this experiment: 1) our solvers are robust enough to simulate highly turbulent astrophysical environments and 2) there are differences between the CT and the Powell method on a quantitative level but both give qualitatively comparable results.

8.4.6 Planet-Disk Interaction

In this simulation, we model the dynamics induced by a planet in a gaseous disk around a central star. We use the (globally) isothermal equation of state with $c_{\mathrm{sd}} = 0.1$, assume that the star has a mass of $M_\star = 1$, work in units where $G = 1$, and place the planet with mass $M_{\mathrm{p}} = 10^{-2}$ on a Keplerian orbit around the star at $R = 1$. This configuration allows for a gap opening because the thermal criterion $M_{\mathrm{p}} \gtrsim M_{\mathrm{thermal}} = c_{\mathrm{sd}}^3/(\Omega_p G)$ is fulfilled where Ω_p is the orbital frequency of the planet (Levy and Lunine, 1993). The potential of the planet is smoothed with $\epsilon = 0.01$ such that the total potential of central star + planet is given by

$$\Phi_{\mathrm{tot}}(\boldsymbol{r}) = -\frac{GM_\star}{|\boldsymbol{r}|} - \frac{GM_{\mathrm{p}}}{\sqrt{|\boldsymbol{r} - \boldsymbol{r}_{\mathrm{p}}(t)|^2 + \epsilon^2}}, \tag{8.139}$$

where $\boldsymbol{r}_{\mathrm{p}}(t)$ is the position of the planet at time t. The disk is set up in 2D cylindrical coordinates in the domain $R \in [0.5, 2]$ and $\varphi \in [-\pi, \pi]$ with no radial velocity on Keplerian orbits around the central star and mass density $\rho = 1$. We use reflective boundary conditions on both R-boundaries. We employ the RK2 time integrator, use $N_R = 768$ cells in radial direction which are logarithmically spaced, $N_\varphi = 2304$ cells in the polar direction, CFL = 0.8, the piecewise-parabolic reconstruction, and the HLLD Riemann solver for isothermal magnetohydrodynamics. Although we do not include magnetic fields, it is beneficial to use the HLLD Riemann solver because it applies a low amount of numerical viscosity to transverse waves in

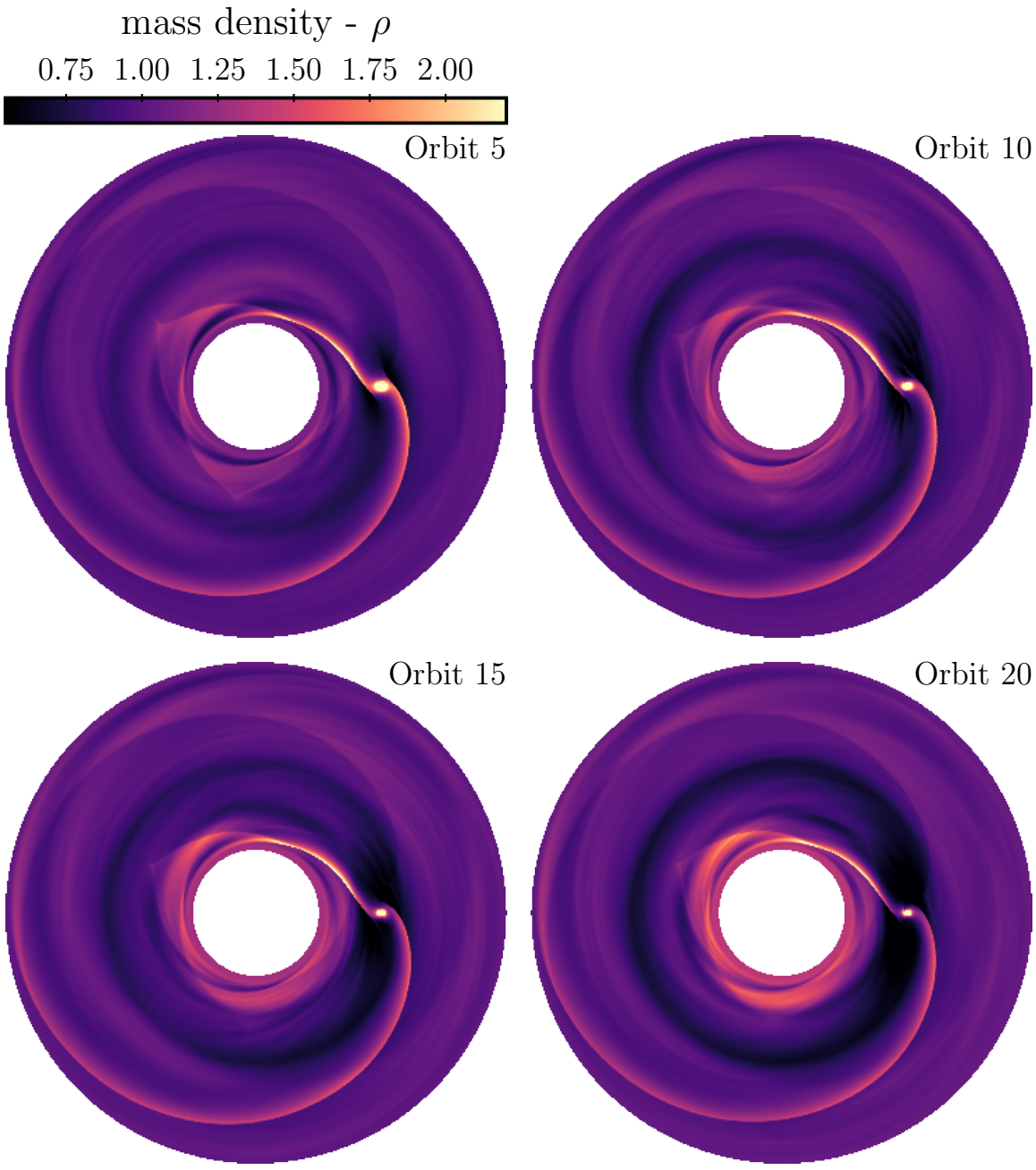

Figure 8.12: Gas density in the planet-disk interaction simulation at $t = 5, 10, 15, 20 \times 2\pi\Omega_{\rm p}^{-1}$.

subsonic flows. We neglect the self-gravity of the gas and do not account for gas accretion onto the planet. The gravitational acceleration process given by the potential in Eq. (8.139) is modelled as a sourceterm and integrated as such by the RK2 time integrator.
In Fig. 8.12, we show the evolution of density inside the disk. The gravity of the planet perturbs the initial Kelperian orbits of the gas. Spiral waves emerge, steepen and start to form the trailing and leading shock waves. They connect to gas that accumulates around the planet. Gas gradually flows out of the horseshoe region which leads to gap opening. The reflective inner boundaries prohibits gas that is driven inwards from leaving the simulation domain. This causes the development of highly patterned and dense structures around the inner boundary. Similarly, the outer reflective boundary conditions seed additional waves that travel through the outer region of the disk.

8.4.7 RHD Test Problems

Here, we compile a suite of test problems for our radiation hydrodynamics solver. Our aim is twofold: 1) we want to show that our implementation is sufficiently robust and accurate and 2) we want to show scenarios in which the M1 closure relation produces results that are in agreement with our expectations for radiation transport and show examples where this is not the case. All simulations use the HLLC Riemann solver, the piecewise-parabolic reconstruction, the RK2 time integrator, CFL $= 0.8$, Cartesian coordinates, and we use units where $c = 1$. In Fig. 8.13, we present the results of these simulations and show the radiation energy density $\varepsilon_{\rm rad}$ for all of them.

Searchlights In this example, we adopt a modified setup of Rosdahl et al. (2013) which considers two isolated sources of beamed radiation. The simulation domain is $(x, y) \in [-1, 5] \times [-3, 3]$ which is initially sampled by 12×6 patches each containing 32^2 cells. The simulation is run with space-and-time AMR. Patches are refined once the maximum value of $\varepsilon_{\rm rad}$ exceeds 10^{-2} inside a patch. We use outflow boundary conditions in all directions. The initial conditions are given by $\varepsilon_{\rm rad} = 10^{-6}$ and $\boldsymbol{F}_{\rm rad} = \boldsymbol{0}$ which represent a quiescent background. The first source injects radiation with $\dot{\varepsilon}_{\rm rad} = 100 \exp(-(\boldsymbol{x} - \boldsymbol{x}_{\rm c})^2/20^2)$ and $\dot{\boldsymbol{F}}_{\rm rad} = \varepsilon_{\rm rad}\boldsymbol{e}_x$ where $\boldsymbol{x}_{\rm c} = (0, -2)$. The second source injects radiation at $\boldsymbol{x}_{\rm c} = (0, -1)$ with the same energy density rate but with $\dot{\boldsymbol{F}}_{\rm rad} = \varepsilon_{\rm rad}(2\boldsymbol{e}_x + \boldsymbol{e}_y)/\sqrt{5}$ - in an oblique direction. The simulation results are shown at $t = 10$. Both radiation beams are well captured. Little to no leakage of radiation from within the beam into the surrounding medium is observed. This is a good showcase which demonstrates that the M1 method can capture non-interacting beams of radiation.

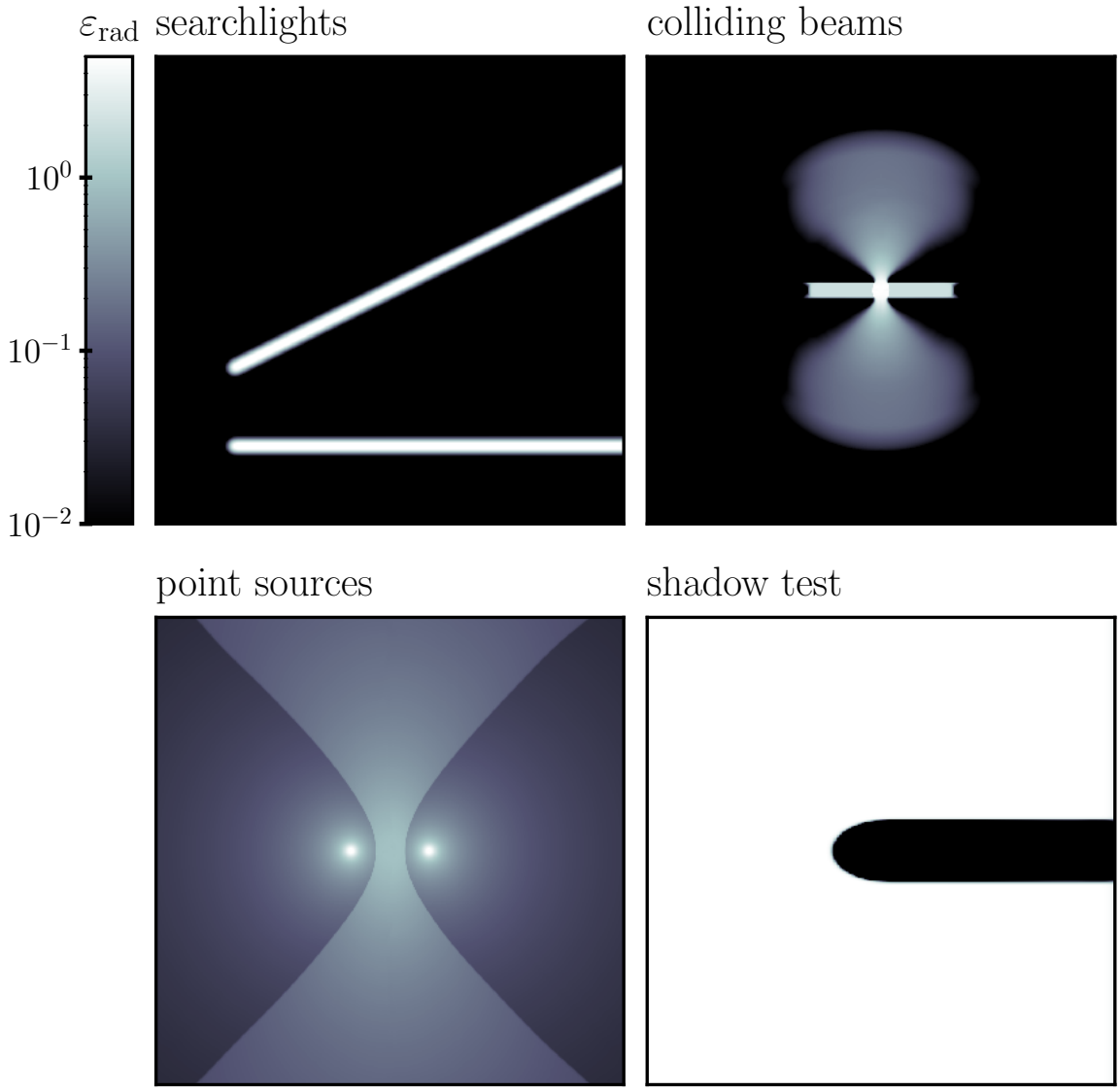

Figure 8.13: Gallery of various test problems for the radiation hyrdrodynamics module.

Colliding Beams For this test, we adapt the colliding beams example of Chan et al. (2021). Our simulation domain $(x, y) \in [-3, 3] \times [-1.5, 1.5]$ is initially sampled with 12×6 patches each containing 32^2 cells. The simulation is run with space-and-time AMR. Patches are refined once the maximum value of $\varepsilon_{\mathrm{rad}}$ exceeds 10^{-2} inside a patch. The radiation field is set up with a uniform density $\varepsilon_{\mathrm{rad}} = 2$ in a stripe where $|y| < 0.1$ and streams towards the centre of the simulations domain with $\boldsymbol{F}_{\mathrm{rad}} = -\mathrm{sign}(x)\varepsilon_{\mathrm{rad}}$. We use the same initial conditions as for the *searchlights* example outside of this stripe. The simulation result are shown at $t = 2$. The counterstreaming beams of radiation interact at the centre although no radiation-matter interacting is included. Thus, the observed dynamics is unphysical. This interaction creates a

central region that is overpressurized in terms of radiation. Because radiation behaves like a fluid if the M1 closure relation is used, radiation starts to flow away in the vertical direction taking the path of least resistance. In the analytic solution to the full radiation transfer equation, no interaction between the two radiation streams takes place and no vertical radiation beams are created. Thus, the M1 scheme is formally inadequate to simulate this problem.

Point Sources This test is similar to the one presented in Rosdahl et al. (2013). Our simulation domain $(x, y) \in [-3, 3]^2$ is sampled with 1024^2 cells. We use the same initial conditions as for the *searchlights* example. We use outflow boundary conditions in all directions. We inject isotropic radiation into the simulation trough $\dot{\varepsilon}_{\rm rad} = 100 \exp(-(\boldsymbol{x} - \boldsymbol{x}_{\rm c})^2/20^2)$ with $\boldsymbol{x}_{\rm c} = (+0.5, 0)$ and $\boldsymbol{x}_{\rm c} = (-0.5, 0)$. We do not include any radiation-matter interaction - our simulation box is completely transparent. The simulation result is shown in Fig. 8.13 at $t = 10$. Radiation freely flows away from the two sources until the two radiation streams meet each other. Both streams shock each other and an hourglass shaped interaction region is created. Radiation streams preferentially in vertical direction in this interaction region. At larger heights, shocked radiation has higher radiation pressure and expands into regions that would otherwise be filled with pristine radiation from both sources. These effects are, again, caused by the fluidization of radiation by the M1 closure relation.

Shadow Test Here, we adopt a modified version of a test present in Hayes and Norman (2003). It demonstrate that simple shadows can be captured with the M1 method. We use a similar configuration as Hayes and Norman (2003) but use dimensionless setup and assume that the gas has a fixed temperature. Our simulation domain $(x, y) \in [-0.5, 0.5]^2$ is sampled with 512^2 cells. We define an absorption coefficient via:

$$\rho = \rho_0 + \frac{\rho_1 - \rho_0}{1 + \exp(\Delta)}, \tag{8.140}$$

$$\Delta = 10 \left[\left(\frac{x}{0.1} \right)^2 + \left(\frac{y}{0.06} \right)^2 - 1 \right], \tag{8.141}$$

$$\kappa = 0.01 \rho, \tag{8.142}$$

where $\rho_0 = 1$ and $\rho_1 = 10^3$. The associated absorption process is integrated at the end of the simulation timestep by multiplying all radiation quantities with $\exp(-\Delta t \kappa \rho)$. We use the same initial conditions as for the *searchlights* example. Radiation is injected through the left x-boundary where we set $\varepsilon_{\rm rad} = 5$ and $\boldsymbol{F}_{\rm rad} = \varepsilon_{\rm rad} \boldsymbol{e}_x$. We use outflow boundary conditions for all other directions. The simulation is run until $t = 10$. The elliptical central overdensity casts

#	ν_{min} [eV]	ν_{max} [eV]	E_{mean} [eV]	$\sigma_{\mathrm{H_2}}$ [cm^{-2}]	σ_{HI} [cm^{-2}]	σ_{HeI} [cm^{-2}]	σ_{HeII} [cm^{-2}]
0	11.20	13.59	12.34	2.1×10^{-19}	0	0	0
1	13.59	24.59	17.79	5.1×10^{-18}	3.4×10^{-18}	0	0
2	24.59	54.42	30.04	2.7×10^{-18}	7.8×10^{-19}	5.6×10^{-18}	0
3	54.42	∞	59.34	4.0×10^{-19}	9.8×10^{-20}	1.4×10^{-18}	1.2×10^{-18}

#	$E_{\mathrm{heat,H_2}}$ [eV]	$E_{\mathrm{heat,HI}}$ [eV]	E_{HeI} [eV]	$E_{\mathrm{heat,HeII}}$ [eV]	$\dot{N}_{\mathrm{source}}$ [s^{-1}]
0	0	0	0	0	1.9×10^{49}
1	2.8	3.0	0	0	4.2×10^{49}
2	12.9	14.7	4.3	0	9.3×10^{48}
3	43.0	44.5	34.0	4.1	3.1×10^{46}

Table 8.1: Parameters of the radiation field in the used four bands. The radiation bands are bounded by the frequencies ν_{min} and ν_{max}. The average photon energy is E_{mean}. The cross sections σ_x are used for the photoionization/photodissociation processes. For each such event, an energy amount of $E_{\mathrm{heat},x}$ is released in the form of heat. The central O-star injects photons with a number luminosity or photon rate of $\dot{N}_{\mathrm{source}}$ into each band.

a shadow. The transition between illuminated and shadow regions is sharp and no radiation leakage between the two regions can be observed.

8.4.8 Strömgren Sphere

We simulate the Strömgren (1939) sphere of an isolated O-star modelled as a black body with an effective temperature $T_{\mathrm{eff}} = 4.87 \times 10^4$ K and luminosity of $L = 7.6 \times 10^6\,\mathrm{L}_\odot$. These parameters are also used in Kannan et al. (2019). The ambient medium of the star has a constant density $n_{\mathrm{H}} = 10^3\,\mathrm{cm}^{-3}$ and is stationary initially. We model radiation using four frequency bands associated with the photoionization edges of H, He, and a lower bound of the Lymann-Werner band. In Tab. 8.1, we list the frequency range of each bin, the associated mean-photon energy, the cross sections used for absorption, and the residual photon energy per photoionization event that heats the absorbing medium. We adopt the approximation of (Nickerson et al., 2018) and model H_2 photoionionzation as H_2 photodissociation. These parameters are comparable to those listed in Kannan et al. (2020). We run two simulations both in spherical coordinates assuming spherical symmetry. Both use the HLLC Riemann solver, the piecewise

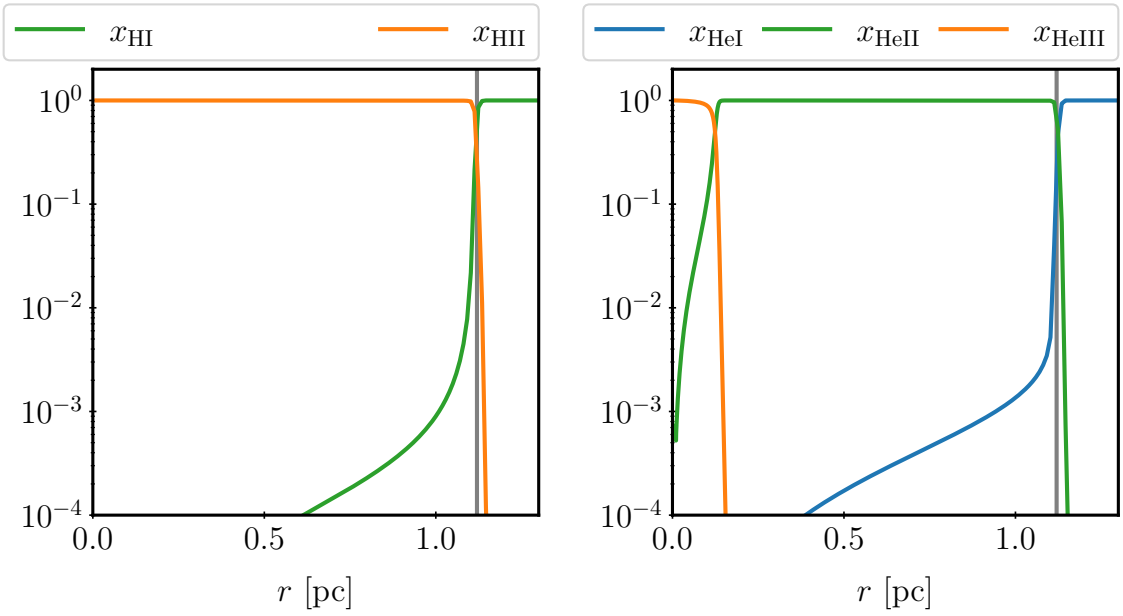

Figure 8.14: Strömgren sphere in an ambient medium with $T = 10^4\,\mathrm{K}$. The vertical grey line marks the analytically expected position of the Strömgren radius. We show the ionization fractions of hydrogen and helium with, e.g., $x_{\mathrm{HI}} = n_{\mathrm{HI}}/n_{\mathrm{H}}$.

linear reconstruction, the RK2 integrator, CFL = 0.4, reflective boundary conditions at the inner boundary, outflow boundary conditions at the outer boundary, and the reduced speed of light approximation with $c = 1000\,\mathrm{km\,s^{-1}}$.

Fixed Temperature The first simulation neglects momentum input from absorbed photons, H_2-chemistry is excluded and we use a fixed gas temperature of $T = 10^4\,\mathrm{K}$. Both hydrogen and helium are initially neutral. The simulation domain $r \in [0.01, 1.5]\,\mathrm{pc}$ is sampled by 512 logarithmically spaced cells. The simulation converges to a steady state which we show in Fig. 8.14. We are able to compare the position of the developing ionization front (I-front) with an analytical estimate in this scenario and validate our numerical scheme. The position of the I-front or the Strömgren radius can be estimated by (Strömgren, 1939):

$$r_{\mathrm{s}} = \left(\frac{3\dot{N}_{\mathrm{LyC}}}{4\pi n_{\mathrm{H}}^2 \alpha_{\mathrm{H}}}\right)^{-1/3} \sim 1.17\,\mathrm{pc} \tag{8.143}$$

where $\dot{N}_{\mathrm{LyC}} = 5.127 \times 10^{49}\,\mathrm{s^{-1}}$ is the Lyman continuum photon number luminosity and $\alpha_{\mathrm{H}} = 2.591 \times 10^{-13}\,\mathrm{cm^3 s^{-1}}$ is the recombination rate of hydrogen. This value overestimates the true position of the I-front because some photons have already been absorbed to create the inner HeIII region and by the HeII region. Using the photon number luminosity in the

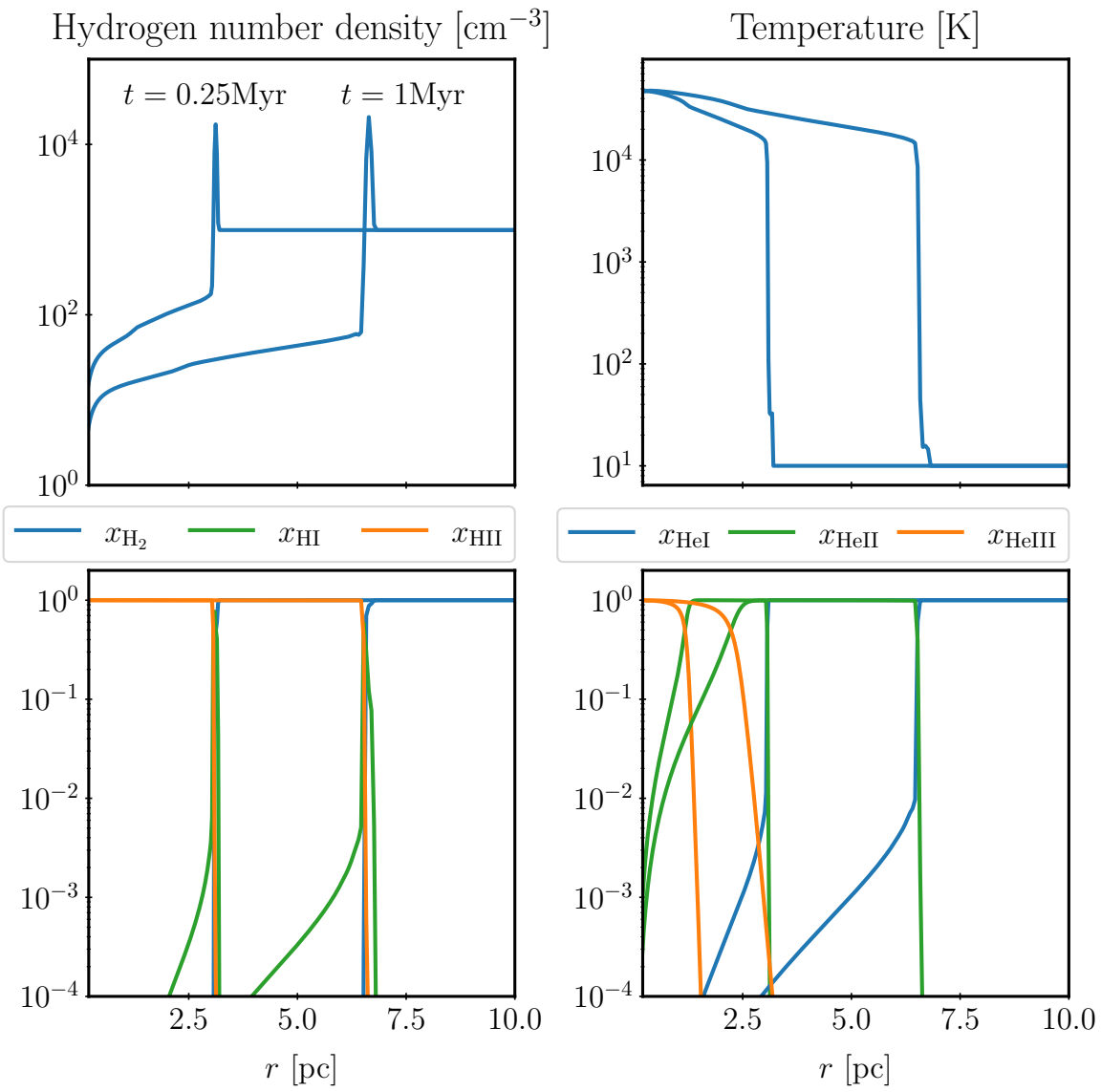

Figure 8.15: Ionization fractions of hydrogen and helium in an expanding HII region. We show the protonized molecular hydrogen fraction $x_{H_2} = 2n_{H_2}/n_H$.

[13.59, 24.59] eV band we calculate $r_s \sim 1.12$ pc which is shown in Fig. 8.14 by a grey line. This estimate aligns with the simulated position of the Strömgren radius.

Expanding HII region The second simulation features the full set of implemented H-He physics including H_2 chemistry. We set up the ambient medium at a temperature of $T = 10$ K which is also set as a temperature floor; helium is neutral and hydrogen is in its molecular phase. We evolve the temperature in time for this simulation. The simulation domain $r \in [0.1, 10]$ pc is sampled by 512 logarithmically spaced cells. The results are presented in Fig. 8.15 at $t =$

0.25 Myr and $t = 1$ Myr. Similar to the first simulation a Strömgren sphere develops. Gas inside this sphere is heated to $T > 10^4$ K and has lower densities $n_{\mathrm{H}} \lesssim 10^2\,\mathrm{cm}^{-3}$ compared to the ambient medium. This heating inside the HII bubble increases its pressure so that it is overpressurized relative to the ambient medium. This leads to an expansion of the HII bubble. Between bubble and ambient medium at the I-front, a thin shell of compressed and swept-up gas forms. Both molecular and neutral hydrogen are dissociated/ionized at the I-front.
Both simulations show no signs of unwanted numerical features although the number densities of the individual ionic species show strong spatial gradients. We conclude that our solver for radiation hydrodynamics and the associated integrator for the radiation-augmented H-He chemistry is stable and accurate.

8.5 Summary

We presented the AMR code Blinc together with finite-volume algorithms for magnetohydrodynmics and radiation hydrodynamics. Algorithms to construct patch-based adaptive meshes on a graph-topology are developed. To share computational work on parallel machines, a diffusive load balancer is described. It that maps the load balancing problem to a physical diffusion process along a Hilbert space-filling curve. We detail how directional-unsplit Godunov/finite-volume schemes are implemented on this mesh framework and which

- coordinate systems can be used in Blinc and how geometrical sourceterms are discretized using the finite-volume idea,
- time integrators are implemented to advance the numerical solution in time using the method of lines,
- reconstruction methods can be employed to achieve higher-order interpolation and to lower numerical diffusivity of the schemes.

To demonstrate the applicability of these general methods, finite-volume methods for the equations of magnetohydrodynamics and radiation hydrodynamics are implemented. The divergence constraint of the magnetic field is handled either by the constrained transport method or by the Powell scheme. Using various test problems and numerical experiments, we show that the resulting schemes are accurate and robust.

9 Conclusions

In this work, I presented a novel theory of CR hydrodynamics, investigated its realm of applicability, developed numerical algorithms to discretize the new equations of CR hydrodynamics in the finite-volume framework, and implemented the resulting schemes in the moving mesh code Arepo. I applied this new theoretical and numerical framework of CR transport in the two astrophysical scenarios. First, I investigated the transport properties of CRs inside the CGM of a simulated galaxy that hosts a CR-driven galactic wind. Second, I proposed that radio-emission of harp-like NTFs in the CMZ originates from CRs propagating in braided magnetic flux tubes. The root cause for these new developments is the empirical finding of Sharma et al. (2009) that the finite-difference approximation of CR streaming in the one-moment CR hydrodynamics demands unphysical numerical regularization techniques to achieve numerical stability. Jiang and Oh (2018) propose to use a two-moment approximation to alleviate this problem. Inspired by their idea, we derived a two-moment hydrodynamical theory for CR transports that consistently accounts for the interaction between CRs and small scale gyroresonant Alfvén waves in the quasilinear limit. All terms up to order $\mathcal{O}(v_\mathrm{a}^2/v^2)$, which describe the interaction between CRs and the magnetic fields of the Alfvén waves, need to be included so that the resulting scattering terms are frame independent. Here, frame independence means that the same derivation executed in a different frame followed by a frame transformation results in the same scattering terms.

The CR fluid is coupled to the MHD equations by forces that are exerted by the CRs through magnetic fields. In the direction perpendicular to a local mean magnetic field, they are caused by the gyromotions of the CRs while forces parallel to this magnetic field are mediated by the interaction of CRs with the gyroresonant Alfvén waves. To arrive at an energy-conserving and -consistent description of this interaction, we model the energy contained in gyroresonant Alfvén waves as a third fluid which resembles the subgrid-scale (SGS) approach to model energy contained in unresolved turbulence. The energy contained in Alfvén waves can be diminished and thermalized through plasma effects which heat the surrounding gas. The balance of Alfvén wave growth and damping sets their local energy density which is then used to model the CR diffusion coefficient using the quasilinear theory. The final set of CR equations is a true extension of the well-established one-moment hydrodynamical theory as our two-moment theory reduces to the one-moment theory in the limit of frequent scattering by Alfvén waves. Furthermore, the transport effects of CR streaming and diffusion are well captured within the new theory and are a self-consistent outcome of the interplay between CRs and gyroresonant Alfvén waves.

Progressing from a one-moment to a two-moment description of transport is reminiscent of the transition from flux-limited diffusion to a higher-order closure-based theory in the context of radiation hydrodynamics. These models for radiation hydrodynamics assume some scattering process which drives the photon distribution towards isotropy. Only a few statistical moments are needed to truthfully represent the radiation field if this distribution is sufficiently isotropic. Capturing the right radiation-propagation properties is difficult for these moment-based descriptions in optical-thin media where no scattering takes place. There, the underlying assumptions of the hydrodynamical theory break down and lead to an unphysical radiation self-interaction.

Both, CR and radiation/photon transport are similar because both topics describe the propagation of relativistic particles. In fact, our new two-moment hydrodynamical model was derived with the P1 or Eddington approximation for radiation in mind and can be considered as a generalisation of this approximation to the CR case. Because of these similarities, the same self-interaction problem is expected to negatively influence the results calculated with our theory for CR hydrodynamics.

We conducted simulations using controlled and idealized initial conditions with absent CR scattering to mimic an optically thin media for CRs. We showed that the self-interaction problem affects CRs less severely. To arrive that this conclusion, we generalised the M1 closure for radiation hydrodynamics to the CR case and derived a four-moment (H1-)approximation for CR transport to compare the base P1-approximation against more sophisticated and arguably more accurate approximations. The main reason for the absence of a strong CR self-interaction effect is the magnetic field. Whilst radiation can freely propagate in any direction, CRs are bound to macroscopic magnetic fields. First, this reduces the dimensionality of the problem, and second, magnetic mirrors provide additional scattering centres for the CRs. If CR scattering by small-scale magnetic fields is included only minuscule differences between the P1, M1, and H1 approximations are observed. We conclude that our P1-based hydrodynamical model is sufficiently accurate to employ it in simulations of astrophysical problems.

To conduct simulations that feature CR transport with our new hydrodynamical description, we developed a finite-volume scheme for the moving-mesh code Arepo. Important terms in our evolution equations cannot be cast into the divergence form of a conservation law. Because some of these terms describe the inertial transport of CRs along magnetic field lines, we carefully discretized these. Path-conservative finite-volume schemes (Parés, 2006) generalize the idea of standard Godunov schemes to non-conservative hyperbolic partial differential equations. We adapt such a scheme to the Voronoi mesh of Arepo. We derive and apply a semi-

implicit 2nd-order Runge-Kutta scheme with adaptive timestepping to solve the sourceterms that describe the scattering process between CRs and Alfvén waves. Through various test problems, these newly developed methods are tested for accuracy and robustness. The new scheme positions itself amongst the finite-volume algorithm of Jiang and Oh (2018) for the AMR-code Athena++ and Chan et al. (2019) for the the meshless finite-mass code Gizmo.

With the help of this new numerical scheme, we investigate large-scale CR transport properties inside the CGM formed by a CR-driven galactic wind. To keep this study focused, we explore a single isolated disc galaxy which is situated inside a $10^{11}\,M_{\odot}$ dark matter halo. Exploring the effects of CRs on galactic winds is a highly active research field (Butsky and Quinn, 2018; Mao and Ostriker, 2018; Chan et al., 2019; Buck et al., 2020; Bustard et al., 2020; Dashyan and Dubois, 2020; Peschken et al., 2021; Hopkins et al., 2020, 2021b; Semenov et al., 2021; Farber et al., 2022; Farcy et al., 2022; Huang and Davis, 2022; Nuñez-Castiñeyra et al., 2022; Quataert et al., 2022c,a). The focus of these works is mostly on aspects that are broadly related to the evolution of the galaxy. This includes the impact of the CRs on energy and mass loading of the wind or the CR influence on the star formation rate. We concentrate our discussion on two facets which received little attention sofar. First, we study the direct wind launching mechanism. We show that the forces exerted by CRs dominate over counteracting forces originating from gravity and magnetic fields at the disk halo interface. We can pinpoint the cause of the momentum transfer to the interaction between CRs and gyroresonant Alfvén waves. The drag between those two agents is mediated by the gyroresonant streaming instability and is dynamically important right at the wind launching site.

Second, we investigate the transport of CRs in our new hydrodynamical model. We find that the CR diffusion coefficient is not a constant value inside the CGM and varies by orders of magnitudes. We found that the outflow contains Alfvén wave dark regions which are localized regions where CRs extract energy from gyroresonant Alfvén waves. This takes place if the effective transport velocity of CRs is slower than the local Alfvén speed and leaves these regions devoid of Alfvén waves. By comparing the effective transport speeds as realized in our two-moment description for CR transport to steady-state expectations, we find that the CR transport in our simulation is neither compatible with the steady-state CR streaming or CR diffusion paradigms nor with a combination of both but is in a state that is only achievable and describable by a two-moment approximation.

In a second application, we propose an explanation for the formation of a peculiar type of NTFs inside the galactic centre. We focus on a subclass of NTFs which are characterized by a group of elongated and parallel filaments that form a triangular structure. They have a harp-like ap-

pearance while their string-like substructure is composed of parallel magnetic field lines. They are visible in the radio map of the CMZ which was recently obtained with the MeerKAT telescope (Heywood et al., 2019, 2022). We speculate that a single point-like source of CRs, such as a pulsar wind or the wind of a massive star, passes through and injects CRs into intermittent magnetic flux tubes of the CMZ. CRs escape from the source region, propagate along these flux tubes and radiate synchrotron emission. Because the source object injects CRs at different times in neighbouring flux tubes, we see the CRs populations at different evolutionary times in their expansion history. This results in a collection of synchrotron-emitting filaments which are seemingly sorted by their length. Through simulations of CR propagation with our new two-moment hydrodynamical theory along a one-dimensional idealized flux tube, we are able to match the morphology of these harp-like NTFs.

Outlook

Our results and discussions consolidate our understanding of CR transport on astrophysical scales. This progress is achieved by our new hydrodyanmical theory for CRs. We showed that this theory can be utilised to explore the effects of small-scale plasma-physical processes in astrophysical contexts. We focused on the self-confinement picture where CRs excite gyroresonant Alfvén waves which in turn scatter CRs through the Lorentz-force. This process is one amongst many that have been proposed to influence the propagation of CRs. Effects such as the intermediate-scale instability (Shalaby et al., 2021), the resonant dust-streaming instability (Squire et al., 2021), external confinement through magnetic turbulence (Yan and Lazarian, 2002; Sampson et al., 2022), interaction of gyroresonantly-generated Alfén waves with the MHD cascade (Farmer and Goldreich, 2004), or their damping through ion-neutral collisions (Zweibel, 2017; Plotnikov et al., 2021) are beyond the scope of this thesis and left for future work.

Beside these micro-physical processes that influence the transport of CRs, investigating the effects of CRs on different environments is valuable. For example: the influence of CRs on the gas dynamics of the ISM is investigated using the one-moment description for CR hydrodynamics by various research groups (c.f. Girichidis et al., 2016; Simpson et al., 2016b; Farber et al., 2017; Simpson et al., 2022) which show that CRs can fundamentally change the outflow properties inside ISM tallbox simulations. These simulations focus on CR diffusion process and neglect CR streaming. Recent post-processing analyses of TIGRESS simulations by Armillotta et al. (2021) and Armillotta et al. (2022) using the two-moment transport description of Jiang

and Oh (2018) demonstrate that CR transport properties differ between the different phases of the ISM and show that ion-neutral damping dominates the energy balance of Alfvén waves at high densities. It would be worthwhile to combine approaches and investigate the impact and transport of CRs in the ISM using the two moment approximation in live tallbox simulations. Recent advancements in the context of high-resolution global-disk simulation of the ISM of dwarf galaxies (Hu et al., 2017; Gutcke et al., 2021) would also allow for such CR-focused investigations inside individual galaxies.

Directly observing CRs is a challening endeavour because there is not an archetypal CR but a population of CRs with energies ranging from MeV to PeV, which implies a range of very distinct physical processes involved that lead to their observational traces. For example, emission from high-energy (GeV to TeV) CRs is accessible by current or upcoming observatories such as Fermi, HESS, MAGIC, VERITAS, and CTA. To interpret gamma-ray observations, understanding the underlying dynamics of the TeV CR subpopulation is crucial. Conversely, the population and transport of MeV CRs can be constrained by observing the chemical composition of nearby giant molecular clouds (GMCs, Padovani et al., 2009). Collisions between MeV CRs and neutrals (atoms and molecules likewise) are a major contributor to the residual ionization inside GMCs and are an important ingredient to understand observations of GMC. Whilst most modern CR hydrodynamical theories aim to understand the dynamics of GeV CRs due to their dominating contribution to the overall CR energy budget, MeV and TeV CR dynamics are currently modelled in galaxy simulations only crudely or not at all (with the exceptions of the works by Girichidis et al. 2022; Hopkins et al. 2022).

In order to leverage the advantages of the two-moment description for transport and to fulfill the desire for a better modelling of high- and low-energy CRs at the same time, the presented grey two-moment approximation for CRs transport needs to be expanded towards a spectrally resolved approximation similar to the one of Hopkins et al. (2021d). This allows for a resolved transport of CRs at different energies and consequently for an in situ modelling of high-energy CR emission and CR-ISM interaction of low-energy CRs.

The Future of Blinc

In addition to these CR related topics, we presented the finite-volume block-structured AMR-code Blinc which is based on a graph-based representation of the patches that form the numerical mesh. It features finite volume solvers for the equations of radiation hydrodynamics with the M1 closure and magnetohydrodynamics. We test these solvers and verify their accuracy

with various standard test problems. While we show that the mesh framework and the associated diffusive load balancer are mature enough to enable simulations in a parallel computing environment, the scalability properties of BLINC are left unexplored. The modularity of the code allows us to easily expand it, include new physics modules, or conduct simulations of new astrophysical scenarios. This ease-of-use enables us to leverage blinc as a testing ground for new numerical schemes and to quickly check ideas concering numerical methods or astrophysical problems. We are currently working on adapting the fast-multipole method (FMM) for gravity which requires a tree representation of the mass contained in the simulation. A working prototype uses the integer coordinates of mesh patches to cost-efficiently construct a tree on-the-fly from the mesh graph which can be utilised for the FMM.

Commented Publication List

Here, I list all my publications. For publications that are part of this thesis, I state my and the contributions of my co-authors. In addition, I summarize the contents of publications that are not part of this thesis.

Publications presented in this thesis

- Cosmic-ray hydrodynamics: Alfvén-wave regulated transport of cosmic rays
  Timon Thomas; Christoph Pfrommer – 2019
  Monthly Notices of the Royal Astronomical Society, Volume 485, Issue 3, p.2977-3008

  Parts of this work have been presented in my master thesis. Following suggestions from the scientific community and referees, we significantly modified the original manuscript and improved the results after publication of the master thesis. Among other improvements, we have added multiple appendices where we provide a covariant derivation of the scattering terms and extended our discussion on aspects of the comoving transport. Furthermore, momentum conservation properties of the coupling between Alfvén waves, CR, and thermal particles were improved by separately considering forces that act parallel and perpendicular to the mean magnetic field. As a result, the manuscript increased in length from 24 to 34 journal pages — the exact changes to the scientific content can be seen by comparing v1 and v3 of https://arxiv.org/abs/1805.11092v3.

  I derived the equations, conducted the simulations, created the figures, and prepared the manuscript. CP helped to conceptualize the manuscript and assisted with the derivations and preparation of the manuscript. Both contributed to the discussion and the interpretation.

- Probing Cosmic-Ray Transport with Radio Synchrotron Harps in the Galactic Center
  Timon Thomas; Christoph Pfrommer; Thorsten Enßlin – 2020
  The Astrophysical Journal Letters, Volume 890, Issue 2, id.L18, 6 pp. (2020)

  I conducted the simulations, created the figures, and prepared the manuscript. CP helped to conceptualize the manuscript. CP and TE suggested this work and assisted in the preparation of the manuscript. All contributed to the discussion and the interpretation.

- A finite volume method for two-moment cosmic ray hydrodynamics on a moving mesh
  Timon Thomas; Christoph Pfrommer; Rüdiger Pakmor – 2021
  Monthly Notices of the Royal Astronomical Society, Volume 503, Issue 2, pp.2242-2264

  I developed the numerical scheme for two-moment CR transport that is built on top of the scheme of Pfrommer et al. (2017a) for one-moment CR transport developed by CP and RP, derived analytic solutions and dispersion relations, conducted the simulations, created the figures, and prepared the manuscript. CP helped to conceptualize the manuscript. All contributed to the discussion and the interpretation.

- Comparing different closure relations for cosmic ray hydrodynamics
  Timon Thomas; Christoph Pfrommer – 2021
  Monthly Notices of the Royal Astronomical Society, Volume 509, Issue 4, pp.4803-4816

  I proposed the general idea of this paper, derived the high-order CR transport models, developed the numerical schemes, conducted the simulations, created the figures, and prepared the manuscript. CP assisted during the conceptualization phase of this paper and with the preparation of this manuscript. Both contributed to the discussion and the interpretation.

- Cosmic ray-driven galactic winds: transport modes of cosmic rays and Alfvén-wave dark regions
  Timon Thomas; Christoph Pfrommer; Rüdiger Pakmor
  arXiv:2203.12029 – submitted to the Monthly Notices of the Royal Astronomical Society

  I conducted the simulation, performed the post-processing, created the figures, and prepared the manuscript. CP and RP assisted during the conceptualization phase of this paper and with the preparation of this manuscript. CP and RP provided the initial conditions for the simulations and the general simulation setup which I adapted to perform simulations with the presented theory for CR hydrodynamics. All contributed to the discussion and the interpretation.

Publications outside this work conducted during my doctoral studies

- A New Cosmic-Ray-driven Instability
  Mohamad Shalaby; **Timon Thomas**; Christoph Pfrommer – 2021
  The Astrophysical Journal, Volume 908, Issue 2, id.206, 17 pp.

  We investigate a new gyroresonant process of CRs – the intermediate scale instability – by analysing plasma dispersion relations and conducting particle-in-cell simulations using the SHARP code.

- Whistler-regulated Magnetohydrodynamics: Transport Equations for Electron Thermal Conduction in the High-β Intracluster Medium of Galaxy Clusters
  Drake, J. F.; Pfrommer, C.; Reynolds, C. S.; Ruszkowski, M.; Swisdak, M.; Einarsson, A.; **Timon Thomas** ; Hassam, A. B.; Roberg-Clark, G. T. – 2021
  The Astrophysical Journal, Volume 923, Issue 2, id.245, 19 pp.

  A derivation for a new fluid theory for thermal conduction mediated by Whistler-waves is given in this paper. I joined the collaboration after the first version of the manuscript was submitted to ApJ and contributed by deriving an improved version of the Whistler-wave-energy transport equation.

- The mechanism of efficient electron acceleration at parallel non-relativistic shocks
  Mohamad Shalaby; Rouven Lemmerz; **Timon Thomas**; Christoph Pfrommer
  arXiv:2202.05288 – accepeted by The Astrophysical Journal

  Through particle-in-cell simulations of parallel non-relativistic shocks, we show that the intermediate scale instability can provide additional scattering of electrons. This allows them to participate in the diffusive shock acceleration process and enables them to reach high energies.

- Comparing energy and entropy formulations for cosmic ray hydrodynamics
  Matthias Weber; **Timon Thomas**; Christoph Pfrommer
  arXiv:2205.12288 – submitted to the Monthly Notices of the Royal Astronomical Society

  In this work, we investigate the differences between numerical solvers for the one-moment description of CR transport that are based either on the CR energy or on the CR entropy. We find that both approaches give in similar results. The energy-based method proves to more stable while the entropy-based method is more accurate if it is stable.

Publications outside this work conducted during my bachelor/master studies

- Radiative waves in stellar winds with line scattering
  Timon Thomas ; Achim Feldmeier – 2016
  Monthly Notices of the Royal Astronomical Society, Volume 460, Issue 2, p.1923-1933

  We investigate the dispersion relation and the (in-) stability of waves driven by the line-force inside the winds of massive stars. This works expands the discussion of Owocki and Rybicki (1986) to include scattered line-radiation. My bachelor thesis is based on this work.

- Non-linear growth of the line-driving instability
  Achim Feldmeier; **Timon Thomas** – 2017
  Monthly Notices of the Royal Astronomical Society, Volume 469, Issue 3, p.3102-3107

  This paper continues the work of the previous publication. We analyse the non-linear stage of the line-driven instability inside the winds of massive stars and investigate the detailed mechanism that forms clumps inside these winds.

Bibliography

Achterberg, A. (1981a). On the propagation of relativistic particles in a high beta plasma. A&A, 98:161–172.

Achterberg, A. (1981b). The ponderomotive force due to cosmic ray generated Alfven waves. A&A, 98(1):195–197.

Amato, E. and Blasi, P. (2006). Non-linear particle acceleration at non-relativistic shock waves in the presence of self-generated turbulence. MNRAS, 371:1251–1258.

Armillotta, L., Ostriker, E. C., and Jiang, Y.-F. (2021). Cosmic-Ray Transport in Simulations of Star-forming Galactic Disks. ApJ, 922(1):11.

Armillotta, L., Ostriker, E. C., and Jiang, Y.-F. (2022). Cosmic-Ray Transport in Varying Galactic Environments. ApJ, 929(2):170.

Aubert, D. and Teyssier, R. (2008). A radiative transfer scheme for cosmological reionization based on a local Eddington tensor. MNRAS, 387(1):295–307.

Axford, W. I., Leer, E., and Skadron, G. (1977). The Acceleration of Cosmic Rays by Shock Waves. In *International Cosmic Ray Conference*, volume 11 of *International Cosmic Ray Conference*, page 132.

Bai, X.-N., Ostriker, E. C., Plotnikov, I., and Stone, J. M. (2019). Magnetohydrodynamic Particle-in-cell Simulations of the Cosmic-Ray Streaming Instability: Linear Growth and Quasi-linear Evolution. ApJ, 876(1):60.

Balsara, D. S. (2004). Second-Order-accurate Schemes for Magnetohydrodynamics with Divergence-free Reconstruction. ApJS, 151(1):149–184.

Balsara, D. S. and Spicer, D. S. (1999). A Staggered Mesh Algorithm Using High Order Godunov Fluxes to Ensure Solenoidal Magnetic Fields in Magnetohydrodynamic Simulations. *Journal of Computational Physics*, 149(2):270–292.

Barkov, M. V. and Lyutikov, M. (2019). On the nature of radio filaments near the Galactic Centre. MNRAS, 489(1):L28–L31.

Barkov, M. V., Lyutikov, M., and Khangulyan, D. (2019). 3D dynamics and morphology of bow-shock pulsar wind nebulae. MNRAS, 484(4):4760–4784.

Bartels, R., Krishnamurthy, S., and Weniger, C. (2016). Strong Support for the Millisecond Pulsar Origin of the Galactic Center GeV Excess. Phys. Rev. Lett., 116(5):051102.

Bell, A. R. (1978). The acceleration of cosmic rays in shock fronts - I. MNRAS, 182:147–156.

Bell, A. R. (2004). Turbulent amplification of magnetic field and diffusive shock acceleration of cosmic rays. MNRAS, 353:550–558.

Benaglia, P., Romero, G. E., Martí, J., Peri, C. S., and Araudo, A. T. (2010). Detection of nonthermal emission from the bow shock of a massive runaway star. A&A, 517:L10.

Beresnyak, A. and Lazarian, A. (2015). MHD Turbulence, Turbulent Dynamo and Applications. In Lazarian, A., de Gouveia Dal Pino, E. M., and Melioli, C., editors, *Magnetic Fields in Diffuse Media*, volume 407 of *Astrophysics and Space Science Library*, page 163.

Berger, M. J. and Colella, P. (1989). Local adaptive mesh refinement for shock hydrodynamics. *Journal of computational Physics*, 82(1):64–84.

Berger, M. J. and Oliger, J. (1984). Adaptive Mesh Refinement for Hyperbolic Partial Differential Equations. *Journal of Computational Physics*, 53(3):484–512.

Berthon, C., Charrier, P., and Dubroca, B. (2007). An hllc scheme to solve the m1 model of radiative transfer in two space dimensions. *Journal of Scientific Computing*, 31:347–389.

Bicknell, G. V. and Li, J. (2001). The Snake: A Reconnecting Coil in a Twisted Magnetic Flux Tube. ApJ, 548(1):L69–L72.

Blandford, R. and Eichler, D. (1987). Particle acceleration at astrophysical shocks: A theory of cosmic ray origin. Phys. Rep., 154(1):1–75.

Blasi, P. and Amato, E. (2012). Diffusive propagation of cosmic rays from supernova remnants in the Galaxy. I: spectrum and chemical composition. J. Cosmology Astropart. Phys., 1:010.

Blasi, P., Amato, E., and Serpico, P. D. (2012). Spectral Breaks as a Signature of Cosmic Ray Induced Turbulence in the Galaxy. Phys. Rev. Lett., 109(6):061101.

Boldyrev, S. and Yusef-Zadeh, F. (2006). Turbulent Origin of the Galactic Center Magnetic Field: Nonthermal Radio Filaments. ApJ, 637(2):L101–L104.

Booth, C. M., Agertz, O., Kravtsov, A. V., and Gnedin, N. Y. (2013). Simulations of Disk Galaxies with Cosmic Ray Driven Galactic Winds. ApJ, 777:L16.

Bordner, J. and Norman, M. L. (2018). Computational Cosmology and Astrophysics on Adaptive Meshes using Charm++. *arXiv e-prints*, page arXiv:1810.01319.

Boris, J. P. (1970). A physically motivated solution of the alfven problem. *Techincal Report NRL Memorandum Report 2167*, page 14.

Boulares, A. and Cox, D. P. (1990). Galactic Hydrostatic Equilibrium with Magnetic Tension and Cosmic-Ray Diffusion. ApJ, 365:544.

Breitschwerdt, D., Dogiel, V. A., and Völk, H. J. (2002). The gradient of diffuse gamma -ray emission in the Galaxy. A&A, 385:216–238.

Breitschwerdt, D., McKenzie, J. F., and Voelk, H. J. (1991). Galactic winds. I. Cosmic ray and wave-driven winds from the galaxy. A&A, 245:79.

Brunetti, G. and Lazarian, A. (2011). Acceleration of primary and secondary particles in galaxy clusters by compressible MHD turbulence: from radio haloes to gamma-rays. MNRAS, 410:127–142.

Bryan, G. L., Norman, M. L., O'Shea, B. W., Abel, T., Wise, J. H., Turk, M. J., Reynolds, D. R., Collins, D. C., Wang, P., Skillman, S. W., Smith, B., Harkness, R. P., Bordner, J., Kim, J.-h., Kuhlen, M., Xu, H., Goldbaum, N., Hummels, C., Kritsuk, A. G., Tasker, E., Skory, S., Simpson, C. M., Hahn, O., Oishi, J. S., So, G. C., Zhao, F., Cen, R., Li, Y., and Enzo Collaboration (2014). ENZO: An Adaptive Mesh Refinement Code for Astrophysics. ApJS, 211(2):19.

Buchler, J. R. (1979). Radiation hydrodynamics in the fluid frame. J. Quant. Spec. Radiat. Transf., 22:293–300.

Buck, T., Pfrommer, C., Pakmor, R., Grand, R. J. J., and Springel, V. (2020). The effects of cosmic rays on the formation of Milky Way-mass galaxies in a cosmological context. MNRAS, 497(2):1712–1737.

Burstedde, C., Wilcox, L. C., and Ghattas, O. (2011). `p4est`: Scalable algorithms for parallel adaptive mesh refinement on forests of octrees. *SIAM Journal on Scientific Computing*, 33(3):1103–1133.

Bustard, C., Zweibel, E. G., D'Onghia, E., Gallagher, J. S., I., and Farber, R. (2020). Cosmic-Ray-driven Outflows from the Large Magellanic Cloud: Contributions to the LMC Filament. ApJ, 893(1):29.

Butsky, I. S. and Quinn, T. R. (2018). The Role of Cosmic-ray Transport in Shaping the Simulated Circumgalactic Medium. ApJ, 868(2):108.

Butsky, I. S., Werk, J. K., Tchernyshyov, K., Fielding, D. B., Breneman, J., Piacitelli, D., Quinn, T. R., Sanchez, N. N., Cruz, A., Hummels, C. B., Burchett, J. N., and Tremmel, M. (2021). The Impact of Cosmic Rays on the Kinematics of the Circumgalactic Medium. *arXiv e-prints*, page arXiv:2106.14889.

Bykov, A. M., Amato, E., Petrov, A. E., Krassilchtchikov, A. M., and Levenfish, K. P. (2017). Pulsar Wind Nebulae with Bow Shocks: Non-thermal Radiation and Cosmic Ray Leptons. Space Sci. Rev., 207(1-4):235–290.

Capdeville, G. (2008). A central weno scheme for solving hyperbolic conservation laws on non-uniform meshes. *Journal of Computational Physics*, 227(5):2977–3014.

Caprioli, D. and Spitkovsky, A. (2013). Cosmic-ray-induced filamentation instability in collisionless shocks. *The Astrophysical Journal Letters*, 765(1):L20.

Caprioli, D. and Spitkovsky, A. (2014). Simulations of Ion Acceleration at Non-relativistic Shocks. I. Acceleration Efficiency. ApJ, 783(2):91.

Castor, J. I. (2007). *Radiation Hydrodynamics*. Cambridge, UK: Cambridge University Press.

Chabrier, G. (2001). The Galactic Disk Mass Budget. I. Stellar Mass Function and Density. ApJ, 554(2):1274–1281.

Chan, T. K., Kereš, D., Hopkins, P. F., Quataert, E., Su, K. Y., Hayward, C. C., and Faucher-Giguère, C. A. (2019). Cosmic ray feedback in the FIRE simulations: constraining cosmic ray propagation with GeV γ-ray emission. MNRAS, 488(3):3716–3744.

Chan, T. K., Theuns, T., Bower, R., and Frenk, C. (2021). Smoothed particle radiation hydrodynamics: two-moment method with local Eddington tensor closure. MNRAS, 505(4):5784–5814.

Chew, G. F., Goldberger, M. L., and Low, F. E. (1956). The Boltzmann Equation and the One-Fluid Hydromagnetic Equations in the Absence of Particle Collisions. *Proceedings of the Royal Society of London Series A*, 236(1204):112–118.

Cioffi, D. F., McKee, C. F., and Bertschinger, E. (1988). Dynamics of Radiative Supernova Remnants. ApJ, 334:252.

Colella, P. and Sekora, M. D. (2008). A limiter for PPM that preserves accuracy at smooth extrema. *Journal of Computational Physics*, 227(15):7069–7076.

Colella, P. and Woodward, P. R. (1984). The piecewise parabolic method (ppm) for gas-dynamical simulations. *Journal of Computational Physics*, 54(1):174–201.

Cox, D. P. (2005). The Three-Phase Interstellar Medium Revisited. ARA&A, 43(1):337–385.

Cravero, I., Puppo, G., Semplice, M., and Visconti, G. (2018). Cweno: uniformly accurate reconstructions for balance laws. *Mathematics of Computation*, 87(312):1689–1719.

Dahlburg, R. B., Einaudi, G., LaRosa, T. N., and Shore, S. N. (2002). Modeling the Galactic Center Nonthermal Filaments as Magnetized Wakes. ApJ, 568(1):220–225.

Dai, W. and Woodward, P. R. (1998). A simple finite difference scheme for multidimensional magnetohydrodynamical equations. *Journal of Computational Physics*, 142(2):331–369.

Dal Maso, G., LeFloch, P. G., and Murat, F. (1995). Definition and weak stability of nonconservative products. *Journal de mathématiques pures et appliquées*, 74(6):483–548.

Dalgarno, A. (2006). Interstellar Chemistry Special Feature: The galactic cosmic ray ionization rate. *Proceedings of the National Academy of Science*, 103:12269–12273.

Dashyan, G. and Dubois, Y. (2020). Cosmic ray feedback from supernovae in dwarf galaxies. A&A, 638:A123.

Davis, S. (1988). Simplified second-order godunov-type methods. *SIAM Journal on Scientific and Statistical Computing*, 9(3):445–473.

de Avillez, M. A. and Breitschwerdt, D. (2005). Global dynamical evolution of the ISM in star forming galaxies. I. High resolution 3D simulations: Effect of the magnetic field. A&A, 436(2):585–600.

del Valle, M. V. and Pohl, M. (2018). Nonthermal Emission from Stellar Bow Shocks. ApJ, 864(1):19.

Dewar, R. L. (1970). Interaction between Hydromagnetic Waves and a Time-Dependent, Inhomogeneous Medium. *Physics of Fluids*, 13:2710–2720.

Díaz, M. J. C., Kurganov, A., and de Luna, T. M. (2019). Path-conservative central-upwind schemes for nonconservative hyperbolic systems. *ESAIM: Mathematical Modelling and Numerical Analysis*, 53(3):959–985.

Dorfi, E. A. and Breitschwerdt, D. (2012). Time-dependent galactic winds. I. Structure and evolution of galactic outflows accompanied by cosmic ray acceleration. A&A, 540:A77.

Drury, L. O. and Falle, S. A. E. G. (1986). On the Stability of Shocks Modified by Particle Acceleration. MNRAS, 223:353.

Drury, L. O. and Völk, J. H. (1981). Hydromagnetic shock structure in the presence of cosmic rays. ApJ, 248:344–351.

Dubois, Y., Commerçon, B., Marcowith, A., and Brahimi, L. (2019). Shock-accelerated cosmic rays and streaming instability in the adaptive mesh refinement code Ramses. A&A, 631:A121.

Dumbser, M. and Balsara, D. S. (2016). A new efficient formulation of the hllem riemann solver for general conservative and non-conservative hyperbolic systems. *J. Comput. Phys.*, 304(C):275–319.

Dumbser, M. and Toro, E. F. (2011). On universal osher-type schemes for general nonlinear hyperbolic conservation laws. *Communications in Computational Physics*, 10(3):635–671.

Dung, R. and Schlickeiser, R. (1990). The influence of the Alfvenic cross and magnetic helicity on the cosmic ray transport equation. I - Isospectral slab turbulence. A&A, 240:537–540.

Dursi, L. J. and Pfrommer, C. (2008). Draping of Cluster Magnetic Fields over Bullets and Bubbles—Morphology and Dynamic Effects. ApJ, 677(2):993–1018.

Earl, J. A. (1973). Diffusion of Charged Particles in a Random Magnetic Field. ApJ, 180:227–238.

Ehlert, K., Weinberger, R., Pfrommer, C., Pakmor, R., and Springel, V. (2018). Simulations of the dynamics of magnetized jets and cosmic rays in galaxy clusters. MNRAS, 481(3):2878–2900.

Einfeldt, B. (1988). On Godunov-Type Methods for Gas Dynamics. *SIAM Journal on Numerical Analysis*, 25:294–318.

Enßlin, T., Pfrommer, C., Miniati, F., and Subramanian, K. (2011). Cosmic ray transport in galaxy clusters: implications for radio halos, gamma-ray signatures, and cool core heating. A&A, 527:A99.

Enßlin, T. A., Pfrommer, C., Springel, V., and Jubelgas, M. (2007). Cosmic ray physics in calculations of cosmological structure formation. A&A, 473(1):41–57.

Evans, C. R. and Hawley, J. F. (1988). Simulation of Magnetohydrodynamic Flows: A Constrained Transport Model. ApJ, 332:659.

Everett, J. E., Zweibel, E. G., Benjamin, R. A., McCammon, D., Rocks, L., and Gallagher, John S., I. (2008). The Milky Way's Kiloparsec-Scale Wind: A Hybrid Cosmic-Ray and Thermally Driven Outflow. ApJ, 674(1):258–270.

Everett, J. E., Zweibel, E. G., Benjamin, R. A., McCammon, D., Rocks, L., and Gallagher III, J. S. (2008). The Milky Way's Kiloparsec-Scale Wind: A Hybrid Cosmic-Ray and Thermally Driven Outflow. ApJ, 674(1):258–270.

Evoli, C., Gaggero, D., Grasso, D., and Maccione, L. (2008). Cosmic ray nuclei, antiprotons and gamma rays in the galaxy: a new diffusion model. J. Cosmology Astropart. Phys., 2008(10):018.

Falle, S. A. E. G. (1991). Self-similar jets. MNRAS, 250:581–596.

Farber, R., Ruszkowski, M., Yang, H.-Y. K., and Zweibel, E. G. (2017). Impact of Cosmic Ray Transport on Galactic Winds. *ArXiv e-prints*.

Farber, R., Ruszkowski, M., Yang, H. Y. K., and Zweibel, E. G. (2018). Impact of Cosmic-Ray Transport on Galactic Winds. ApJ, 856(2):112.

Farber, R. J., Ruszkowski, M., Tonnesen, S., and Holguin, F. (2022). Stress-testing cosmic ray physics: the impact of cosmic rays on the surviving disc of ram-pressure-stripped galaxies. MNRAS, 512(4):5927–5941.

Farcy, M., Rosdahl, J., Dubois, Y., Blaizot, J., and Martin-Alvarez, S. (2022). Radiation-MagnetoHydrodynamics simulations of cosmic ray feedback in disc galaxies. *arXiv e-prints*, page arXiv:2202.01245.

Farmer, A. J. and Goldreich, P. (2004). Wave Damping by Magnetohydrodynamic Turbulence and Its Effect on Cosmic-Ray Propagation in the Interstellar Medium. ApJ, 604:671–674.

Fermi, E. (1949). On the Origin of the Cosmic Radiation. *Physical Review*, 75:1169–1174.

Fermi-LAT Collaboration (2017). Characterizing the population of pulsars in the inner Galaxy with the Fermi Large Area Telescope. *arXiv e-prints*, page arXiv:1705.00009.

Forman, M. A., Jokipii, J. R., and Owens, A. J. (1974). Cosmic-Ray Streaming Perpendicular to the Mean Magnetic Field. ApJ, 192:535–540.

Fromang, S., Hennebelle, P., and Teyssier, R. (2006). A high order Godunov scheme with constrained transport and adaptive mesh refinement for astrophysical magnetohydrodynamics. A&A, 457(2):371–384.

Fujita, Y. and Ohira, Y. (2012). Non-thermal Emissions from Cool Cores Heated by Cosmic Rays in Galaxy Clusters. ApJ, 746:53.

Fuksman, J. D. and Mignone, A. (2019). A Radiative Transfer Module for Relativistic Magnetohydrodynamics in the PLUTO Code. ApJS, 242(2):20.

Fukushima, H. and Yajima, H. (2021). Radiation hydrodynamics simulations of massive star cluster formation in giant molecular clouds. MNRAS, 506(4):5512–5539.

Gabici, S. (2009). Gamma ray astronomy and the origin of galactic cosmic rays. In Király, P., Kudela, K., Stehlík, M., and Wolfendale, A. W., editors, *21st European Cosmic Ray Symposium*, pages 66–77.

Gardiner, T. A. and Stone, J. M. (2005). An unsplit Godunov method for ideal MHD via constrained transport. *Journal of Computational Physics*, 205(2):509–539.

Gardiner, T. A. and Stone, J. M. (2008). An unsplit Godunov method for ideal MHD via constrained transport in three dimensions. *Journal of Computational Physics*, 227(8):4123–4141.

Girichidis, P., Naab, T., Hanasz, M., and Walch, S. (2018). Cooler and smoother - the impact of cosmic rays on the phase structure of galactic outflows. MNRAS, 479(3):3042–3067.

Girichidis, P., Naab, T., Walch, S., and Hanasz, M. (2014). Anisotropic transport and early dynamical impact of Cosmic Rays around Supernova remnants. *arXiv e-prints*, page arXiv:1406.4861.

Girichidis, P., Naab, T., Walch, S., Hanasz, M., Mac Low, M.-M., Ostriker, J. P., Gatto, A., Peters, T., Wünsch, R., Glover, S. C. O., Klessen, R. S., Clark, P. C., and Baczynski, C. (2016). Launching Cosmic-Ray-driven Outflows from the Magnetized Interstellar Medium. ApJ, 816(2):L19.

Girichidis, P., Pfrommer, C., Hanasz, M., and Naab, T. (2020). Spectrally resolved cosmic ray hydrodynamics - I. Spectral scheme. MNRAS, 491(1):993–1007.

Girichidis, P., Pfrommer, C., Pakmor, R., and Springel, V. (2022). Spectrally resolved cosmic rays - II. Momentum-dependent cosmic ray diffusion drives powerful galactic winds. MNRAS, 510(3):3917–3938.

Gittings, M., Weaver, R., Clover, M., Betlach, T., Byrne, N., Coker, R., Dendy, E., Hueckstaedt, R., New, K., Oakes, W. R., Ranta, D., and Stefan, R. (2008). The RAGE radiation-hydrodynamic code. *Computational Science and Discovery*, 1(1):015005.

Gnedin, N. Y. (2016). On the Proper Use of the Reduced Speed of Light Approximation. ApJ, 833(1):66.

Goldreich, P. and Sridhar, S. (1995). Toward a theory of interstellar turbulence. 2: Strong alfvenic turbulence. ApJ, 438:763–775.

Gombosi, T. I., Tóth, G., De Zeeuw, D. L., Hansen, K. C., Kabin, K., and Powell, K. G. (2002). Semirelativistic Magnetohydrodynamics and Physics-Based Convergence Acceleration. *Journal of Computational Physics*, 177:176–205.

González, M., Audit, E., and Huynh, P. (2007). HERACLES: a three-dimensional radiation hydrodynamics code. A&A, 464(2):429–435.

Gottlieb, S., Shu, C.-W., and Tadmor, E. (2001). Strong stability-preserving high-order time discretization methods. *SIAM Review*, 43(1):89–112.

Gronke, M. and Oh, S. P. (2018). The growth and entrainment of cold gas in a hot wind. MNRAS, 480(1):L111–L115.

Guo, F. and Oh, S. P. (2008). Feedback heating by cosmic rays in clusters of galaxies. MNRAS, 384:251–266.

Gutcke, T. A., Pakmor, R., Naab, T., and Springel, V. (2021). LYRA - I. Simulating the multiphase ISM of a dwarf galaxy with variable energy supernovae from individual stars. MNRAS, 501(4):5597–5615.

Haggerty, C. C. and Caprioli, D. (2019). dHybridR: A Hybrid Particle-in-cell Code Including Relativistic Ion Dynamics. ApJ, 887(2):165.

Hanasz, M., Kowal, G., Otmianowska-Mazur, K., and Lesch, H. (2004). Amplification of Galactic Magnetic Fields by the Cosmic-Ray-driven Dynamo. ApJ, 605:L33–L36.

Hanasz, M. and Lesch, H. (2003). Incorporation of cosmic ray transport into the ZEUS MHD code. Application for studies of Parker instability in the ISM. A&A, 412:331–339.

Hanasz, M., Lesch, H., Naab, T., Gawryszczak, A., Kowalik, K., and Wóltański, D. (2013). Cosmic Rays Can Drive Strong Outflows from Gas-rich High-redshift Disk Galaxies. ApJ, 777(2):L38.

Hanasz, M., Strong, A. W., and Girichidis, P. (2021). Simulations of cosmic ray propagation. *Living Reviews in Computational Astrophysics*, 7(1):2.

Hanawa, T. and Audit, E. (2014). Reformulation of the m1 model of radiative transfer. *Journal of Quantitative Spectroscopy and Radiative Transfer*, 145:9–16.

Harten, A., Lax, P. D., and Leer, B. v. (1983). On upstream differencing and godunov-type schemes for hyperbolic conservation laws. *SIAM Review*, 25(1):35–61.

Hayes, J. C. and Norman, M. L. (2003). Beyond Flux-limited Diffusion: Parallel Algorithms for Multidimensional Radiation Hydrodynamics. ApJS, 147(1):197–220.

Heckman, T. M. and Thompson, T. A. (2017). *Galactic Winds and the Role Played by Massive Stars*, page 2431. Springer International Publishing.

Helzel, C., Rossmanith, J. A., and Taetz, B. (2011). An unstaggered constrained transport method for the 3D ideal magnetohydrodynamic equations. *Journal of Computational Physics*, 230(10):3803–3829.

Heywood, I. et al. (2019). Inflation of 430-parsec bipolar radio bubbles in the Galactic Centre by an energetic event. Nature, 573(7773):235–237.

Heywood, I. et al. (2022). The 1.28 GHz MeerKAT Galactic Center Mosaic. ApJ, 925(2):165.

Holcomb, C. and Spitkovsky, A. (2019). On the Growth and Saturation of the Gyroresonant Streaming Instabilities. ApJ, 882(1):3.

Hopkins, P. F., Butsky, I. S., Panopoulou, G. V., Ji, S., Quataert, E., Faucher-Giguere, C.-A., and Keres, D. (2021a). First Predicted Cosmic Ray Spectra, Primary-to-Secondary Ratios, and Ionization Rates from MHD Galaxy Formation Simulations. *arXiv e-prints*, page arXiv:2109.09762.

Hopkins, P. F., Chan, T. K., Garrison-Kimmel, S., Ji, S., Su, K.-Y., Hummels, C. B., Kereš, D., Quataert, E., and Faucher-Giguère, C.-A. (2020). But what about...: cosmic rays, magnetic fields, conduction, and viscosity in galaxy formation. MNRAS, 492(3):3465–3498.

Hopkins, P. F., Chan, T. K., Squire, J., Quataert, E., Ji, S., Kereš, D., and Faucher-Giguère, C.-A. (2021b). Effects of different cosmic ray transport models on galaxy formation. MNRAS, 501(3):3663–3669.

Hopkins, P. F., Squire, J., and Butsky, I. S. (2021c). A Consistent Reduced-Speed-of-Light Formulation of Cosmic Ray Transport Valid in Weak and Strong-Scattering Regimes. *arXiv e-prints*, page arXiv:2103.10443.

Hopkins, P. F., Squire, J., and Butsky, I. S. (2022). A consistent reduced-speed-of-light formulation of cosmic ray transport valid in weak- and strong-scattering regimes. MNRAS, 509(3):3779–3797.

Hopkins, P. F., Squire, J., Butsky, I. S., and Ji, S. (2021d). Standard Self-Confinement and Extrinsic Turbulence Models for Cosmic Ray Transport are Fundamentally Incompatible with Observations. *arXiv e-prints*, page arXiv:2112.02153.

Hu, C.-Y., Naab, T., Glover, S. C. O., Walch, S., and Clark, P. C. (2017). Variable interstellar radiation fields in simulated dwarf galaxies: supernovae versus photoelectric heating. MNRAS, 471(2):2151–2173.

Huang, X. and Davis, S. W. (2022). The launching of cosmic ray-driven outflows. MNRAS, 511(4):5125–5141.

Hummels, C. B., Smith, B. D., Hopkins, P. F., O'Shea, B. W., Silvia, D. W., Werk, J. K., Lehner, N., Wise, J. H., Collins, D. C., and Butsky, I. S. (2019). The Impact of Enhanced Halo Resolution on the Simulated Circumgalactic Medium. ApJ, 882(2):156.

Ichimaru, S. (1973). *Basic principles of plasma physics, a statistical approach.* CRC Press.

Ipavich, F. M. (1975). Galactic winds driven by cosmic rays. ApJ, 196:107–120.

Isaac, T., Burstedde, C., and Ghattas, O. (2012). Low-cost parallel algorithms for 2: 1 octree balance. In *2012 IEEE 26th International Parallel and Distributed Processing Symposium*, pages 426–437. IEEE.

Ivlev, A. V., Dogiel, V. A., Chernyshov, D. O., Caselli, P., Ko, C.-M., and Cheng, K. S. (2018). Penetration of Cosmic Rays into Dense Molecular Clouds: Role of Diffuse Envelopes. ApJ, 855:23.

Jacob, S., Pakmor, R., Simpson, C. M., Springel, V., and Pfrommer, C. (2018). The dependence of cosmic ray-driven galactic winds on halo mass. MNRAS, 475:570–584.

Jacob, S. and Pfrommer, C. (2017a). Cosmic ray heating in cool core clusters - I. Diversity of steady state solutions. MNRAS, 467:1449–1477.

Jacob, S. and Pfrommer, C. (2017b). Cosmic ray heating in cool core clusters - I. Diversity of steady state solutions. MNRAS, 467(2):1449–1477.

Jacob, S. and Pfrommer, C. (2017c). Cosmic ray heating in cool core clusters - II. Self-regulation cycle and non-thermal emission. MNRAS, 467:1478–1495.

Jacques, S. A. (1977). Momentum and energy transport by waves in the solar atmosphere and solar wind. ApJ, 215:942–951.

Ji, S., Kereš, D., Chan, T. K., Stern, J., Hummels, C. B., Hopkins, P. F., Quataert, E., and Faucher-Giguère, C.-A. (2021). Virial shocks are suppressed in cosmic ray-dominated galaxy haloes. MNRAS, 505(1):259–273.

Jiang, Y.-F. and Oh, S. P. (2018). A New Numerical Scheme for Cosmic-Ray Transport. ApJ, 854:5.

Jones, T. W. (1993). Alfven wave transport effects in the time evolution of parallel cosmic-ray-modified shocks. ApJ, 413:619–632.

Jubelgas, M., Springel, V., Enßlin, T., and Pfrommer, C. (2008). Cosmic ray feedback in hydrodynamical simulations of galaxy formation. A&A, 481(1):33–63.

Kannan, R., Marinacci, F., Vogelsberger, M., Sales, L. V., Torrey, P., Springel, V., and Hernquist, L. (2020). Simulating the interstellar medium of galaxies with radiative transfer, non-equilibrium thermochemistry, and dust. MNRAS, 499(4):5732–5748.

Kannan, R., Vogelsberger, M., Marinacci, F., McKinnon, R., Pakmor, R., and Springel, V. (2019). AREPO-RT: radiation hydrodynamics on a moving mesh. MNRAS, 485(1):117–149.

Kempski, P. and Quataert, E. (2021). Reconciling cosmic-ray transport theory with phenomenological models motivated by Milky-Way data. *arXiv e-prints*, page arXiv:2109.10977.

Kennicutt, Robert C., J. (1998). The Global Schmidt Law in Star-forming Galaxies. ApJ, 498(2):541–552.

Kershaw, D. S. (1976). Flux limiting nature‘s own way – a new method for numerical solution of the transport equation. *Lawrence Livermore National Lab Technical Report*.

Kim, C.-G. and Ostriker, E. C. (2015). Momentum Injection by Supernovae in the Interstellar Medium. ApJ, 802(2):99.

Kim, C.-G. and Ostriker, E. C. (2017). Three-phase Interstellar Medium in Galaxies Resolving Evolution with Star Formation and Supernova Feedback (TIGRESS): Algorithms, Fiducial Model, and Convergence. ApJ, 846(2):133.

Kimm, T. and Cen, R. (2014). Escape Fraction of Ionizing Photons during Reionization: Effects due to Supernova Feedback and Runaway OB Stars. ApJ, 788(2):121.

Klimas, A. J. and Sandri, G. (1971). Foundation of the Theory of Cosmic-Ray Transport in Random Magnetic Fields. ApJ, 169:41.

Ko, C. M. (1992). A note on the hydrodynamical description of cosmic ray propagation. A&A, 259(1):377–381.

Kroupa, P. (2001). On the variation of the initial mass function. MNRAS, 322(2):231–246.

Kulsrud, R. and Pearce, W. P. (1969). The Effect of Wave-Particle Interactions on the Propagation of Cosmic Rays. ApJ, 156:445.

Kulsrud, R. M. (2004). *Plasma Physics for Astrophysics*. Princeton University Press.

Lang, C. C., Anantharamaiah, K. R., Kassim, N. E., and Lazio, T. J. W. (1999). Discovery of a Nonthermal Galactic Center Filament (G358.85+0.47) Parallel to the Galactic Plane. ApJ, 521(1):L41–L44.

LaRosa, T. N., Lazio, T. J. W., and Kassim, N. E. (2001). A New System of Parallel Isolated Nonthermal Filaments near the Galactic Center: Evidence for a Local Magnetic Field Gradient. ApJ, 563(1):163–171.

Law, C. J., Yusef-Zadeh, F., and Cotton, W. D. (2008). A Wide-Area VLA Continuum Survey near the Galactic Center at 6 and 20 cm Wavelengths. ApJS, 177(2):515–545.

Lawder, J. and King, P. (2001). Using state diagrams for hilbert curve mappings. *International Journal of Computer Mathematics*, 78(3):327–342.

Lazarian, A. and Beresnyak, A. (2006). Cosmic ray scattering in compressible turbulence. MNRAS, 373(3):1195–1202.

Lazarian, A. and Xu, S. (2022). Damping of Alfvén waves in MHD turbulence and implications for cosmic ray streaming instability and galactic winds. *arXiv e-prints*, page arXiv:2201.05168.

Lazarian, A. and Yan, H. (2014). Superdiffusion of Cosmic Rays: Implications for Cosmic Ray Acceleration. ApJ, 784(1):38.

le Roux, J. A. and Webb, G. M. (2012). A Focused Transport Approach to the Time-dependent Shock Acceleration of Solar Energetic Particles at a Fast Traveling Shock. ApJ, 746:104.

Lebiga, O., Santos-Lima, R., and Yan, H. (2018). Kinetic-MHD simulations of gyroresonance instability driven by CR pressure anisotropy. MNRAS, 476(2):2779–2791.

Lee, M. A. and Voelk, H. J. (1975). Hydromagnetic waves and cosmic-ray diffusion theory. ApJ, 198:485–492.

Lee, M. A. and Völk, H. J. (1973). Damping and Non-Linear Wave-Particle Interactions of Alfvén-Waves in the Solar Wind. Ap&SS, 24:31–49.

Lee, S. K., Lisanti, M., Safdi, B. R., Slatyer, T. R., and Xue, W. (2016). Evidence for Unresolved γ -Ray Point Sources in the Inner Galaxy. Phys. Rev. Lett., 116(5):051103.

Lesch, H. and Reich, W. (1992). The origin of monoenergetic electrons in the arc of the Galactic Center. Particle acceleration by magnetic reconnection. A&A, 264:493–499.

LeVeque, R. J. (1992). *Numerical Methods for Conservation Laws*. Springer-Verlag Berlin Heidelberg.

Levermore, C. D. (1984). Relating Eddington factors to flux limiters. J. Quant. Spec. Radiat. Transf., 31(2):149–160.

Levy, D., Puppo, G., and Russo, G. (1999). Compact Central WENO Schemes for Multidimensional Conservation Laws. *arXiv Mathematics e-prints*, page math/9911089.

Levy, E. H. and Lunine, J. I. (1993). *Protostars and planets III*. University of Arizona Press.

Li, C., Feng, X., Xiang, C., Zhang, M., Li, H., and Wei, F. (2018). Solar Coronal Modeling by Path-conservative HLLEM Riemann Solver. ApJ, 867(1):42.

Li, M., Ostriker, J. P., Cen, R., Bryan, G. L., and Naab, T. (2015). Supernova Feedback and the Hot Gas Filling Fraction of the Interstellar Medium. ApJ, 814(1):4.

Li, S. (2005). An HLLC Riemann solver for magneto-hydrodynamics. *Journal of Computational Physics*, 203(1):344–357.

Li, Z., Hopkins, P. F., Squire, J., and Hummels, C. (2020). On the survival of cool clouds in the circumgalactic medium. MNRAS, 492(2):1841–1854.

Linden, T., Hooper, D., and Yusef-Zadeh, F. (2011). Dark Matter and Synchrotron Emission from Galactic Center Radio Filaments. ApJ, 741(2):95.

Lithwick, Y. and Goldreich, P. (2001). Compressible Magnetohydrodynamic Turbulence in Interstellar Plasmas. ApJ, 562:279–296.

Litvinenko, Y. E. and Noble, P. L. (2013). A Numerical Study of Diffusive Cosmic-Ray Transport with Adiabatic Focusing. ApJ, 765:31.

Litvinenko, Y. E. and Noble, P. L. (2016). Comparison of the telegraph and hyperdiffusion approximations in cosmic-ray transport. *Physics of Plasmas*, 23(6):062901.

Loewenstein, M., Zweibel, E. G., and Begelman, M. C. (1991). Cosmic-ray heating of cooling flows - A critical analysis. ApJ, 377:392–402.

Londrillo, P. and Del Zanna, L. (2000). High-Order Upwind Schemes for Multidimensional Magnetohydrodynamics. ApJ, 530(1):508–524.

Malkov, M. A. (2017). Exact solution of the Fokker-Planck equation for isotropic scattering. Phys. Rev. D, 95(2):023007.

Malkov, M. A. (2018). Propagating Cosmic Rays with exact Solution of Fokker-Planck Equation. *Nuclear and Particle Physics Proceedings*, 297-299:152–157.

Malkov, M. A. and Sagdeev, R. Z. (2015). Cosmic Ray Transport with Magnetic Focusing and the Telegraph Model. ApJ, 808(2):157.

Mao, S. A. and Ostriker, E. C. (2018). Galactic Disk Winds Driven by Cosmic Ray Pressure. ApJ, 854(2):89.

Martizzi, D., Faucher-Giguère, C.-A., and Quataert, E. (2015). Supernova feedback in an inhomogeneous interstellar medium. MNRAS, 450(1):504–522.

McCorquodale, P., Dorr, M. R., Hittinger, J. A. F., and Colella, P. (2015). High-order finite-volume methods for hyperbolic conservation laws on mapped multiblock grids. *Journal of Computational Physics*, 288:181–195.

McKenzie, J. F. and Bond, R. A. B. (1983). The role of non-linear Landau damping in cosmic ray shock acceleration. A&A, 123:111–117.

McKenzie, J. F. and Völk, H. J. (1982). Non-linear theory of cosmic ray shocks including self-generated Alfven waves. A&A, 116:191–200.

McKenzie, J. F. and Webb, G. M. (1984). Magnetohydrodynamic plasma instability driven by Alfvén waves excited by cosmic rays. *Journal of Plasma Physics*, 31(2):275–299.

McNamara, B. R. and Nulsen, P. E. J. (2007). Heating Hot Atmospheres with Active Galactic Nuclei. ARA&A, 45:117–175.

Meyer, C. D., Balsara, D. S., and Aslam, T. D. (2012). A second-order accurate Super TimeStepping formulation for anisotropic thermal conduction. MNRAS, 422:2102–2115.

Mignone, A. (2007). A simple and accurate Riemann solver for isothermal MHD. *Journal of Computational Physics*, 225(2):1427–1441.

Mignone, A. (2014). High-order conservative reconstruction schemes for finite volume methods in cylindrical and spherical coordinates. *Journal of Computational Physics*, 270:784–814.

Mignone, A., Bodo, G., Massaglia, S., Matsakos, T., Tesileanu, O., Zanni, C., and Ferrari, A. (2007). PLUTO: A Numerical Code for Computational Astrophysics. ApJS, 170(1):228–242.

Mignone, A. and Del Zanna, L. (2021). Systematic construction of upwind constrained transport schemes for MHD. *Journal of Computational Physics*, 424:109748.

Mignone, A., Zanni, C., Tzeferacos, P., van Straalen, B., Colella, P., and Bodo, G. (2012). The PLUTO Code for Adaptive Mesh Computations in Astrophysical Fluid Dynamics. ApJS, 198(1):7.

Mihalas, D. and Weibel Mihalas, B. (1984). *Foundations of radiation hydrodynamics*. Oxford University Press.

Miller, J. A. (1991). Magnetohydrodynamic turbulence dissipation and stochastic proton acceleration in solar flares. ApJ, 376:342–354.

Misner, C., Thorne, K., Wheeler, J., and Kaiser, D. (2017). *Gravitation*. Princeton University Press.

Miyoshi, T. and Kusano, K. (2005a). A multi-state HLL approximate Riemann solver for ideal magnetohydrodynamics. *Journal of Computational Physics*, 208(1):315–344.

Miyoshi, T. and Kusano, K. (2005b). A multi-state HLL approximate Riemann solver for ideal magnetohydrodynamics. *Journal of Computational Physics*, 208(1):315–344.

Mo, H. J., Mao, S., and White, S. D. M. (1998). The formation of galactic discs. MNRAS, 295(2):319–336.

Moe, S. A., Rossmanith, J. A., and Seal, D. C. (2015). A Simple and Effective High-Order Shock-Capturing Limiter for Discontinuous Galerkin Methods. *arXiv e-prints*, page arXiv:1507.03024.

Morlino, G. and Caprioli, D. (2012). Strong evidence for hadron acceleration in Tycho's supernova remnant. A&A, 538:A81.

Naab, T. and Ostriker, J. P. (2017). Theoretical Challenges in Galaxy Formation. ARA&A, 55(1):59–109.

Navarro, J. F., Frenk, C. S., and White, S. D. M. (1997). A Universal Density Profile from Hierarchical Clustering. ApJ, 490(2):493–508.

Nickerson, S., Teyssier, R., and Rosdahl, J. (2018). A simple model for molecular hydrogen chemistry coupled to radiation hydrodynamics. MNRAS, 479(3):3206–3226.

Nord, M. E., Lazio, T. J. W., Kassim, N. E., Hyman, S. D., LaRosa, T. N., Brogan, C. L., and Duric, N. (2004). High-Resolution, Wide-Field Imaging of the Galactic Center Region at 330 MHz. AJ, 128(4):1646–1670.

Nuñez-Castiñeyra, A., Grenier, I. A., Bournaud, F., Dubois, Y., Kamal Youssef, F. R., and Hennebelle, P. (2022). Cosmic-ray diffusion and the multi-phase interstellar medium in a dwarf galaxy. I. Large-scale properties and γ-ray luminosities. *arXiv e-prints*, page arXiv:2205.08163.

Ogrodnik, M. A., Hanasz, M., and Wóltański, D. (2021). Implementation of Cosmic Ray Energy Spectrum (CRESP) Algorithm in PIERNIK MHD Code. I. Spectrally Resolved Propagation of Cosmic Ray Electrons on Eulerian Grids. ApJS, 253(1):18.

Olson, G. L., Auer, L. H., and Hall, M. L. (2000). Diffusion, P_1, and other approximate forms of radiation transport. J. Quant. Spec. Radiat. Transf., 64(6):619–634.

Orszag, S. A. and Tang, C. M. (1979). Small-scale structure of two-dimensional magnetohydrodynamic turbulence. *Journal of Fluid Mechanics*, 90:129–143.

Owocki, S. P. and Rybicki, G. B. (1986). Instabilities in Line-driven Stellar Winds. III. Wave Propagation in the Case of Pure Line Absorption. ApJ, 309:127.

Padovani, M., Galli, D., and Glassgold, A. E. (2009). Cosmic-ray ionization of molecular clouds. A&A, 501(2):619–631.

Padovani, M., Ivlev, A. V., Galli, D., Offner, S. S. R., Indriolo, N., Rodgers-Lee, D., Marcowith, A., Girichidis, P., Bykov, A. M., and Kruijssen, J. M. D. (2020). Impact of Low-Energy Cosmic Rays on Star Formation. Space Sci. Rev., 216(2):29.

Pakmor, R., Bauer, A., and Springel, V. (2011). Magnetohydrodynamics on an unstructured moving grid. MNRAS, 418(2):1392–1401.

Pakmor, R., Pfrommer, C., Simpson, C. M., Kannan, R., and Springel, V. (2016a). Semi-implicit anisotropic cosmic ray transport on an unstructured moving mesh. MNRAS, 462(3):2603–2616.

Pakmor, R., Pfrommer, C., Simpson, C. M., and Springel, V. (2016b). Galactic Winds Driven by Isotropic and Anisotropic Cosmic-Ray Diffusion in Disk Galaxies. ApJ, 824(2):L30.

Pakmor, R. and Springel, V. (2013). Simulations of magnetic fields in isolated disc galaxies. MNRAS, 432(1):176–193.

Pakmor, R., Springel, V., Bauer, A., Mocz, P., Munoz, D. J., Ohlmann, S. T., Schaal, K., and Zhu, C. (2016c). Improving the convergence properties of the moving-mesh code AREPO. MNRAS, 455(1):1134–1143.

Parés, C. (2006). Numerical methods for nonconservative hyperbolic systems: A theoretical framework. *SIAM J. Numerical Analysis*, 44:300–321.

Parés, C. and Muñoz-Ruiz, M. L. (2009). On some difficulties of the numerical approximation of nonconservative hyperbolic systems. *Bol. Soc. Esp. Mat. Apl. SeMA*, 47:19–48.

Pareschi, L. and Russo, G. (2005). Implicit–explicit runge–kutta schemes and applications to hyperbolic systems with relaxation. *Journal of Scientific Computing*, 25:129–155.

Parker, E. N. (1958). Dynamics of the Interplanetary Gas and Magnetic Fields. ApJ, 128:664.

Parker, E. N. (1966). The Dynamical State of the Interstellar Gas and Field. ApJ, 145:811.

Peschken, N., Hanasz, M., Naab, T., Wóltański, D., and Gawryszczak, A. (2021). The angular momentum structure of CR-driven galactic outflows triggered by stream accretion. MNRAS, 508(3):4269–4281.

Peterson, J. R. and Fabian, A. C. (2006). X-ray spectroscopy of cooling clusters. Phys. Rep., 427:1–39.

Pfrommer, C. (2013). Toward a Comprehensive Model for Feedback by Active Galactic Nuclei: New Insights from M87 Observations by LOFAR, Fermi, and H.E.S.S. ApJ, 779:10.

Pfrommer, C., Enßlin, T. A., Springel, V., Jubelgas, M., and Dolag, K. (2007). Simulating cosmic rays in clusters of galaxies - I. Effects on the Sunyaev-Zel'dovich effect and the X-ray emission. MNRAS, 378(2):385–408.

Pfrommer, C., Pakmor, R., Schaal, K., Simpson, C. M., and Springel, V. (2017a). Simulating cosmic ray physics on a moving mesh. MNRAS, 465(4):4500–4529.

Pfrommer, C., Pakmor, R., Simpson, C. M., and Springel, V. (2017b). Simulating Gamma-Ray Emission in Star-forming Galaxies. ApJ, 847:L13.

Pfrommer, C., Pakmor, R., Simpson, C. M., and Springel, V. (2017c). Simulating Gamma-Ray Emission in Star-forming Galaxies. ApJ, 847(2):L13.

Pfrommer, C., Springel, V., Enßlin, T. A., and Jubelgas, M. (2006). Detecting shock waves in cosmological smoothed particle hydrodynamics simulations. MNRAS, 367(1):113–131.

Pfrommer, C., Werhahn, M., Pakmor, R., Girichidis, P., and Simpson, C. M. (2021). Simulating radio synchrotron emission in star-forming galaxies: small-scale magnetic dynamo and the origin of the far infrared-radio correlation. *arXiv e-prints*, page arXiv:2105.12132.

Phan, V. H. M., Morlino, G., and Gabici, S. (2018). What causes the ionization rates observed in molecular clouds? The role of cosmic ray protons and electrons. *ArXiv e-prints*.

Pinzke, A., Oh, S. P., and Pfrommer, C. (2017). Turbulence and particle acceleration in giant radio haloes: the origin of seed electrons. MNRAS, 465:4800–4816.

Ploeckinger, S. and Schaye, J. (2020). Radiative cooling rates, ion fractions, molecule abundances, and line emissivities including self-shielding and both local and metagalactic radiation fields. MNRAS, 497(4):4857–4883.

Plotnikov, I., Ostriker, E. C., and Bai, X.-N. (2021). Influence of Ion-Neutral Damping on the Cosmic-Ray Streaming Instability: Magnetohydrodynamic Particle-in-cell Simulations. ApJ, 914(1):3.

Pohl, M., Hoshino, M., and Niemiec, J. (2020). Pic simulation methods for cosmic radiation and plasma instabilities. *Progress in Particle and Nuclear Physics*, 111:103751.

Powell, K. G., Roe, P. L., Linde, T. J., Gombosi, T. I., and Zeeuw], D. L. D. (1999). A solution-adaptive upwind scheme for ideal magnetohydrodynamics. *Journal of Computational Physics*, 154(2):284 – 309.

Ptuskin, V. S., Voelk, H. J., Zirakashvili, V. N., and Breitschwerdt, D. (1997). Transport of relativistic nucleons in a galactic wind driven by cosmic rays. A&A, 321:434–443.

Quataert, E., Jiang, F., and Thompson, T. A. (2022a). The physics of galactic winds driven by cosmic rays - II. Isothermal streaming solutions. MNRAS, 510(1):920–945.

Quataert, E., Thompson, T. A., and Jiang, Y.-F. (2022b). The physics of galactic winds driven by cosmic rays I: Diffusion. MNRAS, 510(1):1184–1203.

Quataert, E., Thompson, T. A., and Jiang, Y.-F. (2022c). The physics of galactic winds driven by cosmic rays I: Diffusion. MNRAS, 510(1):1184–1203.

Rathjen, T.-E., Naab, T., Girichidis, P., Walch, S., Wünsch, R., Dinnbier, F., Seifried, D., Klessen, R. S., and Glover, S. C. O. (2021). SILCC VI - Multiphase ISM structure, stellar clustering, and outflows with supernovae, stellar winds, ionizing radiation, and cosmic rays. MNRAS, 504(1):1039–1061.

Recchia, S., Blasi, P., and Morlino, G. (2016). Cosmic ray driven Galactic winds. MNRAS, 462:4227–4239.

Recchia, S., Blasi, P., and Morlino, G. (2017). Cosmic ray-driven winds in the Galactic environment and the cosmic ray spectrum. MNRAS, 470(1):865–881.

Rodrigues, L. F. S., Sarson, G. R., Shukurov, A., Bushby, P. J., and Fletcher, A. (2016). The Parker Instability in Disk Galaxies. ApJ, 816:2.

Rodrigues, L. F. S., Snodin, A. P., Sarson, G. R., and Shukurov, A. (2018). Fickian and non-Fickian diffusion of cosmic rays. *ArXiv e-prints*, page arXiv:1809.07194.

Rodrigues, L. F. S., Snodin, A. P., Sarson, G. R., and Shukurov, A. (2019). Fickian and non-Fickian diffusion of cosmic rays. MNRAS, 487(1):975–980.

Roe, P. L. (1981). Approximate riemann solvers, parameter vectors, and difference schemes. *Journal of computational physics*, 43(2):357–372.

Rosdahl, J., Blaizot, J., Aubert, D., Stranex, T., and Teyssier, R. (2013). RAMSES-RT: radiation hydrodynamics in the cosmological context. MNRAS, 436(3):2188–2231.

Rosner, R. and Bodo, G. (1996). The Origin of Filaments in the Interstellar Medium. ApJ, 470:L49.

Ruszkowski, M., Yang, H. Y. K., and Zweibel, E. (2017). Global Simulations of Galactic Winds Including Cosmic-ray Streaming. ApJ, 834(2):208.

Salem, M. and Bryan, G. L. (2014). Cosmic ray driven outflows in global galaxy disc models. MNRAS, 437(4):3312–3330.

Salem, M., Bryan, G. L., and Corlies, L. (2016). Role of cosmic rays in the circumgalactic medium. MNRAS, 456(1):582–601.

Salem, M., Bryan, G. L., and Hummels, C. (2014). Cosmological Simulations of Galaxy Formation with Cosmic Rays. ApJ, 797(2):L18.

Sampson, M. L., Beattie, J. R., Krumholz, M. R., Crocker, R. M., Federrath, C., and Seta, A. (2022). Turbulent diffusion of streaming cosmic rays in compressible, partially ionised plasma. *arXiv e-prints*, page arXiv:2205.08174.

Samui, S., Subramanian, K., and Srianand, R. (2018). Efficient cold outflows driven by cosmic rays in high-redshift galaxies and their global effects on the IGM. MNRAS, 476:1680–1695.

Schlickeiser, R. (1989). Cosmic-ray transport and acceleration. I - Derivation of the kinetic equation and application to cosmic rays in static cold media. II - Cosmic rays in moving cold media with application to diffusive shock wave acceleration. ApJ, 336:243–293.

Schlickeiser, R. (2002). *Cosmic Ray Astrophysics*. Springer-Verlag Berlin Heidelberg.

Schmidt, P., Krause, M., Heesen, V., Basu, A., Beck, R., Wiegert, T., Irwin, J. A., Heald, G., Rand, R. J., Li, J.-T., and Murphy, E. J. (2019). CHANG-ES. XVI. An in-depth view of the cosmic-ray transport in the edge-on spiral galaxies NGC 891 and NGC 4565. A&A, 632:A12.

Schneider, E. E. and Robertson, B. E. (2018). Introducing CGOLS: The Cholla Galactic Outflow Simulation Suite. ApJ, 860(2):135.

Schneider, F. (2016). Kershaw closures for linear transport equations in slab geometry I: Model derivation. *Journal of Computational Physics*, 322:905–919.

Schornbaum, F. and Rüde, U. (2018). Extreme-scale block-structured adaptive mesh refinement. *SIAM Journal on Scientific Computing*, 40(3):C358–C387.

Sekora, M. and Colella, P. (2009). Extremum-Preserving Limiters for MUSCL and PPM. *arXiv e-prints*, page arXiv:0903.4200.

Semenov, V. A., Kravtsov, A. V., and Caprioli, D. (2021). Cosmic-Ray Diffusion Suppression in Star-forming Regions Inhibits Clump Formation in Gas-rich Galaxies. ApJ, 910(2):126.

Semplice, M., Coco, A., and Russo, G. (2016). Adaptive mesh refinement for hyperbolic systems based on third-order compact weno reconstruction. *Journal of Scientific Computing*, 66(2):692–724.

Shalaby, M., Lemmerz, R., Thomas, T., and Pfrommer, C. (2022). The mechanism of efficient electron acceleration at parallel non-relativistic shocks. *arXiv e-prints*, page arXiv:2202.05288.

Shalaby, M., Thomas, T., and Pfrommer, C. (2021). A New Cosmic-Ray-driven Instability. ApJ, 908(2):206.

Shalchi, A. (2005). Second-order quasilinear theory of cosmic ray transport. *Physics of Plasmas*, 12(5):052905–052905.

Shalchi, A. (2009a). *Nonlinear Cosmic Ray Diffusion Theories*. Springer-Verlag Berlin Heidelberg.

Shalchi, A., editor (2009b). *Nonlinear Cosmic Ray Diffusion Theories*, volume 362 of *Astrophysics and Space Science Library*.

Shalchi, A. and Schlickeiser, R. (2005). Evidence for the Nonlinear Transport of Galactic Cosmic Rays. ApJ, 626:L97–L99.

Sharma, P., Colella, P., and Martin, D. F. (2009). Numerical Implementation of Streaming Down the Gradient: Application to Fluid Modeling of Cosmic Rays and Saturated Conduction. *arXiv e-prints*, page arXiv:0909.5426.

Sharma, P., Colella, P., and Martin, D. F. (2010). Numerical implementation of streaming down the gradient: Application to fluid modeling of cosmic rays and saturated conduction. *SIAM Journal on Scientific Computing*, 32(6):3564–3583.

Sharma, P. and Hammett, G. W. (2007). Preserving monotonicity in anisotropic diffusion. *Journal of Computational Physics*, 227(1):123–142.

Sharma, P. and Hammett, G. W. (2011). A fast semi-implicit method for anisotropic diffusion. *Journal of Computational Physics*, 230(12):4899–4909.

Shore, S. N. and LaRosa, T. N. (1999). The Galactic Center Isolated Nonthermal Filaments as Analogs of Cometary Plasma Tails. ApJ, 521(2):587–590.

Simpson, C. M., Pakmor, R., Marinacci, F., Pfrommer, C., Springel, V., Glover, S. C. O., Clark, P. C., and Smith, R. J. (2016a). The Role of Cosmic-Ray Pressure in Accelerating Galactic Outflows. ApJ, 827:L29.

Simpson, C. M., Pakmor, R., Marinacci, F., Pfrommer, C., Springel, V., Glover, S. C. O., Clark, P. C., and Smith, R. J. (2016b). The Role of Cosmic-Ray Pressure in Accelerating Galactic Outflows. ApJ, 827(2):L29.

Simpson, C. M., Pakmor, R., Pfrommer, C., Glover, S. C. O., and Smith, R. (2022). How Cosmic Rays Mediate the Evolution of the Interstellar Medium. *arXiv e-prints*, page arXiv:2204.02410.

Skilling, J. (1971). Cosmic Rays in the Galaxy: Convection or Diffusion? ApJ, 170:265.

Skilling, J. (1975). Cosmic ray streaming. I - Effect of Alfven waves on particles. MNRAS, 172:557–566.

Skinner, M. A. and Ostriker, E. C. (2013). A Two-moment Radiation Hydrodynamics Module in Athena Using a Time-explicit Godunov Method. ApJS, 206(2):21.

Snodin, A. P., Brandenburg, A., Mee, A. J., and Shukurov, A. (2006). Simulating field-aligned diffusion of a cosmic ray gas. MNRAS, 373:643–652.

Soler, R., Terradas, J., Oliver, R., and Ballester, J. L. (2016). The role of Alfvén wave heating in solar prominences. A&A, 592.

Sparre, M., Pfrommer, C., and Ehlert, K. (2020). Interaction of a cold cloud with a hot wind: the regimes of cloud growth and destruction and the impact of magnetic fields. MNRAS, 499(3):4261–4281.

Spitkovsky, A. (2008). Particle Acceleration in Relativistic Collisionless Shocks: Fermi Process at Last? ApJ, 682:L5.

Springel, V. (2005). The cosmological simulation code GADGET-2. MNRAS, 364(4):1105–1134.

Springel, V. (2010). E pur si muove: Galilean-invariant cosmological hydrodynamical simulations on a moving mesh. MNRAS, 401(2):791–851.

Springel, V. and Hernquist, L. (2003). Cosmological smoothed particle hydrodynamics simulations: a hybrid multiphase model for star formation. MNRAS, 339(2):289–311.

Squire, J., Hopkins, P. F., Quataert, E., and Kempski, P. (2021). The impact of astrophysical dust grains on the confinement of cosmic rays. MNRAS, 502(2):2630–2644.

Stone, J. M. and Gardiner, T. (2009). A simple unsplit godunov method for multidimensional mhd. *New Astronomy*, 14(2):139–148.

Stone, J. M., Gardiner, T. A., Teuben, P., Hawley, J. F., and Simon, J. B. (2008). Athena: A New Code for Astrophysical MHD. ApJS, 178(1):137–177.

Stone, J. M., Tomida, K., White, C. J., and Felker, K. G. (2020). The Athena++ Adaptive Mesh Refinement Framework: Design and Magnetohydrodynamic Solvers. ApJS, 249(1):4.

Strömgren, B. (1939). The Physical State of Interstellar Hydrogen. ApJ, 89:526.

Strong, A. W., Moskalenko, I. V., and Ptuskin, V. S. (2007). Cosmic-Ray Propagation and Interactions in the Galaxy. *Annual Review of Nuclear and Particle Science*, 57(1):285–327.

Suresh, J., Nelson, D., Genel, S., Rubin, K. H. R., and Hernquist, L. (2019). Zooming in on accretion - II. Cold circumgalactic gas simulated with a super-Lagrangian refinement scheme. MNRAS, 483(3):4040–4059.

Takahashi, H. R. and Ohsuga, K. (2013). A Numerical Treatment of Anisotropic Radiation Fields Coupled with Relativistic Resistive Magnetofluids. ApJ, 772(2):127.

Tautz, R. C. and Lerche, I. (2016). Application of the three-dimensional telegraph equation to cosmic-ray transport. *Research in Astronomy and Astrophysics*, 16:162.

Teufel, A. and Schlickeiser, R. (2002). Analytic calculation of the parallel mean free path of heliospheric cosmic rays. I. Dynamical magnetic slab turbulence and random sweeping slab turbulence. A&A, 393:703–715.

Teyssier, R. (2002). Cosmological hydrodynamics with adaptive mesh refinement. A new high resolution code called RAMSES. A&A, 385:337–364.

Thomas, T. and Pfrommer, C. (2019). Cosmic-ray hydrodynamics: Alfvén-wave regulated transport of cosmic rays. MNRAS, 485(3):2977–3008.

Thomas, T. and Pfrommer, C. (2022). Comparing different closure relations for cosmic ray hydrodynamics. MNRAS, 509(4):4803–4816.

Thomas, T., Pfrommer, C., and Enßlin, T. (2020). Probing Cosmic-Ray Transport with Radio Synchrotron Harps in the Galactic Center. ApJ, 890(2):L18.

Thomas, T., Pfrommer, C., and Pakmor, R. (2021). A finite volume method for two-moment cosmic ray hydrodynamics on a moving mesh. MNRAS, 503(2):2242–2264.

Thompson, K. W. (1990). Time-dependent boundary conditions for hyperbolic systems, ii. *J. Comput. Phys.*, 89(2):439–461.

Toro, E. F. (2009). *Riemann Solvers and Numerical Methods for Fluid Dynamics*. Springer-Verlag Berlin Heidelberg.

Tóth, G. (2000). The $\nabla\cdot$ B=0 Constraint in Shock-Capturing Magnetohydrodynamics Codes. *Journal of Computational Physics*, 161(2):605–652.

Tóth, G. and Roe, P. L. (2002). Divergence- and Curl-Preserving Prolongation and Restriction Formulas. *Journal of Computational Physics*, 180(2):736–750.

Tumlinson, J., Peeples, M. S., and Werk, J. K. (2017). The Circumgalactic Medium. ARA&A, 55(1):389–432.

Uhlig, M., Pfrommer, C., Sharma, M., Nath, B. B., Enßlin, T. A., and Springel, V. (2012). Galactic winds driven by cosmic ray streaming. MNRAS, 423(3):2374–2396.

van de Voort, F., Springel, V., Mandelker, N., van den Bosch, F. C., and Pakmor, R. (2019). Cosmological simulations of the circumgalactic medium with 1 kpc resolution: enhanced H I column densities. MNRAS, 482(1):L85–L89.

Van Leer, B. (1977). Towards the ultimate conservative difference scheme. iv. a new approach to numerical convection. *Journal of Computational Physics*, 23(3):276–299.

van Leer, B. (1979). Towards the Ultimate Conservative Difference Scheme. V. A Second-Order Sequel to Godunov's Method. *Journal of Computational Physics*, 32(1):101–136.

van Leer, B. and Nomura, S. (2005). Discontinuous galerkin for diffusion. In *17th AIAA Computational Fluid Dynamics*, pages 2005–5108. American Institute of Aeronautics and Astronautics, Inc.

Vernotte, P. (1958). Les paradoxes de la theorie continue de l'equation de la chaleur. *Compt. Rendu*, 246:3154–3155.

Völk, H. J., Drury, L. O., and McKenzie, J. F. (1984). Hydrodynamic estimates of cosmic ray acceleration efficiencies in shock waves. A&A, 130:19–28.

Völk, H. J. and McKenzie, J. F. (1981). Characteristics of cosmic ray shocks in the presence of wave dissipation. *International Cosmic Ray Conference*, 9:246–249.

Vukcevic, M. (2013). The scattering mean free path of cosmic ray particles in isotropic damped plasma wave turbulence. A&A, 555:A111.

Waagan, K. (2009). A positive MUSCL-Hancock scheme for ideal magnetohydrodynamics. *Journal of Computational Physics*, 228(23):8609–8626.

Wagner, A. Y., Falle, S. A. E. G., Hartquist, T. W., and Pittard, J. M. (2006). Two-fluid models of cosmic ray modified radiative shocks. A&A, 452(3):763–771.

Walch, S., Girichidis, P., Naab, T., Gatto, A., Glover, S. C. O., Wünsch, R., Klessen, R. S., Clark, P. C., Peters, T., Derigs, D., and Baczynski, C. (2015). The SILCC (SImulating the LifeCycle of molecular Clouds) project - I. Chemical evolution of the supernova-driven ISM. MNRAS, 454(1):238–268.

Webb, G. M. (1985). Relativistic Transport Theory for Cosmic Rays. ApJ, 296:319.

Webb, G. M. (1987). Hydrodynamical Constraints on Cosmic-Ray Acceleration in Relativistic Shocks. ApJ, 319:215.

Werhahn, M., Pfrommer, C., and Girichidis, P. (2021a). Cosmic rays and non-thermal emission in simulated galaxies - III. Probing cosmic-ray calorimetry with radio spectra and the FIR-radio correlation. MNRAS, 508(3):4072–4095.

Werhahn, M., Pfrommer, C., Girichidis, P., Puchwein, E., and Pakmor, R. (2021b). Cosmic rays and non-thermal emission in simulated galaxies. I. Electron and proton spectra compared to Voyager-1 data. MNRAS.

Werhahn, M., Pfrommer, C., Girichidis, P., and Winner, G. (2021c). Cosmic rays and non-thermal emission in simulated galaxies - II. γ-ray maps, spectra, and the far-infrared-γ-ray relation. MNRAS, 505(3):3295–3313.

Whitham, G. B. (1961). Group velocity and energy propagation for three dimensional waves. *Communications on Pure and Applied Mathematics*, 14(3):675–691.

Wibking, B. D. and Krumholz, M. R. (2022). QUOKKA: a code for two-moment AMR radiation hydrodynamics on GPUs. MNRAS, 512(1):1430–1449.

Wiener, J., Oh, S. P., and Guo, F. (2013). Cosmic ray streaming in clusters of galaxies. MNRAS, 434:2209–2228.

Wiener, J., Oh, S. P., and Zweibel, E. G. (2017a). Interaction of cosmic rays with cold clouds in galactic haloes. MNRAS, 467(1):646–660.

Wiener, J., Pfrommer, C., and Oh, S. P. (2017b). Cosmic ray-driven galactic winds: streaming or diffusion? MNRAS, 467:906–921.

Wiener, J., Zweibel, E. G., and Ruszkowski, M. (2019). Cosmic ray acceleration of cool clouds in the circumgalactic medium. MNRAS, 489(1):205–223.

Xu, R., Spitkovsky, A., and Caprioli, D. (2019). Electron acceleration in non-relativistic quasi-perpendicular collisionless shocks. *arXiv e-prints*, page arXiv:1908.07890.

Yan, H. and Lazarian, A. (2002). Scattering of Cosmic Rays by Magnetohydrodynamic Interstellar Turbulence. Phys. Rev. Lett., 89(28):281102.

Yan, H. and Lazarian, A. (2004). Cosmic-Ray Scattering and Streaming in Compressible Magnetohydrodynamic Turbulence. ApJ, 614:757–769.

Yan, H. and Lazarian, A. (2011). Cosmic Ray Transport Through Gyroresonance Instability in Compressible Turbulence. ApJ, 731:35.

Yang, H. Y. K., Gaspari, M., and Marlow, C. (2019). The Impact of Radio AGN Bubble Composition on the Dynamics and Thermal Balance of the Intracluster Medium. ApJ, 871(1):6.

Yang, H. Y. K., Ruszkowski, M., Ricker, P. M., Zweibel, E., and Lee, D. (2012). The Fermi Bubbles: Supersonic Active Galactic Nucleus Jets with Anisotropic Cosmic-Ray Diffusion. ApJ, 761(2):185.

Yee, H. C., Sandham, N. D., and Djomehri, M. J. (1999). Low-Dissipative High-Order Shock-Capturing Methods Using Characteristic-Based Filters. *Journal of Computational Physics*, 150(1):199–238.

Yusef-Zadeh, F. (2003). The Origin of the Galactic Center Nonthermal Radio Filaments: Young Stellar Clusters. ApJ, 598(1):325–333.

Yusef-Zadeh, F., Hewitt, J. W., and Cotton, W. (2004). A 20 Centimeter Survey of the Galactic Center Region. I. Detection of Numerous Linear Filaments. ApJS, 155(2):421–550.

Yusef-Zadeh, F., Morris, M., and Chance, D. (1984). Large, highly organized radio structures near the galactic centre. Nature, 310(5978):557–561.

Yusef-Zadeh, F. and Wardle, M. (2019). Cosmic-ray-driven outflow from the Galactic Centre and the origin of magnetized radio filaments. MNRAS, 490(1):L1–L5.

Zank, G. P. (2014). *Transport Processes in Space Physics and Astrophysics*, volume 877 of *Lecture Notes in Physics, Berlin Springer Verlag*. Berlin Springer Verlag.

Zank, G. P., Lu, J. Y., Rice, W. K. M., and Webb, G. M. (2000). Transport of energetic charged particles in a radial magnetic field. Part 1. Large-angle scattering. *Journal of Plasma Physics*, 64:507–541.

Ziegler, U. (2011). NIRVANA: A Numerical Tool for Astrophysical Gas Dynamics. Astrophysics Source Code Library, record ascl:1101.006.

Zirakashvili, V. N., Breitschwerdt, D., Ptuskin, V. S., and Voelk, H. J. (1996). Magnetohydrodynamic wind driven by cosmic rays in a rotating galaxy. A&A, 311:113–126.

Zweibel, E. G. (2013). The microphysics and macrophysics of cosmic rays. *Physics of Plasmas*, 20(5):055501.

Zweibel, E. G. (2017). The basis for cosmic ray feedback: Written on the wind. *Physics of Plasmas*, 24(5):055402.